


Nenad Mitrovic
Goran Mladenovic
Aleksandra Mitrovic *Editors*

New Trends in Engineering Research

Proceedings of the International
Conference of Experimental and
Numerical Investigations and New
Technologies, CNNTech 2023

Series Editor

Janusz Kacprzyk , *Systems Research Institute, Polish Academy of Sciences
Warsaw, Poland*

Advisory Editors

Fernando Gomide, *Department of Computer Engineering and Automation—DCA,
School of Electrical and Computer Engineering—FEEC, University of
Campinas—UNICAMP, São Paulo, Brazil*

Okay Kaynak, *Department of Electrical and Electronic Engineering
Bogazici University, Istanbul, Türkiye*

Derong Liu, *Department of Electrical and Computer Engineering, University of
Illinois at Chicago, Chicago, USA*

Institute of Automation, Chinese Academy of Sciences, Beijing, China

Witold Pedrycz, *Department of Electrical and Computer Engineering, University of
Alberta, Alberta, Canada*

Systems Research Institute, Polish Academy of Sciences, Warsaw, Poland

Marios M. Polycarpou, *Department of Electrical and Computer Engineering
KIOS Research Center for Intelligent Systems and Networks, University of Cyprus
Nicosia, Cyprus*

Imre J. Rudas, *Óbuda University, Budapest, Hungary*

Jun Wang, *Department of Computer Science, City University of Hong Kong
Kowloon, Hong Kong*

The series “Lecture Notes in Networks and Systems” publishes the latest developments in Networks and Systems—quickly, informally and with high quality. Original research reported in proceedings and post-proceedings represents the core of LNNS.

Volumes published in LNNS embrace all aspects and subfields of, as well as new challenges in, Networks and Systems.

The series contains proceedings and edited volumes in systems and networks, spanning the areas of Cyber-Physical Systems, Autonomous Systems, Sensor Networks, Control Systems, Energy Systems, Automotive Systems, Biological Systems, Vehicular Networking and Connected Vehicles, Aerospace Systems, Automation, Manufacturing, Smart Grids, Nonlinear Systems, Power Systems, Robotics, Social Systems, Economic Systems and other. Of particular value to both the contributors and the readership are the short publication timeframe and the world-wide distribution and exposure which enable both a wide and rapid dissemination of research output.

The series covers the theory, applications, and perspectives on the state of the art and future developments relevant to systems and networks, decision making, control, complex processes and related areas, as embedded in the fields of interdisciplinary and applied sciences, engineering, computer science, physics, economics, social, and life sciences, as well as the paradigms and methodologies behind them.

Indexed by SCOPUS, INSPEC, WTI Frankfurt eG, zbMATH, SCImago.

All books published in the series are submitted for consideration in Web of Science.

For proposals from Asia please contact Aninda Bose (aninda.bose@springer.com).

Nenad Mitrovic · Goran Mladenovic ·
Aleksandra Mitrovic
Editors

New Trends in Engineering Research

Proceedings of the International Conference of
Experimental and Numerical Investigations and
New Technologies, CNNTech 2023

Editors

Nenad Mitrovic
Faculty of Mechanical Engineering
University of Belgrade
Belgrade, Serbia

Goran Mladenovic
Faculty of Mechanical Engineering
University of Belgrade
Belgrade, Serbia

Aleksandra Mitrovic
Faculty of Information Technology
and Engineering
University Union—Nikola Tesla
Belgrade, Serbia

ISSN 2367-3370

ISSN 2367-3389 (electronic)

Lecture Notes in Networks and Systems

ISBN 978-3-031-46431-7

ISBN 978-3-031-46432-4 (eBook)

<https://doi.org/10.1007/978-3-031-46432-4>

© The Editor(s) (if applicable) and The Author(s), under exclusive license to Springer Nature Switzerland AG 2024

This work is subject to copyright. All rights are solely and exclusively licensed by the Publisher, whether the whole or part of the material is concerned, specifically the rights of translation, reprinting, reuse of illustrations, recitation, broadcasting, reproduction on microfilms or in any other physical way, and transmission or information storage and retrieval, electronic adaptation, computer software, or by similar or dissimilar methodology now known or hereafter developed.

The use of general descriptive names, registered names, trademarks, service marks, etc. in this publication does not imply, even in the absence of a specific statement, that such names are exempt from the relevant protective laws and regulations and therefore free for general use.

The publisher, the authors, and the editors are safe to assume that the advice and information in this book are believed to be true and accurate at the date of publication. Neither the publisher nor the authors or the editors give a warranty, expressed or implied, with respect to the material contained herein or for any errors or omissions that may have been made. The publisher remains neutral with regard to jurisdictional claims in published maps and institutional affiliations.

This Springer imprint is published by the registered company Springer Nature Switzerland AG
The registered company address is: Gewerbestrasse 11, 6330 Cham, Switzerland

Paper in this product is recyclable.

Preface

The book is a collection of high-quality peer-reviewed research papers presented at the International Conference of Experimental and Numerical Investigations and New Technologies (CNN Tech 2023) held at Zlatibor, Serbia, from 4 to 7 July 2023. The conference is organized by the Innovation Center of the Faculty of Mechanical Engineering, the Faculty of Mechanical Engineering at the University of Belgrade, and the Center for Business Trainings. A high number of delegates were attending the CNN Tech 2023—academicians, practitioners, and scientists—presenting and authoring more than 100 papers. The Conference Program included 13 Invited Lectures, 4 sessions (oral and poster), and 4 workshops—including the traditional Regional Innovation Forum 2023 and B2B meetings. Twenty-seven selected full papers went through the double-blind reviewing process.

The main goal of the conference is to make a positive atmosphere for the discussion on a wide variety of industrial, engineering, and scientific applications of engineering techniques. Participation of a number of domestic and international authors, as well as the diversity of topics, have justified our efforts to organize this conference and contribute to the exchange of knowledge, research results, and experience of industry experts, research institutions, and faculties which all share a common interest in the field in experimental and numerical investigations.

The CNN Tech 2023 was focused on the following topics:

- Mechanical Engineering,
- Engineering Materials,
- Chemical and Process Engineering,
- Experimental Techniques,
- Numerical Methods,
- New Technologies,
- Clear sky,
- Dental Materials and Structures,
- Advanced Materials and Technology,
- Artificial intelligence,
- Student session and
- Successful Project Stories.

We express our gratitude to all people involved in conference planning, preparation and realization, especially to:

- All authors, specially invited speakers, who have contributed to the high scientific and professional level of the conference,
- All members of the Organizing Committee,

- All members of the International Scientific Committee for reviewing the papers and Chairing the Conference Sessions,
- Ministry of Education of the Republic of Serbia for supporting the Conference,
- Ministry of Science, Technological Development and Innovation of the Republic of Serbia for supporting the Conference.

Belgrade, Serbia

Nenad Mitrovic
Goran Mladenovic
Aleksandra Mitrovic

Scientific Committee

Nenad Mitrović (chairman)	University of Belgrade, Faculty of Mechanical Engineering, Serbia
Miloš Milošević (co-chairman)	University of Belgrade, Faculty of Mechanical Engineering, Serbia
Aleksandar Sedmak	University of Belgrade, Faculty of Mechanical Engineering, Serbia
Hloch Sergej	Technical University of Košice, Faculty of Manufacturing Technologies, Slovakia
Dražan Kozak	University of Osijek, Faculty of Mechanical Engineering in Slavonski Brod, Croatia
Nenad Gubeljak	University of Maribor, Faculty of Mechanical Engineering, Slovenia
Monka Peter	Technical University of Kosice, Faculty of Manufacturing Technologies, Slovakia
Snežana Kirin	University of Belgrade Innovation Center of Faculty of Mechanical Engineering, Serbia
Ivan Samardžić	University of Osijek, Faculty of Mechanical Engineering in Slavonski Brod, Croatia
Martina Balać	University of Belgrade, Faculty of Mechanical Engineering, Serbia
Ludmila Mládková	University of Economics Prague, Czech Republic
Johanyák Zsolt Csaba	Athéné University, Faculty of Engineering and Computer Science, Hungary
Igor Svetel	University of Belgrade, Innovation centre of Faculty of Mechanical Engineering, Serbia
Aleksandra Mitrović	University Union “Nikola Tesla”, Faculty of Information Technology and Engineering, The Academy of Applied Technical Studies Belgrade, Serbia
Valentin Birdeanu	National R&D Institute for Welding and Material Testing—ISIM Timișoara, Romania
Danilo Nikolić	University of Montenegro, Faculty of Mechanical Engineering, Montenegro
Goran Mladenović	University of Belgrade, Faculty of Mechanical Engineering, Serbia
Darko Bajić	University of Montenegro, Faculty of Mechanical Engineering, Montenegro
Tasko Maneski	University of Belgrade, Faculty of Mechanical Engineering, Serbia

Luis Reis	IDMEC Instituto Superior Técnico, University of Lisbon, Portugal
Žarko Mišković	University of Belgrade, Faculty of Mechanical Engineering, Serbia
Tozan Hakan	Istanbul medipol University, School of Engineering and Natural Sciences, Turkey
Traussnigg Udo	Institute for Electrical Machines and Drives University of Technology, Austria
Gordana Bakić	University of Belgrade, Faculty of Mechanical Engineering, Serbia
Katarina Čolić	University of Belgrade, Faculty of Mechanical Engineering, Serbia
Peter Horňák	Technical University of Košice, Faculty of Materials, Metallurgy and Recycling, Slovakia
Robert Huňady	Technical University of Kosice, Faculty of Mechanical Engineering, Slovakia
Martin Hagara	Technical University of Kosice, Faculty of Mechanical Engineering, Slovakia
Jovan Tanasković	University of Belgrade, Faculty of Mechanical Engineering, Serbia
Marija Đurković	University of Belgrade, Faculty of Forestry, Serbia
Tsanka Dikova	Medical University of Varna, Faculty of Dental Medicine, Varna, Bulgaria
Ján Danko	Slovak University of Technology in Bratislava, Faculty of Mechanical Engineering, Slovakia
Ognjen Peković	University of Belgrade, Faculty of Mechanical Engineering, Serbia
Jelena Svorcan	University of Belgrade, Faculty of Mechanical Engineering, Serbia
Suzana Filipović	Institute of Technical Sciences of SASA, Serbia
Darko Kosanović	Institute of Technical Sciences of SASA, Serbia
Nebojša Manić	University of Belgrade, Faculty of Mechanical Engineering, Serbia
Zorana Golubović	University of Belgrade, Faculty of Mechanical Engineering, Serbia
Vera Pavlović	University of Belgrade, Faculty of Mechanical Engineering, Serbia
Aleksandra Dragičević	University of Belgrade, Faculty of Mechanical Engineering, Serbia
Dragan Milković	University of Belgrade, Faculty of Mechanical Engineering, Serbia
Bojan Čudić	University of Maribor, Koroska cesta 160, 2000 Maribor, Slovenia

Dragan Milovanović

University of Banja Luka, Faculty of Economics,
Bosnia and Herzegovina

Nataša Obradović

University of Belgrade, Faculty of Technology
and Metallurgy, Serbia

Branislav Sredanović

University of Banja Luka, Faculty of Mechanical
Engineering, Bosnia and Herzegovina

Contents

Key Factors of Business Sustainability: Analysis of Human Resources' Versus Business Performance in Case of Serbian Companies	1
<i>Iva Dragicevic, Marko Mihic, and Sinisa Arsic</i>	
Robot Movement Programming and Simulation Generation for Pick and Place Materials in ABB Robot Studio	29
<i>Djordje Dihovicni, Petar Jakovljević, Nada Ratković Kovačević, and Dragan Kreculj</i>	
Bucket Wheel Excavator Reliability Improvement by Use of Probabilistic Approach and Fault-Tree Analysis	36
<i>Dušan Arsić, Snežana Kirin, Aleksandra Arsić, Ružica Nikolić, and Ljubica Radović</i>	
Risk Management of Foreign Trade Financing of Bosnia and Herzegovina	54
<i>Dragana Vujičić Stefanović, Boško Mekinjić, and Dragan Milovanović</i>	
CAD/CAM Approach to Automation of the Production Process	65
<i>Djordje Dihovicni and Milan Mišćević</i>	
Bookshelf Scanning Mechanism with Arduino Control	82
<i>Nada V. Ratković Kovačević, Goran Ž. Vojnović, Djordje N. Dihovični, and Dragan D. Kreculj</i>	
Development of a Method for Testing Temperature Distribution During 3D Printing of Specimens with Application in Aerospace Industry	90
<i>Zorana Golubović, Milan Travica, Nenad Mitrović, Isaak Trajković, and Miloš Milošević</i>	
Determination of Compression Response for Various Dried Vegetables	96
<i>Miloš Milošević, Ivana Jevtić, Isaak Trajković, Ivan Zlatanović, Goran Mladenović, and Nenad Korolija</i>	
Energy Efficiency in Serbia: Challenges and Opportunities	105
<i>Nenad Mitrovic and Aleksandra Mitrovic</i>	
Comparative Mechanical Analysis of PLA and ABS Materials in Filament and Resin Form	114
<i>Božica Bojović, Zorana Golubović, Ljubiša Petrov, Aleksa Milovanović, Aleksandar Sedmak, Žarko Mišković, and Miloš Milošević</i>	

Corrosion Damages of Pipelines Assessment by Using the Finite Element Method	132
<i>Vujadin Aleksić, Bojana Zečević, Ana Maksimović, Ljubica Milović, and Srđan Bulatović</i>	
Selection of the Most Suitable Renewable Energy Alternative For Štrpce Municipality	148
<i>Bojan Stojčetić and Živče Šarkočević</i>	
Topology Optimisation as Method for Improving the Design Process of Tipping Semi-trailer	156
<i>Aleksandar Zahariev and Viktor Stojmanovski</i>	
Advances in Additive Manufacturing Application in Military Industry	168
<i>Muhammed Bisić and Adi Pandžić</i>	
A Comprehensive Review of the Effect of Elastane and Common Wet Processes on the Cotton and Cotton/Elastane Knitted Fabrics' Properties and Revalorization of Fabric Waste	188
<i>Aleksandra Ivanovska, Mirjana Reljić, and Biljana Mangovska</i>	
Dimensional Accuracy of Compressive Specimens Obtained by SLS Technology	206
<i>Ivana Jevtić, Goran Mladenović, Miloš Milošević, Aleksa Milovanović, Milan Travica, and Isaak Trajković</i>	
Analysis of Flexural Strength Tiles Made by ABS-X Material with Different Infill	214
<i>Isaak Trajkovic, Aleksandra Dragicevic, Uros Ilic, Marko Djurovic, Goran Mladenovic, and Milos Milosevic</i>	
The Possibility of Applying a Universal Testing Machine for Evaluating Food Textures	222
<i>Ivana Jevtić, Isaak Trajković, Ivan Zlatanović, Goran Mladenović, Nenad Korolija, and Miloš Milošević</i>	
Numerical Simulations for the Optimization of the Position of the Regenerative Burner System for Tundish Preheating	230
<i>Mirjana Stamenic, Branislav Gajic, Aleksandar Milivojevic, Vuk Adzic, and Nikola Tanasic</i>	
Design of Augmented Reality-Based Android App for Simulation and Programming of Industrial Robots	239
<i>Jelena Vidakovic, Andrija Devic, Ilija Lazarevic, and Nikola Zivkovic</i>	

Design of a 6DOF Robot Simulation System in ROS-Gazebo with a Brief Reference to Modern Robot Simulation Software	246
<i>Nikola Zivkovic, Andrija Devic, Jelena Vidakovic, Ilija Lazarevic, and Mihailo Lazarević</i>	
Efficient Computation Method for Total Fatigue Life of Aircraft Structural Components	253
<i>Ivana Vasović Maksimović, Mirko Maksimović, Katarina Maksimović, and Stevan Maksimović</i>	
3D Printing and CNC Machining: Materials, Technologies, and Process Parameters	271
<i>Strahinja Djurović, Dragan Lazarević, Milan Mišić, Živče Šarkoćević, and Zoran Golubović</i>	
The Current State of the Open-Source Engineering Software for Numerical Simulations	277
<i>Ivana B. Ivanovic and Srdjan Tadic</i>	
Aircraft Lug Failure Design Under Fatigue Loading	294
<i>Slobodanka Boljanović</i>	
Structural Analysis of Elements of Passenger Boarding Bridge	309
<i>Martina Balac, Aleksandar Grbovic, and Lajos Sarvas</i>	
Horizontal Boring Mill Machine Feedrate Revitalization with DC Converter and PLC	320
<i>Igor Kocic, Goran Mladenovic, Sasa Nikolic, Darko Mitic, Nikola Dankovic, and Petar Djekic</i>	
Author Index	333



Key Factors of Business Sustainability: Analysis of Human Resources' Versus Business Performance in Case of Serbian Companies

Iva Dragicevic¹, Marko Mihic¹ , and Sinisa Arsic²  

¹ Faculty of Organizational Sciences, University of Belgrade, Belgrade, Serbia

² Telekom Serbia, Belgrade, Serbia

sinisaars@telekom.rs

Abstract. This research paper analyzes the key risk factors within a company, in terms of three main pillars of its sustainability for the long-term: business performance, human resources and financial viability. Scope of research involves for-profit, small and medium-sized manufacturing companies doing business in Serbia. This paper explores efforts of strategic decision makers operating in specific circumstances, by unveiling key correlations between key risk indicators on company sustainability pillars. The quantitative part of this research was conducted during the last quarter of 2022, and it involved 380 companies. Current theory localizes shortcomings of observing and analyzing business performance, employee performance and financial viability as separate indicators of sustainability. As in existing literature, long-term planning (and recognition of possible risk influences) very often covers only one pillar of the envisioned sustainability nexus, key contribution of this paper is that it offers integral view over the influence of risk on all three aspects, which was backed up with results of implementing clustering method, and with the help of applying statistical learning tests. The future work on this research includes extension of the analysis to other countries in the West Balkans region, and comparison of all determined correlations and findings.

Keywords: SME · Risk · Human resources · Performance · Financial viability

1 Introduction

Modest, but constant progress represents the modern-day buzz sentence, of nearly all business worldwide. Business owners, as key strategic decision makers, are facing more influences than ever before, on their path of maintain their business (or company) as a sustainable one. Amidst the current massive shift in economic paradigm of the world, small and medium sized companies (SMEs) are under influence of different sources of risks to their long-term business sustainability.

Moreover, in a special case from Europe, reports show that Serbia's economy is rising within last period of 2021 and 2022 (early announcements for this year suggest GDP growth) and recovering after massive disruption caused by COVID-19 pandemic in 2020. Further analysis is needed in expectations of early reports for 2022, having in

mind the outbreak of war on European soil and its influence on many aspects of life and business.

EU remains the largest foreign trading partner with Serbia, most significant investor and number one recipient of immigrants from Serbia (majority of people leaving Serbia are adults aged between 25 and 50) [1]. In a country economic diagnostics report published by the World Bank group [2], three key enabling factors were identified that could support further economic growth of Serbia as a country and its business subjects. First one is financial viability (limited access to finance, complex tax system appear as the most important constraints to SMEs), it is followed by human capital (most Serbian companies face difficulties when trying to hire and retain employees, especially those with a faculty degree) and employee skills (skills gap between EU average and Serbian average is the second most important business environment obstacle), and lastly third factor is employee productivity (i.e. Serbian manufacturing business needs three times as many workers as the average business in the EU, for the same level of output). Starting as of 2023, USAid in Serbia started a new five year program named “Big small businesses” [3], aimed at empowering SME growth, increase in productivity and profitability, in order to maintain long-term sustainability. Sajc and Haldrup [4] defined means for Serbian SMEs to grow along digital and green transformation efforts, in order to avoid risk to their sustainability in the years to come. Key priorities which were identified were development and retention of skilled human resources and improved access to finance. Ehnert [5] defined human resource management in the context of supporting business sustainability as management of human resource performances, in order to overcome paradoxes and tensions of sustainability between economic, business and social (human) components.

Very few existing research studies focused on analyzing integrally from different perspectives, all the possible influences on company long-term sustainability. Key indicators which appear essential at first sight are business performance and financial viability, but their joint influence has not been analyzed. Additionally, rarely can be found quantitative research conducted in European SMEs, analyzing specific indicators of human resources’ performance, and analysis of statistically determined negative influence on company sustainability. These important research topics can present a research gap, which may be further extrapolated in empirical research presented within this article. Previously there were no similar research attempts conducted in the Balkans region, but certainly these problems can be observed equally in a global context. Therefore, the authors of this paper started from the following research questions in order to address deficiencies within the existing worldwide body of literature:

- RQ1. Is it possible to identify key risk influences over three pillars of company sustainability – business performance, human resources performance and financial viability?
- RQ2. What are the key determinants of each defined sustainability pillar?

The authors of this paper analyzed influence on long-term business sustainability, by determining most important indicators of business performance, human resources performance and finally indicators of financial viability.

Identification of key influences on company long-term sustainability may be determined when examining them integrally:

- Which business performance indicators, and to what extent of risk, are influencing the company sustainability?
- Which indicators of human resources performance, and to what extent of risk are influencing company sustainability?
- Which indicators of financial viability, and to what extent of risk, are influencing company sustainability?

Therefore, it is possible to define the main goal of this research:

- To identify key risk indicators on business sustainability of a company measured through influence on business performance, financial viability and performances of human resources;

Based on literature review and defined research gap, as well as results of discussion with experts, the main purpose of this research was to determine key indicators of each pillar of sustainability, and also to estimate and analyze risk of potential influence of these indicators on sustainability as a whole.

Research methodology in this manuscript involves conducting quantitative research on a selected sample of small and medium sized companies operating in Serbia, by testing several research hypotheses. The authors used gathered data to determine clusters of companies based on similarity, and also to analyze correlations within each cluster. Findings and conclusions were discussed in detail in separate part of this manuscript.

The research itself has been defined through following four chapters. Literature review chapter covers in adequate level of detail, the theoretical review topics, covering possible indicators of sustainability in the domain of business performance, human resources and financial viability.

Next, a separate chapter is dedicated to methodology, as it displays framework presentation and formulation of research hypothesis, developed in order to find answers to two main research questions.

Following that chapter is the specific Results chapter, where authors of this paper presented key research results, by determining similar, homogenous groups of companies, and by analyzing correlations between all indicators. Special attention has been given to hypothesis testing (followed with appropriate tests).

Finally, research results are followed by conclusions and detailed discussion, which provides feedback from research results across existing theory. This chapter includes short elaborations on limitations, practical implications and future plans for research of the re-search team.

2 Literature Review

Even though economies of Europe are nowadays facing changes of great magnitude, regarding political, business, economic and social perspective, national economies and businesses were recovering in the past two years from pandemic outbreak, with success. Damjanovic [6] discovered how strategic outlooks influence success of medium sized companies, making it harder to preserve business sustainability in cases of supply chain disruptions. Schulte and Knuts [7] analyzed different risk influences to sustainability of a business, from a long-term perspective, making it easier to comprehend from a strategic viewpoint.

2.1 Influence of Business Performance Indicators on Company Sustainability

H1: Sustainability of small and medium sized companies is directly influenced by business performance indicators.

Mahmudova and Kovacs [8] defined business performance measurement in SMEs through performance measurement system which examines and inspects every factor that influences a company's business performance. The main purpose of the system is to concentrate on studying the organization's functions at high and low levels of activity which can also be applied effectively to assess the performance of SMEs.

Hristov and Chirico [9] identified several business – economic performance indicators which can influence sustainability, out of which the most important ones are return on sustainable investments and revenues invested rate. Mengistu [10] analyzed business parameters contributing to sustainability in case of SMEs, and within the list of 40 most important indicators, profit, revenue (total and per customer) were the key ones, while R&D expenditure and material and labor costs were identified also as important ones.

In a large-scale research on European SMEs, including a sample from four countries, Moursellas [11] discovered multiple sustainability practices and performance indicators attached to sustainability. Results show that turnover growth as well as market share and return on investment. On the other side, Malesios [12] determines turnover and business growth in a study on influences of SME sustainability practices and performances, while Ciemleja and Lace [13] identified profitability and liquidity as key risks of potential SME decline.

Bae and Smirdon [14] identified profitability and sales as key business performance indicators of sustainability and endangering those two indicators can influence whole sustainability of the company. This is in line with research studies by Soto-Acosta [15] and Broccardo [16] who added effectiveness and competitiveness apart from profitability, as key influences of business performance to sustainability of SMEs.

Sundin [17] identified customer satisfaction and customer retention rate as key business indicators for small and medium sized businesses. Israel [18] adds to it by linking customer retention rate to supply chain performance, making it easier to perceive sustainability issues if supply chain disruptions are causing loss of key customers.

2.2 Influence of Human Resources' Performance on Company Sustainability

H2: Sustainability of small and medium sized companies is directly influenced by performances of company human resources.

According to HRM [19] "Human resources play a key role in maintaining the long-term sustainability of a business".

On the other side, looking at previous similar period after a major economic crisis, in a paper by Rezaee [20], employee productivity has been marked as key for business sustainability. Bartel [21] went further in the analysis of human resources management and company performance, by linking employee satisfaction with overall quality of performance evaluation.

In a study by Woeffray and Chen [22], key conclusions were made about addressing most significant risks to sustainability, such as talent acquisition and maintaining employee numbers at constant rate. Additionally, Hernita [23] introduced "manpower

skills” by placing employee key competences in the epicenter of business effectiveness in SMEs.

Lastly, some authors (Vandenberg [24], Appave [25]) identified outflow migrations towards more prosperous countries of Europe, as the key influences to business sustainability of domestic SMEs.

2.3 Influence of Company Financial Viability on Its Sustainability

H3: Sustainability of small and medium sized companies is directly influenced by financial viability of a company.

Different finance and economic indicators are causing variety of influence on small and medium sized businesses, making it harder to maintain business sustainability. Camberato [26] analyzed inflation rate as the most significant indicator, since over 80% of small-business owners have increased their prices to counter inflation. This fact most certainly causes risk to sustainability, because for the SME to preserve its financial viability, business must define higher price points, and some of their customers may not accept the change. In addition to this.

On the other side, Timm [27] investigated on state support to SME sector in case of Asia and South America, while Risteska [28] analyzed Europe and the EU regarding institutional support to SME sustainability. Conclusions in both papers confirm that this kind of support can represent key enabler for business growth of an SME. Devonshire [29] adds to it by detecting supply chain issues for SMEs, outlining lack of raw materials and rising transport costs.

From perspective of risks deriving from banks, Shihadeh [30] analyzed bank interest rates and their influence of rise on future investment levels. Apart from that Bartolacci [31] discovered capital raising in the scope of overall financing as key indicators of financial viability in a company.

3 Methodology

3.1 Framework

This research presents results of a survey conducted during last quarter of 2022, on a sample of small and medium sized companies from Serbia, who are adequate representatives of economy in every country (and is true also in the case of Serbia), and a good testing ground for estimation of different risk influences on overall business sustainability. The authors decided to perform a survey in order to include risk influence variables based on subjective opinions of CEO as the key decision makers (such as business performance, human resource management, and financial viability). Similar has been performed in papers by Burlea-Schiopoiu [32] and Alvarez Jaramillo [33].

All company owners or CEOs who decided to participate in the survey had to reply to a total of 17 closed questions where they could rank risk influence level, with possible values from 1 to 5, for each of the 17 independent variables. Groups of questions were connected to ranking the following variables:

- Rank key financial viability variables?
- Rank key variables connected with performance of company human resources?
- Rank key variables related to business performance?

Replies from survey participants (CEOs, strategic decision makers) were used to estimate risk influence of multiple indicators, on overall sustainability of their business. These estimations were later used to analyze key correlations within each cluster of companies (SMEs). All survey replies were statistically tested for internal validity, there were no missing replies or mistakes in completion of the survey.

Key findings from literature displayed that companies are under higher risk regarding long-term sustainability if business performance indicators are deteriorating (existing literature is heavily interested around the measurable parameters, such as profitability and investments financing, [34]), or if external economic shocks (such as a major conflict on European soil, energy crisis or pandemics outbreak) are causing financial struggle for SMEs [35]. Very few literature references have statistically determined internal influence of company human resource performances, on company sustainability, and this can be perceived as the gap to be analyzed within this research.

The authors introduced a graphical interpretation of research framework, presented with Fig. 1, which helps the reader better understand the research framework, problem identified from identifying a specific literature gap, discussion with experts about potential indicators for quantitative research, connection with key research goal and research question, and lastly correlation and testing between research hypothesis and research variables within the sustainability nexus.

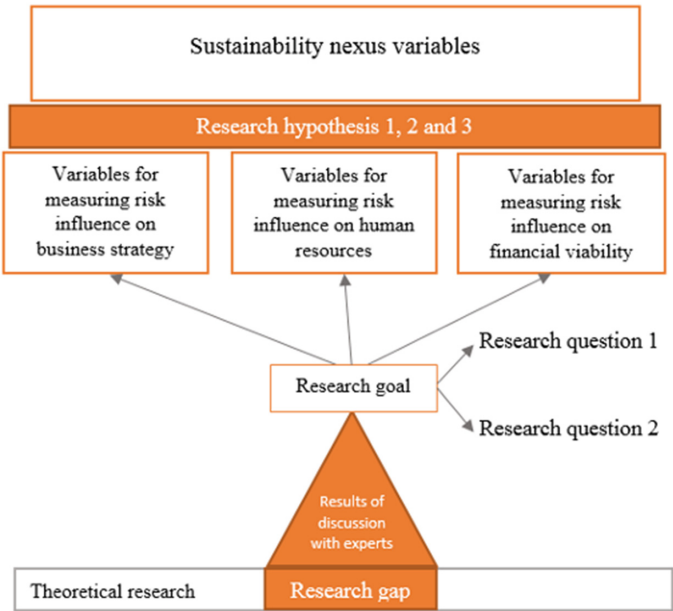


Fig. 1. Research framework

Firstly, from a variety of possible variables established from the literature review (in previous chapter), the authors discussed with 10 experts (with 10+ years of experience) from Serbian Government ministry of economy, National Chamber of Commerce, University professors, banks operating (giving loans) with small and medium sized companies. After the discussion with experts, the list of indicators defined through the literature review was shortlisted (the content of this discussion involving all possible variables analyzed by the experts can be viewed in Appendix B).

The shortlisted research variables are the following:

- financial viability - inflation rate, bank interest rates, capital raising, state support to SME sector, supply chain issues regarding raw materials and energy sources?
- human resource management - productivity issues, employment rate fluctuations, availability of key competences, outflow migrations towards western Europe?
- business performance - decrease in revenue per customer, low or negative profitability, revenue decrease, low retention rate of key customers, low customer satisfaction?

The total sample consisted of contacting again 380 companies from Serbia (who replied to the survey in 2022, out of total 5000 contacted companies), which employed more than 9 employees and up to 249 employees, across different manufacturing or service industries. Description of sampled companies is available in Table 2 as well as in Appendix A.

The research included statistical learning analysis based on clustering homogeneity results, as defined by Hastie [36], with key regressions within each cluster, in order to be able to come to some conclusions on influences of different risks over company sustainability. Methods used are explained in Sect. 3.3.

Taking into consideration measurability and scalability with quantitative methods and techniques, key correlations between business factors were analyzed through methods and techniques of statistical learning, via clustering method as it represents an integral process of discovering statistically significant inference and correlations between similar sampled companies.

3.2 Hypothesis Formulation and Variables Definition

The authors defined three research hypotheses, which could provide answers to which influences are essential for preserving company sustainability, and also what are the most important indicators that influence it. Factors linked with these hypotheses were checked through defined main survey questions and conducted on the sample. The questions present an attempt to measure influence of different indicators, by estimating risk level of influencing company long-term sustainability. Research hypotheses were formulated as following:

- H1: Sustainability of small and medium sized companies is directly influenced by business performance indicators.
- H2: Sustainability of small and medium sized companies is directly influenced by performances of company human resources.
- H3: Sustainability of small and medium sized companies is directly influenced by financial viability of a company.

In order to determine clusters of companies based on similarity (homogeneity), as well as key correlations within the clusters, the authors introduced seventeen independent variables (Table 1), which are then ranked from 1 to 5 (value “1” implies lowest value of rank; value “5” implies highest value rank).

Table 1. Clustering variables

Group of variables	Value of variable	Independent variable	Possible rank value of variable
Financial viability	High inflation rate	Y1	[1, 2, 3, 4, 5]
	High bank interest rates	Y2	[1, 2, 3, 4, 5]
	Low capital raising	Y3	[1, 2, 3, 4, 5]
	Low state support to SME sector	Y4	[1, 2, 3, 4, 5]
	High Cost of raw material	Y5	[1, 2, 3, 4, 5]
	Low availability of raw material	Y6	[1, 2, 3, 4, 5]
	High cost of energy sources	Y7	[1, 2, 3, 4, 5]
	Low availability of energy sources	Y8	[1, 2, 3, 4, 5]
Human resources performance	Low productivity	Y9	[1, 2, 3, 4, 5]
	High fluctuation of work force	Y10	[1, 2, 3, 4, 5]
	Low availability of key competences/expertise	Y11	[1, 2, 3, 4, 5]
	High outflow migrations outside the country	Y12	[1, 2, 3, 4, 5]
Business performance	Decrease in total revenue	Y13	[1, 2, 3, 4, 5]
	Decrease in revenue per customer	Y14	[1, 2, 3, 4, 5]
	Decrease in profitability	Y15	[1, 2, 3, 4, 5]
	Low retention rate of key customers	Y16	[1, 2, 3, 4, 5]
	Low customer satisfaction	Y17	[1, 2, 3, 4, 5]

All research hypotheses were tested using their respective multiple linear regression tests (by analyzing regression coefficients - slopes, adjusted R squared values) and validated for significance (ANOVA, t-test, p-value). All data generated during the survey tests was processed by using Stata16 and it is presented within the Appendix B part of this paper.

3.3 Clustering Method Used for Quantitative Analysis

The research sample data has been processed using the Stata 16 tool. Clustering represents adequate technique in statistical learning, where data points are grouped based on the similarity of some, and on distance of other data points. The basic axiom behind clustering is that it enables grouping of data points, such that those data points present in the same cluster possess a degree of similarity (see Petegrosso in [37]).

The analysis within this paper aims to use clustering as a method of unsupervised learning since there is no external label attached to the object of research. Based on the answers from the sampled business owners, it is not possible to automatically determine what are the key influences on company sustainability, since they estimated risk from 1 to 5 on a number of indicators, which were shortlisted by the experts (before the quantitative research). The Mini Batch K means clustering algorithm learned features and patterns all by itself without any given input–output mapping. The algorithm was then able to extract inferences from the nature of data objects and then create distinct clusters of companies, to be able to distinct them appropriately.

The authors have followed the implementation instructions defined by Xiao [38]. Since the dataset cannot be considered as large (only 380 companies), the Lloyd and Forgys algorithms were left out of the process; therefore, clustering was performed through the McQueen and Hartigan algorithms. In clustering machine learning, the algorithm divides the population into different groups, such that each data point is similar to the data points in the same group and dissimilar from the data points in the other groups. Based on similarity and dissimilarity, the algorithm then assigns an appropriate sub-group to the object. Generally, data should be organized into clusters, should have high level of intra-cluster similarity, but also low level of inter-cluster similarity.

4 Results

4.1 Research Sample

The quantitative research consists of survey questions related to estimations of different risk indicators, on company business sustainability. The survey deals with ranking multiple indicators such as business performance, human resource management, financial viability.

All respondents were given the opportunity to respond to the survey by e-mail, by contacting the authors over online communication tools, or by using the online questionnaire response form. A questionnaire was sent three times to each company during October 2022, to ensure that managers were able to find the time to complete the survey

questionnaire. The validation of the questionnaire was done immediately upon arrival (the e-mail address of the company was checked against the one to which the inquiry was sent), the identity of the owner was validated. All respondents filled in answers to all the questions offered.

The authors contacted 5000 companies in total. Exactly 380 companies replied, and 44 was in the process of closing. Finally, several companies (20 of them) did not have the owner or CEO available at the time of the survey process, due to over-occupation.

On average, sampled companies employ approximately 71 employees in 2022, with a clear increase in employment (compared to the previous year) of an average of 1.5%. Taking the official division of companies by size into consideration (fewer than 249 employees and more than 9 employees – small and medium sized companies), the distribution of the companies surveyed was done according to their overall number of employees, and also by type of business (Table 2):

Table 2. Segmentation of companies surveyed according to their size.

Company size	10–49	50–100	101–200	201–249
No of manufacturing oriented companies (%)	43 (11%)	68 (18%)	38 (10%)	12 (3%)
No of service oriented companies (%)	46 (12%)	76 (20%)	32 (8%)	14 (4%)
No of combined companies (%)	12 (3%)	24 (6%)	11 (3%)	4 (<1%)

The sample does not include companies employing more than 249 employees, and micro companies with less than 10 employees. To be able to include valid sample of companies in terms of size, the precondition was that the company had status of small or medium sized at least for the last 3 years. In the companies surveyed during last quarter of 2022, there were 22,672 employees, while in 2021 and 2020 there were 21,133 and 19,885, respectively. These numbers indicate employment in small and medium-sized companies in Serbia to have increased incrementally, with significant economic growth shown in the national GDP of Serbia during the last period. All surveyed companies are profit oriented and doing business in manufacturing, service or combined industries.

The authors have tried to ensure representativeness of the sample in terms of regional distribution (all 4 regions were represented to be proportionally similar) and industry distribution (there are examples of companies across most of the major industries in Serbia), as it can be viewed in Appendix A. The overall population of companies in Serbia is not defined in literature originating from Serbia, as there is little formalized data on private owned companies (apart from official registry of all businesses from Serbia which includes entrepreneurs, small, medium and large sized companies). All sample data was cross-referenced and tested.

The authors based internal validity of the data gathered from the sample on the authenticity of questions, which was derived from discussion with experts. The questionnaire reflects actual estimations of real-life risk influences on company business

sustainability for the long-term period, to extract maximum information on the topic, from the respondents. Regional representativeness has been ensured (see further statistical breakdown in Appendix A, Table 5), the authors collected data from 380 companies registered in the four main regions of Serbia herein noted:

- Belgrade - 153 companies (11,000 in total, of which 5,000 generate 80% of total revenue for this region)
- Vojvodina - 87 companies (4,000 in total, of which 1,000 generate 80% of total revenue for this region)
- Western Serbia - 81 companies (2,500 in total, out of which 1000 generate 80% of total revenue for this region)
- South and East Serbia – 59 companies (800 in total, of which 300 generate 80% of total revenue for this region).

Now follows a presentation of research findings.

4.2 Research Findings

In order to understand complex influence of different indicators, a total of 5 clusters have been defined, with intra cluster ranges (values) of variables which have highest level of homogeneity. Those correlations have been incorporated into the clustering process. By providing the characteristics of each cluster, key influences on company sustainability can be described, but also it represents a true representation of the mixed influence of different indicators in reality. Cluster descriptions are presented in Table 3.

Table 3. Cluster description of variable ranges

Homogeneity – internal ranges of variables within clusters	Key business performance indicator	Key human resource performance indicator	Key financial viability indicator
C1 - high influence (of all three groups of indicators and very high influence (of human resource performance and financial indicators)	Low retention rate of key customers	Low availability of key competences/expertise	Low availability of energy sources
C2 - medium influence, of all three groups of indicators	Decrease in profitability	Low productivity	High inflation rate
C3 - very low and low influence, of all three groups of indicators	None	High fluctuation of work force	High cost of raw material
C4 - very high influence of business performance indicators	Low customer satisfaction	None	None
C5 - very high influence of human resource performance indicators	None	High outflow migrations outside the country	None

In addition, a brief, simplified graphic display of influence of each indicator has been introduced in Figure, to provide a visualization of the clustering results (Fig. 2).

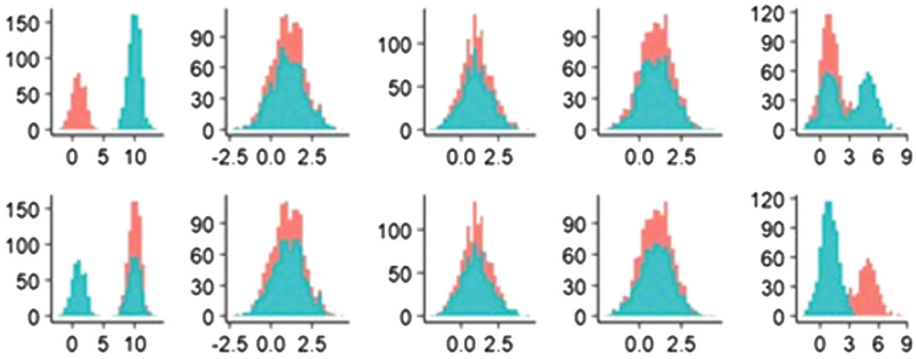


Fig. 2. Visualization of clustering results (importance of key indicators/variables within clusters C1 to C5; blue color – distribution of most important indicator in one cluster; red color – distribution of all other indicators within the same cluster)

Comparison of clustering results across important performance metrics can be seen in Appendix B. It can be concluded that the optimal results of the clustering process are achieved when $k = 5$, considering all important clustering performance measures (when $k = 5$, SSE, ARI, and VI have the minimum recorded values, and NMI has the maximum recorded value, compared with $k = 2, 3, 4, 6$).

Main findings can be defined as the following:

- In terms of the cluster C1 - where the key variables with high influence was “low retention rate of key customers” (business performance), and very high influence was variable “low availability of key competences/expertise” (human resources), as well as variable “low availability of energy sources” (financial viability indicators). Depending on different descriptive characteristics (company size, years of doing business, type of business, region) companies within this cluster are determined in case of manufacturing, medium sized companies doing business more than 5 years across all regions from Serbia;
- Regarding cluster C2 - where the key variables were “decrease in profitability” (business performance), “low productivity” of human resources (human resources), and lastly “high inflation rate” (financial viability). Depending on descriptive characteristics, companies within this cluster are determined in case of mainly manufacturing, small or medium sized companies, doing business less than 5 years in Belgrade and Vojvodina regions.

- Regarding the smallest out of all five clusters – C3 cluster – where the key variables were “high fluctuation of workforce” (human resources), and “high cost of raw material” (financial viability). Depending on descriptive characteristics, companies within this cluster are determined in case of mainly medium sized companies, doing business more than 5 years, mainly in Belgrade region.
- Finally, regarding clusters C4 and C5 - the clusters are described with a single, very high influence indicator – for cluster C4, most important indicator of business performance is “low customer satisfaction”, and regarding fifth cluster, the most important indicator is “high outflow migrations of workers”. Depending on descriptive characteristics, companies within cluster C4 are determined in case of mainly small, service oriented companies, doing business for more than 5 years, originating from East, West and South Serbia, and in case of cluster C5, companies are mainly small, manufacturing oriented, doing business more than 10 years, mainly from Belgrade, West and Vojvodina regions.

4.3 Hypothesis Testing

Statistical ANOVA tests were conducted in order to test statistical significance within and between groups of data, across all five clusters. Results can be viewed in Table 4.

Table 4. ANOVA tests for research hypothesis

Hypothesis	Cluster	Sum of squares		Mean of squares		F test P val
		Between groups	Within groups	Between groups	Within groups	
H1	C1, C2, C3, C4	78,155	7,655	9,337	2,643	F 11,46 p-val <0.01
H2	C1, C2, C3, C5	92,556	8,226	10,353	3,113	F 9,44 p-val <0.01
H3	C1, C2, C3	18,754	4,554	8,664	3,444	F 4,33 p-val <0.01

From results of ANOVA test, regarding groups of data within and between across all five clusters are sufficiently representative to be tested for correlations. With the help of the sampled companies from Serbia, a great deal of variability was described within independent variables (based on the values of the sum of squares and mean of squares, which are significantly larger than zero). Clusters 1, 2 and 3 have the highest score for ANOVA (the biggest difference of variability, depending on the fact of whether the sampled respondents come from different regions in Serbia). In the case of clusters 4

and 5, defining the sole influence of one group of indicators on company sustainability, there is lower, but enough level of difference in variability to be able to confirm the statistical significance of the defined results. When analyzing test results for H1, it can be concluded that there is a statistically significant difference between clusters C1, C2, C3 and C4, suggesting that heterogeneity between clusters included adequate level of variability in data. Similar results have been analyzed also in the case of H2 and H3, confirming the existence of statistical variability across clusters C1, C2, C3 and C5,

To be able to properly test all research hypotheses, it is necessary to conduct appropriate regression tests within separate clusters. To confirm each hypothesis, it is necessary to analyze the impact of each independent variable representing a specific pillar of sustainability (specific indicator of business performance, human resources performance or financial viability).

The regression analysis is conducted by determining the level of regression between cluster centroids (dependent variables) and separate indicators (independent variables), with the help of several statistical indicators:

- Regression coefficients (slope) for specific independent variables (indicators);
- The p-value and comparison based on a confidence interval of 0.05;
- Student's t-test.

The results of the regression tests can be observed in the Appendix B.

Regarding the regression test results between independent variables and the cluster centroids C1, C2, C3 there does exist a significant level of regression. In addition, strong regression can be identified for cluster centroids C4 and C5.

It can be concluded that all hypotheses can be confirmed, but hypothesis H3 could not be described with two clusters, as is the case with hypothesis H1 and H2.

In other words, it was not possible to determine from available data that financial viability indicators have separate, individual significant influence on company sustainability, like it has been determined with business performance indicators and human resources performance indicators.

The adjusted R² parameter is above 0.8 in all cases and it was not displayed in the table. Statistical parameters that also follow the regression coefficients (p-value and Student's t-test) show that adequate independent variables were used in the analysis (there are no cases where the p-value exceeds 0.05 and the t-test is always at a non-zero level) so it can be concluded that the test results are statistically significant at the 95% level.

5 Discussion and Conclusions

5.1 Key Findings and Conclusions

As this research aimed at identifying key risk indicators on business sustainability of a company measured through influence on business performance, financial viability and performances of human resources, and with provided results and analysis, it can be

claimed that the goal has been fulfilled. Key focus of this paper was to analyze small and medium sized businesses in Serbia, which represent the backbone of the economy, and are facing heavy consequences of all global shocks and risks coming to life.

Key correlations were determined for the total of 10 parameters, which were analyzed by the experts, then those parameters were estimated by business owners. Taking into account everything analyzed throughout this research, to comprehensively understand the problem, the existing rationale about influences on sustainability of SMEs in the long run can now be understood with more detail.

Key results of the study displayed five identified clusters of SMEs, depending on the homogeneity between estimated values of different indicators. Most significant influence (highest correlation) was recorded for four human resources indicators of performance. Also, financial viability of SMEs does not influence sustainability individually, but influences jointly with other measured indicators (evidence of this claim was derived from the fact that there was no identified separate cluster with dominant homogeneity of financial viability indicators).

5.2 Discussion of Research Findings

Results of analysis from this study, are complementary with existing research papers, such as the studies by Olah [39], who analyzed financial and economic risk sources in SMEs of Visegrad group and Serbia (based on a sample of 2110 SMEs from Hungary, Poland, Slovakia, the Czech Republic, and Serbia). One of key conclusions identified Serbia as more vulnerable to financial viability threats to sustainability. Advantage of this paper is that it broadens the research by involving influence of human resource performances, while in the study by Olah it was not the case.

Also, while Arsic [40] investigated logistics capacity as a form of business performance indicator of sustainability, it was not the case in this research paper.

Methodologically, this paper is in line with research by Glisovic [41], who also performed cluster analysis on a sample of Serbian SMEs, who assessed sustainability through life cycle management.

As previously also performed by Latip [42], the authors defined the main idea of creating an insightful report on the influences of different indicators on SME sustainability, as well as to determine the specific influence of human resources, so the following conclusions may expand on the following:

- Influences on sustainability with varying levels from medium to very high confirm that key competences and expertise, and low productivity present the key profilers of sustainable SMEs. This conclusion presents an expansion on the results conducted by Aharanwa [43] on strategies for business sustainability of SMEs in South Africa;

- Exclusively, high influence of indicators such as customer satisfaction (business performance), and on the other side high outflow migrations of employees outside Serbia, helps in identifying such massive disruptions to company sustainability, all of which is in line with previous studies by Niedomysl [44] (migration has been analyzed in the case of business owners) and in Cantele [45].

Long-term sustainability of SMEs has been analyzed through ten most important indicators, therefore expanding preliminary findings by Manzaneque Lizano [46], who claimed that customers (business performance perspective) and state or creditor support to SME viability are key indicators to ensure long-term sustainability. Finally, long-term sustainability of SMEs is particularly under influence of family member in case of family-owned SMEs, which has been thoroughly analyzed by Mihic [47].

5.3 Limitations of Conducted Research

This research study had several limitations, apart from the facts that there is an economic crisis rising in Europe, but also a raging war on European soil. Selection of companies for research based on their size and type of industry (business activity) represents an important limitation from the aspect of research inputs.

Since because of these facts, strategic decision makers as the main respondents to the survey (and source of practical confirmation of theoretical findings) were suggestive in form of pessimistic biases, this estimation presents also one of the main limitations of this research. Important limitations of this paper to be noted are also the availability and selection of experts for discussion in qualitative stage, as well as certain level of subjectivity of experts, while defining key parameters for quantitative part of the research.

An overall conclusion may also be made that the sample needs to be broadened, as mostly all surveyed companies in Serbia recorded some form of growth in years until 2022, but also predicted negative effects for 2022, 2023 and long period of years to come.

5.4 Practical Implications

This research contributes to theoretical and practical findings already reported throughout existing literature, by analyzing business indicators who may potentially pretend as sources of risk for maintaining sustainability of a business.

When observing the defined and analyzed research gap, the authors constructed several implications which can be useful when approaching the problem of analyzing risks against sustainability of SMEs in the long run:

- From aspect of business performance indicators, the authors determined that dominantly, SMEs with risk towards sustainability, shall be those SMEs with bad performing post-sales activities, measured through low retention rate of key customers and low customer satisfaction;

- From aspect of human resources performance, research outlined low availability of key competences of employees, low productivity, and finally high fluctuation of work force;
- From financial viability perspective, it is mostly determined by current political, economic and energy issues in Europe, since low availability of energy sources and high inflation rate were marked as key indicators of influence on sustainability of SMEs.

After analyzing all these indicators on SMEs from Serbia, there is one dominant description applicable: only the mixture of different indicators and their estimated influence on sustainability of SMEs, enables best understanding of the topic, and interpretability of the statistical clustering applied.

Therefore, results of this research imply that in order to integrally control sustainability over a longer period of years, it is mandatory to take care about all three dimensions analyzed in this research.

5.5 Future Research Plans

Expansion based on this initial research can investigate deeper the correlations between important indicators, that can be identified with some risk influence on a certain extent. Overall sustainability in limited reach markets and economies such as in the case of Serbia, should also be observed from a regional level, by involving a broader number of experts and SMEs from other countries in the West Balkans region.

Additionally, vision for this research in time to come is to extend scope of research by testing several new variables within defined clusters. One such variable could be related to profile of the organization leader, which has been previously analyzed by Dragicevic and Mihic [48]. Since what has been concluded from this research, findings from analyzed data confirm the initial hypothesis that sustainability of small and medium sized companies are under risk (threat) primarily because of financial viability risk indicators.

Gathering and analyzing more knowledge about businesses from Balkans region, who contribute the most significant share of economic activity within their countries, will certainly provide better understanding of wider variety of influences on company sustainability.

Appendix A

See Tables 5, 6 and 7.

Table 5. Distribution of sampled companies across different descriptive characteristics, and research questions (estimations of risk from 1 to 5)

Person coefficient	Characteristics	Company size (no of employees)				Years of doing business			Type of business		Region (of Serbia)			
		10-49	50-100	101-249	3-5	6-10	10+	Manufacturing	Service	Combined	Belgrade	West	East and south	Vojvodina
	St deviation	1.44	1.21	1.66	1.11	1.45	1.5	1.21	1.2	1.44	1.78	1.54	1.32	1.22
	RQ1-high inflation rate	0.82	0.77	0.85	0.13	0.08	0.05	0.45	0.65	0.55	0.23	0.31	0.20	0.18
	RQ2-high bank interest rates	0.86	0.81	0.79	0.05	0.03	0.02	0.67	0.45	0.34	0.14	0.17	0.09	0.11
	RQ3-low capital raising	0.56	0.49	0.66	0.11	0.02	0.1	0.34	0.23	0.11	0.11	0.09	0.08	0.04
	RQ4-low state support to SME sector	0.68	0.58	0.59	0.15	0.03	0.02	0.65	0.43	0.32	0.06	0.11	0.14	0.15
	RQ5-high Cost of raw material	0.39	0.43	0.52	0.11	0.02	0.1	0.77	0.54	0.43	0.24	0.31	0.22	0.18
	RQ6-low availability of raw material	0.33	0.36	0.76	0.15	0.03	0.02	0.66	0.43	0.56	0.21	0.14	0.16	0.18
	RQ7-high cost of energy sources	0.33	0.56	0.77	0.11	0.02	0.1	0.78	0.71	0.54	0.44	0.43	0.51	0.56
	RQ8-low availability of energy sources	0.45	0.65	0.88	0.15	0.03	0.02	0.86	0.65	0.54	0.32	0.31	0.29	0.21
	RQ9-low productivity	0.21	0.22	0.77	0.11	0.02	0.1	0.65	0.66	0.39	0.05	0.03	0.02	0.09

(continued)

Table 5. (continued)

Characteristics	Company size (no of employees)			Years of doing business			Type of business			Region (of Serbia)			
	10–49	50–100	101–249	3–5	6–10	10+	Manufacturing	Service	Combined	Belgrade	West	East and south	Vojvodina
St deviation	1.44	1.21	1.66	1.11	1.45	1.5	1.21	1.2	1.44	1.78	1.54	1.32	1.22
RQ10-high fluctuation of work force	0.06	0.44	0.65	0.03	0.03	0.02	0.13	0.11	0.19	0.01	0.02	0.1	0.06
RQ11-low availability of key competences/expertise	0.08	0.23	0.83	0.01	0.02	0.1	0.21	0.26	0.27	0.05	0.03	0.07	0.02
RQ12-high outflow migrations outside the country	0.05	0.14	0.32	0.01	0.01	0.02	0.31	0.44	0.43	0.01	0.04	0.34	0.06
RQ13-decrease in total revenue	0.14	0.26	0.65	0.01	0.02	0.1	0.03	0.04	0.3	0.01	0.01	0.01	0.01
RQ14-decrease in revenue per customer	0.12	0.17	0.19	0.04	0.01	0.02	0.01	0.3	0.11	0.01	0.01	0.01	0.01
RQ15-decrease in profitability	0.09	0.55	0.65	0.01	0.02	0.1	0.02	0.06	0.01	0.01	0.01	0.02	0.01
RQ16-low retention rate of key customers	0.68	0.78	0.89	0.09	0.03	0.12	0.03	0.02	0.15	0.01	0.02	0.01	0.01
RQ17-low customer satisfaction	0.24	0.44	0.51	0.01	0.02	0.1	0.11	0.17	0.14	0.02	0.01	0.01	0.01

Pearson correlation coefficient between the sample characteristics and response (rank) by each of the survey respondents

Table 6. Results of survey – sum of replies from 380 business owners

Survey question	Risk influence level estimation on company sustainability				
	1 (Very low)	2 (Low)	3 (Medium)	4 (High)	5 (Very high)
RQ1-high inflation rate	0	0	22	83	275
RQ2-high bank interest rates	0	5	37	218	120
RQ3-low capital raising	4	8	21	204	143
RQ4-low state support to SME sector	29	54	78	99	120
RQ5-high Cost of raw material	42	111	143	47	37
RQ6-low availability of raw material	0	4	14	86	278
RQ7-high cost of energy sources	0	11	22	156	192
RQ8-low availability of energy sources	1	2	30	44	303
RQ9-low productivity	0	2	32	271	75
RQ10-high fluctuation of work force	3	77	123	76	101
RQ11-low availability of key competences/expertise	34	45	51	90	140
RQ12-high outflow migrations outside the country	10	100	67	77	126
RQ13-decrease in total revenue	23	154	144	59	0
RQ14-decrease in revenue per customer	24	56	75	97	128
RQ15-decrease in profitability	13	65	121	101	80
RQ16-low retention rate of key customers	0	5	54	89	232
RQ17-low customer satisfaction	6	44	68	124	138

Table 7. Statistics about surveyed small and medium sized companies

Company size	Average years on the market	Belgrade Metropolitan region	Vojvodina	East and South Serbia	West Serbia
Small	10	88	55	27	35
Medium	11	65	32	32	46

Appendix B

See Tables 8, 9 and 10

Table 8. Variables discussed with experts

Variables deducted from literature review	Key variables after discussion with selected experts
High inflation rate High bank interest rates Low capital raising Low state support to SME sector High Cost of raw material Low availability of raw material High cost of energy sources Low availability of energy sources Low productivity High fluctuation of work force Low availability of key competences/expertise High outflow migrations outside the country Decrease in total revenue Decrease in revenue per customer Decrease in profitability Low retention rate of key customers Low customer satisfaction	Marked as key variables
Return on sustainable investments Revenues invested rate R&D expenditure Material and labor costs Turnover growth Market share Business growth Liquidity Sales Effectiveness Competitiveness Supply chain performance Employee satisfaction Lack of raw materials Transport costs	Marked as less important

Table 9. Hypothesis regression tests for all variables (cluster centroids C1, C2, C3, C4, C5)

Independent variable	Cluster centroid	Regression coefficient	p-value	t-test
High inflation rate	C1	0.24	<0.01	1.38
	C2	1.83	<0.01	1.44
	C3	0.15	<0.01	1.22
	C4	0.14	<0.01	1.25
	C5	0.87	<0.01	1.56
High bank interest rates	C1	0.03	<0.01	1.33
	C2	0.11	<0.01	1.87
	C3	0.54	<0.01	1.24
	C4	0.43	<0.01	1.95
	C5	0.13	<0.01	1.44
Low capital raising	C1	0.11	<0.01	1.42
	C2	0.31	<0.01	1.65
	C3	0.14	<0.01	1.74
	C4	0.14	<0.01	1.34
	C5	0.16	<0.01	1.22
Low state support to SME sector	C1	0.25	<0.01	1.65
	C2	0.14	<0.01	1.74
	C3	0.06	<0.01	1.33
	C4	0.03	<0.01	1.73
	C5	0.02	<0.01	1.22
High cost of raw material	C1	1.24	<0.01	1.05
	C2	1.11	<0.01	1.64
	C3	1.99	<0.01	1.83
	C4	0.32	<0.01	1.95
	C5	0.01	<0.01	1.43
Low availability of raw material	C1	0.43	<0.01	1.53
	C2	0.21	<0.01	1.43
	C3	0.15	<0.01	1.33
	C4	0.53	<0.01	1.14
	C5	0.34	<0.01	1.73

(continued)

Table 9. (continued)

Independent variable	Cluster centroid	Regression coefficient	p-value	t-test
High cost of energy sources	C1	0.32	<0.01	1.32
	C2	0.54	<0.01	1.84
	C3	0.54	<0.01	1.32
	C4	0.64	<0.01	1.24
	C5	0.13	<0.01	1.25
Low availability of energy sources	C1	1.98	<0.01	1.08
	C2	0.43	<0.01	1.21
	C3	0.33	<0.01	1.63
	C4	0.11	<0.01	1.43
	C5	0.34	<0.01	1.36
Low productivity	C1	0.34	<0.01	1.35
	C2	1.86	<0.01	1.74
	C3	0.34	<0.01	1.53
	C4	0.43	<0.01	1.32
	C5	0.13	<0.01	1.22
High fluctuation of work force	C1	0.32	<0.01	1.78
	C2	0.21	<0.01	1.24
	C3	1.98	<0.01	1.43
	C4	0.45	<0.01	1.66
	C5	0.12	<0.01	1.99
Low availability of key competences/expertise	C1	1.89	<0.01	0.99
	C2	0.31	<0.01	1.13
	C3	0.11	<0.01	1.43
	C4	0.31	<0.01	1.34
	C5	0.32	<0.01	1.33
High outflow migrations outside the country	C1	0.43	<0.01	1.66
	C2	0.25	<0.01	1.74
	C3	0.11	<0.01	1.54
	C4	0.32	<0.01	1.74
	C5	1.98	<0.01	1.86

(continued)

Table 9. (continued)

Independent variable	Cluster centroid	Regression coefficient	p-value	t-test
Decrease in total revenue	C1	0.05	<0.01	1.99
	C2	0.11	<0.01	1.88
	C3	0.21	<0.01	1.43
	C4	0.35	<0.01	1.56
	C5	0.54	<0.01	1.84
Decrease in revenue per customer	C1	0.11	<0.01	1.21
	C2	0.02	<0.01	1.63
	C3	0.32	<0.01	1.43
	C4	0.11	<0.01	1.32
	C5	0.32	<0.01	1.54
Decrease in profitability	C1	0.05	<0.01	1.73
	C2	1.67	<0.01	1.43
	C3	0.31	<0.01	1.53
	C4	0.11	<0.01	1.32
	C5	0.06	<0.01	1.21
Low retention rate of key customers	C1	1.78	<0.01	1.19
	C2	0.43	<0.01	1.99
	C3	0.23	<0.01	1.32
	C4	0.11	<0.01	1.53
	C5	0.33	<0.01	1.44
Low customer satisfaction	C1	0.11	<0.01	1.41
	C2	0.34	<0.01	1.21
	C3	0.54	<0.01	1.85
	C4	1.83	<0.01	1.24
	C5	0.65	<0.01	1.93

* C1—centroid for the cluster defining the high and very high risk influences on company sustainability; C2—centroid for the cluster defining medium influences on company sustainability; C3—centroid for the cluster defining very low and low influences on company sustainability; C4—centroid for the cluster defining the very high influence of business performance indicators on company sustainability; C5—centroid for the cluster defining the very high influence of human resource performance indicators on company sustainability.

Table 10. Comparison of clustering performance metrics in case of 2 to 6 clusters ($k = 5$ is optimal)

Clusters C1–C5				
C1—centroid for the cluster defining the high and very high influences on company sustainability; C2—centroid for the cluster defining medium influences on company sustainability; C3—centroid for the cluster defining very low and low influences on company sustainability; C4—centroid for the cluster defining the very high influence of business performance indicators on company sustainability; C5—centroid for the cluster defining the very high influence of human resource performance indicators on company sustainability				
No of clusters	SSE	ARI	VI	NMI
K = 2	1167	0.36	0.77	0.22
K = 3	1073	0.34	0.68	0.29
K = 4	1011	0.31	0.66	0.27
K = 5	955	0.25	0.62	0.79
K = 6	1222	0.33	0.59	0.77

References

1. EU report: Key Findings of the 2021 Report on Serbia: Web report. <https://europa.rs/key-findings-of-the-2022-report-on-serbia/?lang=en> (2021). Accessed 10 Dec 2022
2. World Bank group: Serbia Systematic Country Diagnostic Update: Web report. <https://openknowledge.worldbank.org/entities/publication/33dd90fc-7502-525a-be8e-65352f3e77cc> (2020). Accessed 11 Dec 2022
3. USAid: Big Small business in Serbia: Web report. <https://www.usaid.gov/serbia/fact-sheets/jan-05-2023-big-small-businesses-project> (2023). Accessed 5 Jan 2023
4. Sajc, K., Haldrup, S.: How can Serbian SMEs grow to be more resilient to shocks in the future?, UNDP report. Web report. <https://www.undp.org/serbia/blog/how-can-serbian-smes-grow-be-more-resilient-shocks-future> (2021). Accessed 15 Dec 2022
5. Ehnert, I., Harry, W., Zink, K.J.: Sustainability and HRM. In: Ehnert, I., Harry, W., Zink, K. (eds.) Sustainability and Human Resource Management. CSR, Sustainability, Ethics Governance. Springer, Berlin, Heidelberg (2013). Web report. https://doi.org/10.1007/978-3-642-37524-8_1. Accessed 5 Jan 2023
6. Damjanovic, A.M., Dzafic, G., Nesic, S., Milosevic, D., Mrdak, G., Arsic, S.M.: Strategic management of external disruptions on realization of business plans—case of Serbian manufacturing companies. Sustainability **14**(11583) (2022)
7. Schulte, J., Knuts, S.: Sustainability impact and effects analysis - A risk management tool for sustainable product development. Sustain. Prod. Consum. **30**, 737–751 (2022)
8. Mahmudova, L., Kovacs, J.: Defining the performance of small and medium enterprises **6**(12), (2018). https://seaopenresearch.eu/Journals/articles/NIS_12_5.pdf. Accessed 18 Dec 2022
9. Hristov, I., Chirico, A.: The role of sustainability key performance indicators (KPIs) in implementing sustainable strategies. Sustainability **11**(5742) (2019)

10. Mengistu, A.T., Panizzolo, R.: Tailoring sustainability indicators to small and medium enterprises for measuring industrial sustainability performance. *Meas. Bus. Excel.* (2022)
11. Moursellas, A., De, D., Wurzer, T.: Sustainability practices and performance in european small-and-medium enterprises: insights from multiple case studies. *Circ. Econ. Sust.* (2022)
12. Malesios, C., Skouloudis, A., Kumar Day P., Ben Abdelaziz, F., Kantartzis, A., Evangelinos, K.: The impact of SME sustainability practices and performance on economic growth from a managerial perspective: Some modeling, considerations and empirical analysis results. *Bus. Strat. Environ.* (2022). Web version. https://publications.aston.ac.uk/id/eprint/32482/1/imp_act_of_SME_sustainability_practices.pdf. Accessed 4 Jan 2023
13. Bae, H., Smiridon, R.S.: Indicators of sustainable business practices. *Environmental Management in Practice* (2010)
14. Ciemleja, G., Lace, N.: The sustainable performance of small and medium-sized enterprise: case from Latvia. Web version. <https://sciforum.net/manuscripts/990/original.pdf>, (2020). Accessed 5 Jan 2023
15. Soto-Acosta, P., Cismaru, D.-M., Vătămănescu, E.-M., Ciochină, R.S.: Sustainable entrepreneurship in SMEs: a business performance perspective. *Sustainability* **8**(342) (2016)
16. Broccardo, L., Truant, E.: SMEs and sustainability management: comparison of two case studies **2** (2016). Web report https://www.impresaprogetto.it/sites/impresaprogetto.it/files/articles/new_broccardo_sme_sustainability_10_16.pdf. Accessed 30 Dec 2022
17. Sundin, E., Nasslander, E., Lelah, A.: Sustainability indicators for small and medium sized enterprises in the transition to provide product service systems. *Procedia CIRP* **30**, 149–154 (2015)
18. Israel, B.: Enhancing customer retention in manufacturing SMEs through supply chain innovative practices. *Manag. Dyn. Knowl. Econ.* **10**(3) (2022). Web version. <https://www.managementdynamics.ro/index.php/journal/article/view/473>. Accessed 21 Dec 2022
19. HRM Handbook: Human resources management, a complete and comprehensive guide to Human Resources Management. Web handbook. <https://hrmhandbook.com/agenda/hr-challenges/>, (2021). Accessed 2 Jan 2023
20. Rezaee, Z., Rezaee, H.: Business sustainability and key performance indicators. *J. Bus. Econ.* **5**(9), 1484–1490 (2014)
21. Bartel, A.P.: Human resource management and organizational performance: evidence from retail banking. *ILR Rev.* **57**(2), 181–203 (2004)
22. Woeffray, O., Chen, Z.: How harnessing the power of SMEs and mid-sized companies can shape the future of sustainability, World Economic Forum study. Web report. <https://www.weforum.org/agenda/2022/04/smes-future-of-sustainability/>, (2022). Accessed 27 Dec 2022
23. Hernita, H., Surya, B., Perwira, I., Abubakar, H., Idris, M.: Economic business sustainability and strengthening human resource capacity based on increasing the productivity of small and medium enterprises (SMEs) in Makassar City, Indonesia. *Sustainability* **13**, 3177 (2021)
24. Vandenberg, P.: Micro, small and medium-sized enterprises and the global economic crisis, International Labour Organization. Web version. https://www.ilo.org/wcmsp5/groups/public/@ed_emp/@emp_ent/documents/publication/wcms_108413.pdf, (2009). Accessed 13 Dec 2022
25. Appave, G., Sinha, N.: Migration in the 2030 agenda, International organization for migration. Web report. https://environmentalmigration.iom.int/sites/g/files/tmzbd11411/files/documents/migration_in_the_2030_agenda.pdf, (2017). Accessed 18 Dec 2022
26. Camberato, J.: The impact of inflation on small businesses and how to manage It, Forbes Finance Council (2022), Web report. The Impact Of Inflation On Small Businesses And How To Manage It (forbes.com). Accessed 15 Dec 2022

27. Timm, S.: How the state and private sector can partner to boost support to SMEs: Lessons from Chile Malaysia, Trade and Industrial Policy charges. Web report. https://www.tips.org.za/files/how_the_state_and_private_sector_can_partner_to_boost_support_to_smes.pdf, (2012). Accessed 21 Dec 2022
28. Risteska, A.: The institutional support to SME's development and entrepreneurship in countries of South Eastern Europe, Conference: South-East European Countries towards European Integration (2012)
29. Devonshire, J.: Supply chain issues, recruitment challenges threaten SME manufacturing recovery warns latest Barometer. Web version available at: Supply chain issues, recruitment challenges threaten SME manufacturing recovery warns latest Barometer—The Manufacturer (2021). Accessed 24 Dec 2022
30. Shihadeh, F., Gamage, S.K.N., Hannon, A.: The causal relationship between SME sustainability and banks' risk. *Econ. Res.* **32**(1) (2019)
31. Bartolacci, F., Caputo, A., Soverchia, M.: Sustainability and financial performance of SMEs: a bibliometric and systematic literature review. *Bus. Strat. Environ.* **29**(4) (2019)
32. Burlea-Schiopoiu, A.; Mihai, L.S.: An integrated framework on the sustainability of SMEs. *Sustainability* **11**(6026) (2019)
33. Álvarez Jaramillo, J., Zartha Sossa, J.W., Orozco Mendoza, G.L.: Barriers to sustainability for small and medium enterprises in the framework of sustainable development—literature review. *Bus Strat Env.* **28**, 512–524 (2019)
34. Mulhern, A., Stewart, C.: Long-term decline of small and medium size enterprise share. *Small Bus. Econ.* **21**, 215–228 (2003)
35. OECD: The Impact of the Global Crisis on SME and Entrepreneurship Financing and Policy Responses, OECD Study Report. Web report. <https://www.oecd.org/industry/smes/49316499.pdf>, (2009). Accessed 11 Dec 2022
36. Hastie, T., Tibshirani, R., Friedman, J.: *Elements of Statistical Learning*, 2nd edn. Springer (2017)
37. Petegrosso, R., Li, Z., Kuang, R.: Machine learning and statistical methods for clustering single-cell RNA-sequencing data. *Brief. Bioinform.* **21**(4), 1209–1223 (2020)
38. Xiao, B., Wang, Z., Liu, Q., Liu, X.: SMK means. An improved Mini Batch K means algorithm based on mapreduce with Big Data. *Tech Sci. Press* **1**(1), 1–5 (2018). Web report. <https://www.napier.ac.uk/~media/worktribe/output-1233588/smk-means-an-improved-mini-batch-k-means-algorithm.pdf>. Accessed 28 Dec 2022
39. Oláh, J.; Kovács, S.; Virglerova, Z.; Lakner, Z.; Kovacova, M.; Popp, J.: Analysis and comparison of economic and financial risk sources in SMEs of the Visegrad Group and Serbia. *Sustainability* **11**(1853) (2019)
40. Arsić, M.; Jovanović, Z.; Tomić, R.; Tomović, N.; Arsić, S.; Bodolo, I.: Impact of logistics capacity on economic sustainability of SMEs. *Sustainability* **12**(1911) (2020)
41. Glisovic, S., Stojiljkovic, E., Stojiljkovic, P.: The state of play in disseminating LCM practices in the Western Balkan region: the attitude of Serbian SMEs. *Int. J. Life Cycle Assess.* **23**, 1396–1409 (2018)
42. Latip, M., Sharkawi, I., Mohamed, Z., Kasron, N.: The impact of external stakeholders' pressures on the intention to adopt environmental management practices and the moderating effects of firm size. *J. Small Bus. Strateg.* **32**(3), 45–66 (2022)
43. Aharanwa, C.C.: *Business Sustainability Strategies of Small and Medium Enterprises in South Africa*, Walden University. Web report. <https://scholarworks.waldenu.edu/cgi/viewcontent.cgi?article=11646&context=dissertations>, (2022). Accessed 22 Dec 2022
44. Niedomysl, T., Källström, J., Koster, S., Östh, J.: Interregional migration of business owners: who moves and how does moving affect firm performance? *Reg. Stud.* **53**(4), 503–516 (2019)

45. Cantele, S., Zardini, A.: Is sustainability a competitive advantage for small businesses? An empirical analysis of possible mediators in the sustainability–financial performance relationship. *J. Clean. Prod.* **182**(1) (2018)
46. Manzaneque-Lizano, M.; Alfaro-Cortés, E.; Priego de la Cruz, A.M.: Stakeholders and long-term sustainability of SMEs. who really matters in crisis contexts, and when. *Sustainability* **11**(6551) (2019)
47. Mihic, M., Arsic, S., Arsic, M.: Impacts of entrepreneurs' stress and family members on SMEs' business success in Serbian family-owned firms. *J. East Eur. Manag. Stud.* **20**(4), 452–483 (2015)
48. Dragicevic, I., Mihic, M.: Women leadership in public sector—evidence from Serbia. *Lex Localis* **18**(2) (2020)



Robot Movement Programming and Simulation Generation for Pick and Place Materials in ABB Robot Studio

Djordje Dihovicni¹ (✉) , Petar Jakovljević^{1,2}, Nada Ratković Kovačević¹ ,
and Dragan Kreculj¹ 

¹ The Academy of Applied Technical Studies Belgrade, Boulevard of Zoran Djindjic 152a,
11070 Belgrade, Republic of Serbia

djdihovicni@atssb.edu.rs

² Polytechnic – School for New Technologies, Highway to Zagreb 18, 11070 Belgrade,
Republic of Serbia

Abstract. This paper describes a program for robot movement for pick and place materials using ABB Robot Studio. Program allows its users to make a complete workspace for robot control via virtual work space and make simulation for robot movement. Users can make their own 3D model of the work piece and import it to the virtual workspace. Advantage of making the simulation is exposing errors without direct contact with robot and its workspace. If no errors are present in the simulation users generate the program code for robot movement in accordance with demanding conditions. At the end of the experiment of pick and place materials the users are introduced to the Robot Studio software package. Users are able, after the experiment, to build a robot workspace for transport of materials with the help of the lecturer. The advantage of doing the experiment is that the users get to know the software directly, which enables the design of certain objects within the program itself. In order to improve the experiment, the objects of manipulation has different forms, where users are given the chance to design the parts themselves in the SolidWorks program and to import that 3D model into Robot Studio by saving the modeled part with.SAT extension, then add another task for the robot to move around the contour of the object after placing the part, simulating the type of a milling process, where users use the knowledge gained from placing the targets of the end effectors.

Keywords: Robotics · Artificial intelligence · Simulation · Education

1 Introduction

Industrial robots are used effectively in industry to enhance the production, while at the same time using industrial robots in education has increased over the years, [1, 2]. Advantages applying robots in industry are:

- Production quality
- Increased productivity

- Safety
- Flexibility
- Reducing labor costs.

Robot Studio is a program for off-line robot programming and simulation generating. Robot Studio allows users to make and test complete robot installation for certain tasks made in virtual 3D environment without visiting production line or interrupting the production process, [3–5]. The ability to program a robot in virtual world before the robot completes tasks in real time has drastically changed the perception of most companies regarding robot movement programming, [6]. This method is used for testing robot movement before executing the task to avoid potential collisions, faults or damage, [7–9]. Programming a robot using the device (on-line) is still popular in some tasks, but today robots are applied for complex operations where off line method needs to be used.

Advantages of off-line robot programming are:

- Programming is executed without interrupting the production,
- Risk of damage is reduced,
- Installation of robot line is faster,
- Complex tasks are easily programmed.

2 Making the Work Environment

The first step includes selection and placing the robot in the station. Robot placement is located in the Home tab, via the ABB Library menu. Selecting ABB Library gives a drop-down menu with a selection of robot models. The IRB 1200 model will be selected. After placing the robot, the end effectors are added. The end effectors are located via the Home tab, by selecting the Import Library drop-down menu, then on Equipment, by scrolling down, to the final device named myTool (Fig. 1).



Fig. 1. A robot model and myTool selection.

By selecting myTool places the end effectors are placed at the beginning of the coordinate system of the station and the robot. It is necessary to place the tool on the final segment of the robot. Placement of the end effectors on the last segment of the robot is done in the Layout window, by selecting the end effectors (myTool), as is shown in Fig. 2.

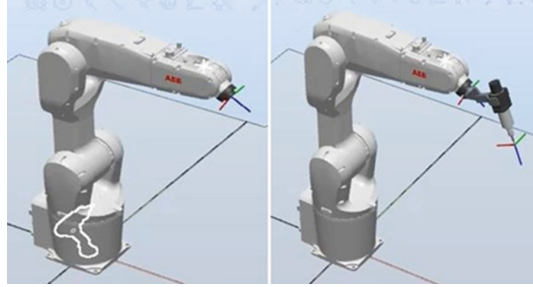


Fig. 2. End effectors position change.

Setting up the controller is done via the Home tab, by selecting Virtual Controller. Virtual Controller gives a drop-down menu with a selection of controllers. For this example controller From Layout is selected.

After controller installation is completed the work table is set. When work table is imported its location needs to be changed. Opening more options on the table in layout window and selecting the position option, entering the values in the axis boxes (X 400, Y 400, Z0) and the rotation of the table around Z axis (90°) (Fig. 3).

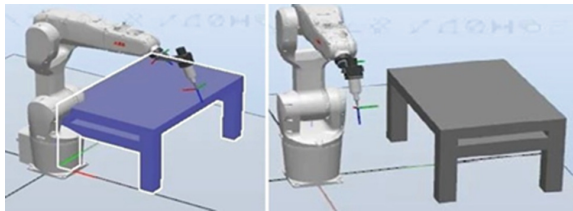


Fig. 3. Table placement (before and after changing the position).

Work-piece should be placed from the floor to the table. From the modeling tab, selecting the solid menu the cylinder will be made with the diameter of 250 mm and height 250 mm. The position of the cylinder will be X 0, Y -700 Z 0 which is placed on the floor. After the creation of the first cylinder, the same cylinder will be created at the table. Second cylinder is created to help for the target placement.

3 Target Placement

Next step is to add the top that the end effectors should reach. The first target is on the upper surface of the cylinder located on the floor (Part_1), at the center of the circle, while the second point is on the upper surface of the second cylinder on the table (Part_2), at the center of the circle (see Fig. 4).

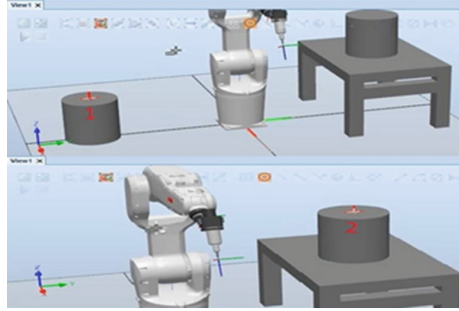


Fig. 4. Target 1 and target 2 placement.

Third target represents the point of guidance of the end effectors (see Fig. 5), since it is necessary to make a path in the form of a circular arc. To add a third target, it is necessary to enter the coordinates of that point in the Create Target window. The coordinates are: X 700, Y 0, Z 550. Target 3 is renamed to “circular”.

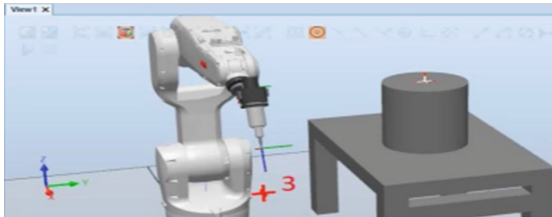


Fig. 5. Third target.

Next step is to check the position of the end effectors for each target. The check is performed by opening more options on an arbitrary Target, View Tool at Target, and name of the final device (myTool).

Next two targets are safe distance targets; they are placed on that way, so when robot is approaching the target it doesn't collide with the work piece. Target 1 and 2 are to be copied and pasted in the layout window but their positions need to be changed to make a distance from the point of end effectors and the surface of the work piece. Safe distance in this example will be 30 mm, which means that in the Z axis box, in the offset window, value – 30 is entered. Value – 30 is entered because the positive direction of the Z axis is upside down due to the tool position changes.

4 Path Generation

Since all the required targets are set, the end effectors path will now be generated based on those targets. By opening more options on the point Target_10_2, then on Add to new path, the generated path Path_10 will appear. Adding the targets to the path is done by dragging the selected target to the last instruction of the path movement. The order of adding targets is:

- Target_10_2 (Approaching the work piece from the floor)
- Target_10 (Picking the work piece)
- Target_10_2 (Lifting the work piece)
- Circular (Moving to Target 3)
- Target_20_2 (Approaching the table)
- Target_20 (Placing the work-piece on the table)
- Target_20_2 (Moving away from the work-piece)
- Home (Returning to the home position).

To make circular arc movement possible, two targets are selected from the Path layout: MoveL circular and MoveL Target_20_2. By opening more options on selected targets in the Modify Instruction menu an option Convert to Move Circular is selected. In order for the robot to have the correct positions during movement, it is necessary to perform calculations for each position. This is done through the Auto Configuration command, which automatically calculates the position for each movement of the robot.

5 Simulation and Code Generation

For the end effectors to pick (attach) the object, it is necessary to add a component that will connect the end effectors to the object. That component is called Attacher. The connection is established by selecting MyTool in the Parent drop-down menu. Parent indicates which object is doing the manipulation. Child indicates which the object of manipulation is; in this case it is the work piece (Part_1).

For the end effectors to place (detach) the object, it is necessary to add a component called Detacher. It is necessary to drop the object of manipulation (work piece). Releasing is done by selecting the Child drop-down menu and selecting Part_1.

Collision sensors are used to detect the distance between two objects in order to avoid a collision. In this case, it is necessary to add two collision sensors:

- The first sensor to when the final device/end effectors approaches the object of manipulation,
- Second sensor when the object of manipulation is left at the desired location.

Method of adding collision sensors is the same as adding the Attacher but instead of parent and child options are Object 1 (parent) and Object 2 (child). In order to detect the presence of the objects by the sensors a distance between those objects will be added in the NearMiss box. The distance between objects in order to be detected is 10 mm.

Reset simulation signals are added from Signals and Connections tab, with Add I/O signals. Type of Signal task requires a digital input signal. Signal Base Name represents

the name of the signal. Since a signal is needed to restore the simulation, reset is entered in the field. Signal Value represents the value of the signal, whose value in this case is 1.

After adding the components that connect the objects in the station as well as adding the signals, it is now necessary to connect the components to synchronize the task functions. Connecting components is done through the Design tab, which displays the components that have been created. The following components need to be connected:

- Reset (1) → Positioner – Execute (0) (Start and repeat program and simulation),
- Collision Sensor – Sensor out (0) → Attacher – Execute (0) (Activation of first collision sensor),
- Collision Sensor_2 – SensorOut (0) → Detacher – Execute (0) (Activation of the second collision sensor) (Fig. 6).

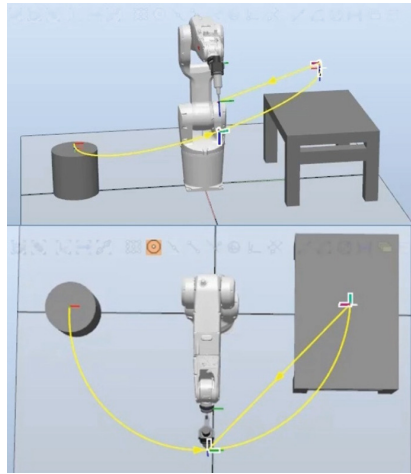


Fig. 6. Robot tool path

The program contains commands that are entered into the robot's control system so that the robot in real time performs the tasks created for it in virtual space. The program is generated via the RAPID tab by selecting Synchronize option. Synchronize opens a new window that allows the selection of objects in the station that the program will affect. Since the entire station is included, all objects and targets need to be checked.

After successful synchronization, the message "Synchronization to RAPID completed" will be displayed in the Output window. The overview of the program can be found in the Layout window, via the drop-down menus RAPID, T_ROB1, by selecting Module1.

6 Conclusion

At the end of the practical demonstration of pick and place materials the users are introduced to the Robot Studio software package. Users are able to build a robot workspace for material transfer by following instructions given from the teacher. The advantage of

doing this practical demonstration is direct introduction to the software, which enables the design of certain objects within the program itself. To implement the generated code in real time it is necessary to make workspace exactly as it is on the simulation, which means placing the same robot and final device like in the simulation, also to equip the robot with sensors which have near miss value exactly as the value set in the simulation. The advantage of the simulation is allowing the users to directly select where will the final device manipulate with work objects via merging the starting points of both coordinate systems of the final device and the work object, also how will the object be manipulated (in this example via attacher and detacher options). For additional tasks the objects of manipulation should have different forms, where users are given the chance to design the parts themselves in the SolidWorks program and to import that 3D model into Robot Studio by saving the modeled part with.SAT extension, then add another task for the robot to move around the contour of the object after placing the part.

References

1. Jakovljevic, P.: Pick and Place, intern script for subject Robots. Academy of Applied Technical Studies. Belgrade (2021)
2. Potkonjak, V.: Robotics. University in Belgrade, Belgrade, Naucna knjiga (1996)
3. Yanna, H., Liying, L.: Application of robotics in higher education in Industry 4.0 Era. *Univers. J. Educ. Res.* **7**(7), 1612–1622 (2019)
4. Mubin, O., Shahid, S., Stevens, C.J., Abdullah, A.M.: A review of the applicability of robots in education (2013). <https://doi.org/10.2316/Journal.209.2013.1.209-0015>
5. Mocan, B., Timoftei, S., Stan, A., Fulea, M.: RobotStudio®, Simulation of Industrial Automation Processes and Offline Programming of ABBs Robots-Practical Guide for Students. U.T. Press, Cluj-Napoca (2017)
6. Eduardo, J., Plata, C., Carbajal, O.M., Lozada, J.C.H., Gutierrez, J.S., Zarate, I.R., Talamantes, J.E.S.: Simulation and implementation of a mobile robot trajectory planning solution by using a genetic micro-algorithm. *Appl. Sci.* **12**, 11284 (2022). <https://doi.org/10.3390/app122111284>
7. Lobbezoo, A., Kwon, H.J.: Simulated and real robotic reach, grasp, and pick-and-place using combined reinforcement learning and traditional controls. *Robotics* **12**, 12 (2023). <https://doi.org/10.3390/robotics12010012>
8. Dihovicni, D., Miscevic, M., Ratkovic Kovacevic, N., Kreculj, D.: Implementation of a fuzzy logic approach for a smart production system. *J. Natl. Sci. Found. Sri Lanka* **50**(3) (2022)
9. Choosing the right robot programming and simulation software. <https://flr.io/choosing-the-right-robot-programming-simulation-software/>. Last Accessed 03 Dec 2023



Bucket Wheel Excavator Reliability Improvement by Use of Probabilistic Approach and Fault-Tree Analysis

Dušan Arsić^{1(✉)}, Snežana Kirin², Aleksandra Arsić³, Ružica Nikolić⁴,
and Ljubica Radović⁵

¹ University of Kragujevac, Faculty of Engineering, Sestre Janjić 6, 34000 Kragujevac, Serbia
dusan.arsic@fink.rs

² Innovation Centre of Faculty of Mechanical Engineering, Kraljice Marije 16, Belgrade, Serbia

³ Faculty of Mechanical Engineering, University of Belgrade, Kraljice Marije 16, Belgrade, Serbia

⁴ Research Centre, University of Žilina, Univerzitná, 8215, 010 26 Žilina, Slovakia

⁵ Military Technical Institute, Ratka Resanovića 1, 11030 Belgrade, Serbia

Abstract. Welded joints' reliability in responsible welded structures is of the utmost importance. If such a structure, for example, a bucket wheel excavator, suffers damage or failure, the financial losses are two-folded – the machine does not deliver the required quantity of coal, while, due to that, the power plant does not deliver sufficient electricity to the industry and households. This paper presents a method, based on the probabilistic and semi-probabilistic approaches to express the coefficient of validity and welded joints weakening, defining reliability as a measure of the quality of installed vital welded structures on the bucket wheel excavators in service. The “fault-tree” analysis was applied to enable a quantitative and qualitative analysis of the welded structure failure causes, diagnostics of behavior, and structural degradation, to evaluate the integrity and estimate the service life of the vital welded structures that have a flaw in the welded joint. The database was created, as well, by which the reliability of the bucket wheel excavators can be increased. The proposed method enables to efficiently test the welded joints during all the phases, from manufacturing, via acceptance to assembling of various welded structures, e.g. machines, like excavators or cranes, or the constructions like bridges, etc.

Keywords: Bucket wheel excavator · Welded structure · Fault-tree analysis · Welded joint reliability

1 Introduction

Bucket-wheel excavators represent extremely complex machines that perform very responsible and demanding tasks. All this imposes the need for all the elements of the assembly to be operational for a long period of time. Excavator consumables are most often replaced through preventive (periodic) maintenance, although certain, most

responsible positions can be monitored with measuring instruments, as well, to be able to react as soon as possible in the case of noticed irregularities. This especially applies to elements that are made by welding. Another way of monitoring the working conditions of such constructions is the fault-tree analysis, through which one is able to identify potential causes of failure and analyze their impact on the integrity and reliability of the construction as a whole.

The objective of this paper was to show/introduce a new method, based on the probabilistic and semi-probabilistic approaches, which predicts that based on possible/potential errors that may occur in the welded joints on the excavator, their impact on the excavator as a whole can be predicted. In addition, the method implies the introduction of the coefficient of validity and welded joints weakening, which defines reliability as a measure of the quality of installed vital welded structures on the bucket wheel excavators in service.

Taking into account all the potential causes of failures and applying the proposed method, it is possible to monitor the condition of the structure during exploitation and to assess its reliability and integrity in operation, as well as to carry out more efficient maintenance of the equipment, which can lead to prevention or delay of accidents and prevention of material (monetary) losses due to replacement of parts or downtime of a machine.

2 Cracks as Causes of Failure of the Bucket-Wheel Excavators and a Role of the Non-destructive Testing in Assemblies State Diagnostics

The stress state in a bucket wheel excavator is complex due to residual stresses after manufacturing and assembling, stationary and dynamic loadings in operation non-stationary dynamic loadings caused by unexpected events. The most critical areas in this respect are welded joints since crack-like defects are always likely to be present. Figure 1 shows the schematic of the bucket wheel excavator complex stress state.

Considering that the bucket wheel excavators have a long service period in very harsh exploitation conditions, their vital welded joints have to be controlled both continuously and periodically since their integrity depends on a large number of technological-metallurgical [1, 2], structural [3, 4] and exploitation factors [5–7]. This explains a wide range of welded joints' fatigue strength values, at different values of the asymmetry coefficient of loading ($R = \sigma_{\min}/\sigma_{\max}$) [8]. Therefore, it is necessary not only to monitor their structural condition [9–15], but to monitor possible defects that can lead to damage of the structure [16–19], as well. One possible way is shown in Fig. 2.

The reason for monitoring this type of equipment is that failures on such complex systems can occur due to improper maintenance or by accident. Accidental failures of the bucket-wheel excavator were considered by authors in [9], which found that by careful analysis of failures, the expected time of proper operation of the excavator, for each year, can be obtained. That is an important factor when considering the maintenance, as well as periodic controls and repairs of parts of the bucket-wheel excavators and mining equipment, in general. In addition, the contribution is that plans for that machine operations, i.e. its expected productivity, can be made. In the case that such machines

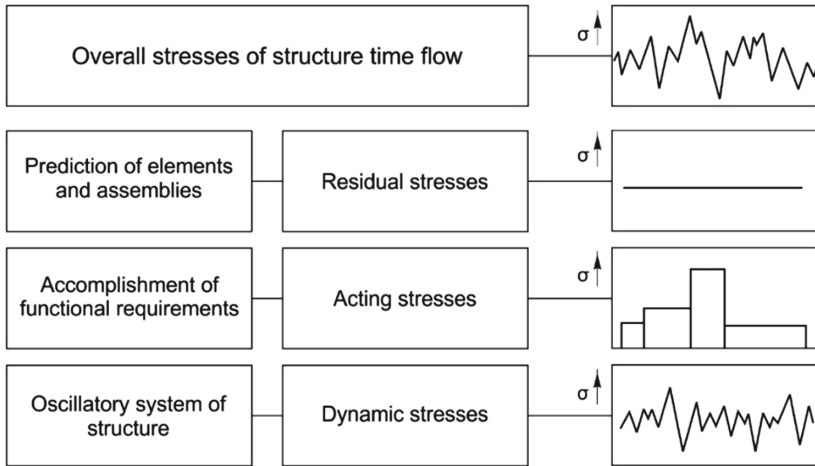


Fig. 1. Presentation of the total stress as divided according to the stress origin.

were loaded more than they should be, i.e. to be exposed to prolonged work in difficult working conditions, failure can occur very easily. The initiator of such a failure can be even a small error, as analyzed by the authors in [10]. They determined that failure of larger excavator components can occur due to fatigue and accelerated/sudden failure. By analyzing the failure of an excavator, they reached the conclusion that even very small errors during the welding, which are most often ignored, can lead to a chain reaction and the failure of a more responsible and expensive working part. The authors of the paper [11] went a step further and conducted research into the causes of damage and an assessment of the integrity of the welded grid structure of the boom of the bucket-wheel excavator's dumper, before and after the repair of vital parts of the structure. The analysis of the results obtained after the non-destructive testing, measurement of the stress state and numerical analysis, determined that there was no danger to the integrity of the grid structure of the boom of the bucket-wheel excavator after repair, if it was executed correctly and if the procedures in working conditions were followed. Similar research was carried out in papers [12–15], where the influence of cracks on various working elements on the integrity of the entire structure was mainly considered. Excavator wheels and tracks [12, 13], bridge conveyor [14] and mine hoist rope attachment elements [15] were analyzed. All the analyses have shown that the impact of cracks on the integrity of the structure is very strong, whether it was already generated in an element during its manufacture or created by welding the entire structure or during the machine's operation. The author's recommendation is that with such complex constructions, in the places that are considered the most critical, constant monitoring of their condition during exploitation, especially when working in very difficult conditions (modes), must be performed.

Classes and quality of the welded joints are defined by the DIN 22261–3 standard [20]; ultrasonic testing of the welded joints is being conducted according to the standard



Fig. 2. Placement of the strain gauges on the welded structure of the bucket wheel boom [6].

SRPS EN ISO 17640 [21]; control of the quality of the welded structures in manufacturing and exploitation of the bucket wheel excavators is done according to standard SRPS EN ISO 5817 [22].

For the non-destructive testing (NDT) of the welded structures the following tests are prescribed by the standard: for the welded joint of the quality class “B” – 100% of joints must be subjected to NDT (visual test – VT, magnetic particles test – MT, ultrasonic test – UT and radiographic test RT); for the quality class “C” – 20% of joints and for the quality class D – 10% of joints must be tested [22]. Performing those tests requires certain labor costs and significant losses in production productivity due to the excavator’s downtime during the tests. No standards, norms, recommendations, or methodology exist in the available literature, which would require some other type of control of the welded structures of the bucket wheel excavators, so these methods can be considered reliable enough [23].

Welded structures of the bucket wheel excavators are made of structural steels S235 and S355 [24]. The plan and program of tests of the welded joints on the bucket wheel excavator predict the tests to be conducted after every 5000 h of exploitation (approximately a period of one year of excavator’s operation). In order to reduce the costs of welded joints’ tests and losses in production due to the excavator’s downtime, a new method was developed, based on the fault-tree analysis, which decreases the testing costs by 70% and the excavator’s downtime by 50%.

Crack-like defects are frequent phenomena during the manufacturing, assembling process and exploitation of the complex welded structures, due to flaws in the production technology, insufficient forming, structural stress concentrators and conditions of the structure realization (Fig. 3).

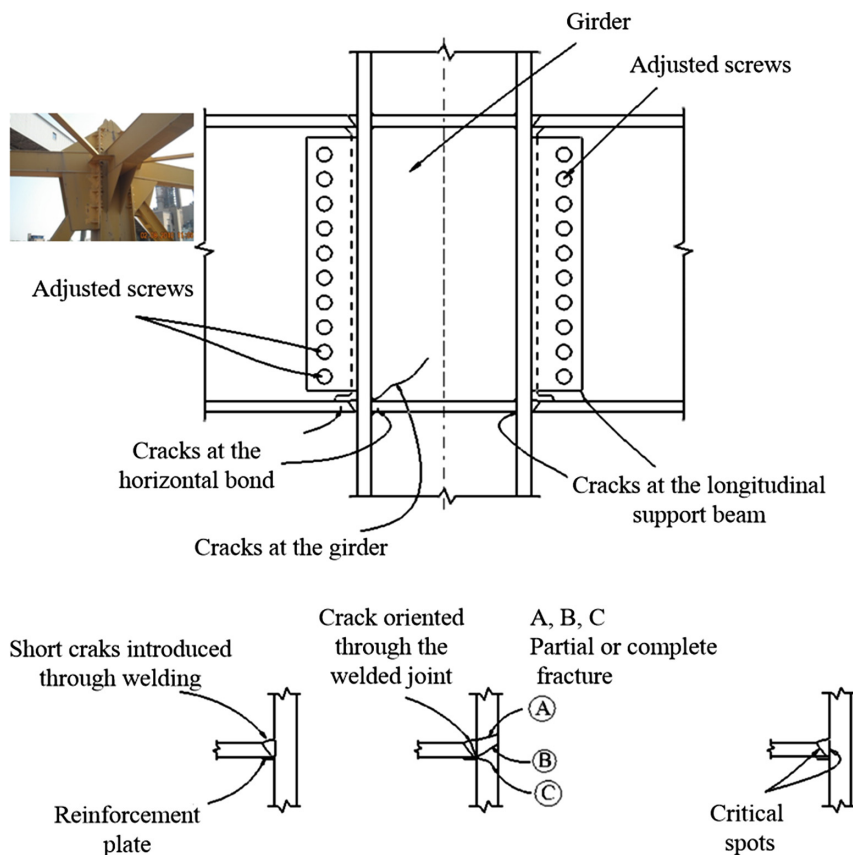


Fig. 3. Locations at which fatigue cracks mainly occur [6].

The characterization of fracture as a multiphase process of crack initiation and growth also includes different starting stages, on which depend the possibilities for further crack growth. The crack can, generally, be stable, subcritical and unstable and possibilities for the crack growth can be along different paths (Fig. 4, paths 1–8). This is especially characteristic of the welded joints and welded structures.

All the bucket wheel excavators at open-pit mines in Serbia are produced by German companies “TAKRAF” and “Thyssen Krupp”, while the excavators on the coal deposits are produced by “Ameco” from France. They are designed according to the DIN 18800 standard.

There are examples of fault-tree analysis application for nuclear power plants, airplanes, communication systems and some other industrial processes, but there are no cases of its application in manufacturing and exploitation of the vital welded structures of the bucket wheel excavators.

Numerical indicators (validity coefficient of the welded joint and weakening coefficient of the welded joint and reliability) for quantitative, as well as qualitative analysis and evaluation of the failure causes of the welded joints in vital welded structures of

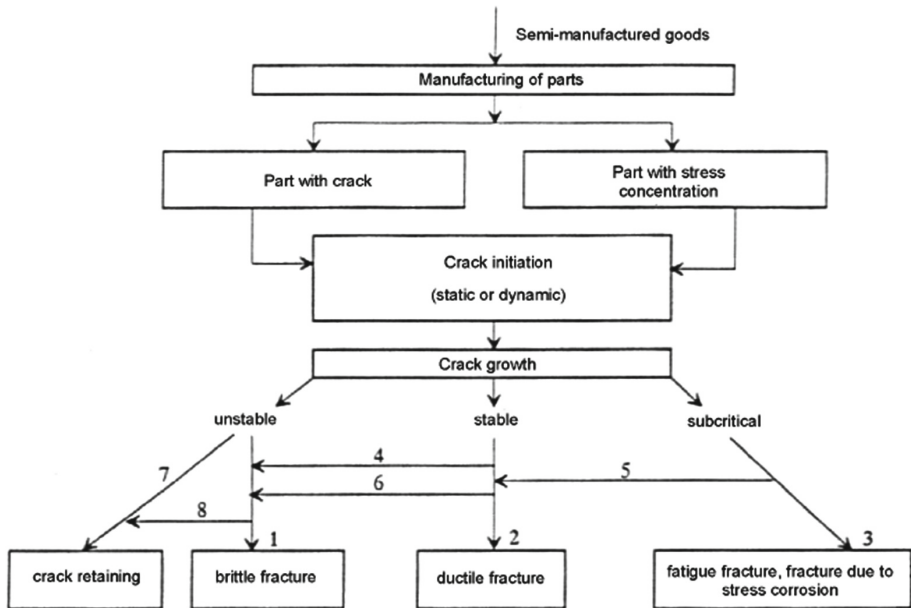


Fig. 4. Options for crack propagation.

the bucket wheel excavators, which appeared as a consequence of manufacturing and/or exploitation, are described in this paper. By analyzing the individual failure cases, one comes up with a conclusion about what their causes were, like wrong material and/or welding technology selection, wrong calculation or the forming method, or deviation from the predicted exploitation conditions.

3 Materials and Methods

The failure analysis is a process where a failed product is investigated in order to find out what caused the failure. Different methods can be used to detect the cause of failure, like the Ishikawa fishbone (cause-and-effect) diagrams, failure modes and effects analysis (FMEA) and fault-tree analysis (FTA).

The basic concept of the Fault-Tree Analysis is the translation of the failure behavior of a physical system into a visual diagram and a logic model. The FTA is an analytical technique, where the undesired state of the system is specified and the system is analyzed to find all the realistic ways why and/or how the undesired event occurred or could occur. The FTA analysis uses the bottom-to-top approach and the undesired event (failure) is the so-called top event.

In the FTA, the diagram presents a visual model that shows system relationships and the root cause paths. The logic segment provides a mechanism for qualitative and/or quantitative evaluation. Events, analyzed as faults by the FTA, can be associated with hardware failure, human or software errors, or any event, which has led to the undesired one. Thus, a fault tree presents the logical interrelationships of basic events that led to

the top event of the fault tree. The FTA is based on reliability theory, Boolean algebra and probability theory and uses a very simple set of rules and symbols to provide a mechanism for the analysis of very complex systems, as well as complex relationships between hardware, software and humans [25, 26].

The FTA is a deductive method, which by analyzing the individual influences, enables a conclusion on causes and individual contributions to failure [27]. The main advantages of the FT method are:

- Simple graphical presentation of the logic of failure,
- Failure logic can be followed gradually,
- Possibility of both qualitative and quantitative analysis by application of the Boolean algebra,
- When the quantitative input data are available both quantitative and qualitative analyses can be performed, in the opposite case only the qualitative analysis is being conducted,
- The computer programs are developed for the fault tree analysis, as well as for its graphical presentation,
- The fault tree analysis can include various influences, unlike some other methods,
- No special training or knowledge is necessary for the application of the fault tree method.

Results of the fault tree analysis are used for failure prevention, analysis of failure causes, namely influences on reliability, clearly defining and quantifying those individual influences, and ensuring conditions that would give good reliability.

Application of the FTA in manufacturing of a welding structure of the bucket wheel excavator, taking into account chemical composition (CC) of the base metal and filler metal (FM), base metal quality, welding parameters, shielding gas and heat treatment, as well as the heterogeneity of welded joints (base metal, BM, weld metal, WM, heat-affected-zone, HAZ), is presented in details in [28]. It was shown that the cooling rate significantly influences the structure of the WM and HAZ, diffused hydrogen and residual stresses.

Application of the FTA during the welding structures of the bucket wheel excavator exploitation is also presented in detail in [29]. It was shown that the undetected flaws have an important effect on the reliability and safety of the bucket wheel excavators since they are frequently causing fractures and sometimes failures. It was also shown that the fatigue crack growth, defined by the Paris Law [30].

$$\frac{da}{dN} = C \cdot (\Delta K)^m, \quad (1)$$

where a is the crack length, N is the number of loading cycles, C and m are the material constants and ΔK is the stress intensity gradient, which presents one of the major problems, if undetected before the crack reached the critical value (a_c).

One should also keep in mind that corrosion plays a significant role in the fatigue process, so special focus should be given to the failure due to corrosion fatigue, as shown in Fig. 5 and explained in [28]. Notation in Fig. 5 is as follows:

T – Fracture due to the corrosion fatigue ($T = F = 1 - R$);

E1 – Flaw was not detected through NDT;

E2 – Crack propagates due to fatigue until reaching the critical length ($a = a_c$);

E3 – Flaw was not detected through the NDT;

E4 – Flaw was not detected through the NDT immediately after the occurrence;

E5 – Flaw was not detected through the NDT in the later phase of inspections;

A – Conditions for the crack propagation;

B – test device did not detect the flaw;

C – The operator did not detect the flaw, which could have been detected by the device.

Derivative of the fault tree in Fig. 5 is then:

$T = E1 \times E2 = E2(B1 + C1) = A(B1 + C1) = A(E4 + E5)(B1 + C1) = A(B2 + C2 + C3)(B1 + C1)$.

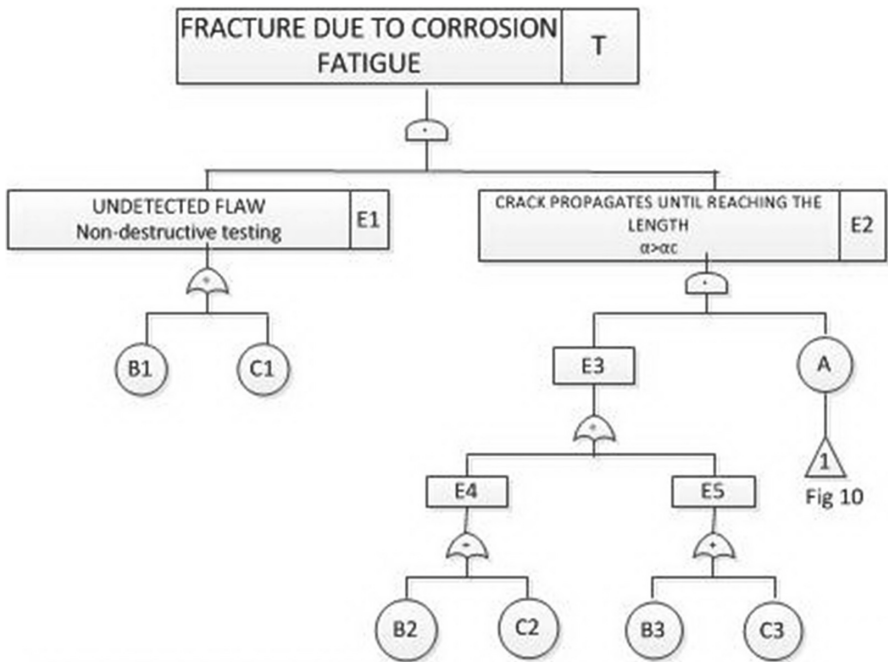


Fig. 5. Appearance of the fault tree due to the corrosion fatigue [27].

For the case when the crack reaches length $a > a_c$ (event A in Fig. 5), the fault tree is shown in Fig. 6.

4 Results

Using the fixed values for calculating the validity and weakening coefficient and the degree of safety of the welded joints is the usual deterministic calculation method. However, the probability of failure can vary from very small to unacceptably large values, for the same values of calculation coefficients and factors, taking into account

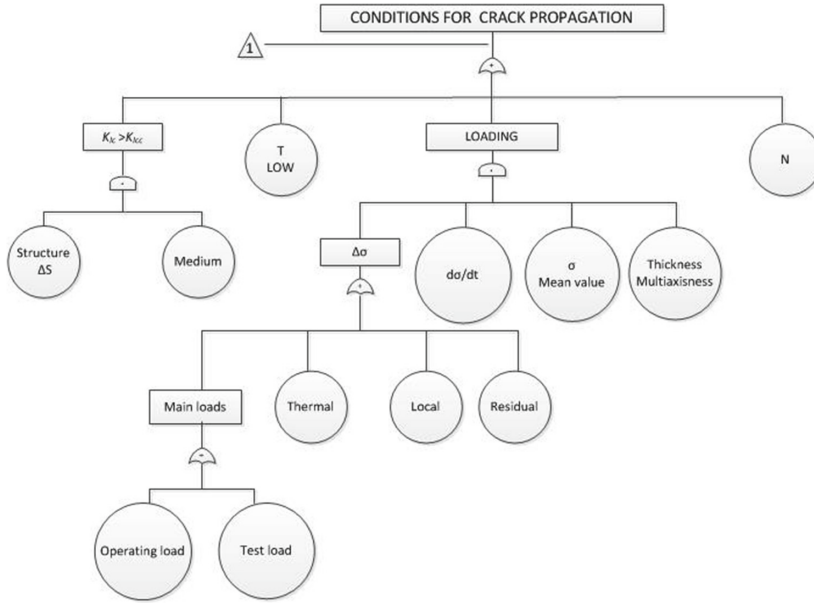


Fig. 6. The fault tree for the crack length $a > a_c$ (event A in Fig. 5)

the smaller or greater possible variability of stress, strength, cross-sections, welded joint flaws and the like.

Since the properties of the welded joint and the base metal, as well as the exploitation conditions, are variable, the more realistic and efficient for the evaluation of various quantities and analysis of the joint's properties and phenomena is the probabilistic approach [27].

The reliability of the welded joints is a numerical probability, with given confidence limits, that the welded joint will execute the set function within the predicted conditions and exploitation time. The probabilistic expression of the welded joint's reliability is more realistic than the reliability factors, which represent a pair of random values.

The bucket wheel excavator design defines the categories (classes) of welded joints that correspond to the predicted reliability of welded joints or welded structures.

Reliability of the welded joint or the welded structure can be calculated by application of the probabilistic model "welded joint yield stress (WJYS) – base metal yield stress (BMYS)" Fig. 7, for the case of the normal distribution by application of Eq. (2), which for the mean distribution value $m = 1$ and when the dissipation of the mean value – the standard deviation is $s = 1$, obtains the form of Eq. (3):

$$R = \int_{-\infty}^{\infty} f(t) dt = \frac{1}{\sigma \sqrt{2\pi}} \int_{-\infty}^{\infty} e^{-\frac{(t-m)^2}{2\sigma^2}} dt, \quad (2)$$

$$R = \int_{-\infty}^{\infty} f(t) dt = \frac{1}{\sqrt{2\pi}} \int_{-\infty}^{\infty} e^{-\frac{t^2}{2}} dt = \Phi(m_1), \quad (3)$$

with

$$m_1 = -\frac{\overline{WJYS} - \overline{BMYS}}{(\sigma_{WJYS}^2 + \sigma_{BMYS}^2)^{\frac{1}{2}}}, \quad (4)$$

where: \overline{WJYS} is the mean value of the welded joint yield stress, \overline{BMYS} is the mean value of the base metal yield stress, σ_{WJYS}^2 is the variance (average value of the square of deviation of the random variable welded joint yield stress), σ_{BMYS}^2 is the variance (average value of the square of deviation of the random variable base metal yield stress).

Equation (2) is valid with the assumption that there is no correlation between the WJ and BMYS properties. The reliability calculated as

$$R_{50\%} = R(\overline{WJYS}, \sigma_{WJYS}, \overline{BMYS}, \sigma_{BMYS}), \quad (5)$$

is an average value for 50% of the reliability estimate and for a single way of failure, only.

The lower limit for reliability R_L , with introducing the number of samples n and confidence limit h_γ , is calculated according to the following expressions:

$$R_L = \Phi(m'_1), \quad (6)$$

$$m'_1 = m_1 + \frac{h_\gamma}{n^{1/2}} \left(1 + \frac{m_1^2}{2}\right)^{1/2}, \quad (7)$$

$$R_L = R_L(\overline{WJYS}, \sigma_{WJYS}, \overline{BMYS}, \sigma_{BMYS}, h_\gamma, n). \quad (8)$$

Figure 7 presents the schematics of distribution of the base metal yield stress, weld metal fatigue strength and base metal fatigue strength. Based on schematics in Fig. 7, the welded joint properties weakening, reliability and weldability can be quantified.

5 The Welded Joint Validity Coefficient

Every test of a certain welded joint (WJ) property – resistance to some failure and comparison to the corresponding base metal (BM) property, is a part of the weldability investigation.

If the individual fixed values are being compared, one obtains indicators of the welded joint validity or exploitation of the base metal properties. The lower the weakening, namely the bigger the welded joint validity coefficient, the weldability is better:

$$v = \frac{\text{Properties of the welded joint}}{\text{Properties of the base metal}} = \frac{WJ}{BM}. \quad (9)$$

Considering that the WJ and BM are the random variables, distributed according to a certain distribution law (Fig. 13), the validity coefficient (v) is a random variable, as

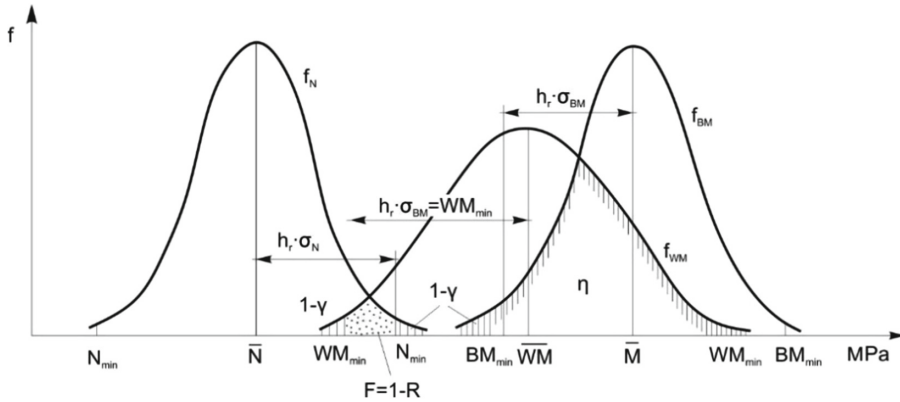


Fig. 7. Schematics of the base metal yield stress distribution (\overline{BMYS} , σ_{BMYS}), weld metal fatigue strength (\overline{WJ} , σ_{WJ}) and fatigue strength of the base metal (\overline{BM} , σ_{BM}).

well. It is usually defined with certain confidence limits and assumption of the normal distribution for a single failure:

$$\nu = \frac{WJ_{min}}{BM_{min}} = \frac{WJ_y}{BM_y} = \frac{\overline{WJ} - h_\gamma \cdot \sigma_{WJ}}{\overline{BM} - h_\gamma \cdot \sigma_{BM}}. \quad (10)$$

Values σ_{WJ} and σ_{BM} are estimates of the standard deviations of the basic sets of welded joint and base metal properties. Values of the h_γ coefficient depend on the required estimate of reliability. For the standardized normal distribution, they are given in Table 1.

Table 1. Recommended values of reliability h_γ in terms of welded joint quality [26]

Reliability estimate γ (%)	h_γ	Welded joint quality level
99.86	3.0	“B”
99.0	2.33	“C”
95.0	1.65	“D”
90.0	1.28	Engineering practice

The validity coefficient ν can be calculated for some other characteristic pairs of properties, like the average values of the WJ and BM properties, or WJ minimal and maximal properties and yield stress (WJYS).

$$\bar{\nu} = \frac{\overline{WJ}}{\overline{BM}}; \nu = \frac{WJ_{min}}{BMYS_{max\ min}}; \nu = \frac{WJ_{max}}{BMYS_{min\ max}}. \quad (11)$$

In a similar manner, one can define the calculated safety degree for the welded joint S_{WJ} and the base metal S_{BM} :

$$S_{WJS} = \frac{WJ_{min}}{BMYS_{max}}; S_{BM} = \frac{BM_{min}}{BMYS_{max}}. \quad (12)$$

In the design of the bucket wheel excavators, one usually uses the safety degree and the weakening coefficients of the welded joints and thus of the welded structures, as well and their experimental verification is usually not required.

Example: Evaluation of the welded joint strength on the bucket wheel excavator SRs 2000 20/5 after 10 years of exploitation

Evaluation of the WJ strength can be equated with the reliability estimate, given here for the bucket wheel excavator SRs 2000 20/5 (manufactured by “Thyssen Krupp” of Germany) (Fig. 8). Based on the test results of the BM and WJ mechanical properties, as well as analysis of flaws discovered by the non-destructive tests in the weld metal of joints made by welding process 111 (SMAW), on the vital constructions of the bucket wheel excavators made of the S235 and S335 steels, the probabilistic model of the reliability calculation, based on the WJ properties, is presented.

By applying Eq. (3), the following relationship between the mean value of the welded joint yields stress \overline{WJYS} and the standard deviation $\sigma_{WJYS} = f(\overline{WJYS})$ can be established. Results of the $(\overline{WJ}, \sigma_{WJ})$ properties investigations are entered into the diagram in Fig. 15 and the level of reliability, namely the level of quality, to which they correspond is being determined. Categories of vital welded structures are denoted by the Roman numerals I through IV (the rest belong to “engineering practice”) and classes of the WJ validity are denoted by the Arabic numbers 1 to 7 (Fig. 9).

Three sets of welded joints are being depicted, which belong to the validity classes “B” (1–3), “C” (4–5) and “D” (6–7). Belonging of a point to a higher level of reliability (the smaller value of the weld weakening coefficient), expressed by the reliability coefficient of reliability m_2 , corresponds to the higher validity coefficient of the welded joint v .

The welded joint weakening coefficient η can be expressed as a numerical probability, with given confidence limits that the WJ properties would be equal to or better than the BM properties. As it is possible to use the numerical probability for reliability R , one can also use the numerical probability for the welded joint weakening coefficient η instead of the welded joint validity coefficient, for a certain way of failure.

When the WJ and BM properties are given by the normal distribution law, analytical expression for value of the weakening coefficient can be obtained in the usual way:

$$\eta = \int_{m_2}^{\infty} f(t)dt = \frac{1}{\sqrt{2\pi}} \int_{m_2}^{\infty} e^{-\frac{t^2}{2}} dt = \Phi(m_2) \quad (13)$$

$$m_2 = -\frac{\overline{WJ} - \overline{BM}}{(\sigma_{WJ}^2 + \sigma_{BM}^2 - 2 \cdot \rho \cdot \sigma_{WJ} \cdot \sigma_{BM})^{1/2}} \quad (14)$$

$$\sigma_{WJ} = \frac{(\overline{WJ}^2 - 2\overline{BMYS} \cdot \overline{WJ} + \overline{BMYS}^2 - m^2 \cdot \sigma_{YS}^2)^{1/2}}{m^2} = f(\overline{WJ}), \quad (15)$$



Fig. 8. The bucket wheel excavator SRs 2000 20/5 in exploitation, Kostolac (Serbia)

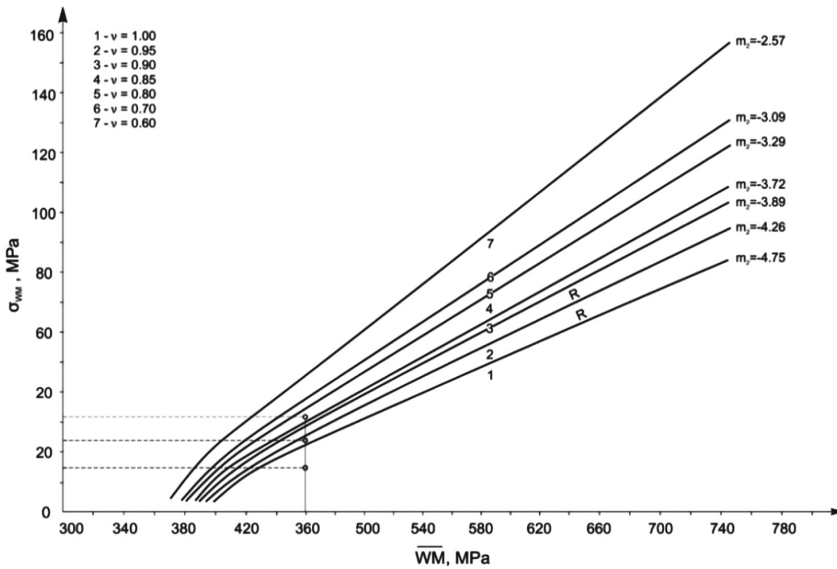


Fig. 9. Influence of the WJ properties on reliability $R(m_2)$, according to Eq. (3)

with ρ being the correlation coefficient between the WJ and BM properties,

$$\eta_{50\%} = \eta(\overline{WJ}, \sigma_{WJ}, \overline{BM}, \sigma_{BM}, \rho). \quad (16)$$

It is also possible to calculate the lower limit of the welded joint weakening, introducing the confidence limits m'_2 and the minimal number of samples n for the WJ and BM properties.

$$\eta_L = \Phi(m'_2) \quad (17)$$

$$m'_2 = m_2 + \frac{h_\gamma}{n^{1/2}} \left(1 + \frac{m_2^2}{2} \right)^{1/2} \quad (18)$$

$$\eta_L = \eta_L(\overline{WJ}, s_{WJ}, \overline{BM} s_{BM}, \rho, n, \gamma). \quad (19)$$

Based on laboratory investigations of the workshop and in-situ executed WJ and their comparison to the initial or the current BM properties, the weldability indicators can be obtained.

If the BM properties are known (\overline{BM} , σ_{BM}), the weakening coefficient of the welded joint η would then numerically represent the WJ weakening. Values of η will be 0.5 when the properties of the WJ and BM are equal ($\overline{WJ} = \overline{BM}$), thus the value for η can be expected within limits 0–0.5 [31]. The equality $WJ \overline{WJ}_{\gamma_{\min}}$ should be additionally checked.

Example: Evaluation of the welded joint strength on the bucket wheel excavator SCh Rs 1400 28/3 during the assembly

The tensile strengths of the BM and WJ, executed by the welding procedure 111 of structures made of the S235 and S335 steels, can be considered according to the normal or Weibull distribution [27], as presented for the bucket wheel excavator SCh Rs 1400 28/3 (produced by “Thyssen Krupp” of Germany) (Fig. 10).



Fig. 10. Bucket wheel excavator Sch Rs 1400 - 28/3 during the assembly, Kostolac (Serbia)

Reliability of the welded joint R , expressed by the weakening coefficient η , or by the reliability coefficient m_2 , for the case of the strong correlation between the tensile strengths of the WJ and BM, namely for the correlation coefficient $\rho = 1$ (though experimental results have shown that the correlation depends on the welding parameters and is within limits from $\rho = 0.75$ to $\rho = 0.85$ [32]) and for medium values of the BM

and WJ tensile strengths, smaller than $\bar{R}_{mbm} = 600$ MPa and $\bar{R}_{mwj} = 590$ MPa for their standard deviations $\sigma_{BM} = 26$ MPa and $\sigma_{WJ} = 33$ MPa, will amount to:

$$\begin{aligned} m_2 &= - \frac{\bar{R}_{mWJ} - \bar{R}_{mBM}}{(\sigma_{WJ}^2 + \sigma_{BM}^2 - 2 \cdot \rho \cdot \sigma_{WJ} \cdot \sigma_{BM})^{\frac{1}{2}}} \\ &= - \frac{590 - 600}{(32^2 + 26^2 - 2 \cdot 1 \cdot 32 \cdot 26)^{\frac{1}{2}}} = 0.20, \end{aligned} \quad (20)$$

with $\eta_{50\%}(m_2) = \eta_{50\%}(0.20) = 0.42$ from the tables of standardized normal distribution.

By establishing changes of mechanical properties of the base metal and the welded joints of structures during the exploitation, by varying the large numbers of influential factors and reducing the undesirable effects to the acceptable values, one can realize the favorable design solution of a bucket wheel excavator as a whole. This paper represents a good basis for creating such a database, a structure of which is presented in Fig. 11.

Application of the presented method also enables efficient reparation and revitalization of the bucket wheel excavator, with savings in the invested labor and reducing the production losses due to shortening the excavator's downtime. The efficient investigation of the welded joints, during the manufacturing, acceptance tests and mounting of the new welded structures, are enabled, as well. In that way, the structure can be monitored during all of the exploitation periods with satisfactory reliability.

6 Conclusions

The method presented in this paper is an efficient and reliable tool to evaluate and improve the safety of vital welded structures of the bucket-wheel excavators, as well as to determine the causes of their failure during the exploitation. The probabilistic and semi-probabilistic approaches are defined for expressing the validity coefficient (ν), weakening coefficient (η) and reliability (R), as measures of reliability in the exploitation of the welded structures, mounted to the bucket wheel excavators. The applied fault tree method enabled qualitative and quantitative analysis of the causes of the welded joint failures and the creation of the corresponding database, which contributes to increasing the bucket wheel excavators' reliability. If still the damage occurs, the data from the proposed database (Fig. 11) can be used to do the reparation of the structure with minimal costs and losses.

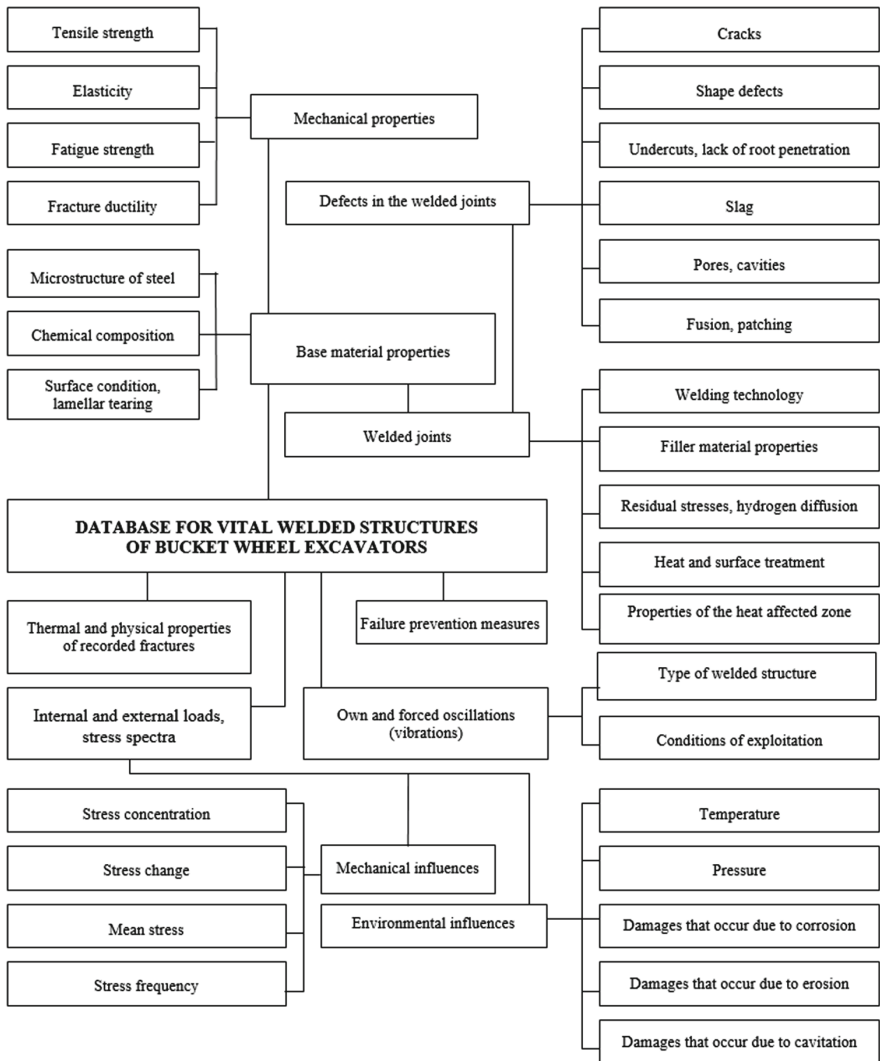


Fig. 11. Database structure for vital welded structures of the bucket wheel excavators

Acknowledgement. This work was supported by the Ministry of Education, Science and Technological Development of the Republic of Serbia through grant TR35024 and by the project “Innovative Solutions for Propulsion, Power and Safety Components of Transport Vehicles” ITMS 313011V334 of the Operational Program Integrated Infrastructure 2014–2020 and co-funded by the European Regional Development Fund.

References

1. Bošnjak, S., Arsić, M., Zrnić, N., Rakin, M., Pantelić, M.: Bucket wheel excavator: integrity assessment of the bucket wheel boom tie-rod welded joint. *Eng. Fail. Anal.* **18**, 212–222 (2011). <https://doi.org/10.1016/j.engfailanal.2010.09.001>
2. Arsić, M., Bošnjak, S., Zrnić, N., Sedmak, A., Gnjatović, N.: Bucket wheel failure caused by residual stresses in welded joints. *Eng. Fail. Anal.* **18**, 700–712 (2011). <https://doi.org/10.1016/j.engfailanal.2010.11.009>
3. Bošnjak, S., Zrnić, N., Simonović, A., Momčilović, D.: Failure analysis of the end eye connection of the bucket wheel excavator portal tie-rod support. *Eng. Fail. Anal.* **16**, 740–750 (2009). <https://doi.org/10.1016/j.engfailanal.2008.06.006>
4. Bošnjak, S., Arsić, M., Gnjatović, N., Milenović, I., Arsić, D.: Failure of the bucket wheel excavator buckets. *Eng. Fail. Anal.* **84**, 247–261 (2018). <https://doi.org/10.1016/j.engfailanal.2017.11.017>
5. Bošnjak, S., Arsić, M., Savićević, S., Milojević, G., Arsić, D.: Fracture analysis of the pulley of a bucket wheel boom hoist system. *Eksplotacija i Niezawodność. Maint. Reliab.* **18**, 155–163 (2016). <https://doi.org/10.17531/ein.2016.2.1>
6. Arsić, D., Gnjatović, N., Sedmak, S., Arsić, A., Uhrčik, M.: Integrity assessment and determination of residual fatigue life of vital parts of bucket wheel excavator operating under dynamic loads. *Eng. Fail. Anal.* **105**, 182–195 (2019). <https://doi.org/10.1016/j.engfailanal.2019.06.072>
7. Đurđević, Đ., Sedmak, S.A., Đurđević, A., Anđelić, N., Maneski, T.: Development and calculation of supporting structure for mining power equipment. *Struct. Integr. Life* **21**, 173–177 (2021)
8. Bartelmus, W., Zimroz, R.: A new feature for monitoring the condition of gearboxes in non-stationary operating conditions. *Mech. Syst. Signal Process.* **23**, 28–34 (2009)
9. Lazarević, Ž., Arandelović, I., Kirin, S.: An analysis of random mechanical failures of bucket wheel excavator. *Struct. Integr. Life* **15**, 143–146 (2015)
10. Daničić, D., Sedmak, S., Blačić, I., Kirin, S.: Scenario of fracture development in bucket wheel excavator. *Struct. Integr. Life* **13**, 189–196 (2013)
11. Arsić, M., Flajs, Z., Sedmak, A., Veg, E., Sedmak, S.: Structural integrity assessment of welded bucket-wheel boom. *Struct. Integr. Life* **21**, 201–206 (2021)
12. Arsić, M., Bošnjak, S., Odanović, Z., Dunjić, M., Simonović, A.: Analysis of the spreader track wheels premature damages. *Eng. Fail. Anal.* **20**, 118–136 (2012). <https://doi.org/10.1016/j.engfailanal.2011.11.005>
13. Tanasković, D., Tatić, U., Đorđević, B., Sedmak, S., Sedmak, A.: The effect of cracks on stress state in crane wheel hard-surface under contact loading. *Tehnički Vjesnik. Technical Gazette* **24**, 169–175 (2017). <https://doi.org/10.17559/TV-20151227221434>
14. Moczko, P., Pietrusiak, D., Wieckowski, J.: Investigation of the failure of the bucket wheel excavator bridge conveyor. *Eng. Fail. Anal.* **106**(104180) (2019), <https://doi.org/10.1016/j.engfailanal.2019.104180>
15. Kačmarčík, J., Hadžalić, M., Konjatić, P.: Structural integrity assessment of a mine hoist rope attachment element with a crack. *Struct. Integr. Life* **21**, 59–64 (2021)
16. Arandelović, M., et al.: Numerical simulation of welded joint with multiple various defects. *Struct. Integr. Life* **21**, 103–107 (2021)
17. Petrović, A., Ignjatović, D., Sedmak, S., Milošević-Mitić, V., Momčilović, N., Trišović, N., Jeremić, L.: Model analysis of bucket wheel excavator SchRs 630 strength. *Eng. Fail. Anal.* **126**(105451) (2021). <https://doi.org/10.1016/j.engfailanal.2021.105451>
18. Jovančić, P., Ignjatović, D., Tanasijević, M., Maneski, T.: Load-bearing steel structure diagnostics on bucket wheel excavator, for the purpose of failure prevention. *Eng. Fail. Anal.* **18**, 1203–1211 (2011). <https://doi.org/10.1016/j.engfailanal.2011.03.001>

19. Arsić, D., et al.: Analysis of the cause of the girth gear tooth fracture occurrence at the bucket wheel excavator. *Transp. Res. Procedia* **40**, 413–418 (2019). <https://doi.org/10.1016/j.trpro.2019.07.060>
20. DIN 22261-3, Excavators, spreaders and auxiliary equipment in opencast lignite mines - Part 3: Execution of steel structures. German National Standard (2015)
21. SRPS EN ISO 17640:2019: Non-destructive testing of welds - Ultrasonic testing - Techniques, testing levels, and assessment
22. SRPS EN ISO 5817: Welding - Fusion-welded joints in steel, nickel, titanium and their alloys (beam welding excluded) - Quality levels for imperfections, European Committee for Standardization (2014)
23. Arsić, M., Arsić, D., Flajs, Ž, Grbović, A., Todić, A.: Application of non-destructive testing for condition analysis, repair of damages and integrity assessment of vital steel structures. *Russ. J. Nondestr. Test.* **57**, 918–931 (2021). <https://doi.org/10.1134/S1061830921100053>
24. EN 10025-2, Hot rolled products of structural steels - Part 2: Technical delivery conditions for non-alloy structural steels, European Committee for Standardization (2011)
25. Ericson, C.: Fault tree analysis—a history. In: *Proceedings of the 17th International System Safety Conference*, System Safety Society of the US, pp. 1–9. Seattle, Washington, USA (1999)
26. Stamatelos, M., Vesely, W.: *Fault tree handbook with aerospace applications*. NASA Office of Safety and Mission Assurance NASA Headquarters, p. 20546. Washington, DC (2002)
27. Ušakov, I.A.: *Handbook of reliability engineering*. Willey, USA (1994)
28. Arsić, D., Kirin, S., Nikolić, R., Arsić, A., Radović, L.: Probabilistic approach and fault-tree analysis for increased bucket wheel excavator welded joints' reliability. *Procedia Struct. Integr.* **42**, 189–195 (2022). <https://doi.org/10.1016/j.prostr.2022.12.023>
29. Sedmak, A., Hemer, A., Sedmak, S.A., Milović, Lj., Grbović, A., Čabrilo, A., Kljajin, M.: Welded joint geometry effect on fatigue crack growth resistance in different metallic materials. *Int. J. Fatigue* **150**(106298) (2021). <https://doi.org/10.1016/j.ijfatigue.2021.106298>
30. Paris, P.C., Erdogan, F.: A critical analysis of crack propagation laws. *J. Basic Eng.* **D85**, 528–534 (1963)
31. Papić, Lj., Pantelić, M.: Implementation methodology for risk minimization into maintenance process of production system at coal mines. Report of Contract No. 4617, DQM Research Center-Kolubara Metal, Prijedor-Vreoci (in Serbian), p. 468. (2009)
32. Rakin, M., Arsić, M., Bošnjak, S., Gnjatović, N., Medo, B.: Integrity assessment of bucket wheel excavator welded structures by using the single selection method. *Tehnički Vjesnik – Technical Gazette* **20**, 811–816 (2013)



Risk Management of Foreign Trade Financing of Bosnia and Herzegovina

Dragana Vujičić Stefanović, Boško Mekinjić, and Dragan Milovanović^(✉)

Faculty of Economics, University of Banja Luka, Majke Jugovića 4, 78000 Banja Luka, Bosnia and Herzegovina

dragan.milovanovic@ef.unibl.org

Abstract. The great wave of changes that began in 2008 with the great economic crisis, continued with the migrant crisis and the COVID 19 crisis, until the events in Ukraine and major geopolitical changes. All this caused enormous tectonic upheavals in the spheres of foreign trade affairs and initiated the need for risk management. In such conditions, the problem of financing foreign trade deals attracts special attention. The aim of the work is to point out the model of optimization of sources of financing foreign trade operations. In our work, we performed modeling in order to optimize the sources of financing foreign trade operations in Bosnia and Herzegovina. Modeling of sources of financing of foreign trade affairs of Bosnia and Herzegovina was carried out on the basis of the simplex model. The results of the research show the necessity of optimizing the sources of financing, as an important segment of the risk management of the financing of Bosnia and Herzegovina.

Keywords: Risk management · Foreign trade · Financing

1 Introduction

In addition to yield, which is the main motive for investment and foreign trade, there is another side related to uncertainty and that a positive result is not guaranteed. This becomes especially important when considering foreign trade transactions at a time of global geopolitical changes taking place today. There is always the danger that there will be no return or that there will be a change or even a fall in prices. The risk speaks of this danger and probability. In the modern world, raising national competitiveness is based on improving the business environment, which should enable an increase in the volume of foreign trade transactions. Foreign trade deals are international transactions of goods, services and intellectual property contracted between legal entities based in different countries, and the basis of a foreign trade deal is the export or import of goods [1].

Business entities engaged in foreign trade need financial resources in order to successfully carry out foreign affairs with foreign partners. The subject of research belongs to the field of risk optimization. The aim of the research is to identify the specifics of the risk management of financing foreign trade operations, to investigate the legality

of financing and their impact on foreign trade operations. The goal is also to perform modeling based on the simplex model. The financing of foreign trade operations is gaining more and more importance, especially at a time when capital knows no borders and export represents one of the basic factors of business competitiveness [2].

Certainly, these forms of financing carry with them certain doses of risk. In the simplest terms, risk is the probability of suffering loss, damage or injury. It is a very complex and multidimensional concept that manifests itself in different ways and in different forms. On the basis of the above, we can confirm the research hypothesis of Ho that, "Risk management implies the optimal combination of sources of financing foreign trade operations in Bosnia and Herzegovina at the most favorable cost of capital". In general, it is considered that all subjects in relation to risk can be divided into three categories - those who love risk and are ready for anything, those who are indifferent or indifferent and those who are averse, that is, they do not like risk. The aim of the work is to develop a risk management model and to model the sources of financing foreign trade operations.

2 Review of Literature Through Previous Research

Globalization processes, major economic crises, business turbulence, migration movements and other processes have significantly affected the other side of foreign trade financing, namely risks. In general, we can say that as much as the possibilities of financing and the number of factors that influence financing increase, the situation in terms of risk and risk management of foreign trade financing becomes more complicated [1]. Risk represents any uncertain situation, that is, possible loss as a result of uncertain events [3–5]. Over time, various methods of risk management have emerged, from classic risk analysis to more modern quantitative methods for risk assessment that are used today by large international banks. The use of complicated methods, i.e. models for risk management, requires the engagement of larger financial resources, but it brings greater precision in risk assessment, thus contributing to the stability and security of business. All participants in risk management cooperate with each other in the adoption of the most important policies and their implementation. A necessary condition for a possible risk assessment is a clear definition of goals, so the company has a clear idea of which way it is going and where it wants to get to [6].

In the first chapters of the ISO 31000 standard, the usual elements of risk management are given, and they include several segments, risk management must create new and protect existing value, risk management must be an integral part of organizational processes, risk management must be part of the decision-making process, risk management must explicitly show uncertainty, risk management must be a systematic, structured and timely process, risk management must be based on the best possible available information, the risk management system must be appropriate for the organization, risk management must take into account human and cultural factors, risk management must be transparent and comprehensive process, risk management must be dynamic, iterative and sensitive to changes and the risk management system must be capable of continuous improvement and improvement [7, 8].

The process of risk management, as well as its development, differs from country to country as well as from organization to organization. These differences are conditioned

primarily by the degree of development of management culture (knowledge and skills), the size and needs of the organization itself [6]. In the practice of risk management, quantitative methods are mostly used, where it is possible to quantify the probability of a harmful event. In addition, in recent times, qualitative methods are widely used, which serve when decision-making about risks cannot be quantified, and other models are used instead. Also, qualitative risk management models are often used as a complement to quantitative models. According to the OECD guidelines, when developing their national standards, countries generally follow the risk management standards recommended by COSO and Turnbull [9]. According to the OECD guidelines, the mentioned models do not provide a sufficiently clear approach to solving problems in real conditions, the shortcomings are primarily reflected in: lack of connection between risk and strategy, definitions of individual risks are often short and insufficiently clear, interest in ensuring the correctness of the risk management process is not sufficiently developed, and another. Figueira-de-Lemos et al. [10] point to internal risk factors that can affect foreign trade operations and thus financing, such as management, internal sources of financing, international strategy business, etc., as well as external ones related to market trends, international economic relations, and related to country risk, risk of interest rate changes, currency risks, inflation risk and others [10].

They can appear independently of the actions of any party in the business, but they can also be a consequence of the subjective actions of the participants in the business [1]. If problems arise in the execution of foreign trade affairs, which are beyond the reach and influence of the decision maker, in that case it is a risk of force majeure, which is based on objective circumstances [11]. In that case, insurance against this type of risk with insurance organizations is recommended. A large number of participants, in itself, also carries great risks that affect the success of the foreign trade business. Risks in foreign trade business can be divided into [1, 5], risks to which the exporter is exposed, risks to which the importer is exposed and risks to which the financial institution that lends or finances the foreign trade business is exposed.

Commercial and non-commercial risks of foreign trade transactions are often classified in practice [12]. The most important risks of financing foreign trade operations can be seen in the following, risks in international lending, risks in international factoring, risks in international forfeiting and risks of self-financing foreign trade operations [13]. In banking-oriented systems, such as in Bosnia and Herzegovina, loans are often the source of financing that is most used in the financing of foreign trade operations. In cases where banks lend to importers, they are secured by bank guarantees issued by export agencies in favor of banks or by a lien on imported goods [14]. However, trends in the EU and the world show that credit-based export financing is greatly reduced [15], Report to the U.S. Congress on Global Export Credit Competition [16].

In many areas of the economy, including foreign trade, the field of risk management has developed as a separate scientific segment. The most common risks to which the exporter is exposed during the implementation of the contract are the risks of non-payment of the delivered goods, which can happen when delivering goods before payment or when delivering goods on credit [1, 12, 17]. On the other hand, the importer can take the risk of paying the agreed advance part, without the delivery even taking place, then paying properly for the goods, which do not correspond to the agreed properties or

do not function in the agreed way [1, 12]. The amount of the loan represents a significant factor, which can generate numerous risks, such as liquidity risk, solvency risk and other risks associated with the exporter or importer who borrows. The risks associated with that issue in the case of fixed interest are linked to the risk of paying a higher cost of capital, if the market interest rate falls in the long term [12]. On the other hand, the factoring contract implies that one contracted party (assignor of claims undertakes to transfer to the other contracted party (the factor current or future claims from the basic business and to pay a commission and interest specified in the contract for the factoring services performed, while on the other the factor undertakes to collect the assigned claim or to perform other factoring services [18, 19].

In the case of factoring with recourse, the factor addresses the client (seller) if the receivables become bad, i.e. if the client does not pay when it is due or if payments start to fall behind [12]. On the other hand, if it is about self-financing export business, a very important issue is the issue of delivery, time period, quantity, timing and quality of delivery of goods.

3 Research Methodology

In order to identify the key segments of risk management for the financing of foreign trade operations in Bosnia and Herzegovina, we analyzed lending factors, factoring factors and factors of self-financing of foreign trade operations. In the first step, we investigated the parameters of the foreign trade policy of Bosnia and Herzegovina, regarding the state of imports and exports. Appropriate dataset with verifiable data source used in research based on database from <https://tradingeconomics.com> which uses data directly from the Central Bank of Bosnia and Herzegovina. The research was carried out in 2023. The period of analysis referred to the last ten years, that is, from 2013 to 2023 (Figs. 1, 2 and 3).

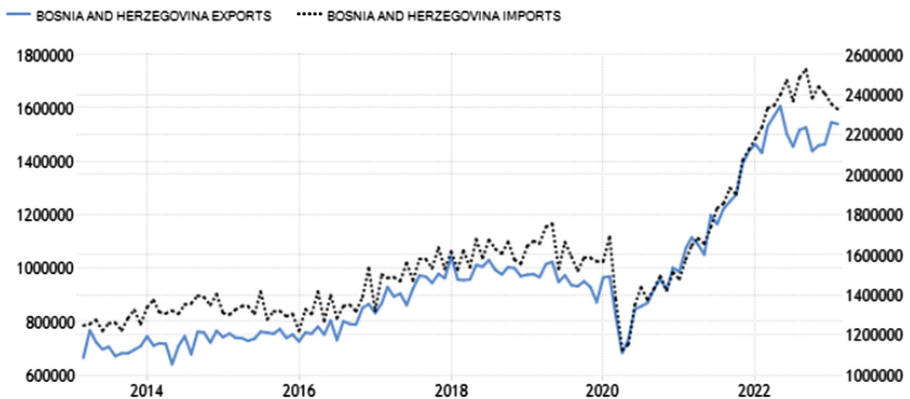


Fig. 1. Research on the relationship between exports and imports in Bosnia and Herzegovina in the period 2013–2023. The author's research is based on <https://tradingeconomics.com>

On the basis of previous data that will also serve us for modeling risk management, we observe a constant intertwining of imports and exports in Bosnia and Herzegovina.

In the last two years, there has been a trend of growth in exports compared to imports. This trend is positive and has positive effects on the foreign trade balance of Bosnia and Herzegovina.

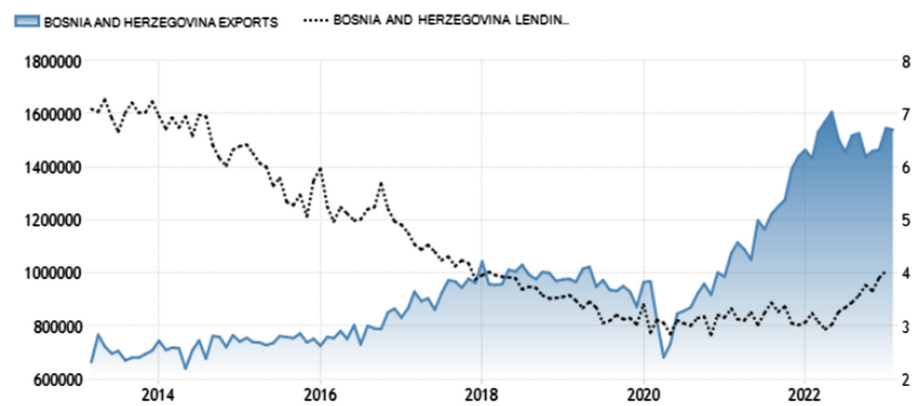


Fig. 2. Research on the relationship between the level of interest rates and exports of Bosnia and Herzegovina in the period 2013–2023. The author’s research is based on <https://tradingeconomics.com>

Based on previous data, it is evident that the level of interest rates on loans in Bosnia and Herzegovina has been constantly decreasing since 2014 until 2020. Most of the loans were placed with a fixed interest rate. After 2022, there will be an increase in interest rates, and the placement of loans with a variable interest rate. This is also a consequence of the growth of the Euribor in that period.

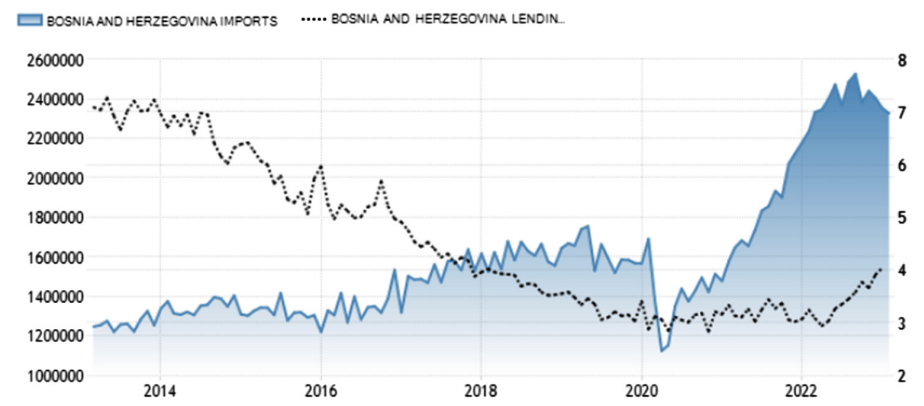


Fig. 3. Research on the relationship between the level of interest rates and imports of Bosnia and Herzegovina in the period 2013–2023. The author’s research is based on <https://tradingeconomics.com>

In order to have high risk management effects, it is necessary to optimize the sources of financing foreign trade operations. Let the linear programming model be given in canonical form [20]:

$$\begin{aligned}
 (1) \text{ (MINIMIZE) } Z &= c_1x_1 + c_2x_2 + \dots + c_nx_n, \\
 a_{11}x_1 + a_{12}x_2 + \dots + a_{1n}x_n &= b_1, \\
 a_{21}x_1 + a_{22}x_2 + \dots + a_{2n}x_n &= b_2, \\
 &\vdots \\
 &\vdots \\
 &\vdots \\
 a_{m1}x_1 + a_{m2}x_2 + \dots + a_{mn}x_n &= b_n, \quad x_1, x_2, \dots, x_n \geq 0,
 \end{aligned}$$

The extended canonical form of the model is given in the following form [20]:

$$\begin{aligned}
 (2) \text{ (MAXIMIZE) } Z &= c_1x_1 + c_2x_2 + \dots + c_{ix}i + \dots + c_nx_n \\
 a_{11}x_1 + a_{12}x_2 + \dots + a_{1ix}i + \dots + a_{1n}x_n &\leq b_1, \\
 &\vdots \\
 &\vdots \\
 &\vdots \\
 a_{j1}x_1 + a_{j2}x_2 + \dots + a_{jix}i + \dots + a_{jn}x_n &\leq b_j, \\
 &\vdots \\
 &\vdots \\
 &\vdots \\
 a_{m1}x_1 + a_{m2}x_2 + \dots + a_{mnx}n + \dots + a_{mn}x_n &\leq b_m,
 \end{aligned}$$

The results of research into the banking sector of Bosnia and Herzegovina show that the annual effective interest rate for financing export and import operations in 2022 in the amount of 100,000.00 BAM and a period of 10 years was at the level of 7%. Research into factoring services by banks in Bosnia and Herzegovina shows that the annual interest rate of factoring was at the level of 5.5%, and that they are used at the level of only 0.3%. Also, the results of the research show that a part of business entities in Bosnia and Herzegovina also use funds from EU funds, through various incentives, programs and projects that are available through development agencies. Research in local agencies and state agencies showed that the share of financing on this basis amounts to only 0.1%, and that their cost is 2%. However, these resources are not free either. You first need to meet high criteria to get funding or make the necessary adjustments to meet the criteria.

Based on the project documentation, they are at the level of 0.01%. The stated results for projects are the result of sampling and practice of development agencies in Bosnia and Herzegovina. In addition to the above, many business entities also use self-financing of certain projects. Even self-financing is not free, given that certain operational activities are required, which causes certain operational costs. On the other hand, there is also opportunity cost, cost of lost opportunity and others. In connection with the previous situation and the research of the situation in Bosnia and Herzegovina, we performed modeling in order to find a risk management model through the optimal combination of sources of financing in Bosnia and Herzegovina. When creating the model, we used the

golden balance rule as a base, where the ratio of our own and other sources of financing (1:1 rule) should be up to an even level.

4 Research Results

Risk management requires consideration of a large number of factors that influence the optimization of financing sources. Certainly, looking at the factors of the model and their further modeling provides the basis for a high level of risk management. The research is of great importance, given that it is about Bosnia and Herzegovina, which has a more pronounced country risk compared to other EU countries. In addition to country risks, there are company risks, as well as part of the risk at the level of held securities. In the following, we carried out optimization and risk analysis, based on the created mathematical model of the optimization of foreign trade financing sources:

(The objective function) (MINIMIZE): $Z = 0,07 X1 + 0,055 X2 + 0,02 X3 + 0,0001 X4$.

Model limitations:

$$\begin{array}{rclclclclcl} X1 & & + & & X2 & & + & & X3 & + & & X4 & & = & & 1 \\ X1 & & & & & & & & & & & & & & \leq & & 0,496 \\ & & X2 & & & & & & & & & & & & \leq & & 0,003 \\ & & & & X3 & & & & & & & & & & \leq & & 0,001 \\ & & & & & & X4 & & & & & & & & \leq & & 0,500 \end{array}$$

$$X1, X2, X3, X4 \geq 0$$

Variables that build the methodological concept of research:

- X1–share of foreign trade financing based on loans, at a rate of 7%
- X2–share of financing foreign trade operations based on factoring at a rate of 5.5%
- X3–share of foreign trade financing based on financing through EU projects and funds (2%)
- X4–share of financing of foreign trade operations based on self-financing (0.01%)

Below is the solution of the optimization model in the risk management function based on the simplex table.

Extended (Canonical) model:

(The objective function) (MAXIMIZE): $Z = - 0,07 X1 - 0,055 X2 - 0,02 X3 - 0,0001 X4 + 0 X5 + 0X6 + 0X7 + 0X8 + 0X9$

Model limitations:

$$\begin{aligned}
 &X_1 + X_2 + X_3 + X_4 + X_9 = 1 \\
 &X_1 + X_5 = 0,496 \\
 &X_2 + X_6 = 0,003 \\
 &X_3 + X_7 = 0,001 \\
 &X_4 + X_8 = 0,500 \\
 &X_1, X_2, X_3, X_4, X_5, X_6, X_7, X_8, X_9 \geq 0
 \end{aligned}$$

The solution was obtained in the sixth iteration of the simplex table.

Table 1 Modeling in the function of risk management

			0	0	0	0	0	0	0	0	−1
Base	Cb	P ₀	P ₁	P ₂	P ₃	P ₄	P ₅	P ₆	P ₇	P ₈	P ₉
P ₉	−1	1	1	1	1	1	0	0	0	0	1
P ₅	0	0.496	1	0	0	0	1	0	0	0	0
P ₆	0	0.003	0	1	0	0	0	1	0	0	0
P ₇	0	0.001	0	0	1	0	0	0	1	0	0
P ₈	0	0.5	0	0	0	1	0	0	0	1	0
Z		−1	−1	−1	−1	−1	0	0	0	0	0

In the Table 1, modeling was performed in the function of risk management. The basic elements of the model are set. Modeling led to Table 2.

Table 2. Modeling in the function of risk management

			0	0	0	0	0	0	0	0	−1
Base	Cb	P ₀	P ₁	P ₂	P ₃	P ₄	P ₅	P ₆	P ₇	P ₈	P ₉
P ₉	−1	0.504	0	1	1	1	−1	0	0	0	1
P ₁	0	0.496	1	0	0	0	1	0	0	0	0
P ₆	0	0.003	0	1	0	0	0	1	0	0	0
P ₇	0	0.001	0	0	1	0	0	0	1	0	0
P ₈	0	0.5	0	0	0	1	0	0	0	1	0
z		−0.504	0	−1	−1	−1	1	0	0	0	0

In Table 2, the modeling is continued, where the value of Z is obtained at the level of −0.504. The achieved result is the result of modeling in 2 iterations.

Table 3. Modeling in the function of risk management

			0	0	0	0	0	0	0	0	−1
Base	Cb	P ₀	P ₁	P ₂	P ₃	P ₄	P ₅	P ₆	P ₇	P ₈	P ₉
P ₉	−1	0.501	0	0	1	1	−1	−1	0	0	1
P ₁	0	0.496	1	0	0	0	1	0	0	0	0
P ₂	0	0.003	0	1	0	0	0	1	0	0	0
P ₇	0	0.001	0	0	1	0	0	0	1	0	0
P ₈	0	0.5	0	0	0	1	0	0	0	1	0
z		−0.501	0	0	−1	−1	1	1	0	0	0

Table 3 continues the modeling towards the final value of the objective function. in the third iteration, its value was −0.501.

Table 4. Modeling in the function of risk management

			−0.07	−0.055	−0.02	−0.0001	0	0	0	0
Base	Cb	P ₀	P ₁	P ₂	P ₃	P ₄	P ₅	P ₆	P ₇	P ₈
P ₄	−0.0001	0.5	0	0	0	1	−1	−1	−1	0
P ₁	−0.07	0.496	1	0	0	0	1	0	0	0
P ₂	−0.055	0.003	0	1	0	0	0	1	0	0
P ₃	−0.02	0.001	0	0	1	0	0	0	1	0
P ₈	0	0	0	0	0	0	1	1	1	1
z		−0.034955	0	0	0	0	−0.0699	−0.0549	−0.0199	0

Below in Table 4, modeling was performed with the aim of installing the final value. In doing so, a critical value was defined on variable P5 (Table 5).

Table 5. Modeling in the function of risk management

			−0.07	−0.055	−0.02	−0.0001	0	0	0	0
Base	Cb	P ₀	P ₁	P ₂	P ₃	P ₄	P ₅	P ₆	P ₇	P ₈
P ₄	−0.0001	0.5	0	0	0	1	0	0	0	1
P ₁	−0.07	0.496	1	0	0	0	0	−1	−1	−1
P ₂	−0.055	0.003	0	1	0	0	0	1	0	0
P ₃	−0.02	0.001	0	0	1	0	0	0	1	0
P ₅	0	0	0	0	0	0	1	1	1	1
z		−0.034955	0	0	0	0	0	0.015	0.05	0.0699

Based on the previous analysis, we obtained the final value of the objective function by modeling, at the level of $Z = 0.034955$.

The optimal solution value is $Z = 0.034955$.

With this structure of sources of financing for foreign trade operations, the minimum average cost of capital of 3.4955% is realized, the SRO creates the most favorable variant of risk management. On the basis of the above, we can confirm the hypothesis of H_0 that "Risk management implies the optimal combination of sources of financing for foreign trade operations at the most favorable cost of capital".

5 Conclusion

Risk management is a central part of the strategic management of every company, but also an integral part of every individual's life. The state of foreign trade policy parameters and results show a positive export trend, but the import trend has also increased. In such circumstances, the need for financing such activities grows, which carries great risks, which need to be managed. Modeling aimed at managing risks and optimizing the financing of foreign trade operations shows that the minimum cost of capital for financing foreign trade operations in Bosnia and Herzegovina is achieved at the amount of 0.034955. Given that risk is based on uncertainty, it is also based on perceptions of that uncertainty, as well as whether we have enough information that can be seen.

Risk management is a scientific approach to the problem of dealing with the full risks that are placed before the individual and the organization. Risk management implies a continuous process of constant monitoring of identified risks, but also the identification of new ones and their treatment. The need for risk management is the basic need for the market operation of the bank and the creation of a competitive advantage. It is particularly important to note that Bosnia and Herzegovina models its system of financial support for foreign trade operations on the model of its most important foreign trade partners. One of the reasons for this is the maintenance of the existing and potential increase of future foreign trade exchange with those countries. The management of any of the risks or the management of all risks requires the formulation of a strategy, policy and process for managing all risks in business.

The research results show that risks can be adequately managed by optimizing the sources of financing of Bosnia and Herzegovina's foreign trade operations, and that such a methodological approach is the basis of the model's basic platform. Certainly with major geopolitical changes on the world stage, risk management and the development of risk management models will gain even more importance in the future.

References

1. Kozomara, J.: Osnove međunarodnog poslovanja. Beograd, Ekonomski fakultet u Beogradu, Institut za međunarodnu politiku i privredu (2012)
2. Ghauria, P., Strange, R., LeeCooke, F.: Research on international business: the new realities. *Int. Bus. Rev.* **30**(2), 1–11 (2021)
3. Crouhy, M., Galai, D., Mark, R.: The Essentials of Risk Management. McGrawHill, New York (2004)

4. Damodaran, A.: Corporate Finance: Theory and Practice. Wiley Series, New York (2001). in Finance
5. Liesch, P.W., Welch, L.S., Buckley, P.J.: Risk and uncertainty in internationalization and international entrepreneurship studies. *Manag. Int. Rev.* **51**(6), 851–873 (2011)
6. Crouhy, M., Galai, D., Mark, R.: The Essentials of Risk Management. McGrawHill, New York (2008)
7. Visick, O.: Loan portfolio value. *Risk Magazine* (2002)
8. Salinger, F.: International factoring and conflicts of law. *Law Financ. Mark. Rev.* **1**(1), 7–10 (2007)
9. OECD: Corporate governance and the financial crisis Conclusions and emerging good practices to enhance implementation of the Principles. str.13–14 (2010)
10. Figueira-de-Lemos, F., Johanson, J., Vahlne, J.E.: Risk management in the internationalization process of the firm: a note on the Uppsala model. *J. World Bus.* **46**(2), 143–153 (2011)
11. Gray, E.R., Smeltzer, L.R.: Management. Mc Millan, New York (1989)
12. Miller, K.D.: A framework for integrated risk management in international business. *J. Int. Bus. Stud.* **23**(2), 311–331 (1992)
13. Fransis, J.C.: Investment: Analysis and Management. Mc Graw-Hill, New York (1991)
14. Olsen, M.G.: Banks in International Trade: Incomplete International Contract Enforcement and Reputation. Harvard University, mimeo (2011)
15. EXIM: Report to the U.S. Congress on Global Export Credit Competition (2021). <https://www.exim.gov>
16. Bessis, J.: Risk Management in Banking. A John Wiley & Sons Ltd, Publication, New Jersey (2011)
17. Saunders, A.: & Cornnett, M.M., Credit Risk Measurement: New Approaches to Value at Risk and Other Paradigms, 2nd edn. Wiley, New York (2005)
18. Klapper, L.: Export financing for SMEs: The role of factoring (World Bank Group Trade Note. No. 29). World Bank (2006)
19. Milošević, M.: Polymerization mechanics of dental composites-advantages and disadvantages. *Procedia Eng.* **149**, 313–320 (2016)
20. Ficken, F.A.: The Simplex Method of Linear Programming. Dover Publications, Harvard (2015) https://www.harvard.com/book/the_simplex_method_of_linear_programming_dover_books_on_mathematics/
21. Trading Economics. <https://tradingeconomics.com>



CAD/CAM Approach to Automation of the Production Process

Djordje Dihovicni¹(✉) and Milan Mišćević²

¹ The Academy of Applied Technical Studies Belgrade, Blv. Zorana Djindjica 152 a, 11070 New Belgrade, Serbia

djdihovicni@atssb.edu.rs

² Teximp d.O.O, 11070 Belgrade, Serbia

Abstract. This paper presents the application of Industry 4.0 in the production of machine parts using a CNC machine and an industrial robot. The functional structure of the flexible production cell, its configuration, programming methods and application in industry are explained in detail. The complete technology design was carried out using the ESPRIT software package, which involved selecting the processing system, introducing auxiliary accessories, selecting the required sequence of operations, defining the tool, defining the processing mode, creating the tool path, and generating the NC code for the CNC machine. With the help of a digital model of the machine (known as a digital twin), a controller emulator, machine parameters and a post processor, the system provides precise simulation and machine-optimized NC code. ESPRIT offers factory-developed post-processors for most types of machines and control units, which generate NC code without requiring subsequent modifications. It is also possible to create special post processors for special types of machines and applications. In this particular case, due to the work piece geometry and production speed, the 4 + 1 strategy was chosen on the 5-axis machine, involving the simultaneous movement of four axes and the indexical movement of one axis. Real-time machine CAM programming represents a fundamental change in the way tool paths are created, resulting in longer tool life, shorter cycle times and better machine utilization.

Keywords: Industry 4.0 · CAD/CAM · Digital twins · Artificial intelligence

1 Introduction

Autonomous systems are characterized by the ability to work successfully in an unstructured work environment, which has an appropriate degree of uncertainty, [1–3]. Namely, modern production systems involve the participation of autonomous industrial robots and machine tools, which perform technological tasks in interactive and cooperative work, in order to successfully implement a technological task in an engineering insufficiently determined environment, [4, 5]. In the case of autonomous industrial robots of the last generation, an empirical management strategy has been established (in research laboratories), which in many ways resembles the actions of humans in the realization of everyday

activities, [6–8]. Human activities in the performance of regular jobs include approaching, grasping and moving objects, with the participation of the sense of sight, motor and mental abilities. At the same time, a person does not solve complex mathematical-mechanical problems (e.g. inverse kinematics problem), [9–11]. Practically, a person's eyes “guide” the hand to the object, and thanks to previously learned motor skills, the correct grasping and manipulation of the object is carried out. The idea that was developed in the conducted research [12–15], is based on an analogy with the described human activity. It implies that, by applying intelligent control of the robot, an analogy with the “biological hardware” of man is realized [16–18], where internal coordinates are systematically generated in the function of solving the task (manipulation, packaging, joining, etc.).

Based on this idea, the scientific goal was set to develop, in the interaction of mechatronic subsystems (machinery, electronics, and information technology), an empirical control strategy of hierarchical intelligent control of autonomous industrial robots based on recognition and learning systems, which is intended for production technologies of the 21st century, [19, 20]. In order to achieve this, it was necessary to improve the control algorithms, and to use and enhance the known principles of the recognition system in new generation robots, using artificial intelligence, [21]. A control algorithm is, in accordance with the need to realize the autonomous behavior of an industrial robot, the key to establishing an empirical control strategy. In order for an autonomous industrial robot to be able to successfully accomplish a technological task in a given real environment, it must recognize changes and disturbances in its working environment, in order to realize autonomous behavior in accordance with its physical limitations and reasoning, i.e. learning, abilities, [22].

Therefore, it is necessary for the robot in its control memory, as an empirical machine, to remember previous events that were based on the appropriate prediction, to check by evaluation (measurement) whether these events are in accordance with the prediction, and finally, based on the obtained results, be able to change the basic prediction, so that in future events he would have to select the highest probability of success in the realization of the technological task. It is very important to emphasize that, if the SENSOR/ACTUATOR relationship has been established, the empirical control system of the robot will, on the basis of prediction, ensure the maintenance of the stability of that relationship, so that after a large number of attempts, the empirical machine-robot becomes intelligent, skilled and careful during realization of favorable opportunities for autonomous behavior in one's own real environment.

What is certain, is that the current downward trend in the need for unskilled labor whose work can be automated will continue, while the need for experts who have the skills to develop, launch and maintain such automated systems will grow year by year.

In this research it is described the industrial automation of the production process, which is based on the fusion of a CNC machine and an industrial robot. After connecting all the elements of the flexible production cell into one unit, generating the NC program for HAAS DM-1 in the CAM software ESPRIT, coding the cycle for process measurement with a measuring probe and programming the robot, the complete system is tested.

2 System Installation

In the implementation of the set task, it is necessary to:

- Install CNC machine, with two-axis tilting table, robot and work piece for clamping systems;
- Connect devices so they can communicate with each other;
- Create NC program for HAAS CNC machine in CAM software;
- Program the robot and align it with the program of the CNC machine.
- Make test pieces within the specified tolerances.

The main problem is to connect these systems and ensure their mutual communication in order to work as a single unit. After the installation of all components at the customer's premises by the service department it is necessary to level and calibrate the machine and the robot.

Leveling the machine is bringing its horizontal axes (mainly X and Y in the case of vertical machining centers) into a parallel position with the horizontal plane.

The leveling of the CNC machine and the robot is carried out with the help of a special digital measuring device for leveling model "Big kaiser", which is presented in Fig. 1.

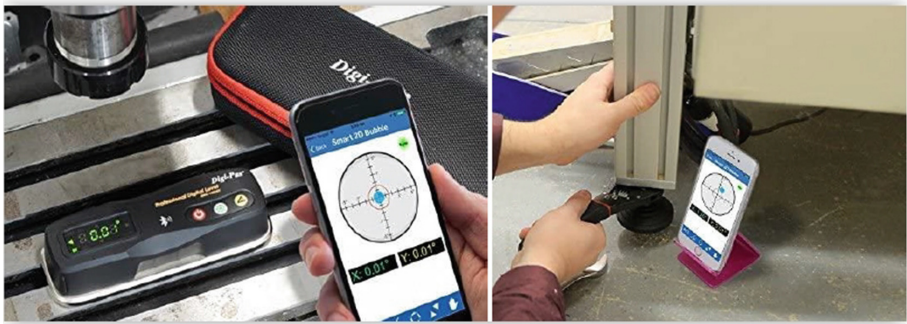


Fig. 1. Special digital measuring device Big kaiser

This device has the ability to connect to mobile devices and computers via Bluetooth connection. By using this device, the leveling process is shortened by 70% compared to the classic variant with analog machine devices for measuring the slope. The resolution is 0.18 mm/m, i.e. 0.01°. Range from 0° to $\pm 90.00^\circ$ for the first axis, from 0° to $\pm 10.00^\circ$ for the second axis.

After leveling, the machines are connected to the electrical network and the robot and the machine are connected to each other with communication cables. The rotary table, which is installed on the machine table, is directly connected to the machine with a voltage-communication cable intended for that purpose.

The HAAS CNC machine communicates with the HAAS two-axis rotary table via the 4th and 5th axis modules that are connected to the machine's control unit.

After installing the device on the machine, it is necessary to physically align the rotating axes of the device with the linear axes of the machine, and then configure the direction of the axes on the control unit in software, as is shown in the Fig. 2.



Fig. 2. Defining rotary axes on the HAAS control unit [26]

The command to open and close the pneumatic chuck is also sent from the machine control unit via G-code (M-function). The same applies to the automatic opening and closing of the cabin door on the machine.

The robot, like the CNC machine, can be specially programmed. Programming this type of robot is much simpler than programming a CNC machine and can be done in several ways:

- by pressing the 3D display arrows on the touch screen of the control unit;
- manually moving the robot, whereby it remembers each position and repeats it later;
- by programming the robot through the machine's HAAS control unit;
- specialized robot programming software.

In order for the robot to receive information when the protective door of the machine is open, i.e. for the machine to have information that the robot is outside the working area and can close the door, they need to communicate with each other. This is also done via the interface, i.e. additional M-functions, which HAAS offers as an option for working with peripheral devices.

The layout of the fully connected system is shown in the Fig. 3, which is taken from the reference [24].



Fig. 3. Flexible production cell [24]

The machine has an ETHERNET network interface (communication between the machine and a computer or server). One of the now very important options for modern production is HaasConnect. HAAS developed this application in response to the requirements of Industry 4.0.

HaasConnect (Fig. 4) is a mobile application that enables remote machine monitoring. The machine must be connected to the Internet via a LAN or Wi-Fi network. The Wi-Fi option on the machine provides a wireless connection between the HAAS control unit and the local network.

The status of the machine can be monitored from a computer or smart phone. Alarms and notifications can be generated for the start of the cycle, the end of the program, as well as any alarms on the machine, or any changes in steps, revolutions, or rapid movements. All notifications are sent to a mobile device or e-mail.

3 System Calibration

After installation and leveling of the machine, it is necessary to calibrate, i.e. correct the movement of the axis of the CNC machine as a whole, which is directly responsible for the precision of the part. This is done with a special device manufactured by RENISHAW, the so-called “Ball bar” test. In this case, the RENISHAW QC20-W model is used.

The popularity of this type of axis calibration is based on the simplicity of the test, the speed of use and the large amount of quantitative information obtained.

In theory, if a CNC machine is programmed to follow an ideal circular path and the positioning accuracy of the machine is perfect, then the actual circle the machine makes will exactly match the ideally programmed circle. In practice, many factors influence

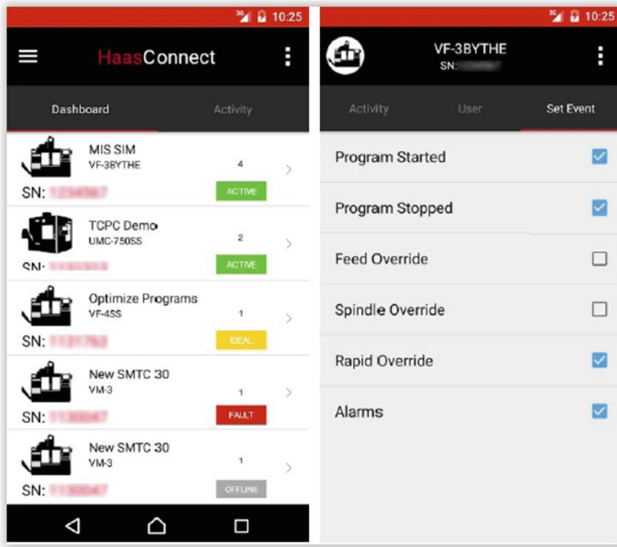


Fig. 4. HaasConnect mobile application [26]

deviations from the ideal circle, starting from the geometry of the machine, through the control system, to the wear and tear of the machine during long-term operation. All of these can cause the radius of the test circle and its shape to deviate from the programmed circle. If they could accurately measure the actual circular path and compare it to the programmed path, they would have a measure of the machine's accuracy. It is the basis of all calibration systems that work this way. Testing consists of 3 simple phases: setup, data collection and analysis.

Connecting to the device is easy thanks to the Bluetooth connection. Testing is quick and easy with Windows-based software that guides the operator through each step. A useful option is the so-called "NC program generator" which helps in writing the appropriate program for the machine tool. In many cases, existing test templates are used. Quick access to templates is done by simply searching for existing files.

The center support is placed on the machine table and (using the adjustment ball supplied in the kit) the spindle is moved to the reference point and set to the test zero coordinate. The spindle is then moved to the initial position to start the test and the magnetic test rod is mounted between the two kinematic magnetic joints. A simple circular interpolation program (G02 and G03) is required to run the test.

Figure 5 presents the beginning of the "Ball bar" test.

In the standard test, the CNC machine performs two consecutive rounds; one clockwise, the other counter-clockwise. In practice, an additional arc is added to the path before and after the test lap to allow the machine to have a constant speed of travel in the lap.



Fig. 5. The beginning of the “Ball bar” test

By using dipstick attachments, a test radius can be selected and will be tailored to machine size and sensitivity to specific problems (e.g. large radius circles are better at finding machine geometry errors, smaller circles are more sensitive to servo misalignment, or drawbar backlash).

The data recording is shown live on the screen; so that any errors or problems can be detected as the test progresses and the test stopped without wasting additional time (this is important if the test is performed with a large radius and slow movement speed). The user has at his disposal several report formats in accordance with international standards (e.g. ISO, ASME) and comprehensive RENISHAW diagnostics (including volumetric analysis) with a number of different screen displays and links to the help manual.

Most reports can be adapted to a specific case, and the end result can be used for written reports. As the technical documentation of the work piece requires certain tolerances that are in the zone of around 0.01mm, and our machine is calibrated with the “Ball bar” test to the maximum precision of exactly 0.01mm, there is a high probability that a certain number of pieces will be at the very limit of tolerance, and that some of the elevations will even exceed the limit tolerances. It follows from this assumption that we need a more accurate calibration system to make the machine even more precise. This is achieved with a sophisticated optoelectronic laser calibration device called a laser interferometer. Measurements can include certain characteristics of the waves themselves and the materials with which the waves interact. In addition, this method is used for techniques that use light waves to study changes in displacement. This displacement measurement method is widely applied for calibration and mechanical control of the degree of displacement in precision machining. The working principle of the used device is based on a Michelson interferometer consisting of a beam splitter (semi-silvered mirror) and two mirrors. When the laser light passes through a semi-silvered splitting mirror, the beam (which is partially reflected) is split into two beams with different optical paths.

The basic components of the system are a compact laser head, an independent ambient temperature compensator system and a specialized software package located on a portable computer. Together with the measuring optics, they form a highly precise system for measurement and analysis.

A laser interferometer manufactured by RENISHAW, a model XL-80, is used to calibrate the machine.

Laser frequency accuracy of ± 0.05 ppm (parts per million) over 3 years is achieved by thermally controlling the length of the laser tube in the nanometer range.

The linear measurement accuracy is ± 0.5 ppm in the entire range of environmental conditions, i.e. from 0 to 40 °C and atmospheric pressure from 650 to 1150 mbar. The reading can be done up to 50 kHz, with a maximum linear measurement speed of 4 m/s and a linear resolution of 1 nm; even at top speed. The XL-80 model has a resolution of $0.001 \mu\text{m}$ (1 nm) in linear measurement, and $\pm 5 \mu\text{m/m}$, i.e. 0.01 arc s, in rotational measurement. Correction of the movement of the machine's axes is performed by entering new, measured values into special tables located in the machine's control unit (so-called mapping). With this system, it is possible to reduce the error of the machine to a level below 0.005 mm within the complete volume of the working space.

In this way, the desired accuracy of the machine is achieved and all tolerances on the work piece are within the prescribed limits. It should be noted that the temperature of the environment plays a very important role in the processing of precision parts. Any change in ambient temperature negatively affects the machine's accuracy. For this reason, the entire production hall is air-conditioned. The device measures air temperature, pressure and humidity, and then calculates the index of refraction of light through the air (and thus the wavelength of the laser). The laser reading is then automatically adjusted to minimize any variations in laser wavelength. The advantage of the automatic system is that no user intervention is required and the compensation is updated automatically.

The calibration of the robot in this case does not require a special approach, because it is a standard "pick and place" operation that does not require particular precision. Allowed position deviations are up to 0.5 mm, which requires only basic calibration with the mandrel on the reference mandrel located on the robot's work table.

The calibration of the robot is given in Fig. 6.

The mandrel located in the robot gripper then needs to be brought to the surface of the machine's worktable to define the zero point of the coordinate system along the Z-axis. The mandrel is then brought to two points on the table (the longer edge of the table) that are parallel to the X-axis to define the X-axis, and then to a point located on the side edge of the table to define the Y-axis. In this way, the initial coordinate system of the working space of the machine is defined for the robot.

4 Program Support

CAM (Computer Aided Manufacturing) represents computer-supported preparation for production and includes the translation of design information into technological information and production with different levels of automation (NC machines, machining centers, etc.), [23].

The design of the complete technology is carried out in the ESPRIT software package, which implies the selection of the processing system, the introduction of auxiliary accessories, the selection of the required sequence (operation), defining the tool, defining the processing mode, creating the tool path and generating the NC code for the CNC machine, [24].



Fig. 6. The calibration of the robot

ESPRIT is the flagship product of DP Technology, one of the leading CAM software development companies and has been in their offering since 1982, [25]. ESPRIT is a highly customizable, high performance CAM system used in industry for CNC machine control, optimization and simulation. It supports all known CNC machine configurations:

Milling (from 2 to 5 axes simultaneously)

- Turning (from 2 to 22 axes simultaneously)
- Wire electro erosion (from 2 to 5 axes simultaneously)
- Multitasking machines, long lathe machines (Swiss-type)
- HSM - high-speed processing (from 3 to 5 axes simultaneously)
- Automated process control on the machine
- Manufacturing by adding materials.

ESPRIT offers 5-axis simultaneous machining cycles that generate tool paths optimized for fully 5-axis machines, as well as indexed 4 + 1 and 3 + 2 applications for the production of complex tools and parts for a variety of industries, including aerospace, automotive, energy and the medical industry. These cycles are optimized to work on all classes of CNC machines with 5-axis movements, including milling machines, multitasking machines and Swiss-type machines.

ESPRIT enables the creation of a so-called “digital twin” by simply importing a 3D model of a machine tool and using it for programming, optimization and simulation. Work pieces, fixtures, and cutting tools are simply placed into the 3D model assembly, resulting in the ability to create demanding simulations, better tool paths, higher-quality manufactured parts, and greater productivity. Whatever happens on the screen will also happen on the real machine in the production plant.

Real-time CAM programming represents a fundamental change in the way tool paths are created, resulting in longer tool life, shorter cycle times and better machine utilization. Unlike traditional CAM software, ESPRIT's machine kinematics and dynamics information is used for setup, programming, optimization and simulation. In this way, CAM programmers make better tool path choices, resulting in improved machining performance.

The application of artificial intelligence in this CAM software simplifies part programming by automatically selecting optimal processes (machining cycles, cutting tools and machining conditions) for part characteristics based on proven best practices. Various machining strategies, tool selection, cutting modes and the like can be saved in ESPRIT's database (Knowledgebase™) and then applied in other cases where the same or similar machining is required.

Another advantage of this software is the integration with cloud-based databases, such as the Machining Cloud database. The Machining Cloud application provides the latest product data from the world's leading suppliers of cutting tools, clamping systems, and CNC machines, eliminating the hassle of manually searching through printed catalogs, phone calls, and extensive Internet searches to find the optimal tool, while removing the burden of manually entering tool data into CAM software.

Data about cutting tools is always up-to-date because it is stored in the cloud and is available to everyone, including global and local availability data. Also, data on HAAS CNC machines is available on Machining Cloud. The files are in GDML format and contain simplified 3D machine models along with machine kinematics, making them ready for use in CAM and simulation software. In this way, the gap between physical tools and digital software has been removed.

Machining Cloud relies on the latest principles of Industry 4.0:

- Interoperability: search, select, and share cutting tools, assemble assemblies, and export data to CAD, CAM, ERP, or other manufacturing software;
- Virtualization: cutting tool data including 2D drawings and 3D models including elements and assemblies, complete descriptive data for CAD/CAM, cutting modes for CNC machines;
- Decentralization: the manufacturer's knowledge base related to the product is in the cloud and makes product recommendations in relation to previous choices. CAD/CAM developers still make the final decision, but manufacturers' recommendations are immediately available to them;
- Real-time capability: cutting tool data is always up-to-date as it is stored in the cloud and is available to everyone, including global and local stock availability, resulting in optimal tool selection and reduced delivery times;
- Service-oriented: simple installation and low-cost operation with all hosting services, databases, servers and catalogs provided as a cloud service.
- Modularity: flexible enough to fit into an engineering, purchasing and workgroup workflow in the cloud, or to retrieve product data for individual items or entire catalogs for use in on-premises software.

As the concept of providing digital tool data on web portals becomes main stream, the ability to integrate that data into other digital systems is transforming industrial production. While digital tool catalogs make it much easier and faster to find the right

tool for the job, a more significant and growing trend is making cutting tool geometry data available as well as 3D models for CAM programming, simulation and verification. The trend of providing complete tool data is more important than ever. The production of industries is increasingly moving to the “digital twin” model, i.e. the synchronization of the digital and physical worlds.

A digital twin is an exact digital replica of a production in a computer. This pairing of the virtual and physical world brings benefits in various applications such as simulation and analysis, visualization, collaboration of multiple teams on the same projects, design and NC programming to eliminate problems before they occur.

In recent years, the Internet of Things (IoT) has made the digital twin model even more cost-effective to implement. Technology is no longer only available to large corporations with big budgets. A manufacturing plant of any size can now benefit from realistic simulation of every aspect of the machining process to improve cycle times, part quality and equipment utilization.

The amount of data available exceeds the digital catalog. There is a growing trend among tool manufacturers to populate digital tool catalogs on their websites to replace the tedious and time-consuming work of searching through thick paper catalogs. While the digital catalog makes it possible to quickly and easily find the necessary tools of a specific supplier, it still requires visiting multiple websites if products from different suppliers are used and the data is isolated in the so-called “information silos”.

Unlocking a huge database offers huge potential for easy integration into other production applications. Direct access to tool data and drawings ensures accurate and reliable tool selection in applications such as CAM programming, tool verification and analysis, enabling the efficient exchange of reliable and accurate data. Integration into other systems is a key function of a centralized database.

Compatibility and function data are also used to optimally create virtual 3D tool assemblies such as combinations of inserts, holders, bodies, adapters, etc. When tools are assembled in the cloud, there is no need to download individual items and assemble them in CAD software. The cloud uses product data provided by the manufacturer to show only those items that can be put together and are available to order. For any selected tool, the software suggests only holders that fit together. This saves hours of searching for the right components and eliminates the uncertainty of whether the components will fit together when shipped.

The two standards provide a communication bridge between cutting tool manufacturers and software manufacturers. ISO 13399 is a set of international standards that regulate the exchange of digital tool data. The ISO 13399 standard is managed by the ISO Technical Committee.

GTC (Generic Tool Catalog) is a digital format that supplements ISO 13399. It enables easy transfer of data on cutting tools. These two standards help advance growing applications for digital tool data.

In this particular case, due to the geometry of the work piece and the production speed, the 4 + 1 strategy was chosen on the 5-axis machine. Thus, simultaneous movement of four axes and indexical movement of one axis are presented in Fig. 7.

After connecting all the elements of the flexible production cell into one unit, generating the NC program for HAAS DM-1 in the CAM software ESPRIT, coding the

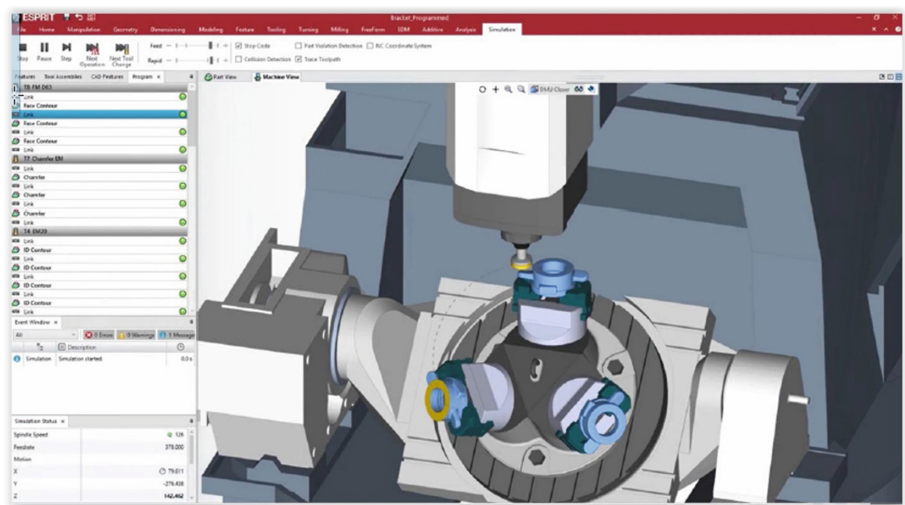


Fig. 7. Simultaneous movement of four axes and indexical movement of one axis [25]

cycle for process measurement with a measuring probe and programming the robot, the complete system is tested.

Figure 8 which is taken from the reference [24], shows the CNC machine and the robot in operation.



Fig. 8. CNC machine and the robot in operation [24]

The precision of the system, especially the HAAS CNC machine, is confirmed by measuring the dimensions on a coordinate measuring machine (CMM) NIKON Altera 7.5.5 (Fig. 9).



Fig. 9. Coordinate measuring machine NIKON Altera 7.5.5

During the measurement, a complete tactile scanning of the surfaces is used (Fig. 10 is taken from the reference [24]). With this measurement strategy, even deformations on the measured surface can be detected, and it is far stricter (more precise) than the tactile measurement of surfaces in points according to a given pattern.

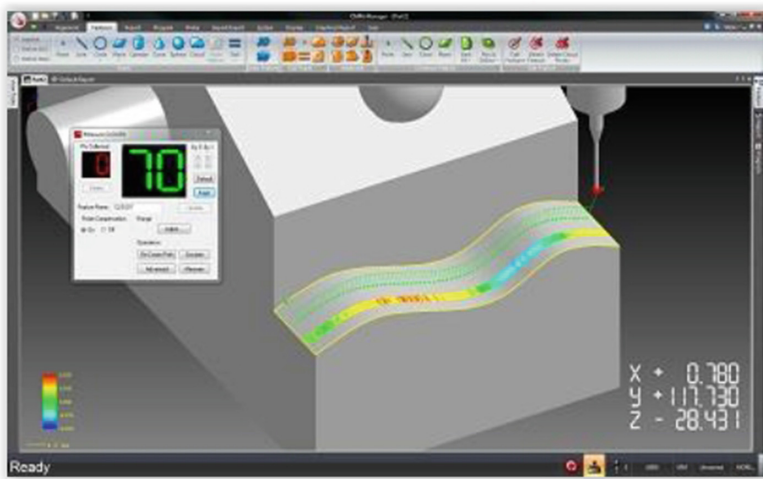


Fig. 10. An example of surface scanning measurement on a CMM [24]

The report from the exit control showed that all the tolerated elevations on the work piece are done within the required tolerance limits (Fig. 11 is taken from the reference [24]).

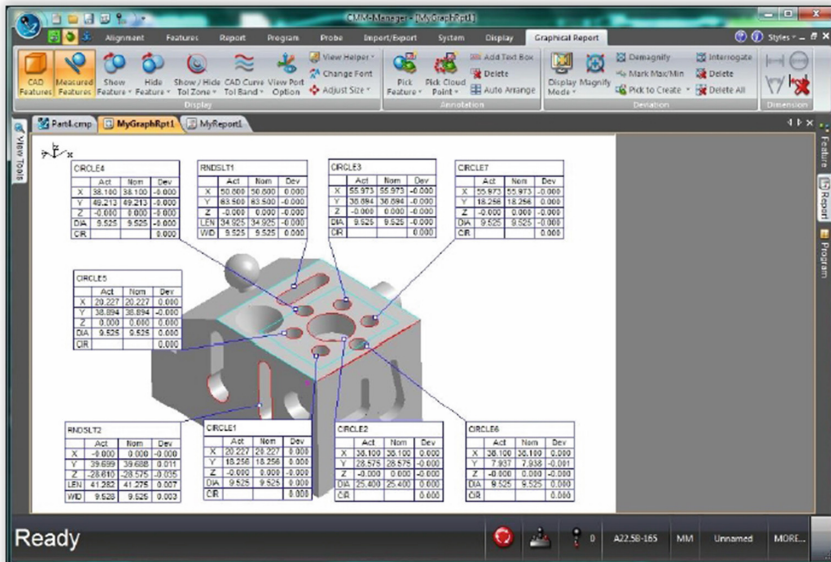


Fig. 11. An example of a graphical report on CMM [24]

In this work, in addition to the ESPRIT program, the FANUC ROBOGUIDE simulation package is used, which simulates both movement commands and robot applications, significantly reducing the time needed to create new movements. The software is autonomous and does not require a constant connection to the network (robot).

To ensure minimal production downtime, cells can be designed using imported CAD models, tested and modified completely offline. It is designed to be intuitive and extremely easy to use. The software requires very little or no additional training to operate.

FANUC HandlingPRO is a module within the FANUC ROBOGUIDE offline simulator that was used in this project. It is an intelligent 3D simulation for programming robots whose purpose is to manipulate work pieces when servicing machines in production. It simulates and tests material handling processes and conducts feasibility studies for robotic applications without the need for physical system installation and the cost of commissioning a trial work cell.

Features of the module:

- Internal robot controller that validates positions and cycle times;
- The virtual panel for manual programming functions like a real panel in a real programming environment;
- Performance and reach checks, collision detection and accurate cycle time estimates;
- Fast connection with the robot;
- Detailed help and "How to" guides make it easy to get started with the software.

Optimization of robot operation offline:

- The Workcell Wizard allows the user to easily step through the development of a material handling program. The process includes a robot model, a controller, a gripper, a machine;
- Workcell Browser provides quick access to every work cell detail that can be expanded, checked and modified;
- Structured menus allow quick access to items needed to adjust the gripper, machine and other elements;
- Machine Tool Workcell Generator wizard helps users create robot cells along with machines.

Advantages

- System evaluation - programming can begin, before the actual robot system is installed;
- Fast and accurate import of CAD data for layout of cell elements
- Simple simulation - simulating the operation of the robotic system and its performance;
- Optimization and debugging - while the production line is running, the user can improve and modify programs without downtime and loss of production time;
- Quick and economical problem solving.

Manual programming:

- HandlingPRO supports automatic robot position optimization;
- It is possible to program the path of the robot through the built-in virtual modules programming;
- Visual representation of the movement of gripping the work piece;
- Path optimization according to process time and robot movement time.

5 Conclusion

In this scientific paper it is described industrial automation of production process based on the application of artificial intelligence, and fusion of the CNC machine and the industrial robot. The research is primarily focused on installation, calibration, and program support of the flexible production cell, and production of machine parts with the use of machines and software of the latest generation. By using this approach in production it is achieved significant shortening of production time from 13 to 7 min, increased productivity to 75000 pieces of machine parts per year per machine, and almost total elimination of scrap.

The direction of further improvement of the existing system would be to install a 3D camera-sensor. In most cases, machines that have a built-in vision system are able to do a specific task for which they are preprogrammed, but recently there are not rare cases where a machine can learn certain things.

The demand for the autonomy of the industrial robot was the starting point for setting up the hypothesis that, based on information from the sensor-camera and learning based on artificial neural networks, it is possible to successfully realize the recognition

of objects, and then the technological task of manipulation, i.e. autonomous positioning and orientation of the gripper of the robot in relation to the recognized object. Intelligent behavior, which implies an autonomous industrial robot, is represented through adequate coordination between the visual information about the object obtained from the sensor-camera and the control system. Realized intelligent control of robots using sensor-cameras and artificial neural networks has proven to be effective in overcoming modeling problems and the appearance of indeterminacy of the real environment (e.g. changing the position of objects), because intelligent control of robots actually represents an adaptive sensor-motor coordination that uses visual mapping realized on the basis of computer vision system. In the further development we expect new approaches and using more factors and operators and thus getting new decision models which would optimize important parameters such as: inspection of rolling stock and machine park, reduced costs, better trained drivers, better service and satisfied customers, increased productivity and efficiency, fewer overtime hours, less idle periods, easy vehicle and machine monitoring, reduced fuel costs, and reduced maintenance and service costs.

During machine learning, visual input signals about the object are processed and combined into a target mapping through adaptive weighting, based on which a control signal for the robot's actuators is generated. The error between the actual control signals at the actuator and the calculated signals, after the acquisition of the signals from the camera, is used to incrementally change the weight ratios. After the successful completion of the learning phase, during association, the learned sensory-motor correlation is used in the recognition and manipulation of objects that are similar to the objects on which the training process was performed.





References

1. Perez, R., Gitierrez, S., Zotovic, R.: A study on robot arm machining. In: 29th Daam International Symposium on Intelligent Manufacturing and Automation, pp. 931–939. (2018)
2. Klimchik, A., Ambiehl, A., Garnier, S., Furet, B., Pashkevich, A.: Efficiency evaluation of robots in machining applications using industrial performance measure. *Robot. Comput.-Integr. Manuf.* **48**, 12–29 (2017)
3. Mikić, D., Desnica, E., Kiss, I., Mikić, V.: Reliability analysis of rolling ball bearings considering the bearing radial clearance and operating temperature. *Adv. Eng. Lett.* **1**(1), 16–22 (2022)
4. Dihovični, D., Ašonja, A., Radivojević, N., Cvijanović, D., Škrbić S.: Stability issues and program support for time delay systems in state over finite time interval. *Phys. A: Stat. Mech. Its Appl.* **538** (2020)s
5. Miljević, N. Ratković Kovačević N., Dihovicni, D.: Automation of cup filling machine by inserting PLC control unit for educational purpose. In: Proceedings of the International Conference of Experimental and Numerical Investigations and New Technologies - CNN TECH, vol. 153, pp. 344–361. (2020). <https://doi.org/10.1007/978-3-030-86009-7>
6. Wu, K., Brueninghaus, J., Johnen, B., Kuhlenkoetter, B.: Applicability of stereo high speed camera systems for robot dynamics analysis. *Int. Conf. Control. Autom. Robot IEEE Singapore* 44–48 (2015). <https://doi.org/10.1109/ICCAR.2015.7155999>
7. Dihovicni, D., Nedic, N.: Application of Finite spectrum assignment method on distillation column. Modeling and simulation in engineering, economics and management, Lecture Notes in Business Information Processing, vol. 145, pp. 232–238. Springer-Verlag (2013)

8. Dihovicni, D., Nedic, N.: Simulation, animation and program support for a high performance pneumatic force actuator system. *Math. Comput. Model.* **48**, 761–768 (2008) (Elsevier, Washington)
9. Ratković Kovačević, N., Škatarić, D.: Multimodeling control via system balancing. *Math. Probl. Eng.* (841830), 20 (2010). <https://doi.org/10.1155/2010/841830>
10. Dihovicni, D., Medenica, M.: mathematical modeling and simulation of pneumatic systems. *Advances in Computer Science and Engineering*, Chapter 9, pp. 161–186. India (2011). <https://doi.org/10.5772/15313>
11. Guatieri, L., Rauch, E., Vidoni, R.: Emerging research fields in safety and ergonomics in industrial collaborative robotics: a systematic literature review. *Robot. Comput. Integr. Manuf.* **67**(101998), 1–30 (2021)
12. Dihovicni, D., Ratković Kovačević, N., Lalić Z., Kreculj, D.: Investigations and results analysis of key parameters of vehicle tracking system. In: *Proceedings of the International Conference of Experimental and Numerical Investigations and New Technologies - CNN TECH 2021*, vol. 323, pp. 105–123. (2021). <https://doi.org/10.1111/s11747-009-0136-2>
13. Dumitrescu, C., Ciotirnae, P., Vizitiu, C.: Fuzzy logic for intelligent control system using soft computing applications. *Sensors* **21**(8), 2617 (2021). <https://doi.org/10.3390/s21082617>
14. Chen, Y., Dong, F.: Robot machining: recent development and future research issues. *Int. J. Adv. Manuf. Technol.* **66**, 1489–1497 (2017). <https://doi.org/10.1016/j.promfg.2017.07.034>
15. Dihovicni, D.: Decision making and fundamental matrix approach in process safety. *Int. J. Comput. Intell. Syst.* **6**(4), 658–668 (2013)
16. Dihovični, D., Škrbić, S.: Fuzzy approach to supply chain management for E-commerce store. *Appl. Eng. Lett.* **5**(2), 62–67 (2020). <https://doi.org/10.18485/aeletters.2020.5.2.4>
17. Raman, S.B., Monga, H.: Method and implementation of data flow. *Appl. Eng. Lett.* **1**(4), 105–110 (2016)
18. Roberti, F., Toiber, J.M., Soria, C., Vassallo, R.F., Carelli, R.: Hybrid Collaborative Stereo Vision System for Mobile Robots Formation. *Int. J. Adv. Robot. Syst.* **6**(4), 7241 (2009)
19. Dihovicni, D.: Fuzzy logic approach in oil treatment. *J. Balk. Tribol. Assoc.* **20**(4), 606–614 (2014)
20. Tyapin, I., Hovland, G., Kosonen, P., Linna, T.: Identification of a static tool force model for robotic face milling. In: *IEEE/ASME 10th International Conference on Mechatronic and Embedded Systems and Applications (MESA 2014)*, pp. 1–6. Senigallia, Italy (2014)
21. Dihovicni, D., Mišević, M., Kovačević, N.R., Kreculj, D.: Implementation of fuzzy logic approach for a smart production system. *J. Natl. Sci. Found. Sri Lanka* **50**(3), 695–703 (2022). <https://doi.org/10.4038/jnsf.sr.v50i3.10440>
22. Pandey, R., Singh, A., Sharma, N., Mikić, D.: A recent role of CAD/CAM in designing, developing and manufacturing in modern manufacturing technologies. *Imp. J. Interdisciplinary Res.* **2**(3), 399 (2016)
23. Maqsood, Z., Rao, P., Abdillahi, T.: CAD/CAM with new trends and advancements using a machine learning: a review. *Int. J. Tech. Innov. Mod. Eng. Sci.* **5**(5), 885–889 (2019)
24. Miscevic, M., Dihovični, D.: Application of robotics and CNC machines in production. *Appl. Eng. Lett.* **5**(4), 135–141 (2020)
25. Esprit Cam, [Internet]. <https://www.espritam.com/>. Accessed 23 May 2023
26. HAAS Automation, [Internet]. <https://www.haascnc.com/>. Accessed 18 Apr 2023



Bookshelf Scanning Mechanism with Arduino Control

Nada V. Ratković Kovačević , Goran Ž. Vojnović , Djordje N. Dihovični ,
and Dragan D. Kreculj 

Computer-Mechanical Engineering Section, The Academy of Applied Technical Studies
Belgrade, 11070 Belgrade, Serbia
gvojinovic@atssb.edu.rs

Abstract. The aim of this paper is to propose a bookshelf scanning mechanism for library inventory, which uses a stepper motor-based linear drive (e.g. slider), controlled by an Arduino board. While exploring different types of slider drives, which could be used in this system, such as linear ball bearing sliders or belt-driven sliders, screw-nut sliders are recommended in here described proposal, because they provide a high level of precision and accuracy. The slider moves a carriage holding a barcode scanner along a sliding track to accurately scan the barcodes of books on a bookshelf. The key components required for the system to function are highlighted, such as a suitable stepper motor driver, an Arduino board with adequate digital input/output pins, and sensors (e.g., limit switches) for detecting the end of the track. The example code is written using Arduino IDE, for controlling the stepper motor. The positioning of the barcode scanner, motor, and sensors is also crucial to ensure the system operates smoothly and accurately. The scanner should be able to read the barcodes of the books accurately and without any errors. In regards to that, the vital role played by Arduino in regulating the slider's speed and position is pointed out. The importance of proper power supply and wiring to prevent potential issues with the motor and Arduino board, is emphasized.

Keywords: Barcode scanning · Embedded systems · Library automation · Linear drives · Mechatronics

1 Introduction

Arduino can be used to control a wide range of electronic devices, including stepper motors. Stepper motors are commonly used in robotics, automation, and other industrial applications. By connecting a stepper motor to an Arduino board, its speed and position can be controlled, making it useful in various projects.

Here a library automation project [1, 2] is further being developed and built. In this case a stepper motor is used to control the linear drive that holds the carriage or a base plate on which the barcode scanner is mounted.

Bookshelf scanning mechanism consists of a barcode scanner mounted onto a linear drive mechanism. The barcode scanner can be mounted on a carriage or a base plate that is able to slide along a track. The slider can be mounted above or below the bookshelf,

with the carriage positioned such that the scanner is able to read the barcodes of the books as it is slid along the track. A motor can be used to move the carriage along the track, and sensors can be used to detect when the carriage has reached the end of the track. Various library automation projects were explored [3–7] and their experiences are used in an endeavor here presented.

2 Hardware Components

2.1 Arduino Microcontroller Board

Arduino Uno or Arduino Mega microcontroller board could be suitable for this library automation project. Both of these models have enough digital input/output pins to control other electrical or electronic components (e.g., limit switches and the motor driver), and both can be powered with a 5 to 12 V external power supply.

2.2 Stepper Motor

The stepper motor chosen should be capable of driving the mechanical transmission and to be able to provide positioning of the barcode scanning equipment. Here a stepper motor 28BYJ-48 was chosen which requires a 5 V DC power supply (Fig. 1).



Fig. 1. A stepper motor 28BYJ-48 (on the left) with motor driver TI ULN2003AN (on the right).

The 28-BYJ48 stepper motor is one of the most commonly used types of stepper motors. This or similar motors can be used in various devices and embedded systems. The 28-BYJ48 motor has four coils powered by unipolar voltage pulses and each coil is rated for + 5V DC voltage [8].

It is relatively easy to control 28-BYJ48 motor with any microcontroller, and here an Advanced Technologies AT mega 328P is used which is ‘heart and brain’ part of an Arduino Uno board. To control the stepper motor 28-BYJ48 for the project described and built here, equivalent electrical scheme given in [8] was implemented.

The code was adapted from [8] and Nikodem Bartnik’s solutions [9, 10].

2.3 Stepper Motor Driver

To power a stepper motor that moves the carriage along the tracks using an Arduino, it is necessary to choose a suitable stepper motor driver that is capable of managing the voltage and current requirements of the motor. After obtaining the stepper motor driver, it can be connected to the Arduino board, and then the Arduino can be programmed to control the motor. Having in mind that the stepper motor chosen was 28BYJ-48 which requires a 5 V power supply, a corresponding driver was used: Texas Instruments ULN2003AN (in Fig. 1 on the right).

2.4 Limit Switches

To determine if the base plate of the mechanism has reached the starting or ending point on either side of the bookshelf, two limit switches were used (shown in Fig. 2).

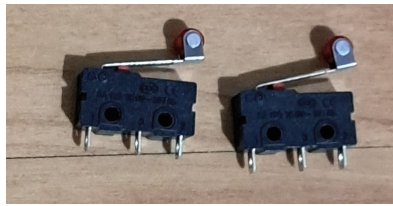


Fig. 2. Two limit switches are used to detect if the slider with plate carrying barcode scanner has reached either end of the bookshelf.

To connect the limit switches so that their activation controls the stepper motor (turn on, turn off, and/or change in direction or rotation) for the project described and built here, equivalent electrical schemes were used and code was adapted [11–13].

3 Challenges of the Device Design

There are four basic types of linear actuators: mechanical/electro-mechanical, hydraulic, pneumatic and piezoelectric. Here a mechanical or electro-mechanical linear drives are considered and explored. Linear drives could be belt drives, screw drives, rack and pinion or linear motor. Figure 3 [14] shows a comparison between these four.

To ensure proper functionality of the bookshelf scanning mechanism, the following considerations should be taken into account:

1. Positioning of the barcode scanner: The barcode scanner should be mounted in a way that allows it to scan the barcodes of the books accurately. Also, it should be positioned at an appropriate distance from the books and at an appropriate angle to ensure that the barcode can be read without any errors. Honeywell Voyager 1250 g barcode scanner was used in this project. Mentioned scanner scans 13 mil bar codes from as far as 447 mm [16, 17]. This particular scanner needs to be on its stand in order to scan barcodes continuously. Optimal distance for it, in order to scan barcodes

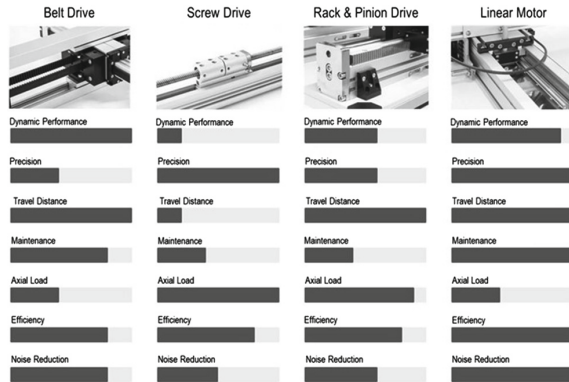


Fig. 3. Comparing modular linear actuator drive types [14].

properly, is 5–10 cm. Even at that distance it periodically skips a barcode. If book spine is too narrow, or if barcode is damaged or not placed correctly, scanner will move on to the next book. In this stage of the project, the program that would detect error (book not being scanned) and report where the error occurred has not been created.

2. Positioning and mechanical coupling of the motor: The motor should be mounted securely to prevent any unwanted movement or oscillation. The positioning of the motor should be such that it can move the carriage smoothly and without any interference with the barcode scanner. Our suggestion is at one end of the slider.
3. Positioning of the sensors: The sensors that detect the end of the track should be mounted at the appropriate locations on the track or fixed on both ends of the bookshelf, so that they can detect the carriage's end-of-travel accurately and consistently.
4. Speed of the slider: The speed of the slider should also be considered and in accordance with the speed at which the barcode scanner scans the books. This will help ensure that the scanner is able to read the barcodes of the books accurately and without any errors. The speed of the slider can be controlled by the motor. It is important to ensure that the speed is not too high or too low, as this can interfere the accuracy of the barcode scanning process. Stepper motor used here, 28BYJ-48, takes 2038 steps per turn. Motor delivers a torque of 34.3 mN.m at a speed of around 15 RPM. Using a delay of 900 μ s between steps. Arbitrary speed is given based on the code example used [8].

```
...  
void loop() {  
    // Rotate CW slowly at 5 RPM  
    myStepper.setSpeed(5);  
    myStepper.step(stepsPerRevolution);  
    delay(1000);  
    ...  
}
```

In this stage of the project, and given the issues that scanner used here has, it is still early to tell the exact speed.

- 5. Power supply: It’s important to make sure that the power supply is capable of providing enough power and current level to both the motor and the Arduino board. If the motor draws too much current, it could cause the voltage to drop, which could potentially cause issues with the Arduino board. In that case, it may be necessary to use a separate power supply for the motor to ensure stable operation of both the motor and the Arduino board.
- 6. Wiring: The wiring of the entire system should be neat and organized to avoid any loose connections or interference between the different components.

When all these considerations are taken into account, the bookshelf scanning mechanism can operate smoothly and accurately.

Table 1. Comparison of available linear drives of 100 cm length [15].

Type of linear drive	Estimated price [Serbian dinars]	Single part or complete mechanism
Screw-nut sliders	2100	Estimate for all parts needed
Linear guides for slider (1 to 3 rods)	2100–3500	Set of parts, need to be assembled
Linear ball bearing sliders	6250	Partially completed mechanism
Leads with carriage	7800	Partially completed mechanism
Linear drive with belt-driven sliders	24000	Completed mechanism

The Table 1 shows the comparison in price of several linear electromechanical drives. The prices are approximate values without VAT [15].

4 Software

4.1 The Code for Arduino Microcontroller Board

Arduino Uno is the microcontroller board which can be programmed and implemented with ease since a numerous projects and solutions exist, available in open access on Arduino Foundation site or in open source in Arduino on line communities. The Arduino IDE (Integrated Development Environment) is an open access and free of charge software which can be used to write the code for regulating the operation of the stepper motor and other hardware components (e.g., limit switches).

The code should include instructions for determining the direction and steps of the motor, based on input from the sensors that detect when the carriage has reached the end of the track. The code was adapted and used from [9–13]. The code of Nikodem Bartnik [9, 10] was used to control the stepper motor and it was combined with the code from Arduino Get Started [11–13] for using the limit switches. Considering whether the limit switch was touched (and which one) the stepper motor is put to a halt or it changes direction of rotation.

An example code is shown below from Arduino Get Started solutions [11–13]:

```
/*
 * Created by ArduinoGetStarted.com This example code is in the public domain
 * Tutorial page: https://arduinogetstarted.com/tutorials/arduino-limit-switch
 */
#include <ezButton.h>
ezButton limitSwitch(7); // create ezButton object that attach to pin 7;
void setup() {
  Serial.begin(9600);
  limitSwitch.setDebounceTime(50); // set debounce time to 50 milliseconds
}
void loop() {
  limitSwitch.loop(); // MUST call the loop() function first
  if(limitSwitch.isPressed())
    Serial.println("The limit switch: UNTOUCHED -> TOUCHED");
  if(limitSwitch.isReleased())
    Serial.println("The limit switch: TOUCHED -> UNTOUCHED");
  int state = limitSwitch.getState();
  if(state == HIGH)
    Serial.println("The limit switch: UNTOUCHED");
  else
    Serial.println("The limit switch: TOUCHED");
}
```

5 Conclusion

Here a project for library automation is further developed and built. Various linear electro-mechanical and/or mechanical drives were compared. The system consists of linear drive with stepper motor, and base plate carrying the barcode scanner and Arduino board. Various linear drives are explored, however, screw-nut sliders are preferred in here described proposal, because they provide a high level of precision and accuracy. The stepper motor requires a driver which should be chosen so that it is capable of providing the required voltage and current consumption of the stepper motor that is used. Various challenges in making successful design are explored and elaborated. Arduino Uno board is chosen and code is implemented to provide control of the stepper motor. Two limit switches are connected to Arduino board to detect the end-of-travel of the base plate on either end of the bookshelf. The code for Arduino Uno is obtained combining two open source and open access resources.

Acknowledgement. Acknowledgements are extended to The Academy of Applied Technical Studies Belgrade for their support.

References

1. Ratkovic Kovacevic, N., Vojnovic, G., Dihovicni, D.: Autonomous shelf scanning system for library. In: Balac, M., Dragicevic, A., Mladenovic, G. (eds.) *The Book of Abstracts (BOA) of the 6th International Conference CNNTech 2022*, Springer, vol. 1, p. 91. Innovation Center of Faculty of Mechanical Engineering, Zlatibor, Serbia (2022). <http://cnntechno.com/docs/Book%20of%20Abstracts%202022.pdf>. Accessed 15 May 2023
2. Vojnovic, G., Ratković Kovačević, N., Dihovicni, D., Kreculj, D.: 3D printing of the parts of the library automation system. In: Programme & BOA of the International Conference SIR-AMM23, H2020-WIDESPREAD-2018–03 Project No. 857124, vol.1, pp. 136–137. Polytechnic University of Timisoara, Timisoara, Romania (2023). https://www.siramm.unipr.it/2_Events/FinalConferenceSIRAMM23/SIRAMM23%20Programme.pdf. Accessed 15 May 2023
3. Yu, X., Fan, Z., Wan, H., He, Y., Du, J., Li, N., Yuan, Z., Xiao, G.: Positioning, navigation, and book accessing/returning in an autonomous library robot using integrated binocular vision and QR code identification systems. *Sensors* **19**(4), 783, 1–26 (2019). <https://doi.org/10.3390/s19040783>. <https://www.mdpi.com/1424-8220/19/4/783>. Accessed 15 May 2023
4. Liu, J.L., Zhu, L.: Library intelligent bookshelf positioning system research. In: 4th Proceedings of the International Conference on Mechatronics, Materials, Chemistry and Computer Engineering ICMCCE 2015, Atlantis Press, vol. 1, pp. 1237–1242. Atlantis Press (2015). <https://doi.org/10.2991/icmmcce-15.2015.238>. Accessed 15 May 2023
5. Dani, A., Patil, R.N.: QR code based library management system. *Int. J. Emerg. Technol. Innov. Res. JETIR* **7**(6), 1876–1883 (2020). <http://www.jetir.org/papers/JETIR2006271.pdf>. Accessed 15 May 2023
6. Chanda, A.: Barcode technology and its application in libraries. *E-J. Libr. Philos. Pract.* **1**(1), 3619, 1–15 (2019). <https://doi.org/10.2139/ssrn.3649957> <https://digitalcommons.unl.edu/libphilprac/3619>. Accessed 15 May 2023
7. Tahil, S.K.: Library automation: an emerging technology for State University and Colleges in Sulu Province. *Nat. Sci. Eng. Technol. J. NASET* **2**(1), 85–89 (2021). <https://doi.org/10.37275/nasetjournal.v2i1.16>. Accessed 15 May 2023

8. Control 28BYJ-48 Stepper Motor with ULN2003 Driver & Arduino. <https://lastminuteengineers.com/28byj48-stepper-motor-arduino-tutorial/>. Accessed 15 May 2023
9. 28BYJ-48 stepper motor and ULN2003 Arduino (Quick tutorial for beginners) [Online Video]. <https://www.youtube.com/watch?v=avrddZD7qEQ/>. Accessed 15 May 2023
10. NikodemBartnik/ArduinoTutorials: <https://github.com/NikodemBartnik/ArduinoTutorials>. Accessed 15 May 2023
11. Arduino: Limit Switch on ARDUINOGETSTARTED.com Homepage. <https://arduinogetstarted.com/tutorials/arduino-limit-switch>. Accessed 15 May 2023
12. Arduino: Button Library (ezButton Library installation) Homepage. https://arduinogetstarted.com/tutorials/arduino-button-library#content_how_to_install_library. Accessed 15 May 2023
13. Arduino: Stepper Motor and Limit Switch Homepage. <https://arduinogetstarted.com/tutorials/arduino-stepper-motor-and-limit-switch>. Accessed 15 May 2023
14. Comparing Modular Linear Actuator Drive Types. <https://www.nookindustries.com/resources/blog/archive/comparing-modular-linear-actuator-drive-types/>. Accessed 15 May 2023
15. Linear Mechanics. (In Serbian). <https://mehatron.rs/linearna-mehanika>. Accessed 15 May 2023
16. Voyager 1250g Single Laser Scanner Data Sheet. https://www.posnet.com.pl/files/products_download/109/voyager1250g-handheld-scanner-data-sheet-en.pdf. Accessed 12 June 2023
17. Voyager 1250g General Duty Scanner Product Description. <https://sps.honeywell.com/gb/en/products/productivity/barcode-scanners/general-purpose-handheld/voyager-1250g-general-duty-scanner>. Accessed 12 June 2023



Development of a Method for Testing Temperature Distribution During 3D Printing of Specimens with Application in Aerospace Industry

Zorana Golubović¹(✉), Milan Travica², Nenad Mitrović¹, Isaak Trajković²,
and Miloš Milošević²

¹ Faculty of Mechanical Engineering, University of Belgrade, Belgrade, Serbia
zzgolubovic@mas.bg.ac.rs

² Innovation Centre of Faculty of Mechanical Engineering, Belgrade, Serbia

Abstract. Additive manufacturing and 3D printing technologies are rapidly evolving and influencing changes in design, prototyping, engineering and manufacturing processes in various industries, including aerospace. In order to use 3D printing processes to produce parts with adequate and satisfactory mechanical properties for aircraft that are constantly exposed to extreme temperatures and environmental conditions, the temperature variations that occur must be taken into account. In this study, small-scale specimens of the thermoplastic polymer material polylactic acid (PLA) were printed using an FDM printer while a thermal imaging camera was used to record the temperature changes during the printing process. The aim was to determine the temperature changes during each step of the printing process of small specimens and to create a future model for testing the temperature distribution.

Keywords: 3D printing · Aerospace industry · FDM · PLA · Heat distribution · Methodology

1 Introduction

The rapid development of additive manufacturing (AM) and 3D printing technologies has led to significant changes in design, prototyping, engineering, and manufacturing processes in various industries, including aerospace. In the last decade, the aerospace industry has been one of the leading sectors using AM [1]. One of the most important features in the aerospace industry is the need for lightweight components with the best possible strength-to-weight ratio to improve safety, fuel efficiency, and reduce emissions [2]. Aerospace engineers are working to reduce the weight of aircraft by minimizing the number of materials used in each component, which increases the complexity of the design in terms of structure and its function [3]. In addition, the materials used for aircraft need to be lighter, more durable, and capable of producing any shape and geometry, making 3D printing the best possible technology for production.

The AM process always starts with the design of the 3D model in the appropriate software. The performance of any product can be improved by using AM, as parts with complex geometry can be produced. To determine the best geometry of the parts for the desired purpose, various parameters must be optimized, such as manufacturing speed, temperature, strength, mass, power and price. In addition, the approach must be tailored and defined for the AM process selected.

In aerospace industry, parts manufactured with AM are divided into metallic and non-metallic parts depending on the criticality of use [1]. Conventional metal parts are being replaced with appropriately strong 3D-printed parts to reduce aircraft weight and part repair time. Research shows that thousands of non-metallic AM parts have been installed in various aircraft in recent years [4]. One of the most commonly used non-metallic AM technologies in the aerospace industry is the Fused Deposition Modelling (FDM) process, in most cases using polymers as non-metallic materials.

Even for the simplest aircraft part, several material performance parameters must be considered, including strength, creep and fatigue resistance, temperature, processing, electrical conductivity, chemical and radiation sensitivity, flammability testing, toxicity, and cost. To produce parts with satisfactory and repeatable mechanical properties and with dimensional control, the temperature distribution in the printing platform must be as uniform as possible. Improved thermal control is required for most thermoplastic polymer printing processes [5].

In this study, specimens of polylactic acid (PLA), a thermoplastic polymer material, were fabricated with an FDM printer using a thermal imaging camera to record temperature changes during the printing process. Various process parameters affect the mechanical properties of the printed parts, such as the material used, the fill density, the pattern, the layer thickness, the screen width and angle, the print orientation and speed, and the nozzle temperature [6]. Since FDM is a thermal process, it is important to observe the temperature changes that occur during the printing process and their influence on the other properties. The temperature evolution during printing depends, on the one hand, on the printing parameters mentioned above and, on the other hand, on the nozzle temperature and the temperature of the build platform [7], and the control of these parameters is important for a better quality and accuracy of the final product produced with the FDM process [8, 9].

Given that the aerospace industry produces both small and large parts, the goal of this research was to first determine the temperature changes on small specimens in order to develop a model for studying thermal imaging tests on large objects.

2 Methodology

The material used in this research is PLA, a thermoplastic, biodegradable and environmentally friendly polymer. It is considered a good material for prototypes and parts that require higher dimensional accuracy. The positive sides of PLA are low material shrinkage, good thermoformability at low processing temperatures, high dimensional accuracy after cooling, and fast crystallization after cooling, while the negative sides are brittleness, degradation behavior, and lower thermal stability [10, 11].

SolidWorks CAD software was used to model the specimens, 5 specimens with dimensions 10 x 5 x 5 mm were produced and then printed on RepRap X400 3D printer (Rep Rap, Germany). The printing parameters are shown in Table 1.

Table 1. Printing parameters.

Printing parameters	Value
Filament diameter	1,75
Infill pattern	Concentric
Infill density	30%
Layer height	0,2 mm
Printing speed	60 mm/s
Nozzle diameter	0,4 mm
Nozzle temperature	195,5 °C
Chamber temperature	33,2 °C
Build platform temperature	48,1 °C

Thermal imaging camera PeakTech 5620 (PeakTech, Germany) as non-invasive, contact free measuring technique was places at the convenient distance of 30 cm from printing specimens (Fig. 1). Chamber of 3D printer was opened in order to avoid poor overview of the printing space due to plexiglas door. Ambient conditions were kept constant, by air cooling and keeping temperature at 23 °C and humidity of 55% RH. Emissivity of PLA material was set to be 0,92 [12].

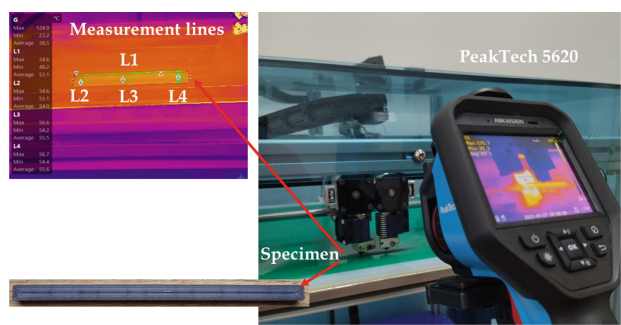


Fig. 1. Experimental setup.

The first specimens was recorded, and additional images were taken every 10 s during printing. The camera recordings are available in raw video and image format for a given position in real time and show the temperature data for each specific point of the specimen.

Previously, it was shown that the effect of temperature on the finished part can be controlled by different settings of the build plate and the pressure chamber temperature [13]. Deformations that occur during printing were monitored during the printing process, observing the influence of the printing temperature, temperature distribution, different layer heights and the subsequent cooling process [8].

3 Results and Discussions

The temperature distribution during the 3D printing process was monitored by thermo-visual measurements, and data were collected for each newly printed layer. Thermal Imaging iVMS-4800 software was used for process monitoring. The images captured by the thermal imaging camera show a variety of colours that correlate with the position of the nozzle as the hottest area. During the solidification of the filaments, there are colour changes ranging from yellow and orange to red, while pink, purple and blue correspond to the lower temperatures of the colder areas.

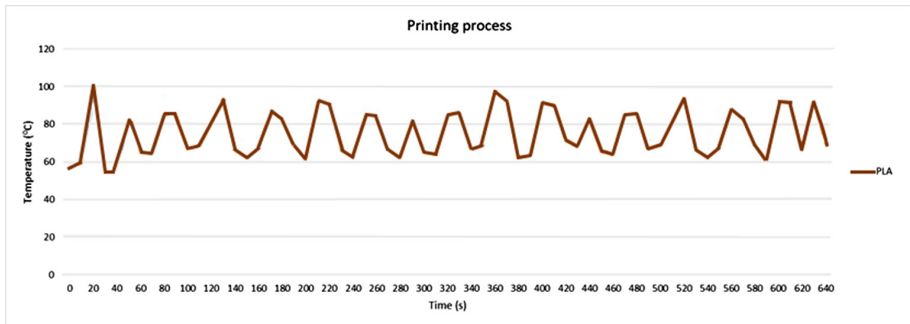


Fig. 2. Software presentation of thermal evolution during printing process.

The graphs show the average temperature in a certain area of the surface of the built-up layer. In this experiment, the temperature changes are sinusoidal, while the temperature values measured at the surface have approximate values at each moment of pressure (Fig. 2). Previously, it was shown that the temporal temperature changes during the cooling process are approximately linear for all measurement lines, and that the cooling rate directly affects the average temperature of the surface layer [14].

4 Conclusions

Additive manufacturing, i.e., 3D printing, was one of the first processes used in the aerospace industry to produce various aircraft parts of different sizes and importance, including aircraft interior components, fuel tanks, etc. [15]. Airplanes are exposed to extreme temperatures and chemicals during their repeated use and therefore need to be as light as possible [16]. Many environmental parameters such as heat, humidity, and radiation must be considered when the part is installed in an aircraft. To obtain the final

part by 3D printing, which is a thermal process, analyzing the effects of temperature changes during the printing process is an important step to obtain complete information and avoid possible negative effects on the final product.

This study has shown that the temperatures of small specimens have a sinusoidal pattern with approximate values at each moment. The temperature changes correspond to the movement of the nozzle. Future research will include in-situ monitoring of temperature changes with thermal imaging on the large specimens to track the thermal evolution in the manufacturing process.

Acknowledgement. This research was financially supported by the Ministry of Science, Technology Development and Innovation of the Republic of Serbia by Contract No. 451-03-47/2023-01/200105 from 03.02.2023.

References

1. Najmon, C., Raeisi, S., Tovar, A.: Review of additive manufacturing technologies and applications in the aerospace industry. In: *Additive Manufacturing for the Aerospace Industry*, pp. 7–31. Elsevier (2019) <https://doi.org/10.1016/B978-0-12-814062-8.00002-9>
2. Braga, D.F.O., Tavaresa, S.M.O., da Silva, L.F.M., Moreira, P.M.G.P., de Castro, P.M.S.T.: Advanced design for lightweight structures: review and prospects. *Prog. Aerosp. Sci.* **69**, 29–39 (2014)
3. Gibson, I., Rosen, D., Stucker, B.: *Additive Manufacturing Technologies: 3D Printing, Rapid Prototyping, and Direct Digital Manufacturing*. Springer, New York (2014)
4. Liu, R., Wang, Z., Sparks, T., Liou, F., Newkirk, J.: 13—Aerospace Applications of Laser Additive Manufacturing A2—Brandt, Milan, *Laser Additive Manufacturing*, pp. 351–371. Woodhead Publishing (2017)
5. Lyons, B.: Additive manufacturing in aerospace: examples and research outlook. *Spring Issue Bridge Front. Eng.* **42**(1) (2012)
6. Abeykoon, C., Sri-Amphorn, P., Fernando, A.: Optimization of fused deposition modeling parameters for improved PLA and ABS 3D printed structures. *Int. J. Lightweight Mater. Manuf.* **3**, 284–297 (2020)
7. Garzon-Hernandes, S., Garcia-Gonzalez, D., Jérusalem, A., Arias, A.: Design of FDM 3D printed polymers: an experimental-modelling methodology for the prediction of mechanical properties. *Mater. Des.* **188**, 108414 (2020)
8. Geng, P., et al.: Effect of thermal processing and heat treatment condition on 3D printing PPS properties. *Polymers* **10**, 875 (2018)
9. Prajapati, H., Salvi, S.S., Ravoori, D., Jain, A.: Measurement of the in-plane temperature field on the build plate during polymer extrusion additive manufacturing using infrared thermometry. *Polym. Test.* **92**, 106866 (2020)
10. Milovanović, A., Milošević, M., Mladenović, G., Likožar, B., Čolić, K., Mitrović, N.: Experimental dimensional accuracy analysis of reformer prototype models produced by FDM and SLA 3D printing technology. In: Mitrović, N., Milošević, M., Mladenović, G. (eds.) *Experimental and Numerical Investigations in Materials Science and Engineering*, pp. 84–95. Springer, Cham (2019)
11. Milovanović, A., Golubović, Z., Trajković, I., Sedmak, A., Milošević, M., Vaele, E., Marsavina, L.: Influence of printing parameters on the eligibility of plain-strain fracture toughness results for PLA polymer. *Proc. Struct. Integ.* **41**, 290–297 (2022). <https://doi.org/10.1016/j.prostr.2022.05.034>

12. Morgan, R., Reid, R., Baker, A., Lucero, B., Bernardin, J.: Emissivity Measurements of Additively Manufactured Materials, Preliminary Report, LA-UR-17-20513. Los Alamos National Laboratory, Los Alamos, N. Mex., USA (2017)
13. Lalegani Dezaki, M., Ariffin M.K.A.M., Hatami, S.: An overview of fused deposition modelling (FDM): research, development and process optimization. *Rapid Prototyp. J.* **27**(3):562–582 (2021)
14. Golubović, Z., Travica, M., Trajković, I., Petrović, A., Misković, Z., Mitrović, N.: Investigation of thermal and dimensional behavior of 3-D printed materials using thermal imaging and 3-D scanning. *Therm. Sci.* **27**, 21–31 (2023). ISSN: 0928–4931 <https://doi.org/10.2298/TSC12301021G>
15. Martinez, D.W., Espino, M.T., Cascolan, H.M., Crisostomo, J.L., Dizon, J.R.C.: A Comprehensive Review on the Application of 3D Printing in the Aerospace Industry. In: *Key engineering materials*, 913:27–34). Trans Tech Publications, Ltd. (2022) <https://doi.org/10.4028/p-94a9zb>
16. Karkun, M., Dharmalingam, S.: 3D printing technology in aerospace industry—a review. *International J. Aviat. Aeronaut. Aerospace* **9**(2) (2022) <https://doi.org/10.15394/ijaaa.2022.1708>



Determination of Compression Response for Various Dried Vegetables

Miloš Milošević¹, Ivana Jevtić¹(✉), Isaak Trajković¹, Ivan Zlatanović²,
Goran Mladenović², and Nenad Korolija³

¹ Innovation Centre of the Faculty of Mechanical Engineering, Kraljice Marije 16 Street, 11120
Belgrade, Serbia

ijevtic@mas.bg.ac.rs

² Faculty of Mechanical Engineering, University of Belgrade, Kraljice Marije 16 Street, 11120
Belgrade, Serbia

³ School of Electrical Engineering, The Department of Computer Science and Information
Technology, University of Belgrade, 11000 Belgrade, Serbia

Abstract. The texture of food plays a vital role in its overall quality, affecting both sensory experience and functional aspects, such as processing and preservation. To study texture in the field of food science and technology, various analytical methods are used to measure mechanical properties such as hardness, cohesiveness, and viscosity. One widely utilized technique for evaluating the texture of solid foods, particularly those with high firmness or brittleness such as dried vegetables, is compression testing. Here, a force is applied to a food sample until it deforms or fractures. In this particular study, dried onions, carrots, and peppers were chosen as test samples to investigate their texture and compression properties. To perform the tests, the researchers employed a Shimadzu AGS-X universal testing machine equipped with a 1 kN load cell capacity. This machine allowed them to compress the samples and measure the force required to achieve a specific deformation. The obtained results revealed that the texture and compression properties of the dried vegetables were significantly influenced by the specific part of the vegetable being tested. For instance, when examining the dried onions, a notable disparity was observed between the inner and outer parts. The basal plate of the onion, in particular, exhibited much greater hardness compared to the middle portion of the dried onion. Consequently, breaking the sample required a higher compression force. This discovery implies that the texture and compression properties of dried vegetables are closely tied to their inherent characteristics, internal structure, and composition.

Keywords: Food textures · Universal testing machine · Compression testing · Dried vegetables

1 Introduction

Food texture refers to the physical properties of food and is one of the key quality attributes used to assess product quality and acceptability. These properties include characteristics such as hardness, chewiness, crispness, smoothness, and viscosity [1, 2]. Food

quality can be evaluated through two approaches - descriptive sensory analysis, which is subjective, and instrumental analysis, which is objective [3–6]. Descriptive sensory analysis is usually performed using a trained panel of sensory evaluation experts. This approach is based on subjective assessment of sensory characteristics of food, such as taste, texture, aroma, and appearance [7, 8]. On the other hand, instrumental analysis is based on objective measurements of the physical, chemical, and microbiological characteristics of food. This method includes the use of various technologies and instruments, such as spectroscopy, chromatography, microscopy, and the assessment of mechanical properties using a universal testing machine [8, 9]. These instruments can provide information on the chemical composition of food, microbiological characteristics, and other physical and mechanical properties of food. Both approaches have their advantages and disadvantages. Descriptive sensory analysis can provide detailed information on the sensory characteristics of food and obtain feedback on consumer tastes and preferences. On the other hand, instrumental analysis can provide objective data on the ingredients and characteristics of food, which can be useful for detecting potential problems in the production process and for evaluating the nutritional value of food.

As already mentioned, testing food texture on a universal testing machine is an objective method that is often used in evaluating food quality. This machine is used to measure various food characteristics, including hardness, elasticity, brittleness, and viscosity. This information can be useful in a variety of food-producing industries, including manufacturers of pasta, meat products, sweets, and ice cream. For example, pasta manufacturers can use a universal testing machine to determine the quality and consistency of the pasta [10]. This process usually consists of measuring the force required to break a pasta sample over a period of time. This measurement is used to determine the resistance of the pasta to breaking, which is an important characteristic when the pasta is cooked. Similarly, researchers investigated the correlation between crispness and mechanical characteristics of potato chips tested under pressure [11, 12]. It is believed that this analysis will contribute to the development of food engineering, providing new methods to quantify the crispness of dry foods [11]. In addition to the crispness of the food, in the works [13–15] measurements of the tomatoes' firmness were examined.

In this work, the compression properties of different types of dried vegetables were determined on a universal tensile testing machine, with a special focus on dried onions, carrots, and peppers. Using the compression method, the resistance of vegetables to pressure and their elasticity is studied. By measuring compression forces and changes in the shape of vegetables during the application of force, obtained data can be useful for determining the quality and usability of dried vegetables in various processes in the food industry. The results of this research will provide valuable information on how the compressive properties of vegetables change during drying and how they differ between different types of vegetables. This knowledge can be useful for food manufacturers when selecting and optimizing the vegetable drying process, as well as for end consumers in terms of selecting the best quality dried vegetables for their needs and preferences.

2 Materials and methods

The products used in this research are dried onions, carrots, and peppers. The samples were cut into discs with a maximum thickness of 10 mm (see Fig. 1). In total, three samples of dried onions and four samples of dried carrots and peppers were examined. The products were placed on an AXIS-BTS11D moisture balance after purchase, where they were dried at a temperature of 60 °C (see Fig. 2). The moisture measurement interval was 160 s, which made it possible to monitor moisture changes in real-time during drying. This is of great importance because moisture is gradually reduced in order to preserve the structure, color, and aroma of the product. The mentioned scale provides precise moisture measurement results, thanks to an accuracy of 0.001g. This makes it possible to detect even the smallest changes in the mass of the sample during the drying process. The scale is equipped with halogen heaters, and the maximum mass of samples that can be dried is 100g.



Fig. 1. Samples of dried onion.

Many methods are used to measure the texture properties of food, such as compression tests, puncture tests, 3-point bending tests, tensile and shear tests, and viscoelasticity tests. The compression test is the most commonly used method for determining food texture, and this method was used in this research. After drying of the samples, the compression tests were performed on a Shimadzu AGS-X universal testing machine at room temperature (about 23 °C) using a load cell with 1kN capacity (see Fig. 3). Pressure tests were performed at a test speed of 1 mm/min, the sampling rate on the machine was 100 Hz. Dedicated software Trapezium-X (Shimadzu Corp., Kyoto, Japan) was used to analyze data from pressure tests. For pressure testing, two plane-parallel plates are needed, in order to adequately apply the pressure load to the tested sample.



Fig. 2. Carrots during drying on a moisture scale.

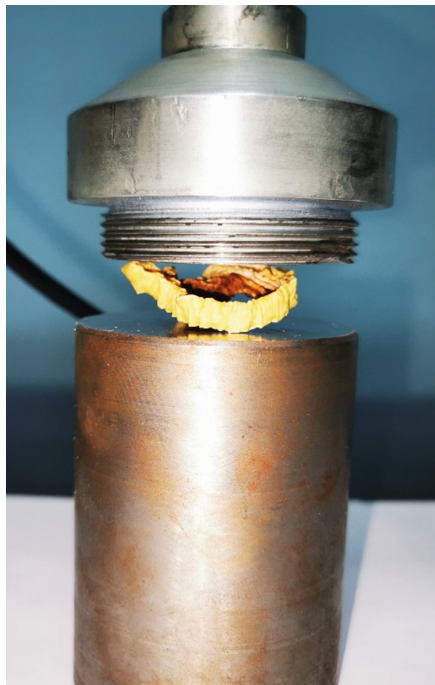


Fig. 3. Samples of onion testing on the universal testing machine.

3 Results and Discussion

The examination of dried vegetables involved analyzing various aspects, and the obtained results are visually represented in the following graphs. Figure 4 illustrates the force-displacement dependence for dried onions. By studying this graph, it becomes evident that there are significant differences among the three samples tested. Upon close examination of the graph, it can be observed that sample number 1 exhibited the least amount of crispness. This implies that it maintained its structural integrity better than the other two samples during examination. The graph likely indicates the force applied to the dried onions versus the resulting displacement or deformation, providing insights on their mechanical properties. Furthermore, Fig. 1, which presents visual representations of the tested samples, provides additional information. It becomes apparent that there were noticeable differences between the samples. Specifically, the first and second samples were cut from the middle of dried onion and appeared relatively softer than the third sample. The third sample, representing the basal plate of the onion, exhibited the highest strength among the three samples.

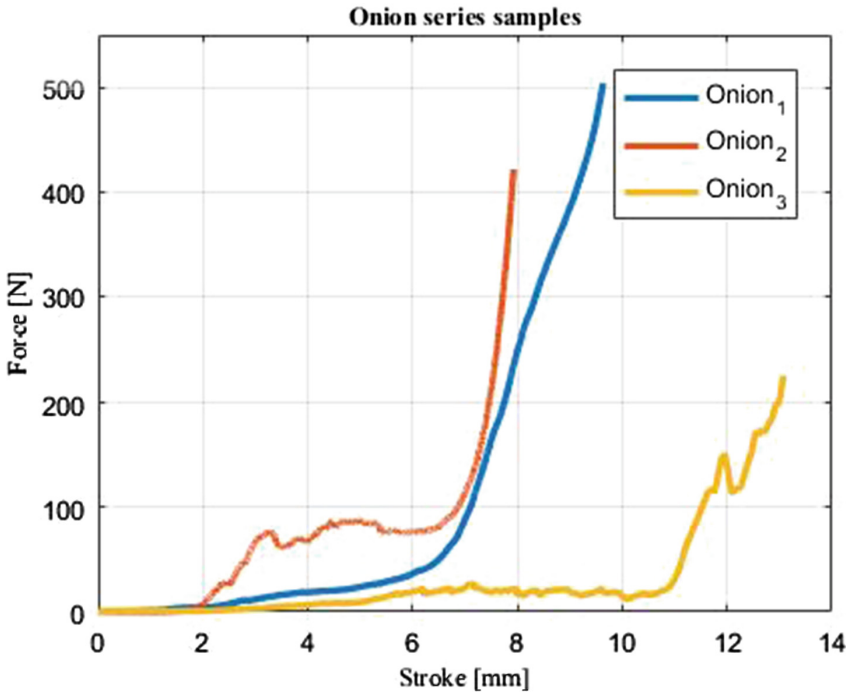


Fig. 4. Force-stroke dependence for onion samples during compression tests.

The force-displacement dependence of dried carrots is shown in Fig. 5. After careful analysis of the provided picture, it becomes evident that the four carrot samples share a considerable degree of similarity, particularly when comparing samples 1, 3, and 4. These three samples exhibit strikingly similar characteristics in terms of force and

stroke values, as well as crispness. However, upon closer inspection, it is discernible that sample number 2 differs slightly from the others, specifically in stroke magnitude. Sample 2 shows a slightly larger and bolder stroke in contrast to the remaining three samples.

Another notable observation is the presence of crispness in all four carrot samples. It is evident that each sample has experienced some degree of crispness, albeit with varying intensities. Among the four samples, sample number 4 stands out as the one with the least noticeable cracking. This sample exhibits a smoother and more intact surface, with minimal evidence of cracking.

These findings shed light on the consistency and quality of the carrot samples depicted in the picture. Despite the slight variation in stroke size observed in sample number 2, the overall similarity among the four samples suggests that they likely belong to the same batch or share common growing conditions.

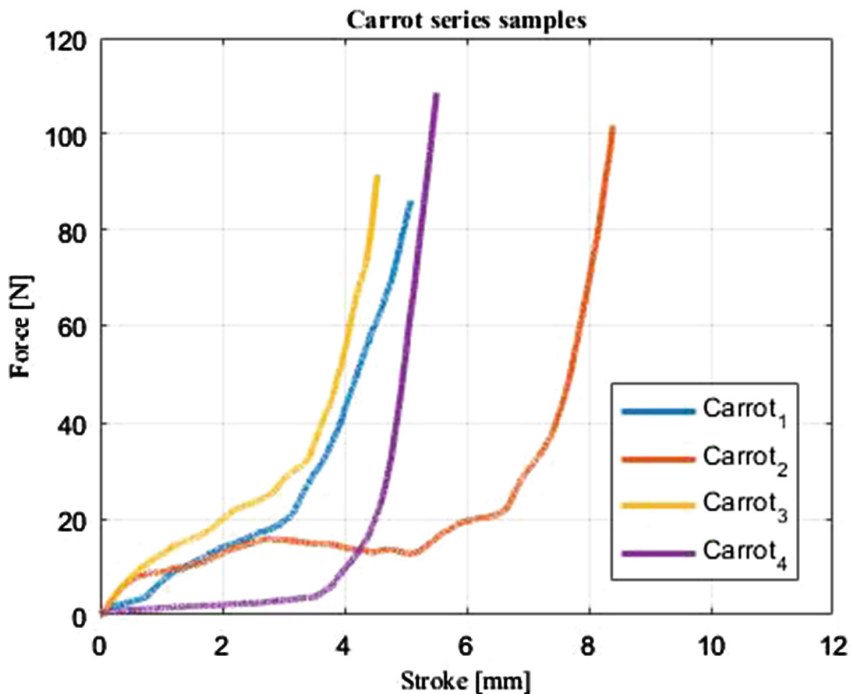


Fig. 5. Force-stroke dependence for carrot samples.

Graphical representation tests on dried pepper samples are shown in Fig. 6. By analyzing the graph, one can deduce that sample 3 exhibits the lowest force and stroke values among all samples. On the other hand, sample number 1 shows nearly double the force value when compared to sample number 3. The variation in the force and stroke values among the dried pepper samples indicates differences in their textural attributes. Sample 3, with the lowest force and stroke values, suggests a relatively softer and less resistant texture compared to the other samples.

Furthermore, all the tested samples display a remarkable level of crispness, characterized by distinct peaks in their respective graphs. Particularly notable are the pronounced peaks observed in samples number 1 and 4. These peaks indicate a significant level of crispness, suggesting that these samples possess a desirable texture and quality.

These findings from the graph provide valuable information about the relative properties and characteristics of the dried pepper samples. The data highlights the considerable differences in force and stroke values between the samples, emphasizing the varying levels of crispness observed. Such insights can help to evaluate and compare the quality of dried pepper samples for various purposes, such as culinary applications or food production.

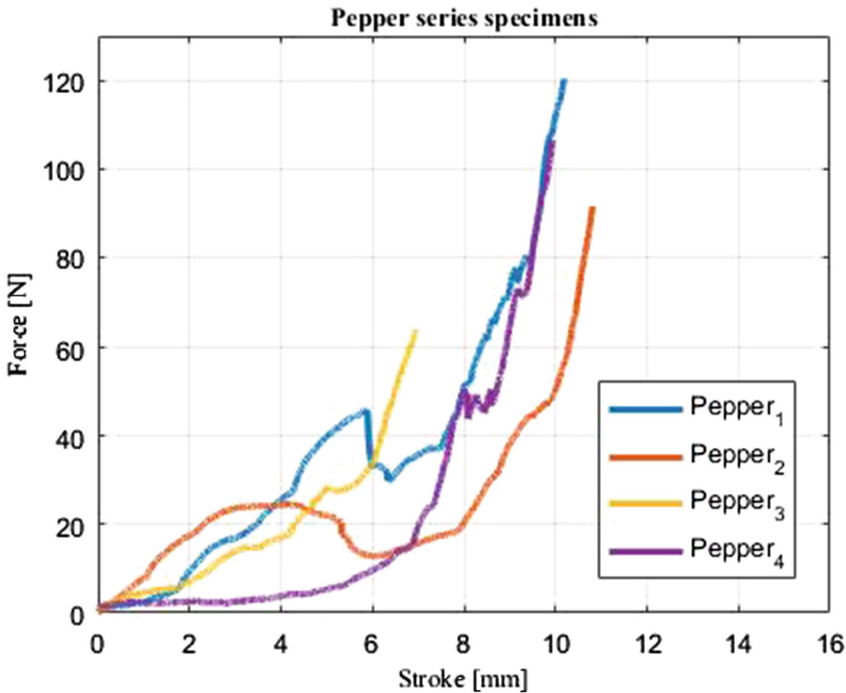


Fig. 6. Force-stroke dependence for pepper samples.

The level of crispness is an important aspect of both food taste and transportation. After collecting the force-stroke dependence for all samples, it was noticed that for certain dried vegetables there are ranges of strokes for which a relatively high number of drops in forces are detected, while the forces are similar in values. An analysis tool is programmed to determine the range of forces for which the most significant amount of forces drops occur. First, raw data from the file was averaged to eliminate noise. Further, consecutive drops in forces are summed, and resulting sums are stored along with forces that correspond to each sum, and stroke values. The following analysis is performed for the case of onion sample number 2. From all drops, those with values less than 10% of the average force found were neglected, eliminating 9 out of 20 detected drops. The

results show that 9 out of 11 forces drop with forces in the range of 63.2 N and 76.9 N. The other two drops were relatively small in terms of forces and occurred in the range of 27.8 N and 29.3 N. These results indicate that it is possible to calculate the amount of vegetables that can be packed together so that the crispness level is well preserved.

4 Conclusions

This research paper presents the results of a vegetable compression experiment. Prior to the experiment, onions, carrots, and peppers were subjected to drying. Upon examination of the dried onions, it was observed that there were significant variations between the samples. The onion sample from the center of the arch exhibited the fewest cracks, while the basal plate sample demonstrated the highest resilience and endured the most shocks. These findings yield valuable insights into the mechanical attributes and structural disparities of dried onions.

Cracking was apparent in all four carrot test samples, with one sample displaying the least amount of cracks. These observations contribute to a comprehensive evaluation of characteristics and potential disparities in the quality of the carrot samples under investigation.

This knowledge empowers decision-makers to make informed choices when selecting the most appropriate samples for specific culinary or food production requirements, considering aspects like spiciness, softness, firmness, and crispness. By utilizing these findings, manufacturers, chefs, and consumers can optimize the use of dried pepper samples to achieve the desired flavor and texture profile in their creations.


References

1. Kadam, S.U., Tiwari, B.K., O'Donnell, C.P.: 6- Improved thermal processing for food texture modification. Woodhead Publishing Ser. Food Sci., Technol. Nutr. **1**, 115–131 (2015)
2. Day, L., Golding, M.: Food Structure, Rheology, and Texture, Encyclopedia of Food Chemistry, pp. 125–129 (2016)
3. Chen, L., Opara, U.M.: Texture measurement approaches in fresh and processed foods—a review. Food Res. Int. **51**, 823–835 (2013)
4. Vernon, K.E.J., Sherman, P.: Evaluation of the firmness of Leicester cheese by compression tests with the Instron universal testing machine. J. Texture Stud. **9**, 311–324 (1978)
5. Shama, F., Sherman, P.: Evaluation of some textural properties of foods with the Instron universal testing machine. J. Texture Stud. **4**, 344–353 (1973)
6. Kohyama, K.: Food texture—sensory evaluation and instrumental measurement, textural characteristics of world foods (2020)
7. Fellows, P.J.: Properties of food and principles of processing. In: Food Processing Technology, pp. 3–200 (2017)
8. Saeleaw, M., Schleining, G.: A review: crispness in dry foods and quality measurements based on acoustic-mechanical destructive techniques. J. Food Eng. **105**, 387–399 (2011)
9. Damez, J.-L.: Meat quality assessment using biophysical methods related to meat structure. Meat Sci. **80**, 132–149 (2008)
10. Shimadzu.com: <https://www.ssi.shimadzu.com/products/materials-testing/uni-ttm-system/ez-test-texture-analyzer/index.html>. Accessed 15 May 2023

11. Aprilia, G.E., Triawan, F., Saville, R.: Crispness measurement of potato crisps by single specimen using compression test. In: The 5th Annual Applied Science and Engineering Conference (AASEC 2020) (2021)
12. Triawan, F., Aprilia, G.E., Saptaji, K., Saville, R., Nandiyanto, A.B.D.: Determining crispness level of dry food through its compressive strain energy. *Ind. J. Comput., Eng., Design* **3**, 106–118 (2021)
13. Holt, C.B.: Measurement of tomato firmness with a universal testing machine. *J. Texture Stud.* **1**, 491–501 (1970)
14. Babarinsa, F.A., Ige, M.T.: Energy absorption capacity of packaged Roma tomatoes under compressive loading. *Int. J. Sci. Eng. Res.* **3** (2012)
15. Babarinsa, F.A., Ige, M.T.: Strength parameters of packaged Roma tomatoes at break point under compressive loading. *Int. J. Sci. Eng. Res.* **3** (2012)



Energy Efficiency in Serbia: Challenges and Opportunities

Nenad Mitrovic¹  and Aleksandra Mitrovic² 

¹ University of Belgrade, Faculty of Mechanical Engineering, Belgrade, Serbia
nmitrovic@mas.bg.ac.rs

² Department of Computer-Machine Engineering, The Academy of Applied Technical Studies
Belgrade, 11000 Belgrade, Serbia

Abstract. Energy efficiency plays a critical role in achieving economic, social, and environmental sustainability. This paper provides an overview of the current state of energy efficiency in Serbia, focusing on the challenges, opportunities, and potential pathways towards a more sustainable energy sector. The country has recognized the importance of energy efficiency in improving energy security, reducing costs, and complying with international environmental standards. However, Serbia faces significant challenges, including a lack of awareness of the benefits of energy efficiency, insufficient financing, and policy support for energy-efficient technologies. Nevertheless, Serbia possesses considerable potential for energy-efficient technologies and practices, particularly in the residential and industrial sectors. By promoting energy efficiency, Serbia can reduce energy costs, improve energy security, and contribute to global climate-change mitigation efforts. The paper also highlights the global challenges faced by the energy sector, such as rising energy demand, climate change, pollution reduction, and energy poverty, emphasizing the need for greening the energy sector and investing in renewable energy sources. The energy consumption trends, energy intensity, energy productivity, and share of renewable energy sources in Serbia were analyzed using EuroStat data. The paper concludes by emphasizing the importance of ambitious goals, public awareness, modernizing infrastructure, and securing adequate financing to drive energy efficiency improvements in Serbia. This overview serves as a valuable resource for policymakers, researchers, and stakeholders interested in promoting sustainable energy practices in Serbia and fostering a transition towards a more energy-efficient and environmentally friendly energy sector.

Keywords: Energy efficiency · Serbia · Energy consumption · Energy intensity · Energy productivity

1 Introduction

Energy efficiency is crucial for achieving economic, social, and environmental sustainability. Energy-efficient technologies and practices can reduce energy consumption, lower costs, and mitigate the impact of climate change [1]. In Serbia, energy efficiency has become a priority in recent years, as the country seeks to improve energy security, reduce energy costs, and comply with international environmental standards [2].

According to the statistical office of the European Union (EuroStat), Serbia's total final energy consumption has been increasing steadily since 2014 [3]. This growth is driven primarily by the transportation and residential sectors, which account for over half of the country's energy consumption. However, Serbia has made progress in improving energy efficiency, with a decrease in energy intensity (energy consumption per unit of GDP) [3].

Despite these positive trends, Serbia still faces significant challenges in promoting energy efficiency. One major challenge is the lack of awareness among businesses and individuals regarding the benefits of energy efficiency [4]. Another challenge is insufficient financing and policy support for energy-efficient technologies and practices [2]. These challenges are compounded by the fact that Serbia is still transitioning from a centralized, state-controlled energy system to a more market-oriented one, creating additional energy efficiency barriers.

However, there are also significant opportunities for improving energy efficiency in Serbia. The country has significant potential for energy-efficient technologies and practices, particularly in the residential and industrial sectors [5]. By promoting energy efficiency, Serbia can reduce its energy costs, increase energy security, and contribute to global efforts to mitigate climate change.

The aim of this paper is to provide a brief overview of energy efficiency, energy intensity and energy productivity in Serbia.

2 Energy Sector in the World: Challenges and Opportunities

As the world's 2.7 billion people lack access to modern energy and the present, highly carbon-intensive energy system relies on reducing fossil fuel reserves, it cannot be sustained at an economic, social, or environmental level. Additionally, the current state of the energy sector exposes many nations to significant fluctuations in the prices of imported oil, resulting in billions of public subsidies.

The goal of 'greening the energy sector', i.e. transforming the energy sector into a green system is to establish a sustainable and renewable energy supply while reducing greenhouse gas (GHG) emissions and pollution. This process involves enhancing energy efficiency, increasing the use of renewable energy sources, and decreasing reliance on fossil fuels, which accounts for the majority of GHG emissions. Improving energy efficiency can often have economic benefits by reducing dependence on fossil fuels. However, with growing population and income levels, energy demand is expected to increase to meet development needs. Greening the sector also aims to end 'energy poverty,' that is, provide electricity access to the 1.4 billion people currently without it and promote healthier and more sustainable cooking technologies for the 2.7 billion people relying on traditional biomass. Modern renewable energy has the potential to improve energy security globally, nationally, and locally, but enabling policies are necessary to ensure investment in greening the energy sector [6].

Governments and the global community face four major challenges in the energy sector [7], namely:

- dealing with rising energy demand and energy security concerns;
- addressing climate change;

- reducing pollution and public-health hazards; and
- tackling energy poverty [7].

Rising energy demand and energy security. Increasing energy demand, along with higher energy prices, raises concerns about the security of the energy supply, including issues such as the reliability and affordability of national sources of energy. These concerns are relevant for low-income countries, as well as emerging and developed economies, where a high dependence on limited imported sources can increase risks to the security of the national energy supply due to political and other developments. The International Energy Agency (IEA) Reference Scenario, which provides a baseline of how global energy markets will evolve without policy changes, shows that fossil fuels are projected to continue dominating energy supply in 2030. Additionally, models predict that greenhouse gas emissions will increase the fastest in high-growth countries, such as China and India. Investing in locally available renewable energy sources, which are often abundant, can improve the energy security in such countries [7].

Climate change. Numerous reports have stressed the significance of both mitigating human-caused climate change, which is largely caused by burning fossil fuels and adapting to irreversible changes. There is a wide range of estimates of the costs of adaptation and damage caused by climate change. The United Nations Environment Programme (UNEP) Report estimates that adapting to climate change would cost at least US\$160–\$340 billion annually by 2030 and US\$315–565 billion by 2050 for developing countries. Other studies that consider the additional direct and indirect impacts of climate change related to water, health, infrastructure, coastal zones, ecosystems, etc., have assessed that the cost of adaptation is several times greater than the UNEP estimate. Switching from fossil fuels to renewable energy sources in the energy supply can contribute to meeting emission-reduction goals, along with improvements in energy efficiency. To lower baseline emissions to a level that would maintain the concentration of GHGs at 450 ppm in 2050, renewable energy would need to account for 27% of the required CO₂ reductions, while the remainder would mostly result from energy efficiency and alternative mitigation options, such as carbon capture. Developing countries would see significant CO₂ reductions as a result of promoting renewables.

Pollution reduction and Public Health Hazards. Burning traditional and fossil fuels has several negative effects on human health. The World Health Organization (WHO) estimated that household air pollution caused 3.2 million deaths per year in 2020, including more than 200 000 deaths of children under the age of 5 [8]. Renewable energy generation has the potential to decrease or even prevent many of the health risks associated with mining, production, and use of fossil fuels. For instance, solar panels and wind turbines do not release air pollutants during their operation.

Energy poverty. Improving access to energy is a major challenge faced by developing nations, as modern and dependable energy services are required for poverty reduction, education, and better health. The challenge is daunting, with 770 million individuals currently lacking access to electricity (mostly in Africa and Asia) and 2.6 billion without access to clean cooking [9]. In sub-Saharan Africa, the number of people with no access to electricity in 2020 increased for the first time since 2013. According to EuroStat, approximately 35 million EU citizens (approximately 8% of the EU population) were

unable to keep their homes adequately warm in 2020 [3]. Utilizing renewable energy sources can be a cost-effective method for addressing energy poverty.

Governments can take advantage of four significant opportunities when implementing a strategy of increased investment in renewable energy as part of their efforts to make the energy sector more environmentally friendly. These include the presence of explicit policy objectives in many nations, advancements in technology that boost competitiveness, a recent upswing in renewable energy investment, and the potential for renewable energy initiatives to generate employment opportunities [7].

3 Energy Consumption in the Republic of Serbia

The EU has an energy efficiency target of reducing energy consumption by 20% by 2020 compared to the 2007 baseline and by 32.5% by 2030. The primary energy consumption should amount to no more than 1312 Mtoe (Million tonnes of oil equivalent) and the final energy consumption to no more than 959 Mtoe in 2020. The EU energy efficiency target for 2030 aims to achieve a primary energy consumption of no more than 1128 Mtoe and a final energy consumption of no more than 846 Mtoe. Primary energy consumption measures the total domestic energy demand, while final energy consumption refers to the actual energy consumed by the end users.

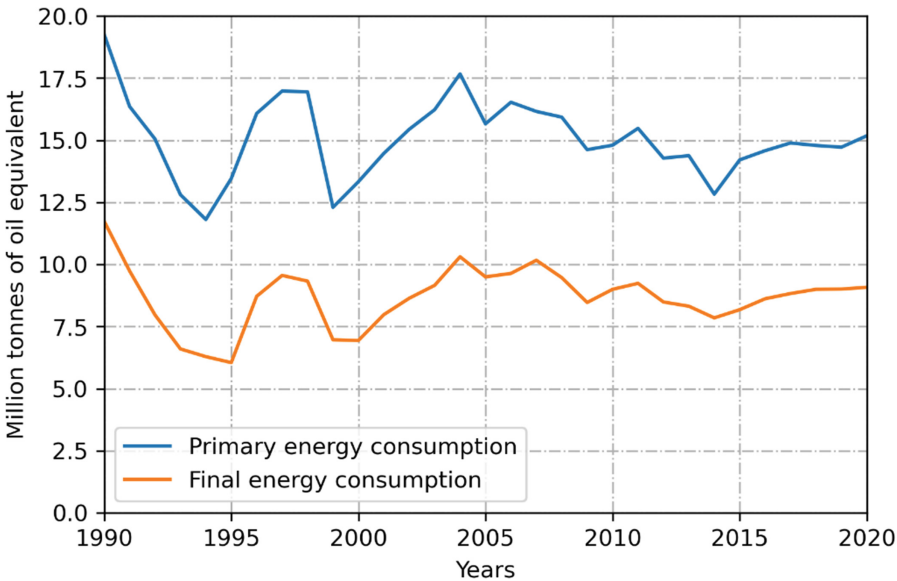


Fig. 1. Energy (primary and final) consumption in Serbia in the period of 1990–2020 (source: EuroStat)

The data presented in Fig. 1 show the level of energy consumption – primary energy consumption and final energy consumption–in the period–1990–2020. Energy saving could improve the security of the energy supply by reducing dependence on fuel imports.

The improvement in energy efficiency also improves the competitiveness of the industry and services, and for households, it reduces the energy bill. Energy savings can also contribute to reducing GHG emissions from fuel combustion.

Energy intensity, often used as an approximation of energy efficiency, is one of the indicators to measure the energy needs of an economy. Many factors influence energy intensity, for example, it reflects on the structure of the economy and its cycle, general standards of living and weather conditions in the reference area. This indicator can be used in the monitoring of several strategies and programs. Figure 2 presents the energy intensity indicator for Serbia from 1995 to 2021. As shown in Fig. 2, energy intensity has been declining in Serbia over the last several decades. The trend of the energy intensity indicator is the same as that of EU countries; however, the actual values of leading EU economies (for example, Germany or France) are much lower, somewhere above 100 kg of oil equivalent per thousand euro.

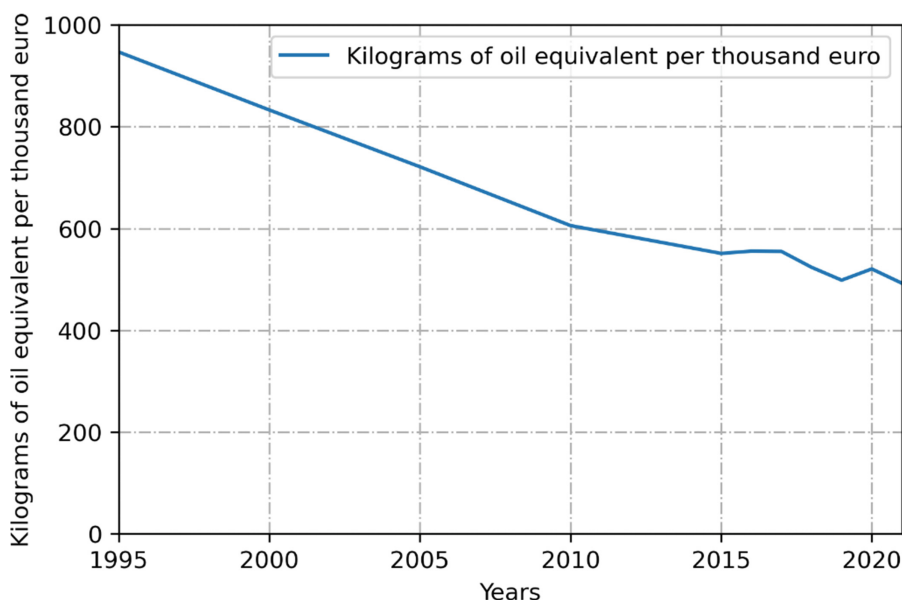


Fig. 2. Energy intensity in Serbia in the period of 1995–2021 (source: EuroStat)

Energy productivity refers to the evaluation of economic output generated per unit of gross available energy. Gross available energy refers to the total energy products required to meet the demands of entities within a specific geographic area. This measure is included in the Sustainable Development Goals (SDGs) set by the European Union (EU). It serves as a tool for tracking advancements in SDG 7, which focuses on accessible and clean energy, as well as SDG 12, which aims to establish sustainable patterns of consumption and production. Energy productivity is computed by dividing the units of GDP by the quantity of energy used. Figure 3 presents the energy productivity indicator for Serbia from 1995 to 2021. The energy productivity indicator has been increasing in recent decades; however, its value has stagnated in the last several years. The same trend

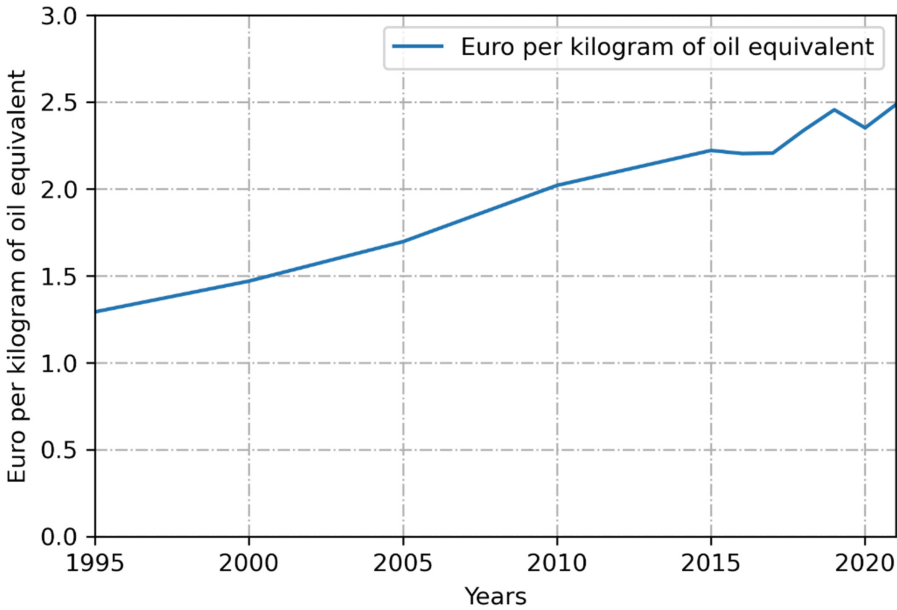


Fig. 3. Energy productivity in Serbia in the period of 1995–2021 (source: EuroStat)

is noticeable for EU countries, although the values are 3–4 times higher compared to Serbia in the previous decade.

Figure 4 presents the share of energy from renewable sources in Serbia from 2004 to 2021. The share of energy from renewable sources is presented for four indicators: Transport, Heating and Cooling, Electricity and Overall share of renewable sources.

Serbia has significant opportunities in the field of energy efficiency. The country has set ambitious goals to increase the share of renewable energy sources and improve energy efficiency in all sectors to ensure energy security, reduce negative environmental impacts, and contribute to global efforts to reduce greenhouse gases [10]. Serbia has economically viable potential for renewable energy sources, and the structure of the production mix in the electricity system should increasingly be based on renewable sources [11]. Investment in energy-efficient solutions, technologies, and practices leads to increased energy productivity [12]. Implementing energy-efficiency programs and using renewable energy sources can lead to sustainable economic development and increased competitiveness. In addition, public awareness about renewable sources can contribute to the social acceptance of sustainable development projects [13]. Additionally, reorganizing the district heating sector and introducing self-sustaining incentives for investments in infrastructure and thermal systems using renewable energy sources can increase efficiency. However, Serbia faces challenges in the field of energy efficiency. The Serbian economy is based on outdated and ‘dirty’ technologies, which results in low energy efficiency [14–17]. The country’s energy infrastructure is outdated, and approximately 66% of its electricity is generated by coal-fired power plants, however, Serbia’s energy strategy is oriented towards clean energy [18]. The implementation of

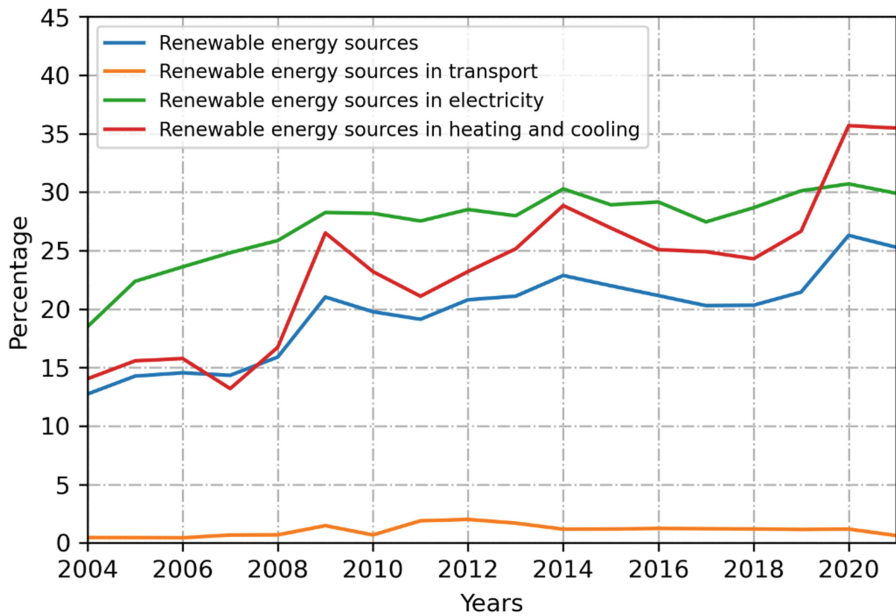


Fig. 4. Share of Energy from Renewable Sources in Serbia in the period of 2004–2021 (source: EuroStat)

energy efficiency programs requires significant investments, which can be a challenge for a country with limited financial resources [10]. Achieving the objectives of an Energy Union requires significant financing, particularly for investments in energy efficiency [19]. Serbia has ratified the Treaty establishing the Energy Community, whose key instrument is in alignment with the regulations of the European Union. Furthermore, the energy sector in Serbia is facing governance issues that can hinder the implementation of energy-efficiency policies [20].

4 Conclusion

The paper discusses the challenges and opportunities in the global energy sector, including rising energy demand, climate change, pollution reduction, and energy poverty. The need to transition to renewable energy sources and improve energy efficiency to address these challenges is emphasized. In the case of Serbia, energy consumption data reveals the importance of energy-saving measures for energy security and competitiveness. Energy intensity and productivity indicators provide insights into energy needs and economic output. An increasing share of renewable energy sources indicates progress in diversifying the energy mix. However, Serbia must overcome obstacles such as outdated technologies, limited resources, and governance issues to fully realize its energy efficiency potential. With strategic investments, the implementation of efficiency programs, and public awareness, Serbia can make significant progress towards sustainable energy development.

References

1. International Energy Agency: Energy Efficiency 2022. (2022)
2. Djordjevic, L., Pekez, J., Novaković, B., Bakator, M., Djurdjev, M., Čočkalović, D., Jovanović, S.: Increasing energy efficiency of buildings in Serbia—a case of an urban neighborhood. *Sustainability* (Switzerland) **15** (2023). <https://doi.org/10.3390/su15076300>
3. Eurostat - statistical office of the European Union: <https://ec.europa.eu/eurostat/web/main/home>. Accessed 11 May 2023
4. Agrawal, R., De Tommasi, L., Lyons, P., Zannoni, S., Papagiannis, G.K., Karakosta, C., Papapostolou, A., Durand, A., Martinez, L., Frigidis, G., Corbella, M., Sileni, L., Neusel, L., Repetto, M., Mariuzzo, I., Kakardakos, T., Güemes, E.L.: Challenges and opportunities for improving energy efficiency in SMEs: learnings from seven European projects. *Energy Effic.* **16** (2023). <https://doi.org/10.1007/s12053-023-10090-z>
5. Nebiu, B., Milanovska, E., Ribic, M., Pasoyan, A.: Gap Analysis of the housing sector in western balkan countries: Bosnia and Herzegovina. North Macedonia, and Serbia Vs. Slovak Republic, Kosovo (2020)
6. dos Santos Bernardes, M.A.: Biofuel Production. IntechOpen, Rijeka (2011). <https://doi.org/10.5772/959>
7. Towards a green economy: Pathways to Sustainable Development and Poverty Eradication. United Nations Publications (2011)
8. World Health Organization. <https://www.who.int/>. Accessed 11 May 2023
9. International Energy Agency: World Energy Outlook 2021 (2021)
10. Ciric, R.M., Mandic, S.N.: A review of challenges and benefits of integration of CHP plant into the grid: a case study in Serbia. *Electr. Eng.* **103**, 2809–2823 (2021). <https://doi.org/10.1007/s00202-021-01271-z>
11. Dragović, N.M., Vuković, M.D., Riznić, D.T.: Potentials and prospects for implementation of renewable energy sources in Serbia. *Therm. Sci.* **23**, 2895–2907 (2019). <https://doi.org/10.2298/TSCI170312056D>
12. Madžar, L.: Modelling the trend of energy productivity in the Serbian economy. *Ekonomika preduzeca* **70**, 179–190 (2022). <https://doi.org/10.5937/ekopre2204179m>
13. Žikić, S., Trifunović, D., Lalić, G., Jovanović, M.: Awareness of the population in rural regions of Serbia about renewable energy sources. *Ekonomika poljoprivrede* **69**, 43–56 (2022). <https://doi.org/10.5937/ekopolj2201043z>
14. Golusin, M., Munitlak Ivanovic, O.: Kyoto protocol implementation in Serbia as precognition of sustainable energetic and economic development. *Energy Policy* **39**, 2800–2807 (2011). <https://doi.org/10.1016/j.enpol.2011.02.052>
15. Tanasić, N., Jankes, G., Stamenić, M., Nikolić, A., Trninić, M., Simonović, T.: Potentials for reducing primary energy consumption through energy audit in the packaging paper factory. In: 3rd International Symposium on Environmental Friendly Energies and Applications (EFEA), pp. 1–5 (2014). <https://doi.org/10.1109/EFEA.2014.7059957>
16. Stamenić, M., Simonović, T., Tanasić, N.: Efficient technology for combustion of low calorific gaseous fuels. In: 2018 5th International Symposium on Environment-Friendly Energies and Applications (EFEA), pp. 1–5 (2018). <https://doi.org/10.1109/EFEA.2018.8617090>
17. Stamenić, M., Jankes, G., Tanasić, N., Trninić, M., Simonović, T.: Energy audit as a tool for improving overall energy efficiency in Serbian industrial sector. In: 2012 2nd International Symposium on Environment Friendly Energies And Applications, pp. 118–122 (2012). <https://doi.org/10.1109/EFEA.2012.6294075>
18. Spasenić, Ž., Benković, S., Sredojević, S.: Financing of wind energy projects in Serbia: current status and future prospects. In: Contemporary Financial Management, pp. 453–464. Institute for Local Self-Government Maribor (2023). <https://doi.org/10.4335/2023.3.23>

19. Đukić, M., Zidar, M.: Sustainability of investment projects with energy efficiency and non-energy efficiency costs: case examples of public buildings. *Sustainability (Switzerland)* **13** (2021). <https://doi.org/10.3390/su13115837>
20. Četković, S.: Energy governance in Serbia. In: Knodt Michèle and Kemmerzell, J. (ed.) *Handbook of Energy Governance in Europe*, pp. 1–17. Springer International Publishing, Cham (2020). https://doi.org/10.1007/978-3-319-73526-9_26-1



Comparative Mechanical Analysis of PLA and ABS Materials in Filament and Resin Form

Božica Bojović¹(✉), Zorana Golubović¹, Ljubiša Petrov², Aleksa Milovanović², Aleksandar Sedmak¹, Žarko Mišković¹, and Miloš Milošević²

¹ University of Belgrade, Faculty of Mechanical Engineering, Belgrade, Serbia
bbojovic@mas.bg.ac.rs

² Innovation Centre of Faculty of Mechanical Engineering, Belgrade, Serbia

Abstract. Additive manufacturing (AM), also known as 3D printing, represent technologies where the production of physical models with complex shapes is performed in a layer-by-layer manner, directly from the CAD model. With these processes, there is no need for additional tools or fixtures, and there is no excess material. There are seven different AM technologies, all utilizing different materials depending on the needed final part properties. Recent years were particularly significant for the development and advancement of polymer materials in AM. Among available technologies where polymer materials are used, this research covers extrusion-based Fused Deposition Modeling (FDM) and liquid resin photopolymerization technology called Digital Light Processing (DLP). Concerning the fact that these technologies process materials from different forms, the filament and resin form, the goal of this research was to compare the mechanical properties of two of the most widespread materials in AM, Acrylonitrile Butadiene Styrene (ABS) and PolyLactic Acid (PLA), in filament and resin form. Specimen geometry and test protocols followed the dedicated standards. For a comprehensive analysis tensile, compression, and (three-point) bending tests were utilized here, along with surface fracture 2D optical microscopy and Shore A hardness test.

Keywords: Additive manufacturing · FDM · DLP · ABS · ABS resin · PLA · PLA resin · Mechanical properties · Optical 2D microscopy · Hardness

1 Introduction

Since their beginnings in the 1980's Additive Manufacturing (AM) technologies revolutionized the production process. Several terms are used alongside AM, e.g., additive fabrication, rapid prototyping, rapid manufacturing, direct digital manufacturing, and the more commonly used term "3D printing". All names have in common the bottom-up approach to manufacturing. Until now, all AM technologies are divided into seven categories, different in manufacturing style and materials utilized for component production. They are named as follows: (1) binder jetting, (2) material jetting, (3) material extrusion, (4) directed energy deposition, (5) powder bed fusion, (6) sheet lamination, (7) vat photopolymerization [1]. Due to abundant possibilities offered by AM technologies, it is a necessity to be familiar with process-specific differences in order to comprehend all the

possibilities offered by the technology. Each of the AM technologies have different sets of available production parameters, which influence on the process adjustment and final part properties. In fact, these possibilities led to the broad range of AM applications in various industries such as large-scale production [2], architecture [3], automotive [4], railway [5], aerospace industry [6], biomedical [7], dentistry [8] and pharmacy [9] in particular, and not to forget the significance of the technology for science and education [10]. What makes this technology unique is the fact that it enables a less complicated workflow with the possibility of final object customization. The most challenging task for conventional manufacturing technologies is creating objects with complex geometries, which from the manufacturers' perspective AM overcomes effortlessly [11]. This bottom-up approach eliminates the need for the production processes that require complex tooling and machining, thereby creating a lot of scrap material [12].

After AM process is chosen with corresponding materials, in order to completely experimentally characterize properties of the final parts several techniques can be utilized, both during manufacturing process and after the part is finished. These techniques embrace: thermal properties characterization [13], ultrasonic monitoring of the layer build-up [14, 15], mechanical testing [16, 17], digital image correlation (DIC) [18, 19], hardness testing [20], microscopy [21], 3D scanning [22].

Improvement in mechanical properties and overall performance of polymers used in AM is a highly-researched topic in the last years. The mechanical properties of AM components not only derive from the raw materials' properties but also from AM process parameters utilized. Hence, in order to obtain a final part with adequate properties it is necessary to keep in mind all of these variables [23].

The widespread use of AM technologies is mainly due to devices' low-cost and availability of build materials. Based on the stated, two AM categories stand out: material extrusion and vat photopolymerization. Fused Deposition Modeling (FDM) and Digital Light Processing (DLP) are the most utilized AM technologies in material extrusion and vat photopolymerization categories, respectively. Both AM technologies use low-cost devices and affordable build materials [24]. In FDM build material is supplied in the form of a filament wrapped around a spool, guided to the extruder where the material is heated and deposited from a nozzle onto a build platform [25]. Process parameters depend from the build material and specific application of the final component [26, 27]. In FDM important parameters include layer thickness, infill pattern, infill orientation, infill density, raster angle, build direction, printing speed, and nozzle temperature [28, 29]. For example, an uneven heating of the component during FDM fabrication also is a significant factor, which can be comprehended via thermal analysis [13]. Vat photopolymerization process is based on selective photo-curing of the resin material using an UV light source. The low-cost of the device mostly depends on the cost of the light source. Hence, the DLP technology stands out, where UV source is from an affordable LCD screen. Not only due to devices' cost but also the time consumption is the reason for the high interest for this technology [30]. Here, printing parameters have to be set based on the pre-cured resin properties, such as UV light wavelength, in order to create solid components [31]. Layer height, speed of the light source and post-curing procedures are affecting the properties of the components [32]. Unlike other vat photopolymerization technologies,

in DLP process it is possible to customize printing parameters, such as UV light source (wavelength and intensity) and exposure time [33].

Most commonly used polymer materials in FDM are PolyLactic Acid (PLA) and Acrylonitrile Butadiene Styrene (ABS). The biggest concern in FDM is the amorphous nature of polymer materials, which only complicates with numerous of available AM parameters [34]. As for that, both PLA and ABS have been widely researched in recent years. These materials differ; PLA is made from renewable resources (i.e., corn starch, cassava roots, etc.) and is a biodegradable polymer, in contrast to petroleum-based ABS material, known for emitting the unpleasant odors during AM process. ABS has good mechanical properties but lacks in dimensional accuracy due to material shrinkage while cooling after the extrusion process [35]. On the other hand, PLA has better dimensional accuracy of final components [36]. However, PLA's downsides are brittleness and low impact strength [37, 38]. Printing parameters have a substantial effect on both PLA and ABS, e.g., the decrease of overall mechanical properties of ABS is apparent with lower infill densities [39, 40], and an increase of Young modulus is the case with higher infill densities [41]. Compared to PLA and ABS materials used in FDM, there is a very limited data addressed to assessment of mechanical properties and characterization of materials with similar properties but in a resin form dedicated for vat AM processes. New photocurable formulations of standard resins developed by manufacturers allows for a wider range of available properties [42]. Newly developed PLA-like resins hold high strength and stiffness but their drawback is low toughness. The resin materials can be tailored and the key to that is in the chemical and molecular control during the resin fabrication [43]. To improve PLA-like resin properties, changes can be made via blending, copolymerization, reinforcement with fibers, fillers, or by processing material to a composite [44–46]. ABS-like resins consist of three components: copolymer of styrene and acrylonitrile with additional rubber phase of polymer or copolymer containing butadiene, where each of these components affects certain properties of the resin [47, 48]. Recent research shows that building direction has an effect on surface roughness, stiffness and ultimate tensile strength (UTS). Namely, horizontally built specimens here have lower values of stiffness and UTS compared to vertical ones [49].

Except for mechanical properties, for some applications the materials' surface state is also important [50]. Hence, material property characterization includes different approaches namely, mechanical tests (tensile, bending, compressive, fatigue, impact), morphology evaluation (microscopy, hardness, roughness), dimensional accuracy (3D scanning) etc.

Objective of this research is a comprehensive comparison of mechanical properties of PLA and ABS materials used in FDM and DLP technology, in filament and resin form. It is well-known that components made from these two AM technologies differ significantly, however the intention here is to acquire a more detailed insight and comparison between these materials supplied in the different form, in the means of mechanical properties, hardness, and morphology.

2 Methodology

2.1 Specimen Preparation

AM process is based on the material layering until the final component is produced. Before AM process, the part model has to be created in the dedicated CAD (Computer Aided Design) software and saved in a distinct file format- usually “stl”, which is an industry-standard stereo-lithography format. Afterward, such a file is utilized for so-called “slicing” in dedicated software. The term “slicing” refers to CAD model partitioning into exact layers, needed to perform AM process [51]. An output of slicer software is a well-known G-code file, which contains defined process parameters and exact working tool trajectories for the application of the material.

Four commercially available materials were used in this study: ABS (Creality, Shenzhen, China), PLA (Creality, Shenzhen, China), ABS-like resin (Creality, Shenzhen, China), PLA-like resin (eSUN, Shenzhen, China). Specimens were modeled in CAD software (SolidWorks, Dassault Systèmes SE, Vélizy-Villacoublay, France), then converted to STL file format and sliced in the corresponding software’s for FDM (Simplify3D, Cincinnati, OH, USA) and DLP (ChiTuBox, Shenzhen, China) printers. Specimen’s geometry respects the ISO 527-2 standard for tensile testing, ISO 604:2002 for compression testing, and ISO 178:2019 for three-point bending testing. Fifteen specimens were prepared for each material, i.e., five specimens per each mechanical test- 60 in total (Table 1).

Table 1. Specimen’s distribution.

		FDM						DLP				
		T	3 p.b.	C	Σ			T	3 p.b.	C	Σ	
ABS	90°	5	5	5	15	ABS resin	90°	5	5	5	15	
PLA	90°	5	5	5	15	PLA resin	90°	5	5	5	15	
					30						30	60

The devices used here are: Creality CR-10 smart pro FDM (Creality, Shenzhen, China) and Creality LD -002R DLP (Creality, Shenzhen, China) device. All specimens were made with full infill density, grid infill pattern and 90° raster orientation. Other parameters can be found in the Table 2. All specimens were printed, stored and tested at room temperature (23°C) and relative humidity of 55% RH.

2.2 Mechanical Testing

Tensile, three-point bending and compression tests were performed on the Shimadzu AGS-X universal testing machine (Shimadzu Corp., Kyoto, Japan) equipped with a 100 kN load cell. The testing speed was set at 1 mm/min.

Table 2. FDM and DLP printing parameters, relative to materials.

Description	FDM		Description	DLP	
Material	ABS	PLA	Material	ABS	PLA
Layer thickness	0.24 mm	0.24 mm	Layer height	0.05 mm	0.05 mm
Nozzle diameter	0.4 mm	0.4 mm	Bottom layer count	10	10
Filament diameter	1.75 mm	1.75 mm	Exposure time	8 s	8 s
Printing temperature	250 °C	215 °C	Bottom exposure time	80 s	50 s
Build platform temperature	90 °C	65 °C	Bottom lift distance	5 mm	5 mm
Printing speed	60 mm/s	60 mm/s	Bottom lift speed	100 s	

2.3 Hardness

Important aspect of material testing is the hardness measurement, giving the information about the capability of the material to resist deformation and to recover after an induced mechanical indentation [52, 53]. Materials' hardness is important both for FDM [54], and DLP AM components [55].

Commercial Shore A hardness measurement device (SAUTER HDA100–1; Conrad, Berlin, Germany) was used here. Indentations were taken 5 times for each surface, as per ASTM D2240 standard.

2.4 Microscopy

In order to determine surface features, and evaluate the crack site structure, an optical 2D microscopy was utilized after mechanical testing. Micrographs were taken with a Mustool G600 Digital Portable Microscope (Shenzhen, China). Magnification range was between 50 and 100x, depending on the specimen. The surface morphology of the finished components plays significant role in better understanding of the surface finish and continuity of the materials' printed structure, for possible enhancing the component characteristics and performance [49].

3 Results and Discussions

AMed components may be subjected to various impact loads in certain engineering applications. Therefore, it is necessary to investigate the strain-rate dependent mechanical properties of AM materials. The available studies of ABS and PLA filaments' mechanical properties used in FDM are comprehensive. For instance, DLP process has higher printing accuracy than FDM thus, ABS and PLA-like resins used in DLP ought to be investigated as well. In this study the mechanical performance of ABS and PLA filaments and corresponding resins are presented to ratify printed components' suitability for particular applications.

The average stress–strain curves for each test type for both FDM and DLP technology, i.e., for both filament and resin ABS and PLA material are computed in Matlab software and all test results are presented in nine figures (Figs. 1, 2, 3, 4, 5, 6, 7, 8 and 9).

3.1 Tensile Testing

Tensile tests were performed for five specimens per printing technology and material. Twenty specimens are presented in Fig. 1c–f, where fracture cites in the narrow section of specimens can be observed. The most deformed specimens are FDM printed PLA, see Fig. 1e. Stress-strain curves for five FDM printed specimens (see Fig. 1a,b) exhibit very good repeatability. On the other hand, repeatability of stress-strain curves of DLP printed specimens is not so representative. Overall, the FDM printed specimens have higher UTS than DLP printed ones.

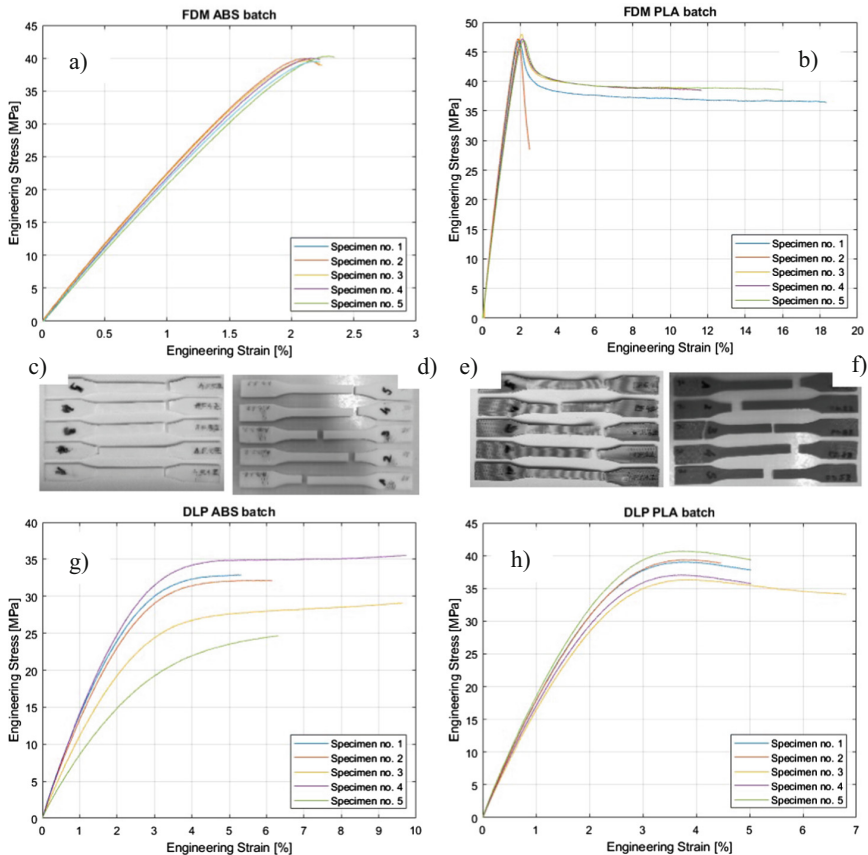


Fig. 1. Tensile stress-strain curves for: a) FDM printed ABS, b) FDM printed PLA, g) DLP printed ABS, h) DLP printed PLA; Specimens after tensile test: c) FDM printed ABS, d) DLP printed ABS, e) FDM printed PLA, f) DLP printed PLA.

Charts in Fig. 2 reveal that FDM printed PLA specimens have the highest value of all calculated tensile properties. PLA elastic modulus value for DLP is 60% of FDM ones. PLA UTS for DLP is 20% lower than FDM one. Although, elongation at yield is the highest for FDM PLA specimens, in the same time the elongation at break is the lowest. FDM PLA specimens absorbs 50% more energy than DLP printed PLA resin. Considering tensile stress, FDM prints are stronger and tougher than DLP ones.

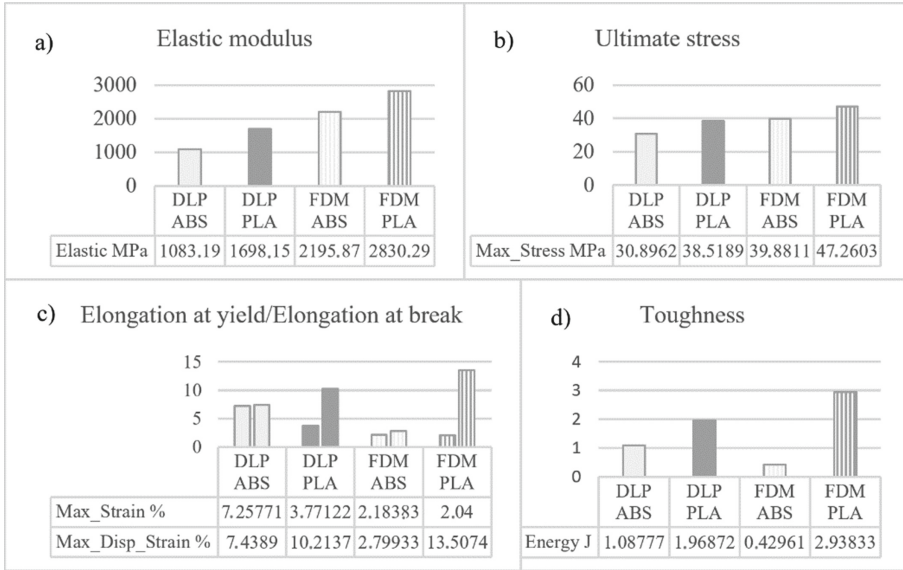


Fig. 2. Tensile properties: a) elastic modulus, b) ultimate stress, c) elongations and d) toughness.

Digital optical microscope was used to investigate the failure mode and fracture morphology of the specimens after tensile mechanical tests. Micrographs taken at a magnification of 50x are shown in Fig. 3a,b. In Fig. 3a the tiny bubble defects in the fractured surface of DLP printed ABS specimen can be noticed. Those bubbles (denoted as zone I) are entrapped air that was induced in resin during bottle shaking before pouring in vat. The bubble defects present in the specimen gradually enlarge during tension testing, thus reducing the overall mechanical properties of the ABS resin specimen compared to others. This observation is detected in stress-strain diagram (see Fig. 3e). DLP printed PLA fractured surface (Fig. 3b) can be divided into two regions: the rough fracture surface as initiation region denoted as (II) and smooth fracture surface as propagation region denoted as (III). As can be observed on Fig. 3c-d, the fracture surface of FDM printed specimens under tension has distinctive circles at filaments' cross-section in central layer that undergo the higher deformation during tension. Also, both materials have two-level fracture surface (see red arrows in Fig. 3) as a consequence of initial fracture of specimen along one surface and ending fracture along another. Worth pointing out is that FDM printed ABS has step-like fractured surface and FDM printed PLA has wedge-like surface.

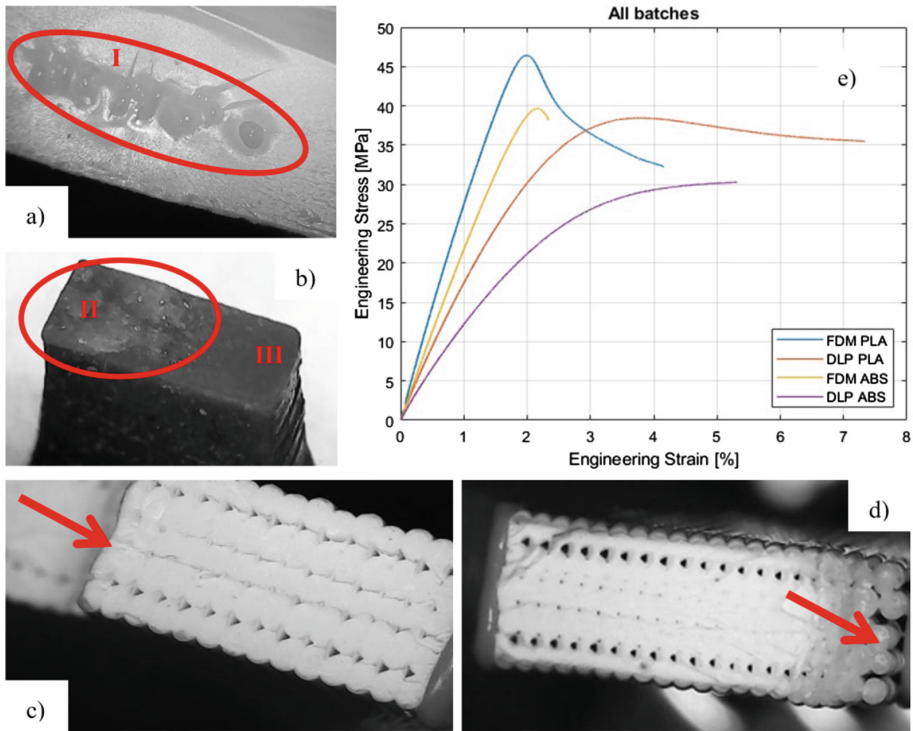


Fig. 3. Fractured surface's image of a) DLP ABS, b) DLP PLA, c) FDM ABS, d) FDM PLA tensile specimen, e) Tensile stress-strain curves for all batches.

3.2 Bending Testing

Bending tests were performed for five specimens per printing technology and material. Twenty specimens are present in Fig. 4c-f where position of fractures in a middle of a component can be observed. The V-shaped partially broken specimens are FDM printed ABS (Fig. 4c) and FDM printed PLA (Fig. 4e). Stress-strain curves for five FDM printed specimens (see Fig. 4a and b) exhibit very good repeatability. On the other hand, five broken DLP printed ABS specimens (Fig. 4d) and three DLP printed PLA (Fig. 4f) are shown. Two of the DLP PLA specimens just bended to 90° shape during test remaining its structure, without any surfaces fracture. These two specimens are denoted by arrows in Fig. 4f. As can be seen on stress-strain curves presented in Figs. 4g-h, DLP specimens don't have such repeatability as FDM ones. On average, FDM specimens have higher UTS that DLP ones, but DLPs are tougher. Generally, PLA material regardless of printing technology has proven to have good bending properties, with some specimens that haven't experience fracture even after high deflection.

Charts in Fig. 5. Show that PLA material, either filament or resin, has better behavior in three-point bending tests. PLA ultimate flexural strength value for DLP is 68% of

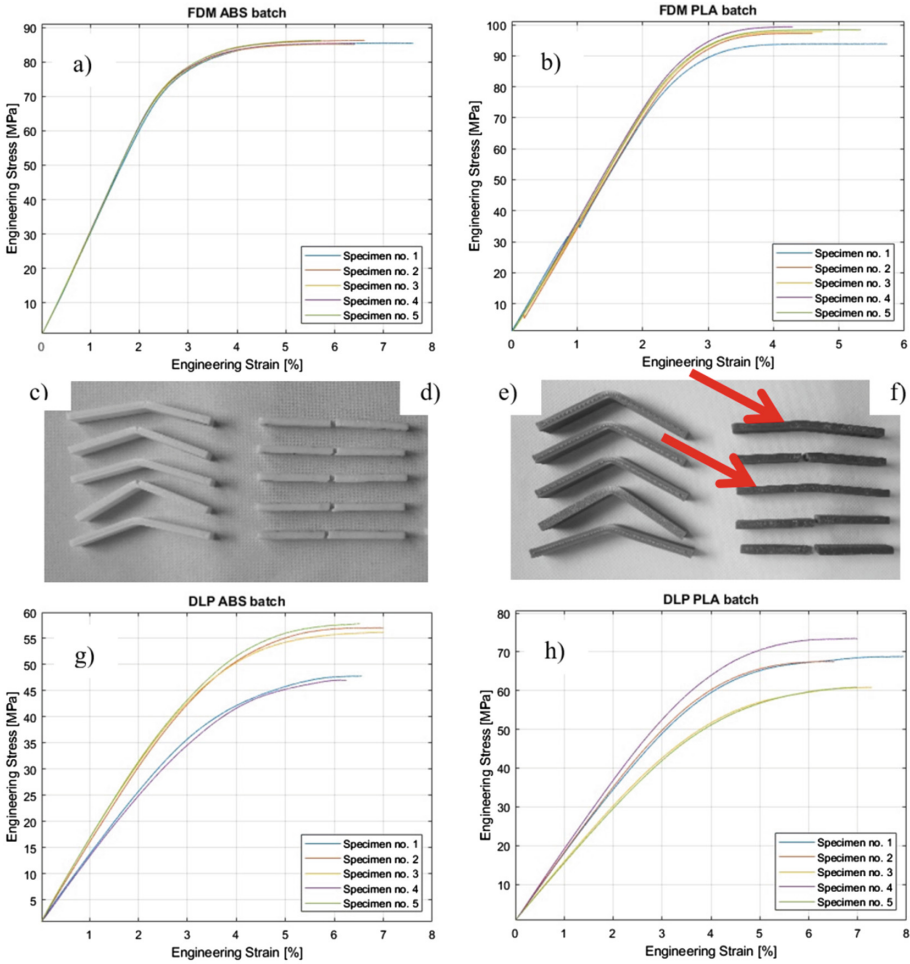


Fig. 4. Bending stress-strain curves for a) FDM printed ABS, b) FDM printed PLA, g) DLP printed ABS, h) DLP printed PLA; Specimens after bending tests, c) FDM printed ABS, d) DLP printed ABS, e) FDM printed PLA, f) DLP printed PLA.

that in FDM. PLA flexural modulus for DLP is more than 50% lower than FDM flexural modulus. Though, strain at ultimate flexural strength is the highest for DLP PLA specimens. Considering flexural strain, DLP fabricates better components than FDM.

Digital optical microscopy was used to investigate the failure and fracture morphology of the specimens after bending tests. Images are gathered at a magnification of 50x and 100x (see Fig. 6). The stress-whitening lines are visible on FDM bending specimens from the side. Fracture on ABS (Fig. 3a) is incomplete and failed specimens endure in one piece. In case of the PLA (Fig. 6b), the specimens didn't disengage, with also visible plastic deformation along the side surface of the specimen. However, the DLP

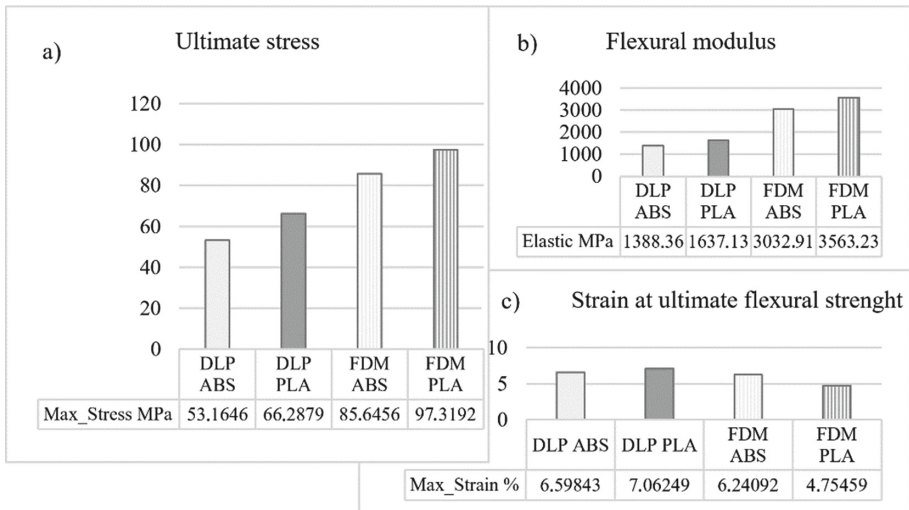


Fig. 5. Flexural properties: a) ultimate strength, b) flexural modulus, c) strain at ultimate flexural strength.

printed ABS resin specimens have been separated into two pieces and clean brittle fracture is obvious (see Fig. 6c). Fractured surface differentiates two zones: brittle denoted as (I) and ductile denoted as (II)- Fig. 6c. DLP printed PLA resin differentiates three zones: smooth denoted as (I), rough denoted as (II) and cutoff fracture denoted as (III) in Fig. 6d. The average stress-strain curves (Fig. 6e) show better mechanical response of FDM specimens, especially PLA.

3.3 Compression Testing

Compression tests were performed for five specimens per technology and per material. Twenty specimens are present in Fig. 7c-f, where “buckling effect” cannot be observed. PLA material FDM specimen’s end up being flattened without distinct failure (Fig. 7e), while ABS ones become flat with popping edges (see Fig. 7c) due to certain porosity between printed lines. DLP printed specimens exhibit “split effect” from the sides, due to intensive shear (see Fig. 7f). Such splitting become apparent after the specimen failure (see Fig. c-d). Stress-strain curves for five FDM printed specimens (see Fig. 7a-b) show better repeatability compared to DLP printed specimens (see Fig. 7g-h). Regardless of material type, FDM printed specimens undergo intensive densification, detectable in stress-strain chart. Clearly, FDM PLA proved to be strong and tough material that hasn’t experienced failure during the compression tests.

Values from compressive tests are present in Fig. 8. Here, elastic modulus is higher for PLA material, compared to ABS. The lowest value of elastic modulus has DLP ABS specimen. Considering the amount of energy that material can absorb, FDM fabricated specimens, regardless of material type, are better than DLP fabricated ones. PLA specimens have similar yield stress values, regardless to printing technology. On the other side, ABS specimens’ ultimate compressive strength has similar values, regardless to

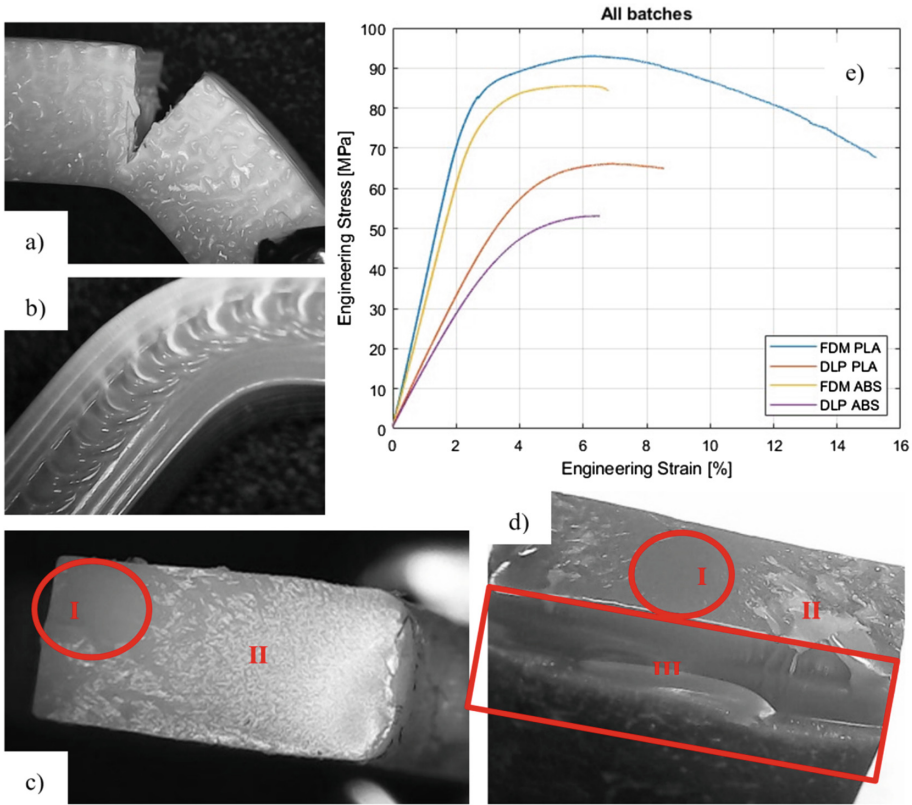


Fig. 6. Fracture surface image of flexural specimens: a) FDM ABS, b) FDM PLA, c) DLP ABS, d) DLP PLA, e) Flexural stress-strain curves for all batches.

printing technology. Strain at ultimate compression strength and strain at break have similar pattern for all cases. It's obvious that FDM technology provides higher values for compression regardless to material type.

Digital optical microscope was used to investigate the failure and fracture morphology of the specimens after compression tests. Images are gathered at a magnification of 50x and 100x, and are shown in Fig. 9. During compression, FDM printed ABS specimens' exhibit symmetric convex deformation and pops along the edges (see Fig. 8a). After compression, PLA FDM specimens were intact (see Fig. 8b), very densely packed in the form of "button-like" prism, without any cracks. DLP printed specimens have similar "blooming" crack behavior with sharp splinter separation. Afterward, the remaining core reveals shiny and smooth surface (Fig. 8c and d) with stress lines (see red arrows), attributed to the inconsistent mechanical properties in areas close to the specimen's side. Under compression, FDM PLA printed specimens show dominant mechanical response as can be seen from stress-strain curves (see Fig. 8e).

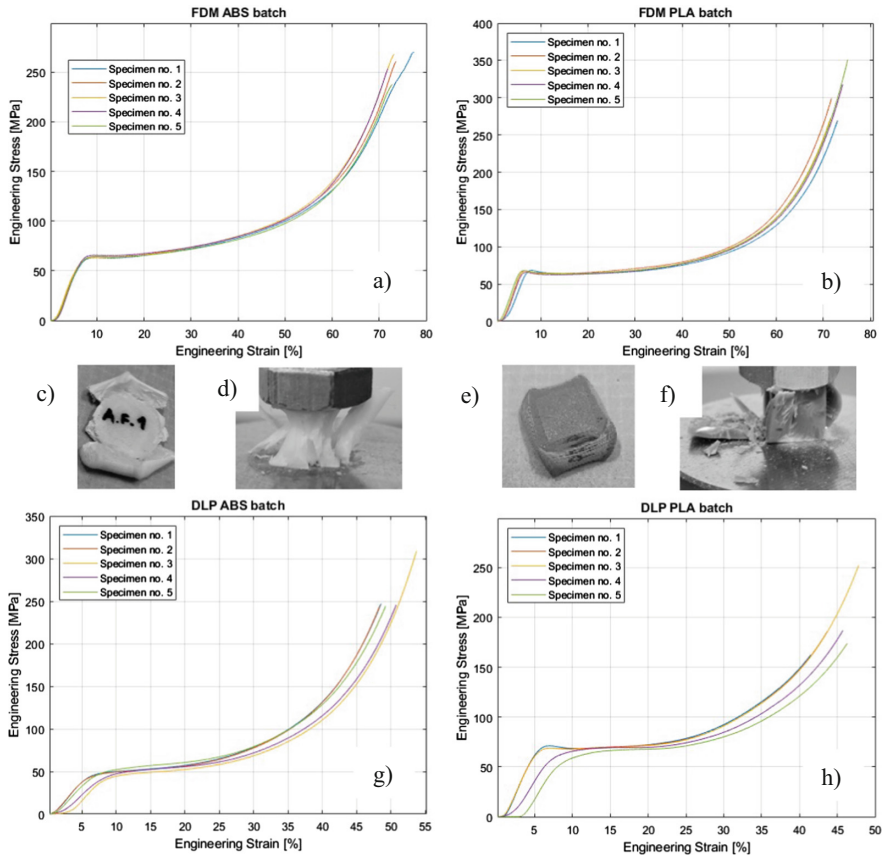


Fig. 7. Compressive stress-strain curves for: a) FDM printed ABS, b) FDM printed PLA, g) DLP printed ABS, h) DLP printed PLA; Specimens after compressive test: c) FDM printed ABS, d) DLP printed ABS, e) FDM printed PLA, f) DLP printed PLA.

3.4 Hardness

Shore A Hardness, as a conventional test covered by ISO 868 standard for elastomers, was performed five times per each type of the printed specimens. Calculated average values of the hardness for ABS material made using FDM and DLP technology are 90A and 85A, respectively. Calculated average hardness values of FDM and DLP PLA material are 83A and 81A, respectively. Therefore, filament and resin printed specimens show distinctive hardness, regardless to the 3D printing technology in both cases. Specimens made from ABS filament are considered as hard elastomers. Otherwise, the specimens made of the ABS resin as well as the PLA resin are considered to be medium to hard elastomers. The ABS resins have lower Shore hardness, compared to the filament and therefore are more flexible, making DLP printed ABS resin suitable for applications that require bending or stretching and FDM printed ABS filament may withstand stresses (or pressures) like harder materials. PLA filament or resin are definitely more flexible than ABS material.

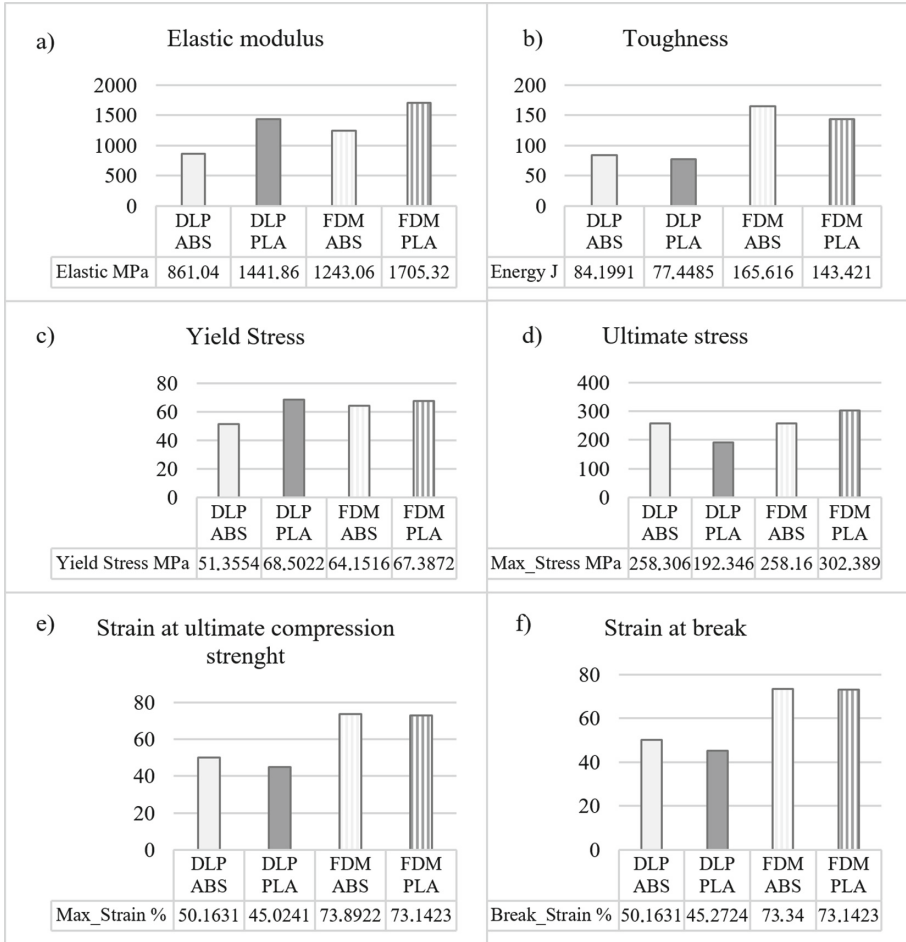


Fig. 8. Compression properties: a) elastic modulus, b) toughness, c) yield stress, d) ultimate strength, e) strain at ultimate strength, f) strain at break.

4 Conclusions

AM processes are a complex phenomenon, due to many crucial parameters and interactions that should be taken into account. Type of the 3D process and the print parameters have shown to influence significantly on the surface structure and the mechanical properties of the manufactured parts.

Studies of mechanical properties of FDM printed ABS and PLA filaments cannot be taken into account for predictions of mechanical behavior of insufficiently investigated ABS or PLA resin. Thus, this study enhances the knowledge about mechanical properties based on experimental examination and comparison among two frequently used AM technologies.

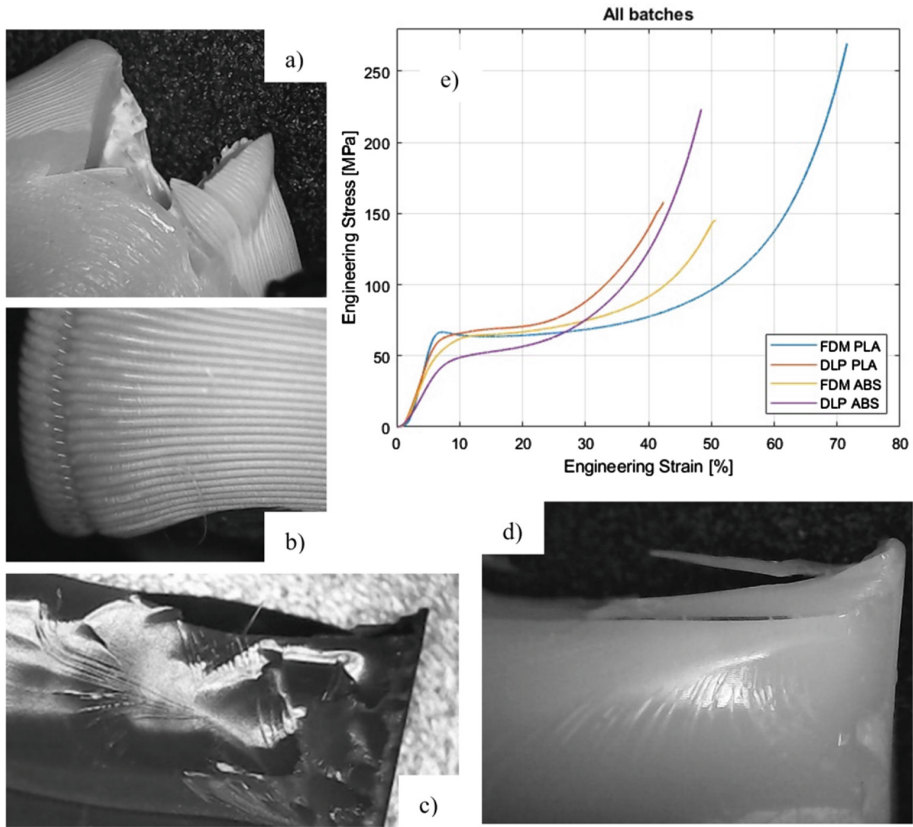


Fig. 9. Compressed surface image of a) FMD ABS, b) FDM PLA, c) DLP ABS, d) DLP PLA compression specimen; and e) Stress-strain compression curves for all batches.

Present research showed comparison in specimen's mechanical behavior between two different additive manufacturing processes, FDM and DLP. Further, two different thermoplastic materials were used, ABS and PLA, both in the form of filament and in the form of the resin. Experimental results showed the obvious strain rate effect, anisotropy, and ductile or brittle behavior, depending on the materials, for the 3D printed specimens.

Generally, conclusions are:

- Considering the tensile mechanical performances, FDM AM process manufactures stronger parts, while DLP makes tougher parts.
- Considering the flexural performance, FDM has an advantage, printing the stronger and tougher parts.
- Considering the compressive performance, PLA parts are stronger and tougher especially the ones built by FDM AM processes.
- It is found that if the degree of curing of each printing layer is too high, inadequate cross-linking of the neighboring printed layers may occur, resulting in low interface strength. Hence, the selection of proper light intensity and exposure time is

very important for ensuring good mechanical properties for DLP products. Further investigation will be based on curing and post-curing process effect.

Acknowledgments. This research was financially supported by the Ministry of Education, Science and Technological Development of the Republic of Serbia by Contract No. 451–03-47/2023–01/ 200105 from 03.02.2023.

References

1. ISO/ASTM 52900:2021: <https://www.iso.org/obp/ui/#iso:std:iso-astm:52900:ed-2:v1:en>. Accessed 18 May 2023
2. Lipton, J.I., Cutler, M., Nigl, F., Cohen, D., Lipson, H.: Additive manufacturing for the food industry. *Trends in Food Sci. Technol.* **43**(1), 114–123 (2015). <https://doi.org/10.1016/j.tifs.2015.02.004>
3. Paoletti, I.: Mass customization with additive manufacturing: new perspectives for multi performative building components in architecture. *Procedia Eng.* **180**, 1150–1159 (2017). <https://doi.org/10.1016/j.proeng.2017.04.275>
4. Leal, R., et al.: Additive manufacturing tooling for the automotive industry. *The Int. J. Adv. Manuf. Technol.* **92**, 1671–1676 (2017). <https://doi.org/10.1007/s00170-017-0239-8>
5. Fu, H., Kaewunruen, S.: State-of-the-art review on additive manufacturing technology in railway infrastructure systems. *J. Compos. Sci.* **6**, 7 (2022). <https://doi.org/10.3390/jcs6010007>
6. Shapiro, A.A., Borgonia, J. P., Chen, Q.N., Dillon, R.P., Mc Enerney, B., Polit-Casillas, R., Soloway, L.: Additive manufacturing for aerospace flight applications. *J. Spacecraft Rockets*, 952–959 (2016). <https://doi.org/10.2514/1.A33544>
7. Calignano, F., Galati, M., Iuliano, L., Minetola, P.: Design of additively manufactured structures for biomedical applications: a review of the additive manufacturing processes applied to the biomedical sector. *J. Healthcare Eng.* **2019**, Article ID 9748212 (2019). <https://doi.org/10.1155/2019/9748212>
8. Golubović, Z., Mitrović, A., Mitrović, N.: 3D printing in contemporary dentistry. In: Mitrovic N., Mladenovic G., Mitrovic A. (eds.) *Experimental Research and Numerical Simulation in Applied Sciences. CNNTech 2022. Lecture Notes in Networks and Systems*, vol. 564, Springer, pp. 213–232 (2023). https://doi.org/10.1007/978-3-031-19499-3_12
9. Jamróz, W., Szafraniec, J., Kurek, M., Jachowicz, R.: 3D printing in pharmaceutical and medical applications—recent achievements and challenges. *Pharm. Res.* **35**, 176 (2018). <https://doi.org/10.1007/s11095-018-2454-x>
10. Jakovljević, P., Dihovični, Đ, Bijelić, I., Kreculj, D., Ratković Kovačević, N.: Experiences in 3D printing applied in education. *Struct. Integrity and Life* **22**(1), 43–47 (2021)
11. Ailinei, I.I., Galațanu, S.V., Marșavina, L.: Influence of deposition direction on vibration characteristics of 3D printed ABS test specimens. *Struct. Integrity Life* **22**(1), 25–28 (2022)
12. Gao, W., Zhang, Y., Ramanujana, D., Ramani, K., Chenc, Y., Williams, C.B., Wang, C.C.L., Shina, Y.C., Zhang, S., Zavattieri, P.D.: The status, challenges, and future of additive manufacturing in engineering. *Comput.-Aided Design* **69**, 65–89 (2015). <https://doi.org/10.1016/j.cad.2015.04.001>
13. Golubović, Z., Travica, M., Trajković, I., Petrović, A., Misković, Ž., Mitrović, N.: Investigation of thermal and dimensional behavior of 3-D printed materials using thermal imaging and 3-D scanning. *Thermal Sci.* **27**, 21–31 (2023). ISSN: 0928-4931. <https://doi.org/10.2298/TSCI2301021G>

14. Rieder, H., Spies, M., Bamberg, J., Henkel, B.: On- and offline ultrasonic characterization of components built by SLM additive manufacturing (2016). <https://doi.org/10.1063/1.4940605>
15. Honarvar, F., Varvani-Farahani, A.: A review of ultrasonic testing applications in additive manufacturing: defect evaluation, material characterization, and process control. *ultrasonics*, 106227 (2020). <https://doi.org/10.1016/j.ultras.2020.106227>
16. Letcher, T., Waytashek, M.: Material property testing of 3D-printed specimen in PLA on an entry-level 3D printer. In: Proceedings of the ASME 2014 International Mechanical Engineering Congress & Exposition (IMECE2014), Montreal (2014)
17. Dizon, J.R.C., Espera, A.H., Chen, Q., Advincula, R.C.: Mechanical characterization of 3D-printed polymers. *Addit. Manuf.* **20**, 44–67 (2018). <https://doi.org/10.1016/j.addma.2017.12.002>
18. Schnittker, K., Arrieta, E., Jimenez, X., Espalin, D., Wicker, R.B., Roberson, D.A.: Integrating digital image correlation in mechanical testing for the materials characterization of big area additive manufacturing feedstock. *Addit. Manuf.* **26**, 129–137 (2019). <https://doi.org/10.1016/j.addma.2018.12.016>
19. Trajković, I., Milosević, M., Travica, M., Rakin, M., Mladenović, G., Kudrjavceva, L.J., Medo, B.: Novel method for measurement of pipeline materials fracture resistance-examination on selective laser sintered cylindrical specimens. *Sci. Sintering* **54**(3), 373–386 (2022). <https://doi.org/10.2298/SOS2203373T>
20. Neikter, M., Åkerfeldt, P., Pederson, R., Antti, M.-L., Sandell, V.: Microstructural characterization and comparison of Ti-6Al-4V manufactured with different additive manufacturing processes. *Mater. Charact.* (2018). <https://doi.org/10.1016/j.matchar.2018.02.003>
21. Parandoush, P., Lin, D.: A review on additive manufacturing of polymer-fiber composites. *Compos. Struct.* **182**, 36–53 (2017). <https://doi.org/10.1016/j.compstruct.2017.08>
22. Jevtić, I., Mladenović, G., Milošević, M., Milovanović, A., Trajković, I., Travica, M.: Dimensional accuracy of parts obtained by SIs technology. *Struct. Integrity Life* **22**(3), 288–329 (2022)
23. Yang, Y., Li, L., Zhao, J.: Mechanical property modeling of photosensitive liquid resin in stereolithography additive manufacturing: Bridging degree of cure with tensile strength and hardness. *Mater. Des.* **162**, 418–428 (2019). <https://doi.org/10.1016/j.matdes.2018.12.009>
24. Ngo, T.D., Kashan, A., Imbalzano, G., Nguyen, K.T.Q., Hui, D.: Additive manufacturing (3D printing): a review of materials, methods, applications and challenges. *Compos. Part B Eng.* **143**, 172–196 (2018). <https://doi.org/10.1016/j.compositesb.2018.02.012>
25. Milovanović, A., Golubović, Z., Babinský, T., Šulák, I., Mitrović, A.: Tensile properties of polypropylene additively manufactured by FDM. *Struct. Integrity Life* **22**(3), 305–308 (2022)
26. Amendola, C., et al.: Optical characterization of 3D printed PLA and ABS filaments for diffuse optics applications. *PLoS ONE* **16**(6), e0253181 (2021). <https://doi.org/10.1371/journal.pone.0253181>
27. Solomon, I.J., Sevvell, P., Gunasekaran, J.: A review on the various processing parameters in FDM. *Mater. Today Proc.* **37**(2), 509–514 (2021). <https://doi.org/10.1016/j.matpr.2020.05.484>
28. Sood, A.K., Ohdar, R.K., Mahapatra, S.S.: Parametric appraisal of mechanical property of fused deposition modelling processed parts. *Mater. Des.*, **31**(1), 287e295 (2010). <https://doi.org/10.1016/j.matdes.2009.06.016>. Elsevier Ltd.
29. Doshi, M., Mahale, A., Singh, S.K., Deshmukh, S.: Printing parameters and materials affecting mechanical properties of FDM-3D printed parts: perspective and prospects. *Mater. Today: Proc.* **50**, 2269–2275 (2022). <https://doi.org/10.1016/j.matpr.2021.10.003>
30. Lai, J., Wang, C., Wang, M.: 3D printing in biomedical engineering: processes, materials, and applications. *Appl. Phys. Rev.* **8**, 021322 (2021). <https://doi.org/10.1063/5.0024177>

31. Shah, D.M., Morris, J., Plaisted, T.A., Amirkhizi, A.V., Hansen, C.J.: Highly filled resins for DLP-based printing of low density, high modulus materials. *Addit. Manuf.* (2020). <https://doi.org/10.1016/j.addma.2020.101736>
32. Wu, D., Zhao, Z., Zhang, Q., H. Qi, H.J., Fang, D.: Mechanics of shape distortion of DLP 3D printed structures during UV post-curing. *Soft Matter*. **15**, 6151–6159 (2019). <https://doi.org/10.1039/C9SM00725C>
33. Kadry, H., Wadnap, S., Xu, C., Ahsan, F.: Digital light processing (DLP) 3D-printing technology and photoreactive polymers in fabrication of modified-release tablets. *Eur. J. Pharm. Sci.* **135**, 60–67 (2019). <https://doi.org/10.1016/j.ejps.2019.05.008>
34. Milovanović, A., et al.: Influence of printing parameters on the eligibility of plain-strain fracture toughness results for PLA polymer. *Procedia Struct. Integrity* **41**, 290–297 (2022). <https://doi.org/10.1016/j.prostr.2022.05.034>
35. Milovanović, A., et al.: Comparative analysis of printing parameters effect on mechanical properties of natural PLA and advanced PLA-X material. *Procedia Struct. Integrity* **28**, 1963–1968 (2020). <https://doi.org/10.1016/j.prostr.2020.11.019>
36. Milovanović, A., Milošević, M., Mladenović, G., Likozar, B., Čolić, K., Mitrović, N.: Experimental dimensional accuracy analysis of reformer prototype models produced by FDM and SLA 3D printing technology. In: Mitrović, N., Milošević, M., Mladenović, G. (ed.) *Experimental and Numerical Investigations in Materials Science and Engineering*, pp. 84–95. Springer, Cham (2019)
37. Lee, J.T., Kim, M.W., Song, Y.S., Kang, T.J., Youn, J.R.: Mechanical properties of denim fabric reinforced poly(lactic acid). *Fibers Polym.* **11**, 60–66 (2010). <https://doi.org/10.1007/s12221-010-0060-6>
38. Bajpai, P.K., Singh, I., Madaan, J.: Tribological behavior of natural fiber reinforced PLA composites. *Wear* **297**(1–2), 829–840 (2013). <https://doi.org/10.1016/j.wear.2012.10.019>
39. Baich, L., Manogharan, G., Marie, H.: Study of infill print design on production cost-time of 3D printed ABS parts. *Int. J. Rapid Manuf.* **5**(3/4), 308 (2015). <https://doi.org/10.1504/IJR-APIDM.2015.074809>
40. Popović, M., Pjević, M., Milovanović, A., Mladenović, G., Milošević, M.: Printing parameter optimization of PLA material concerning geometrical accuracy and tensile properties relative to FDM process productivity. *J. Mech. Sci. Technol.* **37**(1) (2023). <https://doi.org/10.1007/s12206-023-0113-6>
41. Dudescu, C., Botean, A., Hardau, M.: Thermal expansion coefficient determination of polymeric materials using digital image correlation. *Materiale Plastice* **50**(1) (2013)
42. Kafle, A., Luis, E., Silwal, R., Pan, H.M., Shrestha, P.L., Bastola, A.K.: 3D/4D printing of polymers: fused deposition modelling (FDM), selective laser sintering (SLS), and stereolithography (SLA). *Polymers* **13**(18), 3101 (2021). <https://doi.org/10.3390/polym13183101>
43. Drumright, R.E., Gruber, P.R., Henton, D.E.: Polylactic acid technology. *Adv. Mater.* **12**(23), 1841–1846 (2000). [https://doi.org/10.1002/1521-4095\(200012\)12:23%3c1841::aid-adma1841%3e3.0.co;2-e](https://doi.org/10.1002/1521-4095(200012)12:23%3c1841::aid-adma1841%3e3.0.co;2-e)
44. Lipson, H., Kurman, M.: *Fabricated: the new world of 3D printing*. Wiley (2013)
45. Li, N., Li, Y., Liu, S.: Rapid prototyping of continuous carbon fiber reinforced polylactic acid composites by 3D printing. *J. Mater. Process. Technol.* **238**, 218–225 (2016). <https://doi.org/10.1016/j.jmatprotec.2016.07.025>
46. Getme, A.S., Patel, B.: A review: bio-fiber's as reinforcement in composites of polylactic acid (PLA). *Mater. Today: Proc.* **26**, 2116–2122 (2020). <https://doi.org/10.1016/j.matpr.2020.02.457>
47. Moore, J.D.: Acrylonitrile-butadiene-styrene (ABS)-a review. *Composites* **4**(3), 118–130 (1973)

48. Wypych, G.: Odor in relation to different polymers. handbook of odors in materials, ChemTec Publishing, Elsevier, pp. 73–99 (2013). <https://doi.org/10.1016/B978-1-895198-51-5.50010-3>
49. Poyraz, O.: Influence of build direction and post processes on the material and part attributes of hard. *Mat. Res.* **26** (2023). <https://doi.org/10.1590/1980-5373-MR-2022-0362>
50. Hanon, M.M., Zsidai, L.: Sliding surface structure comparison of 3D printed polymers using FDM and DLP technologies. *IOP Conf. Ser.: Mater. Sci. Eng.* **749**, 012015 (2020). <https://doi.org/10.1088/1757-899X/749/1/012015>
51. Berman, B.: 3-D printing: the new industrial revolution. *Bus. Horiz.* **55**, 155–162 (2012). <https://doi.org/10.1016/j.bushor.2011.11.003>
52. Kumar, N., Kumar Jain, P., Tandon, P., Pandey, P.M.: Extrusion-based additive manufacturing process for producing flexible parts. *J. Braz. Soc. Mech. Sci. Eng.* **40**, 143 (2018). [https://doi.org/10.1007/s40430-018-1068-x\(0123](https://doi.org/10.1007/s40430-018-1068-x(0123)
53. Lovo, J.F.P., de Camargo, I.L., Erberelia, R., Moraisa, M.M., Fortulana, C.A.: Vat photopolymerization additive manufacturing resins: analysis and case study. *Mater. Res.* **23**(4), e20200010 (2020). <https://doi.org/10.1590/1980-5373-MR-2020-0010>
54. Singh, R., Trivedi, A., Singh, S.: Experimental investigation on shore hardness of barrel-finished FDM patterns. *Sādhana* **42**(9), 1579–1584 (2017). <https://doi.org/10.1007/s12046-017-0709-6>
55. Monzón, M., Ortega, Z., Hernández, A., Paz, R., Ortega, F.: Anisotropy of photopolymer parts made by digital light processing. *Materials* **10**(1), 64 (2017). <https://doi.org/10.3390/ma10010064>



Corrosion Damages of Pipelines Assessment by Using the Finite Element Method

Vujadin Aleksić¹ , Bojana Zečević² , Ana Maksimović² ,
Ljubica Milović³ , and Srđan Bulatović¹

¹ Institute for Testing of Materials-IMS Institute, Bulevar Vojvode Mišića 43, Belgrade, Serbia

² Innovation Centre of the Faculty of Technology and Metallurgy, Karnegijeva 4, Belgrade, Serbia

aprodanovic@tmf.bg.ac.rs

³ Faculty of Technology and Metallurgy, University of Belgrade, Karnegijeva 4, Belgrade, Serbia

Abstract. In order to ensure pipeline safety during their service life, all relevant construction, testing and safety requirements must be met. Corrosion damage is a major hazard to the steel pipeline as a whole, and it is necessary to comply with inspections and adequate maintenance so that destruction with catastrophic consequences would be avoided. In this paper, the standard calculation for determining the maximum acceptable corrosion damage length according to the RSTRENG method is presented using the calculation of the corrosion-damaged structure of the ammonia (NH₃) transfer pipeline. After that, the methodological approach to calculation using the finite element method (FEM) is presented in accordance with the methods defined by the new and general approach to standardization and technical harmonization for pressure equipment (Pressure Equipment Directive). The aim of the work was to present advanced modeling techniques of corroded surfaces based on FEM in order to develop a procedure for evaluating the residual strength of steel pipelines in the chemical industry.

Keywords: Pipeline · Corrosion damage · Corrosion assessment · FEM

1 Introduction

Corrosion damage, in which the load-bearing capacity of the section is reduced, greatly endangers the steel pipelines as a whole. Failure to perform required periodic and emergency inspections, as well as inadequate maintenance, can result in destruction with catastrophic consequences.

Improper maintenance of steel pipelines from the aspect of corrosion protection entails very expensive repairs, therefore it is necessary to thoroughly study the issues of protection, durability and maintenance of steel pipelines, as well as the possibility of monitoring corrosion aggression in operation. In this regard, it is necessary to assess the condition or the remaining strength of the steel pipeline subject to corrosion after long-term use, after which certain tests should be carried out using non-destructive methods to

determine the actual degree of damage to the vital parts of the structure. Inspection and testing of the corroded zones of the supporting elements of the steel support structure of the pipelines by non-destructive methods must be accompanied by standard inspection calculations, as well as FME calculations, in order to evaluate the remaining strength of the steel pipelines; the inspection and testing must also include opinions and recommendations. In uncertain situations, the calculations must be confirmed by experimental analysis.

Prior to inspection and testing by non-destructive methods, the steel support structure of the pipelines must be cleaned (e.g., by sandblasting), and the necessary interventions in the form of modifications to critical elements must be immediately followed by corrosion protection.

Pipelines must be designed to be safe throughout their service life, taking into account all relevant influences, with special requirements for design, construction, testing and safety.

Allowable stresses must be limited by possible errors in operating conditions to fully eliminate uncertainties resulting from manufacturing, the calculation model, actual operating conditions, and the properties and behavior of the material.

Due to the risk of corrosion to which the steel support structure are exposed, a number of corrosion protection measures are prescribed during the construction phase:

- Use of clean and non-corroded sheet metal, profiles and binding material with corrosion protection.
- Protection of parts that need to be protected prior to installation against the effects of corrosive agents that may occur on site.
- During the construction phase, sensors and measuring tapes must be installed in order to monitor changes in the aggressiveness of the environment, stress and strain of the responsible supporting parts of the steel pipelines which are connected to a computer that processes the data and makes appropriate decisions.

After installation and prior to commissioning, steel pipelines are subject to inspection in order to obtain a work permit.

Despite numerous methods of protection, corrosion of steel pipelines is inevitable due to the harsh environmental conditions in the industry. It occurs in various forms, such as general corrosion with uniform loss of wall thickness or pitting corrosion associated with localized reduction of wall thickness. In practice, it happens that the steel embedded in the pipeline partially or completely corrodes, thus reducing the cross-section and thus the load-bearing capacity of the structure. In more severe cases, accidents with catastrophic consequences for production, facilities, production means, equipment and human lives can occur. Such accidents lead to pollution and harmful effects on flora and fauna, air, watercourses and groundwater.

Examples of corrosion of steel pipelines structures in the chemical industry are shown in Fig. 1.

Corrosion manifests itself as follows: appearance of cracks, loss of strength, swelling and loss of mass, corrosion spots and weakening of the cross-section. Visual signs of destruction are: erosion, flaking and crumbling, bruising, softening, cracking, crystallization, appearance of so-called “popcorn cracking”. Point corrosion is especially dangerous on parts of the structure exposed to stresses. Due to the reduction in cross-section and high



Fig. 1. Examples of corrosion damage to steel support structures of pipelines [1, 2]

stress, occasional damage can lead to the formation of cracks and stress concentrations. [3, 4].

During operation, legally required inspections are performed to ensure safe and reliable operation of the steel pipelines. In addition to proper and timely maintenance, it is also necessary to monitor corrosion processes during operation. These processes can be monitored directly or indirectly. Direct monitoring involves checking the condition of the steel surface and the aggressiveness of the environment surrounding the pipeline steel support structure. In indirect monitoring, the corrosion effect is measured on samples made of the same material as the steel support structure of the pipeline.

Monitoring is very present in the world, especially monitoring the behavior of dynamically loaded structures, such as steel pipelines that operate in aggressive environments, especially those offered by the chemical industry. The value of the installed monitoring equipment is negligible compared to the value of the construction of steel pipelines or the value of rehabilitation works carried out after years of inadequate maintenance.

The direct and indirect costs caused by corrosion in the chemical industry are enormous. In the U.S., the total annual cost of corrosion is estimated at \$1.7 billion, or about 8 percent of total capital costs [5]. The indirect costs of production stoppage due to failure or catastrophic destruction have not been calculated, but are estimated to be much higher.

The durability of steel for pipelines in the chemical industry depends on the properties of the corrosive environment and the ability to withstand internal and external influences, the character and intensity of which depend on the operating conditions of the steel pipelines. The internal influence is reflected by the purpose and type of fluid in the steel pipelines, which may be of different aggressiveness, toxicity and explosiveness, different pressures, temperatures and flows. The external influence depends on the type, composition and temperature of the exhaust gases and air surrounding the objects in question, the velocity, flow and pressure of the gases, as well as the powdery substances in the gas flow.

External influences also include: the chemical effect of water - the environment and the substances dissolved in it, the changing effect of temperature changes (which leads to expansion changes of the steel), the changing humidification and drying of the steel, and the effect of dissolved salts in contaminated water. The emission of pollutants, which are

almost always present in the ambient atmosphere of the chemical industry, has a great influence. It includes gases O_2 , CO , CO_2 , SO_2 , NO , NO_2 , NO_x , H_2S , water vapor, and particles of solids such as KCl , K_2SO_4 , $(NH_4)_2SO_4$, $CO(NH_2)_2$ etc. The composition of exhaust gases and solids, their velocity, flow and increased concentration also affect the rate of corrosion and erosion of steel pipelines.

Pipes of appropriate diameter and wall thickness are used for the construction of steel pipelines, as well as various profiles in some qualities of general and fine-grained structural steel.

Steel pipelines made of steel elements require precision, great attention and trained and professional labor in their manufacture. They are made by welding or joining pipe flanges of suitable quality. They are equipped with suitable devices such as load cell, level gauges, safety valves, filling, draining and overflow valves, etc.

Depending on the aggressiveness of the transported fluid, steel pipelines are exposed to internal corrosion, depending on the environmental conditions and the effect of external corrosion.

The side of steel pipelines facing the sources of pollutant emissions, which is supported by airflow from that direction, is more exposed to corrosion due to the direct impact of pollutants on the structure of the steel pipeline. With poor air circulation, steel pipelines can be exposed to constant moisture, which, along with the emission of pollutants, can have disastrous consequences for the structure.

All defects, whether installed or created during the explosion, are investigated over a period of time, providing realistic insight into the potential damage progression, which in turn has a direct impact on reducing the number of failures, scheduling plant shutdowns, and significantly reduces overall costs.

To prevent defects and ensure safe operation, corrosion should be detected, measured and the remaining strength of the corroded surface of the element needs to be evaluated.

Inspections and tests should be documented with sketches and photographs to ensure the reproducibility of tests and updating the file, i.e. the “passport” of the steel pipeline.

In order to evaluate the residual strength of corroded elements of steel pipelines using any of the existing methods, the corrosion defect must be accurately measured. Currently, the ultrasonic method with associated equipment is the most commonly used method for testing corrosion damage to steel pipelines. The test and inspection results are processed manually or automatically with the help of computer programs. The programs can work in such a way that we provide them with data collected by the classic method of measuring the maximum corrosion depth (the minimum thickness of the pipe wall), or the program is integrated with a measuring instrument which scans the tested surface and compares the obtained results with the standard prescribed acceptance criteria. As a result, we obtain, by classical calculation or automatically, the remaining strength of the tested steel pipeline and on this basis determine the maximum allowable operating pressure.

2 Methods for Assessing Corrosion Damage to Steel Pipelines

There are several methods for evaluating the residual strength of corroded pipelines. Some of them are very simple and rely only on the length and depth of the fault, while others are much more complicated based on finite element modeling (FEM).

ASME B31G [3] is one of the most widely accepted solutions for evaluating corrosion damage in steel pipelines. The improvement of the method [6, 7] was achieved by introducing the damage factor, material loading and detailed consideration of the damage shape by calculations. This method is included in the program known as RSTRENG (Remaining Strength of Corroded Pipe). ASME B31G and RSTRENG have found wide application in the assessment of corrosion damage to steel pipelines in industry.

The presented methods allow the evaluation of longitudinal corrosion defects. The role of transversely oriented defects is usually denied. Kastner's standard for the drop-in plasticity at the defect location can be used for transversely oriented defects [8].

However, these criteria are too conservative when applied to damage in steel pipelines made of high-strength materials. Based on the experimental observations, a specific finite element framework called PCORRC has been developed, and solutions have been proposed for the evaluation of pipes made of medium- to high-strength steels, based on a large series of experiments and FEM calculations [9–25].

Corrosion defects are asymmetric defects that extend in any direction on the inner or outer surface of the pipeline. Therefore, in order to assess the remaining strength of the FEM and thus the service life, they should be modeled as realistically as possible.

The aim of this work is to present advanced modeling techniques of corroded surfaces based on FEM in order to develop a method for evaluating the residual strength of steel pipelines operating under the environmental conditions of the chemical industry.

2.1 Data for the Calculation of Corrosion Damage to the Steel Pipelines

The data required for the calculation of corrosion damage to pipelines, Fig. 2, using the RSTRENG method and FEM are:

- The nominal value of the outer diameter of the pipeline, $D = 125 \text{ mm}$;
- Nominal wall thickness of the pipeline, $t = 5 \text{ mm}$;
- Maximum depth of corrosion damage, $d = 2 \text{ mm}$;
- Measured (longitudinal) length of the corrosion damage, $L_m = 70 \text{ mm}$;

The pipeline is made of steel with the following mechanical properties, determined by experimental tests:

- Modulus of elasticity, $E = 211500 \text{ MPa}$;
- Poisson's ratio, $\nu = 0.3$;
- Yield stress, $S_{eH} = 813.4 \text{ MPa}$;
- Tensile strength, $S_M = 854.8 \text{ MPa}$;
- The pipe is subjected to pressure during operation, $P = 60 \text{ MPa}$.

Figure 3 shows the recommendations of the ASME B31G-Manual for Determining the Remaining Strength of Corroded Pipelines standard for evaluating corrosion damage.

2.2 Determination of the Maximum Acceptable Length of Corrosion Damage Using the RSTRENG Method

The depth of corrosion damage can be expressed as a percentage of the nominal value of the pipeline wall thickness. If the depth of corrosion of the part is more than 10% or less

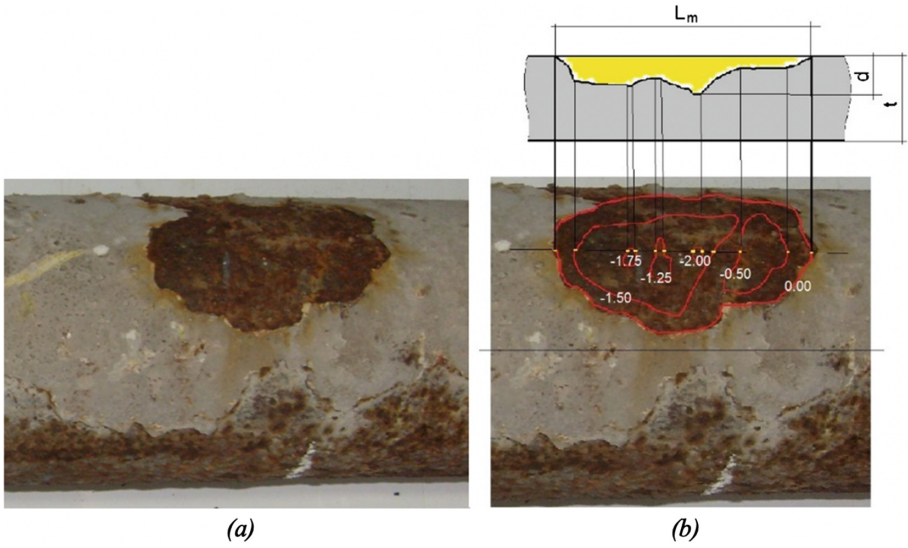


Fig. 2. Corrosion-damaged pipeline (a), and measured values of the asymmetric corrosion damage to the pipeline (b)

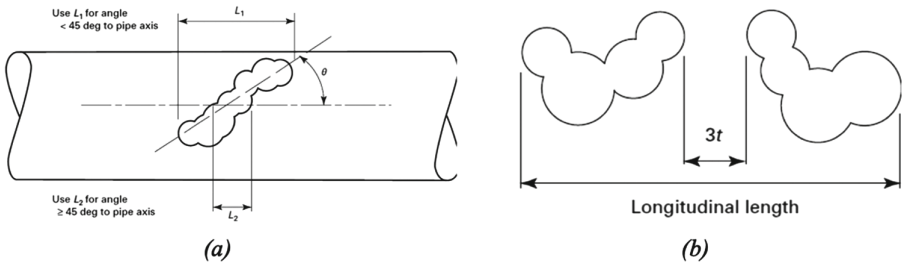


Fig. 3. Recommendations of standards for evaluation of corrosion damage, orientation of corrosion damage (a), and influence of mutual distance of corrosion damage (b) [3]

than 80% of the nominal value of the pipeline wall thickness, the length of corrosion damage shall not exceed the value determined by Eq. (1).

$$L = 1.12 \cdot B \cdot \sqrt{D \cdot t} \quad (1)$$

whereby:

- L - maximum allowable length of corrosion damage;
- B - value determined according to Eq. (2).

The maximum depth of corrosion damage is: $d = 2 \text{ mm}$, $40\% = 100 \cdot 2/5$.

$$B = \sqrt{\left(\frac{d/t}{1.1 \cdot \frac{d}{t} - 0.15}\right)^2 - 1} = \sqrt{\left(\frac{2/5}{1.1 \cdot \frac{2}{5} - 0.15}\right)^2 - 1} = 0,949998 \quad (2)$$

The maximum length of corrosion damage is:

$$L = 1.12 \cdot B \cdot \sqrt{D \cdot t} = 1.12 \cdot 0.949998 \cdot \sqrt{125 \cdot 5} = 26.6 \text{ mm}$$

Figure 4 shows the relationship between corrosion damage and the criteria for accepting corrosion damage to pipelines. The criterion is that they must withstand a pressure equal to the lower yield strength SeL . The figure represents a parabolic section of the corroded part, where the y-axis shows the value of the maximum depth of the corrosion damage divided by the thickness of the pipeline wall, while the x-axis shows the length of the corrosion damage divided by the square root of the product of the pipe radius and the pipeline wall thickness.

$$d/t = 0.400; \frac{L}{\sqrt{R \cdot t}} = \frac{26.6}{\sqrt{\frac{125}{2} \cdot 5}} = 1.505 \quad (3)$$

The coordinates of the point from Eq. (3) are exactly on the line of the diagram, Fig. 4. Considering that the actual measured length of the corrosion damage is $L = 70 \text{ mm}$, the operating pressure should be reduced or the pipe with the corrosion damage should be replaced or repaired.

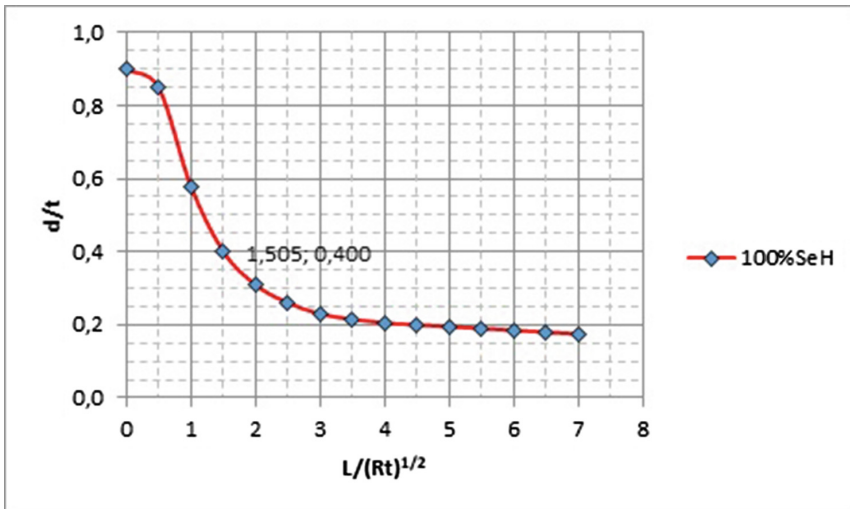


Fig. 4. Corrosion damage assessment diagram

If the maximum measured depth of corrosion damage is more than 10% of the nominal value of the pipe wall thickness and less than 80% of the nominal value of the pipeline wall thickness, and the measured length of corrosion damage is greater than the value determined according to Eq. 1, a calculation is required:

$$P_f = 1.1 \cdot P \left[\frac{1 - \frac{2}{3} \cdot \left(\frac{d}{t} \right)}{1 - \frac{2}{3} \left(\frac{d}{t \cdot \sqrt{A^2 + 1}} \right)} \right] \quad (4)$$

whereby:

- P' - maximum allowable pressure for L_m and cannot be greater than P ;
- P - determined pressure value in the pipe or:

$$P = 2 \cdot SeH \cdot t \cdot F \cdot \frac{T}{D} = 2 \cdot 813.4 \cdot 5 \cdot 1 \cdot \frac{1}{125} = 65.1 \text{ MPa} \quad (5)$$

whereby:

- F - corresponding factor from ASME B31.4 [26], ASME B31.8 [27];
- T - corresponding temperature value based on B31 regulation (if not specified, $T = 1$).

$$A = 0.893 \left(\frac{L_m}{\sqrt{Dt}} \right) = 0.893 \left(\frac{70}{\sqrt{125 \cdot 5}} \right) = 2.50 \quad (6)$$

For a damage depth of 40% of the nominal thickness of the pipeline wall, the maximum allowable corrosion damage length of $L = 26.6$ mm was calculated. This corrosion damage length is smaller than the actual measured corrosion damage length of $L = 70$ mm, so it is necessary to calculate the maximum allowable pressure (P') of the corroded pipeline for this damage case, and it is:

$$P' = 1.1 \cdot P \left[\frac{1 - \frac{2}{3} \cdot \left(\frac{d}{t} \right)}{1 - \frac{2}{3} \left(\frac{d}{t \cdot \sqrt{A^2 + 1}} \right)} \right] = 1.1 \cdot 65.1 \left[\frac{1 - \frac{2}{3} \left(\frac{2}{5} \right)}{1 - \frac{2}{3} \left(\frac{2}{2 \sqrt{2.50^2 + 1}} \right)} \right] = 3.9 \text{ MPa} \quad (7)$$

3 Evaluation of the Residual Strength of FEM Steel Pipelines

In order to evaluate the residual strength of steel pipelines FEM [2, 7], the processed test results can be implemented as a model in one of the commercial programs for FEM calculation, taking into account the PCORRC rules. Due to the asymmetry of the corrosion damage, a part of the corrosion damaged pipeline is modeled with an approximate shape to the actual shape. The model is created by connecting isoperimetric elements, where the number of elements depends on the size of the corrosion damage. It is necessary to represent the bottom of the damaged area with a sufficient number of elements determined by the analysis of the previous section. The inside of the model is exposed to the operating pressure, i.e. the test pressure. Symmetry planes are locations where boundary conditions are specified, i.e. motions in certain planes are constrained.

All numerical simulations in this work were performed using the Solid Works software package, which is based on FEM. The accuracy of the results depends on the precise modeling of the shape of the pipeline and the corrosion damage, as well as on the choice of the type and density of the final elements, so our task was to model the corrosion damage in Fig. 2 as realistically as possible. First, we created a model of a pipeline without corrosion damage, Fig. 5(a), and then a model of a pipeline with corrosion damage, Fig. 5(b).

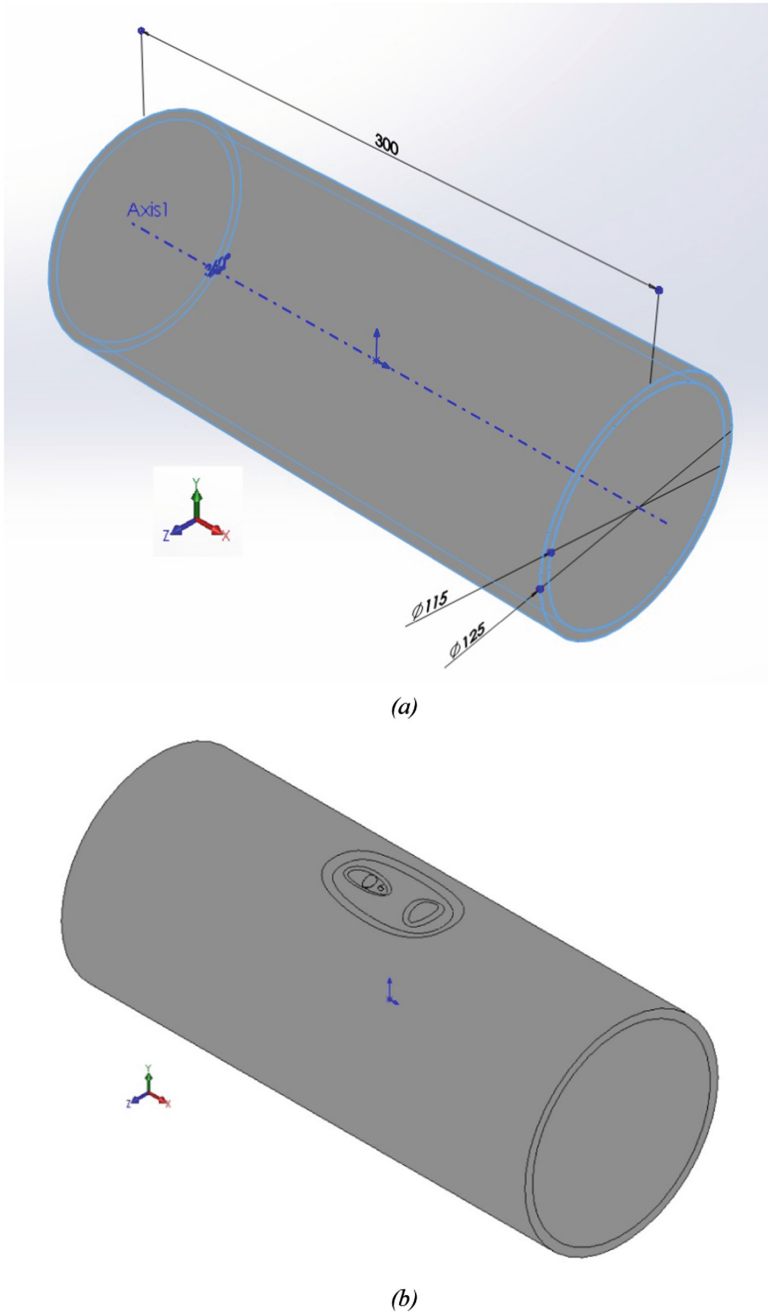


Fig. 5. Appearance of the pipeline model without corrosion damage (a), and the pipeline model with corrosion damage (b)

The material properties were determined based on experiments, after which the data regarding the material and the boundary conditions were used in the calculation, Fig. 6. Then, a finite element mesh was generated for both the model without corrosion damage, Fig. 7(a), and the model with corrosion damage, Fig. 7(b).

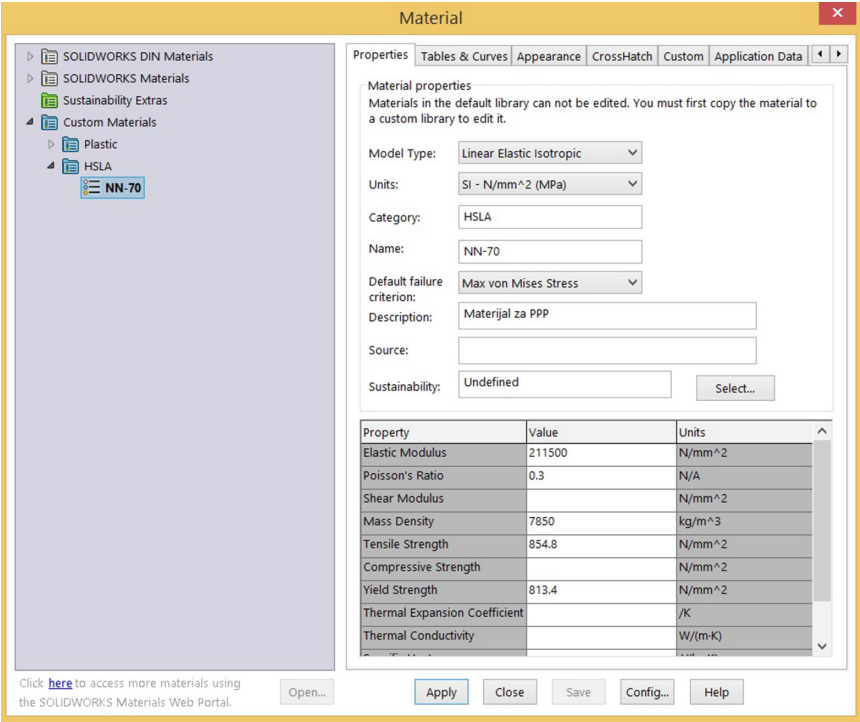
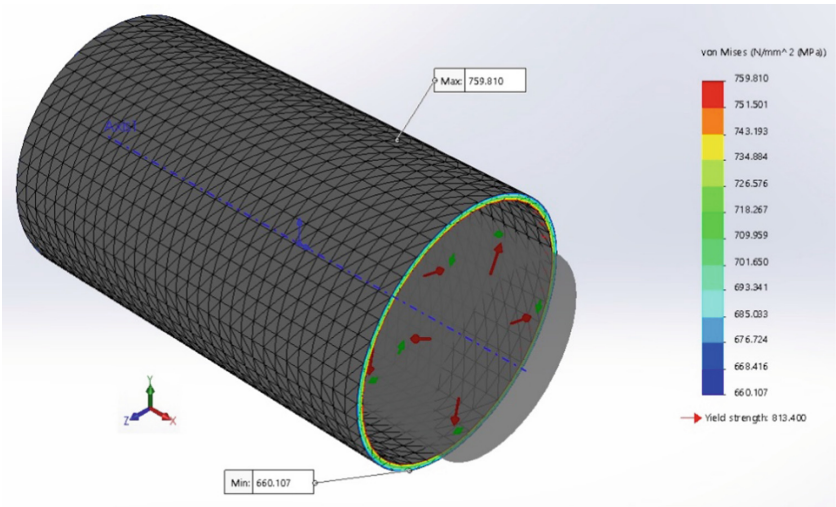


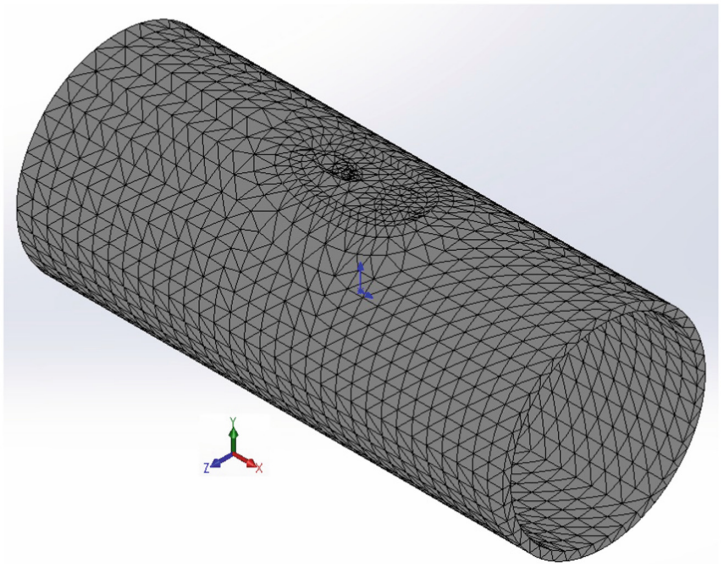
Fig. 6. Pipeline material properties and boundary conditions

In the finite element mesh of pipeline with corrosion damage, Fig. 7(b), the size of the elements varied depending on their location. Smaller elements were used at locations where corrosion damage occurred, while larger elements were used at locations far from the critical locations to keep the number of nodes as small as possible so that the calculation would be simplified to some extent.

Figures 8, 9, 10 and 11 show the calculation results of pipeline with asymmetric corrosion damage. The calculation was performed for the operating pressure of the undamaged pipe 60 MPa, the pressure calculated according to ASME B31.G of 3 MPa and the pressure 22 MPa, which ensures the operation of the pipeline with $\nu = 1$, which means that the pressure in the pipe must not exceed this value.



(a)



(b)

Fig. 7. Representation of the finite element mesh on the pipeline without corrosion damage (a), and on the pipeline with corrosion damage (b)

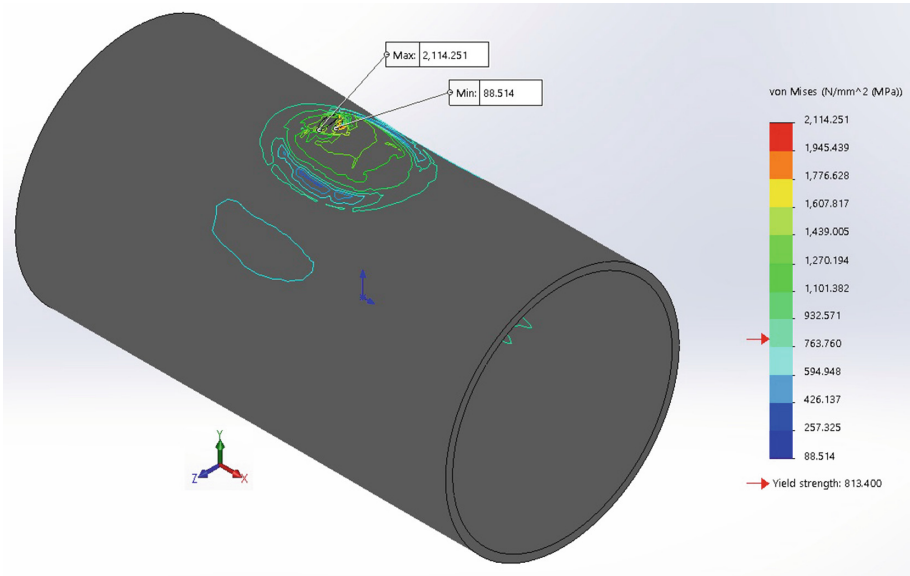


Fig. 8. Distribution and stress values on pipeline with corrosion damage for a pressure 60 MPa

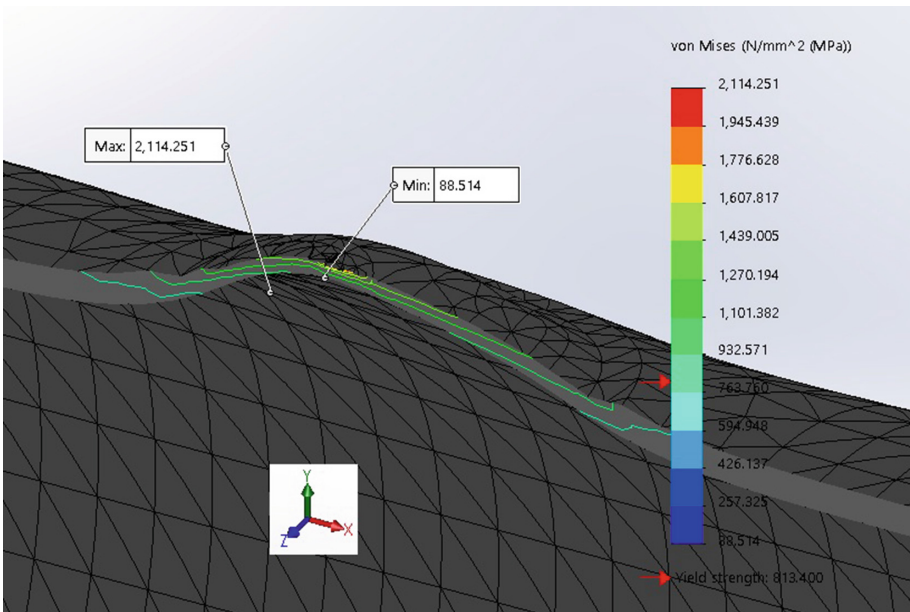


Fig. 9. Section through a model of corrosion damage to a pipeline that has been subjected to a pressure 60MPa

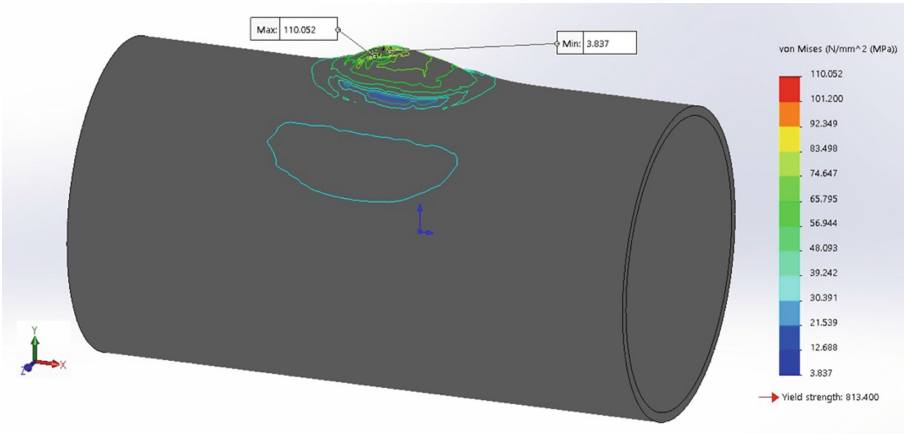


Fig. 10. Distribution and stress values on pipeline with corrosion damage for a pressure 3MPa

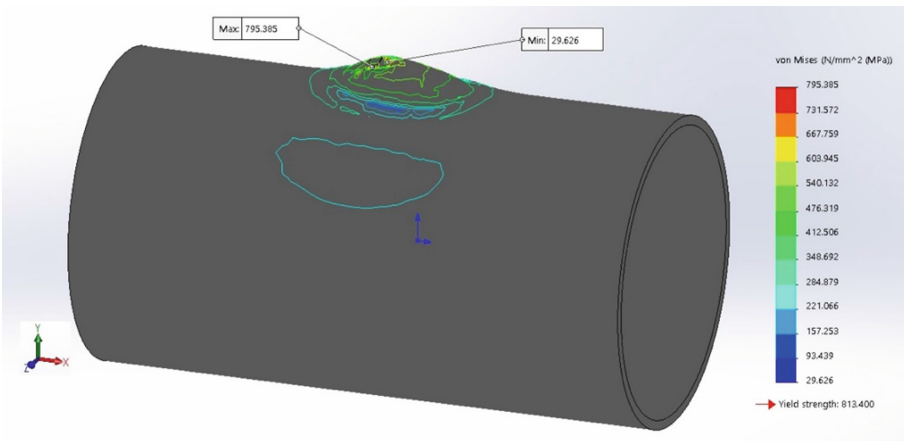


Fig. 11. Distribution and stress values on pipeline with corrosion damage for a pressure 22MPa

4 Results and Discussion

The standard calculation for determining the maximum acceptable length of corrosion damage using the RSTRENG method resulted in an operating pressure of an undamaged pipeline of 65.1 MPa, while the pressure of a damaged corroded pipeline calculated according to ASME B31.G is 3.9 MPa.

A finite element method calculation was performed in Solid Works, and Table 1 shows the maximum and minimum stress values on pipeline with corrosion damage for different operating pressures - for the operating pressure of an undamaged pipeline of 60 MPa and for the pressure of 3 MPa calculated according to ASME B31.G.

As evident in Table 1, the maximum stress value for the working pressure of the undamaged pipeline 60 MPa is 2144.5 MPa, which is much higher than the yield stress

Table 1. Stress values on pipeline with corrosion damage

Stress, MPa	FEM (von Mises stress)	
	σ_{\min} , MPa	σ_{\max} , MPa
60	2144.5	187.9
3	110.0	3.8
22	795.3	29.6

813.4 MPa, while for the calculated ASME B31.G pressure 3 MPa, the maximum stress value is 110.0 MPa, which again is much lower than what the corroded pipeline can withstand. This is due to the fact that the standard calculation is quite conservative. For this reason, through calculations with FEM, we have shown that this type of corrosion damage can withstand a pressure of 22 MPa when the pipeline would work with $\nu = 1$, and the maximum stress in this case is 795.3 MPa.

5 Conclusion

Corrosion damages the steel pipelines. It is therefore important to carry out regular and extraordinary inspections and adequately maintain the steel pipelines to avoid destruction with catastrophic consequences. The inspection by nondestructive testing of the corroded zones of the supporting elements of the steel pipelines constructions must be followed by inspection calculations using standard methods and FEM to assess the remaining strength of the steel pipeline.

In this paper, advanced modeling techniques for corroded surfaces based on FEM were presented with the aim of developing a procedure to evaluate the residual strength of steel pipelines operating in the environmental conditions of the chemical industry.

By analyzing the stress distribution on the corrosion-damaged pipeline for the operating pressure of the undamaged pipeline 60 MPa, the pressure 3 MPa calculated according to ASME B31G and the pressure 22 MPa, which ensures the operation of the pipeline with $\nu = 1$. After the FEM calculation, a completely different picture of the stress distribution can be seen, which is to be expected, and it tells us that for a complete understanding of the behavior of a corroded pipeline for the purpose of control calculation, the FEM calculation is mandatory on a model where all significant corrosion damage is modeled as realistically as possible.

Acknowledgements. This work was supported by the Ministry of Science, Technological Development and Innovation of the Republic of Serbia (Contracts: No. 451–03-47/2023–02/200012 and No. 451–03-47/2023–01/200287).

References

1. Aleksić, V.: Causes and consequences of corrosion damage to steel spherical tanks and pipelines in the chemical industry, XI YUCORR. In: International Conference, Collaboration

- of Researchers from Different Professions in the Field of Corrosion, Material Protection and the Environment, Tara, pp. 109–114 (2009)
2. Aleksić, V.: Assessment of residual strength using the finite element method of corrosion-damaged steel pipelines in the chemical industry, I International Congress, Engineering, materials and management in the process industry, pp. 98–102. Jahorina, Republika Srpska (2009)
 3. ASME B31G-2012 (Revision of ASME B31G-2009): Manual for Determining the Remaining Strength of Corroded Pipelines, Supplement to ASME B31 Code for Pressure Piping
 4. Koch, G.H.: Corrosion costs and preventive strategies in the United States, Publication No. FH WA-RD-01–156, CC Technologies, Dublin, Ohio (2002)
 5. Pressure Equipment Directive
 6. Kiefner, J., Vieth, P.: Evaluating pipe-1 new method corrects criterion for evaluating corroded pipe. *Oil & Gas J.* (1990)
 7. Szary, T.: The Finite Element Method Analysis for Assessing the Remaining Strength of Corroded Oil Field Casing and Tubing, Ph.D. dissertation, Der Fakultät für Geowissenschaften, Geotechnik und Bergbau der Technischen Universität Bergakademie, Freiberg (2006)
 8. Kastner, W.: Critical crack sizes in ductile piping. *Int. J. Press. Vessels Pip.* **9**, 197–219 (1981)
 9. Aleksić, B., Aleksić, V., Milović, L.J.: Finite element method pressure vessel calculation and analysis of the effects of the butt welded joints on a carrying capacity of a structure. In: 16th International Conference on New Trends in Fatigue and Fracture (NT2F16), pp. 153–154. Dubrovnik, Croatia (2016)
 10. Aleksić, B., Aleksić, V., Milović, L.J.: Analysis of the effects of butt welded joints on a carrying capacity of a structure tank. *Zaštita Materijala* **58**(4), 462–468 (2017)
 11. Aleksić, B., Milović, Lj., Grbović, A., Hemer, A., Aleksić, V., Zrilić, M.: Experimental and numerical investigations of the critical values of J-integral for the steel of steam pipelines, *Procedia Structural Integrity* **13**, 22st European Conference on Fracture-ECF22, pp. 1589–1594, Belgrade, Serbia (2018)
 12. Aleksić, V., Jaković, D., Kovačević, Z.: SolidWorks used for the process of optimization of supporting structure of a pressure vessel, international virtual journal for science, technics and innovations for the industry „MTM MACHINES TECHNOLOGIES MATERIALS“. *YEAR V*, Issue **6**, 3–6 (2011)
 13. Bulatović, S., Aleksić, V., Milović, L.J.: Failure of steam line causes determined by NDT testing in power and heating plants, *Frattura ed integrità strutturale*. The Int. J. Italian Group of Fracture, Anno VI, Numero **26**, 41–48 (2013)
 14. Cosham, A., Hopkins, P.: The Assessment of Corrosion in Pipelines – Guidance in the Pipeline Defect Assessment Manual (PDAM), Pipeline Pigging and Integrity Management Conference, Amsterdam, The Netherlands, pp. 1–31 (2004)
 15. Medjo, B., Rakin, M., Arsić, M., Šarkočević, Ž, Zrilić, M., Putić, S.: Determination of the load carrying capacity of damaged pipes using local approach to fracture. *Mater. Trans.* **53**(1), 185–190 (2012)
 16. Šarkočević, Ž, Arsić, M., Međo, B., Kozak, D., Rakin, M., Burzić, Z.: Damage level estimate of API J55 steel for welded seam casing pipes. *Strojarstvo* **51**(4), 303–311 (2009)
 17. Šarkočević, Ž, Rakin, M., Arsić, M., Sedmak, A.: Fabrication of high strength seam welded steel tubes and quality indicator testing. *Struct. Integrity Life* **8**, 81–98 (2008)
 18. Šarkočević, Ž, Arsić, M., Rakin, M., Međo, B., Mišić, M.: Otpornost na koroziju zavarenih cevi u naftnim bušotinama. *Zaštita materijala* **54**, 57–63 (2013)
 19. Sedmak, A., et al.: Corrosion effects on structural integrity and life of oil rig drill pipes. *Hemijaska Industrija* **76**(3), 167–177 (2022)
 20. Zaidi, R., Sedmak, A., Kirin, S., Martić, I., Šarkočević, Ž: Structural integrity and life assessment of oil drilling rig pipes using analytical method. *Struct. Integrity Life* **22**(1), 63–68 (2022)

21. Sedmak, A., Arsić, M., Šarkočević, Ž., Medjo, B., Rakin, M., Arsić, D., Lazić, V.: Remaining strength of API J55 steel casing pipes damaged by corrosion. *Int. J. Pressure Vessels and Piping* **188** (2020)
22. Kirin, S., Sedmak, A., Zaidi, R., Grbović, A., Šarkočević, Ž.: Comparison of experimental, numerical and analytical risk assessment of oil drilling rig welded pipe based on fracture mechanics parameters. *Eng. Failure Anal.* **114** (2020)
23. Krechkovska, H., Student, O., Zvirko, O., Hredil, M., Svirska, L., Tsybailo, I., Solovei, P.: Substantiation of the critical structural and mechanical state of low-alloy heat-resistant steel from steam pipelines of thermal power plant. *Eng. Failure Anal.* **150** (2023)
24. Qiao, Q., Cheng, G., Wu, W., Li, Y., Huang, H., Wei, Z.: Failure analysis of corrosion at an inhomogeneous welded joint in a natural gas gathering pipeline considering the combined action of multiple factors. *Eng. Fail. Anal.* **64**, 126–143 (2016)
25. Černý, I., Linhart, V.: An evaluation of the resistance of pipeline steels to initiation and early growth of stress corrosion cracks. *Eng. Fract. Mech.* **71**(4–6), 913–921 (2004)
26. ASME B31.4–2002 (Revision of ASME B31.4–1998), Pipeline Transportation System for Liquid Hydrocarbons and other Liquids, ASME Code for Pressure Piping, B31
27. ASME B31.8–2014 (Revision of ASME B31.8–2012), Gas Transmission and Distribution Piping Systems, ASME Code for Pressure Piping, B31



Selection of the Most Suitable Renewable Energy Alternative For Štrpce Municipality

Bojan Stojćetović¹ (✉) and Živče Šarkoćević²

¹ Kosovo and Metohija Academy of Professional Studies, Leposavić, Serbia
bojan.stojcetovic@akademijakm.edu.rs

² Faculty of Technical Sciences, Kosovska Mitrovica, Serbia

Abstract. Energy is a prerequisite for the development of today's companies, municipalities and whole societies. Renewable energy sources (RES) are gaining increasing importance and share in the energy systems of many countries. But, selection among different renewable energy sources request analyzing numerous criteria, stakeholders' interests, costs, legal regulations etc. For this reason, multi-criteria decision-making methods (MCDM) are often used for the selection of renewable energy alternatives. There are numerous MCDM methods that are used in literature and practice to select the most suitable renewable energy alternative. In this paper, the analytical hierarchy process (AHP) is applied to assess four renewable energy alternatives (hydro, wind, photovoltaic and biomass) in Štrpce municipality. Also, there are numerous criteria in the literature that are used to select renewable energy alternatives. In this paper six criteria are used: investment, efficiency, land requirements, GHG emissions, price of energy and operation and maintenance jobs. According to obtained results, the hydro alternative is ranked first.

Keywords: Analytical hierarchy process AHP · Renewable energy · Štrpce

1 Introduction

A secure and uninterrupted supply of energy is a condition for the development of today's societies. The importance of energy came to the fore during the COVID-19 pandemic. During this period, many countries were faced with energy security problems. In addition to the aforementioned crisis Kosovo's*¹ energy sector has other problems too, such as delays in building new capacity for lignite production, significant technical and commercial losses of electricity in the distribution network, insufficient production capacity to cover peak loads in the winter season, inappropriate use of the potential of renewable energy sources, etc. [1]. Due to all of the above, many municipalities across Kosovo* have problems with regular electricity supply. According to [2] the number of public consumers of electricity in the municipality of Štrpce is 54 while the number of

¹ This designation is without prejudice to positions on status, and is in line with UNSCR 1244/1999 and the ICJ Opinion on the Kosovo* declaration of independence.

private consumers is 3.800, and the average annual electricity consumption in Štrpce is 11 MWh in the household and 7 MWh in the apartments. One of the issues is the only route of supply of Štrpce, which comes from Urosevac. The network obsolescence, illegal network connections, frequent system failures, intentional exclusion, as well as the difficult terrain for maintenance makes this supply route quite unstable [3]. Due to all of the above, the question arises as to whether renewable energy sources can help improve the supply of electricity in Štrpce, because according to [4] developing RES capacity, certain regions can provide enough energy for their needs, which certainly leads to improved energy security. However, in order to select adequate RES, it is necessary to consider a number of criteria that are most often grouped in the literature into economic, environmental, technical and social. Numerous factors that need to be analyzed impose the need to apply multicriteria decision-making (MCDM) methods. Various MCDM methods are applied in theory and practice. However, one of the most frequently used methods is an analytical hierarchical process (AHP). It is used in numerous fields: energy [5], environment [6], and agriculture [7]. Also, AHP is used in renewable energy selection [8–10].

2 Methodology

In this paper, the selection of the most suitable renewable energy alternative is proposed through the implementation of several steps: defining the list of potential renewable alternatives, defining the list of decision criteria, evaluating the criteria, and a final ranking of renewable energy alternatives.

Due to its simplicity and proven advantages for the assessment of criteria (step 3), this paper will apply the AHP methodology, which is described in more detail as follows.

The AHP was developed by Thomas Saaty [11]. The AHP methodology can be explained step by step approach as follows: (1) in the first step, the problem is formulated in a hierarchical manner. In this step, the aim, main criteria, sub-criteria and alternatives should be identified clearly; (2) paired comparisons are performed and the relative importance is determined; (3) the consistency of pair-wise comparison matrices is determined. If the consistency ratio (CR) is equal to or smaller than 0.1 value, the comparisons are consistent; (4) in the final step, priorities of alternatives are found by combining the weights of criteria and the ratings of the alternatives.

To perform a pairwise comparison by all relevant criteria/alternatives, an $n \times n$ matrix A is formed:

$$A = \begin{pmatrix} a_{11} & a_{12} & \dots & a_{1n} \\ a_{21} & a_{22} & \dots & a_{2n} \\ \dots & \dots & \dots & \dots \\ a_{n1} & a_{n2} & \dots & a_{nn} \end{pmatrix} \quad (1)$$

where a_{ij} values are obtained using a 9-point scale (Table 1).

Matrix A is a positive reciprocal matrix in which a_{ij} represents the relationship of preference of alternative i and in relation to alternative j . The value of a_{ij} is the reciprocal of the value of a_{ji} . That is,

$$a_{ij} = \frac{1}{a_{ji}} \quad (2)$$

Table 1. Saaty's 1–9 scale of pairwise comparisons

Intensity of importance	Definition	Explanation
1	Equal importance	Two activities contribute equally to the objective
3	Moderate importance	Experience and judgment slightly favor one activity over another
5	Strong Importance	Experience and judgment strongly favor one activity over another
7	Very Strong	An activity is favored very strongly over another
9	Extreme Importance	The evidence favoring one activity over another is of the highest possible order of affirmation
2, 4, 6, 8	Intermediate results	They are used to present a compromise between the priorities listed above

If the pairwise comparisons are consistent, then the elements of the matrix A satisfy the equation:

$$a_{ij} * a_{jk} = a_{ik}, \text{ for each } i, j, k. \quad (3)$$

The weighting factor of the criterion / alternative can be denoted by w_i . If the matrix A is consistent a_{ij} can be represented as

$$a_{ij} = \frac{w_i}{w_j} \text{ for each } i \text{ and } j. \quad (4)$$

Therefore, if A is consistent then it is:

$$A * W = \begin{pmatrix} \frac{w_1}{w_1} & \frac{w_1}{w_2} & \dots & \frac{w_1}{w_n} \\ \frac{w_2}{w_1} & \frac{w_2}{w_2} & \dots & \frac{w_2}{w_n} \\ \dots & \dots & \dots & \dots \\ \frac{w_n}{w_1} & \frac{w_n}{w_2} & \dots & \frac{w_n}{w_n} \end{pmatrix} * \begin{pmatrix} w_1 \\ w_2 \\ \dots \\ w_n \end{pmatrix} = n * \begin{pmatrix} w_1 \\ w_2 \\ \dots \\ w_n \end{pmatrix} \quad (5)$$

By normalizing the matrix $A = [a_{ij}]_{n \times n}$ the weight factor is calculated as follows:

$$a^*_{ij} = \frac{a_{ij}}{\sum_{i=1}^n a_{ij}}, \quad (6)$$

for each $j = 1, 2, \dots, n$. Then, it is:

$$w_i = \frac{\sum_{i=1}^n a^*_{ij}}{n}, \quad (7)$$

for each $j = 1, 2, \dots, n$.

To determine the level of consistency, Saaty proposed the Consistency Index (CI), which can be calculated according to the following equation:

$$CI = \frac{(\lambda_{\max} - n)}{(n - 1)} \quad (8)$$

where λ_{\max} is the validation parameter in AHP. The closer the value of λ_{\max} is to n , the more consistent the estimate is. The Consistency Ratio (CR) can be calculated by the following formula:

$$CR = \frac{CI}{RI}, \quad (9)$$

where RI (Random Index) is a random consistency index. When $CR < 0.10$, the matrix can be assessed as acceptable, otherwise, the matrix should be modified until an acceptable value is reached. The homogeneity of factors within each group, fewer factors in the group, and a better understanding of decision problems can improve the consistency index [12].

3 Case Municipality of Štrpce

As mentioned in Chap. 2 there are several steps applied to select the most appropriate renewable energy alternative in Štrpce municipality.

Defining the list of potential renewable alternatives – Each area has different renewable energy sources and different potentials. Therefore, before starting the decision-making process, it is necessary to determine which RES have the greatest potential in the observed area. By analyzing the literature, it can be concluded that the potential of hydro, wind, solar and biomass can be used in the territory of Štrpce.

Decision-making criteria selection - A large number of criteria are used in the literature for renewable energy alternative assessment. However, each case has its own specifics and goals that should be taken into account when choosing decision criteria. For the purposes of this work, six criteria were selected, the values of which are shown in Table 2.

Evaluation of the criteria - for the evaluation of the criteria AHP method was applied. In the first step, the criteria were evaluated in relation to the decision-making goal (Table 3). Then, the alternative is compared in relation to the criteria (Table 4).

Final ranking of renewable energy alternative - after all comparisons are done, all results are synthesized and RES rank is obtained and shown in Fig. 1. According decision-making results obtained the most suitable renewable energy alternative is A2. This alternative is ranked first because it meets the selected decision criteria to the greatest extent.

4 Conclusion

In this paper, four RES alternatives (PV, hydro, wind and biomass) are evaluated in order to select the most suitable one for the municipality of Štrpce. In the decision-making process, six criteria were included and evaluated using the AHP method. According results obtained the most suitable renewable alternative for Štrpce municipality is A2 (hydro).

Table 2. Decision making criteria

	PV (A1)	Hydro (A2)	Biomass (A3)	Wind (A4)	Reference
Investment (EUR/kW) (C1)	1,303	1,500	4,500*	1,569	IRENA [13]; *expert
Operation and maintenance jobs (jobs/MW) (C2)	0.3	2.4	1.5	0.2	Meyer and Sommer [14]
Efficiency (%) (C3)	4–22%	80–90%	28%	24–54%	Evans et al. [15]; Chatzimouratidis and Pilavachi [16]
LAND km ² /1000 MW (C4)	35	750	5,000	100	Chatzimouratidis and Pilavachi [17]
GHG emissions gCO ₂ eq/kWh (C5)	85	26	45	26	Chatzimouratidis and Pilavachi [17]
The price of energy (C6)	0.085	0.047	0.062	0.056	IRENA [18]

Table 3. Pairwise comparison in relation to the goal

	C1	C2	C3	C4	C5	C6
C1	1	3	1	1/2	1/2	1/3
C2		1	1	1/2	1/2	1/3
C3			1	2	1/3	1
C4				1	1/3	1/2
C5					1	1/2
C6						1
Inconsistency 0.09						

The paper can be used by researchers and practitioners, as well as by the municipal administration that works in the energy sector as a starting point in RES planning. Also, stakeholders can use this paper as the base for determining and using different criteria for negotiation and decision-making with municipal representatives in RES planning. In future research, this paper can be improved by including all relevant parties in the municipality (stakeholders, experts, municipal representatives etc.) in order to get results which reflect the position of all interested parties. Also, to avoid subjectivity in the

Table 4. Alternative pairwise comparison in relation to the criteria

Pairwise comparison in relation to criterion C1					Pairwise comparison in relation to criterion C2				
	A1	A2	A3	A4		A1	A2	A3	A4
A1	1	3	5	3	A1	1	4	3	1/2
A2		1	4	1	A2		1	1/3	1/5
A3			1	1/4	A3			1	1/3
A4				1	A4				1
Inconsistency 0.04					Inconsistency 0.04				
Pairwise comparison in relation to criterion C3					Pairwise comparison in relation to criterion C4				
	A1	A2	A3	A4		A1	A2	A3	A4
A1	1	1/7	1/2	1/3	A1	1	5	9	4
A2		1	5	5	A2		1	5	1/3
A3			1	2	A3			1	1/6
A4				1	A4				1
Inconsistency 0.06					Inconsistency 0.09				
Pairwise comparison in relation to criterion C5					Pairwise comparison in relation to criterion C6				
	A1	A2	A3	A4		A1	A2	A3	A4
A1	1	1/5	1/4	1/4	A1	1	1/4	1/3	1/4
A2		1	3	1	A2		1	3	3
A3			1	1/3	A3			1	1/2
A4				1	A4				1
Inconsistency 0.05					Inconsistency 0.06				

decision-making process a fuzzy environment can be used to further determine the reliability of the results obtained and to avoid inaccuracies.

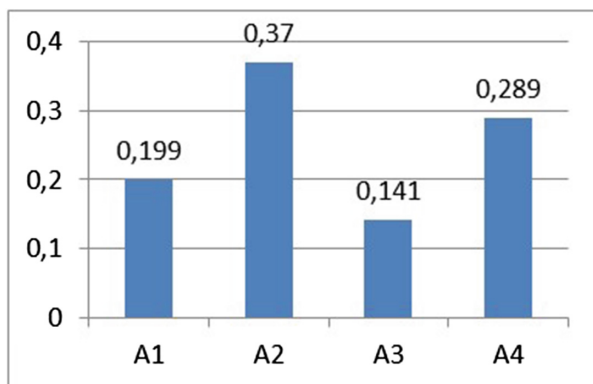


Fig. 1. Renewable alternative rank

References

1. Energy strategy of Kosovo* 2017–2026, Ministry of economic development, Pristina (2017)
2. Municipal Energy Efficiency Plan 2016–2021 – MEEP (in Serbian language), USAID (2016)
3. Stojčetiović, B., Nikolić Đ., Živković, Ž., Bogdanović D.: SWOT-AHP method application to determine current energy situation and define strategies for energy security improvement. *Thermal Sci.* **23**(2b), str. 861–872 (2019)
4. Proskuryakova, L.: Updating energy security and environmental policy: energy security theories revisited. *J. Environ. Manage.* **223**, 203–214 (2018)
5. Stojčetiović, B., Nikolić, Đ., Velinov, V., Bogdanović, D.: Application of integrated strengths, weaknesses, opportunities, and threats and analytic hierarchy process methodology to renewable energy project selection in Serbia. *J. Renew. Sustain. Energy* **8**, 035906 (2016)
6. Kurttila, M., Pesonen, U.M., Kangas, J., Kajanus, M.: Utilizing the analytic hierarchy process AHP in SWOT analysis - a hybrid method and its application to a forest certification case. *Forest Policy Econ.* **1**(1), 41–52 (2000)
7. Shrestha, R.K., Alavalapati, J.R.R., Kalmbacher, R.S.: Exploring the potential for silvopasture adoption in south-central Florida: an application of SWOT-AHP method. *Agric. Syst.* **81**(3), 185–199 (2004)
8. Al Garni, H., Kassem, A., Awasthi, A., Komljenovic, D., Al-Haddad, K.: A multicriteria decision making approach for evaluating renewable power generation sources in Saudi Arabia. *Sustain. Energy Technol. Assess.* **16**, 137–150 (2016)
9. Haddad, B., Liazid, A., Ferreira, P.: A multi-criteria approach to rank renewable for the Algerian electricity system. *Renew. Energy* **107**, 462–472 (2017)
10. Stojčetiović, B., Mišić, M., Đorđević, A.: Multicriteria assessment of renewable energy sources in Serbia. *Tehnika* **3**, 379–385 (2021)
11. Saaty, T.L.: *The Analytic Hierarchy Process: Planning*. McGraw-Hill, New York, USA (1980)
12. Saaty, T.L.: The analytic hierarchy process: a 1993 overview. *Central Eur. J. Oper. Res. Econ.* **2**(2), 119–137 (1993)
13. *Cost-Competitive Renewable Power Generation: Potential across South East Europe*, IRENA (2017)
14. Meyer, I., Sommer, W.M.: Employment effects of renewable energy supply - a meta analysis. *Int. J. Sustain. Dev.* **10**, 1–29 (2014)
15. Evans, A., Strezov, V., Evans, T.J.: Assessment of sustainability indicators for renewable energy technologies. *Renew. Sustain. Energy Rev.* **13**, 1082–1088 (2009)

16. Chatzimouratidis, A.I. Pilavachi, P.A.: Sensitivity analysis of technological, economic and sustainability evaluation of power plants using the analytic hierarchy process. *Energy Policy* **137**, 788–798 (2009)
17. Chatzimouratidis, A.I., Pilavachi, P.A.: Multicriteria evaluation of power plants impact on the living standard using the analytic hierarchy process. *Energy Policy* **36**, 1074–1089 (2008)
18. Renewable Power Generation Costs in 2018, International Renewable Energy Agency, Abu Dhabi (2019)



Topology Optimisation as Method for Improving the Design Process of Tipping Semi-trailer

Aleksandar Zahariev¹(✉) and Viktor Stojmanovski²

¹ Rugjer Boskovikj 8/1/14, 1000 Skopje, Republic of North Macedonia
aleksandar.zahariev@gmail.com

² Faculty of Mechanical Engineering, Ss Cyril and Methodius University in Skopje, Rudjer Boskovic 18, PO Box 464, 1000 Skopje, Republic of North Macedonia

Abstract. When designing a new better product, besides all the engineering knowledge, time and money, more modern techniques as possible should be presented at any stage of the development process. Hence, “brainstorming” as the earliest stage in the process can be more accurate and productive for the development team with data of initial material distribution in the form of a typical “topology optimization - TO” result based upon the predetermined technological, geometrical, economical and homologation constraints. Design objectives such as lowering mass or displacements are tangible variables when using the TO approach and are suitably desired by the development team. This paper presents a simulation study based on the finite element method used in the development process for designing a chassis for a typical tipping semi-trailer vehicle. The expected load cases are described and calculated for a specific direction of movement. The tipping sequence described as longitudinal bending, the tipping on uneven ground is longitudinal torsion or the short turning is lateral bending of the potential new chassis. Based on the envelope simulation results from the multiple scenarios with the pre-defined constraints a topology geometry model has been created. For that, a two-stage process of optimizing is presented. First optimizing the 2D initial area, then a 3D solution for minimum structural compliance of the extruded initial 2D design. As a main tool for pre-processing and post-processing, Siemens Simcenter is used. The solving is performed with Nastran’s topology optimization SOL200 solver.

Keywords: Tipper trailer engineering · Product development process · Topology optimization · Nastran SOL200

1 Introduction

Most companies that produce products with similar complexity such as the later used tipping semi-trailer, are nowadays developing mainly using traditional techniques (see Fig. 1). Based on the product necessity the development team brainstorms solutions to their problem or new design, mainly based on: engineer knowledge and experience, already produced products in their portfolio or based on solutions from their competitors. Then development is done with CAD software and optimization is done by simple hand

or Excel calculations. With this approach no significantly better design than the current can be achieved [1].

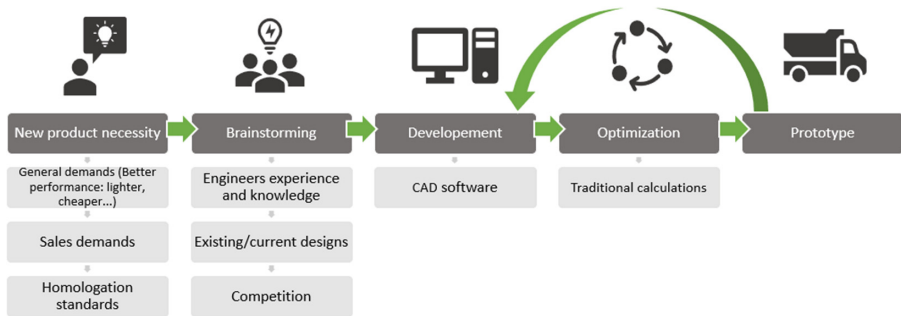


Fig. 1. Experience-based development – “Traditional way”

In order to create a better product, besides all the engineering knowledge, time and money mentioned above as more modern techniques as possible should be presented at any stage of the development process. In this situation, brainstorming can be more productive with TO results in front of the development team. Also, FE simulations can be used in the development, optimization and validation process. Adding all of these modern techniques can potentially create new products with better characteristics or can be described as a “future way” of development (presented in Fig. 2) [2].

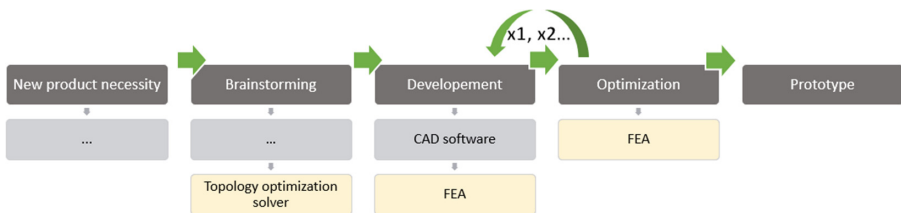


Fig. 2. Science-based development – “Future way”

In this project, the FE simulations are proposed as an addition in all stages of the development process for a new trailer tipper chassis. The expected load cases are described and simulated, and based on the results and constraints a topology optimization model has been created as well. Topology optimization usually takes place towards the end of the design process, when the desired part needs optimization so it has a lower weight or uses less materials, but in this case, the geometry created from the TO result is finally used for better brainstorming and developing a new potentially better design.

2 Geometry limits

The geometry limits for designing a new trailer's chassis can come from different areas such as homologation, weight distribution [3], size demands, as well as market perception [4].

The location of the kingpin, tipping cylinder and axles (axle distance and wheelbase) can be calculated based on the weight distribution of axles and king pin which can vary from market to market. The width of the chassis and the ISO-curve [5] (location needed for the pulling truck) are typical homologation constraints. Below are given the maximized dimensions (limits) where a new potential chassis can be created. Besides those limits also the location of the suspension mounts, tipping hinge, lifting cylinder brackets and kingpin are depicted in Table 1.

3 Load cases

The first scenario of usage for a trailer like this is driving around with a body rested on the chassis (see the scenario in Fig. 4), but fully loaded. Despite that the bulk payload is resting on the body while being transported also its unloading and loading should be done. The unloading is also known as tipping [6]. The tipping sequence (Fig. 3) is a time-based occurrence, where the tipping cylinder starts to lift so the body rotates around the tipping axle. At first, the forces are bigger on the front part (also known as the head section) where the cylinder brackets for moving the lifting cylinder to the welded frame are located. When the body is fully lifted (usually around 45 degrees) the forces around the tipping axle are bigger, since the bulk load has been transferred from the front and middle to the back. In that situation two stages of the tipping sequence are interesting to be simulated: the start and end of tipping (Fig. 7). Both of them represent longitudinal normal bending of the welded frame structure [7].

Typical scenarios of additional real-life behavior while both properly or improperly usage of the tipper can be torsion (Fig. 5) and lateral bending [8] (Fig. 6). Using the basic rules of statics, a calculation for the maximum cylinder force acting on the body through the brackets was made. The trailer was calculated as a simple two-dimensional beam where the body is completely rigid and its mass is concentrated in the center of gravity (CoG). Below are given the used scenarios for making the TO simulation model (Fig. 7).

Lateral bending can happen in a typical short-turn scenario. When the truck is normal to the trailer and immediately starts to pull. That can be simulated by applying a lateral force on the kingpin and the wheels are fixed in all degrees of freedom.

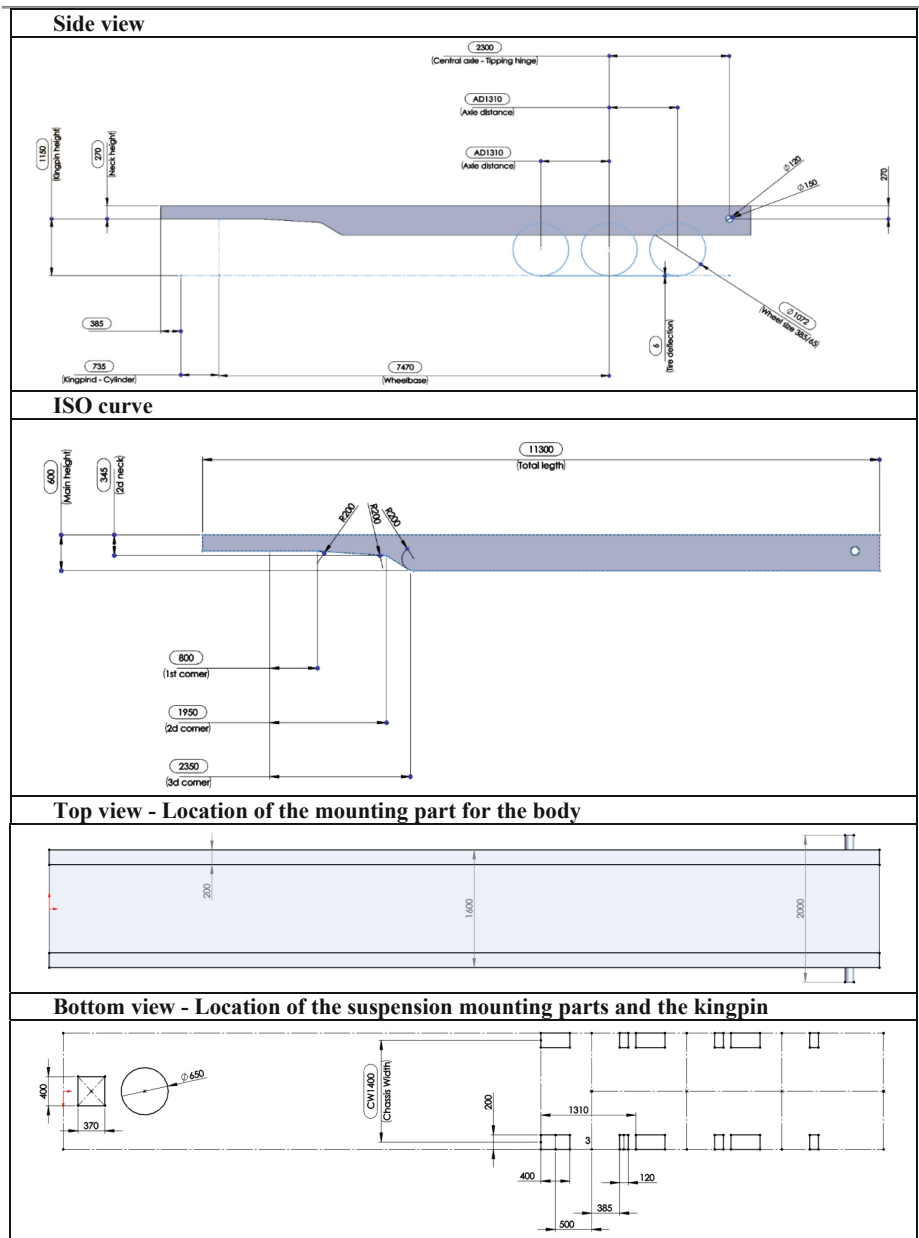
Typical calculation¹ of the input forces (F_1 ; F_2) for the end of tipping scenario uses the basic laws of statics (Fig. 8):

$$a_1 = (L_1 + L_2) \cdot \cos\alpha; a_2 = L_3 \cdot \cos\alpha; h = \sqrt{(L_1 + L_2 + L_3)^2 - (a_1 + a_2)^2} \quad (1)$$

$$\sum M_o = 0; M \cdot g \cdot a_2 - F_1 \cdot (a_1 + a_2) \cdot \cos\beta - F_1 \cdot h \cdot \sin\beta = 0 \quad (2)$$

¹ Jacobson Bengt "Vehicle Dynamics" Compendium, Chalmers university 2017.

Table 1. Geometrical constraints of a new trailer tipper chassis' welded frame



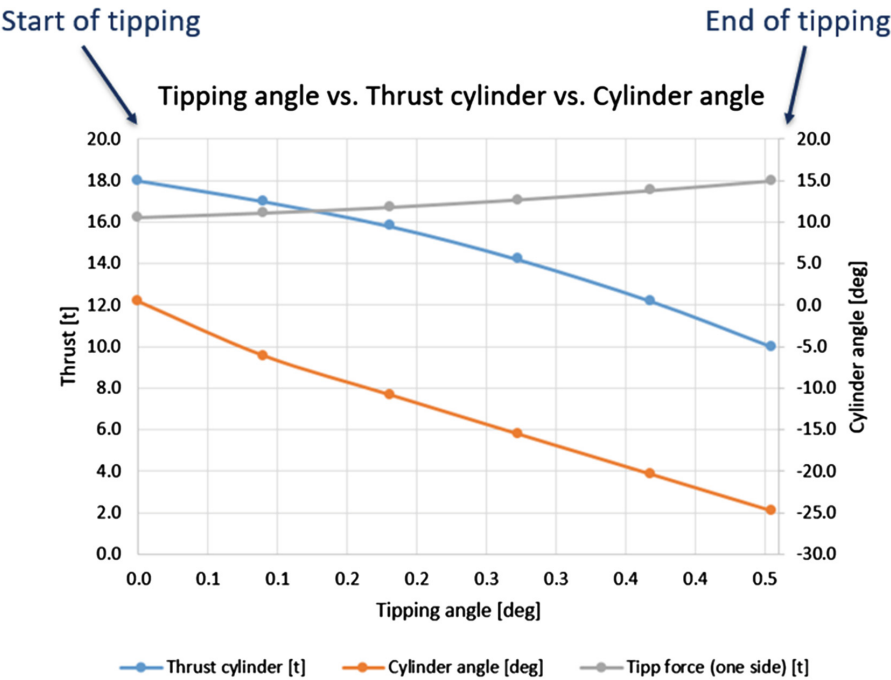


Fig. 3. Typical tipping sequence representing the main forces acting on the welded frame in the time domain as well as the angle of the lifted body.

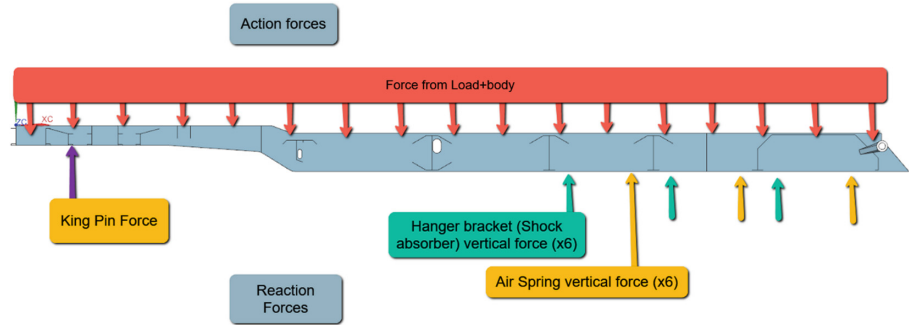


Fig. 4. Body rested on chassis, loads and constraints coming from the bulk load, suspension and the pulling truck.

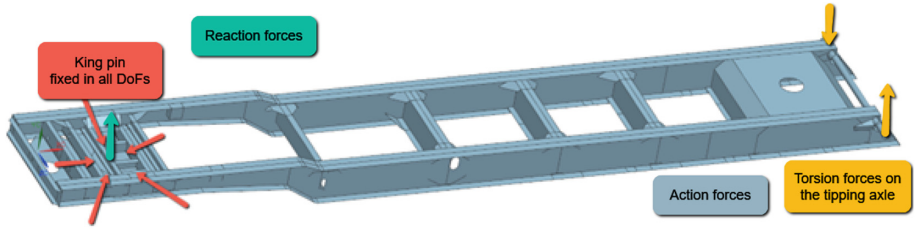


Fig. 5. Longitudinal torsion on chassis, loads and constraints. The kingpin area is fully fixed while a set of forces with opposite directions are acting on the left and right rear ends of the tipping axle.

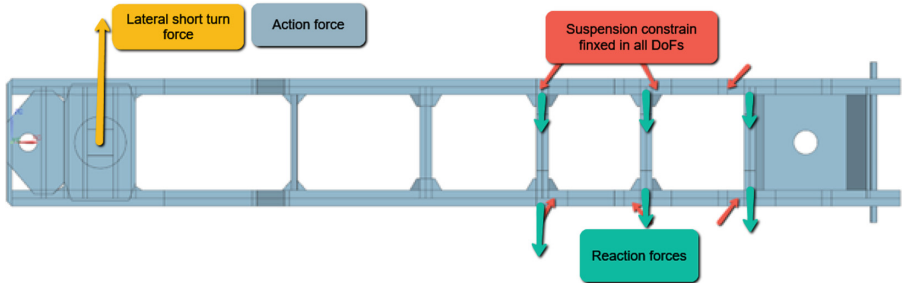


Fig. 6. Lateral bending on chassis, loads and constraints. The frame is fixed at the mounts of the suspension and a certain lateral force is applied in the kingpin representing sudden normal pulling from the truck.

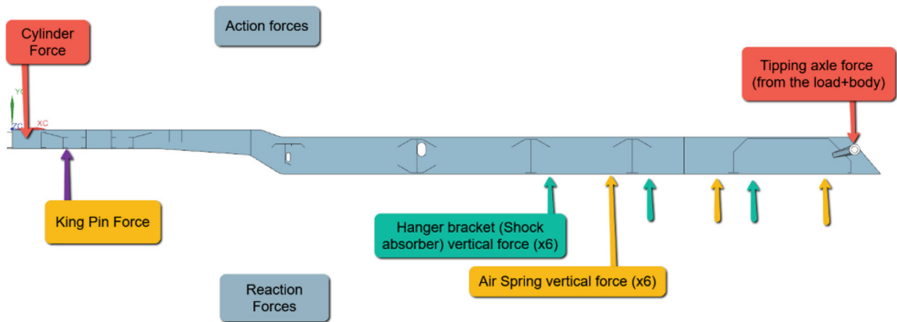


Fig. 7. Start/end of tipping, loads and constraints.

$$\sum F_y = 0; F_1 + F_2 - M \cdot g = 0 \quad (3)$$

$\rightarrow F_1; F_2$

L – Length of the trailer;

L_1 – Distance between the cylinder brackets and the frontend of the body;

L_2 – Distance from the frontend of the body to the CoG;

L_3 – Distance from the CoG to the rear hinge;

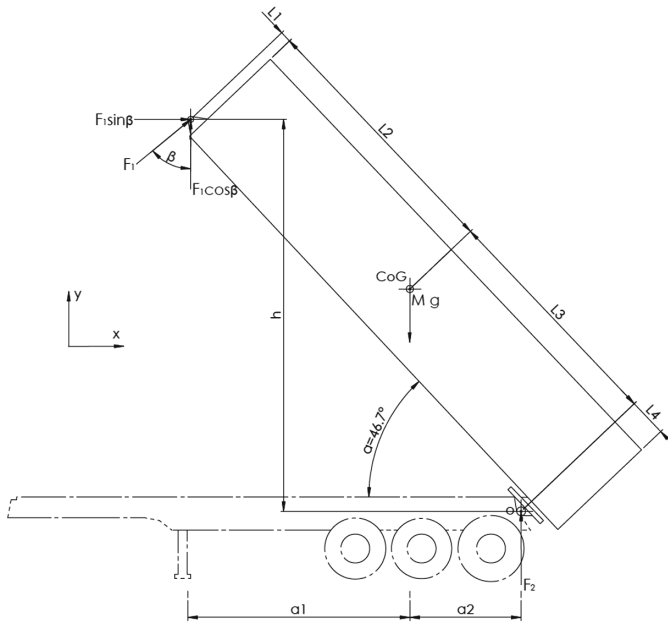


Fig. 8. End of tipping, force analysis

L_4 – Distance from the rear hinge to the rear end of the body.

$M \cdot g$ – Maximum weight including a load of the body.

4 Simulation model

Topology optimization (TO) is an engineering method that can optimize material composition within a given geometry, for predefined load cases in order to maximize certain performance. Such a load case can mimic a real-life problem modelled with a set of loads and constraints based on the laws of physics and mathematics. Performance desired to be maximized can vary, from lowering mass or displacement to better stress distribution etc. To set a TO analysis certain data is needed, from geometry limits and multiple design and manufacturing objectives, all of them suitably described in the following text.

Regarding the element type, linear elements are sufficient for TO. Therefore, mesh-wise, in this type of analysis, it is best to use a “low order” element and invest the computational power in a small mesh size. A smaller element size is needed, as this dictates the resolution of the design solution itself [9].

In this case, are used:

- CTETRA(4), Elem Size = 50mm for the 3D model;
- CQUAD(4), Elem Size = 50mm for the 2D model. (it is shown in Fig. 9).

The goal for a new chassis is to withstand the desired loads and be as light as possible. For that reason, the main objective is to take the “Compliance” Response Type. The solver will minimize the mass so that the solver keeps the structural performance in mind. The



Fig. 9. Mesh model of the 2D shell model

compliance method uses both displacement and stress distribution of the results of the simulated model to propose which location material can be additionally removed.

The design area (depicted for both 2D and 3D models in Fig. 10) consists of two groups of elements:

- optimized area, an area where elements (mass) can be removed – green/grey mesh, depicted below;
- frozen area, area to maintain in the simulation results – orange mesh.

Certain geometry so-called “frozen” areas should always contain material in the optimized model. Such as the mounting points of the suspension, the ends of the tipping axle and tipping cylinder bracket where the body is attached, or the kingpin plate where the chassis is rested over the pulling truck.

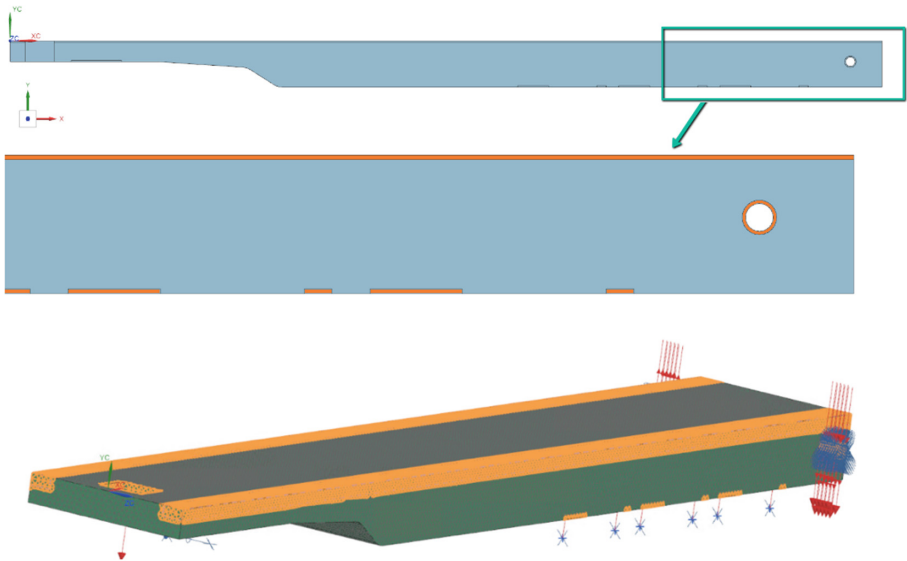


Fig. 10. Design area of 2D and 3D mesh model

The design constraint is an empirical description of the desired amount that is in direct relation to the design objective. In this situation, it gives the amount of mass that needs to be removed according to the initial mass of the design area mesh.

On a first run, the advice is to start with something “gentler” like 20% (or 50%). For example, if the initial mass is 10t, the “upper” limit (amount of desired mass for the optimized model) should be added $10 \cdot 0.5$ (5t) for a 50% reduction of mass.

The good practice is to increase this number (“upper limit”) as long as the solver is giving results that match the engineer’s expectations.

For creating an initial geometry for a new potential chassis designs the only manufacturing constraint is to have a symmetrical design for both left and right wheels this is usually known as planar symmetry constrain. It is advisable to constrain also on the minimum size of the member in order to have structures thick enough to be manufacturable. In the engineer’s practice, a possible rule of thumb is to add this as twice your element size (in this model 100mm).

This TO simulation is done using Nastran solver SOL200 from Siemens. In this situation, certain “Bulk Data” parameters should be defined to run the model.

- The most relevant ones would be the Max Number of Design Cycles, at least 50 to start for good results.
- Penalty Law (first run with RAMP with a Penalty Factor of 5 and increase it max to 8) The penalty law in Nastran is case dependent, being that, the good practice is to start with RAMP 5 and once the rest of the analysis is well set up, to try different laws and choose the one that outputs better results.






5 Topology optimization simulation and results discussion

As the initial run is taken only a 2D mesh (Fig. 9), created with CQUAD elements according to the constraints given in Table 1 of the side view of a new potential chassis. The results for each scenario as well as for a combination of all scenarios are given in Table 2.

In the results, blue is an area where the material is likely to be excluded, whereas red is an area where the material is crucial to have in the design for the simulated load case.

At the start of the tipping scenario, the frame is expected to bend longitudinally forming a “banana shape”, where the middle is displacing vertically upwards and the front and rear ends are displacing downwards. This occurs because of the force created by the lifting cylinder and the force transferred to the tipping axle coming from the load on the tipper body. Because of that reason, a generally continuous material distribution on the whole length of the chassis is expected. The 2D TO result of this scenario clearly shows that it adds material to the top and bottom of the beam, representing a potential I-beam design, or a beam with flanges or slats on its top and bottom location. The top and the bottom parts are connected with diagonal portions of material, that could be either made as tubular frames, or all of those connecting points could be replaced with a thinner sheet metal plate. It is also clear that the material behind the tipping hinge is not needed. At the end of the tipping scenario, the frame is still longitudinally bent but the force acting from the lifting cylinder is smaller than before, since the body is rotated, the CoG (centre of gravity) is transferred to the rear and some of the bulk material is unloaded. But in this situation, the forces acting on the tipping hinges are higher than before. In this scenario TO result it is still visible that the top and bottom of the beam adding material is significant, but also adds more material to the rear of the chassis, hence the largest forces there. For the torsion scenario in the result, it is clear that the front of the chassis or the so-called head section adding material is vital. For the lateral bending scenario, a larger portion of the material, maybe an extra cross-member is needed around the ISO

Table 2. TO results for each scenario

Start of Tipping

End of Tipping

Torsion

Lateral bending (short turn)

Combination of the above


curve area of the welded frame. Finally, a combination TO plot result is made of all of the described scenarios, which is extracted as a separate 2D geometry (Fig. 11).



Fig. 11. Extracted 2D geometry from the Combination plot

Extruding [10] the 2D geometry (as shown in Fig. 12) in a lateral direction to the width limit as described in Chapter “Robot Movement Programming and Simulation Generation for Pick and Place Materials in ABB Robot Studio”, which represents the maximum possible width of a new chassis, with a suitable location for all the forces, or a location where the suspension or the kingpin is located.

The extruded newly created geometry is created from 3D CTETRA mesh (Fig. 12). On this mesh a new, second integration of TO simulation for the same combination of

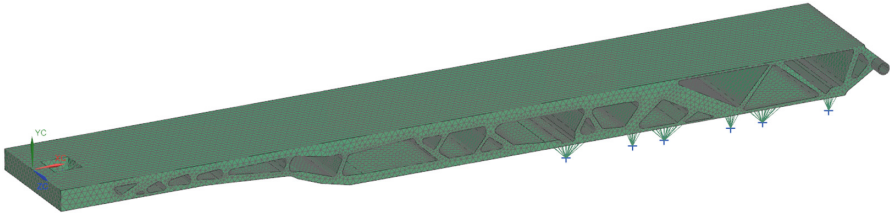


Fig. 12. 3D extruded model – Tetra mesh

load-cases is performed. The combination plot of the final results is given in Fig. 13, and its shape is further discussed.

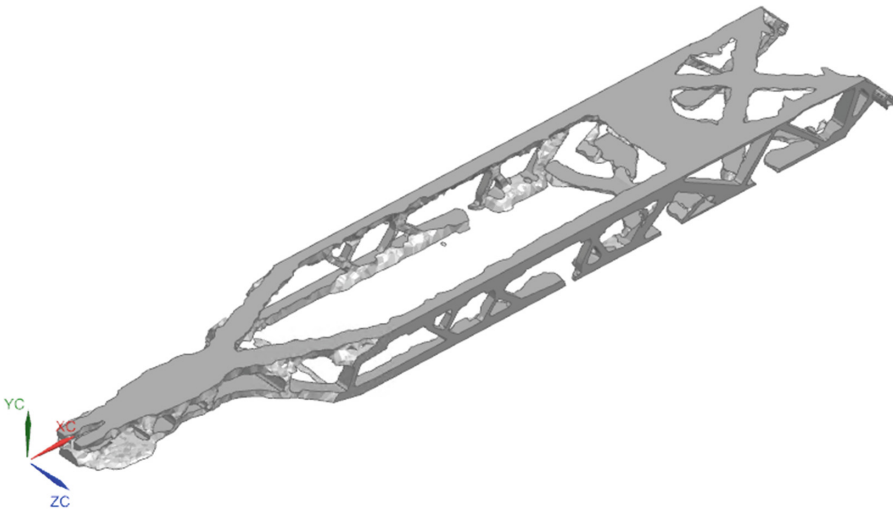


Fig. 13. Extracted 3D geometry from the Combination plot

6 Conclusion

Based on the extracted 3D geometry from the combination plots of the simulated scenarios, certain geometrical conclusions useful for brainstorming for a new welded frame for a tipper chassis can be made.

The head section or the front of the chassis where it is landed over the fifth wheel of the pulling truck can have an A-shape design, or material should be placed only for supporting the chassis to the truck and diagonally connecting to the beams and the rest of the chassis. This design is forced by the TO solver not only because the front corners are structurally not useful but also because this design could behave better in a short-turn scenario.

The main beams are no longer typical of a ladder frame chassis, where two parallel beams suitably connected are on the whole length of the chassis. I-beams are traditionally

seen as the best shape for making a chassis beam, but in this result, it is clear that the beam could maybe be made out of more complex sheet metal with no continuous shape throw its whole length. The middle of the beam should not have material, possible cutouts can be made.

The cross-members that connect the main beams, are not present in the middle of the chassis, meaning they could be thin members just for attaching equipment. In the front, close to the ISO-curve two parallel round cross-members can be placed. In the rear on large crossmember or an X-shaped crossmember should be placed that could provide better torsional stiffens to the chassis.

The tipping axle is possible to be made of two separate hinges, not one common tube. Also, the connection to the rest of the chassis asks for more material concentration, which means a potential casting on that area could be included.

With this general conclusion for each location of the welded frame, significantly easier brainstorming for a new potentially better design of a welded frame could be achieved. That also proves that adding TO in the brainstorming process makes more reliable and scientifically supported discussions between any development team.

Acknowledgement. This research as part of a larger project is supported by STAS. The company STAS as (a trailer) constructor is an established name in Belgium, today is one of the largest manufacturers of tipping trailers and moving-floor trailers in Europe. Their trailers can be aluminum and steel, but mainly they are famous for their extremely solid aluminum chassis, also separately supplied.

References

1. Illes, M., Wilson, P., Bruce, C.: Forensic epistemology: a need for research and pedagogy **2**, 51–59 (2019). <https://doi.org/10.1016/j.fsism.2019.11.004>
2. Zeid, I., Chin, J., Duggan, C., Kamarthi, S.: Engineering based learning: a paradigm shift for high school STEM teaching. *Int. J. Eng. Educ.* **30**, 876–887 (2014)
3. International Organization for Standardization: Road vehicles—Product data exchange between chassis and bodywork manufacturers (BEP)—Part 3: General, mass and administrative exchange parameters (ISO/DIS Standard No. 21308) (2020)
4. International Organization for Standardization: Road vehicles—Product data exchange between chassis and bodywork manufacturers (BEP) — Part 2: Dimensional bodywork exchange parameters (ISO/DIS Standard No. 21308) (2020)
5. International Organization for Standardization: Heavy commercial vehicles and buses—Vehicle dynamics simulation and validation—Closing-curve test (ISO/DIS Standard No. 21233) (2021)
6. International Organization for Standardization: Heavy commercial vehicles—Vehicle stability during tipper body operation—Tilt-table test method (ISO/DIS Standard No. 22138) (2022)
7. Baryshnikov, Y.N.: IOP Conf. Ser.: Mater. Sci. Eng. **468** 012022 (2018)
8. International Organization for Standardization: Heavy commercial vehicles and buses—Vehicle dynamics simulation and validation—Lateral dynamic stability of vehicle combinations (ISO/DIS Standard No. 19586) (2019)
9. Jacobson, B.: “Vehicle Dynamics” Compendium, Chalmers university (2017)
10. Cavazzuti, M., Splendi, L., D’Agostino, L., Torricelli, E., Costi, D., Baldini, A.: Structural optimization of automotive chassis: theory, set up, design (2012)



Advances in Additive Manufacturing Application in Military Industry

Muhamed Bisić^(✉) and Adi Pandžić

Faculty of Mechanical Engineering, University of Sarajevo, 71000 Sarajevo, Bosnia and Herzegovina
mbisic@gmail.com

Abstract. Additive manufacturing (AM) is recognized as a valuable method for producing functional parts in many global industries. It has been increasingly applied even in military manufacturing companies due to its specific characteristics. What started as a simple technique several decades ago, mostly used for rapid prototyping, now takes an important place in military industry when it comes to producing completely functional parts and mechanisms for weapon and different types of equipment. Understanding of different 3D printing methods and compatible materials allows engineers to create standard parts with reduced manufacturing costs and parts that are difficult to machine. One of the crucial benefits of 3D printing application in military industry is flexibility in manufacturing process, especially in terms of production site mobility. That literally means that it is now possible for soldiers to create new parts on 3D printers directly in battlefield, just by receiving right files for 3D printing from engineers. This paper reviews advances in AM application for military industry through different examples of 3D printed weapon and military equipment. Relevant 3D printing technologies are described, along with the discussion of potential problems in this area of manufacturing and possible solutions. The perspective of this method was analyzed based on current challenges, compatibility with experimental techniques and numerical methods, along with some suggestions for modernization and new areas of military application.

Keywords: Additive manufacturing · Military · Weapon · Flexibility · 3D printing

1 Introduction

The fourth industrial revolution, particularly additive manufacturing as a significant part of it, brings numerous changes in all fields of engineering [1]. Accordingly, the military industry has adopted 3D printing in its daily operations. Such a combination is potentially very powerful, but also dangerous due to insufficient understanding of the technology and its control. It is necessary to devote a lot of attention to this topic in order to explore all aspects, which would lead to a higher rate of safety for civilians who could potentially be endangered due to the misuse of 3D printed weapons. This paper provides an overview of previous achievements in the fields of 3D printed weapons and

military equipment fabrication through a review of the possible dangers and benefits of these discoveries. The paper focuses on the specific presentation of representatives of 3D printed weapons and equipment from different groups. It is important to emphasize that this is a rapidly developing but relatively young trend, and that the libraries of available scientific research papers on this topic are quite poor. Another complicating factor in researching this topic is that these are often researches that are only placed in secret specialized military archives. Therefore, this paper relies to some extent on investigative journalism articles, amateur publications, and current works by authors.

In order to raise awareness of the real danger that the combination of 3D printing and the military industry brings, it is primarily necessary to familiarize public with additive technology in a general sense. Additive technologies include manufacturing technologies that allow the production of three-dimensional objects based on a 3D model in a digital format, by adding material layer by layer [2]. These technologies do not use tools like conventional machining technologies, so they are characterized by a high degree of flexibility [3]. At the same time, multiple products of completely different geometries can be produced on one machine [4]. Additive manufacturing is a process opposite to subtractive manufacturing, in which the object is made by removing material to the final product. To avoid confusion, the term AM can refer to any process where the product is made by “stacking” something, such as making molds, but it mostly refers to 3D printing [5, 6]. This type of technology was first used for prototyping in the 1980s [7]. This process is known as rapid prototyping because it allows users to quickly create a scaled model of the final product without the standard preparations and costs associated with prototyping. As the technology improved, its application expanded to the production of tools, which were used to make molds for final products. At the beginning of this century, AM began to be used for the production of final products. A good example connected with this research is that Boeing chose 3D printing as one of the ways to produce important parts in aircraft production [8, 9].

1.1 3D Printing Explained

To create parts using 3D printing, design is primarily required. The design is usually obtained by modeling using some CAD software (Computer Aided Design), and it is also possible to 3D scan the part that needs to be 3D printed. Then, a certain software (e.g. Ultimaker Cura) transforms the design into a layer-by-layer order that the printing machine will follow. The data is sent to the 3D printer and the part is immediately 3D printed [10]. Depending on the type and material of the 3D printer, a division of 3D printing is created. The most widespread and cheapest 3D printing technology that first appeared in 1992 in the patent of the Israeli company “Startasys” is FDM (Fused Deposition Modeling) [11]. The material for FDM 3D printers is called filament, and it is a plastic thread wound on a spool. In the head of the FDM 3D printer, there are gears that pull the plastic thread to the heater that melts the plastic. The melted plastic comes out through the nozzle located close to the printing surface. As the FDM printer head moves, the melted plastic threads are laid on the printing surface and the object is made layer by layer. The surface can be heated or not. After the entire layer is finished, the FDM printer head moves up by the height of one layer and printing of a new layer begins. Some FDM printers do not move the head, but the printing surface moves down

while the head stays at the same height [12–14]. The main parameters of an FDM 3D printer are print speed, nozzle temperature, layer height, and filament uptake speed. Almost every FDM 3D printer offers users to adjust these parameters using software that controls the 3D printer. All these parameters affect the print quality and depend on the type of material used and the required properties of the final product. If objects with parts at an angle less than 45 degrees are being made, support structures are used. Support structures are very thin to save materials, but also to make them easy to remove after printing. FDM 3D printers with two or more nozzles can use special filaments that break down into liquid to make support structures. After printing is finished, the support structures that are water-soluble are suitable. Also, a very important parameter in FDM 3D printing is filling, i.e. infill density. Variation is possible in the range from 0 to 100%. It is also possible to vary the shape of the infill. Understanding of all of these parameters is crucial when it comes to 3D printing parts for military purposes [15, 16].

The basic materials used in FDM technology are usually thermoplastic polymers. These materials do not change their chemical structure when heated to their melting or softening temperature, but only their aggregate state, making them reusable. Thermoplastic polymers are most suitable for functional applications, including the production of functional prototypes and functional parts for final use [17]. They have very good mechanical properties, high impact resistance, wear resistance, and chemical resistance. In recent times, composite thermoplastic polymers containing reinforcing fibers (such as carbon fibers, glass fibers, etc.) can also be used for additive manufacturing, significantly improving the properties of the base material. The so-called engineering class of thermoplastic materials is widely used in industry today [18]. The most commonly used material for FDM 3D printing is PLA (Polylactic Acid) plastic, which is also the easiest to print. It is a thermoplastic polymer obtained by condensation of lactic acid with loss of water. It is biodegradable, without any harmful environmental impact, and is obtained from fermented plant starch, usually from corn, sugarcane, or sugar beet pulp. It does not crumble, allows for coloring and finishing, and withstands temperatures up to 60 °C without deformation. It is an optimal choice for prototypes with special requirements and complex geometry. It is not a flexible material, and its properties weaken if exposed to sunlight for a long time. Due to its additional strength, this material is less suitable for developing complex mechanisms and fitting elements, so it is mainly used for functional and conceptual prototypes. It is printed at a nozzle temperature in the range of 195–225 °C, on a bed heated to 60 °C. The material density is 1.24 g/cm³, and the maximum print speed is up to 120 mm/s. There are also certain modifications of PLA that allow it to withstand temperatures up to 110 °C [19]. It is an excellent combination with water-soluble PVA (polyvinyl acetate) plastic, making it possible to create complex structures. In addition to PLA and PVA, FDM technology supports a large number of different thermoplastic polymers, and the number is increasing every day with the discovery of new suitable materials. Nylon has the highest density (1.54 g/cm³), and the optimal material is chosen based on the desired characteristics of the final product. SLA (Stereolithography) is another 3D printing technology that uses light to solidify a photopolymer, creating a thin layer of solidified material. The light source is usually an LCD screen, and the process is repeated by lowering the platform into the liquid resin. Support structures are often used due to the complexity of the object's construction [20].

The group of polymers used in additive manufacturing technologies with SLA 3D printers are thermosets. Unlike thermoplastics, thermosets cannot be reused by changing their aggregate state. Typically, in additive manufacturing, thermosets are obtained by polymerizing resins using a light source. The light source can be a laser beam, lamp, or diode, and the material can be located in a building tank or fed through a print head. Accordingly, these technologies are classified and divided. SLA, DLP, and LCD technologies keep the material in tanks in a liquid state and illuminate the building layer zone using different light sources [21]. Thermosets are better suited for applications where product aesthetics are a key factor, as the technologies that use them are capable of producing parts with almost smooth surfaces that simulate the finishing of parts made in a traditional way. Generally speaking, thermosets are stiffer and more brittle than thermoplastics, so they have limited usability in functional parameters. They show signs of aging, especially if exposed to external light [22]. When it comes to available thermosets, there is also a large group, and standard thermosets with mechanical properties that simulate ABS thermoplastics, thermosets with increased toughness that simulate PP thermoplastics, transparent materials, elastic materials, and materials with increased temperature resistance are well-known [23]. More and more work is being done on the development of biocompatible thermosets, which otherwise have toxicity as a property. After 3D printing, the sintered product needs to be UV treated with a natural or artificial UV source, which has been proven to affect the mechanical properties of the elements [24]. Figure 1 shows main principle of FDM (left) and SLA (right) 3D printing technologies.

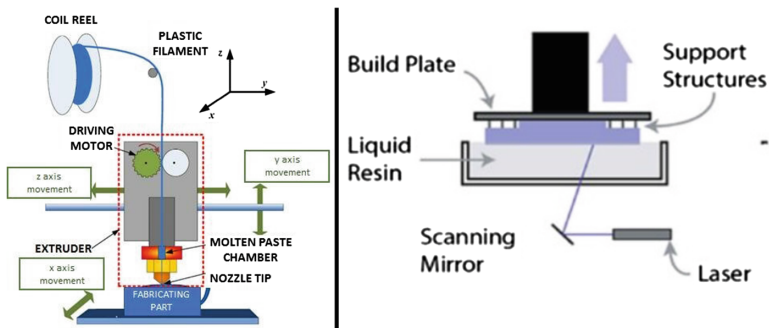


Fig. 1. FDM 3D printer (left) and SLA 3D printer (right) [25, 26].

1.2 Advantages and Disadvantages of AM in Military Industry

Additive technologies have some specific advantages. The traditional production process can take months and require huge amounts of investment, and it only pays off for mass production. With the introduction of additive technology, the entire process can be changed and some steps can be eliminated. The biggest advantages of 3D printing could be the ability to print extremely small dimensions and complex geometry, unlike the subtractive method. Using additive technologies, it is also possible to reduce the total

weight of the final product, which is very important in the automotive and space industries [27]. It is also believed that the use of 3D printing simplifies the production of more complex assemblies and reduces waste with a “just in time” approach to production. In addition, it is easier to make smaller series of an element because production is done directly on the computer-3D printer line [28]. The possibility of personalizing objects is particularly interesting, especially when it comes to prostheses, implants, and especially hearing aids, which are almost all 3D printed because each one is unique [29, 30].

Additive technology also brings certain challenges. 3D printers are devices with a wide range of prices, ranging from a hundred dollars to several hundred thousand dollars. Their use for the production of large parts and large quantities is much slower than traditional production. Also, a large number of products made with 3D printers require finishing to remove defects, clean the part, and process the edges, among other things. One of the biggest challenges is to adjust the parameters to obtain guaranteed product properties. From the materials science perspective, this is probably the biggest challenge that this technique brings with it. The disadvantages and problems in 3D printing are never the same and depend on many parameters such as material and its storage, print parameters, atmospheric conditions, machine condition, and many others [31].

2 Literature Review

Production of parts and products directly on the locations where military or humanitarian missions take place represents a promising solution for armies and organizations [32]. Operations that take place in remote locations often require extensive and well-organized supply chains that are completely different from standard ones [33]. By positioning additive manufacturing equipment closer to the end user in the chain, delivery time and logistics costs are significantly reduced [34]. Challenges in logistics in the military industry are always problematic, not only from a financial perspective, but also from the standpoint of personnel safety, military detachment on the battlefield, etc. [35, 36]. With easier overcoming of the described problems, additive manufacturing also emerges as a form of environmentally friendly way of supplying the military with spare parts [37]. Since the military industry involves complex types of weapons and equipment, supplying the same with spare parts can be achieved either by constant production or by creating large stocks in advance. Both cases represent an extremely expensive and economically unfavorable approach, and the end user pays the highest price [38]. In addition, many elements and assemblies are produced in such small quantities that tooling for them represents the most significant share of the cost [39]. The potential best solution for reducing stocks is the “on-demand” production system, which primarily relies on additive manufacturing [40]. Such an approach would contribute to the relief of the entire logistics network and increase the reliability of supplying spare parts directly on the battlefield [41]. The use of 3D printed replacement parts could result in shorter periods of time when equipment is out of use [42]. The focus for 3D printed spare parts should be on parts with lower or unknown demand and short production times [43]. Reducing stocks of spare parts in mission preparations would give the military additional space for carrying basic necessities. However, as a potential problem for the

use of 3D printers, the terrain on which the mission is carried out should be observed in advance, due to the assessment of the impact of atmospheric conditions, energy supply, etc. [44]. As for the tactics of warfare, it is believed that the use of 3D printers directly on the battlefield could confuse the opponent who would not be able to have insight into the army's equipment and its warehouse [45].

The ecological aspect is certainly worth mentioning, and it is believed that this approach encourages the use of recycled materials [46]. Within the research conducted in the work [32], it was concluded that due to the great possibility of personalization of 3D printed elements, soldiers show satisfaction in using them. A specific case is the application of night vision goggles, where the element that rests on the soldier's face is personalized by a 3D printer, making it much more comfortable for longer wear and use than the standard universal one.

Despite the described advantages of using additive technology in the military industry, a certain number of works also deal with the issue of moral use of additive manufacturing [47]. Given its potential and almost endless possibilities, there is a justified fear of misuse of this technology, and it is being considered whether it is justified to use it for military purposes [48]. However, the answer to such a question is difficult to give, especially when it comes to the lives of soldiers who are already deployed on the battlefield. When their safety is at stake, there is also a justified fear because, as already mentioned, it is an insufficiently researched field. Not all safety aspects, reliability, and performance of 3D printed weapons and equipment are fully known yet [49].

It is also believed that a lack of knowledge about the described technology and errors in its use could result in the production of elements that would not be able to provide the desired mechanical characteristics for real use [50]. Despite this, there have already been publicly announced cases of direct use of 3D printers on the battlefield by many armies around the world for the production of spare parts, suicide drones, and many other products. One of the better-known examples of adopting additive manufacturing into their ranks is the case of the Canadian military, which is working on adopting this technology to the fullest extent possible through the "Beyond the Horizon" project [51]. Personalization of equipment is also considered one of the main arguments for introducing AM into full use for military purposes, so that equipment can be adapted for special purposes [52].

The authors give preference to additive technology through their research due to the possibility of producing disposable devices, whether it be even telephone sets, suicide drones, or other means of communication and jammers, all in order to create a safer environment for those participating in the mission [49]. The Canadian military extensively uses 3D printed reconnaissance drones, citing only rough advantages [53]. The fact that the danger is real is evidenced by the fact that the number of forensic experts specializing in 3D printed weapons and ammunition has been increasing lately. Some of them claim that hybrid weapons are a great danger, while completely plastic ones still pose the primary danger to the user [54].

3 3D Printed Guns and Ammunition

The current topic of many world media in recent years is precisely 3D printed guns, the so-called “ghost guns”. The name is justified because it is literally impossible to trace the weapon that it is easy to produce, use, and even easier to destroy. One of the focuses of this work is to come to the conclusion by citing many examples of the use of additive technology for this purpose, whether 3D printed weapons are a myth or a real danger. To qualify as 3D printed, it is enough for only some components to be printed and combined with metal parts. The process is even easier now that it is possible to 3D print metal, but it is an expensive process, so only plastic weapons will be considered. It is already possible to find a certain number of articles, laws, and even examples of criminal offenses using this type of weapon on the internet. According to one definition, 3D printed weapons are weapons primarily produced on a 3D printer. They can be classified based on the type of printer used, whether plastic, metal, or combined. While plastic is used as improvised weapons to avoid control, metal printed guns are already used in the legal manufacturing industry. Although it is possible to produce a completely plastic functional gun, such a weapon has a short lifespan, and it is common practice to print a plastic frame and combine it with metal for the firing process (combustion chamber) and barrel, resulting in a so-called hybrid weapon. Metal parts can also be made at home. Another controversy related to plastic guns is the problem of producing parts for standard weapons. Such additions maximize the potential of real weapons and often take them out of the legal framework [54]. The first example of a 3D printed functional gun is the so-called “Liberator,” which allowed for the firing of one bullet, made entirely of polymer and presented in 2013. After just 2 days, US authorities deleted the published designs for the Liberator and filed charges against the designer, Cody Wilson [55]. Figure 2 shows all parts of Liberator.

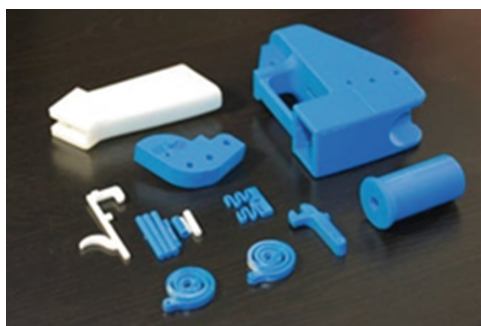


Fig. 2. First functional 3D printed gun – “Liberator” [54].

The test results conducted with the Liberator, in which one projectile was fired from 6 pieces of the weapon, showed that the muzzle tends to break at the moment between igniting the propellant charge in the bullet and leaving the muzzle. The velocity of the projectile at the muzzle exit in the case of muzzle breakage is about 140 m/s, and 170 m/s in the case of no muzzle breakage. The trajectory is very complex to describe.

The penetration of the projectile measured in ballistic soap goes up to 21 cm, and the projectile is considered lethal. The entire analysis was conducted to gather information for forensic examinations [56].

In the same year that the controversy surrounding the Liberator arose, the American company Solid Concepts presented the first 3D printed metal gun, a replica of the Colt 1911 model. Over the years, the development of plastic weapons has grown exponentially, and even in 2021, there was a case where guerrillas in Myanmar used 3D printed semi-automatic weapons in armed conflicts [55]. In all European countries, the production and possession of 3D printed weapons is strictly prohibited. In some countries, even possessing the blueprints is illegal. Despite this, there is an increasing percentage of such weapons found in raids and criminal activities. The seriousness of the situation is evidenced by the recent request of the American president to adopt laws that will fully control and supervise the entire 3D printing industry. Something like this already exists in certain parts of China, where all companies that use additive technology must register as a special industry, providing details about the equipment they use, security measures, and detailed information about all employees. In Australia, a penalty of up to 14 years is planned for the discovery and use of 3D printed weapons, while in Singapore, the death penalty is imposed for this [55].

The main question is whether all of this is justified, or how real the danger of plastic weapons is. The answer is still not entirely clear and it will require a lot of academic research (within which dealing with this topic is legal) to define some clear guidelines and parameters. Since the emergence of this type of weapon, it is considered prone to breakage and even explosion in the hands of the user. 3D printed weapons are considered extremely dangerous for users. A documentary that followed a competition in the production of plastic weapons with printers in 2021 recorded that none of the products worked without difficulty. Since it is amateur production, an important factor is precisely the knowledge and ability of the person involved. From a technological standpoint, improvement is constant, number of technology users is growing, and it is clear that the efficiency of 3D printed weapons will only increase. A major concern is partial understanding of polymers available in the form of materials for FDM technology. Uncertainties arise because, theoretically, the performance of the material cannot keep up with the processes that occur during the firing of ammunition, but in practice, these processes take place in thousandths of a second and the effect on the material is not entirely clear. It is certain that production with the development of materials will be much more serious and that legal regulations related to this topic will be more than justified. However, one of the forensic analysis papers [54] shows rapid progress when it comes to reducing original metal parts in hybrid weapons, which proves that designs and materials are becoming more advanced. Figure 3 shows variants of 3D printed weapons based on AR15 in 2015 (left image) and 2019 (right image).

The first version consisted of only a few 3D printed components that replaced the original ones (modular approach), while the latest version only has the original firing mechanism and gun handle. In this year, several models can already be found that have been declared by users as completely successful and durable. One such model is the "Lifecard 0.22 lr," a 3D printed version of the world's thinnest folding pistol produced by Trailblazers Firearms. Its components and ammunition are shown in Fig. 4.



Fig. 3. Difference in 3D printed AR15 in 4 years [54].



Fig. 4. 3D printed “lifecard” gun.

The difficulty in controlling the sharing of designs and the production of different models is demonstrated by the example in Fig. 5a, which shows all 35 parts of the most common gun worldwide, the Glock 17. With minor hybrid combination (replacement of certain elements with metal), a fully functional prototype of 9 mm caliber is obtained. Through experimental methods, it is possible to test the ability of this prototype made from different materials, in hybrid and fully plastic variants, to fire real ammunition, with varying masses of propellant. The ease of illegally manipulating ammunition is demonstrated by the example that a completely legal kinetic hammer can be used to disassemble a bullet without damage, remove a certain part of the filling, and then reassemble the bullet and use it for 3D printed guns. This process will reduce the pressure and temperature in the combustion chamber, bringing us one step closer to a completely perfect prototype. Figure 5b shows the appearance of a disassembled bullet that can have a part of the filling removed and then reassembled into a single unit.

In the context of this topic, the possibility of using plastic projectiles, or “ghost” ammunition, will also be considered in the future. Varying the mass of the filling allows for such production, and one example is the production of projectiles (bullets) for 5.56 × 45 mm ammunition. Plastic cases are already being manufactured and represent a

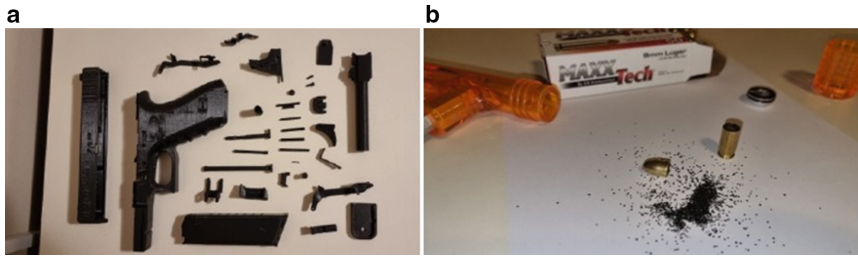


Fig. 5. a) 3D printed Glock 17, b) disassembled 9 mm bullet.

popular trend in military industry (TrueVelocity). The appearance of the projectile and the complete bullet is shown in Fig. 6.



Fig. 6. 3D printed projectile for 5.56 × 45 mm bullet.

In addition to the inability to track, the greatest danger of printed weapons lies in the fact that they can be completely melted using certain, also easily available, acids and substances. The power of ordinary PLA plastic was accidentally demonstrated during an experiment at the Faculty of Mechanical Engineering at the University of Sarajevo, where 3D printed sabots were used to stabilize metal projectiles. In the experiment using a wooden board, 25 mm thick (the American standard for testing the effectiveness of small caliber ammunition), the sabots penetrated several millimeters [57]. The unexpected outcome can be seen best in Fig. 7, which shows the appearance of the sabot.

This result led to the development of 3D printed polymer penetrators that could be used as fully effective ammunition. In their work testing polymer projectiles, authors used 5 different UM materials (PLA, Tough PLA, Nylon, PETG, and PC). A compressed air-powered gun was used to fire the projectiles, with a pressure of 50 bar for each experiment. The velocity of the projectiles was measured using a Doppler effect chronograph. The design concept for statically stabilized plastic projectiles is shown in Fig. 8a. A wooden board with a thickness of 2.54 cm was used as the target. The paper describes in detail the

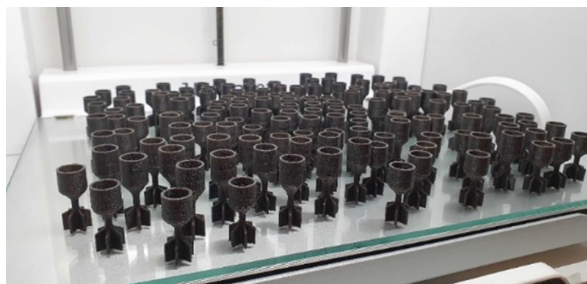


Fig. 7. 3D printed PLA sabots.

process of designing and 3D printing the projectiles, as well as the entire experimental process with accompanying calculations. The experimental setup is shown in Fig. 8b.

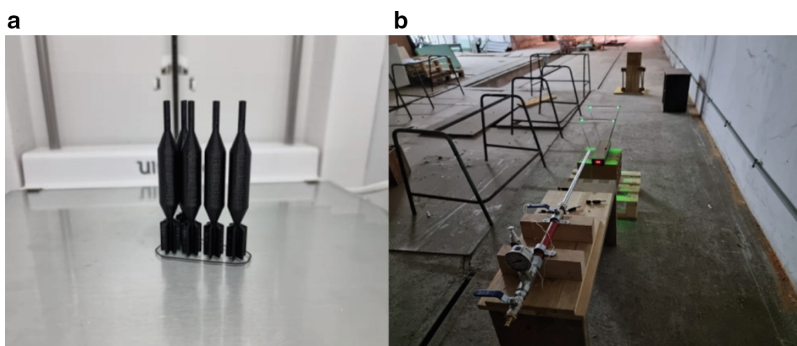


Fig. 8. a) 3D printed projectile, b) experiment setup [57].

After experimental measurements, it was found that Tough PLA polymer achieves complete penetration of the wooden board with each firing, which could ultimately mean that it is a potentially lethal projectile [57]. Further work on improving the design of the projectiles, as well as the systems for firing them, could result in the most dangerous combination of today - “ghost” weapons and “ghost” ammunition. Research of this type is important in order to show the skeptical public the real danger of this specific topic, and to develop the defense sector against plastic weapons and ammunition in step with their development. The penetration of the projectile into the wooden board is shown in Fig. 9.

In one of the experiments using a compressed air gun, a barrel made entirely of PLA plastic was used, on which even a thread was cut without compromising the structure of the material. The barrel proved to be fully functional, and after multiple firings, there was no compromise to its structural integrity [57].



Fig. 9. Penetration of 3D printed polymer projectile into the wooden board [57].

4 3D Printed Bombs, Drones and Spare Parts

In step with the development of Airsoft competitions and weapons, it has been found that it is possible to make a bomb that contains preformed fragments, in this case airsoft metal balls. Further testing has shown that traditional hand grenades are a design that has been present for decades and that throughout that period the grenade has a very unfavorable ratio of body mass to explosive filling. That ratio, and therefore the effectiveness of the hand grenade, could be greatly improved by 3D printing it. So, the idea is to make the bodies of hand grenades from different polymers, ideally PETG. PETG is a material for FDM 3D printers that is characterized by good strength, hardness, and toughness parameters, with excellent resistance to atmospheric influences, unlike its competitor PLA. PETG also has a higher melting point than PLA and casting TNT into a PETG shell would proceed without problems. The use of 3D printed elements for explosive devices with preformed fragments has been successfully demonstrated and explained experimentally in some ongoing military projects. However, in the case of mass production, due to the high cost and time required to make one piece, 3D printing would only be used to make a prototype of the grenade body. On the other hand, when it comes to directed explosions, control of explosion power, etc., 3D printing is undoubtedly the number one method by which such personalization can be carried out, and follow the trend of “on-demand” production. There is currently no specific work on this topic in online databases, and it is possible to lay a solid foundation for this topic. One of the conceptual solutions is shown in Fig. 10a, which is a cross-section of a PLA material grenade body. The intended slots would be filled with tungsten or steel balls that have small dimensions, high density, and strength, making them an ideal choice for preformed fragments.

In addition to introducing new designs, where testing would determine whether the optimal design is a cylinder with a hollow or solid bottom, a sphere, or something else, it is also possible to 3D print a standard design of a hand grenade, as seen in the Fig. 10b.

3D printing is an indispensable process in the industrial production of drones today. The reason is that all modern military drones must be lightweight and to some extent resistant to external influences. The Turkish drone Bayraktar TB2 consists of many components that are 3D printed. In addition, the Pentagon is developing secret reconnaissance drones that are completely 3D printed, made for each different purpose (customized) and

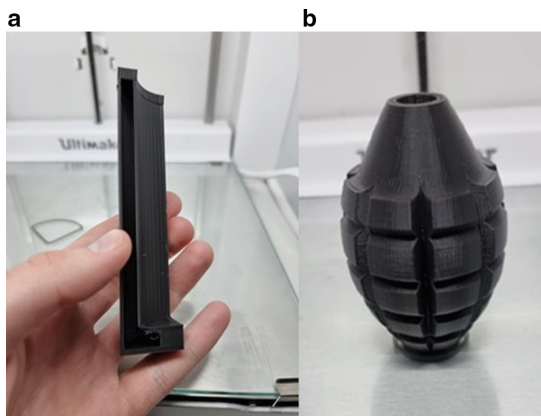


Fig. 10. a) Cylindrical 3D printed grenade shell, b) 3D printed standard hand grenade.

even capable of carrying certain amounts of explosives - suicide drones [58]. In addition to complete products, many parts are made on conventional 3D printers in armies around the world. Some of them are: parts for submarines, parts for tanks and armored vehicles, parts of the US strategic bomber B-52, sending parts as electronic files and then their production for the purpose of keeping secrets (AirForce bombers), Biomedical aids, unique tools, turbines, etc. [58].

5 3D Printed Explosive Materials

In the last 2 years, the idea of 3D printing of energy materials, i.e. secondary high explosives and fuel, has come to life to a certain extent. It is possible to find works on this topic on the Internet, and due to the specificity and sensitivity of the topic, many people are unable to use the example without security checks. One of the specific ones is work dealing with 3D printing of explosives based on RDX. Research has shown that it is possible to make one such filament that will have improved thermal stability and suppress the formation of hot spots within the gradient explosive (gradient explosive is an explosive whose structure has been changed). The critical dimension of detonation indicates that the critical size of the explosive charge. For the last 2 years, the idea of 3D printing of energy materials, i.e. secondary high explosives and fuel, has come to life to a certain extent. It is possible to find works on this topic on the Internet, and due to the specificity and sensitivity of the topic, many people are unable to use the example without security checks. One of the “hidden” ones is work dealing with 3D printing of explosives based on RDX. Research has shown that it is possible to make one such filament that will have improved thermal stability and suppress the formation of hot spots within the gradient explosive (gradient explosive is an explosive whose structure has been changed). The critical dimension of detonation indicates that the critical size of the explosive with the structure gradient is significantly increased. This represents a major shift and a huge advantage of the explosives 3D printing method when it comes to the production of large caliber ammunition with structural and functional improved properties [59].

The next topic that researchers are exploring is 3D printing of propellants for conventional weapons. Most modern weapons use propellants with the same ingredients that were introduced in the late 19th and early 20th centuries. The ballistic performance of all propellants essentially depends on the geometry of the propellant charge [60]. Large calibers usually use perforated charges or tube-shaped charges obtained by extruding wet charges that are further processed. The development of more powerful weapons in modern times requires a more complex geometry and a complex structure that is almost impossible to obtain with conventional methods of charge production. Therefore, there is a need for 3D printing of propellant charges to eliminate restrictions and expand the design possibilities of propellant charges that would directly affect ballistic performance. Similarly, 3D printing could also focus on printing explosives and pyrotechnic mixtures. In addition to enabling ballistic improvements, the introduction of 3D printing will also cause positive economic changes. Large and expensive facilities can be broken down into smaller ones, increasing facility safety, reducing storage costs, and developing a new trend popular in today's world known as "print on demand" or printing on demand, which is increasingly used in the military industry and reduces pressure on logistics, increases flexibility, and eliminates restrictions in daily activities. In the described work, the authors compared the internal ballistic parameters of conventional explosive charges with 7 perforations of different geometries to 3D printed solutions. The design and geometry of the 3D printed charge were obtained by parametric modeling in the C program, where the ideal shape was obtained based on the required parameters and the design of the barrel and combustion chamber. The analysis of the results showed that the 3D printed charge gave a muzzle velocity over 10% higher than conventional charges, with reduced pressure. The reason is that the complete burning surface is optimally utilized. The authors cite the experiment as successful and the only problem they mention is the development of high-quality materials for this method, with a potential solution being the use of SLA 3D printers [61].

In addition to the aforementioned topics, intensive work is also being done on the development of 3D printed granules for rocket fuels. Since this is a very important group of fuels, research has been conducted with the aim of eliminating the boundaries in terms of the geometry of conventional granules. Researchers have used an improvised FDM 3D printer to create granules with oxidizers by layering material layer by layer [62]. The process of making rocket fuel with a 3D printer is shown in Fig. 11.



Fig. 11. 3D printing rocket fuel [62].

Improving this method would bring great advantages when it comes to the complexity of the geometry of the propellant and the size of the granules, while retaining the mechanical properties of conventional granules. 3D printing could eliminate pore incompleteness at the microscopic level. It could directly improve the properties of the granules by printing certain complex structures and mixing them with different components (dual extrude). It is expected that this method will make a huge leap in the quality of rocket propellants, combustion, and pressure control, which will have an impact on potential missions and the like [62].

The biggest breakthrough when it comes to 3D printing of energetic materials will be caused by the examination of the nanostructure of the materials. The basic idea is to introduce nano-particles of strong secondary explosives into materials for conventional 3D printing (for FDM, SLA, or SLS methods). Some progress has been made, but work is still being done to define the properties of such materials to ensure the safety of the method [63].

6 3D Printed Safety Equipment and Structures

New research in the fields of nanomaterials and the development of ultra-strong polymers has unlocked a totally new sphere when it comes to “plastic” armor. One of the researches currently being done in collaboration between MIT, Caltech, ETH Zurich and the US Army Research Laboratory claims to have used 3D printing technology to form a nano-level material that is said to have less penetration than Kevlar or steel. The material is thinner than a human hair and made of tiny carbon particles grouped into interconnected tetrakaidekahedra (structures with 14 surfaces) formed by two-photon lithography. This material should be able to replace Kevlar in a wide range of applications [64]. Structure is shown in Fig. 12.

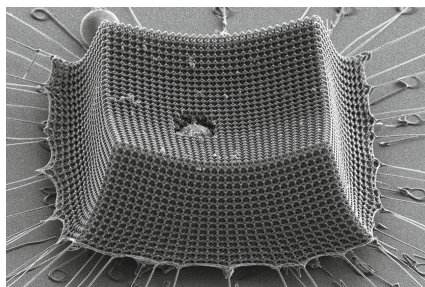


Fig. 12. 3D printed structure for armor [64].

The second method also combines carbon fibers, but in a different structure. The importance of structure is demonstrated by the fact that a bullet traveling at a speed of 5800 km/h penetrated a solid material cube, while a cube made of tubular structure stopped the same projectile on the second layer. Tubular structures are made of interwoven carbon nano-fibers and are still largely unexplored and until recently only theoretical. However, 3D printing has enabled the production of cubes like those shown

in Fig. 13 and these truly incredible results. The lattice of holes causes a strengthening effect on the structure and for this reason, in all 10 tests, this type of cube was more efficient than a solid one [65].

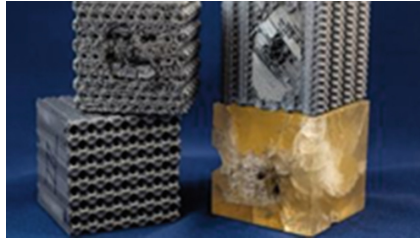


Fig. 13. 3D printed tubular structure.

For some time now, the US military has been using large FDM 3D printers to build barracks and temporary storage facilities. The nozzles print concrete and provide complete structures in just 36 h. The structures are so large that multiple rocket launchers can be housed in them. Such structures are much cheaper and simpler to produce than conventional temporary military buildings [66].

7 3D CAD/CAM Compatibility with Numerical Simulations

The use of additive technology, specifically 3D printing, is another method that saves time and resources in the development and improvement of new and old weapons and ammunition in the modern world, along with numerical simulations. In combination with powerful computer modeling tools and 3D printers, engineers can obtain a finished physical model faster than ever before. With this CAM method, designers can obtain a realistically looking model and visually capture all potential shortcomings. With the adoption of 3D printing technology in the military industry, it is realistic to expect an expansion of projectiles or projectile elements made of polymer bodies. Such a trend could direct the explosive energy required to break the projectile shell primarily into the target effect, and can be specifically demonstrated in the case of forming a cumulative jet in the HEAT projectile for the M80 “Zolja” handheld rocket launcher. The appearance of the 3D printed body of the warhead is shown in Fig. 14.

The compatibility of using such a projectile body in real conditions or just during static testing (exceptional economic efficiency compared to aluminum projectile body) has been confirmed by numerical simulations in the Ansys Autodyn program. The numerical simulation showed the process of forming a jet in cases where the warhead body is made of aluminum alloy Al6061-T6 and in the case of polyethylene (3D printable polymer). In both cases, the explosive filling is LX-14-0 and the cumulative funnel is made of copper. The maximum velocity of the formed jet for the warhead using the aluminum alloy body is 6939 m/s, while the polyethylene warhead forms a jet of maximum velocity 6381 m/s (deviation of about 1.5%). This result supports the hypothesis that tests using metal bodies for warheads, shells, etc. could be conducted with 3D printed



Fig. 14. 3D printed warhead body for HEAT 64 mm projectile.

polymer options. Such an approach would greatly reduce the cost and speed up testing, creating space for more detailed experiments.

8 Conclusion

Through the presented and described examples of direct use of additive technology in the military industry, it is possible to recognize its good and bad sides. As a positive aspect of its application, the defense sector and its improvement, accompanied by ecological and economic savings in production, should certainly be emphasized.

The development of 3D printed weapons, ammunition, and military equipment is inevitable in the coming period, and as such, it is necessary to constantly monitor and point out the increasingly serious danger of such products.

Based on the described examples of use, the fact is that it is no longer a myth and non-functional prototypes, but a serious and fully functional danger about which many regional security services are not sufficiently informed. Monitoring and bringing such production under control is a logical step in the future to preserve the safety of people and property, especially in public spaces. The fact is that conventional metal detectors and security systems are not fully up to this challenge of the 21st century and that the growth of the use of additive technology in the military industry will inevitably cause innovations in the defense sector. In any case, it is necessary to extract the maximum from this topic and use it in the best possible way for the development of new defense systems.

References

1. Vaidya, S., Ambad, P., Bhosle, S.: Industry 4.0 – a glimpse. *Procedia Manuf.* **20**, 233–238 (2018)
2. Praveena, B.A., Lokesh, N., Buradi, A., Santhosh, N., Praveena, B.L., Vignesh, R.: A comprehensive review of emerging additive manufacturing (3D printing technology): methods, materials, applications, challenges, trends and future potential. *Mater. Today: Proc.* **52**(part 3), 1309–1313 (2022)
3. Joel, C.N., Raeisi, S., Tovar, A.: Review of additive manufacturing technologies and applications in the aerospace industry. In: *Additive Manufacturing for the Aerospace Industry*, pp. 7–31. Elsevier (2019)

4. Wong, K.V., Hernandez, A.: A review of additive manufacturing. *ISRN Mech. Eng.* (2012)
5. Sathish, K., et al.: A comparative study on subtractive manufacturing and additive manufacturing. *Adv. Mater. Sci. Eng.* **2022**, 1–8 (2022)
6. Magnien, J., Cosemans, P., Nutal, N., Kairet, T.: Current surface issues in additive manufacturing. *Plasma Process. Polym.* (2020)
7. Singh, A., Singh, H.: Metal additive manufacturing: from history to applications. In: Khan, M.A., Jappes, J.T.W. (eds.) *Innovations in Additive Manufacturing*. Springer Tracts in Additive Manufacturing. Springer, Cham (2022)
8. Linke, R.: Additive manufacturing, explained. <https://mitsloan.mit.edu/ideas-made-to-matter/additive-manufacturing-explained> (2017). Last accessed 22 Apr 2023
9. Ghimire, T., Joshi, A., Sen, S., Kapruan, C., Chadha, U., Kumaran, S.S.: Blockchain in additive manufacturing processes: recent trends & its future possibilities. *Mater. Today: Proc.* **50**(part 5), 2170–2180 (2022)
10. Bevrnja, M., Imamović, Z., Bisić, M.: Additive manufacturing application for the inclusion of the vision impaired population in public transport. In: *Proceedings of the 33rd DAAAM International Symposium*, pp. 0519–0525. DAAAM International, Vienna, Austria (2022)
11. Kechagias, J., Chaidas, D.: Fused filament fabrication parameter adjustments for sustainable 3D printing. *Mater. Manuf. Processes* **38**(8), 933–940 (2023)
12. Nasir, M.H.M., Taha, M.M., Razali, N., Ilyas, R.A., Knight, V.F., Norrrahim, M.N.F.: Effect of chemical treatment of sugar palm fibre on rheological and thermal properties of the PLA composites filament for FDM 3D printing. *Materials* **15**, 8082 (2022)
13. Wang, J., Wang, M., Xu, C., Han, Y., Qin, X., Zhang, L.: Tailored dynamic viscoelasticity of polyurethanes based on different diols. *Polymers* **15**, 2623 (2023)
14. Jung, Y.S., Lee, S., Park, J., Shin, E.J.: Synthesis of novel shape memory thermoplastic polyurethanes (SMTPUs) from bio-based materials for application in 3D/4D printing filaments. *Materials (Basel, Switzerland)* **16**(3), 1072 (2023)
15. Pandžić, A., Hodžić, D.: Tensile mechanical properties comparison of PETG, ASA and PLA-Strongman FDM 3D printed materials with and without infill structure. In: *Proceedings of the 33rd DAAAM International Symposium*, pp. 0221–0230. DAAAM International, Vienna (2022)
16. Doshi, M., Mahale, A., Kumar, S.S., Deshmukh, S.: Printing parameters and materials affecting mechanical properties of FDM 3D printed parts: perspective and prospects. *Mater. Today: Proc.* **50**(part 5), 2269–2275 (2022)
17. Tripathy, C.R., Sharma, R.K., Rattan, V.K.: Effect of printing parameters on the mechanical behaviour of the thermoplastic polymer processed by FDM technique: a research review. *Adv. Prod. Eng. Manag.* **17**(3), 279–294 (2022)
18. Patel, R., Desai, C., Kushwah, S., Mangrola, M.H.: A review article on FDM process parameters in 3D printing for composite materials. *Mater. Today: Proc.* **60**(part 3), 2162–2166 (2022)
19. Arrigo, R., Frache, A.: FDM printability of PLA based-materials: the key role of the rheological behavior. *Polymers* **14**, 1754 (2022)
20. Wang, S., et al.: A review of 3D printing technology in pharmaceuticals: technology and applications, now and future. *Pharmaceutics* **15**, 416 (2023)
21. Pariskar, A., Sharma, K.P., Murty, U.S., Benerjee, S.: Effect of tatzine as photoabsorber for improved printing resolution of 3D printed “ghost tablets”: non-erodible inert matrices. *J. Pharm. Sci.* **112**(4), 1020–1031 (2023)
22. Pandžić, A.: Influence of layer height, build orientation and post curing on tensile mechanical properties of SLA 3D printed material. In: *Proceedings of the 32nd DAAAM International Symposium*, pp. 0200–0208. DAAAM International, Vienna (2021)
23. Kumar, R.: Functionalities of ZnO reinforced thermoplastics composite materials: a state of the art review. *Mater. Today: Proc.* **51**(part 1), 972–976 (2022)

24. Bisić, M., Pandžić, A.: Experimental analysis and comparison of mechanical properties of standard grey resins, with and without post-curing, and biocompatible SLA printed materials. In: Mitrovic, N., Mladenovic, G., Mitrovic, A. (eds.) *Experimental Research and Numerical Simulation in Applied Sciences*. CNNTech 2022. Lecture Notes in Networks and Systems, vol. 564. Springer, Cham (2023)
25. Zaharin, H.A., Rani, A.M.A., Ginta, T.L., Azam, F.: Additive manufacturing technology for biomedical components: a review. *IOP Conf. Ser.: Mater. Sci. Eng.* **328** (2017)
26. Ans, R., Waqas, A., Khalid, M. Y., Koc, M.: Vat photopolymerization of polymers and polymer composites: processes and applications. *Addit. Manuf.* **47** (2021)
27. Syrlybayev, D., Zharylkassyn, B., Seisekulova, A., Akhmetov, M., Perveen, A., Talamona, D.: Optimisation of strength properties of FDM printed parts—a critical review. *Polymers* **13**, 1587 (2021)
28. Jabil homepage. <https://www.jabil.com/blog/3d-printing-in-aerospace-and-defense-manufacturing.html>. Last accessed 26 May 2023
29. Lopez-Vivero, M., et al.: Anti-biofilm multi drug-loaded 3D printed hearing aids. *Mater. Sci. Eng.: C* **119** (2021)
30. Mitsloan homepage. <https://mitsloan.mit.edu/ideas-made-to-matter/additive-manufacturing-explained>. Last accessed 27 May 2023
31. Pandžić, A., Hodžić, D., Kadrić, E.: Experimental investigation on influence of infill density on tensile mechanical properties of different FDM 3D printed materials. *TEM J.* **10**(3), 1195–1201 (2021)
32. Boer, D., Lambrechts, W., Krikke, H.: Additive manufacturing in military and humanitarian missions: advantages and challenges in the spare parts supply chain. *J. Clean. Prod.* **257** (2021)
33. De la Torre, N., Espinosa, M.M., Domínguez, M.: Rapid prototyping in humanitarian aid to manufacture last mile vehicles spare parts: an implementation plan. *Hum. Factors Ergon. Manuf. Serv. Ind.* **26**(5) (2016)
34. Durao, L.F.C.S., Christ, A., Zancul, E., Anderl, R., Schützer, K.: Additive manufacturing scenarios for distributed production of spare parts. *Int. J. Adv. Manuf. Technol.* **1e12** (2017)
35. Kovacs, G., Tatham, P.H.: Responding to disruptions in the supply network—from dormant to action. *J. Bus. Logist.* **30**(2), 215e229 (2009)
36. Yoho, K.D., Rietjens, S., Tatham, P.: Defence logistics: an important research field in need of Researchers. *Int. J. Phys. Distrib. Logist. Manag.* **43**(2), 80e96 (2013)
37. Kellens, K., Mertens, R., Paraskevas, D., Dewulf, W., Duflou, J.R.: Environmental impact of additive manufacturing processes: does AM contribute to a more sustainable way of part manufacturing? *Procedia CIRP* **61**(3), 582e587 (2017)
38. Peres, F., Noyes, D.: Envisioning e-logistics developments: making spare parts in situ and on demand. State of the art and guidelines for future developments. *Comput. Ind.* **57**(6), 490e503 (2006)
39. Conner, B.P.: Paradigm shift. *Def. AT&L* 35e37 (2016)
40. Ford, S., Despeisse, M.: Additive manufacturing and sustainability: an exploratory study of the advantages and challenges. *J. Clean. Prod.* **137** (2016)
41. Antill, P., Smith, J.: The British Army in transition: from army 2020 to the strike brigades and the logistics of future operations. *RUSI J.* **162**(3), 50e58 (2017)
42. Westerweel, B., Basten, R.J.I., van Houtum, G.J.: Traditional or additive manufacturing? Assessing component design options through lifecycle cost analysis. In: *Beta Working Paper Series*, vol. 519 (2016)
43. Liu, P., Huang, S.H., Mokasdar, A., Zhou, H., Hou, L.: The impact of additive manufacturing in the aircraft spare parts supply chain: supply chain operation reference (scor) model based analysis. *Prod. Plann. Contr.* **25** (2014)

44. Holmstream, J., Partanen, J., Tuomi, J., Walter, M.: Rapid manufacturing in the spare parts supply chain: alternative approaches to capacity deployment. *J. Manuf. Technol. Manag.* **21**(6), 687e697 (2010)
45. Atlason, R.S., Gerstlberger, W.: Which factors characterize sustainable behavior of defense forces? *J. Clean. Prod.* **164**, 230e241 (2017)
46. Mohr, S., Khan, O.: 3D printing and its disruptive impacts on supply chains of the future. *Technol. Innov. Manag. Rev.* **5**(11), 20e24 (2015)
47. Lau, G.: Expanding additive manufacturing beyond the sustainment framework to evolve Canadian Special Operations Force Command's competitive advantage. JSCP 48, Service Paper, Canada (2022)
48. Mattox, J.: Additive manufacturing and its implications for military ethics. *J. Mil. Ethics* **12**(3), 225 (2013)
49. Ford, S.L.N.: Additive manufacturing technology: potential implications for U.S. manufacturing competitiveness. U.S. Int. Trade Comm., J. Int. Commer. Econ. (2014)
50. Saunders, L.: Implications of additive manufacturing deployed at the tactical edge. The Defense Acquisition University (2015)
51. Bayley, C., Kopac, M.: The implications of additive manufacturing on Canadian Armed Forces operational functions. *Can. Mil. J.* **18**(3) (2018)
52. Meisel, N.A., Williams, C.B., Ellis, K.P., Taylor, D.: Decision support for additive manufacturing deployment in remote or austere environments. *J. Manuf. Technol. Manag.* **27**(7), 889 (2016)
53. Department of National Defence: Beyond the Horizon – A Strategy for Canada's Special Operations Forces in an Evolving Security Environment, p. 28 (2020)
54. Pavlovich, S.: 3D print applications of illicit firearms manufacture: a review. College of Science, Health, Engineering and Education, Murdoch University (2023)
55. All3Dp homepage. <https://all3dp.com/1/3d-printed-gun-firearm-weapon-parts/>. Last accessed 29 May 2023
56. Honsberger, H., et al.: How to recognise the traces left on a crime scene by a 3D-printed liberator? Part 2. Elements of ammunition, marks on the weapons and polymer fragments. *Forensic Sci. Int.* **295**, 137–144 (2019)
57. Bisić, M., Razić, F., Pandžić, A., Bevrnja, M.: Penetration testing of 3D printed projectiles made of various types of polymers. *J. Mech. Sci. Technol.* **37**(9) (2023)
58. Fabbaloo homepage. <https://www.fabbaloo.com/news/drone-wars-and-3d-printing>. Last accessed 30 May 2023
59. Zhou, X., Mao, Y., Zheng, D.: 3D printing of RDX-based aluminized high explosives with gradient structure, significantly altering the critical dimensions. *J. Mater. Sci.* (2021)
60. Pepekin, V.I., Gubin, S.A.: Propellant performance of organic explosives and their energy output and detonation velocity limits. *Combust. Explos. Shock Waves* **43**, 84–95 (2007)
61. Dolman, B., Hart, A., Johnston, I., Prior, C.: Advanced munitions: 3D printed firepower. Defence Science and Technology Group, Edinburgh
62. Chandru, R.A., Balasubramanian, N., Oomen, C., Raghunadandan, B.N.: Additive manufacturing of solid rocket propellant grains. *J. Propuls. Power* (2018)
63. Hudryashova, O., Lerner, M., Vorozhtsov, A., Sokolov, S., Promakhov, V.: Review of the problems of additive manufacturing of nanostructured high-energy materials. *Materials* (2021)
64. Lifeboat homepage. <https://lifeboat.com/blog/2022/02/3d-printed-nanomaterial-could-replace-kevlar-and-steel-for-bulletproof-armor>. Last accessed 30 May 2023
65. Techradar homepage. <https://www.techradar.com/news/3d-printers-have-made-bulletproof-cubes-vests-and-tank-armor-next>. Last accessed 30 May 2023
66. Forbes homepage. <https://www.forbes.com/sites/carolynschwaar/2022/02/27/us-military-to-3d-print-its-way-out-of-supply-chain-woes/?sh=5772ff6f275d>. Last accessed 30 May 2023



A Comprehensive Review of the Effect of Elastane and Common Wet Processes on the Cotton and Cotton/Elastane Knitted Fabrics' Properties and Revalorization of Fabric Waste

Aleksandra Ivanovska¹(✉), Mirjana Reljić^{2,3}, and Biljana Mangovska⁴

¹ University of Belgrade, Innovation Center of the Faculty of Technology and Metallurgy,
Karnegijeva 4, 11000 Belgrade, Serbia
aivanovska@tmf.bg.ac.rs

² CIS Institut, Vojislava Ilića 88, 11000 Belgrade, Serbia

³ Academy of Technical and Art Applied Studies, Starine Novaka 24, 11000 Belgrade, Serbia

⁴ Ss. Cyril and Methodius University in Skopje, Faculty of Technology and Metallurgy, Ruger
Boskovic 16, 1000 Skopje, North Macedonia

Abstract. This paper represents a comprehensive review of the effect of elastane and common wet processes (bleaching, dyeing, and softening) on the properties of 100% cotton and half or full plated cotton/elastane single jersey knitted fabrics. The fabrics were characterized in terms of their structural (fabric weight, thickness, and stitch density), comfort (air permeability and water vapor resistance), mechanical (stiffness, bursting elongation, and bursting strength), and antistatic (volume electrical resistivity) properties. Fabrics' antistatic properties were further improved by *in situ* synthesis of Cu-based nanoparticles (CuNPs) on their surfaces. Such fabrics can be also considered as bioactive since they possessed excellent antioxidant (determined using the ABTS method) and antimicrobial (against *E. Coli*, *S. aureus*, and *C. albicans*) activities. The last section of this chapter is focused on proposing a novel circular economy solution for the disposal of softened cotton and cotton/elastane knitted fabric waste collected from the textile industry (i.e., after clothing cutting). For that purpose, selected fabrics were revalorized as adsorbents for the widely used textile dye Congo Red and the maximum dye adsorption was tested using isotherm models. Thereafter, the fabrics with adsorbed Congo Red dye were evaluated as antistatic and dissipative fabrics, i.e., as alternative non-metal-based conductive textiles.

Keywords: Knitted bioactive fabrics · Softener · Properties

1 Introduction

Knitted fabric quality represents a kind of puzzle comprised of many pieces such as comfort, mechanical, antistatic, antioxidant, and antimicrobial properties. These fabric properties can be tailored by choosing different types of fibers, knitting patterns, wet

processes as well as various functional finishings in such a way that they can fit a particular application [1]. Single jersey knitted fabrics made of cotton or its blends with synthetic fibers are widely used for the production of underwear which quality is under constant consumer scrutiny.

Cotton, the most abundant natural cellulosic fiber, can satisfy some of the consumers' demands like good comfort and hygienic properties, softness, breathability, and high moisture absorbency. However, underwear should also fit the body and should have satisfactory mechanical properties, good elasticity, dimensional stability, and the ability to recover. Moreover, low electrical resistivity is not essential but is one of the desired fabric properties that strongly affect its ability to produce static electricity [2]. To achieve all the above-mentioned, underwear is usually made from cotton or cotton/elastane blends. Elastane (known as Lycra, Spandex, or Dorlastan) is a man-made fiber that has an extension-at-break higher than 200% and rapid recovery after the tension is released [3]. It can be introduced in two ways: by using it as a core in the core-spun yarns with cotton fibers or as additional yarn during circular knitting.

It should be emphasized that the introduction of elastane is not the only way for improving the overall fabric quality. Namely, before sewing, fabrics undergo a series of different wet processes like scouring (removal of non-cellulosic components and yielding the fabric absorbency), bleaching (improving whiteness), dyeing (to render color to fabrics), and softening (improving fabric softness, fullness, handle, elastic resilience, sewability, and reducing the coefficient of friction between fibers, yarns, and between fabrics and other surfaces) that can alter the fabrics' properties [4]. The neglected area in the knitting industry is the possibility of obtaining comfortable bioactive underwear characterized by antioxidant and antimicrobial activities.

This review provides a comprehensive understanding of the effect of elastane incorporation (0, 1.5, or 3%), bleaching or dyeing, and cationic softening as well as their synergistic effects on the comfort and mechanical properties, volume electrical resistivity, and antimicrobial and antioxidant activities of cotton and cotton/elastane knitted fabrics. In order to decrease the fabrics' volume electrical resistivities and at the same time to obtain bioactive fabrics, copper-based nanoparticles (CuNPs) were *in situ* synthesized on their surfaces. Among different metal NPs, the synthesis of CuNPs is of great interest for fabric functionalization since the process is low cost (the copper precursor salts are much cheaper than those of silver) and nontoxic, while the CuNPs show catalytic, antimicrobial (cause the disassembly of the bacterial membrane [5]), anti-cancer, and antioxidant activity, or cytotoxicity. Enormously large quantities of already finished textile materials remain as waste after clothing cutting, causing many environmental problems, such as landfills occupation, contamination, and global warming [6]. Here, we proposed a simple way for revalorization of softened cotton and cotton/elastane knitted fabric waste collected from the textile industry as adsorbents for the textile dye Congo Red. On the other hand, disposing of such waste with adsorbed Congo Red dye can cause secondary pollution, which represents one of the most important challenges for all researchers focused on adsorption as a method for wastewater purification. Therefore, the last part of this review is focused on developing a new circular economy solution for the disposal of knitted fabric waste with adsorbed Congo Red and converting them into dissipative materials that could be used for providing antistatic protection.

2 Experimental

The cotton ring-spun yarn of 20 tex and elastane yarn of 22 dtex were used for the production of 100% cotton, half or full plated cotton/elastane (containing 1.5% or 3.0% elastane, respectively) single jersey knitted fabrics. After knitting, 100% cotton raw tubular knitted fabric was kept on a flat surface under standard atmospheric conditions and dry relaxed, while elastane-containing fabrics were open heat set at 193 °C with minimal traverse tension. Then, fabrics were bleached with H₂O₂ and optical brightened or dyed with reactive dyes in the dark blue shade. Half of the bleached and dyed knitted fabrics were subjected to softening with cationic softener, while the other halves were not softened. Bleached 100% cotton and full plated cotton/elastane fabrics were softened with silicone softener and they were used only for adsorption experiments, Sect. 8. All fabrics (Table 1) were prepared in industrial conditions (Zona-Triko from Vinica, Republic of North Macedonia) according to the standard recipes used for finishing the commercial knitted fabrics, detail information can be found in Ivanovska et al. [4].

Table 1. Knitted fabric codes.

Fabric code	Explanation
CoR	100% cotton raw fabric
CoB	100% cotton bleached fabric
CoD	100% cotton dyed fabric
CoBC	100% cotton bleached fabric softened with cationic softener
CoDC	100% cotton dyed fabric softened with cationic softener
Co2ELR	Cotton/elastane half plated raw fabric
Co2ELB	Cotton/elastane half plated bleached fabric
Co2ELD	Cotton/elastane half plated dyed fabric
Co2ELBC	Cotton/elastane half plated bleached fabric softened with cationic softener
Co2ELDC	Cotton/elastane half plated dyed fabric softened with cationic softener
CoELR	Cotton/elastane full plated raw fabric
CoELB	Cotton/elastane full plated bleached fabric
CoELD	Cotton/elastane full plated dyed fabric
CoELBC	Cotton/elastane full plated bleached fabric softened with cationic softener
CoELDC	Cotton/elastane full plated dyed fabric softened with cationic softener

The fabric thickness, weight, and stitch density were determined according to the standards ASTM D 1777-96 (2011) (SiroFAST apparatus under the pressure of 10 kPa), ISO 3801:1977, and BS 5441:1988, respectively.

The fabrics' air permeability was tested on the Air Permeability Tester (M021A) at a constant pressure of 100 kPa (20 cm² test area) according to the standard EN ISO

9237:1995. The water vapor resistance was assessed based on the hot plate method (sweating guarded hotplate test) reported in the literature Reljic et al. [7].

The cationic softener pick-up was evaluated using the method outlined by Ivanovska et al. [4].

The fabric stiffness was measured on a Digital Pneumatic Stiffness Tester M003F (SDLATLAS, USA) according to ASTM D 4032-94 standard. The bursting strength and bursting elongation were determined on the H5KT dynamometer (Tinius Olsen, USA) following ASTM D 6797-02 standard.

The measurement of fabric volume electrical resistivity (in course direction) was performed using the voltage method that has been presented by Kramar et al. [8]. The content of copper in the fabrics with *in situ* synthesized CuNPs was determined following the procedure given in the above-mentioned literature.

The fabrics' antimicrobial activity was determined against Gram-negative bacteria *E. coli* ATCC 25922 and Gram-positive bacteria *S. aureus* ATCC 25923, and yeast *C. albicans* ATCC 2443 according to ASTM E 2149-01 (2001) standard, while their antioxidant activities were determined following the procedure described by Shabbir et al. [9].

To obtain fabrics with *in situ* synthesized CuNPs, they were first immersed in a 2% sodium alginate aqueous solution for 1 h at room temperature. After squeezing and drying at 100 °C for 10 min, the *in situ* synthesis of CuNPs was performed in two steps: (1) each fabric was immersed in 10 mM of CuSO₄ solution for 2 h, 1:100 fabric-to-liquid ratio, rinsed with distilled water and immediately dipped into the 0.2 M of ascorbic acid solution (pH 6.50) and the reduction process took place in the following 2 h at 80 °C. The fabrics were thoroughly rinsed with deionized water and dried at room temperature; they contain NPs in their codes [2].

FESEM microscopy (Tescan MIRA 3 XMU) was used to prove the existence of CuNPs on the knitted fabrics' surfaces.

The dye adsorption study was performed by immersing 0.5 g of each fabric waste in 100 ml of freshly prepared Congo Red (in further text: CR) solution (having an initial dye concentration of 25, 50, 75, or 100 mg/l) containing 15 g/l NaCl. Adsorption experiments were conducted under the previously optimized dyebath pH of 10.00 (for bleached full plated cotton/elastane fabrics softened with cationic (CoELS) softener) or 11.00 (for 100% cotton bleached fabrics softened with cationic (CoC) or silicone (CoS) softener) at room temperature with constant shaking for 4 h. The dye concentration in the aqueous solution was determined based on the UV-Vis spectrophotometer (Shimadzu 1700) absorbance spectra at $\lambda_{\max} = 486$ nm. The mass of dye adsorbed per gram fabric waste (q , mg/g) was calculated according to Eq. (1):

$$q = \frac{C_0 - C_t}{m} \cdot V \quad (1)$$

where: C_0 and C_t (mg/l) are the dye concentrations in the aqueous solution before and after a defined period of adsorption, respectively, V (l) is solution volume, and m (g) is the mass of dry fabric.

In other to find the maximum adsorbent capacity for CR, the equilibrium data generated from isotherm experiments (initial CR concentration of 25, 50, 75, and 100 mg/l) was modeled according to the Langmuir and Freundlich isotherm models [10].

All of the above-mentioned experiments were done in triplicate, wherein the coefficients of variation were below 2.75%.

3 Structural Characteristics of Knitted Fabrics

Knitted fabrics' structural characteristics depend on various factors like the yarns' chemical composition, fineness, and type, the knitting machine characteristics, the loops' arrangement, the applied wet protocols, etc. [4]. Within this investigation, the following variables were introduced: the elastane content and different wet processes (bleaching, dyeing, and softening). Before discussing their effect on fabric weight, stitch density, and thickness, some general comments should be given.

Cotton fiber is recognized for its ability to swell by about 40% by volume in water, while its length increased by about 1–2%. Within the spun yarns (as used in the current study), fibers are arranged in a spiral configuration, whereby the radial fiber swelling with no significant increase in fiber length leads to a reduction in spiral length and, hence, yarn shrinkage. As a consequence, wet-processed 100% cotton knitted fabrics (CoB and CoD) have higher stitch densities and weights compared to 100% cotton raw fabric (CoR), Table 2. On the other hand, CoB and CoD possessed lower thicknesses than CoR. This is more pronounced for CoB since the bleaching was carried out under more severe conditions (under high alkali conditions at boiling temperature) than dyeing (under milder alkali conditions and at 60 °C). Moreover, during the scouring and bleaching, the yarn diameter decreased (due to the removal of non-cellulosic components) and flattened to an elliptical cross-section by calendaring, which altogether resulted in increased adhesion between the loops [4].

Table 2. Knitted fabric structural characteristics [4].

Sample code	Fabric weight (gm ⁻²)	Fabric thickness (mm)	Fabric stitch density (cm ⁻¹)
CoR	135.15	0.487	236.18
CoB	137.12	0.415	255.33
CoD	144.96	0.457	266.46
Co2ELR	159.67	0.542	256.72
Co2ELB	149.88	0.462	253.21
Co2ELD	156.36	0.481	252.07
CoELR	204.55	0.685	314.4
CoELB	158.9	0.478	262.22
CoELD	175.54	0.530	286.65

After both bleaching and dyeing protocols, the elastane-containing fabrics possessed lower structural parameters' values compared to their raw counterparts, which is more noticeable for the full than for the half-platted fabrics, Table 2. Such decline in CoELB

and CoELD fabrics' structural characteristics can be explained by the fact that during their heat setting under tension, the loops' shape and orientation probably changed without the change in their length, i.e. the loops become rounder resulting in weight loss, decreased thickness, and lower stitch density [4]. Besides elastane content, wet processes also influence the structural characteristics of cotton/elastane fabrics, Table 1. CoELB has 22.3%, 16.6%, and 30.2%, while CoELD has 14.1%, 8.8%, and 22.6% has lower fabric weight, fabric thickness, and stitch density than CoELR, respectively. These results are in accordance with the earlier mentioned severity of performed wet processes.

As expected, softening with cationic softener did not give any significant changes in the knitted fabrics' structural characteristics.

4 Knitted Fabrics' Comfort Properties

According to Saville [11], comfort is a complex matter, with physical, physiological, and psychological factors interrelated in an unpredictable combination that constantly undergoes variation. In this study, air permeability (i.e., the volume of air (in liters) passed during 1 s through 1 m² fabric at the defined pressure [12]) and water vapor resistance (the material's reluctance to let water vapor pass through it [13]) were considered as very important fabric comfort properties, Table 3.

Table 3. Knitted fabric air permeability and water vapor resistance vs. cationic softener pick-up [4].

Sample code	Air permeability (lm ⁻² s ⁻¹)	Water vapor resistance, (m ² PaW ⁻¹)	Cationic softener pick-up (%)
CoR	1319.0	1.35	/
CoB	615.7	1.07	/
CoD	529.0	1.15	/
Co2ELR	601.4	1.48	/
Co2ELB	415.4	0.95	/
Co2ELD	382.1	1.00	/
CoELR	374.3	1.85	/
CoELB	371.6	1.01	/
CoELD	259.9	1.07	/
CoBC	624.6	1.07	0.645
Co2ELBC	406.4	1.01	0.706
CoELBC	298.1	1.05	0.872
CoDC	569.8	1.15	0.706
Co2ELDC	375.0	1.11	0.720
CoELDC	251.3	1.15	1.282

Bleaching and dyeing induced a decline in the fabrics' air permeability, whereby the highest reduction was observed in the case of 100% cotton fabrics CoB and CoD. Before wet processes, CoR was subjected to dry relaxation leading to increased stitch densities of CoB and CoD (Fig. 1), i.e. decreased spaces between the loops, which is the main reason for their lower air permeability compared to CoR [14], Table 3. All bleached fabrics showed slightly higher air permeability compared to the dyed ones which can be described by their lower structural characteristics' values (Table 2) and the discussed higher adhesion between fibers resulting in lower spaces between yarns. Moreover, with increasing the elastane content from 1 to 3%, fabrics' air permeability decreases, while the combination of higher elastane content and bleaching did not change the CoELB air permeability compared to its raw counterpart CoELR (Table 3) [4]. The calculated inverse relationships (ranging between -0.967 and -0.997) between air permeability of bleached and dyed fabrics and their appropriate thicknesses and weights pointed out that with increasing the fabric thickness and weight of wet-processed fabrics, they become less permeable to air [4].

The air spaces between fibers and yarns and fibers themselves are not important only for fabrics' air permeability, they are also essential for the transfer of moisture through the fabrics. An inverse relation between the air permeability and water vapor resistance is observed for differently finished knitted fabrics (Table 3), which is not the case for the raw one. CoR, Co2ELR, and CoELR are characterized by higher water vapor resistance than wet-processed fabrics since the present hydrophobic non-cellulosic components disturb the moisture diffusion and its transfer through the raw fabrics. The highest differences (45.4 and 42.2%) between the water vapor resistance of raw and wet-processed fabrics were observed for full plated fabrics (CoELR vs. CoELB and CoELD). Such behavior is attributed to plating (i.e. the fact that the cotton yarn is placed under the elastane yarn which hard crystalline segments limited the water vapor adsorption) and significantly decreased fabrics' CoELB and CoELD structural properties (Table 2) causing the reduction of their water vapor resistance [4]. By observing in parallel the results for the water vapor resistance of dyed and bleached fabrics, it can be concluded that bleached ones have lower water vapor resistance which is in line with the results published by Cubric et al. [14]. During the scouring and bleaching, the used alkali and hydrogen peroxide leads to the complete removal of hydrophobic non-cellulosic components resulting in more hydrophilic fibers that allow the passage of a higher amount of water vapor through the fabrics. Knitted fabrics characterized by lower water vapor resistance allow cooling of the human body due to sweating and is also essential to avoid or lessen water buildup in garments leading to uncomfortable feelings [15].

Besides bleaching and dyeing, softening represents the most common textile wet finishing stage since it reduces the coefficient of friction between fibers, yarns, and between fabrics and other surfaces, and therefore, improves fabric softness, fullness, handle, elastic resilience, sewability, etc. [16]. In this section, another variable, i.e., softening with cationic softener was introduced and its influence on fabrics' comfort properties was given in Table 3. Softening contributed to obtaining bleached and dyed 100% knitted fabrics (CoBC and CoDC) with slightly enhanced air permeability compared to CoR which is owed to the cationic softener pick-up mechanism. Theoretically, when cotton

and cotton/elastane fabrics were immersed in cationic softener macroemulsion, the softener is deposited on the yarns' surfaces in such a way that its positively charged ends are oriented toward the negatively charged cotton surface while creating a new surface of hydrophobic carbon chains that provide excellent softening and lubricity [17]. On the other hand, charged ends will repel each other resulting in high fabric voluminosity, i.e. yarn hairiness, and hence, the fibers sticking out away from yarns can represent a kind of barrier for air [4] as was the case for half and full plated knitted fabrics, Table 3. Another important fact that can be seen from this table is an increase in cationic softener pick-up with increasing elastane content. For example, compared to CoBC and CoDC, the cationic softener pick-up by CoELBC and CoELDC increases by 35.2%, and 81.6%, resulting in 2.1 times and 2.3 times lower air permeabilities, respectively. Furthermore, softened dyed fabrics have lower air permeability than softened bleached fabrics, which is probably due to the interaction between reactive dyestuff and cationic softener, resulting in higher cationic softener pick-up, and consequently lower air permeability [4].

The important role of the cationic softener pick-up was also evident when fabrics' water vapor resistance was considered, Table 3. The existence of long hydrophobic carbon chains on the knitted fabrics' surfaces (due to the cationic softening) decreased their wettability, i.e. increased their water vapor resistance [18]. Higher cationic softener pick-up by dyed fabrics induced their higher water vapor resistance (up to 9.9%) compared to the bleached one. Based on the Hohenstein Institute (Germany) ranking system of water vapor resistance, all examined fabrics are extremely breathable and comfortable at a higher level of activity since their water vapor resistance values are below $1.3 \text{ m}^2 \text{PaW}^{-1}$ [7]. The findings of this section revealed that softened elastane-containing fabrics can allow a lower amount of air and water vapor to pass through the other side of the fabric than the non-softened one.

5 Mechanical Properties of Selected Knitted Fabrics

Knitted fabrics' mechanical properties were evaluated through the determination of their stiffness, bursting strength, and bursting elongation. From the results given in Fig. 1, it is evident that the incorporation of elastane yarn in the cotton knitted fabrics and softening with cationic softener contributed to some changes in the fabrics' mechanical properties.

Belonging to a group of highly elastic fibers, elastane is comprised of soft segments that provide stretching and hard segments that hold the chains together [4]. Cotton fibers have much lower breaking elongation (5.6–7.1% vs. 400–700%) and higher tenacity (27–44 cN/tex vs. 5.4–7.2 cN/tex) compared to elastane fibers, so, it was reasonable to expect that the introduction of elastane at the same time will improve the fabrics' bursting elongation (from 36.82 to 42.82 mm for CoB and Co2ELB) and decline their bursting strength (from 402.8 down to 359.6 N for CoB and Co2ELB). The last one can be also ascribed to the performed heat setting of Co2ELR, which is not the case for CoR that after knitting was dry relaxed under standard atmospheric conditions [4]. Besides the fact that the elastane soft segments affect the fabric bursting elongation, its hard segments increased fabric compactness (Fig. 1) and have a dominant influence on fabric stiffness which increased by about 8% after elastane incorporation [4].

Fabric bursting elongation and stiffness are not associated only with the product's durability but also with its sensorial comfort [19]. Cationic softener acts as a lubricant

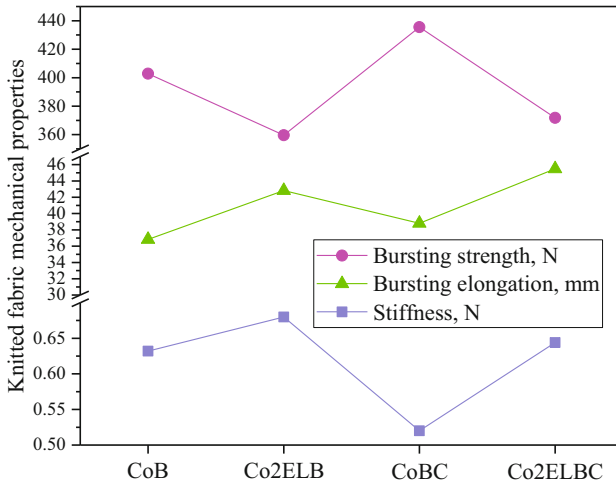


Fig. 1. Mechanical properties of knitted fabrics [2].

and reduces the coefficient of friction between yarns within the fabric and facilitates their slipping resulting in 18 and 6% lower stiffness of CoBC and Co2ELBC compared to their non-softened counterparts. Moreover, softened fabrics possessed a slight increase in bursting elongation which contributed to improved fabric bursting strength, Fig. 1.

6 Volume Electrical Resistivity of Knitted Fabrics

Since the studied fabrics intended for underwear could be used in different humidities that indirectly affect their comfort properties, another step in the fabrics' characterization was the estimation of their tendency to produce static electricity at 65, 60, and 55% relative air humidity (in further text: RH). For that purpose, the volume electrical resistivity (in further text: resistivity) of selected fabrics was measured by decreasing the humidity in the chamber, Table 4. By decreasing the RH from 65 to 55%, the fabrics' resistivities increased by about 1.8–2.1 times which can be explained by the fact that RH induced partly ionization of water molecules located around the fabrics, and neutralized the electric charges on the fabric surface [20].

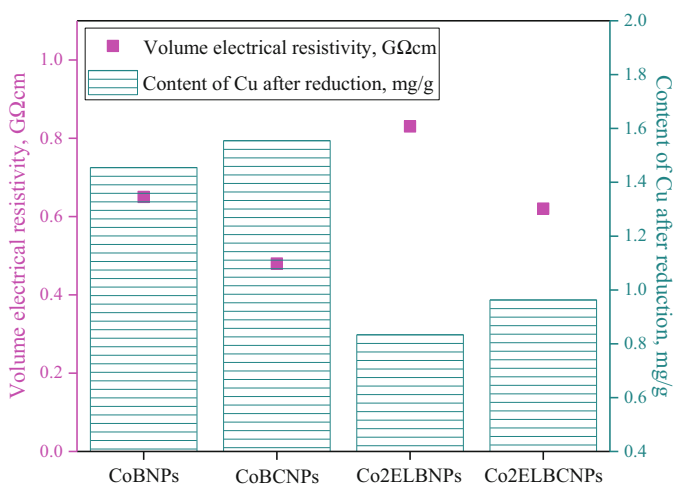
The elastane incorporation into non-softened cotton fabric induced a decrease in the resistivity by 23–27% (CoB vs. Co2ELB) which is due to the increased fabric compactness (i.e., increased weight and thickness, Table 2) enabling better contact between the loops, and hence, the easier flow of charge through them. The situation is different in the case of softened fabrics; they have a more compact structure than the non-softened ones (Table 2) and possessed about 23–93% higher resistivities (Table 4) indicating that another factor affects such behavior. The previously described mechanism of cationic softener pick-up could be found as a possible explanation for such unexpected high resistivity values of softened fabrics. Precisely, hydrophobic carbon chains which contribute to high yarns' volume could disturb the electric flow through the fabric resulting in higher resistivity of softened fabrics [2].

Table 4. The influence of relative humidity (RH), elastane incorporation, and softening on the resistivity of knitted fabrics [2].

Fabric codes	Volume electrical resistivity at different RH, GΩcm		
	65%	60%	55%
CoB	1.85	2.54	3.67
Co2ELB	1.35	1.87	2.84
CoBC	2.28	3.31	4.61
Co2ELBC	2.52	3.61	4.56

7 Obtaining Bioactive Knitted Fabrics

In the previous section, it was shown that the resistivities of studied fabrics at RH of 55% ranged between 2.84 and 4.61 GΩcm. Having in mind the increased demand for comfortable and multifunctional underwear as well as the metals' high conductivity, we decided to further decrease the fabrics' resistivity, and hence, to improve their overall quality by *in situ* synthesis of CuNPs on their surfaces according to the method described in the experimental part of this paper. The results presented in Fig. 2 pointed out that knitted fabrics with *in situ* synthesized CuNPs have about 3.4–9.6 times lower resistivities, i.e., lower ability to produce static electricity than fabrics without NPs, which is in line with the Cu content determined after the reduction [2].

**Fig. 2.** Comparison between the fabrics' resistivities (at 55% RH) before and after *in situ* synthesis of CuNPs and the content of Cu after reduction [2].

It has to be emphasized that non-softened knitted fabrics CoBNPs and Co2ELBNPs have lower Cu content than softened which undoubtedly lies in the putative adsorption

mechanism and the intensity of the interaction between fabric surface and alginate [2]. Namely, the interactions between cotton fibers and alginate are mainly achieved through the hydrogen bonds since both of them contain hydroxyl groups. On the other hand, alginate chains are stabilized and crosslinked by Cu^{2+} -ions through chelate formation among themselves [21]. After dipping in ascorbic acid, the reduction of Cu^{2+} -ions takes place providing material bearing CuNPs. Co2ELBNPs and Co2ELBCNPs fabrics have much lower Cu content when compared to corresponding fabrics without elastane (CoBNPs and CoBCNPs) which is due to the more hydrophobic nature of elastane-containing fabrics having a lower affinity towards highly hydrophilic alginate chains.

The existence of smaller and higher unevenly distributed agglomerates of NPs (having particle sizes between 10 and 80 nm) was clearly seen on the CoBNPs fabric surface, while CoB possessed typical cotton fiber surface morphology with a pronounced convolution, Fig. 3.

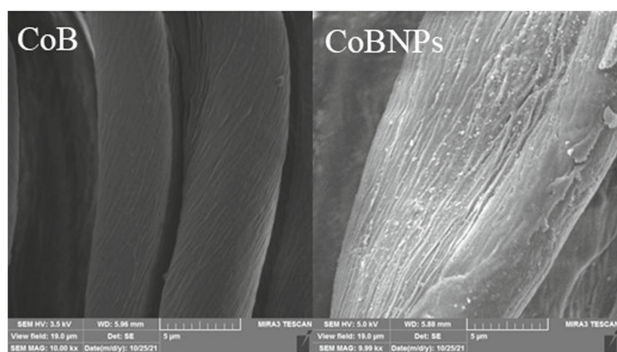


Fig. 3. FESEM images of cotton CoB and CoBNPs.

Apart from lowering the fabrics' resistivities for providing better comfort properties, the *in-situ* synthesis of CuNPs contributed to obtaining bioactive fabrics having significant antioxidant and antimicrobial properties, Table 5. Weak antioxidant activity of cotton and cotton/elastane fabrics (33–41%) originating from the cellulose hydroxyl groups was enhanced by up to 2.5 times after the *in-situ* synthesis of CuNPs. Furthermore, it was observed that fabrics with CuNPs possessed maximum microbial reduction (99.99%) for three microorganisms *E. Coli*, *S. aureus*, and *C. albicans* which is ascribed to the existence of nanoparticles, Table 5.

Fabrics with *in situ* synthesized CuNPs can be considered as bioactive fabrics with excellent antimicrobial activity and a higher ability for trapping the free radical of oxygen species and preventing cell deterioration. Medical bioactive textile plays an important role in the technical textiles sector as one of the most rapidly growing sectors in the technical textile market [22].

Table 5. Comparison between the knitted fabric antioxidant and antimicrobial activities before and after in situ synthesis of Cu-based NPs [2].

Fabric codes	Antioxidant activity (%)	<i>E. coli</i> , (%)	<i>S. aureus</i> (%)	<i>C. albicans</i> (%)
CoB	34.24	0	0	0
CoBC	86.75	0	0	0
Co2ELB	41.26	0	0	97.8
Co2ELBC	78.71	0	0	0
CoBNPs	32.97	99.99	99.99	99.99
CoBCNPs	62.13	99.99	99.99	99.99
Co2ELBNPs	28.55	99.99	99.99	99.99
Co2ELBCNPs	69.75	99.99	99.99	99.99

8 Reuse and Revalorization of Knitted Fabric Waste

The last section of this chapter is focused on proposing a novel circular economy solution for the disposal of softened cotton and cotton/elastane knitted fabric waste collected from the textile industry, Table 5. For that purpose, CoC, CoS, CoELC, and CoELS were considered as adsorbents for water-soluble and widely used azo dye Congo Red (in further text: CR) (Table 6).

Table 6. Knitted fabric codes.

Fabric codes	Explanation	
CoC and CoS	100% cotton	C - softened with cationic softener
CoELC and CoELS	Cotton/elastane full plating	S - softened with silicone softener

The results given in Fig. 4 revealed that the amount of dye adsorbed per gram adsorbent (q_e) increased by about 2.0–2.5 times when the initial concentration of CR (C_0) increased from 25 to 100 mg/l. This trend is attributed to the intensified collision among the dye molecules and adsorbent and lower mass transfer resistance at high dye concentrations, both contributing to an increased fabrics' adsorption capacity (q_e) [23]. The equilibrium adsorption data presented in Fig. 4 were then analyzed by using linearized forms of Langmuir and Freundlich isotherm models. From the corresponding coefficients of determination (R^2 , Table 7), it is evident that the Langmuir model provided a better description of the adsorption of CR onto cationic softened fabrics (CoC and CoELC) than the Freundlich isotherm model. This behavior implies a monolayer pollutant adsorption onto CoC and CoELC surfaces having a finite number of uniformly distributed adsorption sites and homogeneous adsorption [24]. The monolayer maximum adsorption capacity (q_m) estimated from the Langmuir isotherm for CoC and CoELC was found to increase from 9.897 to 12.533 mg/g with increasing of the cationic softener

pick-up from 0.645 to 0.872% [4] and elastane incorporation [10], Table 7. Fitting of the isotherm experimental data obtained for CoS and CoELS pointed out that equilibrium data were better described by the Freundlich isotherm. The applicability of this model confirmed the multilayer adsorption, i.e., heterogeneous surface nature with non-uniform distribution of adsorption sites and affinities over the heterogeneous fabrics' CoS and CoELS surfaces [10]. Taking into account a significantly higher Freundlich constant (K_f) value obtained for CoS compared to CoELS, it can be concluded that CoS has better adsorption efficiency for CR, which conforms with the results shown in Fig. 4. This statement is additionally supported by the facts that CoS has a more heterogeneous surface (i.e., the smaller $1/n$, the greater the expected heterogeneity, Table 7), which is in accordance with the higher content of silicon indicating a higher content of silicon softener (158.30 vs. 112.06 $\mu\text{g/g}$).

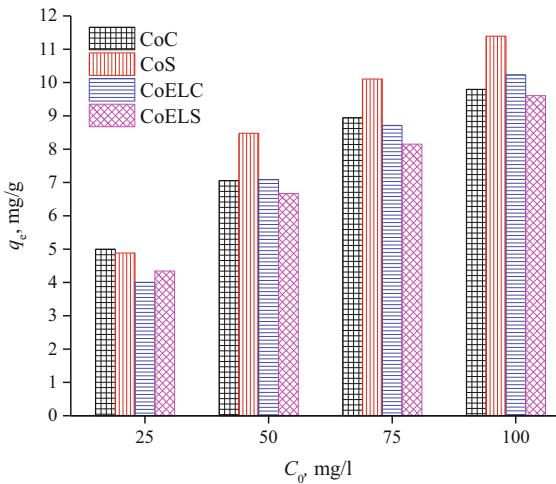


Fig. 4. Equilibrium adsorption (q_e) of CR as a function of initial concentration (C_0) of CR. [10] (Reprinted by permission from [Springer Nature Customer Service Centre GmbH]: [Springer Nature] [Fibers and Polymers] [Revalorization of Cotton and Cotton/Elastane Knitted Fabric Waste, Ivanovska A, Lađarević J, Asanovic K, Pavun L, Kostic M, Mangovska B.], [COPYRIGHT] (2023)).

It seems this is the right place to discuss the essence of the different behavior of CR on the knitted fabric wastes, which is the different softeners' fixation onto fabrics. The used softeners are of different chemical compositions and have different particle sizes, i.e., the used cationic softener is in the form of macroemulsion, while the silicone softener is in the form of microemulsion. It is commonly known that when the cotton and cotton/elastane fabrics were immersed in water, their surfaces become negatively charged, while the cationic softener's positively charged ends are oriented towards the partially negative charged fibers due to the electrostatic interactions, leaving hydrophobic carbon chains on the fibers' surfaces [10], Fig. 5a. In contrast, the used silicone microemulsion besides fixation to cotton fabrics, can penetrate between and inside the yarns and deposit onto the fibers' surfaces thus forming a network of elastic silicone polymers, Fig. 5b. The

Table 7. Langmuir and Freundlich isotherm parameters for CR adsorption onto fabric waste (Some of the results were previously published in [10]).

Adsorption isotherm	Isotherm parameters	Knitted fabric waste			
		CoC	CoS	CoELC	CoELS
		R^2			
		0.989	0.984	0.991	0.980
Langmuir	K_L , l/mg	0.498	0.390	0.078	0.118
	q_m , mg/g	9.897	11.667	12.533	10.821
		R^2			
		0.936	0.994	0.963	0.999
Freundlich	K_f , (mg/g)(l/mg) $^{-1/n}$	6.944	5.666	1.999	2.832
	$1/n$	0.071	0.177	0.422	0.306

interactions between cotton and cotton/elastane fabrics and silicone softener are mainly governed by hydrogen bonds between the silicone softener’s electronegative oxygen atom and hydrogen atom of the surface OH groups, on one hand, and between softener’s terminal amino groups and OH groups, on the other hand, Fig. 10b [10]. In such a way, a hydrophobic layer consisting of methyl groups that are arranged orderly on the fabric surface is formed [25].

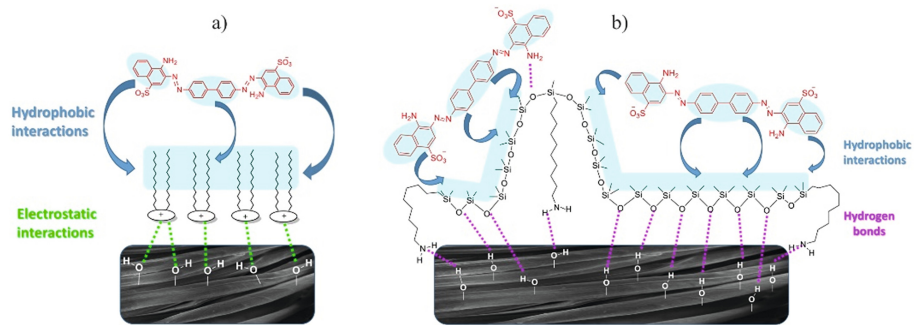


Fig. 5. Adsorption mechanism of CR onto: a) cationic and b) silicone softened knitted fabric wastes. [10] (Reprinted by permission from [Springer Nature Customer Service Centre GmbH]: [Springer Nature] [Fibers and Polymers] [Revalorization of Cotton and Cotton/Elastane Knitted Fabric Waste, Ivanovska A, Ladarević J, Asanovic K, Pavun L, Kostic M, Mangovska B.], [COPYRIGHT] (2023)).

Kumar et al. [26] concluded that both electrostatic (originating from ionized groups) and hydrophobic (originating from aromatic rings) components of CR are crucial for interaction with different surfactants. On the other hand, research conducted by Chakraborty et al. [27] and Wu et al. [28] indicated that increasing the surface hydrophobicity enhances the adsorption capacity of different organic aromatic dyes independently

of their structures and charges which is attributed to the hydrophobic interactions. Considering in parallel the high propensity of CR to form hydrophobic interactions and the change of the cotton surface from hydrophilic to hydrophobic upon softening, it can be assumed that external softener hydrophobic groups interact with the aromatic ring imparted by CR [10]. Due to the earlier mentioned fabric surface heterogeneity, the interactions of CR with the fabric surface could be established through randomly distributed hydrogen bonds, Fig. 5b.

Regardless of the adsorption capacities of the knitted fabrics, the disposal of such solid waste containing organic matter represents the utmost challenge since it undoubtedly causes secondary pollution. The last one along with the significantly low volume electrical resistivity of CR (0.0064 GΩcm) inspired us to develop a new idea for the revalorization of knitted fabric waste with adsorbed CR as antistatic and dissipative fabrics. For that purpose, volume electrical resistivity (measured at different relative air humidity's according to Ivanovska et al. [10]) was selected as the most appropriate method for the evaluation of the mentioned fabrics' characteristics.

As expected, the knitted fabric wastes' volume electrical resistivities decreased 169–494 and 205–737 times, and ranged between 0.008 and 0.0337 GΩcm (at 60 and 50% humidity, respectively) after the CR adsorption ($C_0 = 100$ mg/l), Fig. 6. Fabrics CoC and CoELS possessed almost the same adsorption efficiencies for CR (9.789 vs. 9.609 mg/g), while fabric CoELSCR has about 60–65% lower volume electrical resistivities than CoCCR. At first glance, it seems that the adsorption of CR is not in agreement with the fabrics' volume electrical resistivities [10]. However, having in mind that these two fabrics (CoC and CoELS) have different weights (140.42 and 167.61 g/m², Table 2), as well as that the volume electrical resistivity was measured at the fixed area of 2 cm², it is

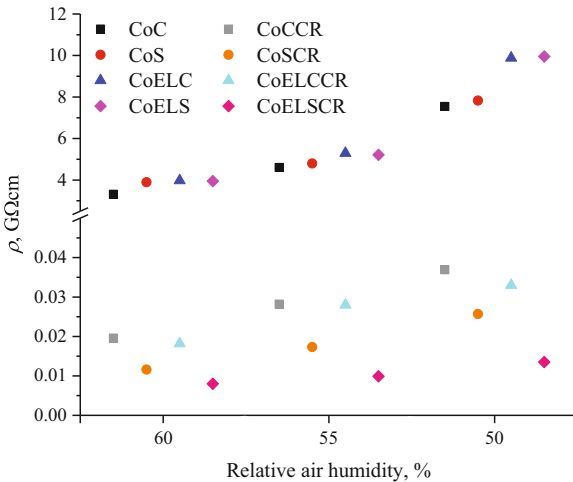


Fig. 6. Knitted fabric wastes' volume electrical resistivities (ρ) before and after adsorption of CR ($C_0 = 100$ mg/l). [10] (Reprinted by permission from [Springer Nature Customer Service Centre GmbH]: [Springer Nature] [Fibers and Polymers] [Revalorization of Cotton and Cotton/Elastane Knitted Fabric Waste, Ivanovska A, Lađarević J, Asanovic K, Pavun L, Kostic M, Mangovska B.], [COPYRIGHT] (2023)).

clear that in this area, CoC and CoELS are capable of adsorbing 0.275 and 0.322 mg CR, respectively. In other words, an inversely proportional correlation exists between fabrics' adsorption efficiencies and their volume electrical resistivities after CR adsorption [10]. The results given in Fig. 6 prove that knitted fabric waste with adsorbed CR can be defined as dissipative materials (ESD Association standard) and are suitable for antistatic protection [29]. The findings of this section are very important since they put knitted fabric waste with adsorbed CR into the new circular economy solution contributing to reducing the environmental burden while generating additional revenues [10].

9 Conclusion

The results of this review confirmed that knitted fabrics of 100% cotton or half plated cotton/elastane along with cationic finishing significantly affect the fabrics' structural characteristics, comfort and mechanical properties and volume electrical resistivity. *In situ* synthesis of CuNPs contributed to obtain bioactive fabrics with significantly lower volume electrical resistivities. The present work provides a new perspective on textile industry waste by its revalorization as an efficient adsorbent for textile dye.

Acknowledgment. This work was supported by the CIS Institute d.o.o. Belgrade and the Ministry of Science, Technological Development and Innovation of the Republic of Serbia, Contract No. 451-03-47/2023-01/200287.

References

1. Dinh, T.D., Weeger, O., Kaijima, S., Yeung, S.-K.: Prediction of mechanical properties of knitted fabrics under tensile and shear loading: mesoscale analysis using representative unit cells and its validation. *Compos. B Eng.* **148**, 91–82 (2018)
2. Ivanovska, A., et al.: Quality of cotton and cotton/elastane single jersey knitted fabrics before and after softening and *in situ* synthesis of Cu-based nanoparticles. *J. Nat. Fibers* **19**(16), 15139–15150 (2022)
3. Vasile, S., De Raeve, A., Malengier, B., Cools, J.: Effect of biaxial stretch and domestic washing on air permeability of elastic knitted fabrics for sportswear. *Fibers Polym.* **20**(4), 868–875 (2019)
4. Ivanovska, A., Reljic, M., Kostic, M., Asanovic, K., Mangovska, B.: Air permeability and water vapor resistance of differently finished cotton and cotton/elastane single jersey knitted fabrics. *J. Nat. Fibers* **19**(13), 5465–5477 (2022)
5. Ermini, M.L., Voliani, V.: Antimicrobial nano-agents: the copper age. *ACS Nano* **15**(4), 6008–60029 (2021)
6. Gun, A.D., Kuyucak, C.N.: Performance properties of plain knitted fabrics made from open end recycled acrylic yarn with the effects of covered and PBT elastic yarns. *Fibers Polym.* **23**, 282–294 (2022)
7. Reljic, M., Stojiljkovic, S., Stepanovic, J., Lazic, B., Stojiljkovic, M.: Study of water vapor resistance of Co/PES fabrics properties during maintenance. In: *Experimental and Numerical Investigations in Materials Science and Engineering*, vol. 54, 1st ed., pp. 72–83. Springer, Cham (2018)

8. Kramar, A.D., Asanović, K.A., Obradović, B.M., Kuraica, M.M., Kostić, M.M.: Electrical resistivity of plasma treated viscose and cotton fabrics with incorporated metal ions. *Fibers Polym.* **19**(3), 571–579 (2018)
9. Shabbir, M., Rather, L.J., Mohammad, F.: Economically viable UV-protective and antioxidant finishing of wool fabric dyed with *Tagetes erecta* flower extract: Valorization of marigold. *Ind. Crops Prod.* **119**, 277–282 (2018)
10. Ivanovska, A., Ladarević, J., Asanović, K., Pavun, L., Kostić, M., Mangovska, B.: Revalorization of cotton and cotton/elastane knitted fabric waste. *Fibers Polym.* **24**(2), 749–758 (2023)
11. Saville, B.P.: *Physical Testing of Textiles*, 1st edn. Woodhead Publishing Limited, Cambridge (2002)
12. Dehkordi, S.S.H., Ghane, M., Abdellahi, S.B., Babadi Soultanzadeh, M.: Numerical modeling of the air permeability of knitted fabric using computational fluid dynamics (CFD) method. *Fibers Polym.* **18**(9), 1804–1809 (2017)
13. Reljic, M., Mitrovic, A., Stojiljkovic, S., Stojiljkovic, M., Kocareva M.: Study of mechanical and physical properties of clothing in maintenance. *Computational and Experimental Approaches in Materials Science and Engineering*, vol. 90, pp. 477–497. Springer (2019)
14. Cubric, I.S., Skenderi, Z., Havenith, G.: Impact of raw material, yarn and fabric parameters, and finishing on water vapor resistance. *Text. Res. J.* **83**(12), 1215–1228 (2013)
15. Badr, A.A., Hassanin, A., Moursey, M.: Influence of tencel/cotton blends on knitted fabric performance. *Alex. Eng. J.* **55**(3), 2439–2447 (2016)
16. Crutzen, A.: Fabric softeners. In: *Liquid Detergents*, 2nd edn, pp. 488–554. CRC Press Taylor and Francis Group, Boca Raton (2006)
17. Cimilli Duru, S., Şahin, U.K.: Effects of yarn type, process history, softener type and concentration on wicking and drying properties of cotton plain knitted fabrics. *J. Text. Inst.* **111**(8), 1166–1175 (2020)
18. Tang, K.-P.M., Kan, C.-W., Fan, J.-T., Tso, S.-L.: Effect of softener and wetting agent on improving the flammability, comfort, and mechanical properties of flame-retardant finished cotton fabric. *Cellulose* **24**(6), 2619–2634 (2017)
19. Ivanovska, A., Dojčinović, B., Mangovska, B.: Studying the influence of common wet processes on the quality of 1 × 1 rib cotton/elastane knitted fabrics. *J. Eng. Fibers Fabr.* **17**, (2022)
20. Ivanovska, A., Asanovic, K., Jankoska, M., Mihajlovski, K., Pavun, L., Kostic, M.: Multifunctional jute fabrics obtained by different chemical modifications. *Cellulose* **27**(14), 8485–8502 (2020)
21. Cao, L., Lu, W., Mata, A., Nishinari, K., Fang, Y.: Egg-box model-based gelation of alginate and pectin: a review. *Carbohydr. Polym.* **242**, 116389 (2020)
22. Mitrovic, N., Mitrovic, A., Reljic, M.: Strain Measurement of Medical Textile Using 2D Digital Image Correlation Method, *Experimental and Computational Investigations in Engineering*, vol. 153, pp. 447–464. Springer (2020)
23. Ivanovska, A., et al.: Obtaining polysaccharide-based fabrics with improved moisture sorption and dye adsorption properties. *Appl. Sci.* **13**(4), 2512 (2023)
24. Ivanovska, A., et al.: Recovering the soybean hulls after peroxidase extraction and their application as adsorbent for metal ions and dyes. *Adsorpt. Sci. Technol.* **2023**, 8532316 (2023)
25. Wei, Y., et al.: Synthesis of multiblock linear polyether functional amino silicone softener and its modification of surface properties on cotton fabrics. *Polym. Bull.* **76**(1), 447–467 (2019)
26. Kumar, V., Patel, D., Pal, H., Kuperkar, K.: A comprehensive insight on H-type aggregation in Congo red-surfactant systems revealed through spectroscopic and electrochemical study unified with a simulation framework. *Phys. Chem. Chem. Phys.* **21**(28), 15584–15594 (2019)

27. Chakraborty, P., Nagarajan, R.: Efficient adsorption of malachite green and Congo red dyes by the surfactant (DS) intercalated layered hydroxide containing Zn^{2+} and Y^{3+} -ions. *Appl. Clay Sci.* **118**, 308–315 (2015)
28. Wu, P., Wu, T., He, W., Sun, L., Li, Y., Sun, D.: Adsorption properties of dodecylsulfate-intercalated layered double hydroxide for various dyes in water. *Colloids Surf. A* **436**, 726–731 (2013)
29. González, J.T., Ovejero, R.G., Murciego, Á.L., González, G.V., De Paz, J.F.: Effects of environmental conditions and composition on the electrical properties of textile fabrics. *Sensors* **19**(23), 5145 (2019)



Dimensional Accuracy of Compressive Specimens Obtained by SLS Technology

Ivana Jevtić¹✉, Goran Mladenović², Miloš Milošević¹, Aleksa Milovanović¹,
Milan Travica¹, and Isaak Trajković¹

¹ Innovation Centre of the Faculty of Mechanical Engineering, University of Belgrade, Kraljice
Marije 16 Street, 11120 Belgrade, Serbia

ijevtic@mas.bg.ac.rs

² Faculty of Mechanical Engineering, University of Belgrade, Kraljice Marije 16 Street, 11120
Belgrade, Serbia

Abstract. The objective of this study is to examine the accuracy of dimensional measurements for parts produced using Additive Manufacturing (AM) technology. The specific 3D printer employed in this research is Fuse 1 (FormLabs, Summerville, MA). The printer operates on the Selective Laser Sintering (SLS) method, enabling the simultaneous creation of objects with diverse shapes and sizes, as long as they are printed at a minimum separation distance of 5 mm. The printing process involved a layer thickness of 110 microns. To assess the dimensional accuracy, a particular type of specimen adhering to the ISO 604 standard for compressive specimens was analyzed. These compressive specimens possess dimensions of $\varnothing 10 \times 20$ mm. Four sets of specimens were fabricated, differing in their printing orientation (horizontal or vertical) and printing location (edge or middle of the powder bed). Polyamide (PA 12) was the chosen material for printing the specimens, known to exhibit compressive strength values of 13/24/55 MPa at 1%/2%/5% strain, respectively. After printing, the specimens were subjected to a 3D scanner Atos Core 200. The most significant deviations observed across all four series of specimens were primarily in terms of height, ranging from 0.1 to 0.15 mm. In the case of vertically printed specimens positioned in the middle of the powder bed, variations in the width of the specimens were also noted.

Keywords: SLS · Universal testing machine · Compressive specimens · PA12 material

1 Introduction

Additive manufacturing, also known as 3D printing, is a revolutionary manufacturing process that involves creating three-dimensional objects by building them layer by layer [1–6]. Unlike traditional subtractive manufacturing methods, such as cutting or drilling, which remove material to create the desired shape, additive manufacturing adds material to form the final product [1, 4, 7]. Additive manufacturing offers numerous advantages over traditional manufacturing methods. Additive manufacturing allows for the creation

of complex and intricate geometries that are difficult or even impossible to produce using conventional methods. This freedom enables the production of highly customized and optimized designs. Since additive manufacturing adds material selectively, it minimizes material waste compared to subtractive manufacturing. This can lead to significant cost savings and reduced environmental impact [8–10]. Also, additive manufacturing is particularly beneficial for rapid prototyping. It enables designers and engineers to quickly produce physical prototypes, allowing for faster iteration and design refinement. The process of additive manufacturing begins with the creation of a digital 3D model using computer-aided design (CAD) software. This virtual model serves as a blueprint for the physical object. The 3D printer then reads this digital file and constructs the object layer by layer, following the instructions provided. There are several different additive manufacturing technologies available, each with its unique approach to building objects. Some of the commonly used techniques include FDM (Fused Deposition Modeling), SLS (Selective Laser Sintering), SLA (Stereolithography), SLM (Selective Laser Melting), DLP (Digital Light Processing), DMLS (Direct Metal Laser Sintering), EBM (Electron Beam Melting) [1]. FDM printing technology has become widely embraced as an additive manufacturing technique [10]. Nevertheless, it is worth highlighting that SLS 3D printing technology has also found extensive application in the industry. SLS is a type of additive manufacturing technology that belongs to the Powder Bed Fusion family [1]. SLS forms 3D objects by laser energy to selectively heat powder particles which results in fusion. The fused particles subsequently solidify to form a 3D structure. Post-processing is the next step in the procedure. It involves the extraction of the model from the unsintered powder solution and its subsequent sandblasting. This crucial stage showcases the true advantages of SLS technology. Unlike FDM, SLS has the remarkable ability to create 3D models with intricate geometry without the need for support structures. This is made possible because the models are suspended within the powder [11].

In this study, we investigate the dimensional accuracy of specimens produced using Selective Laser Sintering (SLS) technology and composed of polyamide 12 (PA12) material. The research focuses on four batches of specimens that undergo compression in different orientations and are printed at various locations within the powder bed. To evaluate the dimensional accuracy, we employ a 3D scanner called Atos Core 200. The main goal is to examine the variations in dimensional accuracy between specimens compressed horizontally and vertically, as well as those printed in the middle or on the edge of the powder bed. Additionally, we explore the impact of the printing location within the powder bed on dimensional accuracy. By comparing specimens printed in the middle of the bed to those printed on the edge, we aim to determine if the position within the bed significantly affects the dimensional accuracy of the parts.

2 Materials and Methods

2.1 Preparing Specimens

This research employed the ISO 604:2002 standard [12] to fabricate compressive specimens with the recommended dimensions. The specimens were designed as 3D models using CAD software (SolidWorks, Dassault Systèmes, Vélizy-Villacoublay, France) and

saved in the STL format. These models were then “sliced” using PreForm software (Formlabs, Sommerville, MA, USA). The specimens have bulk dimensions of $\text{Ø}10 \times 20$ mm, as depicted in Fig. 1. A total of four batches, each consisting of ten specimens, were 3D printed. The batches varied in terms of printing orientation and location. Specifically, both vertical and horizontal orientations were utilized, and each orientation was combined with printing in either the middle or on the edge of the powder bed. The specimens were produced using Selective Laser Sintering (SLS) technology on the Fuse 1 3D printer (Formlabs, Somerville, Massachusetts). The typical thickness of printing layers ranges from 20 to 150 microns, but for this study, a powder thickness of 110 microns was employed. During the printing process, all models were positioned at least 5 mm apart. The SLS printer operated at a laser power of 63–70 W while maintaining a working temperature of 180 °C. It is worth noting that the build volume for this 3D printer measures $165 \times 165 \times 300$ mm.

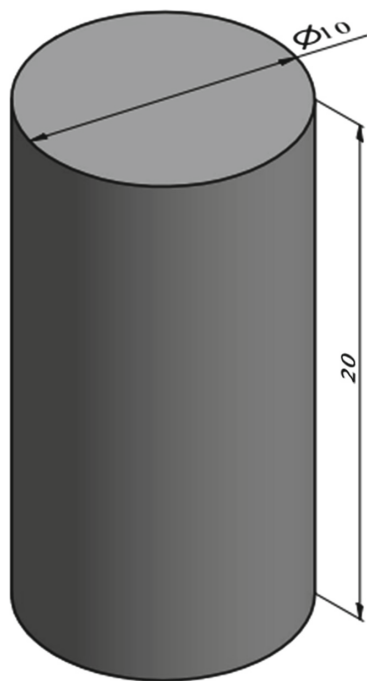


Fig. 1. Compressive specimen dimensions.

2.2 Materials

In this study, the specimens utilized for research purposes were generated using PA12 material (Formlabs, Sommerville, MA, USA). Among the variety of materials available, PA12 is a popular choice for both intricate assemblies and prototypes. This material boasts impressive attributes such as strength, longevity, flexibility, heat resistance, and

satisfactory mechanical qualities [13]. PA12 finds widespread usage in the automotive, aerospace, and industrial domains, particularly for the production of gears, bearings, and pump components [14]. The glass transition temperature of PA12 stands at approximately 48.8 °C, while its melting point ranges from 178 to 180 °C, representing the lowest melting temperature among all polyamides. Some noteworthy properties of PA12 include its minimal water absorption, density of 1.01 g/cm³, chemical resistance, and resistance to stress cracking [15]. Some of the mechanical characteristics of this material are 50 MPa tensile strength, flexural strength of 66 MPa, and a modulus of elasticity of 1850 MPa [16]. The combination of the mentioned tensile strength, flexural strength, and modulus of elasticity highlights the mechanical robustness and versatility of this material. These properties make it a promising choice for a wide range of applications, including but not limited to structural engineering, automotive components, aerospace structures, and manufacturing processes that require high-strength materials capable of withstanding demanding mechanical forces.

2.3 Testing Procedure

The research involved printing a total of forty specimens, which were divided into four batches, each containing ten specimens. The batches were differentiated based on variations in printing orientation and location. Both vertical and horizontal orientations were used, and each orientation was combined with a specific printing location either in the middle or on the edge of the powder bed.

In this research, Atos Core 200 3D scanner (GOM, Braunschweig, Germany) was used to determine the dimensional accuracy of compression specimens. This 3D scanner is a non-contact optical scanner equipped with GOM Inspect software, which served as the data acquisition software for the scanner. Consistent environmental conditions were maintained throughout the scanning process, including a constant temperature of 23 °C with air conditioning. The Atos 3-D scanner utilized optical triangulation, fringe projection, and photometry techniques for optical measurements. This system allowed for the rapid digitization of observed objects, resulting in relatively high precision and resolution. The scanner is designed for quality control and reverse engineering applications, and can be used to capture high-resolution 3D data of complex parts and surfaces. The scanner uses blue light projection and structured white light technology to capture accurate and detailed 3D data (see Fig. 2). The measurement volume of this scanner is 200 × 150 × 250 mm, the point spacing is 0.08 mm, and the operating temperature range is from 5 to 40 °C [17]. It's crucial to ensure that the scanner remains within this range during operation to maintain its optimal performance and prevent any potential issues that may arise from operating outside of this temperature range. Apart from the utilization of 3D scanners, optical systems can also incorporate digital image collection (DIC) techniques. This approach allows for the evaluation of deformations occurring in diverse shapes, ranging from simple to complex, as a consequence of different types of loading [18–26].

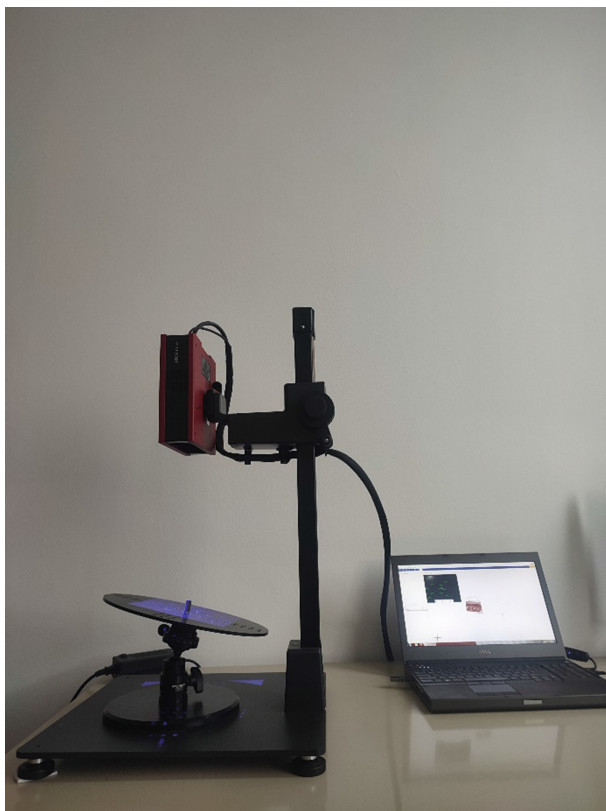


Fig. 2. 3D scanning of the compressive specimen.

3 Results and Discussions

The following figures provide a clear visualization of the disparities between the 3D scanned model and the CAD model, highlighting the precise locations of significant and maximum deviations. Figures 3 and 4 display dimensional discrepancies observed in horizontally oriented 3D scanned compressive specimens. Both figures showcase different specimen positions: Fig. 3 exhibits the printed specimen positioned at the edge of the powder bed, while Fig. 4 represents the printed specimen located in the middle of the powder bed. The CAD model exhibits its greatest deviations in specimen height, with a maximum deviation of 0.12 mm observed in horizontally printed specimens located at the edge of the powder bed. In the case of horizontally printed specimens positioned in the middle of the powder bed, the maximum height deviation amounts to 0.18 mm.

Figures 5 and 6 illustrate the dimensional discrepancies observed in 3D scanned compressive specimens with a vertical orientation. Each figure showcases a distinct specimen position: Fig. 5 exhibits a printed specimen placed at the edge of the powder bed, whereas Fig. 6 demonstrates a printed specimen positioned in the middle of the powder bed. The CAD model displays its most significant discrepancies in terms of specimen height, with

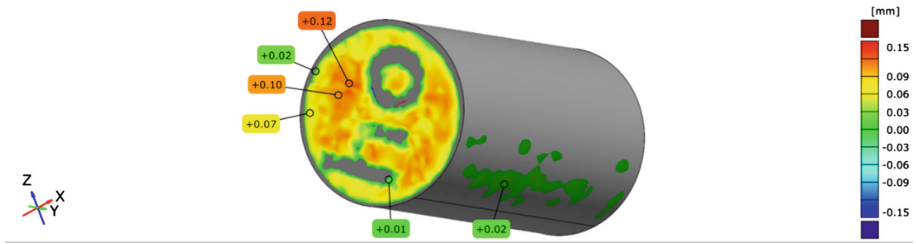


Fig. 3. Horizontally printed specimen on the edge of the powder bed.

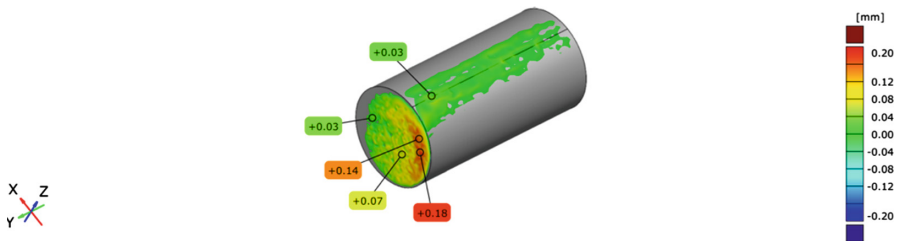


Fig. 4. Horizontally printed specimen in the middle of the powder bed.

a maximum deviation of 0.09 mm observed in vertically printed specimens situated at the powder bed's perimeter. Similarly, for vertically printed specimens positioned in the center of the powder bed, the highest height deviation reaches 0.11 mm. Additionally, deviations in specimen width are also evident for vertically printed specimens located in the middle of the powder bed. Furthermore, the width discrepancies in vertically printed specimens positioned in the middle of the powder bed are primarily attributed to the inherent nature of the additive manufacturing process. These variations arise from factors such as material shrinkage, thermal effects, and the accumulation of residual stresses during the printing process.

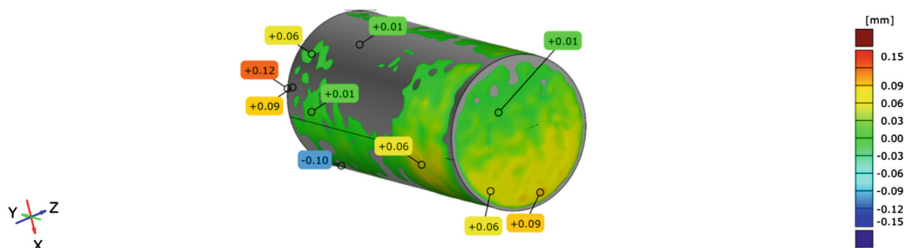


Fig. 5. The vertically printed specimen on the edge of the powder bed.

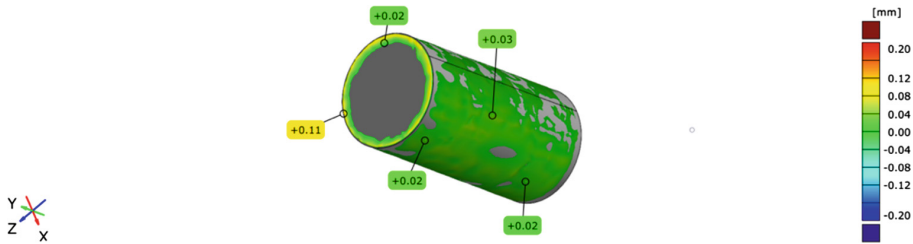


Fig. 6. The vertically printed specimen in the middle of the powder bed.

4 Conclusions

This research investigates the dimensional accuracy assessment of parts manufactured through additive SLS technology, specifically utilizing PA12 material. The evaluation involves comparing 3D scanned specimens to the original CAD model using dedicated software. The analysis is conducted using GOM Inspect software, which generates visual representations illustrating the deviations and marked peaks. The study findings reveal that the most significant dimensional deviations are observed in the height of the specimens. In all four specimen series, the height discrepancies range between 0.1 and 0.15 mm. Furthermore, when printing vertical specimens at the center of the powder bed, variations in specimen width are also evident.

The variations in specimen width are attributed to the uneven thermal distribution during the additive SLS printing process. This uneven distribution can lead to localized melting and cooling inconsistencies, resulting in slight dimensional variations. However, despite these discrepancies, the overall dimensional accuracy of the parts manufactured using PA12 material through additive SLS technology is found to be within acceptable tolerances for many applications.

Overall, this research contributes to the understanding of dimensional accuracy assessment in additive SLS manufacturing, particularly with PA12 material. The findings provide valuable insights for industries and researchers seeking to optimize the process parameters and improve the quality control of parts produced through additive SLS technology.

References

1. ASTM F2792-12a: Standard Terminology for Additive Manufacturing Technologies (2013)
2. Golubovic, Z., Travica, M., Trajkovic, I., Petrovic, A., Miskovic, Z., Mitrovic, N.: Investigation of thermal and dimensional behavior of 3-D printed materials using thermal imaging and 3-D scanning. *Therm. Sci.* **27**, 21–31 (2023)
3. Milovanovic, A., et al.: Side-groove effect on fracture mechanical fatigue testing of PLA material. *Procedia Struct. Integr.* **42**, 847–856 (2022)
4. Jevtic, I., Mladenovic, G., Milosevic, M., Milovanovic, A., Trajkovic, I., Travica, M.: Dimensional accuracy of parts obtained by SLS technology. *Struct. Integr. Life* **22**, 288–292 (2022)

5. Golubovic, A., Mitrovic, A., Mitrovic, N.: 3D printing in contemporary dentistry. In: *Experimental Research and Numerical Simulation in Applied Sciences*, vol. 564, pp. 213–232. Springer (2022)
6. Golubović, Z., Travica, M., Mitrović, A., Trajković, I., Mitrović, N.: Mogućnosti praćenja temperaturnog polja nakon procesa 3d štampe. In: *Šesti naučno-stručni skup POLITEHNIKA*, Beograd, pp. 577–583 (2021)
7. Prakash, K.S., Nancharaih, T., Subba Rao, V.V.: Additive manufacturing techniques in manufacturing – an overview. *Mater. Today Proc.* **5**, 3873–3882 (2018)
8. Rasiya, G., Shukla, A., Saran, K.: Additive manufacturing – a review. *Mate. Today Proc.* **47**, 6896–6901 (2021)
9. Durakovic, B.: Design for additive manufacturing: benefits, trends and challenges. *Period. Eng. Nat. Sci.* **6**, 179–191 (2018)
10. Vorkapic, M., et al.: Enhancing mechanical properties of 3D printed thermoplastic polymers by annealing in moulds. *Adv. Mech. Eng.* **14**, 1–15 (2022)
11. Trajkovic, I., et al.: Novel method for measurement of pipeline materials fracture resistance-examination on selective laser sintering cylindrical specimens. *Sci. Sinter.* **54**, 373–386 (2022)
12. ISO 604:2002: Plastics – Determination of Compressive Properties (2002)
13. Martynková, G.S., et al.: Polyamide 12 materials study of morpho-structural changes during laser sintering of 3D printing. *Polymers* **13**, 810 (2021)
14. Crompton, T.R.: *Engineering Plastics* (2014)
15. Touris, A., et al.: Effect of molecular weight and hydration on the tensile properties of polyamide 12. *Results Mater.* **8** (2020)
16. Formlabs.com.: <https://formlabs-media.formlabs.com/datasheets/2001447-TDS-ENUS-0.pdf>. Accessed 5 June 2023
17. ATOS Core scanner by GOM, Official Website of the Manufacturer: https://www.gom.com/en/products/3d-scanning?keyword=atos%20%2Bcore%20%2B200&device=c&network=g&gclid=CjwKCAjwp7eUBhBeEiwAZbHwkWgccIllecq91NkpE0UCMIEaFF9SNRuMKNBr-wNyBy-RutejLQfxoCLwkQAvD_BwE. Accessed 5 June 2023
18. Milovanovic, A., Milosevic, M., Trajkovic, I., Sedmak, A., Razavi, M.J., Berto, F.: Crack path direction in plane-strain fracture toughness assessment tests of quasi-brittle PLA polymer and ductile PLA-X composite. *Procedia Struct. Integr.* **42**, 1376–1381 (2022)
19. Nikitovic, A., et al.: 3D digital image correlation analysis of local deformation field of different endodontic calcium silicate cements. *Appl. Sci.* **13**, 1633 (2023)
20. Travica, M., et al.: Experimental evaluation of hoop stress-strain state of 3D-printed pipe ring tensile specimens. *Metals - Open Access Metall. J.* **12**, 1560 (2022)
21. Milosevic, M., et al.: Development of methodologies for experimental analysis of neck deformations caused by impact forces in martial arts. *Adv. Mech. Eng.* **14**, 1–14 (2022)
22. Mitrovic, N., et al.: Experimental and numerical study of globe valve housing. *Hem. Ind.* **71**(3), 251–257 (2017)
23. Kovacevic, T., et al.: Effects of oxidized/treated non-metallic fillers obtained from waste printed circuit boards on mechanical properties and shrinkage of unsaturated polyester-based composites. *Polym. Compos.* **40**(3), 1170–1186 (2019)
24. Mitrovic, N., et al.: Experimental and numerical analysis of local mechanical properties of globe valve housing. *Chem. Listy* **106**(3), 491–494 (2012)
25. Mitrovic, N., Milosevic, M., Sedmak, A., Petrovic, A., Prokic-Cvetkovic, R.: Application and mode of operation of non-contact stereometric measuring system of biomaterials. *FME Trans.* **39**(2), 55–60 (2011)
26. Milosevic, M., et al.: Measurement of local tensile properties of welded joint using digital image correlation method. *Chem. Listy* **106**, 485–488 (2012)



Analysis of Flexural Strength Tiles Made by ABS-X Material with Different Infill

Isaak Trajkovic¹ (✉) , Aleksandra Dragicevic² , Uros Ilic² , Marko Djurovic² ,
Goran Mladenovic² , and Milos Milosevic¹

¹ Innovation Centre of the Faculty of Mechanical Engineering, Kraljice Marije 16 Street, 11120 Belgrade, Serbia

trajkovicisaak@gmail.com

² Faculty of Mechanical Engineering, University of Belgrade, Kraljice Marije 16 Street, 11120 Belgrade, Serbia

Abstract. This paper presents the results of bending tests of tiles made of ABS X material and analysis of mechanical characteristics. The tested tiles were made of ABS X material with an infill that has a Honeycomb sample structure, assuming that this type of infill has the highest values of modulus of elasticity and mechanical properties. The ABS X material performed very satisfactorily, with less cracking, excellent adhesion to the layer and improved mechanical properties. As the main advantage of a three-point bend test is its simplicity, the method used in testing tiles is precisely the three-point bend test. The orientation of the 3D printing while making the tiles was vertical, and the tile infills were made with a density of 50 and 100%. When analyzing the obtained results of the mechanical properties of the tiles, special attention was paid to the influence of the infill density on the mechanical properties. The results and analyzes obtained in this work can be used in practice and in further research, with the tendency to examine and compare as many materials as possible, with different structures and infill densities.

Keywords: 3D printing · Tiles · ABS X · Honeycomb structure · Three-point bending

1 Introduction

Research and testing of polymer-based materials, such as plastics, are of key importance for the development and improvement of many industries. In addition to the standard tests of the mechanical characteristics of materials that were done in studies in the currently available literature [1–3], examinations were also done on some non-standard shapes obtained by 3D printing techniques [4–6], all with the aim of better understanding the material's reactions.

Often, the mechanical characteristics of materials are tested using equipment such as universal material testing machines, which are often found in the available literature [7–10], and optical measurement procedures such as the digital image correlation method and thermal imaging and 3D scanning are becoming more common [11–15].

In addition to a wide range of commercially available materials whose specific mechanical properties are known thanks to the aforementioned equipment and methods, ABS-X material is a recently developed new type of ABS material with added reinforcements of unknown chemical composition. Such examples are already known in practice [16] and the differences in the mechanical characteristics of the material are known.

In order to increase the application of commercially available materials with unknown fillers both in the industrial sector and in the research sector, additional tests are necessary for a better understanding of the behavior of these materials.

The aim of this work lies in providing a deeper understanding of how this material reacts to stress and load at different amounts of filling the samples with the material. Through the three-point bending method, we can evaluate the strength and flexibility of ABS-X material, which are key characteristics in many application situations, including engineering, construction, medicine and manufacturing.

2 Experimental Setup

In order to compare and examine the influence of infill density on mechanical properties, tiles with infill density of 50% (5 pieces) and 100% (5 pieces) were tested, so a total of 10 tiles were tested. All tested tiles were made on a 3D printer (German RepRap x400) [17] in laboratory of Center for Optical Measurement and Rapid Prototyping at Innovation Center of Faculty of Mechanical Engineering and Faculty of Mechanical Engineering University of Belgrade. The chosen tile material is ABS-X (acrylonitrile butadiene styrene with an unknown filler), one of the most common plastics used in injection-molding.

When printing the tiles, it was decided to make them all with the geometry of the fill structure Honeycomb comb (Fig. 1), and to compare their results.

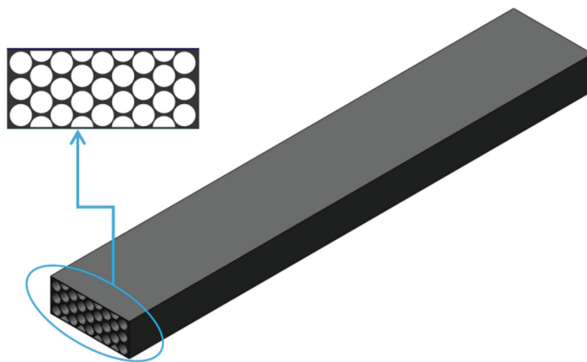


Fig. 1. 3D model of a tile with a honeycomb infill structure. Note: depending on the infill density (50 or 100%), the dimensions of the honeycomb structure differ.

Printing parameters are:

- Nozzle diameter: 0.4 mm
- Extruder temperature: 235 °C
- Bed temperature: 105 °C
- Layer high: 0.200 mm
- Printing speed: 50 mm/s

During the experiment setup, the title sample is supported on two rollers and centrally loaded (under constant load) in a three-point bend configuration as shown in Fig. 2. Determination of the flexural strength of tiles made of ABS-X plastic was done according to the ISO 178 standard as applied in research Milovanovic et al. [1].

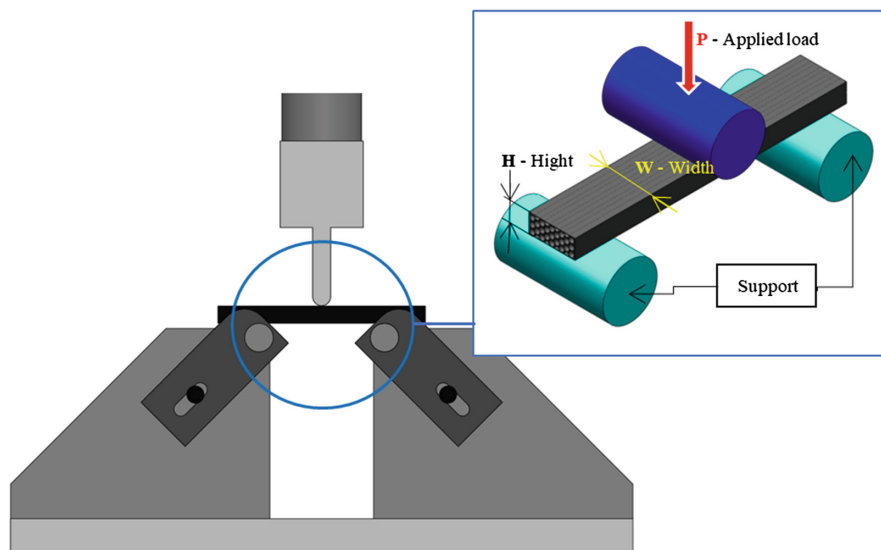


Fig. 2. Display of the setting of the tile on the breaker in the initial position, where P is the applied load, H and W are the thickness and width of the sample beam.

For each flexure experiment, the obtained Load-Deflection curve was used to extract and estimate the flexural properties (the flexural strength (σ_f), the modulus (E_f) and the strain to failure (ϵ_f)) as shown in Table 2. Also, according to similar or even same mechanisms of break appear in both samples, which are not dependent of dimensions of cross section or wall thickness of samples (Fig. 3).

With this approach, only some of the mechanical characteristics of the material were determined. For both complex and simple geometries, there are several approaches to determine the mechanical characteristics of materials that vary with the types of loading [18–23].

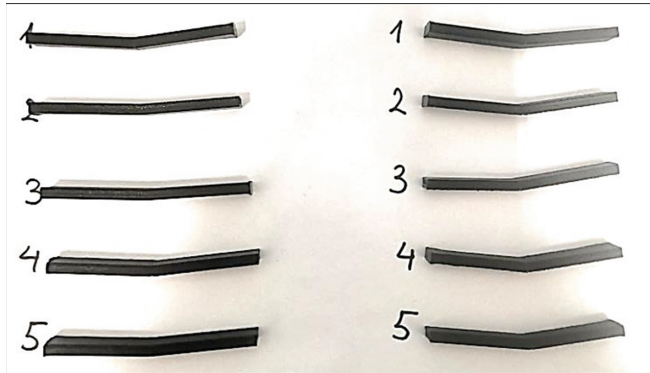


Fig. 3. Image of all 10 tiles after folding (left 50% infill, right 100% infill).

3 Results and Discussion

Due to the observed discrepancies in the results, three of the five samples (Table 1) with the closest values were taken as the relevant results, taking into account the test results obtained by testing the remaining samples.

Table 1. Results for five tiles

Name	Max_force	Max_stress	Max_strain
Parameter	Calc. at entire areas	Calc. at entire areas	Calc. at entire areas
Unit	N	MPa	%
1 (100%)	78.694	37.8853	3.89662
2 (100%)	80.7921	39.0851	4.03518
3 (100%)	76.6118	36.1803	3.36381
4 (100%)	82.3498	40.0339	4.09535
5 (100%)	74.5614	36.0708	3.40892
1 (50%)	77.0251	38.1943	3.58832
2 (50%)	67.1705	32.3375	2.69564
3 (50%)	70.7467	34.0593	3.04262
4 (50%)	71.907	34.6179	3.22846
5 (50%)	62.8313	30.2485	2.54202

Table 1 shows the maximum values of force, stress and deformation for each tested sample. The differences in the maximum values between the samples have statistical significance, which will be given more attention when additional tests are performed.

Table 2. Results for chosen tiles with average and standard deviation

Name	Max_force	Max_stress	Max_disp.	Max_strain	Elastic
Unit	N	MPa	mm	%	MPa
Infill 100%					
Average	80.61196667	39.00143333	6.2201	4.00905	1351.196667
Standard deviation	1.834544746	1.076740718	0.158114117	0.101909204	58.52080171
Infill 50%					
Average	69.9414	33.67156667	4.63733	2.988906667	1401.1
Standard deviation	2.468803178	1.188616378	0.419587582	0.270440621	35.56542703

Table 2 shows the average values with standard deviations for the samples with the smallest deviation. The values in the table indicate the difference in the bending resistance of the material for two different amounts of infill.

By testing the flexural strength of samples with 100% infill, an average value of 39.00 MPa was obtained at a flexural strain value of 4%. For samples with twice as much infill, the average value of flexural strength was 33.67 MPa and flexural strain was 2.99%.

In addition to the differences in the maximum values of the flexural strength of these samples, a difference was observed in the maximum values of the measured parameters within both series. This difference is more pronounced in the series of samples where the infill is 50%. For representative samples taken from both series, the difference in standard deviation values is twice as large for samples with a smaller amount of infill.

The differences in the scatter values of three representative samples from both series are shown in Figs. 4 and 5 for the series of samples with 50% and 100% infill, respectively.

In Fig. 4, we can see the dispersion of the results, the difference in the maximum values of which indicates statistical significance, although the nature of the behavior of the samples is approximately the same up to the deformation value of 2.5%.

Figure 5 shows the diagrams of 3 representative samples for a series of 100% filling samples, where the nature of the behavior of the samples under load is almost identical and without a large scattering of results.

The differences in the behavior of the two tested series of samples are the result of filling the samples with material. A large influence on the consistency of the results is obviously due to the amount of material within the samples. Samples filled with 50% showed a lower flexural strength by approximately 18%, while the measured deformations on the samples were lower by approximately 33%.

A series of samples whose filling was 100% showed much less dispersion of results. Bearing in mind that the only parameter that was varied was the amount of filling of the samples with the material, we can assume that it affects not only the mechanical

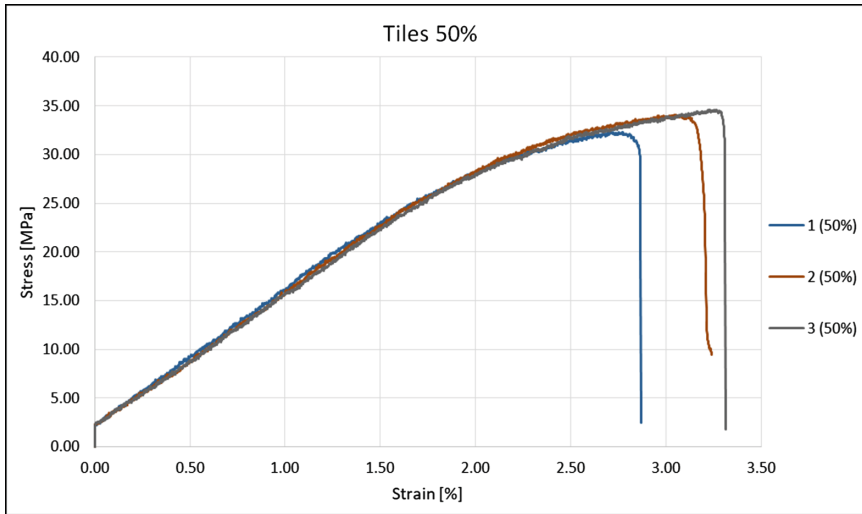


Fig. 4. Plot of flexural stress versus flexural strain for tiles of 50%.

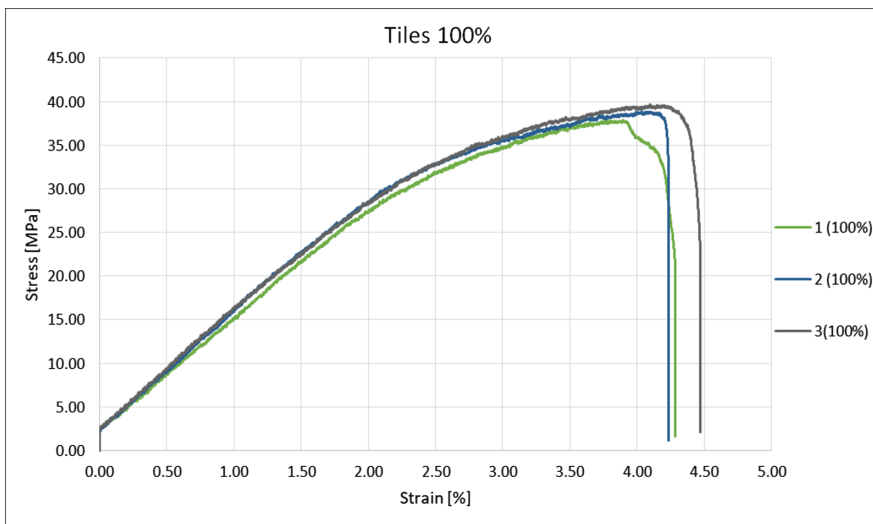


Fig. 5. Plot of flexural stress versus flexural strain for tiles of 100%.

characteristics of the material, but also their reproducibility. This can be very important information when it comes to functional parts of equipment obtained by additive manufacturing, especially equipment that works under elevated pressure.

4 Conclusion

By testing the flexural strength of the samples tested for three-point bending, results were obtained that indicate non-negligible differences in the values of flexural strength and flexural strain. Samples with 100% infill showed approximately 18% higher flexural strength compared to samples with twice as much infilling. The amount of sample infill was also reflected in the higher flexural strain. The flexural strain is approximately 33% higher for samples with a larger amount of infill compared to the other types of tested samples. We can conclude that the testing tiles with 100% infill showed better mechanical properties in terms of flexural strength. A smaller amount of infill with material, in addition to having lower values of the mechanical characteristics obtained by bending, also gives a greater dispersion of the results, which can have a great influence when choosing the amount of filling of the object with material.

A smaller amount of material infill, in addition to resulting in lower values of the mechanical properties acquired by bending, also results in a higher dispersion of the results, which can have a significant effect when deciding the amount of material filling of the object. This result, although expected, will be very useful in further work. In the following period, the flexural strength of samples with 100% infill will be compared to the samples of the same infill, but treated with acetone.

References

1. Milovanovic, A., et al.: The effect of time on mechanical properties of biocompatible photopolymer resins used for fabrication of clear dental aligners. *J. Mech. Behav. Biomed. Mater.* **119** (2021)
2. Milovanovic, A., Golubovic, Z., Babinsky, T., Sulak, I., Mitrovic, A.: Tensile properties of polypropylene additively manufactured by FDM. *Struct. Integr. Life* **22**(3), 305–308 (2022)
3. Vorkapic, M., et al.: Enhancing mechanical properties of 3D printed thermoplastic polymers by annealing in moulds. *Adv. Mech. Eng.* **8** (2022)
4. Trajkovic, I., et al.: Novel method for measurement of pipeline materials fracture resistance-examination on selective laser sintered cylindrical specimens. *Sci. Sinter.* **54**, 373–386 (2022)
5. Travica, M., et al.: Experimental evaluation of hoop stress-strain state of 3D-printed pipe ring tensile specimens. *Metals - Open Access Metall. J.* **12**, 1560 (2022)
6. Trajkovic, I., Milosevic, M., Rakin, M., Sedmak, A., Medjo, B.: Additively manufactured tensile ring-shaped specimens for pipeline material fracture examination-influence of geometry. *Procedia Struct. Integr.* **42**, 1314–1319 (2022)
7. Milosevic, M., et al.: Measurement of local tensile properties of welded joint using digital image correlation method. *Chem. Listy* **106**, 485–488 (2012)
8. Tanasic, I., et al.: An attempt to create a standardized (reference) model for experimental investigations on implant's sample. *Measurement* **72**, 37–42 (2015)
9. Milosevic, M., et al.: Digital image correlation in analysis of stiffness in local zones of welded joints. *Tech. Gaz.* **23**, 19–24 (2016)
10. Mitrovic, N., et al.: Experimental and numerical study of globe valve housing. *Chem. Ind.* **71**(3), 251–257 (2017)
11. Balac, M., Grbovic, A., Petrovic, A., Popovic, V.: Fem analysis of pressure vessel with an investigation of crack growth on cylindrical surface. *Eksplot. Niezawodn. – Maint. Reliab.* **20**(3), 378–386 (2018)

12. Milosevic, M., et al.: Development of methodologies for experimental analysis of neck deformations caused by impact forces in martial arts. *Adv. Mech. Eng.* **14**, 1–14 (2022)
13. Jevtic, I., Mladenovic, G., Milosevic, M., Milovanovic, A., Trajkovic, I., Travica, M.: Dimensional accuracy of parts obtained by SLS technology. **22**, 288–292 (2022)
14. Nikitovic, A., et al.: 3D digital image correlation analysis of local deformation field of different endodontic calcium silicate cements. *Appl. Sci.* **13**, 1633 (2023)
15. Golubovic, Z., Travica, M., Trajkovic, I., Petrović, A., Miskovic, Z., Mitrovic, N.: Investigation of thermal and dimensional behavior of 3-D printed materials using thermal imaging and 3-D scanning. *Therm. Sci.* **27**, 21–31 (2023)
16. Milovanovic, A., Milosevic, M., Trajkovic, I., Sedmak, A., Razavi, M.J., Berto, F.: Crack path direction in plane-strain fracture toughness assessment tests of quasi-brittle PLA polymer and ductile PLA-X composite. *Procedia Struct. Integr.* **42**, 1376–1381 (2022)
17. Golubovic, A., Mitrovic, A., Mitrovic, N.: 3D printing in contemporary dentistry. In: *Experimental Research and Numerical Simulation in Applied Sciences*, vol. 564, pp. 213–232. Springer (2022).
18. Compton, B., Lewis, J.: 3D-printing of lightweight cellular composites. *Adv. Mater.* **26**(34) (2014)
19. Jemii, H., Bahri, A., Taktak, R., Guermazi, N., Lebon, F.: Mechanical behavior and fracture characteristics of polymeric pipes under curved three-point bending tests: experimental and numerical approaches. *Eng. Fail. Anal.* **138** (2022)
20. Guermazi, N., Tarjem, A.B., Ksouri, I., Ayedi, H.F.: On the durability of FRP composites for aircraft structures in hygrothermal conditioning. *Compos. B Eng.* **85**, 294–304 (2016)
21. Mazlan, N.C., Hua, T., Ramli, N., Abdan, K., Zin, M.: Thermoplastics for aircraft cabin applications. In: *Encyclopedia of Materials: Plastics and Polymers*, vol. 4, pp. 482–497 (2022).
22. Miloichikova, I., Stuchebrov, S., Verigin, D., Danilova, I.: Simulation of the X-ray beam absorption by the ABS-plastic filled with different metallic additives. *J. Phys: Conf. Ser.* **769**(1), 012014 (2016)
23. Zhu, W., Zhang, X., Li, D.: Flexible all-plastic aircraft models built by additive manufacturing for transonic wind tunnel tests. *Aerosp. Sci. Technol.* **84** (2018)



The Possibility of Applying a Universal Testing Machine for Evaluating Food Textures

Ivana Jevtić¹(✉), Isaak Trajković¹, Ivan Zlatanović², Goran Mladenović²,
Nenad Korolija³, and Miloš Milošević¹

¹ Innovation Centre of the Faculty of Mechanical Engineering, Kraljice Marije 16, 11120
Belgrade, Serbia

ijevtic@mas.bg.ac.rs

² Faculty of Mechanical Engineering, University of Belgrade, Kraljice Marije 16, 11120
Belgrade, Serbia

³ The Department of Computer Science and Information Technology, University of Belgrade -
School of Electrical Engineering, 11000 Belgrade, Serbia

Abstract. The evaluation of food texture is an essential aspect of food quality control, directly influencing consumer acceptance and preference. Various methods have been developed to assess food texture, including sensory evaluation, rheological measurements, and instrumental analysis. Among the versatile instruments used for measuring the mechanical properties of food, the universal testing machine (UTM) stands out. Traditionally used in the field of materials science and engineering, the possibility of applying UTM for evaluating food textures has gained significant attention in recent years. The UTM can perform compression, tension, bending, and shear tests on food samples, providing objective and quantifiable data on their mechanical properties. Compression testing involves measuring the force required to compress a food sample between two plates, shear testing measures the force required to cut through a food sample, while puncture testing measures the force required to puncture a food sample with a probe. This paper reviews the current state-of-the-art of UTM in the evaluation of food textures, including the types of tests that can be performed, the parameters that can be measured, and the challenges and limitations associated with the technique. The potential of utilizing UTMs in the food industry for quality control and product development, instead of traditional sensory evaluation methods, is discussed, along with its advantages and disadvantages. Overall, UTM represents a promising tool for the objective evaluation of food textures, and further research is needed to optimize its application in this field.

Keywords: Food textures · Universal testing machine · Compression testing · Mechanical properties

1 Introduction

A universal testing machine (UTM), also known as a universal testing instrument or materials testing machine, is a versatile mechanical testing device used to determine the mechanical properties and behavior of various materials. It is commonly used in

materials science, engineering, manufacturing, and quality control laboratories. The primary purpose of a universal testing machine is to apply controlled forces and measure the corresponding responses of materials under different test conditions. This machine can perform various types of mechanical tests, including tension (pull), compression (push), bending, shear, and torsion tests. Through these tests, engineers and scientists can evaluate the strength, stiffness, ductility, toughness, fatigue resistance, and other mechanical properties of materials, as demonstrated in many papers [1–8]. Universal testing machines find applications in a wide range of industries, including aerospace, automotive, construction, materials manufacturing, biomedical, and research institutions. Additionally, universal machines are also utilized in the food industry. In the food industry, UTMs can be utilized for different purposes related to quality control, research, development, and examination of food textures. Food texture, a crucial component of product assessment and consumer satisfaction, refers to the tangible properties exhibited by food. These properties encompass a diverse range of characteristics, such as hardness, chewiness, crispness, smoothness, and viscosity [9, 10]. Food quality assessment can be approached through two methods: descriptive sensory analysis, which is subjective, and instrumental analysis, which is objective [11–14]. Universal testing machines provide a means for instrumental analysis in the food industry, enabling the quantification and measurement of texture-related parameters. By subjecting food samples to controlled forces and recording their responses, such as deformation or rupture, UTMs enable the objective evaluation of textural properties. This information aids in understanding the sensory experience and quality attributes of various food products, leading to improvements in formulation, process optimization, and consumer acceptance. The application of UTMs in the food industry continues to expand, contributing to advancements in food research, development, and overall quality assurance.

This comprehensive paper aims to provide a detailed overview of the testing methodologies employed when evaluating various types of food using a UTM. One of the key aspects covered in this paper is the selection of appropriate testing techniques for different food types. Foods possess diverse compositions and physical characteristics, requiring tailored approaches to accurately evaluate their mechanical properties. Various testing methods can be employed, such as compression testing, tensile testing, shear testing, and puncture testing, depending on the specific attributes of the food being analyzed.

2 Destructive Methods

There are two primary methods frequently employed to assess food texture properties: compression tests and puncture tests. These techniques are widely recognized and utilized due to their effectiveness. Food samples used in texture analysis can vary in consistency, ranging from solid to semi-solid. Moreover, depending on the specific research objectives, texture tests can be conducted on entire fruits or specific components such as the skin, pulp, or a combination of both. The choice of testing methodology and sample selection depends on the desired outcomes of the research study.

2.1 Compressive Tests on Vegetables and Fruits

During the compression tests, different vegetables including tomatoes, peppers, and eggplants were subjected to controlled forces to determine their mechanical properties and resistance to compression.

In the study described in research [15], the compression test on tomato fruits involved compressive forces at three different speeds across fruit's cross-section. However, researchers in research [16, 17] chose to use a single compression speed when examining tomatoes at their ultimate tensile strength (UTS). The variation in testing protocols could have been influenced by specific research objectives or experimental considerations.

In another research paper [18], the mechanical properties of pepper fruits were investigated. Two filling positions were tested, and each pepper fruit was placed between two compression plates. The compression test was conducted at a constant speed of 10 mm/min. By subjecting the pepper fruits to controlled compression, the researchers aimed to understand their behavior under external forces and assess their structural integrity.

Moving on to eggplants, experiments described in research papers [19–22] were conducted to evaluate the resistance to compression of intact eggplant fruits. A universal testing machine was used for these tests. The procedure involved placing a designated area of the eggplant between the stationery and compression components of the machine. A controlled loading rate of 20 mm/min was applied until the fruit ruptured. This method allowed researchers to quantify the eggplant's ability to withstand compressive forces and provided insights into its mechanical properties.

In a separate paper [23], a series of experiments were conducted to evaluate the performance of a universal machine in testing various substances, including vegetables, bread, and agar gel. The researchers aimed to assess the machine's ability to handle different types of materials and determine if it could provide consistent results across a diverse range of samples. In addition to vegetables, the study included bread, a commonly consumed food item known for its varying textures and densities. The bread was cut to a standardized thickness of 10 mm to ensure consistent measurements. By subjecting the bread samples to the universal testing machine, the study aimed to investigate how effectively the UTM could assess the properties and characteristics of this widely consumed food product.

2.2 Puncture Tests on Vegetables

In addition to conduct compression tests on various food varieties, the research paper [24] also investigated the puncture behavior of a pepper sample (see Fig. 1). For this specific test, a stainless-steel probe with a circular tip measuring 6 mm in diameter was used. The probe was attached to the loading cell of the machine and used to pierce the vegetable to a predetermined depth, equivalent to 50% of the vegetable's diameter, before quickly returning to its initial position. The research paper [24] presented the results of the puncture tests, including force-displacement curves and statistical analyses of the data. These findings enabled researchers and food scientists to develop a deeper understanding of the pepper's puncture behavior, contributing to the improvement of food processing techniques, packaging designs, and culinary applications.



Fig. 1. Pepper's puncture [24].

2.3 Other Tests on Food

Research [25] examines various types of food and suggests testing methods for each of them. Multi-piercing jigs are innovative tools that offer significant advantages in the evaluating hardness or cohesiveness in samples consisting of small food pieces with diverse shapes or samples containing dispersed air bubbles. By utilizing this specialized apparatus, researchers and food manufacturers can obtain accurate and reliable measurements, leading to valuable insights into the properties of different food items. One of the primary benefits of using multi-piercing jigs is their effectiveness in assessing the characteristics of food products that incorporate solid components, such as jam with fruit chunks, cookie-laden ice cream, or mixed vegetables [25]. These samples often present challenges when it comes to measuring their hardness or cohesiveness due to the presence of distinct textures or heterogeneous structures. However, the multi-piercing jig overcomes these difficulties by providing a standardized method for piercing and probing the samples.

When it comes to assessing properties like hardness and spreadability in materials that exhibit thermal plasticity, such as butter, margarine, and bar soap, conical press jigs play a crucial role [25]. These specialized jigs provide an invaluable means of conducting compression or piercing tests on these specimens, enabling precise measurements and analysis. Butter, margarine, and bar soap are examples of materials that undergo changes in their physical properties when exposed to temperature variations. Thermal plasticity refers to their ability to soften, deform, or undergo structural transformations under the influence of heat. Evaluating characteristics like hardness and spreadability in these materials is essential for quality control, product development, and research purposes. Piercing tests involve driving the pointed tip of the conical press jig into the material to evaluate its spreadability. This test determines how easily the material can be penetrated or spread, which is particularly relevant for substances like butter or margarine that are

meant to be spread onto bread or other food items. By quantifying the force required to pierce the material or the depth of penetration, valuable information can be obtained about its consistency and texture.

The three-point bending test is a valuable method for assessing the fracture resistance and brittleness of samples. By subjecting a specimen to a controlled bending force, this test provides valuable insights into the strength and structural integrity of various materials. While commonly used in engineering and material science, the three-point bending test can also be applied to evaluate the properties of food products such as biscuits or chocolate bars [25] (see Fig. 2). During the test, the specimen is placed on two lower supports, known as lower shocks, while a single upper shock or support is positioned above the sample, creating a span between the supports. The choice of upper shock or support can vary depending on the specific characteristics and properties of the sample being tested. For instance, a rigid upper support may be suitable for materials that exhibit high strength and resilience, while a flexible or cushioned upper support might be more appropriate for brittle or delicate samples.



Fig. 2. 3-point bending test on biscuits [26].

3 Conclusions

This research paper highlights the substantial potential of UTMs as a valuable tool for assessing and characterizing the textural properties of food products. By employing objective and standardized measurements, UTMs offer several advantages over traditional sensory evaluation methods, providing a more efficient and reliable approach to texture analysis.

One of the key benefits of using UTMs is their ability to provide precise and quantitative measurements of food textures. Unlike sensory evaluation, which relies on subjective perceptions and individual preferences, UTMs employ instrumental techniques that yield objective data. This objectivity ensures consistency and repeatability in texture analysis, enabling researchers and food manufacturers to make informed decisions based on reliable measurements.

The application of UTMs in food texture analysis has wide-ranging implications for various food markets in the food industry. Firstly, UTMs can enhance the understanding of food textures by providing detailed information about the physical properties of different food products. Researchers can investigate the relationships between texture attributes and the composition, processing methods, and storage conditions of foods, leading to deeper insights into the factors influencing texture.

Moreover, UTMs play a crucial role in facilitating product development. Food scientists and product developers can use UTMs to precisely measure and evaluate the impact of recipe modifications, ingredient substitutions, or processing techniques on the texture of food products. This enables them to optimize formulations and processes to achieve desired textural characteristics, ultimately leading to the creation of innovative and appealing food products.

In addition to aiding product development, UTMs are invaluable for ensuring consistent quality control in the food industry. By implementing UTMs as part of quality assurance protocols, manufacturers can objectively assess the texture of their products at different stages of production. This helps detect any deviations or inconsistencies in texture, allowing for timely adjustments and improvements to maintain uniform quality across batches and production lines.

While UTMs have demonstrated significant potentials, further research and development in this field are necessary to unlock their full capabilities and establish them as a universal approach for evaluating food textures. Ongoing studies can focus on refining measurement techniques, expanding the range of textural properties captured by UTMs, and exploring their applications in different food categories.

Moreover, efforts should be directed towards standardizing UTM methodologies and establishing industry-wide guidelines for texture analysis. This would promote consistency and comparability of results across different laboratories and research studies, further enhancing the reliability and acceptance of UTMs in the food industry.



References

1. Milovanovic, A., Golubovic, Z., Babinský, T., Šulák, I., Mitrovic, A.: Tensile properties of polypropylene additively manufactured by FDM. *Struct. Integr. Life* **22**, 305–308 (2022)
2. Milovanovic, A., et al.: Influence of printing parameters on the eligibility of plane-strain fracture toughness results for PLA polymer. *Procedia Struct. Integr.* **41**, 290–297 (2022)
3. Milovanovic, A., et al.: Comparative analysis of printing parameters effect on mechanical properties of natural PLA and advanced PLA-X material. *Procedia Struct. Integr.* **28**, 1963–1968 (2020)
4. Trajkovic, I., Milosevic, M., Rakin, M., Sedmak, A., Medjo, B.: Additively manufactured tensile ring-shaped specimens for pipeline material fracture examination - influence of geometry. *Procedia Struct. Integr.* **42**, 1314–1319 (2022)
5. Mitrovic, N., et al.: Experimental and numerical study of globe valve housing. *Hem. Ind.* **71**(3), 251–257 (2017)
6. Tanasic, I., Tihacek-Sojic, Lj., Mitrovic, N., Milic-Lemic, A., Vukadinovic, M., Markovic, A., Milosevic, M.: An attempt to create a standardized (reference) model for experimental investigations on implant's sample. *Meas.: J. Int. Meas. Confed.* **72**, 37–42 (2017)
7. Milosevic, M., et al.: Digital image correlation in analysis of stiffness in local zones of welded joints. *Teh. Vjesn.* **23**(1), 19–24 (2016)
8. Milosevic, M., et al.: Measurement of local tensile properties of welded joint using digital image correlation method. *Chem. Listy* **106**, 485–488 (2012)
9. Kadam, S.U., Tiwari, B.K., O'Donnell, C.P.: 6 - Improved thermal processing for food texture modification. In: *Woodhead Publishing Series in Food Science, Technology and Nutrition*, vol. 1, pp. 115–131 (2015)
10. Day, L., Golding, M.: Food structure, rheology, and texture. In: *Encyclopedia of Food Chemistry*, pp. 125–129 (2016)
11. Chen, L., Opara, U.M.: Texture measurement approaches in fresh and processed foods—a review. *Food Res. Int.* **51**, 823–835 (2013)
12. Vernon, K.E.J., Sherman, P.: Evaluation of the firmness of Leicester cheese by compression tests with the Instron universal testing machine. *J. Texture Stud.* **9**, 311–324 (1978)
13. Shama, F., Sherman, P.: Evaluation of some textural properties of foods with the Instron universal testing machine. *J. Texture Stud.* **4**, 344–353 (1973)
14. Kohyama, K.: Food texture – sensory evaluation and instrumental measurement. In: *Textural Characteristics of World Foods* (2020)
15. Idama, O., Uguru, H.: Robotization of tomato fruits production to enhance food security. *J. Eng. Res. Rep.* **20**, 67–75 (2021)
16. Ekruyota, O.G., Akpenyi-Aboh, O.N., Uguru, H.: Evaluation of the mechanical properties of tomato (Cv.Roma) fruits as related to the design of harvesting and packaging autonomous system. *Direct Res. J. Agric. Food Sci.* **9**, 174–180 (2021)
17. Edafeadhe, G.O.I., Uguru, H.: Evaluation of engineering properties of tomato (cv. Cobra 26) fruit, necessary for its' automated harvesting and processing. *Direct Res. J. Eng. Inf. Technol.* **7**, 27–33 (2020)
18. Idama, O., Uguru, H., Akpokodje, O.I.: Mechanical properties of bell pepper fruits, as related to the development of its harvesting robot. *Turk. J. Agric. Eng. Res.* **2**, 193–205 (2021)
19. Ekruyota, O.G., Uguru, H.: Characterizing the mechanical properties of eggplant (Melina F1) fruits, for the design and production of agricultural robots. *Direct Res. J. Eng. Inf. Technol.* **8**, 21–29 (2021)
20. Idama, O., Azodo, A.P.: An evaluation of African eggplant fruits engineering properties in relation to robotic harvesting. *Appl. J. Phys. Sci.* **4**, 15–21 (2022)

21. Nwanze, N.E., Uguru, H.: Optimizing the efficiency of eggplant fruits harvesting and handling machines. *J. Mater. Sci. Res. Rev.* **6**, 1–10 (2020)
22. Bratte, A.G., Uguru, H.: Evaluating the influence of pre-harvest hybrid treatments (compost manure and potassium nitrate fertilizer) on the mechanical properties of eggplant (cv. Bello) fruits. *J. Agric. Sci. Pract.* **6**, 60–66 (2021)
23. Kohyama, K., Sasaki, T., Dan, H.: Active stress during compression testing of various foods measured using a multiple-point sheet sensor. *Biosci. Biotechnol. Biochem.* **67**, 1492–1498 (2014)
24. Uguru, H., Akpenyi-Aboh, O.N.: Optimization of agricultural machines through the pre-harvest treatment of sweet paper (cv. Goliath) fruits. *Direct Res. J. Agric. Food Sci.* **9**, 167–173 (2021)
25. Shimadzu.com: <https://www.ssi.shimadzu.com/products/materials-testing/uni-ttm-system/ez-test-texture-analyzer/index.html>. Accessed 14 June 2023
26. <https://textureanalysisprofessionals.blogspot.com/2015/04/texture-analysis-in-action-three-point.html>. Accessed 14 June 2023



Numerical Simulations for the Optimization of the Position of the Regenerative Burner System for Tundish Preheating

Mirjana Stamenic¹ , Branislav Gajic¹, Aleksandar Milivojevic¹ , Vuk Adzic¹,
and Nikola Tanasic²

¹ Faculty of Mechanical Engineering, University of Belgrade, Belgrade, Serbia
mstamenic@mas.bg.ac.rs

² The Academy of Applied Technical Studies Belgrade, 11000 Belgrade, Serbia

Abstract. The paper presents the result of numerical simulations performed to optimize the position of burners and off-gas exit for a tundish preheating system. The optimization of the position of burner heads and off-gas exit at the tundish top cover has been done by application of StarCD CFD software for numerical simulations. Optimisation of the position for burner heads and off-gas exhaust in the tundish top cover brought a uniform temperature field inside the tundish refractory layer during the transient preheating process with minimal fuel consumption.

Keywords: Numerical CFD simulation · Tundish preheating system · Design optimization · Transient heating process

1 Introduction

The iron and steel production process is highly energy intensive. Thus, efficient energy conversion is one of the most relevant and mandatory tasks. Reducing the fuel consumption and air pollution of industrial furnaces in the iron and steel industry is one of the most significant objectives. High-temperature air combustion (HiTAC) has become a leading technology in energy-efficient fossil fuel conversion in high-temperature processes [1]. In recent years, different technologies have been developed for the utilisation of waste heat as a possibility of primary energy savings in steel and iron production processes. One of the available energy-efficient technologies is a regenerative burner system for tundish preheating. Tundish is used within the continuous casting line in the steel mill. Before use, tundish should be preheated at the prescribed temperature during a defined time. After the preheating phase, the steel is poured into the tundish, and from the tundish, the steel flows into the continuous casting machine, where the slabs are formed for the next operation – rolling and producing the steel sheets.

2 State-of-the-Art Regenerative Burner Systems

Regenerative burner systems are suitable for improving the energy efficiency of high-temperature processes with fuel combustion by using the energy of the exhaust gasses to preheat the combustion air. Today, there are several types of regenerative burner systems to choose from, each with specific advantages and disadvantages for different applications. There is a system with a central regenerator and separate regenerative burners. A central regenerator offers several advantages: (1) the number and types of burners are not limited and can be chosen as desired; (2) it is possible to use high-velocity burners; (3) the point at which the exhaust gas is taken from the furnace can be optimized; (4) the temperature field inside the furnace is uniform and allows efficient heat transfer from the gasses to the material in the furnace. Due to the special operating conditions (alternating heating and cooling phase), the main problem of the central regenerator is the switching between combustion air and exhaust gas flow through the regenerator units. In [7], the solution with two hot blast dampers is described as expensive and energetically unattractive, as the water cooling required for the dampers leads to heat losses and therefore reduces the overall thermal efficiency. In [7], it is also mentioned that frequent switching between regenerator units reduces the lifetime of the dampers, and regenerator units have to be very large, which makes such an option expensive.

It is possible to use a regenerator with a rotating bed [2], but this option has a limited operating temperature for combustion air of about 1,000 °C and for exhaust gas of about 1,200 °C. The heat recovery of such a system is limited to about 80%.

There are two other modern regenerative burner systems: (1) classical regenerative burners and (2) flameless regenerative burners (FLOX-Flameless oxidation). These systems have at least two drawbacks. First, it is impossible to optimise the point of extraction of exhaust gases from the furnace. The number of regenerative burners is the same for each furnace side (the system requires twice the number of burner heads). While one group of burners is in “burning mode”, the other group, mounted on the opposite side of the furnace, is in “heating mode”, and the combustion products flow through it, so it is impossible to optimize the position of the exhaust gas extraction in the furnace. Due to the small cross-section of the burner head, only 85% of the exhaust gas can be discharged through the regenerator thus, 15% leaves the furnace directly through the stack; therefore, the overall efficiency of heat recovery reaches at most 72%, although the available regenerators (with axial flow) have efficiencies up to 85% [7]. Regenerative burners are not suitable for operation in high-velocity regimes. The benefit of using high-velocity burners is that the temperature field in the furnace is uniform.

Flameless oxidation burners (FLOX) operate with highly preheated combustion air. The air temperature is well above the ignition point of the combustible mixture, resulting in combustion without a visible flame, which positively influences NO_x emissions [5]. According to [7], the small ceramic heat storage elements of FLOX burners can easily be clogged with dust, limiting their application to exhaust gasses with low dust content; another disadvantage is that FLOX burners do not operate in high-velocity mode, and the heat recovery efficiency is approximately 65%.

The regenerative burners presented in this paper consist of two regenerative pebble bed heaters (PH), a fluid-dynamic valve (FDV), two burners, a four-way valve, an exhaust

fan, and a combustion air supply fan. This system has several advantages compared to the above-mentioned regenerative burner systems:

- FDV is part of the installation that makes it possible to rapidly switch between two hot gas streams (exhaust gas and preheated combustion air) without movable mechanical parts. Its operating principle is based on the interaction between velocity and pressure field in the FDV channels [7]. By optimizing the dimensions of FDV's flow ducts, it is possible to achieve such a pressure field so that two hot gas streams flow in different directions without considerable mixing. FDV is an economically feasible option compared to a conventional switching valve on the hot gas side.
- The four-way valve is located on the cold side of the installation, which is more favorable from technical and economic aspects.
- If the heat storage bed of the PB heater is made of tabular alumina balls, the regenerator units can operate in a high-temperature regime, allowing a very high preheating temperature of combustion air (up to 1,300 °C). The frequent switching between the heating and blast periods enables the compact construction of PB units. Such a construction is characterised by low heat losses through the outer walls and low investment costs.
- The radial flow of gases through the porous bed, where the heat is stored, allows for more effective heat transfer than axial flow regenerators. The gradient of temperature in a radial direction is high (up to 1,100 °C), allowing the temperature on the cool grid in PBH to be as low as 200 °C.

Preheating the combustion air up to 1,300 °C in the PBH systems, energy consumption can be reduced, and, respectively, CO₂ emissions. With a controlled mixing of two streams (exhaust gas and preheated combustion air) in the FDV, the NO_x concentration can be reduced to below 200 mg/m³ ($p = 101,325 \text{ Pa}$, $T = 27,315 \text{ K}$) [7]. Additionally, the exhaust gas extraction position can be optimised, resulting in a more uniform temperature field and higher furnace capacity.

Figure 1 shows the regenerative burner system PH-FDV.

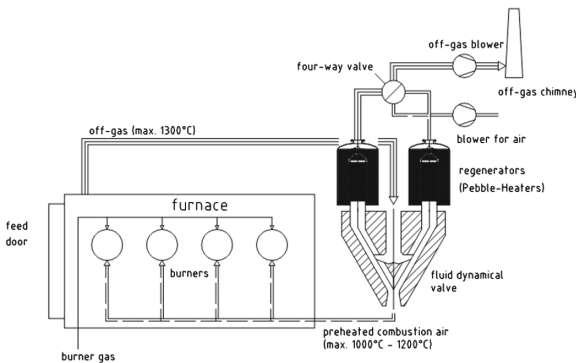


Fig. 1. Regenerative burner system with PH-FDV [7]

3 Test Facility

The test facility presented in this paper consists of PH-FDV regenerative burner system for $2,000 \text{ m}^3/\text{h}$ ($p = 101,325 \text{ Pa}$, $T = 0 \text{ K}$) and $1,200^\circ\text{C}$ flow and it will be installed instead of the old tundish preheating system presented in Fig. 2.



Fig. 2. Old tundish preheating system

Figure 3 presents the newly designed preheating system (PH-FDV regenerative burners connected to the tundish).

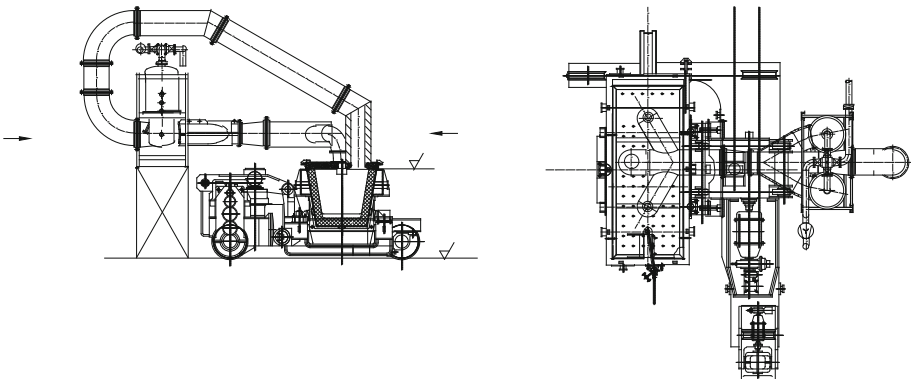


Fig. 3. Newly designed preheating system – PH-FDV regenerative burners connected to the tundish

4 Numerical Simulation of a Tundish Preheating

The burner and off-gas positioning at the tundish top cover have been done by the numerical CFD code StarCD. The simulation of transient heating of tundish with optimized top cover geometry and position of burner heads and off-gas exhaust has been performed

using real geometry of tundish without any simplification. The real geometry of a tundish stand for preheating is shown in Fig. 4, while the tundish model is shown in Fig. 5.

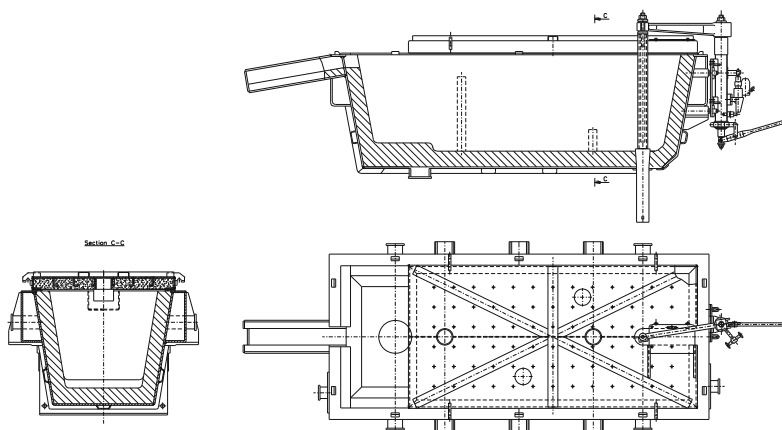


Fig. 4. Geometry of tundish on the stand for preheating in a steel plant

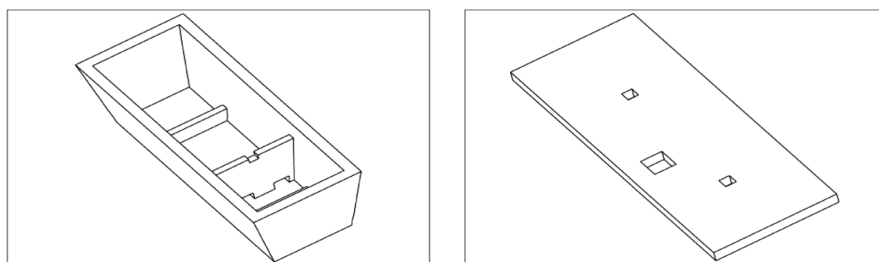


Fig. 5. Geometry of tundish model in numerical simulation

Tundish has to be heated up to 1100 °C in 5–6 h. In the present situation, average fuel consumption is 200–250 m³/h, and the combustion is irregular.

Parameters presented in Tables 1 and 2 have been used for numerical modeling. The radiation model coupled with conjugate heat transfer has been used for numerical simulation and optimization of top cover geometry (steady state and transient solution method have been done with solution algorithm - Simple and Pisco, respectively). First, we solved a stationary problem, resulting in the final temperature field at the inner surface of the tundish presented in Fig. 6. It could be seen that the uniformity of the temperature field is satisfying, and as is presented in Fig. 6, the temperature is in the range of 1028–1096 °C (pink), 1096–1164 °C (violet) and 1164–1232 °C (red). Maximal temperature (red field) is obtained at the point where a high-velocity stream of hot combustion products contacts with a tundish bottom. The maximum average temperature difference is 136 °C and the middle part of the tundish is at the lowest temperature.

On the other hand, the transient problem for 6 h of tundish preheating has been analyzed. This is a real case in this solution. The result of this analysis is presented in

Fig. 7, where the time interval of 6 h is divided into 12 short intervals of 30 min, lined in counterclockwise from case (a) to case (c).

Table 1. Characteristic parameters in numerical modeling and design optimization of tundish top cover

Item	Characteristics
Number of blocks	1,009
Number of cells in the grid	300,195
Type of the grid	Uniform
Type of analysis	Steady state & transient
Geometry of:	Identical geometry with real tundish
<i>–Inlets:</i>	
Burner 1	$\phi_{ekv} = 160 \text{ mm}$
Burner 2	$\phi_{ekv} = 160 \text{ mm}$
<i>–Outlets:</i>	
Off-gas	$\phi_{ekv} = 350 \text{ mm}$
<i>Boundary conditions:</i>	
<i>–Inlets:</i>	
Burner 1	$V = 93.9 \text{ m/s}$, $t = 1,450 \text{ }^{\circ}\text{C}$, $\rho = 0.205 \text{ kg/m}^3$
Burner 2	$V = 93.9 \text{ m/s}$, $t = 1,450 \text{ }^{\circ}\text{C}$, $\rho = 0.205 \text{ kg/m}^3$
<i>–Outlet:</i>	
Off-gas	Split
Reference pressure	101,325 Pa
Used models in simulation:	K- ϵ High Reynolds number
Turbulence model	Calculation of temperature field
Thermal model	Radiation model coupled with conjugated heat transfer

The solution of transient heating after 6 h is presented in case (c). The maximum temperature in the right separated part of the tundish after 6 h of preheating was 1193 °C - darker ochre color (at the same position as in the stationary case). The temperature field on the inner side of the tundish refractory is uniform and is in the range of 1089–1193 °C prevalence of yellow color and light ochre, with satisfactory uniformity of the temperature field and maximal average difference 104 °C.

The positions of the burner heads and exhaust outlets have been determined in this simulation. Both burner heads are positioned on a symmetrical axis of the tundish top cover. The exhaust outlet is not symmetric, and during simulation, it has been shown that there is little or no influence on whether there are two symmetric or one unsymmetrical openings for exhaust gases. Due to the simplicity of the experimental installation, it was decided to use one exhaust opening. One burner head is positioned exactly above the first, smaller step of the tundish, and the other in the right separated part of the tundish

Table 2. Parameters used in solution and numerical simulation for tundish top cover optimization

Solution method		Steady state/transient		
Solution algorithm		Simple/Pisco		
Max. global residual tolerance		1×10^{-4}		
Solver-type		Scalar		
Primary variables	Relaxation factor	Number of sweeps	Residual tolerance	Difference scheme
<i>U</i> -momentum	0.5	100	0.01	UD
<i>V</i> -momentum	0.5	100	0.01	
<i>W</i> -momentum	0.5	100	0.01	
Pressure	0.15	1,000	0.005	UD
Turbulence K-ε	0.5	100	0.01	UD
Turbulence dissipation	0.5	100	0.01	
Temperature	0.7	100	0.01	UD
Density	1			MARS
Viscosity	1			

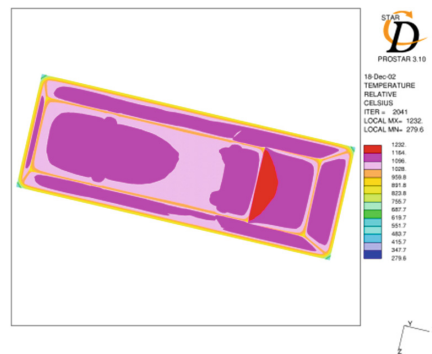


Fig. 6. Temperature field inside the refractory layer in the tundish (stationary solution)

where melted metal first touches the tundish surface when the melted steel is poured. It is essential to keep a high temperature at this surface since high-temperature differences could damage the refractory surface or cause problems in the casting of steel. A uniform temperature field at the inner side of the tundish was obtained with considerable fuel reduction (all numerical simulations have been performed with 100 m³/h of natural gas consumption) by using high-preheated air for combustion (up to 1100 °C) and high-velocity burner heads.

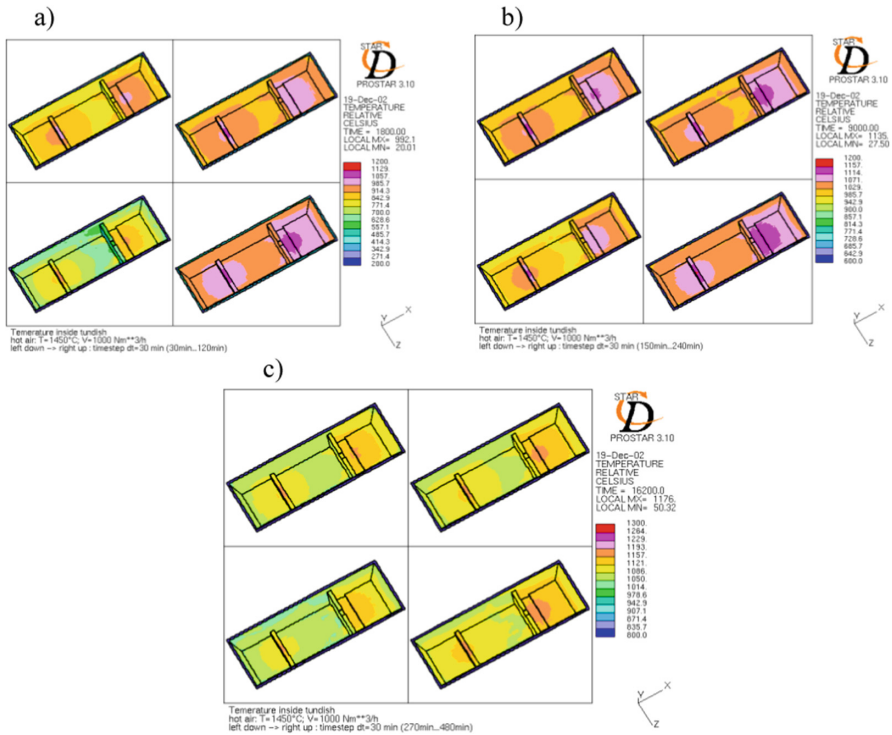


Fig. 7. Temperature field development during 6 h (transient problem)

5 Conclusions

With existing physical models, CFD can offer cost-effective solutions for many complex systems of interest in different engineering fields. Numerical simulations in designing and optimizing elements of experimental installation of regenerative burners for tundish preheating have been performed using CFD code StarCD v 3.15.

Positions of burner heads and off-gas openings have been determined in this simulation. Both burner heads are positioned on a symmetrical axis of the tundish top cover. In this paper, two cases of tundish preheating were studied (stationary and transient). For both cases, the uniformity of the temperature field was satisfactory and the temperature was in the range of 1028–1232 °C for stationary and 1089–1193 °C for transient solution. Maximum temperatures are obtained when a high-velocity stream of hot combustion products contacts a tundish bottom. A uniform temperature field at the inner side of the tundish was obtained as a result of the optimization of the position of the burner heads. Numerical simulations showed that considerable fuel reduction, up to 50%, could be obtained; however, this will be verified in further experiments.

References

1. Weber, R., Gupta, A.K., Mochida, S.: High-temperature air combustion (HiTAC): how it all started for applications in industrial furnaces and future prospects. *Appl. Energy* **278**, 115551 (2020)
2. Jasper, D.: Energieeinsparung und Verfahrensverbesserung in Aluminiumschmelzöfen. *Gaswärme International* No. 4, July/August 1998
3. Rich, L.V.: Regenerative burners in reheat furnaces. In: *Iron and Steel Engineer*, October 1989
4. Dormire, J.C.: Benefits of applying regenerative burner technology to continuous reheat furnaces. *AISE Steel Technology*, April 2000
5. Wüning, J.A., Wüning, J.G.: Keramische Brenner und Gasstrahlrohre für die Hochtemperaturanwendung. *Gaswärme International*, No. 45, June 1996
6. Stamenić, M., Jankes, G., Stevanović, D.: Numerical simulations in design and optimization of elements of experimental installation of regenerative burners for tundish preheating in steel plant US Steel – Sartid Smederevo. *Metalurgy* **10**(1), 51–69 (2004)
7. Stavanović, D., Fischer, W.: Pebble-heater twins with fluid dynamical valve – an efficient possibility for high combustion air preheating



Design of Augmented Reality-Based Android App for Simulation and Programming of Industrial Robots

Jelena Vidakovic¹  , Andrija Devic¹ , Ilija Lazarevic² ,
and Nikola Zivkovic¹ 

¹ Lola Institute, Belgrade, Serbia
jelena.vidakovic@li.rs

² Military Technical Institute, Ratka Resanovića 2, 11030 Belgrade, Serbia

Abstract. Growing customer requirements and global competition are factors that cause the integration of industrial robots and Industry 4.0 solutions increasingly. There is a high demand for robotics and automation solutions that are cost-effective, safe, and easy to install and reprogram, where the operator can work with the complex robots to solve unpredictable problems, and that can be adapted by small and medium-sized enterprises (SME). The Industry 4.0 paradigm triggered the use of Augmented Reality (AR), which has become a popular multidisciplinary research field over the last decade, in industrial facilities. In this paper, the application of AR for the simulation and programming of industrial robots is presented and demonstrated for a case of 6DoF industrial robot RL15. The design of an AR-based mobile Android app that facilitates the simulation and programming of industrial robots is proposed. The virtual robot model has been developed in Unity software based on the robot CAD model. Simulation of robot movements using the designed AR android app allows users to program, test and verify the desired robot trajectories by incorporating 3D robot virtual model motion into a real-world environment obtained from an android device in real-time.

Keywords: Industrial robot · Augmented reality · Simulation

1 Introduction

Growing customer requirements and global competition are factors that cause global industrial leaders to increasingly apply industrial robots and solutions of Industry 4.0 [1]. Industry 4.0 is the concept that encompasses digitization of manufacturing with smart factories as the primary outcome, which are being developed with the aid of advanced robotics, massive data, cloud computing, solid safety, intelligent sensors, the Internet of things, and other advanced technological developments [2]. There is a high demand for the development of robotics and automation solutions that are less expensive, safer, easier to install and re-program, where the operator can work as an assistant with the complex robots to solve unpredictable problems, and that can be adapted by small and medium-sized enterprises (SME) [3, 4]. Regarding industrial robots, Industry 4.0

solutions have been implemented in the domains of collaborative robotics, assembly tasks, inspection, pick and place tasks, packaging applications, and in various industries such as the automotive industry, logistics and warehouses, etc. [2].

The Industry 4.0 paradigm triggered the use of Augmented Reality (AR), which has become a popular multidisciplinary research field over the last decade, in networks of connected physical systems and human-machine communication [5]. The most common definition of AR by Azuma [6] states that in AR “3D virtual objects are integrated into a 3D real environment in real-time”. One of the domains of AR application in robotics is interactive robot trajectory planning and simulation [3].

A robot application program is a set of instructions that cause the robot system to move the robot’s end effector, i.e. Tool Center Point (TCP), in order to perform the desired robot task correctly [7, 8]. User-friendly robot programming methods are an essential tool and a key factor in enabling the wider application of robots in industrial production facilities [7]. AR enriches the way that users experience the real world by embedding virtual objects to coexist and interact with real objects in the real world [9]. xR (extended reality) technologies comprised of virtual reality (VR) and AR represent the technological basis for the building of a new generation of human-machine interfaces [10, 11], which allow users to give instructions to the robot in a simpler, more natural and intuitive way [12]. By reducing programming time, simplifying changes and reprogramming, and simplifying training methods, AR-based robot programming technologies provides foundations for wider usage of robots, especially in small-scale productions and SMEs.

In this study, the AR-based simulation and programming system of industrial robots developed in Unity is presented. 6DoF industrial robot RL15 installed at the Laboratory for Robotics and machine tools in Lola institute is used for demonstration. In this stage of development, for the solution of an inverse kinematic problem, RoboDK’s [13] integrated inverse kinematics solver has been used for the created robot model. The creation of the robot RL15 simulation model in Unity based on the designed CAD model is shown. The creation of a Unity-RoboDk programming and simulation environment is proposed. The main component of this research is the design of the AR-based mobile Android app for the simulation and programming of robot motions.

2 Creation of Robot Simulation Model in Unity-RoboDk Programming and Simulation Environment

Unity is one of the first freely available game engines whose popularity has only continued to increase. It has been adopted as a stand-alone simulator in several robotics areas. However, it lacks many of the tools suitable for the development of robot programming/control systems [14]. Thus, it is desirable to integrate Unity as a simulator with a dedicated robotics development framework [15]. This is commonly done using ROS [16], yielding the ROS-Unity robotics simulation suite. Other integrations are possible, such as with 3D simulation and offline/online programming environment RoboDK [13], which is used in this study.

2.1 Design of 3D Model of RL15 Robot in Unity

CAD 3D model of the robot RL15 in the laboratory environment was created in CATIA [17] software, Fig. 1, and exported into STEP (Standard for the Exchange of Product Data) file format. Prior to export, all part elements belonging to specific links are grouped, and coordinate frames attached to robot links are placed into robot joints. In order to import the robot model in Unity, the STEP file is converted into glTF file format [18]. glTF (GL Transmission Format) is an open-source standard for the efficient transfer of 3D models and scenes from one application to another. The glTF format enables the minimization of the required memory space for the transfer of 3D models. It also reduces the time required to unpack the model, which is significant with sophisticated 3D models [11].



Fig. 1. Render of the 6DoF robot RL15 in the laboratory environment.

A script performing transformations of rotational matrixes due to different orientations of frames attached to robot joints between Unity and RoboDK development environments is developed in C# language. After the glTF files are accordingly altered, they are imported into Unity. A parent-child hierarchical structure is designed according to the CAD model. In Unity, robot links are coupled by joints with specified rotational axis and their orientations.

2.2 Integration of Unity with RoboDK Software

RoboDK is a commercial cross-platform robot simulation and programming environment [13]. In this stage of development, RoboDK's integrated inverse kinematics solver has been used for the created robot model, as well as for achieving one of the two provided means for robot programming - "programming by demonstration".

In RoboDK, robot RL15 assembly is created using 'Model Mechanism or Robot' input form where dimensions of robot links are specified manually by the designer, while the STEP file for every link (part) obtained from CAD software is imported.

After transferring the 3D model from the CAD modeller to the AR development system (Unity), it was necessary to write a script that allows interaction between Unity and RoboDK via RoboDK API. Code written in C# executes mapping of robot motion in RoboDK with robot motion in Unity in real-time. Figure 2 shows programming by demonstration of RL15 robot in RoboDk (achieved by dragging of robot tool centre point by user) that has been transferred in a simulation environment in Unity in real-time. Here, the robot inverse kinematics problem has been solved by RoboDK in real-time.

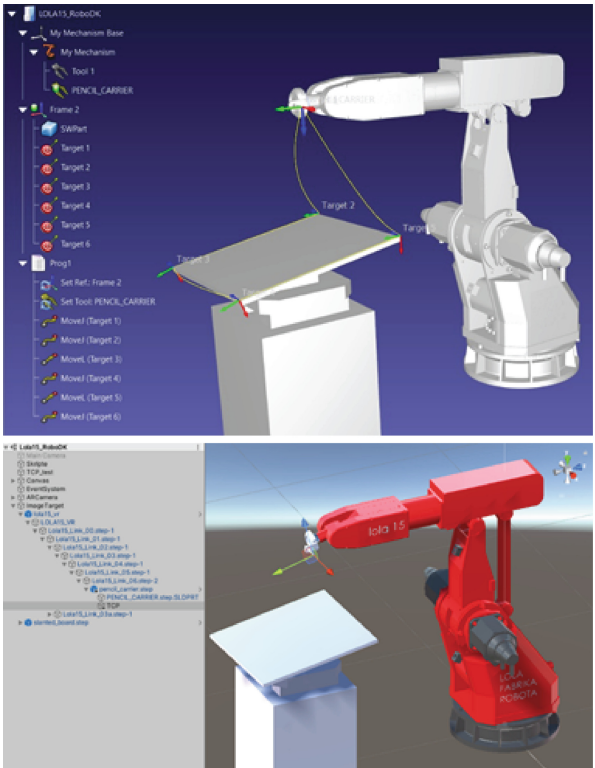


Fig. 2. Unity-RoboDk programming and simulation environment.

3 Design of AR Robot Simulation and Programming Android App in Unity

The main component of this research is the design of the AR-based mobile Android app for the simulation and programming of robot motions. Android is a Linux-based mobile operating system primarily developed for touchscreen mobiles [19]. Simulation of robot movements using the Android app allows users to test and verify the desired robot trajectories by incorporating 3D robot virtual model motion into a real-world

environment obtained from an Android device cam in real-time. For instance, robot programming can be performed in RoboDK software, and the AR-based app can be used for program verification, Fig. 3.

In marker-based AR, scanning a marker triggers an augmented experience. Vuforia [20], an AR Software Development Kit for mobile devices that provide essential tools for the creation of Augmented Reality applications, is used for generating AR robot image in a real laboratory environment, Fig. 3.



Fig. 3. AR integration of robot model in the real-world laboratory environment for simulation and verification of programmed robot motions

Another possibility of robot programming the app is allowing it by using user interface (UI) input from the phone touch-screen. In this case, an Android device is used as the simplified form of a teaching pendant. GUI for the designed AR-based Android robot programming app, with the designed buttons that allow for robot programming by manually setting the values of TCP position (x, y, z coordinate) and orientation (RPY angles), by increasing and decreasing their value is shown in Fig. 4.

Using Vuforia SDK provided a possibility to compile the designed application on devices from different manufacturers. One of the main challenges in the presented research was to ensure compatibility for different development environments (i.e. to adjust the frame settings between different software).

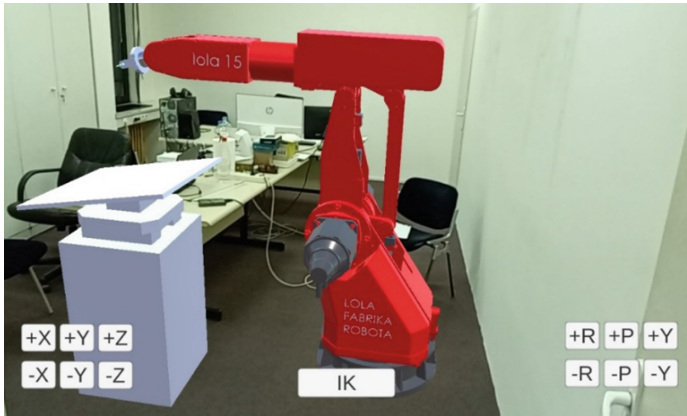


Fig. 4. GUI of AR-based Android robot programming app

4 Conclusion

In this paper, one simple application of AR for the simulation and programming of industrial robots is presented. 6DoF industrial robot RL15 installed at the Laboratory for Robotics and machine tools in Lola institute is used for demonstration. The creation of the robot simulation model in Unity based on the designed CAD model is shown. In this stage of development, to solve the inverse kinematic problem, RoboDK's integrated inverse kinematics solver has been used for the created robot model. The creation of Unity-RoboDK programming and simulation environment is described. The design of the programming and simulation Android app that facilitates the simulation and programming of industrial robots is presented. One of the main challenges was to ensure compatibility for different development environments. Simulation of robot movements using the designed AR android app allows users to program, test and verify the desired robot trajectories by incorporating 3D robot virtual model motion into a real-world environment obtained from an Android device in real-time.

Acknowledgement. This research has been supported by the research grants of the Serbian Ministry of Science, Technological Development and Innovations, grant No. 451-03-68/2023-14/200066 from 03.02.2023.

References

1. Kutia, V., Ruchel, F.L., Chrapek, K.: Simulation and programming of an industrial robot based on augmented reality. In: Modeling, Control and Information Technologies: Proceedings of International Scientific and Practical Conference, pp. 184–186. National University of Water and Environmental Engineering, Rivne, Ukraine (2019)
2. Javaid, M., Haleem, A., Singh, R.P., Suman, R.: Substantial capabilities of robotics in enhancing industry 4.0 implementation. *Cogn. Robot.* **1**, 58–75 (2021)
3. Fang, H.C., Ong, S.K., Nee, A.Y.C.: Interactive robot trajectory planning and simulation using augmented reality. *Robot. Comput.-Integr. Manuf.* **28**(2), 227–237 (2012)

4. Brogårdh, T.: Present and future robot control development—an industrial perspective. *Annu. Rev. Control* **31**(1), 69–79 (2007)
5. Makhataeva, Z., Varol, H.: Augmented reality for robotics: a review. *Robotics* **9**(2), 21 (2020)
6. Azuma, R.T.: A survey of augmented reality. *Presence: Teleoperators Virtual Environ.* **6**(4), 355–385 (1997)
7. Vidaković, J., Kvrđić, V., Lazarević, M., Dimić, Z., Mitrović, S.: Procedure for definition of end-effector orientation in planar surfaces robot applications. *Tehnika* **72**(6), 845–851 (2017)
8. Biggs, G., MacDonald, B.: A survey of robot programming systems. In: *Proceedings of the Australasian Conference on Robotics and Automation ACRA*, p. 27. Brisbane, Australia (2003)
9. Kaarlela, T., Padrao, P., Pitkäaho, T., Pieskä, S., Bobadilla, L.: Digital twins utilizing XR-technology as robotic training tools. *Machines* **11**(1), 13 (2022)
10. Fuchs, P.: *Virtual Reality Headsets—A Theoretical and Pragmatic Approach*, 1st edn. CRC Press, London (2017)
11. Dević, A., Lukić, N., Matijašević, L., Petrović, P.: Linking cad modeler and XR engine for digital twin-based collaborative robotic assembly. In: *Proceedings of the 38th International Conference on Production Engineering-ICPE-S 2021*, Čačak, Serbia, pp. 144–148, 14–15 Oct 2021
12. Ong, S.K., Yew, A.W.W., Thanigaivel, N.K., Nee, A.Y.: Augmented reality-assisted robot programming system for industrial applications. *Robot. Comput.-Integr. Manuf.* **61**, 101820 (2020)
13. RoboDK: Simulate robot applications, homepage. <https://robodk.com/>. Last accessed 15 June 2023
14. Platt, J., Ricks, K.: Comparative analysis of ROS-Unity3D and ROS-Gazebo for mobile ground robot simulation. *J. Intell. Rob. Syst.* **106**(4), 80 (2022)
15. Meng, W., Hu, Y., Lin, J., Lin, F., Teo, R.: ROS+unity: an efficient high-fidelity 3D multi-UAV navigation and control simulator in GPS-denied environments. In: *IECON 2015 - 41st Annual Conference of the IEEE Industrial Electronics Society*, Yokohama, Japan, pp. 002562–002567 (2015)
16. ROS homepage. <https://www.ros.org/>. Last accessed 14 June 2023
17. CATIA homepage. <https://www.3ds.com/products-services/catia/>. Last accessed 14 June 2023
18. glTF, homepage. <https://www.khronos.org/glTF/>. Last accessed 10 June 2021
19. Subin, E.K., Hameed, A., Sudheer, A.P.: Android based augmented reality as a social interface for low cost social robots. In: *Proceedings of the Advances in Robotics*, pp. 1–4. Association for Computing Machinery, New York, NY, United States (2017)
20. Vuforia, homepage. <https://library.vuforia.com/>. Last accessed 14 June 2023



Design of a 6DOF Robot Simulation System in ROS-Gazebo with a Brief Reference to Modern Robot Simulation Software

Nikola Zivkovic¹(✉) , Andrija Devic¹ , Jelena Vidakovic¹ , Ilija Lazarevic² ,
and Mihailo Lazarević³

¹ Lola Institute, Kneza Višeslava 70a, 11030 Belgrade, Serbia
nikola.zivkovic@li.rs

² Military Technical Institute, Ratka Resanovića 2, 11030 Belgrade, Serbia

³ Faculty of Mechanical Engineering, University of Belgrade, Kraljice Marije 16, 11120
Belgrade, Serbia

Abstract. Simulators have become indispensable tools in the field of robotics, providing researchers and engineers with a means to design, develop, and test various aspects of robotic systems in a safe, time and cost-efficient way. Currently, several robot simulation environments exist, each with its own benefits in terms of physical realism, visual realism, simulation speed, and industry support. Gazebo combined with ROS is a popular choice when it comes to simulating robots. This study presents the development of a 6DoF robot simulator in a ROS-Gazebo environment. 6DoF industrial robot RL15, installed at Laboratory for Robotics and machine tools in Lola Institute, is used for demonstration. Modelling of robot links in ROS-Gazebo environment based on the designed robot model in 3D modeller, URDF and SDF file formats, mesh files, including the inertial properties, is presented. Robot trajectory planning, trajectory generation and control design with ROS are described. A brief reference to modern software simulation tools is given.

Keywords: Industrial robot · ROS-Gazebo · Simulation

1 Introduction

Industrial systems are becoming increasingly autonomous. Simulators have become indispensable tools in the field of robotics, providing researchers and engineers with a means to design, develop, and test various aspects of robotic systems in a safe, time and cost-efficient way. The ultimate goal of the abovementioned virtual environments is to enable users to simulate and analyze the operation of robots, their interactions with the physical world, and the performance of different algorithms and control strategies, in order to refine and optimize robotic applications before implementing them in the real world. In order to accomplish this, they have to achieve faithful reproduction of the various aspects of the physical properties of robots and their surroundings. Simulators also play a crucial role in robotics education and training. They provide an accessible platform for students and beginners to learn about robotics concepts, practice programming, and gain hands-on experience with robot design and control.

Robot simulators have different quality levels in accuracy (physical or visual realism), speed of simulation, and industry support [1]. A priority list of mentioned quality-determining elements depends on the specific application. Robotic simulators come in various forms, ranging from simple 2D platforms to complex 3D environments that closely resemble real-world scenarios. They can be free or proprietary licensed, with closed or open-source architecture. Three of the most used ones by the robotic community are V-Rep (CoppeliaSim), Gazebo, and Unity [2]. Gazebo [3], paired with the Robot Operating System (ROS) [4], consistently ranks as one of the most popular robot simulators [1, 2] with a large community of users.

In this paper, a design of a simulator for the 6DoF robot in a ROS-Gazebo [5] environment is presented. 6DoF industrial robot RL15 installed at Laboratory for Robotics and machine tools in Lola Institute is used for demonstration. Modelling of robot links in ROS-Gazebo environment based on the designed robot model in 3D modeller, URDF [6] and SDF file formats, mesh files, including the inertial properties, is presented. Based on the 3D robot model in Blender, the inertia tensor for every robot link is computed using MeshLab software. Robot trajectory planning, trajectory generation and control design with ROS is described. A brief reference to other modern software simulation tools such as Unity is given.

2 Design of a Robot Simulation System in ROS-Gazebo for 6DoF Industrial Robot RL15

Robot Operating System (ROS) is an open-source Linux-based software framework extensively used in robotics, robot collaboration and machine vision research [4]. ROS ecosystem provides tools, libraries, and conventions targeted towards building applications in robotics, and is compatible with various robotic platforms [4]. It has an Industrial ROS extension [7] that is aimed at industrial robots rather than general and mobile robotics, and it is often paired with the open-source 3D robotics simulator Gazebo [8, 9]. Gazebo has OpenGL rendering, integrated several physics engines, and support code for sensor simulation and actuator control [4].

The first step in the design of a robot simulation system is to define the robot's kinematic and dynamic properties using XML file formats such as URDF (Universal Robot Description Format) or SDF (Simulation Description Format), which are equipped with elements and attributes specific to robot kinematic structure. The URDF is primarily developed for ROS purposes, while SDF is specifically designed for the Gazebo simulator. SDF file defines a simulation world or environment and multiple models inside that world. URDF uses the '<robot>' element to define one model per file, Fig. 1.

2.1 Modeling of Robot Links in ROS-Gazebo Environment

A 3D model of each link must be defined to visually represent the robot in the Gazebo simulator. Simple robots can be directly modelled inside URDF or SDF files using built-in XML elements of primitive geometric shapes; however, to avoid cumbersome and inefficient modelling for any real-world robot, the links are designed in 3D modelling software and reference file of the link model with the '<mesh>' element. The URDF



Fig. 1. URDF (left) and SDF (right) file minimal example

and SDF have a '`<mesh>`' element with a filename attribute, which needs to be set as the path to the 3D model file. The mesh files are usually STL (.stl), Wavefront (.obj) or Collada DAE (.dae) formats. The coordinate systems of each element in the URDF or SDF file are defined with Cartesian coordinates for origin position and roll, pitch and yaw angles for orientation. Coordinate systems are rigidly attached relative to the element in which they are defined. For our purposes, a 3D simplified model of each robot link of the RL15 robot is modelled in Blender [10] and exported as a .obj file. Besides visual representation, the mesh of the 3D models of robot links can be used as a boundary for collision detection (Fig. 2).

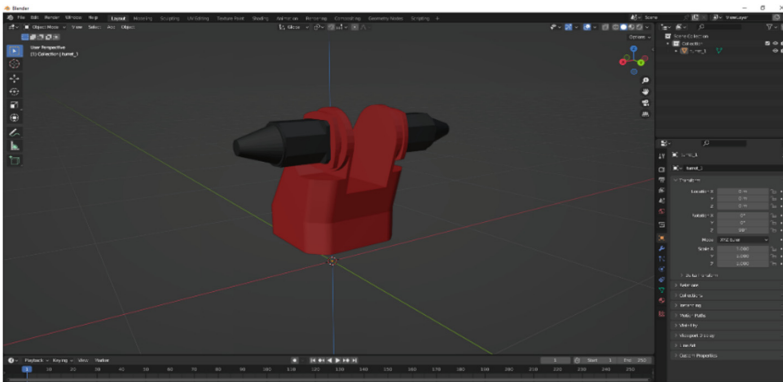


Fig. 2. Simplified model of the robot RL15 link in Blender

The inertial properties of the robot are crucial for the simulation within the physics engine in Gazebo to be as accurate as possible. Mass, the center of mass and inertia tensor are externally computed and defined inside the '`<inertial>`' element of the URDF or SDF file. Based on the 3D robot model from the Blender file, the inertia tensor for every robot link is computed using MeshLab software [11]. MeshLab calculates inertia tensors based on the volume of the mesh and unit density. The numerical values of inertia tensors

are obtained by multiplying inertia tensor elements with appropriate density calculated from mass and volume (Fig. 3).

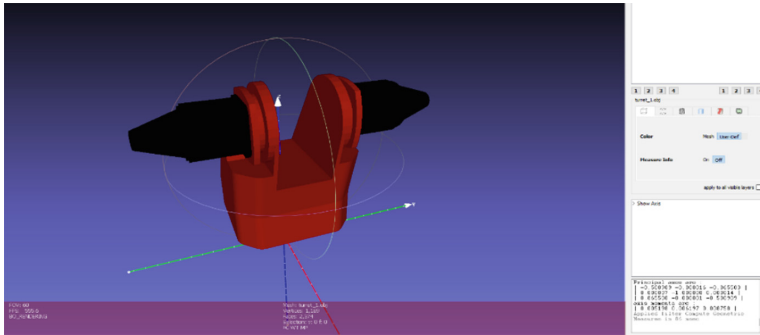


Fig. 3. RL15 link in MeshLab

2.2 Trajectory Planning, Programming and Control Design with ROS

At its core, ROS is the middleware used for inter-process communication via a publish/subscribe pattern. The second component of the ROS ecosystem is ROS packages that provide specific functionalities needed in building robotic projects. The best example in this context is the ‘ros_control’ package [12] which provides ready-for-use controllers for the most common types of robots and the necessary framework for users to develop their own controllers or modify existing ones. The package ‘move_it’ (MoveIt) provides a solution to the motion planning and trajectory programming problem [13]. The communication between ROS nodes and Gazebo is achieved using special inter-faces from package ‘gazebo_ros_pkgs’ [5]. This package defines topics, services and dynamic reconfiguration for Gazebo and exposes them to ROS nodes. The simulation process of the 6DoF industrial robot RL15 can be summarized in the following steps:

1. User specifies the desired path of the end-effector using MoveIt graphic interface;
2. MoveIt use inverse kinematics to convert the desired path from operational-space coordinates (end-effector position and orientation) to joint-space coordinates (joint angles);
3. The desired path in joint space coordinates is fed to the joint trajectory controller which generates interpolated desired joint-space trajectory. The desired joint-space trajectory can be defined as a linear, cubic, or quintic polynomial;
4. Joint trajectory controller parses desired joint-space trajectory to the PID controller;
5. Joint trajectory controller further sends an actuation signal to the Gazebo, where joints of the RL15 are actuated (Fig. 4).

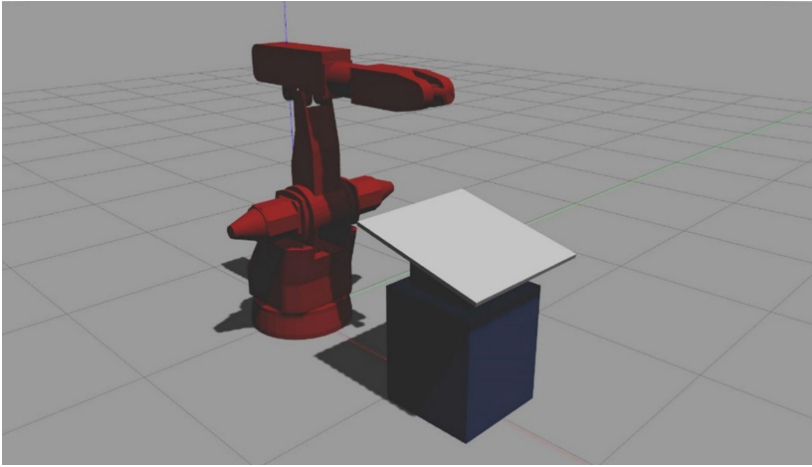


Fig. 4. Model of the RL15 in laboratory environment in Gazebo.

3 Reference to Other Notable Robot Simulation Environment

Despite the powerful capabilities of ROS-Gazebo, there is still a desire within the research community for simulation environments with improved visual fidelity [1]. Thus, many have begun to turn their attention towards the usage of game engines, such as Unity [14], due to their higher visual fidelity and developer-friendly architectures [1, 15]. When choosing an environment for robotics applications, it is important to consider features such as user-friendliness, affordability, and open-source availability. In addition, the existence of the community of users, support and accessible examples are highly valuable merits [8].

V-Rep and Unity offer a user-friendly interface and considerable flexibility when it comes to scene editing, while Gazebo demonstrated fewer capabilities in that aspect [2]. For all three simulators (V-Rep, Gazebo, and Unity), it is possible to perform a connection with ROS, but with different complexities, Gazebo and V-Rep being the easiest ones [2]. While Gazebo and V-Rep are open-source software, Unity is not. Unity provides extended reality (XR) development which has been increasingly used in the robotics domain [16]. Generally, V-Rep is tried and tested for industrial purposes, followed by Unity (which has major potential regarding XR capabilities) while Gazebo is dominant in mobile and hobby robotics. Another significant robot simulation system is the commercial cross-platform simulation environment RoboDK [8, 9, 17], which can be installed on a RaspberryPI which helps using low-cost controllers. RoboDK can also be integrated with Unity, providing inverse kinematics solutions and an applicative programming environment. In Fig. 5, the simulation environment for the RL15 robot designed in Unity is presented.

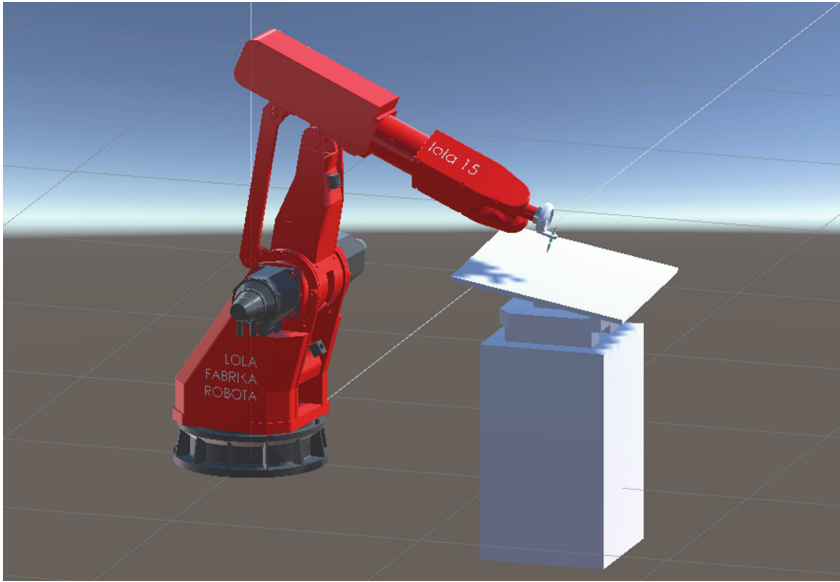


Fig. 5. Robot simulation environment for robot RL15 created in Unity.

4 Conclusion

In the presented paper, a design of a simulator for a 6DoF robot in a ROS-Gazebo environment is presented. Modelling of robot links in ROS-Gazebo based on designed robot model in 3D modeller, URDF and SDF file formats, mesh files, including the inertial properties, is presented. Based on the 3D robot model from the Blender file, the inertia tensor for every robot link is computed using MeshLab software. Robot trajectory planning, generation and control design with ROS are described. A brief reference to modern software simulation tools such as Unity is given. 6DoF industrial robot installed RL15 at Laboratory for Robotics and machine tools in Lola institute is used for demonstration.

Acknowledgment. This research has been supported by the research grants of the Serbian Ministry of Science, Technological Development and Innovations, grant No. 451-03-68/2023-14/200066 and 451-03-47/2023-01/ 200105 from 03.02.2023.

References

1. Platt, J., Ricks, K.: Comparative analysis of ROS-Unity3D and ROS-Gazebo for mobile ground robot simulation. *J. Intell. Rob. Syst.* **106**(4), 80 (2022)
2. De Melo, M.S.P., da Silva Neto, J.G., Da Silva, P.J.L., Teixeira, J.M.X.N., Teichrieb, V.: Analysis and comparison of robotics 3d simulators. In *21st Symposium on Virtual and Augmented Reality (SVR)*, pp. 242–251. IEEE (2019)
3. Gazebo 11 Homepage, <https://classic.gazebosim.org/>. Accessed 14 June 2023

4. ROS Homepage, <https://www.ros.org/>. Accessed 14 June 2023
5. Gazebo-ROS packages Github page, https://github.com/ros-simulation/gazebo_ros_pkgs. Accessed 14 June 2023
6. Tola, D., Corke, P.: Understanding URDF: a survey based on user experience. arXiv preprint [arXiv:2302.13442](https://arxiv.org/abs/2302.13442)
7. ROS Industrial, <https://rosindustrial.org/>. Accessed 14 June 2023
8. Al-Geddawy, T.: A digital twin creation method for an open source low-cost changeable learning factory. *Procedia Manuf.* **51**, 1799–1805 (2020)
9. Kousi, N., Gkournelos, C., Aivaliotis, S., Giannoulis, C., Michalos, G., Makris, S.: Digital twin for adaptation of robots' behavior in flexible robotic assembly lines. *Procedia Manuf.* **28**, 121–126 (2019)
10. Blender Homepage, <https://www.blender.org/>. Accessed 14 June 2023
11. MeshLab Homepage, <https://www.meshlab.net/>. Accessed 14 June 2023
12. Chitta, S., Marder-Eppstein, E., Meeussen, W., Pradeep, V., Rodríguez Tsouroukdissian, A., Bohren, J., Coleman, D., Magyar, B., Raiola, G., Lüdtkke, M., Fernandez Perdomo, E.: *ros_control*: a generic and simple control framework for ROS. *J. Open Source Soft.* **2**(20), 456 (2017)
13. Chitta, S., Sucan, I., Cousins, S.: MoveIt! [ROS Topics]. *IEEE Robot. Autom. Mag.* **19**(1), 18–19 (2012). <https://doi.org/10.1109/MRA.2011.2181749>
14. Unity Homepage, <https://unity.com/>. Accessed 14 June 2023
15. Mattingly, W.A., Chang, D.-J., Paris, R., Smith, N., Blevins, J., Ouyang, M.: Robot design using unity for computer games and robotic simulations. In: 17th International Conference on Computer Games (CGAMES), pp. 56–59 (2012). <https://doi.org/10.1109/CGames.2012.6314552>
16. Makhataeva, Z., Varol, H.A.: Augmented reality for robotics: a review. *Robotics* **9**(2), 21 (2020)
17. RoboDK. Simulate Robot Applications. In: <https://robodk.com/>. Accessed 12 June 2023



Efficient Computation Method for Total Fatigue Life of Aircraft Structural Components

Ivana Vasović Maksimović¹(✉), Mirko Maksimović², Katarina Maksimović³,
and Stevan Maksimović⁴

¹ Lola Institute, Kneza Višeslava 70, Belgrade, Serbia
ivanavvasovic@gmail.com

² Belgrade Waterworks and Sewerage, Kneza Miloša 27, Belgrade, Serbia

³ City of Belgrade – City Government, Belgrade, Serbia

⁴ Military Technical Institute, Belgrade, Serbia

Abstract. The primary focus of this study is the development of efficient calculation methods and application software for the fatigue strength analysis of aircraft structural elements. This primarily indicates the long life of aircraft structure elements exposed to the spectrum of cyclical loads. Therefore, the total fatigue life can be divided into two parts: the first until the appearance of the initial damage, and the second after the appearance of the initial damage, that is, crack propagation. The conventional approach uses small-cycle fatigue characteristics to estimate the life until the appearance of an initial crack and dynamic characteristics to analyze crack propagation. In order to avoid very expensive and time-consuming tests, the Strain Energy Density (SED) method was used here, which uses the same low-cycle characteristics for both appearance and crack propagation. The Finite Element Method (FEM) was used to assess the life of complex constructions, such as aircraft, for the analysis of the stress state. By combining the SED method with FEM for stress state analysis, a reliable and efficient method for estimating the total life of aircraft structural elements is obtained. The results show that the predicted results agree well with the test data.

Keywords: Aircraft structures · Fatigue · Crack initiation · Crack growth · Total fatigue life · Strain Energy Density (SED) · Finite Element Method (FEM)

1 Introduction

The research in this work is primarily focused on the development of suitable methods and application software for the lifetime verification of the metal elements of an aircraft structure exposed to cyclic loads in the form of spectra. One of the primary goals of this research is to establish effective calculation methods for estimating the life of aircraft elements under the influence of the load spectrum. In work related to the fatigue behavior

of real aircraft structural components under service loading, one of the fundamental issues is the evaluation and formulation of adequate relations that should describe fatigue life. Fatigue, as a very complex process, can be considered and analyzed as: (1) the crack initiation phase and (2) the crack propagation phase. In this paper, a computational model to estimate the total fatigue life of aircraft structural components was developed.

The aircraft structural components and structural components of other mechanical systems are components with geometrical discontinuities, known as components with notches or notched structural components. As a rule, cracks appear at critical points that lie at the bases of the notches. Therefore, notches play an important role in the investigation of fatigue life. The Total Fatigue Life (TFL) of concrete aircraft structural components is the sum of the Crack Initiation and Crack Growth Life (CIL and CGL, respectively) and mainly depends on the number, form, size, position, and arrangement of its notches.

CIL computation of aircraft structural components understands knowing aircraft flight cycles, cyclic events in flight cycles, cyclic properties of the material used or nominated for workmanship, the stress-strain response at critical points or points of expected crack initiation, and damages initiated by all cyclic events.

The stress-strain response at the critical point (local stress-strain response) for all cyclic events and the method of identification and counting of those events have special importance. The local stress-strain response may be determined by strain gauge measurement, the Finite Element Method (FEM), and methods that relate local stresses (σ_{loc}) and strains (ϵ_{loc}) to nominal values. The identification and counting of cyclic events in aircraft flight cycles may be carried out using the rain flow counting method, range pair method [1], and similar good methods of the reservoir [2].

The method of exact damages and CIL computation still does not always exist. All these are based on numerous hypotheses (rules). Because of its simplicity, Palmgreen-Miner's linear damage accumulation rule is mostly used [1–5].

For TFL computation, several investigators [6, 7] have combined the two approaches by combining the computed results for crack initiation and crack growth.

The aim of this paper was to compute (to predict) the TFL ($TFL = CIL + CGL$) of notched structural components using the same input parameters (cyclic properties) for the CIL and CGL computations. Methodologies of CIL and CGL computation of notched structural components based on the criteria of low-cycle fatigue (LCF) [1, 8] and Strain Energy Density (SED) [9] are described in this paper. The aim was to predict the total fatigue life of structural components using the same input parameters (low cyclic properties) for the crack initiation and crack growth propagation stages. Therefore, the formulated model presents an effective procedure that enables us to predict the CIL and CGL life and establish an estimated fatigue life schedule by combining the finite element and strain life methods, as well as the strain density theory. The initiation phase is modeled using strain-life and cyclic stress-strain curves, whereas the propagation phase uses the crack growth rate versus stress intensity curves. In this work, the crack growth rate is analyzed by using the SED theory. Therefore, the same parameters were

used to predict the fatigue life to crack growth, as well as to estimate the fatigue life to crack initiation.

2 Initial Fatigue Life Estimation

To estimate the life until the appearance of the initial damage of structural elements subjected to cyclic loads and where material plasticity occurs in critical zones, it is necessary to use the cyclic behavior curves of the material. Here, a complete procedure for estimating the lifetime until the appearance of initial damage is presented, where the Manson-Coffin relation was used for estimating the lifetime

$$\frac{\Delta \varepsilon}{2} = \frac{\sigma_f'}{E} N_f^b + \varepsilon_f' N_f^c \quad (1)$$

where: σ_f' - coefficient of fatigue strength, b - exponent of fatigue strength (Basquin's exponent), ε_f' - coefficient of fatigue ductility, c - exponent of fatigue ductility, E - modulus of elasticity and N_f - number of cycles until the appearance of initial cracking. In Eq. (1), the total deformation $\Delta \varepsilon$ is equal to the sum of elastic, $\Delta \varepsilon_e$ and plastic deformation, $\Delta \varepsilon_p$ and has the form:

$$\frac{\Delta \varepsilon}{2} = \frac{\Delta \varepsilon_e}{2} + \frac{\Delta \varepsilon_p}{2} \quad (2)$$

The Manson-Coffin Eq. (1) represents the simplest relationship for estimating the age until the appearance of initial damage. Equation (1) can be expressed graphically, and Fig. 1 represents the sum of the elastic and plastic deformations ($\varepsilon_t = \varepsilon_e + \varepsilon_p$).

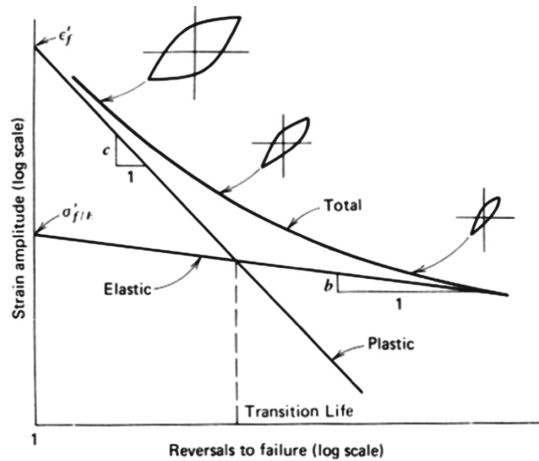


Fig. 1. Curve ε - N for total fatigue life estimation

In the case of a “graded” load spectrum, such as usually occurs (or is defined) in the flight of an airplane, mean stress, σ_m , occurs. Earlier research has shown that the influence of medium stress on age until the appearance of initial damage is important, but the same does not exist in the Manson-Coffin relationship. In order to include the influence of medium stresses on the estimation of the lifetime until the appearance of the initial damage, various relations were established, of which the following relations are often used: Morrow, Manson-Halford, and Smith-Watson-Topper low-cycle fatigue curve [10–12].

Morrow’s relation for estimating the life to the onset of initial damage

Morrow was the first to propose a modification to include the effect of medium stress in the lifetime estimate in the form:

$$\frac{\Delta \varepsilon}{2} = \frac{\sigma_f' - \sigma_m}{E} N_f^b + \varepsilon_f' N_f^c \quad (3)$$

The difference between this curve and the basic low-cycle fatigue curve is that considering the mean stress σ_m , only the elastic component of the total amplitude deformation is modified.

Manson-Halford’s relation

In the Manson–Halford low-cycle fatigue curve equation has the form:

$$\frac{\Delta \varepsilon}{2} = \frac{\sigma_f' - \sigma_m}{E} N_f^b + \left(\frac{\sigma_f' - \sigma_m}{\sigma_f'} \right)^{\frac{c}{b}} \varepsilon_f' N_f^c \quad (4)$$

Smith-Watson-Topper relation

The Smith-Watson-Topper (SWT) relation for describing the low-cycle fatigue curve has the form:

$$P_{SWT} = \sqrt{(\sigma_f')^2 (N_f)^{2b + E \sigma_f' \varepsilon_f' (N_f)^{b+c}}} \sqrt{\sigma \frac{\Delta \varepsilon}{2}}_{max} \quad (5)$$

whereby the influence of medium stresses is included via the dependence

$$\sigma_m \frac{\Delta \sigma}{2}_{max} \quad (6)$$

The notation P_{SWT} in (5) refers to the Smith-Watson-Topper parameter. The relation SWT (5) defines that there is no fatigue damage in situations where the value of the maximum stress, σ_{max} , is zero or has a negative value, which is not entirely true.

3 Estimate of the Remaining Life of the Wing-Fuselage Connection

3.1 Crack Growth Based on the Theory of Strain Energy Density

In this section, the procedure for crack growth computation is established based on SED theory. The key value in the process of crack growth analysis is the stress intensity factor range, ΔK_I . Near the stress intensity factor range ΔK_I , a threshold stress intensity factor range ΔK_{th} exists, that is the value below which fatigue cracks do not grow. Therefore, we will formulate a relation for crack growth rate da/dN_p as a function of a stress intensity range ΔK_I as well as a threshold stress intensity factor range ΔK_{th} .

The first important parameter in fatigue crack analysis is the length of the process zone ahead of the crack tip, d^* (Fig. 2). This parameter can be considered as a constant by the same authors [13] and as a variable (as a function of ΔK_I) by others [14, 15]. The length d^* can be expressed as a function of ΔK_I and ΔK_{th} [15], as follows:

$$d^* = \frac{\Delta K_I^2 - \Delta K_{th}^2}{\pi E \sigma_y'} \quad (7)$$

where ΔK_{th} is the range of the threshold stress intensity factor and σ_y' is the cyclic yield stress. In order to define the required relation based on parameters ϵ_f' , σ_f' and n' , we first need to define a relation for the cyclic plastic strain energy density ΔW_p in the units of Joule per cycle per unit volume [6, 7] as:

$$\Delta W_p = \left(\frac{1 - n'}{1 + n'} \right) \Delta \sigma_{eq} \Delta \epsilon_{eq} \quad (8)$$

where are $\Delta \sigma_{eq}$, $\Delta \epsilon_{eq}$ equivalent stress and strain along the crack line ($\theta = 0$), respectively, or

$$\Delta W_p = \left(\frac{1 - n'}{1 + n'} \right) \frac{\Delta K_I^2 \overline{\sigma_{eq}}(0; n') \overline{\epsilon_{eq}}(0; n')}{E I_{n'} r} \quad (9)$$

where ΔK_I is the range of stress intensity factors under mode I loading, or for the plate with a central hole and crack ΔK_I can be expressed as [16]:

$$\Delta K_I = \Delta \sigma \sqrt{\pi a} \left[1 + 2.365 \left(\frac{R}{R + a} \right)^{2.4} \right] \quad (10)$$

where a is the crack length, $\Delta \sigma$ - stress range, R - the radius of a central hole, and $I_{n'}$ is the non-dimensional parameter of exponent n' . Terms r and θ are the radial and angular positions, respectively, of any point from the crack tip, as shown in Fig. 8.

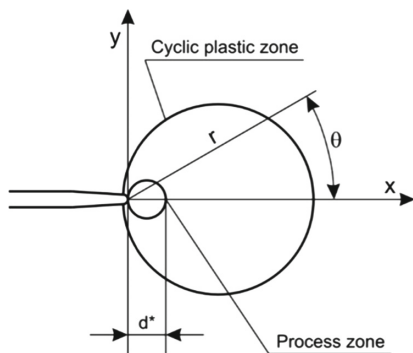


Fig. 2. A crack tip zones of damage

Furthermore, and $\overline{\sigma_{eq}}(0; n')$, $\overline{\varepsilon_{eq}}(0; n')$ are non-dimensional angular ($\theta = 0$) distribution functions for stress and strain, respectively.

Equation (9) presents the distribution of the plastic strain energy density per cycle ahead of the crack tip. The unknown values are the angular distribution functions of the equivalent stress, strain, and parameter I_n' . The area near the crack tip is known as the process zone [14]. The next area is the region between the cyclic plastic zone and the process zone. The area where the damage is mainly accumulated is the process zone.

Since we defined the length d^* it was possible to determine the plastic energy ω_p dissipated per cycle per unit growth. The required relation for ω_p can be obtained by integrating the relation for the plastic strain energy density (11) and if r is substituted by d^* , or:

$$\omega_p = \int_0^{d^*} \left(\frac{1 - n'}{1 + n'} \right) \frac{\Delta K_I^2 \psi(n')}{EI_n' d^*} dr \quad (11)$$

after integrating,

$$\omega_p = \left(\frac{1 - n'}{1 + n'} \right) \frac{\Delta K_I^2 \psi}{EI_n'} \quad (12)$$

where $\psi = (\overline{\sigma_{ij}}(0; n') \overline{\varepsilon_{ij}}(0; n'))$ and can be determined experimentally. It is known that the external load increases from zero at the crack tip; it is blunted first and starts to open when the stress intensity factor reaches the threshold value, K_{th} . After that, loading blunts the crack tip, and when the load reaches the maximum value, the crack tip becomes blunter, causing the crack to move by a certain distance. Based on the previous statement, it is possible to formulate $\Delta K_I = K_{max} - K_{min}$ instead of $\Delta K_I = K_{max} - K_{th}$, as follows:

$$\omega_p = \left(\frac{1 - n'}{1 + n'} \right) \frac{\psi (K_{max} - K_{th})}{EI_n'} \quad (13)$$

The plastic energy dissipated per cycle per unit growth can be formulated as a function of the energy absorbed until fracture, W_c , as follows:

$$W_c \delta a = \omega_p \quad (14)$$

Therefore, the relation for δa becomes:

$$\delta a = \frac{da}{dN_p} = \frac{(1 - n')\psi}{4EI_{n'}\sigma_f'\varepsilon_f'}(K_{max} - K_{th})^2 \quad (15)$$

Equation (15) presents a special case for $R = 0$ ($R = K_{min}/K_{max}$). In that case, $K_{max} = \Delta K$, $K_{th} = \Delta K_{th}$, where is ΔK_{th} a material constant and it is sensitive to stress ratio R . An important aspect of the fatigue design of structural elements is the "design of safe cracks" based on the crack growth threshold. Of much concern, however, is the effect of the stress ratio on the fatigue threshold stress intensity range ΔK_{th} . Regarding the R -effect on ΔK_{th} , many relations, mostly empirical, have been proposed, some of which are [17]:

$$\begin{aligned} \Delta K_{th} &= K_{max}(1 - R); \Delta K_{th} = K_{th0}(1 - R)^{\frac{1}{2}}; \Delta K_{th} = K_{th0}(1 - R)^\gamma; \\ \Delta K_{th} &= K_{th0}(1 - R^2); \Delta K_{th} = K_{th0}\left(\frac{1 - R}{1 + R}\right)^{\frac{1}{2}} \end{aligned} \quad (16)$$

where ΔK_{th0} is the threshold stress intensity range at $R = 0$ and γ is a material constant that varies from zero to unity. For most materials, γ was 0.71 [14]. Despite the large number of proposed relations (16) between ΔK_{th} and R , a general relation does not appear to exist. Such a general relation would be most welcome.

By substituting the values of K_{max} and K_{th} for the general stress ratio R , the fatigue crack growth relations are expressed as follows:

$$\delta a = \frac{da}{dN_p} = \frac{(1 - n')\psi}{4EI_{n'}\sigma_f'\varepsilon_f'}[\Delta K_I - \Delta K_{th0}(1 - R)^\gamma]^2 \quad (17)$$

$$\delta a = \frac{da}{dN_p} = \frac{(1 - n')\psi}{4EI_{n'}\sigma_f'\varepsilon_f'}\left[\Delta K_I - \Delta K_{th0}\left(\frac{1 - R}{1 + R}\right)^{\frac{1}{2}}\right]^2 \quad (18)$$

It is clear from Eqs. (17) and (18) that with an increase in the stress ratio R , ΔK_{th} decreases and ΔK_I increases, increasing the fatigue crack growth rate. However, the influence is more pronounced in stage I (near-threshold region of da/dN_p vs ΔK_I plot) where ΔK_I and ΔK_{th} are comparable to those in other regions of the plot. This is consistent with the experimental results [14].

From the fatigue crack growth relations (15) and (16) or (17) and (18), it can be seen that they require only the mechanical and fatigue properties E , σ'_f , ε'_f and n' , which presents a great advantage in the application of this procedure.

3.2 Crack Growth Life Computation

To compute the CGL, Eq. (18) was used. A crack growth model of the flat specimen with a central hole with two cracks was considered. For this purpose, the stress intensity factor is defined by Eq. (10): Fig. 10 are shown computation (prediction) results - the relation between crack length a and the number of blocks of variable force.

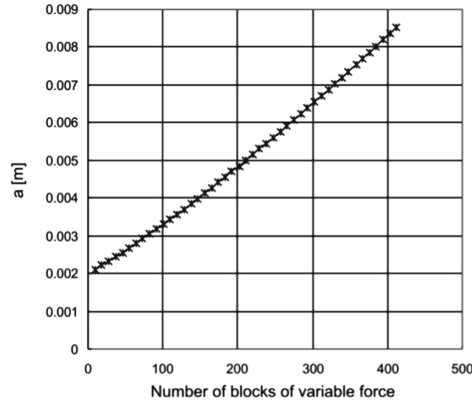


Fig. 3. Graphical interpretation of CGL computation of flat specimen with a central hole

The CGL obtained by computation, according to Fig. 3, amounts to 412 blocks, and this result has a good correlation with the experimentally obtained results (See Table 2).

3.3 Numerical Examples

The validity of the presented strain energy density method can only be assessed through a comparison with experimental data, which is the focus of this section. In addition, stress intensity factors were obtained using analytical and numerical approaches. When the numerical simulation was used for the stress intensity factor for crack growth life estimation, the evaluated polynomial expressions were used for the corrective function, which included the geometry of the structural element.

4 Structural Analysis of Aircraft Wing-Fuselage Connection Using FEM

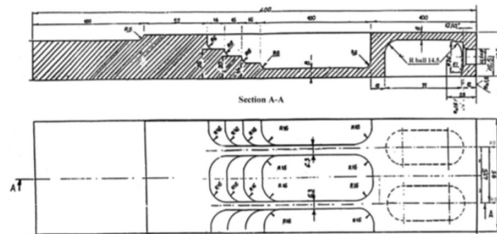
Calculation estimates of the total life were made here, which included calculations until the appearance of the initial damage, as well as an estimate of the remaining life after the appearance of the initial crack, that is, during crack propagation. For this purpose, part of the wing structure at the wing/fuselage junction was considered. In order to verify the calculation procedure for the estimation of the life, representative parts of the wing were made in the form of “complex” test tubes, which represent a real part of the structure of the wing of the aircraft. Calculation estimates of life and tests were performed using the same (“real”) load spectrum. In the following discussion, only the essential part of the research results will be presented, both in the domain of calculation estimates and the results of fatigue tests.

4.1 Life Estimation Until the Appearance of the Initial Damage

Figure 4 shows the part of the wing-fuselage connection (the part on the side of the wing), which is practically the subject of the analysis. A similar part of the structure, with which this part is connected with special screws, is located on the other side. The analysis of the stress state was performed using FEM. For this purpose, due to the systematicity of the research, a linear analysis of FEM, Figs. 7 and 8, as well as an elastoplastic analysis of FME, Figs. 10 and 11. Elastoplastic analysis was performed using FEM for the cyclic characteristics of the behavior of duralumin, Fig. 9.



a) The critical zone of the wing-fuselage connection



b) Part of the wing connection in the critical zone

Fig. 4. Part of the aircraft wing-fuselage connection (part on the wing side)

Figure 5 shows the load spectrum of the part of the wing-fuselage connection (one block corresponds to 50 h of aircraft flight). Table 1 shows the load spectrum as well as the corresponding stresses for each load level in the spectrum. To determine the stress state for certain load levels, the elastic-plastic analysis of FEM was used. The material of the wing joint, that is, the part of the wing that is the subject of analysis, is made of duralumin alloy 2024-T351. The cyclic behavior curve of the material is shown in Fig. 9.

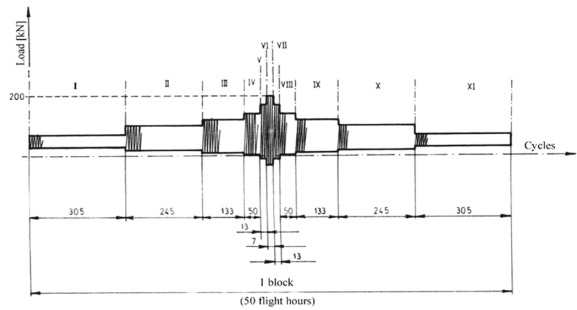


Fig. 5. Load spectrum in the wing-fuselage connection (per one screw in the wing-fuselage connection)

Table 1. Load spectrum and corresponding stresses in the critical position in the wing/fuselage connection section

Load level	n_i	$F_{\min}[\text{kN}]$	$F_{\max}[\text{kN}]$	$\sigma_{\min}[\text{MPa}]$	$\sigma_{\max}[\text{MPa}]$
I	305	13.3	33.3	58.8	147.2
II	245	9.30	46.6	41.0	205.5
III	133	6.0	60.0	28.0	279.8
IV	50	3.0	73.3	13.3	313.8
V	13	-4.6	86.6	20.3	336.5
VI	7	-14.0	100.0	61.9	366.4
VII	13	-4.6	86.6	20.3	336.5
VIII	50	3.0	73.3	13.3	313.8
IX	133	6.0	60.0	28.0	279.8
X	245	9.3	46.6	41.0	205.5
XI	305	13.3	33.3	58.8	147.2

Figure 6 shows the finite element model of the wing part at the point of connection of the wing to the aircraft's fuselage. When it comes to structural elements with complex geometric shapes and loads, it is necessary first to determine the potentially critical zone in which the appearance of damage under the effect of cyclic loads is first expected. For this purpose, FEM was used. When estimating the age until the appearance of initial damage, a precise calculation of stress states is required, especially in the critical zone of the structure. Two methods can be used to determine the elastoplastic stress state:

- Using the linear analysis of FEM, Figs. 7 and 8, cyclic material behavior curves and Neuber curves, the intersection of which determines the elastoplastic stress state;
- Using elastoplastic FEM analysis for all load levels within the spectrum, Figs. 10 and 11.

The elastoplastic analysis of the FEM was used for the calculation assessment of the life until the appearance of initial damage, and the calculation results are given in Table 1. Neuber's approach based on linear FEM analysis is used here only as a control calculation.

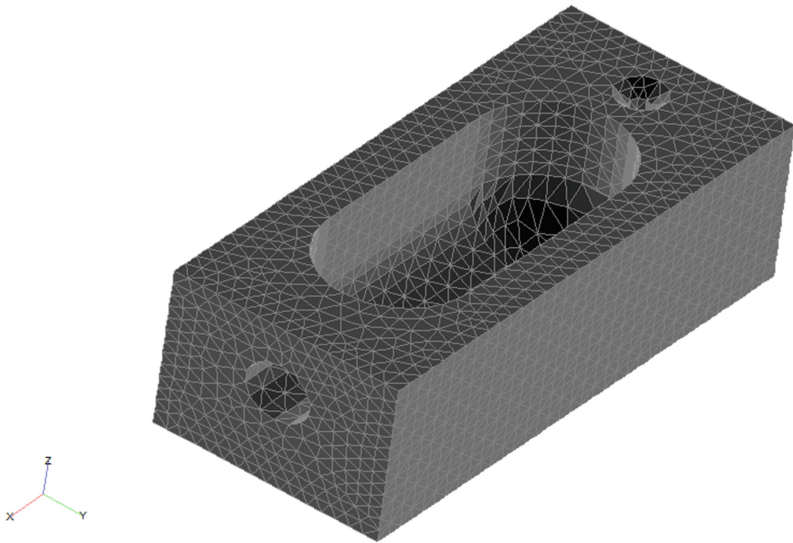


Fig. 6. Finite element model of the wing-fuselage connection part of the aircraft

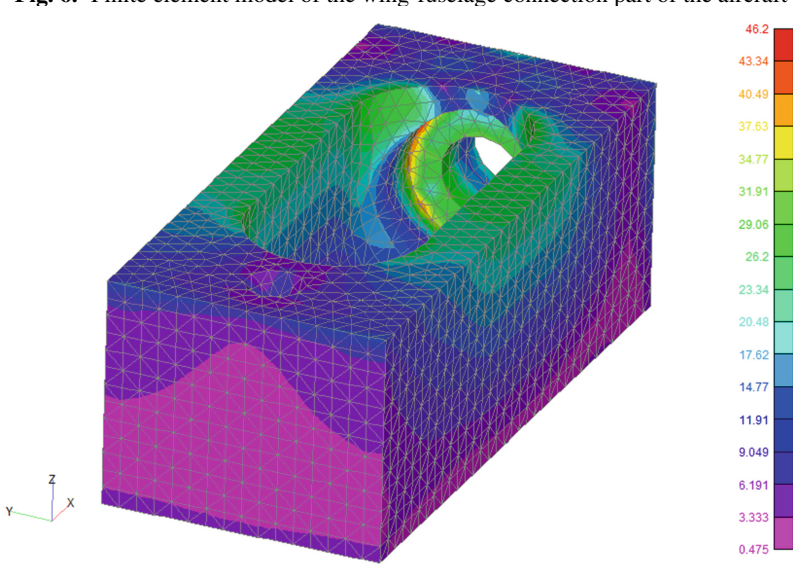


Fig. 7. Linear FEM analysis in the part of the wing structure for the maximum load in the spectrum (Level VI in the spectrum)

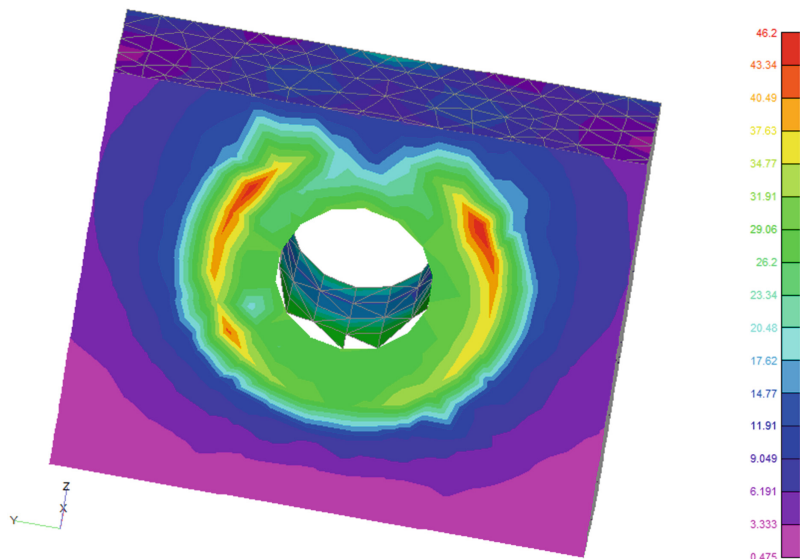


Fig. 8. Detail of the stress distribution in the critical part of the wing-fuselage connection using linear FEM analysis (for load level VI in the spectrum)

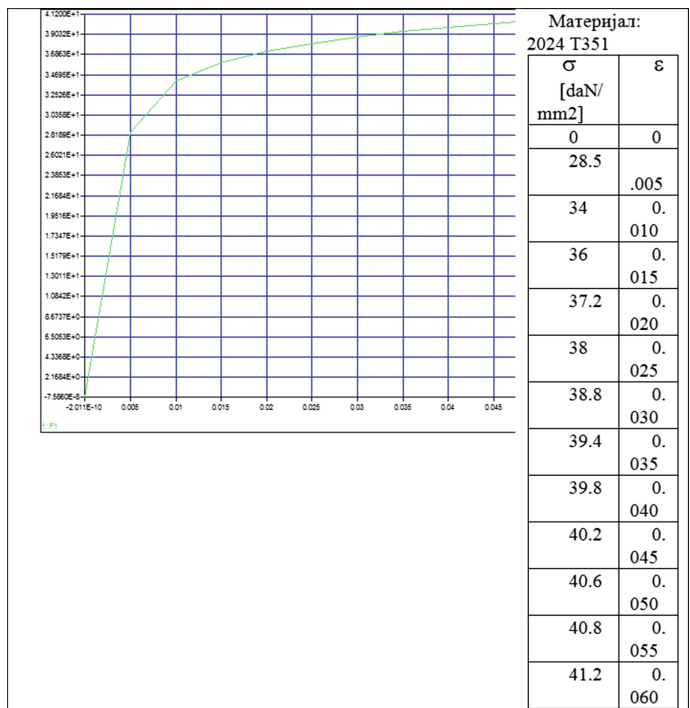


Fig. 9. Curve of elastic-plastic behavior of the material (2024 T351 duralumin)

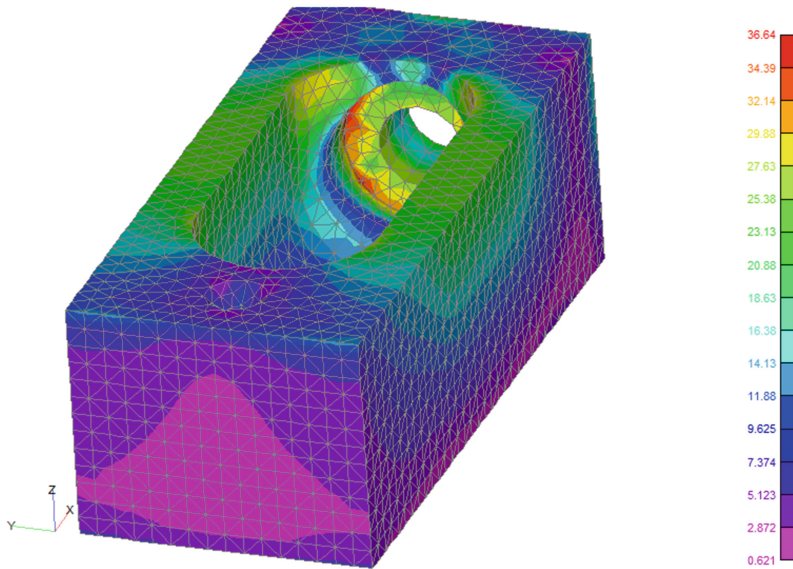


Fig. 10. Elastoplastic FEM analysis in the part of the wing structure for the maximum load in the spectrum (Level VI in the spectrum)

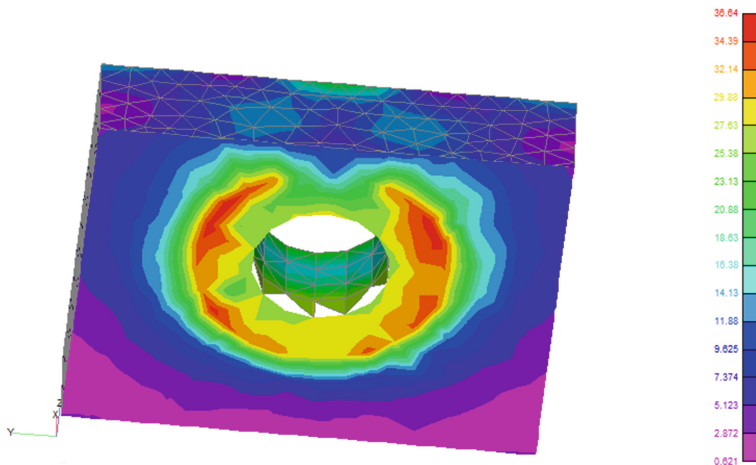


Fig. 11. Detail of the stress distribution in the critical part of the wing-fuselage connection using elastoplastic FEM analysis (for load level VI in the spectrum)

4.2 Assessment of the Age Until the Appearance of Initial Damage

For a given load block, Fig. 3, as well as the stress states determined for each load level, the number of blocks until the appearance of initial damage can be determined. To estimate the lifetime until the appearance of initial damage, expressed through the number of blocks N_{bl} , the Morrow (3) and SWT (Swith-Watson-Topper) relations, given

by (5), were used. Remaining life and experience have shown that it is the most accurate for century estimates with the influence of medium stresses. Finally, to estimate the lifetime until the appearance of initial damage, the elastoplastic analysis of FEM was used to determine the stress states in conjunction with the SWT (Swth-Watson-Topper) relation. This approach determined the number of blocks until the appearance of initial damage, $N_{bl,i}$. The life determined by calculation until the appearance of initial damage, expressed through the number of blocks, using the previous relations, is given in Table 2.

Table 2. Life to damage assessment of the wing-fuselage connection according to (SWT) and Morrow

Do pojave inicijalnog oštećenja

Podaci o opterećenju

2024 T351 Naziv: 2024 T351

Smin1	58.800	Smax1	147.200	n1	305
Smin2	41.000	Smax2	205.500	n2	245
Smin3	28.000	Smax3	279.800	n3	133
Smin4	13.300	Smax4	313.800	n4	50
Smin5	20.300	Smax5	336.500	n5	13
Smin6	61.900	Smax6	366.400	n6	7
Smin7	20.300	Smax7	336.500	n7	13
Smin8	13.300	Smax8	313.800	n8	50
Smin9	28.000	Smax9	279.800	n9	133
Smin10	41.000	Smax10	205.500	n10	245
Smin11	58.800	Smax11	147.200	n11	305
Smin12	0.000	Smax12	0.000	n12	0
Smin13	0.000	Smax13	0.000	n13	0
Smin14	0.000	Smax14	0.000	n14	0
Smin15	0.000	Smax15	0.000	n15	0
Smin16	0.000	Smax16	0.000	n16	0
Smin17	0.000	Smax17	0.000	n17	0
Smin18	0.000	Smax18	0.000	n18	0
Smin19	0.000	Smax19	0.000	n19	0
Smin20	0.000	Smax20	0.000	n20	0
Smin21	0.000	Smax21	0.000	n21	0

Podaci o materijalu

Naziv Materijala: 2024 T351

E: 70430 Kprim: 794

Epsilon: 0.334 n prim: 0.0919

Sigma: 740 b: -0.0701

Kt: 1.49 c: -1.2

Broj blokova SWT: 480.1830472088

Broj blokova Morrow: 505.5855210519

Broj nivoa: 11

Izračunaj

Makim	Minima	sig1	sig2	eps1	eps2	E1	Broj Ciklusa	DeltaH/Ni	Izabrani test
147.2	58.8	219.2995	87.582719	0.0031145	0.00124	0.00209	5522804.3	18107.555	Morrow
205.5	41	305.1526	60.047720	0.0043629	0.00088	0.00291	3501810.8	14293.105	Morrow
279.8	28	398.5146	23.342555	0.0062108	0.00088	0.00398	971327.44	7303.2139	Morrow
313.8	13.3	428.6573	-19.01452	0.0073078	0.00094	0.00449	125191.51	2503.8303	Morrow
336.5	20.3	445.1848	-25.82688	0.0081647	0.00147	0.00486	53123.145	4086.3957	Morrow
366.4	61.9	464.2674	10.641242	0.0095030	0.00306	0.00542	42304.004	6403.4232	Morrow
336.5	20.3	445.1848	-25.82688	0.0081647	0.00147	0.00486	53123.145	4086.3957	Morrow
313.8	13.3	428.6573	-19.01452	0.0073078	0.00094	0.00449	125191.51	2503.8303	Morrow
279.8	28	398.5146	23.342555	0.0062108	0.00088	0.00398	971327.44	7303.2139	Morrow
205.5	41	305.1526	60.047720	0.0043629	0.00088	0.00291	3501810.8	14293.105	Morrow
147.2	58.8	219.2995	87.582719	0.0031145	0.00124	0.00209	5522804.3	18107.555	Morrow
147.2	58.8	219.2995	87.582719	0.0031145	0.00124	0.00209	3413680.8	11192.396	SWT
205.5	41	305.1526	60.047720	0.0043629	0.00088	0.00291	2376607.9	9700.4406	SWT
279.8	28	398.5146	23.342555	0.0062108	0.00088	0.00398	688602.92	5177.4655	SWT
313.8	13.3	428.6573	-19.01452	0.0073078	0.00094	0.00449	123980.54	2479.6108	SWT
336.5	20.3	445.1848	-25.82688	0.0081647	0.00147	0.00486	65790.842	5060.8340	SWT
366.4	61.9	464.2674	10.641242	0.0095030	0.00306	0.00542	63862.278	9123.1825	SWT
336.5	20.3	445.1848	-25.82688	0.0081647	0.00147	0.00486	65790.842	5060.8340	SWT
313.8	13.3	428.6573	-19.01452	0.0073078	0.00094	0.00449	123980.54	2479.6108	SWT
279.8	28	398.5146	23.342555	0.0062108	0.00088	0.00398	688602.92	5177.4655	SWT
205.5	41	305.1526	60.047720	0.0043629	0.00088	0.00291	2376607.9	9700.4406	SWT
147.2	58.8	219.2995	87.582719	0.0031145	0.00124	0.00209	3413680.8	11192.396	SWT

Faktor skaliranja: 1

$N_{bl,i} = 480$ (SWT) (Computation estimate of the life until the appearance of the initial damage).
 $N_{bl, i} = 505$ (Morrow) (Computation estimate of the life until the appearance of the initial damage)

5 Residual Life Estimation

In addition to the age estimation until the initial damage, it is necessary to carry out a calculation assessment of the remaining life, i.e., during the crack propagation. To estimate the remaining life, it is necessary to assume initial damage in the form of surface cracking. Based on the maximum stress value, determined by elastoplastic analysis of FEM, the critical position is defined in Fig. 10. Here, the initial damage is defined in the form of an initial surface crack.

The calculation estimate of the remaining life is based on the stress intensity factor in analytical form. Since it is a complex construct, there are no known analytical expressions for FIN. For this purpose, the finite element method was used to determine the analytical expression of FIN. 3-D singular finite elements around the assumed surface crack line were used to determine the FIN. Figure 12 shows the finite element model of a part of the wing structure with an assumed initial surface crack.

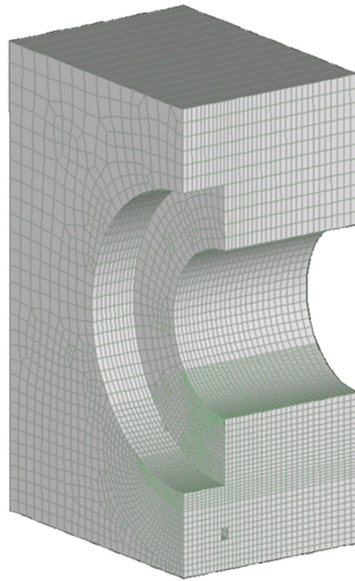


Fig. 12. Finite element model for a part of the wing structure with an initial surface crack

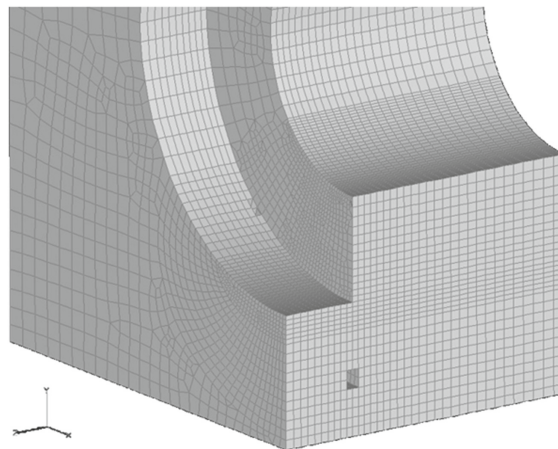


Fig. 13. FEM detail for a part of the wing structure with an initial surface crack

As mentioned before, in order to establish an analytical expression for FIN, FEM was used again, assuming several depths of surface cracks. For this purpose, singular finite elements around the tip of the crack were used. Figures 13, 14, 15 and 16 show the stress state for two “depths” of cracks.

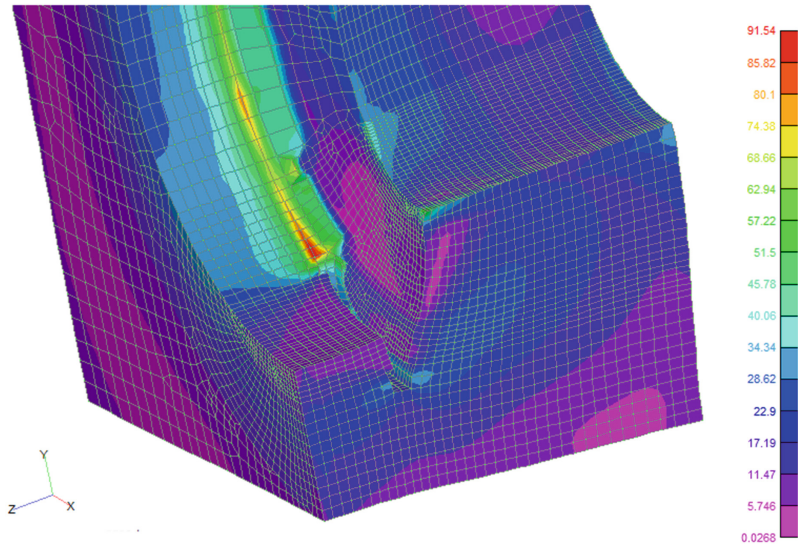


Fig. 14. Detail of the distribution of the stress state for a crack depth of 3.5 mm

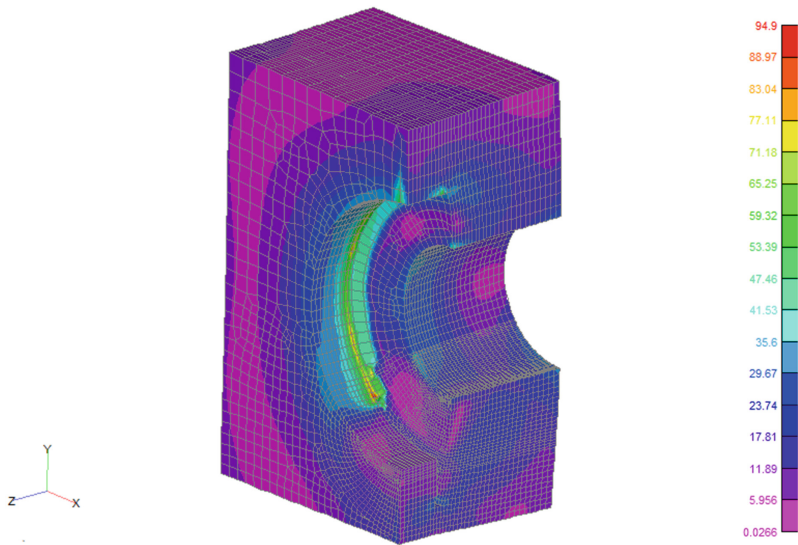


Fig. 15. Distribution of the stress state for the crack depth of 5.5 m

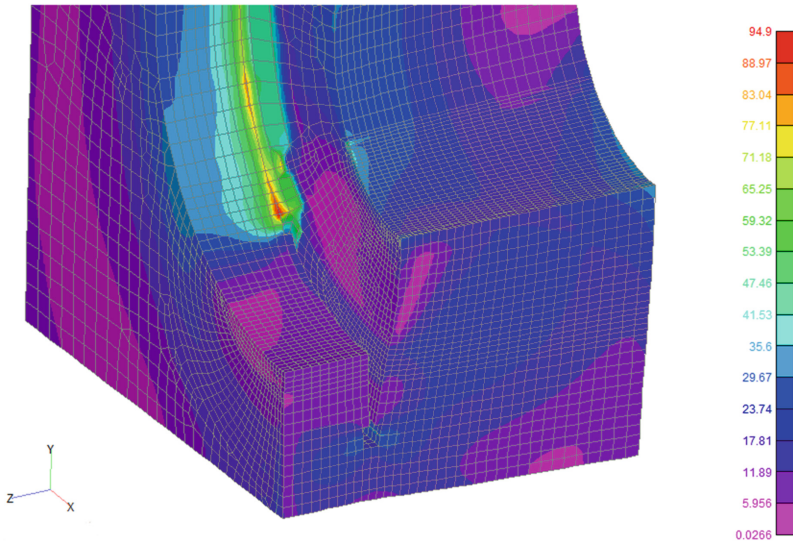


Fig. 16. Detail of the distribution of the stress state for a crack depth of 5.5 mm

For the analysis of crack propagation, i.e., for the estimation of the remaining life, the strain energy density method was used.

The estimate of the remaining life during the crack propagation, expressed through the number of blocks, is $N_{bl,p} = 52$ (Calculation estimate of the remaining, i.e., during the crack propagation). So, to estimate the remaining life, the SED method, described in detail in the paper, was used, on the one hand, with the establishment of analytical expressions for FIN using FEM, on the other hand.

6 Conclusion

This paper deals with research in the domain of estimating the total fatigue life of aircraft structures under the effect of cyclic loads. *The goal is to provide an efficient calculation method.* For this purpose, the strain energy density method was developed for crack propagation analysis. Unlike the conventional method, which uses the dynamic characteristics of the material for calculation, this method uses the low-cycle fatigue characteristics of the material, which are also used in the estimation of the life until the appearance of initial damage. This, in turn, reduces the additional experimental tests required for the experimental determination of the dynamic characteristics of the material. *This approach finds particular application in the domain of aircraft structures, both in the design phase and in the phase of aircraft exploitation, when NDT methods are used to monitor damage to aircraft structural elements, especially in critical zones.*

Acknowledgment. This research has been supported by the research grant No. 451–03-47/2023–14/200066 of the Serbian Ministry of Education, Science and Technological Development.

References

1. Maksimović, K., Maksimović, S.: Structural analysis and optimizations of layered composite structures: numerical and experimental investigations, dynamics of hybrid systems of complex structures, mathematical institute of the Serbian academy of sciences and arts. Ed. Katica Stevanović Hedrih **19**(21), 293–236 (2022)
2. Maksimovic, S., Kozic, M., Stetic- Kozic, S., Maksimovic, K., Vasovic, I., Maksimovic, M.: Determination of load distributions on main helicopter rotor blades and strength analysis and its structural components. *J. Aeros. Eng.* [https://doi.org/10.1061/\(ASCE\)AS.1943-5525.0000301](https://doi.org/10.1061/(ASCE)AS.1943-5525.0000301), Posted ahead of print 23 (Nov 2012)
3. Boljanović, S., Maksimović, S.: Fatigue crack growth modeling of attachment lugs. *Int. J. Fatigue* **58**(1), 66–74 (2014)
4. Sehitoglu, H., Gall, K., Garcia, A.M.: Recent advances in fatigue crack growth modeling. *Int. J. Fract.* **80**, 165–192 (1996)
5. Pantelakis, Sp.G., Kermanidis, Th.B., Pavlou, D.G.: Fatigue crack growth retardation assessment of 2024-T3 and 6061-T6 aluminum specimens. *J. Theoret. Appl. Fract. Mech.* **22**, 43–47 (1995)
6. Ellyin, F.: Fatigue damage, crack growth and life prediction. *Fracture Mech.* Chapman & Hall., **48**(1), 9–15 (1997)
7. Maksimovic, K., Nikolic, V., Maksimovic, S.: Efficient computation method in fatigue life estimation of damaged structural components. *FACTA UNIVERSITATIS Ser. Mech. Autom. Control Robot.* **4**(16) (2006)
8. Izumi, Y., Fine, M.E., Mura, T.: Energy consideration in fatigue crack propagation. *Int. J. Fract.* **17**(1), 15–25 (1981)
9. Bannantine, J.A., Comer, J., Handrock, J.: *Fundamentals of Material Fatigue Analysis*. Prentice-Hall, Englewood Cliffs, New Jersey (1990)
10. Kostaes, D.: *Fatigue Behaviour and Analysis*, Talat Lecture 2401, Technische Universität München, EAA – European Aluminium Association (1994)
11. Palmgren, A.: *Die Lebensdauer von Kugellagern*. *Verfahrenstechnik*, Berlin **68**, 339–341 (1924)
12. Miner, M.A.: Cumulative damage in fatigue. *J. Appl. Mech.* **67**, A159–A164 (1945)
13. Fatemi, A., Yang, L.: Cumulative fatigue damage and life prediction theories: a survey of the state of the art for homogeneous materials. *Int. J. Fatigue* **20**(1), 9–34 (1998)
14. Vasic, Z., Maksimovic, K., Maksimovic, M., Vasovic, I., Vidanovic, N., Simonovic, A.: Buckling and postbuckling behavior of shell type structures under thermo-mechanical loads. *Therm. Sci.* **25**(6), 2334–7163 (2021)
15. Vasovic, I., Maksimovic, S., Stamenkovic, D., Stupar, S., Maksimovic, M., Bakic, G.: Fracture mechanics analysis of damaged turbine rotor discs using finite element method. *Therm. Sci.* **1**(18), S107–S112 (2014)
16. Maksimović, K., Vasović, I.: Strength analysis of aircraft structural components with respect to fracture mechanics by finite elements, 70 years of the Mathematical Institute SASA, Belgrade, Serbia, International Mini-Symposium “Fracture Mechanics and Numerical Methods” Mathematical Institute of SASA and Project OI 174001, Belgrade, Serbia, (ISBN 978–86–7746–628–2), November 16 (2016)
17. Jankovic, D, Maksimovic, S., Kozic, M., Stupar, S., Maksimovic, K., Vasovic, I., Maksimovic, M.: CFD calculation of helicopter tail rotor airloads for fatigue strength experiments. *J. Aerosp. Eng.* **30**(5) (2017)



3D Printing and CNC Machining: Materials, Technologies, and Process Parameters

Strahinja Djurović¹(✉), Dragan Lazarević², Milan Mišić¹, Živče Šarkoćević²,
and Zoran Golubović²

¹ Academy of Applied Science Kosovo and Metohija, 38227 Leposavić, Serbia
strahinja.djurovic@akademijakm.edu.rs,
strahinjadjurovic55@gmail.com

² Faculty of Technical Science, Kosovska Mitrovica, 38220 Mitrovica, Serbia

Abstract. Industry and industrial production in today's world represent one of the main drivers of the economy and development. One of the relatively newer methods of production is additive manufacturing or better known as 3D printing. Unlike traditional ways of manufacturing parts, 3D printing adds material layer-by-layer and gives the possibility of creating complex shapes that are almost impossible to create with classical methods. In order to improve the surface quality of 3D printed parts, CNC technologies can be used for part finishing. This paper presents an overview of the possibilities of combining 3D printing and CNC technologies, recommendations for material selection, process parameters, technical data, as well as their use in the finishing process.

Keywords: 3D printing · CNC · Machining · Quality

1 Introduction

Industry and industrial production, technologies, materials, and equipment in use are advancing very rapidly. In addition to CNC technologies, which represent traditional manufacturing technologies, one of the technologies that is gaining ground is certainly 3D printing. 3D printing is a generally faster, cheaper, and easier solution than other technologies for the production of 3D objects. It enables the production of parts and assemblies from many different materials, with different mechanical and physical properties. This technology produces models that faithfully imitate the appearance, impression, and functionality of the product as a prototype [1]. 3D printing technology can produce parts of any complex shape, without having to consider processing problems, and solves the problems of designing and manufacturing complex parts. Therefore, 3D printing technology is a very important production method in the industry [2]. When we have a complex geometry that is ideal for FDM, however, the part requires critical dimensions and fine features that cannot be achieved by printing alone, thus CNC processing after 3D printing is one of the solutions that will lead to the geometrically and dimensionally accurate part that is needed [3, 4]. Many researchers have been engaged in investigating the post-processing of 3D-printed parts with CNC machining as well as the possibility of combining 3D printing and CNC technology.

Kulkarni, P. et al. integrated additive manufacturing and traditional material removal processes into an integrated production process in their work. Processes under which this integration would be useful were identified and algorithms for the integration were developed. As examples, they looked at two additive manufacturing technologies that use material removal operations as part of their process [5]. Boschetto et al. has developed a methodology in their work that can unlock the possibility of parts made by Fused Deposition Modeling to be machined using computer numerical control. A different depth of the cut was considered to avoid defects and eliminate initial surface morphology. The experiment made it possible to determine how the depth of the cut should be adjusted. A case study characterized by functional surfaces confirmed the applicability of the method to complex geometry: A large reduction in average roughness and reliability of finished surfaces was achieved [6]. Pamarac and Petruse determined in their study the best parameters for milling 3D printed parts at a constant spindle speed of 3500 (rpm). Some important observations are: for ABS, low cutting speeds give better roughness quality. For PLA, the situation is reversed, better surface quality is obtained when a higher cutting speed is used. This is due to the lower melting temperatures of PLA, which implies that if the cutting tools remain in contact with the part more heat will be generated and would damage the part surface [7]. Li et al. studied additive and subtractive processes, which are presented as a hybrid manufacturing process. Specifically, the authors manufactured PLA pieces using a Fused Deposition Modeling printing head and a milling head. The measured surface roughness varied depending on the printing angle (from 20 to 90°). The hybrid process by adding, the milling post-processing, allowed for the reduction of the surface roughness from a range of 17.332 and 56.021 mm to 4.870 and 24.511 mm [8]. Guo et al. analyzed the surface roughness after machining of AISI 316L samples produced by direct laser deposition. They obtained surface roughness between 0.2 and 0.4 mm after dry finish milling. Cutting conditions included a feed rate of 0.05 mm/tooth, depth of cut of 0.1 mm, and cutting speed between 60 and 150 m/min. They did not provide the values of the surface roughness before machining but, regarding the post-process, they showed how by increasing the cutting speed, the surface roughness can be reduced [9]. Cococcetta et al. investigated the effects of the printing process and milling process on the post-processing quality of thermoplastic composites. The results showed that deep cooling reduced tool wear during milling and was able to completely eliminate or reduce burrs [10]. Noorani identified characteristics of additive and subtractive machining processes. 3D printing offers advantages such as its adequacy for manufacturing entire assemblies, where high complexity can be obtained, including small holes of unlimited length. However, it is still an expensive technology, and the part size is a limitation. Subtractive manufacturing offers advantages such as no part size limitations and cost because it is a conventional and widespread technology. Moreover, it allows for achieving high accuracy and excellent surface finish, which is still a limitation for AM [11].

2 Machining 3D Printed Parts with CNC Technologies

The finishing of additively manufactured (AM) components may be categorized into three mechanisms, namely: (i) mechanical conversion, and machining e.g., grinding, milling, and shot-peening; (ii) thermal processes including electron beam and laser melting; (iii) electrochemical and chemical processes, such as electropolishing and etching. Several subtractive processes have been vastly used in near-net shaping processes, such as die-casting, casting, and molding. This has now been extended to additive manufacturing, allowing feature geometries to be realized with greater accuracy and surface quality via subtractive processing [12].

Milling is a typical AM post-processing method that eliminates the effect of the surface staircase effect on the parts, expands the range of applications for 3D-printed parts, and increases durability. The combination of FDM and milling post-processing technology is an AM method with low energy consumption, low cost, and sustainable potential [13]. According to an insight into the literature, the three most frequently used factors in post-processing are feed rate (Vf), speed (n), and depth of cut (ap).

Companies often AM plastic or metal parts and then process them on a CNC machine for the following reasons:

- **Dimensional accuracy** – Industries with high functional and tolerance requirements, such as automotive, medical, and consumer products manufacturing, need to hit repeatable, tight specs. Most additive manufacturing technologies, such as Fused Deposition Modeling (FDM) can achieve up to ± 0.005 mm, but that's not enough for some critical part features. With CNC machining you can bring tolerance down to ± 0.002 mm. Which can make a huge difference if you're producing an assembly aid, manufacturing fixture, or any in-process tool with a long service life.
- **Speed** – The second reason why companies combine the two technologies is speed. Accounting for print time, CAD/CAM set up and machining, the process is still much faster than designing and producing a tool for injection molding. And 3D printing and machining give engineers more flexibility in the timeline to make design improvements. It just involves updating CAD/CAM files, and printing and machining a new part, whereas making changes to an injection molding tool can be nearly impossible and expensive, causing major delays in production [14].

In addition to the above reasons, one of the most important is certainly the improvement of surface quality. 3D printing generally does not provide a good enough surface quality and therefore post-processing is necessary. Table 1 shows the results of individual researchers who dealt with this problem and machined 3D-printed polymer.

3 The Combination of 3D Printing and CNC Machining

Hybrid manufacturing is a relatively new method that combines additive manufacturing and subtractive manufacturing technologies in one machine (Fig. 1). These machines use 3D printing to produce the basic, near-net shape of the part in metal or plastic. Then, another unit or tool head mills the part to the required tolerances. As a result, manufacturers (and their customers) have gained complex part geometries via additive manufacturing and the detailed surface quality by milling those components [16].

Table 1. Surface roughness measured in both additively manufactured and machined parts [15].

Material	AM technology	Subtractive technology	Ra before	Ra after
ABS	Fused Deposition Modeling	Milling	From 17 to 50	From 1 to 35
VeroClear	Material Jetting	Turning	From 0.14 to 1.07	From 0.14 to 0.32
Polyamid	Selective Laser Sintering	Grinding	Over 15	2.85
PLA	Fused Deposition Modeling	Milling	From 17.332 to 56.021	From 4.870 to 24.511

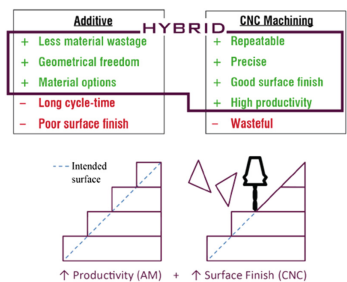


Fig. 1. Hybrid process of Additive Manufacturing and CNC [17]

Combining both processes in the same machine provides additional benefits not possible through tandem use with separate machines. First, it provides the opportunity to realize both metal addition and removal in the same setup, thus eliminating the transfer step between systems. It also enables both deposition and removal processes to be programmed in the same way (as opposed to writing different kinds of programs for robotic deposition versus machine tool finishing). It also provides access to the inside of the part in the manufacturing process for inspection and heat/compressive treatments (helpful in managing residual stresses). This can even allow defect identification and re-work of a part before it becomes scrap. Perhaps most importantly, it provides access to both technologies at a lower capital investment threshold than acquiring two separate systems [18].

As manufacturing and design techniques get progressively “smarter” with CAM/CAD programs offering generative design and artificial intelligence, these hybrid machines could become a new standard in high-end machine shops working in advanced manufacturing industries like aerospace, medical, defense, and the mold, tool & die market [19].

4 Conclusion

3D printing or additive manufacturing is a trend that is increasingly prevalent in industrial production. Lower production costs, reduced development time and costs (increased pace of product design), environmental friendliness, shorter delivery time, and complex products that are relatively easy to make, are just some of the advantages that 3D printing brings. However, there are also some disadvantages, such as certainly worse surface quality, higher tolerances, and lower dimensional accuracy. In order to improve these parameters, post-processing with CNC technologies as well as the possibility of hybrid production (combining 3D printers and CNC machines) represents a trend that will continue to develop and enable researchers to improve both methods of production.

References

1. <https://www.industrija.rs/vesti/clanak/3d-stampa>. Accessed 29 May 2023
2. Botao, H., Guomin, L.: 3D printing technology and its application in Industrial Manufacturing. IOP Conference Series: Materials Science and Engineering 782. 022065. EMCME 2019. IOP Publishing. <https://doi.org/10.1088/1757-899X/782/2/022065> (2020)
3. <https://www.stratasysdirect.com/technologies/cnc-machining/cnc-machining-3d-printed-parts>. Accessed 29 May 2023
4. <https://www.sculpteo.com/blog/2019/10/23/3d-printing-and-machining-how-to-combine-them-for-your-benefits/>. Accessed 29 May 2023
5. Kulkarni, P., Dutta, D.: On the integration of layered manufacturing and material removal process. *J. Manuf. Sci. Eng.* (122), 100–108 (2000)
6. Boschetto, A., Bottini, L., Veniali, F.: Finishing of fused deposition modeling parts by CNC machining. *Robot. Comput. Integr. Manuf.* (41), 92–101 (2016)
7. Pămărac, R.G., Petruse, R.E.: Study regarding the optimal milling parameters for finishing 3D printed parts from abs and pla materials. *Acta universitatis cibiniensis – technical series*, vol. Lxx. <https://doi.org/10.2478/aucts-2018-0009> (2018)
8. Li, L., Haghighi, A., Yang, Y.: Theoretical modelling and prediction of surface roughness for hybrid additive/subtractive manufacturing processes. *IISE Trans.* 51 (2), 124e135 (2019). <https://doi.org/10.1080/24725854.2018.1458268>
9. Guo, P., Zou, B., Huang, C., Gao, H.: Study on microstructure, mechanical properties and machinability of efficiently additive manufactured AISI 316L stainless steel by high-power direct laser deposition. *J. Mater. Process. Technol.*, 240 (2017)
10. Cococetta, N., Jahan, M.P., Schoop, J., Ma, J., Pearl, D., Hassan, M.: Post-processing of 3D printed thermoplastic CFRP composites using cryogenic machining. *J. Manuf. Process.* 68, 332–346 (2021)
11. Noorani, R.: 3D Printing. Technology, Applications and Selection. CRC Press, Boca Ratón, Florida (US) (2018)
12. Amanullah, T., Tanveer, S., Raisuddin, K.: Improvement of dimensional accuracy of 3-D printed parts using an additive/subtractive based hybrid prototyping approach IOP Conference Series: Materials Science and Engineering 260 (2017). <https://doi.org/10.1088/1757-899X/260/1/012031>
13. Zhou, H., Cheng, X., Jiang, X., Zheng, G., Zhang, J., Li, Y., Tang, M., Lv, F.: Green manufacturing-oriented Polyetheretherketone additive manufacturing and dry milling post-processing process research. *Processes* (2022). <https://doi.org/10.3390/pr10122561>
14. <https://www.stratasys.com/en/stratasysdirect/resources/articles/cnc-machining-3d-printed-parts/> last accessed 2023/05/29

15. Pérez, M., García-Collado, A., Carou, D., Medina-Sánchez, G., Dorado-Vicente, R.: On surface quality of engineered parts manufactured by additive manufacturing and postfin-ishing by machining
16. <https://all3dp.com/1/3d-printing-cnc-guide-to-hybrid-additive-subtractive-manufacturing/>. Accessed 29 May 2023
17. Jones, J.B.: SME Technical Paper TP14PUB77: The Synergies of Hybridizing CNC and Additive Manufacturing. Presented at the RAPID 2014 and 3D Imaging Conferences & Exposition, Detroit, MI, USA (2014)
18. Jones, J.B.: Repurposing mainstream CNC machine tools for laser based additive manufacturing. Proceedings SPIE 9738, Laser 3D Manufacturing III, 973811 (2016). <https://doi.org/10.1117/12.2217901>
19. <https://www.harveyperformance.com/in-the-loupe/cnc-machining-3d-printing/>. Accessed 29 May 2023



The Current State of the Open-Source Engineering Software for Numerical Simulations

Ivana B. Ivanovic^(✉)  and Srdjan Tadic

Innovation Center, Faculty of Mechanical Engineering, University of Belgrade, Kraljice Marije
16, 11120 Belgrade 35, Republic of Serbia
ivanovicivana@hotmail.com

Abstract. This work is an overview of open-source engineering software for numerical simulations running on a desktop or laptop since most of the research still begins and ends on a personal computer. An attempt was made to analyze what the current state is, and how it developed in the last two decades. Although comparisons with corresponding commercial software were made, the main goal was to analyze how extensive is the use in research, especially in the last couple of years, what are the latest innovations, how the verification and validation process is developing. Special attention was paid to the most advanced software. More recent are also mentioned, the one that are imposing due to new models which are the main topic of recent research, and, in general, due to the new way of thinking. The Windows Subsystem for Linux is highlighted as novelty that can bring a solution to well-known problem of the lack of Windows versions of the open-source Linux software.

Keywords: Numerical simulations · Open-source software · FEM · FVM · CAELinux · Windows Subsystem for Linux (WSL2) · Salome platform · CFD · OpenFOAM · Elmer FEM · NETGEN · Gmsh · ParaView · Python3

1 Introduction

In recent times, software for numerical simulations is expected to provide advanced tools for all steps in the process: a version for each operating system with installation instructions and user support; a choice between graphical and command interface; pre-processors for geometry and mesh; solvers, preferably coupled, for different physical phenomenon; postprocessors for visualization of the results, with the most beautiful 3D graphics if possible; extensive documentation with tutorials, validation and benchmark examples included. In the case of commercial software, all needed is available in one package. Couple of examples of a successful use of commercial FEM software are given in [10].

When look back at a period of a little more than two decades ago, one would say many years, but again a little when it comes to scientific research, every postgraduate student or researcher in the field of numerical simulations would write bunch of code during coursework and research or would use in-house code previously made by the fellow

researchers. The imperative was to know how and to know what was behind commercial software that was already in widespread use. That was a time of Computational Fluid Dynamics (CFD) commercial software Fluent, around version 5, and before it become Ansys Fluent, [11]. Fluent was composed of solvers and post-processor, and sufficiently user-friendly mesh generation software Gambit was commonly used as pre-processor. At the same time Ansys [11], Abaqus [12], and Comsol [13] were with some multiphysics capabilities, but more oriented towards structural analysis, and there was a need for better and better pre-processors, especially mesh generation software. In addition to usual programming tools, programming and numeric computing platforms like Wolfram Mathematica [14] and MathWorks Matlab [15] have already been used extensively.

Increasing interest in mesh generation, CFD, parallel computing, design optimization, and due to numerous postgraduate students and all other researchers who used commercial software, but also did a lot from scratch, where the main reasons why the creation of so much quality open-source numerical simulation software started at that time. When glance through the history of some, for example Gmesh [16], finite element mesh generator, but also pre- and post-processor, was the product of a joint effort of Christophe Geuzaine and Jean-Francois Remacle, and said in their own words, at the beginning more a hobby than official work [17], on the website of CalculiX [18], finite element solver written by Guido Dhondt, and pre and post-processor written by Klaus Wittig it is written: “The CalculiX package was developed by a team of enthusiasts in their rare spare time”, OpenFOAM [19, 20], in the beginning as FOAM, was not intended to be open-source, but later it became the most famous open-source CFD software [21]. It is important to highlight here CAELinux [22], special engineering Linux distribution which was created in 2005 as a personal project of Joël Cugnon [23], and looks like it still is, for the most part, a personal effort with continuous new releases, at the moment version 2020.

On the other hand, Salome platform [24], the open-source platform for numerical simulation, with all additional tools, and with accompanying solver for structural mechanics and heat transfer Code_aster [25], and CFD solver Code_Saturn [26], is the project of The French National Network for Research and Innovation in Software Technologies, from 2005 the French National Agency for Research (ANR) [27]. The network was initiated by OPEN CASCADE [28] and was created by the French Ministry of Research and the French Ministry of Industry in September 2000 [29].

The experience of every researcher is that getting used to the use of new software for numerical simulations, commercial or open-source, is always difficult at the beginning. Even more difficult is a transition from one to another, certain habits are created, each software requires a certain way of thinking, and new one requires the creation of new habits. In general, the easier and more comfortable to use the better for the end user. Open-source software is the constant effort of the few, and, additionally, the effort of the many. For that reason, being comfortable to use is not the primary goal, but it is increasingly present. The software is distributed under GNU General Public License (GPL), GNU Lesser General Public License (LGPL) [30], or Berkeley Source Distribution Licenses (BSD). The source code is opened, it can be seen, tested, upgraded, redistributed under conditions of previously mentioned licenses, which makes it perfect for research and development (R&D). Since you can see what you get, it can be very

useful in mastering existing methods and can be effectively used as highly advanced tool for educational purposes. An example is a course “CFD with OpenSource software” at Chalmers University of Technology given by professor Håkan Nilsson [31].

Usually, this type of software is originally made for Linux, and CAELinux is Linux operating system (OS) with specific characteristics. In this work, the most attention will be paid to the software that has version or is not difficult to be installed under other operating systems.

2 Windows Subsystem for Linux

Since most of the open-source software for numerical simulations is Linux based, frequently asked question in the research community is the one about Windows versions. The subject of this work is the open-source software, but the incredibly fast development of information technologies pushes the limits, force the communication between operating systems, and Windows Subsystem for Linux (WSL) is one of the results. It is probably the solution of the problem for Windows users, and as such it must be mentioned here.

WSL is a real subsystem that gives the possibility to Windows users to run Linux without living Windows, and without virtual machine or dual-boot [32].

```

ivana@DESKTOP-DT2Q5K8: ~
ivana$ cp -ar $FOAM_TUTORIALS/incompressible/icoFoam/cavity/cavity .
openfoam2212:/mnt/d/openfoam_tutorials/
ivana$ cd cavity
openfoam2212:/mnt/d/openfoam_tutorials/cavity/
ivana$ blockMesh

*****
//      F ield      | OpenFOAM: The Open Source CFD Toolbox
//      O peration   | Version: 2212
//      A nd         | Website: www.openfoam.com
//      M anipulation|
*****

Build : f8a05934-20230403 OPENFOAM=2212 patch=230110 version=2212
Arch  : "LSB;label=32;scalar=64"
Exec  : blockMesh
Date  : Jun 11 2023
Time  : 11:51:50
Host  : DESKTOP-DT2Q5K8
PID   : 11187
I/O   : uncollated
Case  : /mnt/d/openfoam_tutorials/cavity
nProcs : 1
trapFpe: Floating point exception trapping enabled (FOAM_SIGFPE).
fileModificationChecking : Monitoring run-time modified files using timeStampMaster (fileModificationSkew 5, maxFileModificationPolls 20)

```

Fig. 1. Lid-driven cavity flow tutorial example from OpenFOAM tutorials executed in Ubuntu 22.04.2 terminal on Windows with WSL2 using latest Ubuntu OpenFOAM version 2212

The latest version from November 2022 is WSL2, and it comes with the latest version of Ubuntu, Ubuntu 22.04.2. WSL2 is easy to install, the one line of commands, executed from Windows PowerShell, will get the job done:

```
wsl --install.
```

After installation, the Ubuntu terminal is available from Start menu, and the Ubuntu directory tree is available in Windows File Explorer. Through WSL the systems are interchangeable with each other, for example, the new directory made from Ubuntu terminal can be placed in the Windows directory tree. Now, with WSL2 it is also possible to run Linux graphical applications.

Detailed information about advantages of OpenFOAM installation using WSL is already given at OpenFOAM websites. Illustration of Ubuntu terminal running OpenFOAM tutorial case on WSL2 is presented in Fig. 1.

3 CAELinux

CAELinux is a unique engineering Linux distribution coming with numerous open-source software for numerical simulations, programing tools, and much more. It is based on Ubuntu Linux. Latest version is CAELinux 2020, released in January 2019, and is based on Xubuntu 18.04 [22] (Latest stable version of Ubuntu is 22.04).

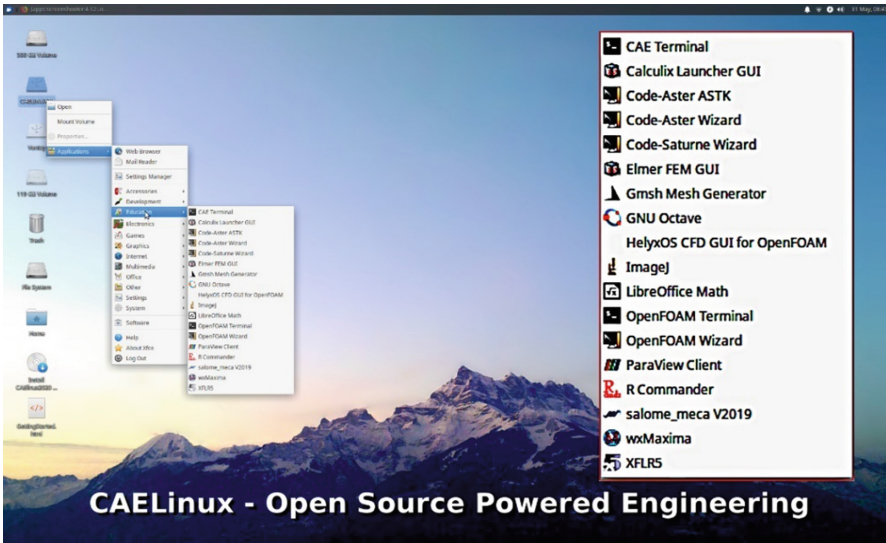


Fig. 2. CAELinux desktop with enlarged image of educational menu of CAELinux 2020

Live distribution of CAELinux can be run from USB flash drive so that a user who wants to try how it works, and wants to familiarize with the installed software, can do it without installation of an operating system. System is easy to install, single-boot or dual-boot, parallel to the operating system to which the user is accustomed, or maybe lately through WSL. This range of capabilities is of great significance for beginners, students, or educators who wants to introduce their students to numerical simulation in general.

Desktop of CAELinux 2020 running from USB flash drive is presented in Fig. 2. Educational menu is enlarged at right to illustrate available numerical simulation software. In addition to standard compilers such as gcc, gfortran, java, perl, tcl/tk, Qt, latest

distribution comes with Spyder [33], open-source integrated development environment (IDE) for scientific programming, and with Python 3 [34].

4 Salome Platform and Code_Aster

Salome is a product of many years of work of researchers from R&D organizations from French universities, small, medium-sized and large enterprises, joint on a project managed by a government institution. What is available in the public domain of Salome platform, in appearance and in capabilities, is closest to what one would expect from commercial software [29], and much more. It should be pointed out that graphical user interface (GUI) is in English and all modules have detailed documentation translated into English.

Several Linux versions of Salome_meca, which is the combination of structural mechanics and heat transfer module Code_aster and Salome pre- and post-processors, can be downloaded from Code_aster website [25]. Latest versions of the software are distributed as Singularity container image which needs Singularity to be previously installed on the system [35]. If container is not already installed, or if user is not familiar with containers, the installation process will be longer and more complicated than it was before. There is a warning that Salome_meca needs Nvidia-like device, which means that other types of graphics can cause problems during execution. On the other hand, in the case of Windows version of Salome_meca [36], Code_aster and Salome have to be installed separately, but the process is straightforward, and software is running without any problems.

4.1 Salome Geometry Module

The Salome geometry module is comfortable to use and easy to master 3D CAD software. Geometry can be programmed in Python and loaded into module, drawn directly in the module, or imported from BREP, STEP, IGES, STL, XAO file formats. It can also be exported in previously mentioned formats, in VTK format, and as Python script.

In the references, where Salome platform is used for research, the Salome mesh module, or some other modules, are emphasized, but it is often difficult to conclude whether the geometry module was applied to draw the model. Recent examples, where it is explicitly indicated that CAD model was built with Salome, are references in which programming of geometry becomes important. For example, reference [37] where the gas entrainment in sodium-cooled fast breeder reactor pools was analyzed experimentally and numerically. It is interesting that in this work Salome was used only for geometry, and a commercial software Ansys ICEM CFD for mesh generation. The numerical simulations, more precisely the CFD calculations, are performed in TrioCFD, another powerful open-source CFD code developed by Nuclear Energy Division of French Alternative Energies and Atomic Energy Commission (CEA) [38, 39]. Some verifications and comparisons are performed in Ansys Fluent.

The same group of software was selected in reference [40] for CFD analysis of the cross-section of pressurized water reactor fuel assemblies. Python programming of geometry in Salome geometry module was used to facilitate modification of the model.

In the CFD simulation of control rod guide tube of pressurized water reactor [41], Salome geometry and mesh module are used, but numerical analysis was performed in Code_Saturn and Ansys Fluent. Options of using Python programming of geometry in Salome for design optimization are discussed in reference [42] where CFD analysis with OpenFOAM was applied for numerical simulations of wine tank. Optimization was performed with open-source Design Analysis Kit for Optimization and Terascale (DAKOTA), project of Sandia National Laboratories [43].

The illustration of relatively complex geometry made in Salome geometry module from reference [44] is presented in Fig. 3.

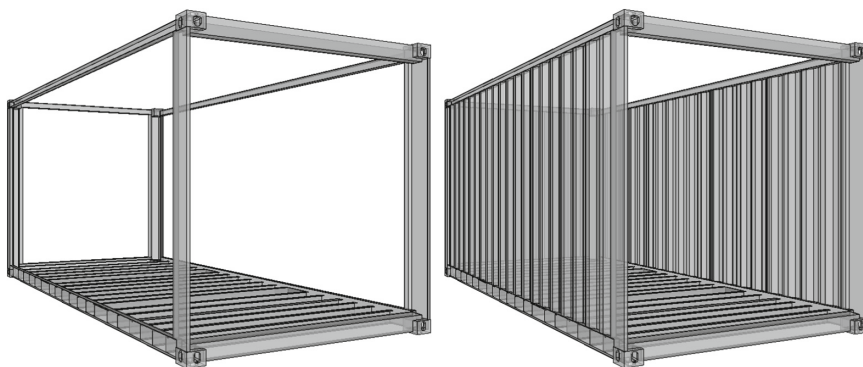


Fig. 3. Geometry of shipping container drawn in Salome geometry module

Since a shipping container is composed of parts that are repeating two or more times, all parts were drawn separately using Graphical User Interface (GUI) of Salome, exported in BREP file format, and imported and combined as needed. It is interesting to mention that the HDF files (binary file format that Salome uses to save the work) from 2013, made on CAELinux installation of Salome_meca, loaded without any problem on current Windows Salome_meca installation. It was possible to read geometry of the parts and mesh, but the Code_Aster command file was showing errors while loading, and, obviously, lot of updating needs to be done for file to be customized for new Linux or Windows settings of Salome_meca. Also, it was impossible to read old results, prepared and saved in the default post-processor at the time.

In 2019 new Salome CAD module was introduced, Salome Shaper, which is more advanced than geometry module, and brings a more modern approach to geometry construction to Salome [45]. Now the pieces of geometry can be drawn as separate parts in Shaper which solves the problem of geometry module tree which is pretty linear and becomes complex for complex geometry. Also, the parameters of the part can be changed as needed, and there is a possibility to export drawing to geometry module.

4.2 Salome Mesh Module

The main components of Salome mesh module are SMECH, or Salome MESH, and an open-source automatic 3D tetrahedral mesh generator Netgen [46]. Some other software is supported through plugins.

When talking about standard meshing algorithms in Salome mesh module, the simplest is an automatic mesh generation through the assignment of automatic hypothesis. The automatic tetrahedralization with default values preselected by mesh module applied to the shipping container corner fitting is illustrated in Fig. 4. When this option is selected, Salome uses NETGEN for mesh generation.

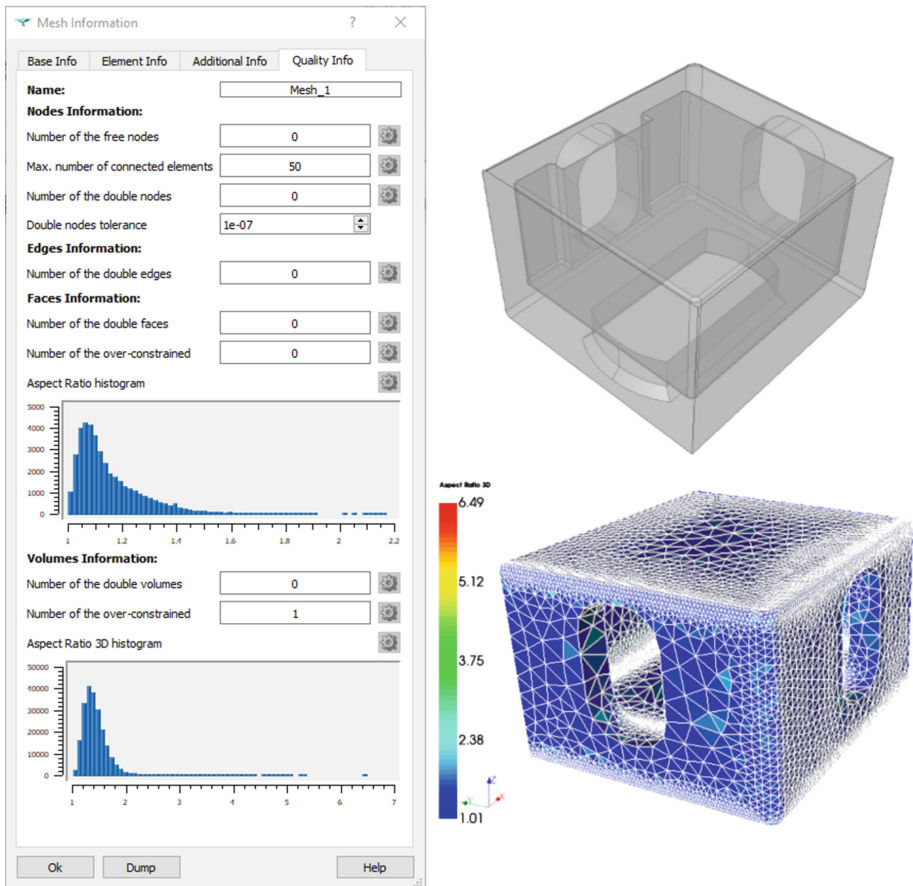


Fig. 4. Mesh information window (left), shipping container corner fitting geometry (top right), and aspect ratio 3D of the mesh obtained using automatic tetrahedralization algorithm with default values (bottom right)

A plugin for Gmsh, an open-source 3D finite element mesh generator mentioned in the introduction, is recently added, and it looks like it is not available for Windows

version of Salome. There is a series of plugins for MeshGems, suite is available in the menu, but a license error occurs during runtime since MeshGems is not open-source software. The product was developed by company Distene, but it is obviously acquired by Dassault Systemes since all web links connected to MeshGems and Distene lead to Dassault Systemes website.

4.3 Code_Aster

Code_aster is open-source set of finite element solvers for structural mechanics and heat transfer. The software can be installed separately or as module of Salome_meca. It comes with documentation, French and English, and with numerous test cases that can be loaded into the software, and are product of long-time work of researchers from Électricité de France (EDF).

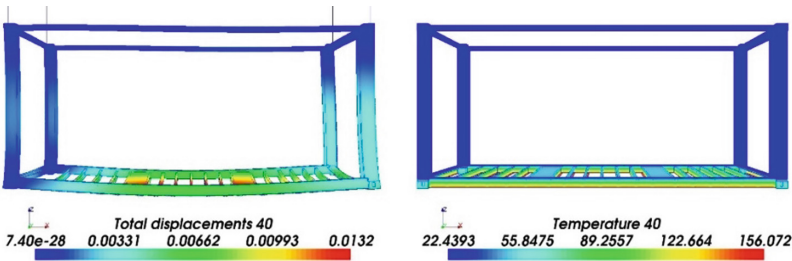


Fig. 5. Results for temperature and displacement from transient thermo-mechanical simulations of the skeleton of the shipping container performed in Code_Aster

Some examples of transient thermo-mechanical simulations from reference [44] are presented in Fig. 5. These simulations do not really represent state-of-the-art numerical calculations related to the subject of presented research; they are more a product of fascination of the authors with the possibilities that this open-source software brought with it in one package at the time.

Structural mechanics and heat transfer solvers in Code_Aster are not coupled. The heat transfer simulations had to be performed first, followed by structural mechanics simulations applied to the results obtained from transient heat transfer simulations. Since the object was supposed to be gradually exposed to a certain temperature, it was hung on cables to make the model as realistic as possible. All steps: pre-processing, calculations, and post-processing of the results, were performed using Salome_meca.

The transient thermal simulations of welding problem with Goldak's moving heat source from reference [47] are presented in Figs. 6 and 7. The moving heat source was introduced into calculations using formula command.

Salome_meca comes with GUI that tends to be more and more advanced with each new version. All test cases that are in public domain can be selected and added from the list, not always without errors. If the test case is not loading easily, the Code_Aster code can be seen, and the steps can be entered manually trough GUI or as text. There is also a possibility to add case, or more precisely stage of the Code_Aster case, with

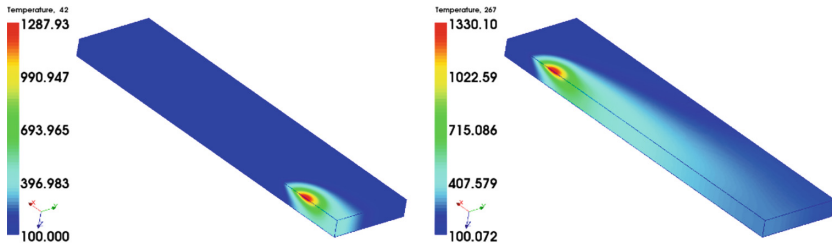


Fig. 6. Temperature distribution as example for the transient welding simulations with Goldak's moving heat source performed in Salome_meca with Code_aster

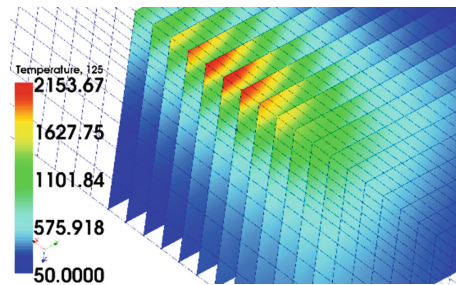


Fig. 7. Temperature distribution in 2 mm cut planes as example for the transient welding simulations with Goldak's moving heat source performed in Salome_meca with Code_Aster

assistant which is a series of templates with procedures prepared in advanced for thermo-mechanical analysis, fracture analysis, etc.

Code_Aster is supported by an extensive literature with examples following the development of the solvers. Presentations from 1991 to 2019 containing literature about specific fields of research can be found at the web link given in reference [48]. Many of the listed texts and all PhD Thesis are in French, but there are references to published papers which are in English.

5 CFD Open-Source Solvers

5.1 Code_Saturne

There is a number of open-source solvers for fluid dynamics, but there are often no provided versions that are easy to install on all operating systems. An example is Code_Saturne [16], a finite volume CFD software mentioned in the introduction as one of the solvers from the group of software around Salome platform. Of course, the native OS is Linux, the version for Windows existed until version 5 (current version is 7, and version 8 is expected in June 2023), but is not available anymore and they welcome help from anyone who is prepared to work on the version for Windows OS [16].

The new Windows version may not be necessary since Ubuntu Code_Saturne can be installed using WSL2 following the instructions for Ubuntu installation. On Ubuntu, Salome or Salome_CFD would be used for pre- and post-processing, on Windows,

Salome_meca for Windows or some other software for pre-processing and ParaView for post-processing.

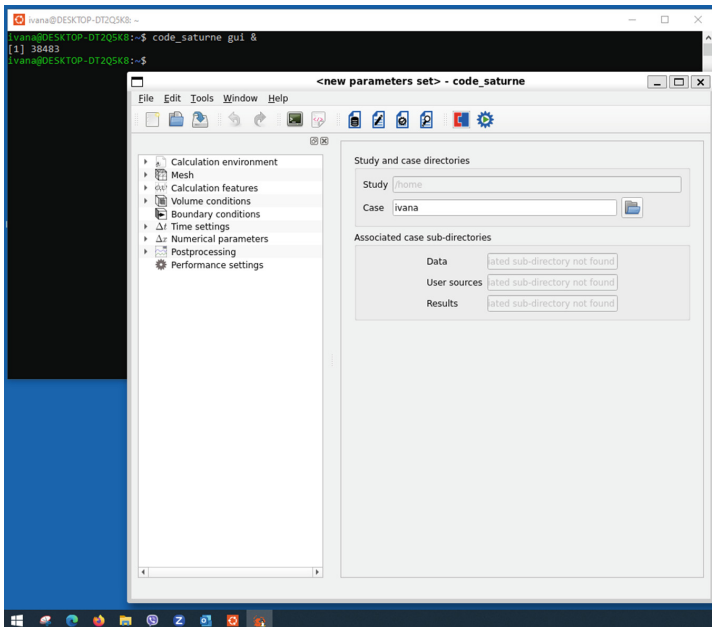


Fig. 8. Code_Saturne GUI running on Windows through WSL2

A GUI of Code_Saturne 7.0.6 installed through WSL2 is illustrated in Fig. 8. It is extremely user-friendly, especially for novice in CFD, since the necessary steps required for setting a CFD model are listed in the GUI, and can be simply followed.

In order to get a feel for how Code_Saturne works, a heated square cavity flow tutorial example was chosen from reference [49] and was made slightly more complex through the changes applied to boundary conditions.

Information and files necessary for square cavity heated from the side wall are given at Code_Saturne website or GitHub page of Code_Saturne. The study laminar solution in the tutorial was obtained using transient, incompressible flow equations with a buoyance term added to momentum equations through Boussinesq approximation, and without using any turbulent model. The buoyance source term needs to be programmed, and code has to be added while defining physical properties of the model through user law. In Code_Saturne, model is always three dimensional, for two dimensional cases like this one, one mesh cell is added in third dimension, and the symmetry boundary conditions are imposed to a front and rear wall. The adiabatic boundary conditions were applied to horizontal walls and two vertical walls were kept at different temperatures. The results in the tutorial were validate by comparing with the benchmark solution.

In this work, the settings for the solver with minor changes were used for the simulation of the cavity partially heated at the bottom wall. The part of the bottom wall was

exposed to a higher temperature while the side walls were exposed to lower temperature. Adiabatic boundary conditions were imposed to the rest of the walls. The results of one execution for the cavity where 0.8 of the length of the bottom wall was heated are illustrated in Fig. 9.

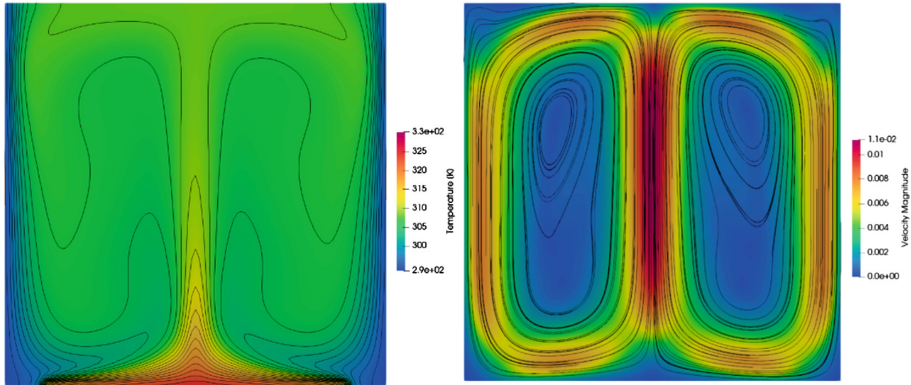


Fig. 9. Isotherms and streamlines for the cavity partially heated from the bottom. Streamlines were drawn in ParaView over surface plot of velocity using “Stream Tracer with Custom Source Filter”, afterwards lines were colored in black using “Solid Color” option. Isotherms were drawn in the same manner using solid and black color for “Contour” filter lines

Details for the model parameters will not be given here since it is not a subject of this work. The model was used to examine the procedures in Code_Saturne. For example, the possibility of programming geometry, and afterwards mesh, can be useful for the change of length of the heated part of the bottom wall.

Post-processing was performed in ParaView without any difficulties. The details are given in paragraph 6.

5.2 OpenFOAM

The open-source CFD software that stands out by its popularity among researchers worldwide from the very beginning is OpenFOAM. Without going into the turbulent history, and into the dispute about the first developer, the creation of OpenFOAM started at the Imperial College, University of London, an inspiring place known for its tradition through one of the pioneers of CFD Brian Spalding, and people from his group like Suhas Patankar or David Gosman. The tradition obviously continued since OpenFOAM began its development as product of PhD research or work under the mentorship of professor David Gosman.

The first developers are still active participants in the development of OpenFOAM, the first one, Henry Weller, together with Chris Greenshields through The OpenFOAM Foundation [19]; Hrvoje Jasak, the one that was responsible for the most of the fundamental development at the beginning, and Gavin Tabor through ESI Group [20]. Also, on the website for developers [50], one can find names from the list of the first, Andrew Heather and Mattijs Janssens, constantly active in current development.

From 2004 a new version of software has been released at least once a year. Installation procedure is usually explained in details. Example is the last version, coming with the step-by-step explanation of the Windows installation under WSL2. OpenFOAM comes with numerous examples that can be found in the tutorials' directory of the software. The examples are often followed by text file containing references for the model used in example, and with data for validation of the results.

Details for the creation of the models and the steps needed for the execution of the simulations can be found at websites already mentioned in references. There is still no GUI, the execution of the simulations is done through the terminal. Mesh generation can be done using OpenFOAM tools for mesh generation, or using other software and afterward convert the mesh using OpenFOAM converters. ParaView is used for post-processing, but also EnSight, Fieldview and Fluent.

In OpenFOAM, there is already a series of prepared solvers for buoyancy driven flows, and there are constantly developing. In this work, one such solver was selected for the simulation example. The heat transfer tutorial case using buoyantSimpleFoam solver was chosen as starting point. The solver is for steady turbulent buoyancy driven flow which is in the latest version merged with transient buoyantPimpleFoam solver into one buoyantFoam solver. In the OpenFOAM tutorial, the model was turbulent natural convection in an enclosed tall cavity from experimental study given in reference [51]. The test and the data for validation of the results are provided in the tutorial directory. In this work, the boundary conditions were changed to simulate the natural convection in shallow enclosure. The temperature difference was imposed to horizontal walls, higher temperature at the bottom and lower at the top wall. The case is two-dimensional, but the solution is three-dimensional, one mesh cell had to be added in third dimension and OpenFOAM boundary type "empty" had to be selected for those boundaries.

The illustration for two different aspect ratios of the enclosure are given in figure Fig. 10. As in the case of Code_Saturne example, the details of simulations and the parameters used in simulations will not be given here.

OpenFOAM can be, and has often been used, in advanced CFD courses. As mentioned earlier, an outstanding example is PhD course "CFD with OpenSource Software" of professor Håkan Nilsson [31] who is also responsible for turbomachinery applications at ESI Group Technical Committees for OpenFOAM. Among other, the website of this course contains tutorials made by students, some of which are worthy of attention.

6 Post-Processing with ParaView

ParaView is the most widely used open-source data analysis and visualization software. Nearly every open-source software for numerical simulations relies upon ParaView for post-processing. Detailed information about software usage, development, and webinars can be found on ParaView website [52]. The software was released in 2002 as a project of Kitware and Los Alamos National Laboratory, and as a product built on Visualization Toolkit (VTK) libraries of Kitware – a company dedicated to R&D of open-source 3D visualization tools. It is difficult to describe all the power of ParaView in few lines, therefore the emphasis will be placed on several elementary flow field post-processing examples.

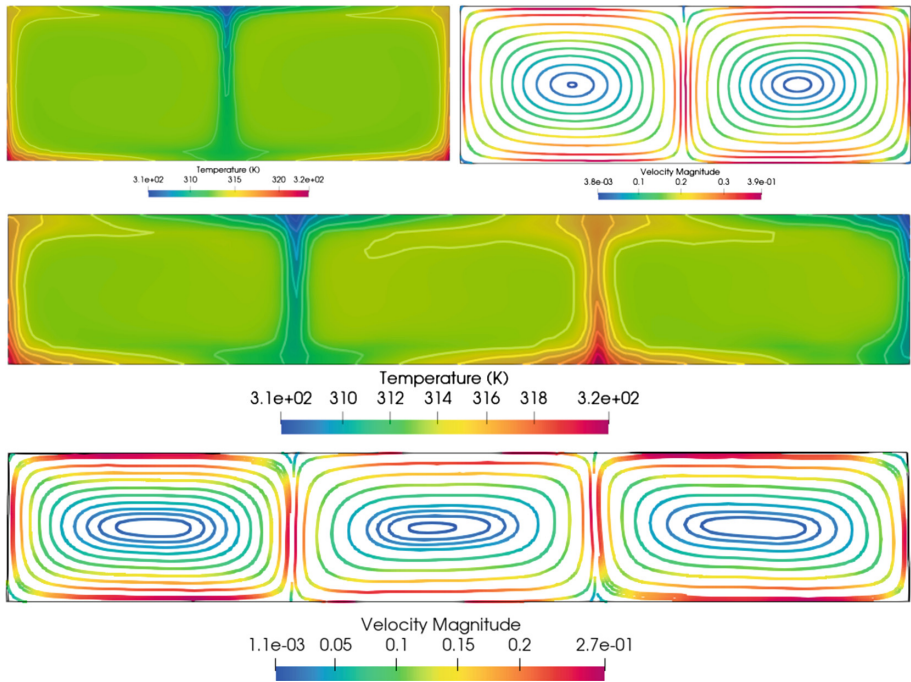


Fig. 10. Isotherms and streamlines for shallow enclosure with aspect ratio approximately 3 (top two) and aspect ratio approximately 6 (bottom). Stream lines were drawn in ParaView using “Evenly Spaced Streamlines 2D” filter, afterwards the “Point” representation was selected in order to ensure better line visibility

Since the mesh from previous examples is simple, flange mesh obtained from OpenFOAM snappyHexMesh tutorial (OpenFOAM tutorials/mesh/snappyHexMesh/flange) is used to demonstrate geometry and mesh visualization in ParaView. The solid color surface representation of the object mesh is illustrated in Fig. 11. Followed by two cuts combined in one presentation.

Wireframe of the flange mesh, and surface mesh of one boundary defined in advance, are also presented in Fig. 11. Boundaries which are defined on a model can be selected as mesh regions in ParaView, and they can be visualized separately along with the fluid or solid properties for those boundaries calculated in the simulations.

Two methods of streamline presentation were already used and the results were illustrated in Figs. 9 and 10. For the presentation in Fig. 9, “Stream Tracer with Custom Source” filter was applied, “CellDatatoPointData” filter was used as stream tracer input, and “MaskPoints” filter was used as stream tracer seed source. Streamlines were colored with solid black color, and visualized together with surface plot of velocity.

For the presentation in Fig. 10, “CellDatatoPointData” filter was applied first, then the “Slice” filter parallel to the enclosure, and finally “Evenly Spaced Streamlines 2D” filter to draw evenly spaced streamlines.

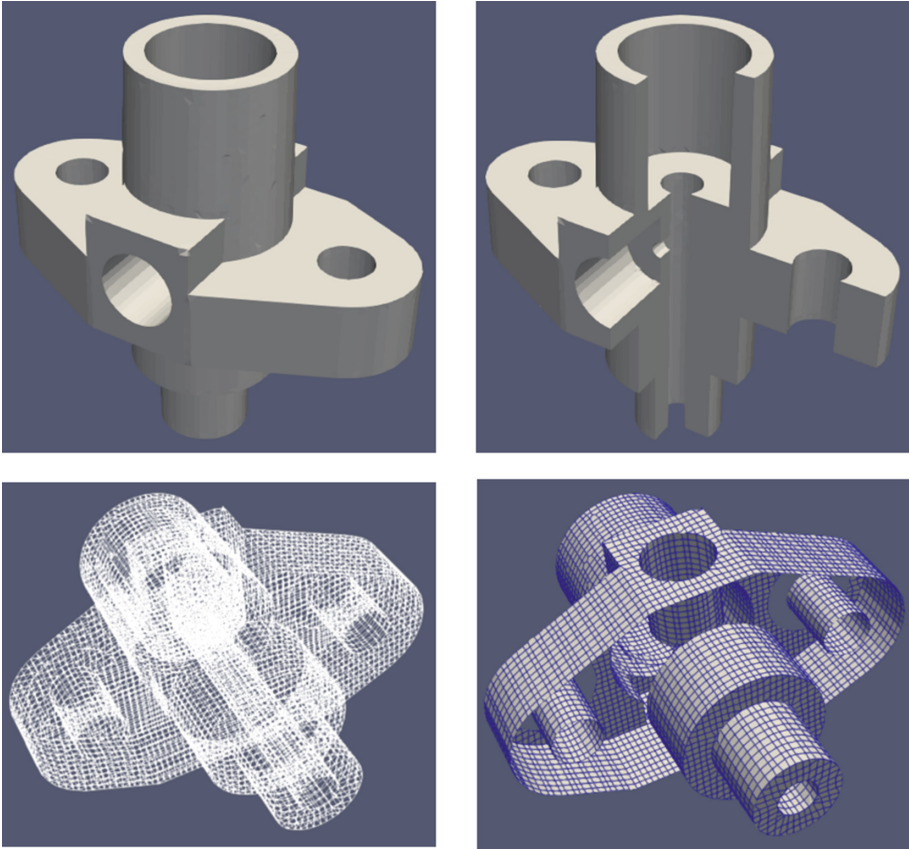


Fig. 11. ParaView visualization of the flange obtained from OpenFOAM snappyHexMesh tutorial example (top left), the image of the object's two cuts obtained using "Clip" filter in x and y direction and combined (top right), wireframe presentation (bottom left), and surface mesh of one boundary (bottom right)

In Fig. 12 the results for velocity of the shorter enclosure from Fig. 10 are presented using "Glyph" filter. First "CellDatatoPointData" filter was used, then "Stream Tracer" filter, and, at the end, "Glyph" filter was applied to draw vectors along streamlines with intensity and orientation.

Important to mention is that ParaView has numerous readers, tools for reading different file types like: CGNS, EnSight, Fluent, Plot3D, Tecplot and many more. In addition to being used as post-processor for numerical simulations, it is also a powerful tool for material, medical and other types of computer visualization.

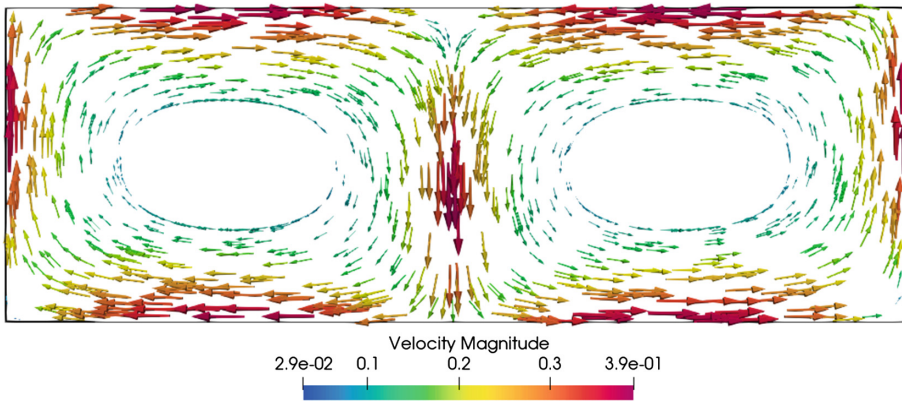


Fig. 12. Vector presentation of velocity magnitude

7 Conclusion

The attention was paid to most popular open-source software for numerical simulations, and there is a lot more to say about the one we mentioned. Of course, there are many more that we haven't and won't be able to process: Elmer FEM [53], one other joint effort between government organization, Finnish IT Center for Science (CSC), and Finnish universities, research laboratories, and industry – from the beginning, the main idea was to make a multiphysics software, and Elmer was built in such a way; one other multiphysics project – an open-source, parallel, finite element framework Moose [54] draws attention with fantastic gallery of simulations already done in it; there is a lot of new research that uses TrioCFD [38] for fluid calculations, but the problem is that aside from research papers most of the information about software is in French. The list is infinite, and on top of it all Python, modern object-oriented programming language that is everywhere and in almost all we mentioned.

Acknowledgement. This work was supported by the Ministry of Science, Technological Development, and Innovations (Serbia) by Contract No. 451-03-47/2023-01/200213.

References

1. Sedmak, A.: Computational fracture mechanics: an overview from early efforts to recent achievements. *Fatigue Fract. Eng. Mater. Struct.* **41**(12), 2438–2474 (2018). <https://doi.org/10.1111/ffe.12912>
2. Milosevic, N., Younise, B., Sedmak, A., Travica, M., Mitrovic, A.: Evaluation of true stress–strain diagrams for welded joints by application of digital image correlation. *Eng. Failure Anal.*, 128 (2021). <https://doi.org/10.1016/j.engfailanal.2021.105609>
3. Kirin, S., Sedmak, A., Zaidi, R., Grbović, A., & Šarkochević, Ž.: Comparison of experimental, numerical and analytical risk assessment of oil drilling rig welded pipe based on fracture mechanics parameters. *Eng. Failure Anal.*, 114 (2020). <https://doi.org/10.1016/j.engfailanal.2020.104600>

4. Milovanović, N., Sedmak, A., Arsic, M., Sedmak, S.A., Božić, Ž.: Structural integrity and life assessment of rotating equipment. *Eng. Failure Anal.*, 113 (2020). <https://doi.org/10.1016/j.engfailanal.2020.10456>
5. Sedmak, A., Čolić, K., Grbović, A., Balać, I., Burzić, M.: Numerical analysis of fatigue crack growth of hip implant. *Eng. Fracture Mech.*, 216 (2019). <https://doi.org/10.1016/j.engfracmech.2019.106492>
6. Grbović, A., Kastratović, G., Sedmak, A., Balać, I., Popović, M.D.: Fatigue crack paths in light aircraft wing spars. *Int. J. Fatigue* **123**, 96–104 (2019). <https://doi.org/10.1016/j.ijfatigue.2019.02.013>
7. Sedmak, A.S., et al.: Heat input effect of friction stir welding on aluminum alloy AA 6061–T6 welded joint. *Therm. Sci.* **20**(2), 637–641 (2016). <https://doi.org/10.2298/TSCI150814147D>
8. Sedmak, A., Čolić, K., Burzić, Z., Tadić, S.: Structural integrity assessment of hip implant made of cobalt chromium multiphase alloy. *Struct. Integrity Life* **10**(2), 161–164 (2010)
9. Veljić, D., et al.: Numerical simulation of the plunge stage in friction stir welding. *Struct. Integrity Life* **11**(2), 131–134 (2011)
10. Ivanović, I.B., Sedmak, A.S., Miloš, M.V., Živković, A.B., Lazić, M.M.: Numerical study of transient three-dimensional heat conduction problem with a moving heat source. *Therm. Sci.* **15**(1), 257–266 (2011). <https://doi.org/10.2298/TSCI1101257I>
11. “Ansys,” [Online]. Available: <https://www.ansys.com/>
12. “Abaqus,” [Online]. Available: <https://www.3ds.com/products-services/simulia/products/abacus/>
13. “COMSOL Multiphysics,” [Online]. Available: <https://www.comsol.com/>
14. “Wolfram Mathematica,” [Online]. Available: <https://www.wolfram.com/mathematica/>
15. “MathWorks Matlab,” [Online]. Available: <https://www.mathworks.com/>
16. “Gmesh,” [Online]. Available: <https://gmsh.info/>
17. Geuzaine, C., Remacle, J.-F.: Gmsh: a three-dimensional finite element mesh generator with built-in pre- and post-processing facilities. *Int. J. Numer. Meth. Eng.* **79**(11), 1309–1442 (2009)
18. “CalculiX, A Free Software Three-Dimensional Structural Finite Element Program,” [Online]. Available: <http://www.calculix.de/>
19. “OpenFOAM, The OpenFOAM Fondation,” [Online]. Available: <https://openfoam.org/>
20. “OpenFOAM,” [Online]. Available: <https://www.openfoam.com/>
21. Chen, G., Xiong, Q., Morris, P.J., Paterson, E.G., Sergeev, A., Wang, Y.-C.: OpenFOAM for computational fluid dynamics. *Not. Am. Math. Soc.* **61**(4), 354–363 (2014)
22. “CAELinux,” [Online]. Available: <https://www.caelinux.com/CMS3/>
23. J. Cugnon, “CAELinux: an open source engineering platform,” <https://www.caelinux.com/CMS3/images/caelinuxpresentation2015.pdf> (2015)
24. “Salome platform, The open-source platform for numerical simulation,” [Online]. Available: <https://www.salome-platform.org/>
25. “Code_Aster, Structures and Thermomechanics Analysis for Studies and Research,” [Online]. Available: <https://code-aster.org>
26. “Code_Saturne, the free, open-source software for computational fluid dynamics (CFD) applications,” [Online]. Available: <https://www.code-saturne.org/>
27. “The French National Research Agency (ANR),” [Online]. Available: <https://anr.fr/en/anrs-role-in-research/about-us/missions/>
28. “Open Cascade Technology,” [Online]. Available: <https://dev.opencascade.org/>
29. “History of SALOME,” [Online]. Available: https://www.salome-platform.org/?page_id=676
30. “GNU Operating System, Licenses,” [Online]. Available: <https://www.gnu.org/licenses/licenses.html>

31. H. Nilsson, "CFD with OpenSource Software, PhD course at Chalmers University of Technology," [Online]. Available: https://www.tfd.chalmers.se/~hani/kurser/OS_CFD/#YEAR_2023
32. "Ubuntu on WSL," [Online]. Available: <https://ubuntu.com/wsl>
33. "Spyder," [Online]. Available: <https://www.spyder-ide.org/>
34. "Python," [Online]. Available: <https://www.python.org/>
35. "Syngularity," [Online]. Available: <https://docs.sylabs.io>
36. "Salome-Meca v2021 and Code_Aster v2021 for Windows," [Online]. Available: <https://code-aster-windows.com/2022/04/22/salome-meca-2021-for-windows/>
37. Bhatia, H., Bieder, U., Guenadou, D.: Rankine-vortex model based assessment of CFD methods for simulating the effect of gas entrainment observed in the hot-pool of sodium cooled fast breeder reactors. *Progress Nucl. Energy* **137** (2021)
38. "TrioCFD," [Online]. Available: <https://trio CFD.ceea.fr/>
39. Angeli, P.-E., Puscas, M.-A., Fauchet, G., Cartalade, A.: FVCA8 benchmark for the stokes and Navier-stokes equations with the TrioCFD code—benchmark session. In: *Finite Volumes for Complex Applications 8*, Lille, France (2017)
40. Bieder, U., Genrault, C., Ledac, P.: Hydraulic forces acting on full cross section fuel assemblies with 17×17 fuel rods. *Progress Nucl. Energy* **130** (2020)
41. Zhang, C., Wang, L., Wang, M., Xu, T., Barthet, A., Liu, Y., Tian, W., Qiu, S., Su, G.: Numerical simulation of pressure force for control rod guide tube in PWR. *Progress Nucl. Energy* **148** (2022)
42. Müller, J., Velten, K.: Application of computational fluid dynamics for the optimization of homogenization processes in wine tanks. In: *BIO Web of Conferences 5* (2015)
43. "DAKOTA," [Online]. Available: <https://dakota.sandia.gov/>
44. Ivanovic, I., Sedmak, A., Rudolf, R., Gusel, L., Grujic, B.: Distortion of the substructure of a 20-ft shipping container exposed to zinc hot-dip galvanizing. *Mater. Technol.* **47**(2) (2013)
45. Marc, R.: A short introduction to SHAPER (2019). [Online]. Available: https://events.prace-ri.eu/event/896/sessions/2723/attachments/998/1676/SHAPER_AShortIntro_2.pdf
46. "Netgen/NGSolve," [Online]. Available: <https://ngsolve.org/>
47. Lazic, V., Ivanovic, I., Sedmak, A., Rudolf, R., Lazic, M., Radakovic, Z.: Numerical analysis of temperature field during Hardfacing process and comparison with experimental results. *Thermal Sci.* **18** (2014)
48. "Code_Aster study examples," [Online]. Available: <https://code-aster.org/V2/spip.php?article14>
49. EDF R&D, Fluid Dynamics, Power Generation and Environment Department, Single Phase Thermal-Hydraulics Group, "Code saturne version 7.0 tutorial: Heated Square Cavity Flow," (2022)
50. "OpenFOAM development," [Online]. Available: https://develop.openfoam.com/groups/Development/-/group_members
51. Betts, P.L., Bokhari, I.H.: Experiments on turbulent natural convection in an enclosed tall cavity. *Int. J. Heat Fluid Flow* **21**(6), 675–683 (2000)
52. "ParaView," [Online]. Available: <https://www.paraview.org/>
53. "Elmer FEM," [Online]. Available: <http://www.elmerfem.org>
54. "MOOSE," [Online]. Available: <https://mooseframework.inl.gov/>



Aircraft Lug Failure Design Under Fatigue Loading

Slobodanka Boljanovic^(✉)

Mathematical Institute of the Serbian Academy of Sciences and Arts, Kneza Mihaila 35, 11000
Belgrade, Serbia
slobodanka.boljanovic@gmail.com

Abstract. For high speed systems, fatigue relevant analysis of lug-type joints plays an important role in preventing sudden hazard events. Dynamic loads are one of the main causes of system disturbance during service operations. In the present research, thus, the stress state of the lug with an elliptical corner crack-like flaw was explored, and prognostic analysis in terms of residual life was performed using a new computational framework. This study provides valuable information for both academia and industry on the detrimental effects of stress raisers for improving the optimal and safe design of fatigue-critical lug type joints.

Keywords: Computational design · Elliptical flaw · Fatigue life · Lug-Pin joint

1 Introduction

Large moving systems face a loss of stability due to crack-like flaws, and damage tolerance requirements under dynamic load impose significant challenges in terms of the safe-integrity design. The problem's complexity increases due to the hotspots where stress concentrators such as lug-type joints participate in the load transfer for relevant operations. In the contact linkage zone, evidently, the presence of a strong notch effect causes the lug-pin joints to be highly susceptible to the sudden formation of part-through crack-like flaws. Thus, it is necessary to efficiently combine appropriate sets of damage tolerance-based strategies within computational design models to assess the fatigue response of quarter-elliptical or semi-elliptical flaws at the lug-type joint.

The presence of continuous concern about the increased risk of fatigue-driven hazard events motivated researchers to pay special attention to the surface part-through phenomena through relevant fracture mechanics-based concepts. Thus, the stability of lug with an elliptical corner crack or a through-the-thickness crack has been assessed by Kathiresan and Brussat [1] by applying Forman and Walker crack growth concepts [2, 3], the Green's function method [4] and the finite element method [5]. Guo [6] suggested that an analytical crack growth model can be employed for analyzing the same fatigue flaws under biaxial and pin loading. Rigby and Aliabadi [7] explored the behavior of the elliptical corner flaw coupled with the pin-loaded effect by using the J -integral method

and the boundary element method. Later, Mikheevskiy et al. [8] analyzed the same linkage via the weight function method and the UnuGrow software framework based on the Noroozi et al. concept [9].

Through safety-relevant design of the lug with elliptical corner flaw, Boljanović et al. [10] introduced novel damage-tolerance based solutions by combining the modified Zhan et al. concept [11] with the J -integral method. Further, Boljanović and Carpinteri [12] performed the fatigue analysis in the case of the same flaw by means of the modified two parameter driving force model.

Moreover, Jones et al. [13] demonstrated that the behavior of semi-elliptical flaws can be evaluated through the weight function method and the CTOD crack growth model. Boljanović et al. [14] examined such a stress raiser located at a hole taking into account the crack growth concept proposed by Kujawski [15] and the finite element method. Later, Boljanović and Carpinteri [16] proposed novel stress ratio dependent solutions to generate the mode progression due to semi-elliptical flaw.

The present research study aims to develop a computational model for the failure resistance assessment of pin-loaded lugs under the threat of defect-related hotspot formation in a dynamic load environment. The analysis uses sets of analytical solutions to quantify the bearing capacity degradation due to stress raiser interactions. Such novel damage tolerance-based formula, successfully verified, can be used for a reliable design of lug with the elliptical corner flaw, enabling the adjustment of relevant performance characteristics according to long-term durability requirements.

2 Failure Mode Analysis Under Dynamic Load

The driving mode of an elliptical corner flaw was assessed here via crack growth rates in depth and surface direction, modifying the fracture mechanics concept proposed by Huang and Moan [17], expressed as follows:

$$\frac{da}{dN} = C_A (M \Delta K_A)^{m_A}, \quad \frac{db}{dN} = C_B (M \Delta K_B)^{m_B} \quad (1)$$

where ΔK_A , ΔK_B and da/dN , db/dN are stress intensity factor ranges and corresponding crack growth rates in depth and surface direction, respectively, C_A , C_B , m_A , m_B represent material parameters generated through fatigue experiments.

Through safety-relevant linkage assessments, the interaction between service loadings and environmental factors was quantified by means of the fracture mechanics parameter M [17], i.e.

$$M = \begin{cases} (1 - R)^{-\beta_1} & -5 \leq R < 0 \\ (1 - R)^{-\beta} & 0 \leq R < 0.5 \\ (1.05 - 1.4R + 0.6R^2)^{-\beta} & 0.5 \leq R < 1 \end{cases} \quad (2)$$

where R is stress ratio, β and β_1 are crack growth exponents, experimentally obtained in the case of positive and negative values of loading.

Moreover, to achieve effective and efficient decision making in a complex load environment, the number of loading cycles N was generated for two critical (depth and surface) directions integrating relevant crack growth rates, defined by

$$N = \int_{a_0}^{a_f} \frac{da}{C_A (M \Delta K_A)^{m_A}}, \quad N = \int_{b_0}^{b_f} \frac{db}{C_B (M \Delta K_B)^{m_B}} \quad (3)$$

where (a_0, b_0) and (a_f, b_f) are initial and final crack growth length in depth and surface direction, respectively.

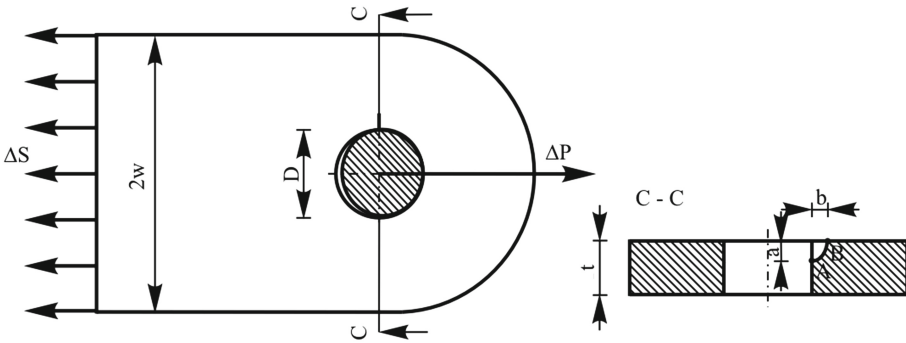


Fig. 1. Cyclically loaded lug with quarter-elliptical crack

The necessity to progress towards sustainability has inspired modern researchers in the aeronautical sector to theoretically examine the interaction between stress raiser effects and in-service loading on the fatigue response of large moving systems. Therefore, in the present research study, a novel computational design model was developed to generate the fatigue stability of pin-loaded lug with elliptical corner flaw. In order to solve novel damage tolerance-based solutions herein discussed, the Euler's numerical integration algorithm for functions of a complex variable was employed.

3 Stress Intensity Evaluation for a Corner Flaw

A long-duration aircrafts designed for relevant missions must include adequate protection against sudden failures in hotspots, where stress raisers exist, by implementing fracture mechanics-based analytical and/or numerical approaches [18–28]. In this context, the performance of lug-type joint with elliptical flaw (Fig. 1) was analyzed through the stress intensity factor [29], expressed as follows:

$$\Delta K = F_{qec} \Delta S \sqrt{\frac{\pi a}{Q}} \quad (4)$$

where a and Q are the crack length in depth direction and the ellipse shape factor, respectively, ΔK denotes the stress intensity factor and ΔS is applied stress range.

Fatigue-induced degradation is evaluated taking into account the effect of elliptical corner crack and the lug-hole effect through the correction factor F_{qec} [29], i.e.

$$F_{qec} = \left[M_1 + M_2 \left(\frac{a}{t} \right)^2 + M_3 \left(\frac{a}{t} \right)^4 \right] g_1 g_2 g_3 g_4 f_{\phi} f_{w1} G_1 \quad (5)$$

where a and t are crack length in depth direction and lug thickness, respectively, G_1 is the correction factor for the lug with one crack, and f_w is the correction factor related to the lug-width effect, respectively.

Further, stress disturbance caused by the quarter-elliptical crack, in the case of $a/b \leq 1$, was generated considering the crack size effect and the crack shape associated with the location angle on the crack front in terms of relevant correction factors $M_1, M_2, M_3, g_1, g_2, g_3, Q$, given by

$$M_1 = 1.13 - 0.09 \left(\frac{a}{b} \right) \quad (6)$$

$$M_2 = -0.54 + \frac{0.89}{0.2 + \frac{a}{b}} \quad (7)$$

$$M_3 = 0.5 - \frac{1}{0.65 + \frac{a}{b}} + 14 \left(1 - \frac{a}{b} \right)^{24} \quad (8)$$

$$g_1 = 1 + \left[0.1 + 0.35 \left(\frac{a}{t} \right)^2 \right] (1 - \sin \varphi)^2 \quad (9)$$

$$g_2 = \frac{1 + 0.358\lambda + 1.425\lambda^2 - 1.578\lambda^3 + 2.156\lambda^4}{1 + 0.13\lambda^2} \quad (10)$$

$$\lambda = \frac{1}{1 + \frac{b}{r} \cos(0.85\varphi)} \quad (11)$$

$$g_3 = \left(1 + 0.04 \frac{a}{b} \right) \left[1 + 0.1(1 - \cos \varphi)^2 \right] \cdot \left[0.85 + 0.15 \left(\frac{a}{t} \right)^{\frac{1}{4}} \right] \quad (12)$$

$$g_4 = 1 - 0.7 \left(1 - \frac{a}{t} \right) \left(\frac{a}{b} - 0.2 \right) \left(1 - \frac{a}{b} \right) \quad (13)$$

$$Q = 1 + 1.464 \left(\frac{a}{b} \right)^{1.65} \quad (14)$$

where ϕ represents the location angle at a crack front and r denotes the radius of the lug hole, respectively.

Through the failure resistance analysis, the pin-loaded effect, the location angle effect and the lug-width effect are theoretically examined by means of the correction factors G_1, f_{ϕ} and f_w , respectively, expressed as follows

$$G_1 = \frac{1}{2} + \frac{2w}{\pi(2r+b)} \sqrt{\frac{r}{r+b}} \quad (15)$$

$$f_{\phi} = \left[\left(\frac{a}{b} \right)^2 \cos^2 \varphi + \sin^2 \varphi \right]^{0.25} \quad (16)$$

$$f_{w1} = \left\{ \sec \left(\frac{\pi r}{2w} \right) \sec \left[\frac{\pi}{4} \frac{(2r+b)}{w+b} \sqrt{\frac{a}{t}} \right] \right\}^{0.5} \quad (17)$$

4 Stability Analysis of Lug with Part-Through Corner Flaw

4.1 Life Assessment of Pin-Loaded Lug

In the first section, the fatigue endurance of damaged lug (Fig. 1) was explored via residual life evaluation. Initial quarter-elliptical crack-like flaw is characterized by the following lengths $a_0 = b_0 = 0.635$ mm in depth and surface direction, respectively. Through failure analysis the lugs ($D = 38.1$ mm, $t = 12.7$ mm), made of 7075 T851 Al Alloy ($C_A = 4.0 \times 10^{-10}$, $m_A = m_B = 2.9$, with da/dN , db/dN in m/cycles and ΔK_A , ΔK_B in MPam^{0.5}), were subjected to two different stress ratios $R = 0.1$ and 0.5 . Note that, applied maximum stresses and corresponding stress ratios in the case of two lug widths ($2w = 57.15$ mm and 114.3 mm) are shown in Table 1.

Table 1. Maximum stress S_{max} , stress ratio R and width $2w$ for relevant lug configurations [1] examined through this research work.

Lug ID [1]	S_{max} (MPa)	R	$2w$ (mm)
ABPLC21	41.38	0.1	57.15
ABPLC18, ABPLC22	41.38	0.5	57.15
ABPLC6, ABPLC56	41.38	0.1	114.3
8ABPLC88, ABPLC55	103.31	0.5	114.3

The interest in surface phenomena under dynamic load has increased due to high performance requirements of modern large systems during service operations. In this context, the interaction between the elliptical-flaw effect and the stress ratio effect coupled with pin-loaded effect is herein examined in terms of the lug life through a novel damage tolerance-based analytical model, employing Eqs. (4) to (17) together with Eqs. (2) and (3), respectively. The evaluated number of loading cycles, as a function of crack length, is shown in Figs. 2, 3, 4 and 5 for two different lug widths.

Relevant fatigue outcomes obtained in the case of two values of stress ratios are then compared with experiments tested by Kathiresan and Brussat [1] and theoretical results generated by Boljanović and Maksimović [30], as is shown in Figs. 2, 3, 4 and 5 and Table 2.

From different comparisons, it can be deduced that the developed computational model provides reliable fatigue evaluations for the lug with elliptical corner flaw subjected to dynamic loads. It should be also noted that, in the case of stress ratio equal to $R = 0.1$, theoretical outcomes obtained through this research work are less conservative than those previously discussed [30] with respect to literature-based experiments [1].

Further, the safety relevant analysis demonstrates that if the lug width increases from $2w = 57.15$ mm to 114.3 mm, the number of loading cycles increased from 28100 to 32900 according to experiments, while obtained estimates have approximately the same values under maximum stress and stress ratio equal to $S_{max} = 41.38$ MPa and $R = 0.1$, respectively. Moreover, for a lug subjected to the same value of maximum stress, increasing the stress ratio from 0.1 to 0.5 leads to an increase in residual life more than

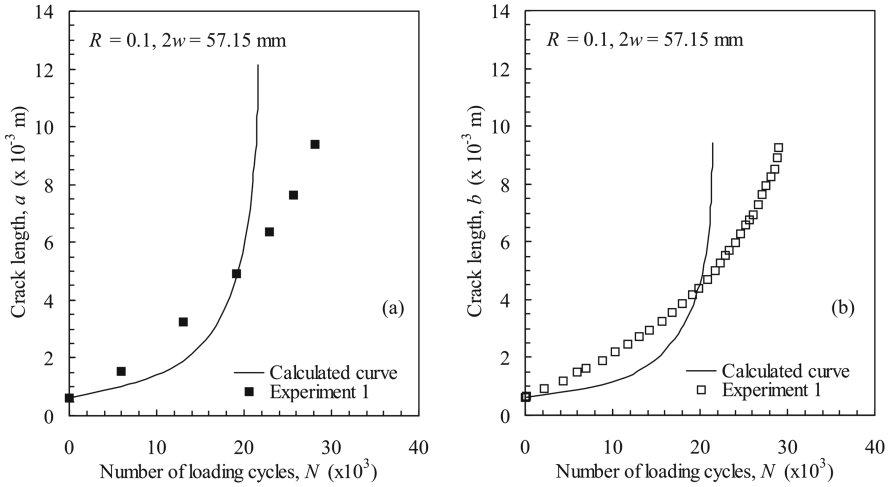


Fig. 2. Fatigue life evaluations ($R = 0.1$, $2w = 57.15$ mm): (a) a versus N and (b) b versus N ; calculated curves are generated within the present work and experiments (1 – ABPLC21) discussed by Kathiresan and Brussat [1].

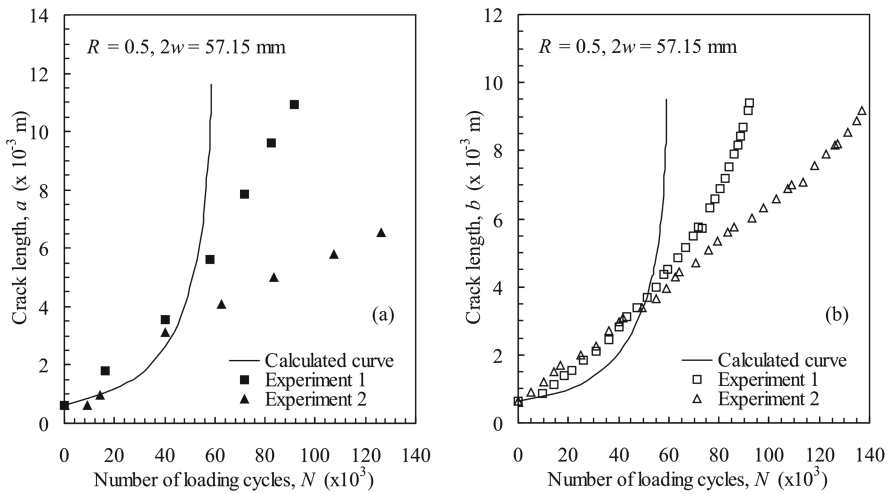


Fig. 3. Fatigue life evaluations ($R = 0.5$, $2w = 57.15$ mm): (a) a versus N , (b) b versus N ; calculated curves are generated within the present work and experiments (1 – ABPLC18 and 2 – ABPLC22) discussed by Kathiresan and Brussat [1].

two and a half times if the lug width and hole-diameter are equal $2w = 57.15$ mm and $D = 38.1$ mm, respectively.

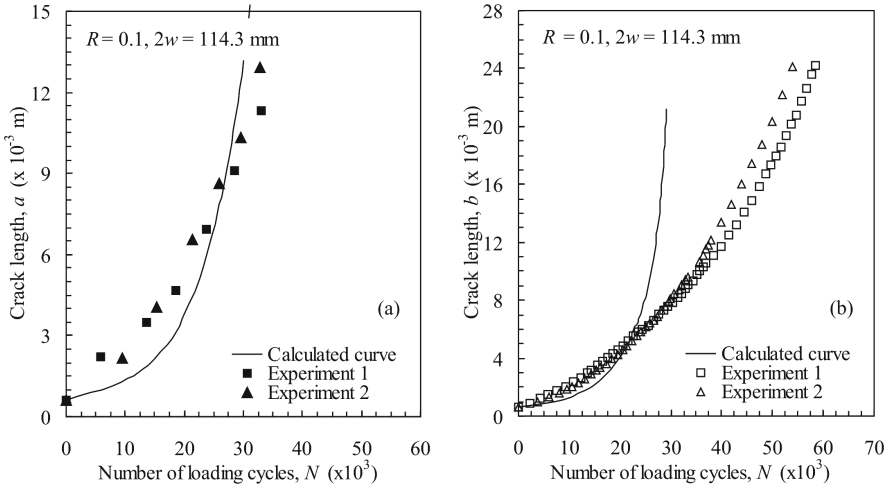


Fig. 4. Fatigue life evaluations ($R = 0.1$, $2w = 114.3$ mm): (a) a versus N , (b) b versus N ; calculated curves are generated within the present work and experiments (1 – ABPLC6 and 2 – ABPLC56) discussed by Kathiresan and Brussat [1].

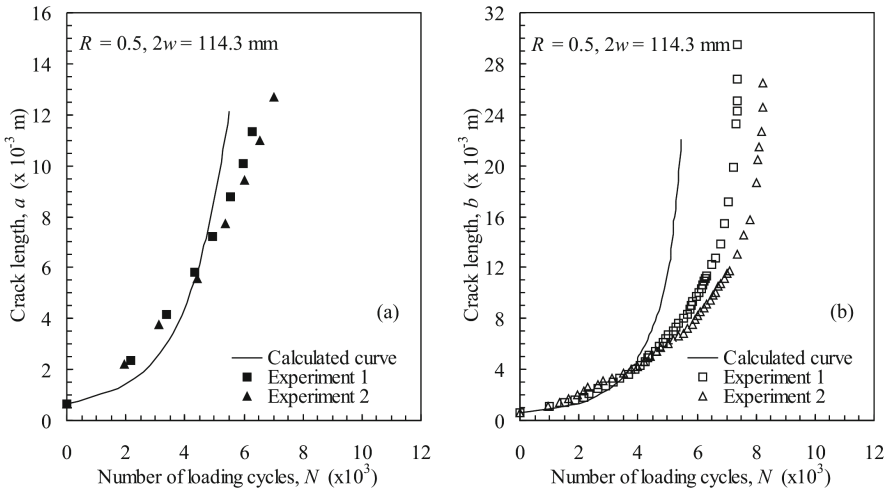


Fig. 5. Fatigue life evaluations ($R = 0.5$, $2w = 114.3$ mm): (a) a versus N , (b) b versus N ; calculated curves are generated within the present work and experiments (1 – ABPLC88 and 2 – ABPLC55) discussed by Kathiresan and Brussat [1].

4.2 Stress Intensity Calculation in the Vicinity of Crack Tip

Through this section, the stability of the pin-loaded lug (Fig. 1), made of 7075 T851 Al Alloy, was analyzed via the stress intensity factor. Such fatigue evaluations were performed in the case of maximum stress equal to $S_{max} = 48.8$ MPa and stress ratio $R = 0.3$, assuming that initial elliptical flaw is characterized by the following sizes:

Table 2. Evaluated number of loading cycles (N^{*cal} . Discussed by Boljanović et al. [30] and N^{cal} . from the present work) and experiments (N^{exp}) reported by Kathiresan and Brussat [1].

Lug ID [1]	$2w$ (mm)	N^{exp} . (cycles) [1]	N^{*cal} .(cycles) [30]	N^{cal} .(cycles)
ABPLC21-51,52	57.15	28100	19100	21400
ABPLC18, ABPLC22	57.15	91400; 126100	62380	58590
ABPLC6, ABPLC56	114.3	36356; 32900	19220	21190
8ABPLC88, ABPLC55	114.3	6300; 7015	4060	5440

$a_0 = 1.64$ mm, $b_0 = 1.97$ mm in depth and surface directions, whereas the lug width, hole-diameter and thickness are equal to $2w = 70$ mm, $D = 26$ mm, and $t = 12$ mm, respectively.

Considering the significant influence of driving forces on fatigue response of lug-type joint, it is important to carefully examine the stress raiser effects at damaged hole under service loading. Therefore, by employing Eqs. (4) and (5) coupled with Eqs. (6) to (17), the stress intensity factor was evaluated with respect to depth and surface directions, as it is shown in Fig. 6a and b, respectively.

Furthermore, the predictive-capability of obtained estimates was verified using appropriate theoretical results generated through analytical solutions, discussed by Boljanović and Maksimović [30], as is listed in Table 3. From such comparisons, it can be deduced that different stress intensity outcomes agree quite well for considered lug with the elliptical corner flaw.

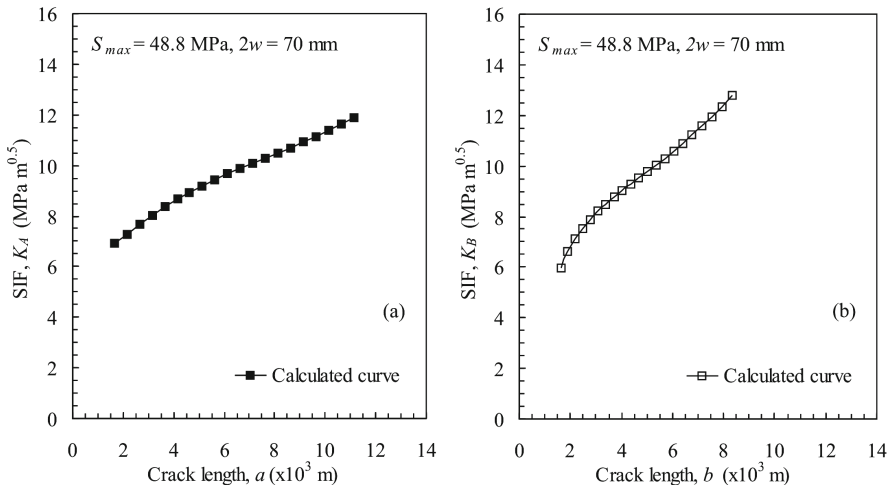


Fig. 6. Stress intensity analysis of the lug with elliptical corner flaw: (a) K_A versus a , (b) K_B versus b ; calculated curves are generated within the present work.

Table 3. Stress intensity calculation for elliptical corner crack-like flaw.

a (mm)	ΔK_A (MPam ^{0.5})	ΔK_B (MPam ^{0.5})	$\Delta K_A \cdot$ (MPam ^{0.5}) [30]	ΔK_B (MPam ^{0.5}) [30]
3.14	8.021	7.543	8.446	7.328
4.64	8.941	8.490	8.964	7.626
7.14	10.080	9.770	9.636	8.252
9.14	10.920	10.892	10.200	9.002

4.3 Crack Growth Evaluations at a Lug Hole

Now fatigue performance design examines the failure of pin-loaded lug (Fig. 7) in terms of crack path. Applied dynamic load is characterized by maximum stress equal to $S_{max} = 120$ MPa with stress ratio $R = 0.33$. The lug with initial elliptical crack ($a_0 = b_0 = 0.25$ mm, $2w = 60$ mm, $t = 9.6$ mm and $D = 25$ mm), is made of 7075 T851 Al Alloy ($S_u = 568$ MPa, $S_{0.2} = 506.5$ MPa, $C_A = 4 \times 10^{-10}$, $m_A = m_B = 2.9$, with da/dN , db/dN in m/cycles and ΔK_A , ΔK_B in MPam^{0.5}).

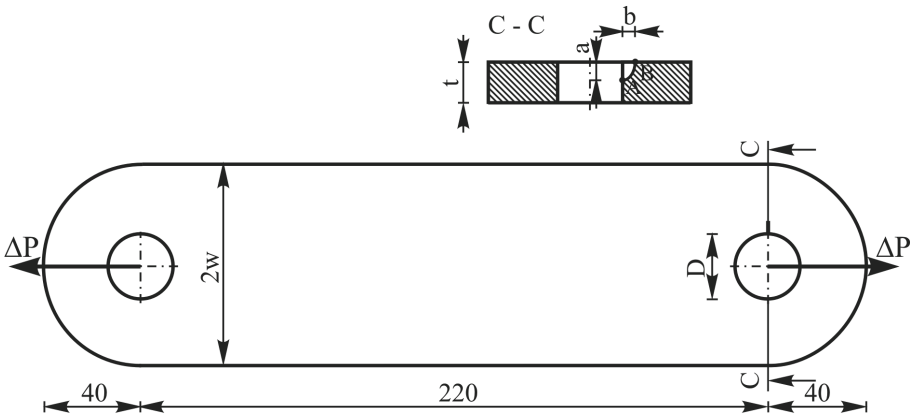


Fig. 7. The lug specimen with elliptical corner crack experimentally tested by Friedrich and Schijve [31].

One of the primary mission risks that must be monitored for large moving systems in a fatigue environment is that caused by surface crack-like flaw. Therefore, the stability of lug-type joint with elliptical corner flaw was generated via crack growth paths, using Eqs. (1) and (2) together with Eqs. (4) to (17). Relevant theoretical outcomes are plotted in Figs. 8, 9 and 10 for six different crack lengths in depth direction, adopting that the vertical axis and horizontal axis coincide with the lug hole and the front face of the lug, respectively.

Furthermore, in order to verify the computational design model, generated crack paths were compared with those experimentally tested by Friedrich and Schijve [31], as is

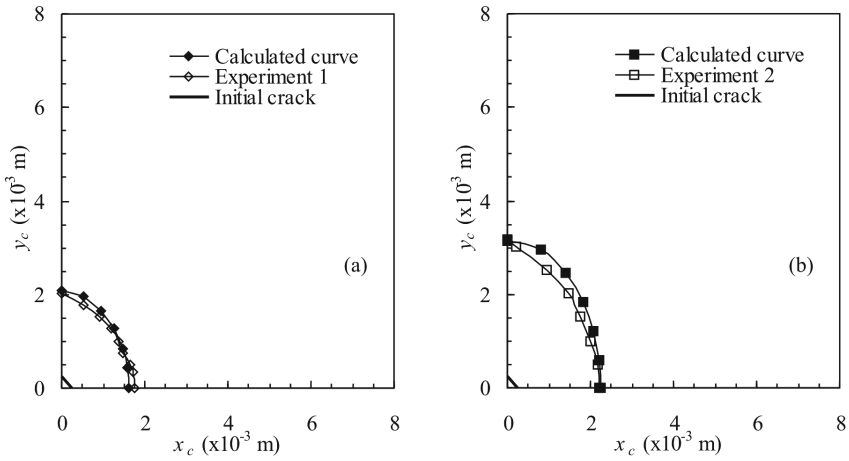


Fig. 8. Fatigue crack path evolutions: (a) $a = 2.07$ mm, (b) $a = 3.16$ mm; calculated curves are generated within the present work and experiments reported by Friedrich and Schijve [31].

shown in the same Figures. Examining relevant comparisons, it can be deduced that modeled crack growth paths adequately correlate with those obtained through experimental observations [31].

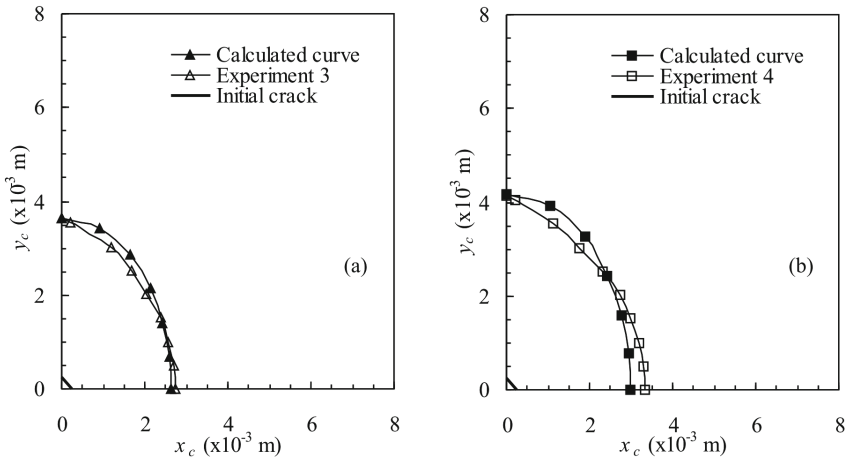


Fig. 9. Fatigue crack path evolutions: (a) $a = 3.64$ mm, (b) $a = 4.14$ mm; calculated curves are generated within the present work and experiments reported by Friedrich and Schijve [31].

4.4 Lug Failure Strength and the Hole-Diameter Effect

Fatigue stability evaluations are performed here in order to analyze the impact of the lug diameter (Fig. 1) on the failure strength. Thus, residual life of three different lugs ($2w =$

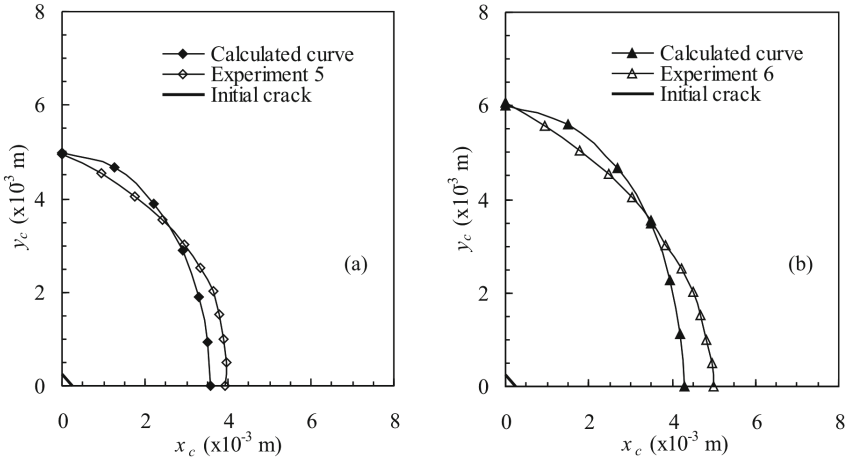


Fig. 10. Fatigue crack path evolutions: (a) $a = 4.95$ mm, (b) $a = 6.06$ mm; calculated curves are generated within the present work and experiments reported by Friedrich and Schijve [31].

90 mm, $t = 14$ mm, $a_0 = 1.86$ mm and $b_0 = 2.53$ mm), made of 7075 T851 Al Alloy, are assessed in the case of lug-hole diameters equal to $D = 32$ mm, 44.8 mm and 57.6 mm. Also, it was assumed that maximum force and stress ratio are equal to $P_{max} = 57000$ N and $R = 0.3$, respectively and material parameters are the same as those examined in Sect. 4.1.

Knowledge-based damage tolerance analysis represents an effective way to interpret the lug-failure due to elliptical corner flaw. Thus, the fatigue response was herein evaluated via the crack growth rate and residual life using Eqs. (1) to (3) coupled with Eqs. (4) to (17), respectively. Relevant analytical outcomes obtained in the case of three values of lug-hole diameters are shown in Fig. 11a and b for crack growth length in depth and surface direction, respectively.

Different comparisons indicate that if the lug diameter D increases from 32 mm to 44.8 mm, the residual life N decreases about 30%. Further, if the diameter increases from 44.8 mm to 57.6 mm, it causes the linkage capacity to decrease by about 50% for considered lug configurations with elliptical flaws. It is evident that increasing the lug-diameter can worsen the disturbed stress state of crack-like flaw, endangering the fatigue performance of lug-pin joint.

4.5 Impact of Stress Ratio and Crack Shape on the Fatigue Life of Lug

Finally, the failure performance of lugs with elliptical corner flaw ($2w = 80$ mm, $t = 10$ mm, $D = 30$ mm, $a_0 = 2.34$ mm and $b_0 = 3.19$ mm), made of 7075 T851 Al Alloy, was evaluated under dynamic load characterized by maximum force equal to $P_{max} = 32000$ N and three different values of stress ratios $R = 0.1$, 0.2 or 0.4, respectively.

Through the safety-relevant analysis, the lug life was estimated via a computational model generated within this research work, taking into account the stress ratio effect and pin loaded effect. Generated number of loading cycles, as a function of crack length

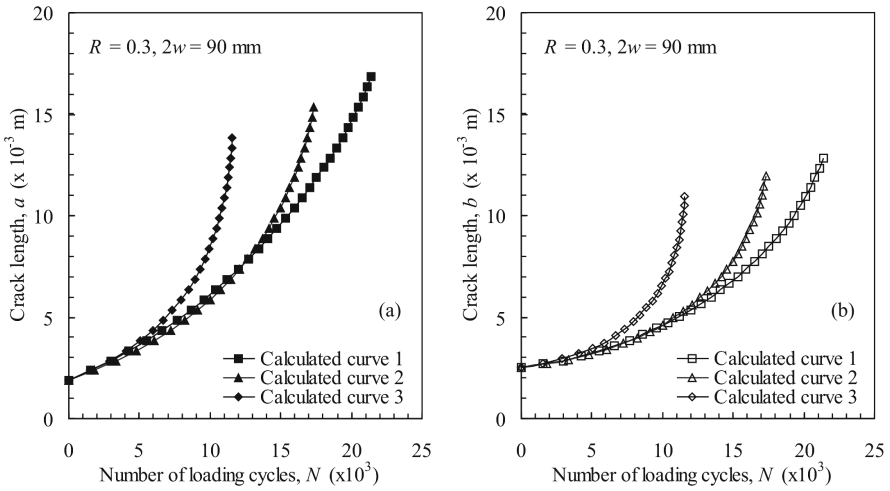


Fig. 11. Fatigue life evaluations ($a_0 = 1.86$ mm, $b_0 = 2.53$ mm): (a) a versus N , (b) b versus N ; 1- $D = 32$ mm, 2- $D = 44.8$ mm, 3- $D = 57.6$ mm, calculated curves are generated within the present work.

in depth and surface direction, are shown in Fig. 12a and b, respectively. Such damage tolerance-based outcomes indicate that if the stress ratio R increases from 0.2 to 0.4, the residual life increases about 28% in the case of considered lug with corner flaw.

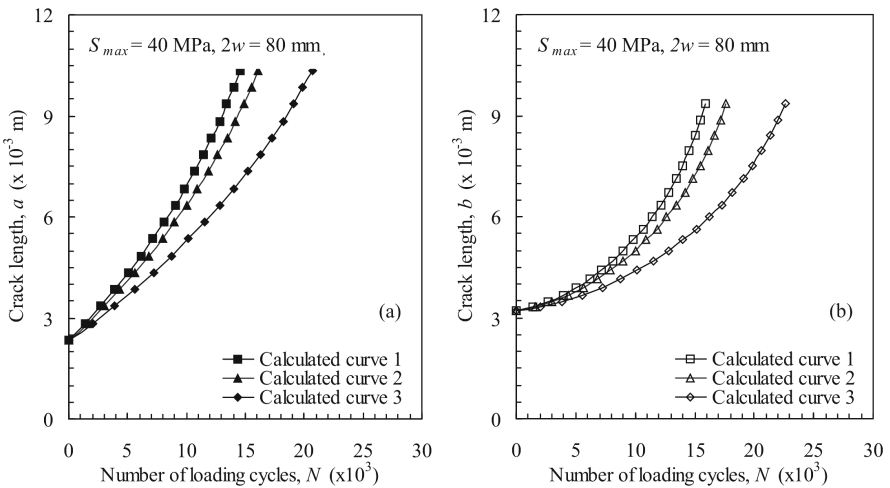


Fig. 12. Fatigue life evaluations ($a_0 = 2.34$ mm, $b_0 = 3.19$ mm): (a) a versus N , (b) b versus N ; 1- $R = 0.1$, 2- $R = 0.2$, 3- $R = 0.4$, calculated curves are generated within the present work.

Furthermore, the lug life was explored here in the case of three different corner flaws, whose sizes in depth and surface directions are equal to $a_0 = 1.9$ mm, 2.47 mm, 3.21 mm

and $b_0 = 3.41$ mm, assuming the following geometrical and loading parameters $2w = 86$ mm, $t = 15$ mm, $D = 32$ mm, $P_{max} = 44000$ N, $R = 0.2$, respectively. Fatigue-induced degradation of lug in terms of number of loading cycles, as a function of crack growth length in depth and surface direction, is plotted in Fig. 13a and b, respectively.

From relevant comparisons, it can be concluded that if the crack length in depth direction increases from 1.9 mm to 3.21 mm, it leads to a reduction in the number of loading cycles by 10% for fatigue-critical linkage examined. Since an increase in crack length in depth direction by less than 1.5 mm can cause a decrease in residual life by about 10%, it is clear that the application of reliable computational design models has a key role in ensuring the full functioning of large systems in a dynamic load environment.

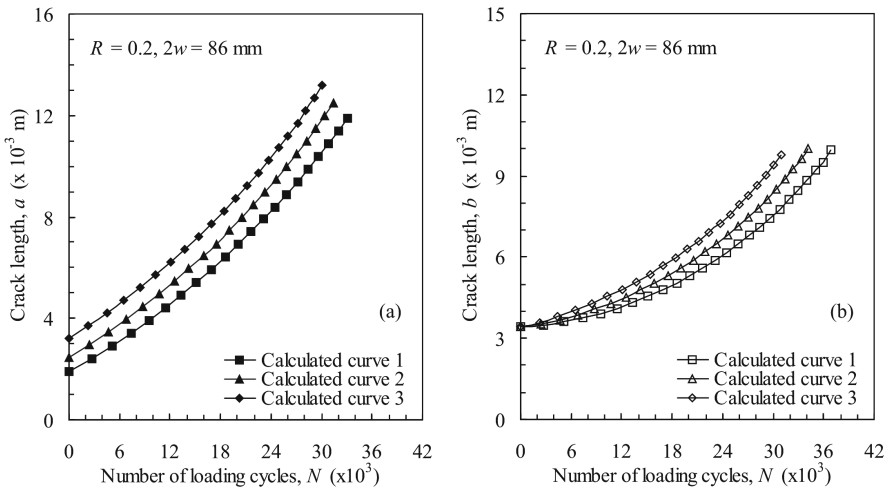


Fig. 13. Fatigue life evaluations ($b_0 = 3.41$ mm): (a) a versus N , (b) b versus N ; $1-a_0 = 1.9$ mm, $2-a_0 = 2.47$ mm, $3-a_0 = 3.21$ mm, calculated curves are generated within the present work.

5 Conclusions

How well large moving systems resist the damage that can occur during complex operations at high speeds is one of the main design configurations for aircrafts continuously exposed to dynamic load environments. Thus, this research proposes a novel computational model to evaluate the fatigue response of the elliptical corner flaw in order to achieve long-term durability of the lug-type joints. It was demonstrated that changes of driving forces result in direct variation on stress intensities at a damaged hole endangering residual life, which can suddenly lead to loss of lug stability. Analytical solutions were developed to assure that the formation targeted can be employed for crack growth path evaluations. Damage tolerance-based outcomes agree well with experimentally tested results, providing good confidence in the use of computational model to assess the failure strength and to generate safety-relevant performances of lug-type joints under service loading.

Acknowledgement. The scientific research presented in this chapter was supported by the Mathematical Institute of the Serbian Academy of Sciences and Arts, the Ministry of Education, Science and Technological Development of the Republic of Serbia and the COST Association, Brussels, Belgium within the Action CA18203, which is gratefully acknowledged.

References

1. Kathiresan, K., Brussat, T.R.: Advanced life analysis methods, AFWAL-TR-3080, Air Force Wright Aeronautical Laboratories, Ohio, United States (1984)
2. Forman, R.G., Kearney, V.E., Engle, R.M.: Numerical analysis of crack propagation in cyclic-loaded structures. *Trans. ASME. J. Basic Eng.* **89**, 453–464 (1967)
3. Walker, K.: The effect of stress ratio during crack propagation and fatigue for 2024–T3 and 7075–T6 aluminum, ASTM STP 462, pp. 1–14. American Society for Testing and Materials, PA (1970)
4. Rice, J.R.: Some remarks on elastic crack-tip stress fields. *Int. J. Solids Struct.* **8**, 751–758 (1972)
5. Tracey, D.M.: 3-D elastic singularity element for evaluation of K along an arbitrary crack front. *Int. J. Fract.* **9**(3), 340–343 (1973)
6. Guo, W.: Stress intensity factors for corner cracks at holes subjected to biaxial and pin loads. *Eng. Fract. Mech.* **46**, 473–479 (1993)
7. Rigby, R., Aliabadi, M.H.: Stress intensity factors for cracks at attachment lugs. *Eng. Fail. Anal.* **4**(2), 133–146 (1997)
8. Mikheevskiy, S., Glinka, G., Algera, D.: Analysis of fatigue crack growth in an attachment lug based on the weight function technique and the UniGrow fatigue crack growth model. *Int. J. Fatigue* **42**, 88–94 (2012)
9. Noroozi, A.H., Glinka, G., Lamber, S.: A study of stress ratio effects on fatigue crack growth using the unified two-parameter fatigue crack growth driving force. *Int. J. Fatigue* **29**, 1616–1633 (2007)
10. Boljanović, S., Maksimović, S., Carpinteri, A., Jovanović, B.: Computational fatigue analysis of the pin-loaded lug with quarter-elliptical corner crack. *Int. J. Appl. Mech.* **9**, 1750058 (2017)
11. Zhan, W., Lu, N., Zhang, C.: A new approximate model for the R -ratio effect on fatigue crack growth rate. *Eng. Fract. Mech.* **119**, 85–96 (2014)
12. Boljanović, S., Carpinteri, A.: Computational analysis of a surface corner crack under cyclic loading. *Procedia Struct. Integrity* **28**, 2370–2377 (2020)
13. Jones, R., Peng, D., Pitt, S., Wallbrink, C.: Weight functions, CTOD and related solutions for cracks at notches. *Eng. Fail. Anal.* **11**(1), 79–114 (2004)
14. Boljanović, S., Maksimović, S., Djurić, M.: Fatigue strength assessment of initial semi-elliptical cracks located at a hole. *Int. J. Fatigue* **92**, 548–556 (2016)
15. Kujawski D.: A new $(\Delta K + K_{\max})^{0.5}$ driving force parameter for crack growth in aluminum alloy. *Int. J. Fatigue* **23**, 733–740 (2001)
16. Boljanović, S., Carpinteri, A.: Modelling of the fatigue strength degradation due to a semi-elliptical flaw. *Forces Mech.* **4**, 100020 (2021)
17. Huang, X., Moan, T.: Improved modeling of the effect of R -ratio on crack growth rate. *Int. J. Fatigue* **29**, 591–602 (2007)
18. Boljanović, S.: Computational modeling of aircraft lugs failure under fatigue loading. *Int. J. Fatigue* **114**, 252–261 (2018)
19. Boljanović, S.: Fatigue performance evaluation for crack-like surface flaws. *Int. J. Fatigue* **124**, 371–379 (2019)

20. Boljanović, S., Maksimović, S., Carpinteri, A., Ćosić, M.: Fatigue endurance design of plates with two semicircular edge notches and one quarter-elliptical corner crack or through-the-thickness crack. *Int. J. Fatigue* **127**, 45–52 (2019)
21. Boljanović, S., Carpinteri, A.: Modelling the residual strength of fatigue damage at a single semicircular edge notch: semielliptical crack and through-the-thickness crack. *Fatigue Fract. Eng. Mater. Struct.* **42**, 1010–1021 (2019)
22. Boljanović, S., Maksimović, S.: Fatigue failure analysis of pin-loaded lugs. *Frattura ed Integrità Strutturale* **35**, 313–321 (2016)
23. Maksimović, S., Posavljak, S., Maksimović, K., Nikolić, V., Djurković, V.: Total fatigue life estimation of notched structural components using low-cycle properties. *Strain* **47**(Suppl. 2), 341–349 (2011)
24. Antoni, N., Gaisne, F.: Analytical modelling for static stress analysis of pin-loaded lugs with bush fitting. *Appl. Math. Model.* **35**, 1–21 (2011)
25. Carpinteri, A., Brighnetti, R., Huth, H.J., Vantadori, S.: Fatigue growth of a surface crack in a welded T-joint. *Int. J. Fatigue* **27**(1), 59–69 (2005)
26. Carpinteri, A., Brighnetti, R., Vantadori, S.: Notched double-curvature shells with cracks under pulsating internal pressure. *Int. J. Press. Vessels Pip.* **86**(7), 443–453 (2009)
27. Vasović, I., Maksimović, S., Maksimović, K., Stupar, S., Bakić, G.: Maksimović, M.: Determination of stress intensity factors in low pressure turbine rotor disks. *Math. Problems Eng.*, 304638 (2014)
28. Belinha, J., Azevedo, J.M.C., Dinis, L.M.J.S., Natal, Jorge R.: The natural neighbour radial point interpolation method extended to the crack growth simulation. *Int. J. Appl. Mech.* **8**(1), 1650006/1-32 (2016)
29. Newman, Jr. J.C., Raju, I.S.: Stress-intensity factor equations for cracks in three-dimensional finite bodies subjected to tension and bending loads, NASA Technical Memorandum 85793, National Aeronautics and Space Administration, Langley Research Center, Hampton, Virginia, United States (1984)
30. Boljanović, S., Maksimović, S.: Fatigue crack growth modeling of attachment lugs under fatigue loading. *Int. J. Fatigue* **58**, 66–74 (2014)
31. Friedrich, S., Schijve, J.: Fatigue crack growth of corner cracks in lug specimens, Delft University of Technology, Report LR-375 (1983)



Structural Analysis of Elements of Passenger Boarding Bridge

Martina Balac¹✉, Aleksandar Grbovic¹, and Lajos Sarvas²

¹ Faculty of Mechanical Engineering, University of Belgrade, 11000 Belgrade, Serbia
mbalac@mas.bg.ac.rs

² JT2 Batajnicki Drum 261a, 11000 Belgrade, Serbia

Abstract. Structural analysis of elements of passenger boarding bridge is necessary to achieve endurance and safety in transport network. Elements of pivoting joint which are enclosed by protective bellows have been the subject of these analysis. Aluminum frames connected by protective bellows and attached to the circular rod might be in two operating positions of special interest: the position where two rigid sections connected by articulation make an angle of 0° (firm position) and position where two rigid sections connected by articulation make an angle of 45° (maximum angle position). For the purpose of simplifying the calculation, five aluminum frames have been extracted from the original geometry in a firm position, and to simulate the influence of protective bellows attached to aluminum frames, springs have been added. The main dilemma in the analysis was how to estimate the stiffness of springs. Using data from the protective bellows manufacturer stiffness coefficient of springs was evaluated. However, the stiffness coefficient value was varied through the analysis to assess the influence of this parameter on stress/displacement values, and the difference in obtained results is commented later in this report. Values of displacements and stresses obtained using finite element analyses (FEA) for both positions of frames are given.

Keywords: Passenger boarding bridge · Forces · FE analysis · Stiffness coefficient

1 Introduction

With the recent developments in technology, significant improvements have been achieved in transportation both on sea, land, and air routes. Bridge construction is changing swiftly since it is so important to the transportation system. Passengers can enter and depart ships or plane through weather-protected tunnels provided by the Passenger Boarding Bridge (PBB). Sea transport has been widely used especially in international transportation. Around 90% of the world trade is carried out by sea transportation [1–4]. The main elements of the maritime transport are sea vehicles and ports. Vessels such as oil tankers, bulk carriers, general cargo, containers, ferries, and cruise ships contribute to the national economy with domestic and foreign transportation [5]. Clearly, the strength and safety of such structures are of utmost importance. Application of the finite element

method (FEM) is of particular importance in different industrial sectors in terms to evaluate the life time of the structure based on the predefined geometry of the structure, the mechanical characteristics of the applied material, the position, geometry and dimension of different components [6–9].

Subject of this structural analysis are elements of pivoting joint which are enclosed by protective bellows. Five aluminum frames connected by protective bellows and attached to the circular rod might be in two operating positions of special interest.

The aim of this research is to determine values of displacements and stresses obtained using finite element analyses (FEA) for both positions of frames. For this analysis Ansys 2020 software was used.

2 Materials and Methods

The PBB described in this paper (Fig. 1) must be highly operational, adaptable, lightweight, and fault-free while yet offering passengers a great boarding experience.

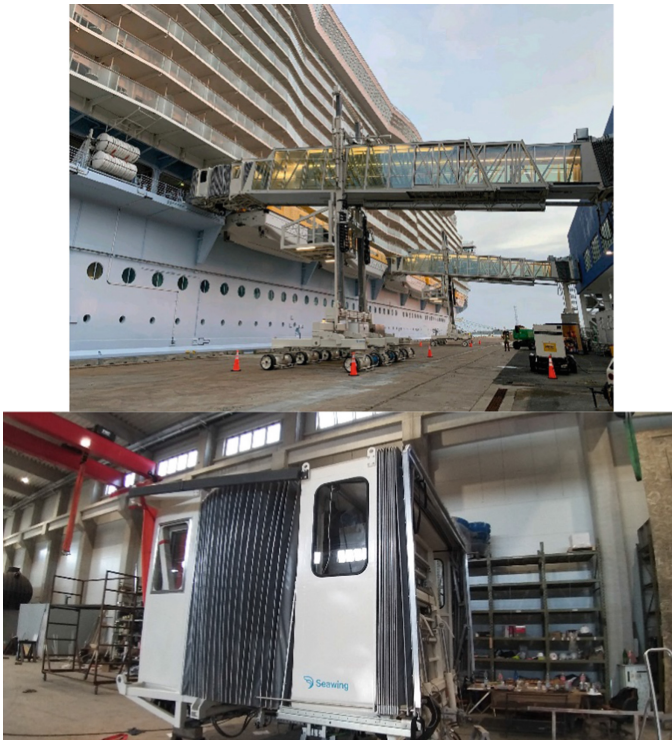


Fig. 1. Passenger boarding bridge

Aluminum frames connected by protective bellows and attached to the circular rod (with cross-section defined by the manufacturer) might be in two operating positions of special interest: the position where two rigid sections connected by articulation make an angle of 0° (firm position, Fig. 2) and position where two rigid sections connected by articulation make an angle of 45° (maximum angle position, Fig. 3).

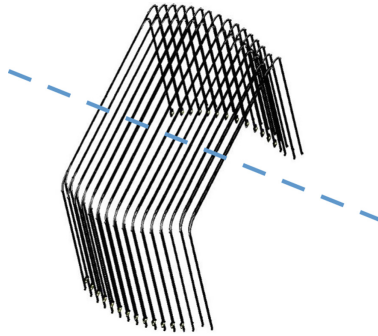


Fig. 2. Firm position of frames ($\alpha = 0^\circ$)

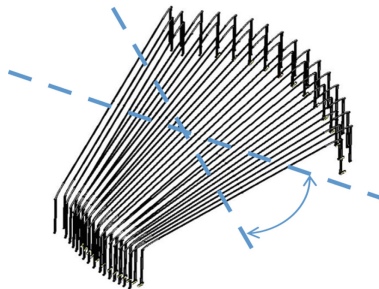


Fig. 3. Maximum angle position of frames ($\alpha = 45^\circ$)

For the purpose of simplifying the calculation, five aluminum frames have been extracted from the original geometry in a firm position (Fig. 4), and to simulate the influence of protective bellows attached to aluminum frames, springs have been added (Fig. 5).

The main dilemma in the analysis was how to estimate the stiffness of springs. Using data from the protective bellows manufacturer (modulus of elasticity of the material used in production) stiffness coefficient of springs was evaluated as $c = 70 \text{ N/mm}$. However, the stiffness coefficient value was varied through the analysis to assess the influence of this parameter on stress/displacement values, and the difference in obtained results is commented later in this report.

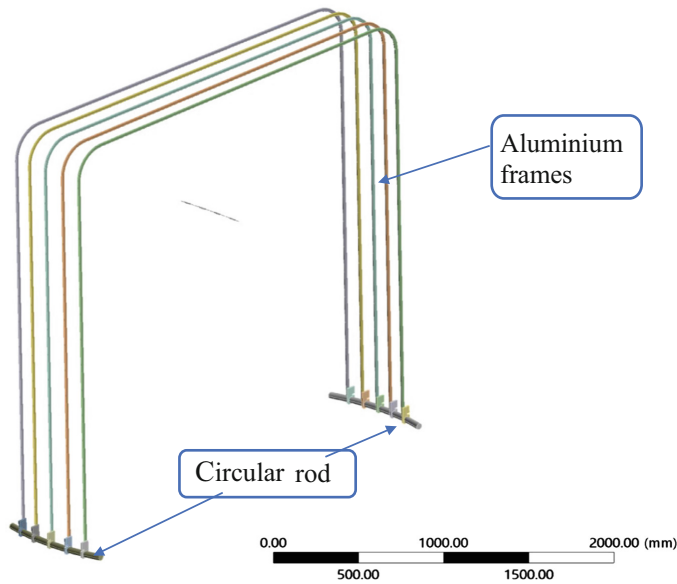


Fig. 4. Five frames connected to the circular rod in a firm position ($\alpha = 0^\circ$)

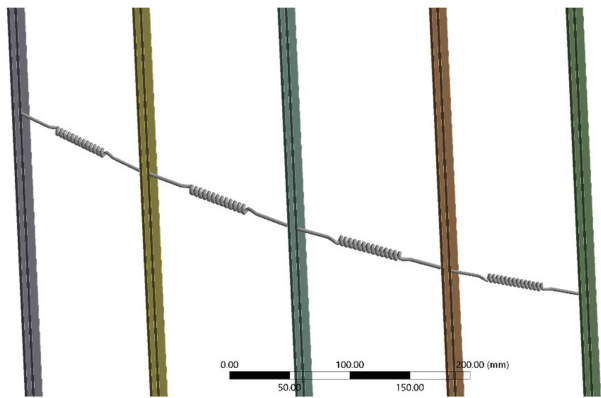


Fig. 5. Protective bellows were simulated using springs

The main (and only) load considered in the analysis was a force of 2,500 N (simulating the mass of 250 kg) acting perpendicularly to three middle frames. Three frames were loaded because it had been estimated that an average person can apply pressure (with his/her body) on a maximum of three frames at once. The average person is considered to have a mass of 80–100 kg, but the mass of 250 kg was used in calculations to ensure the value of safety factor $\nu = 2.5$. On the subject of boundary conditions, it was assumed that the circular rod was fixed (Fig. 6) since the main emphasis in the analysis was on the displacements and stresses of aluminum frames, not the rod.

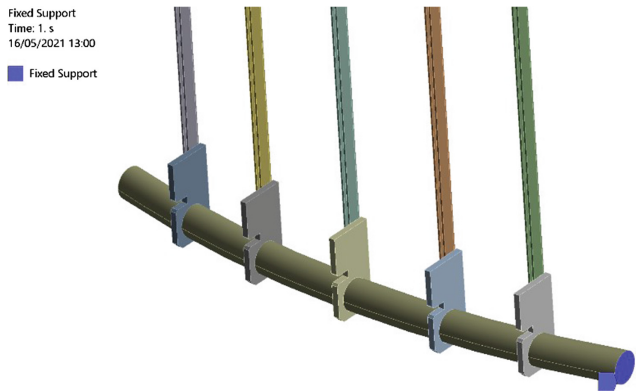


Fig. 6. Circular rod is fixed

Since no data were available about the type of contact between the rod and ends of frames, two approaches were used in the analysis: 1st approach: contact was considered to be sliding without friction (so-called No separation contact), and 2nd approach: contact was considered to be sliding with friction (so-called Frictional contact) with the value of friction coefficient $\mu = 0.2$.

3 Results and Discussion

Values of displacements and stresses obtained using finite element analyses (FEA) for both approaches and both positions of frames (firm and max. Angle) are given below.

Firm position of frames, sliding without friction

Values of displacements are given in Figs. 7 and 8.

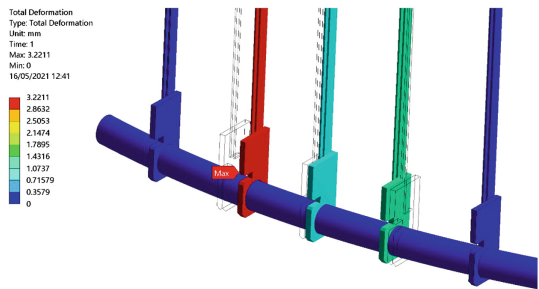


Fig. 7. Displacements on the left-hand side of pivoting joint (maximum 3.2 mm)

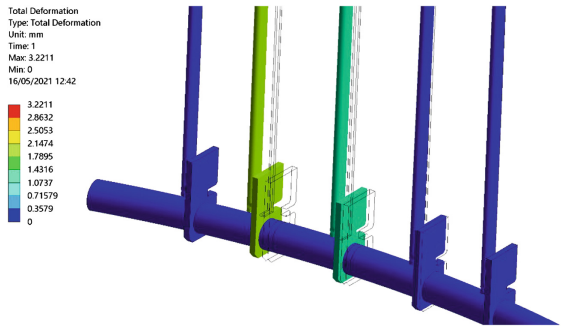


Fig. 8. Displacements on the right-hand side of pivoting joint (maximum 2.1 mm)

Values of stress are given in Fig. 9.

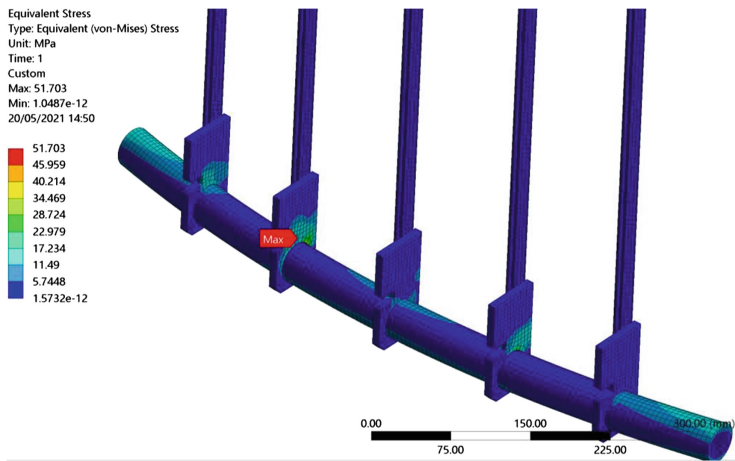


Fig. 9. Maximum value of stress 51.7 MPa obtained on the left-hand side of pivoting joint

Firm position of frames, sliding with friction $\mu = 0.2$

As can be seen in Fig. 10, values of displacements, as expected, are significantly smaller than in the case when friction was not considered (0.72 mm versus 3.2 mm). However, friction produces higher stresses in the contact areas and these stresses cannot be correctly evaluated without further analysis which includes nonlinear properties of materials in contact.

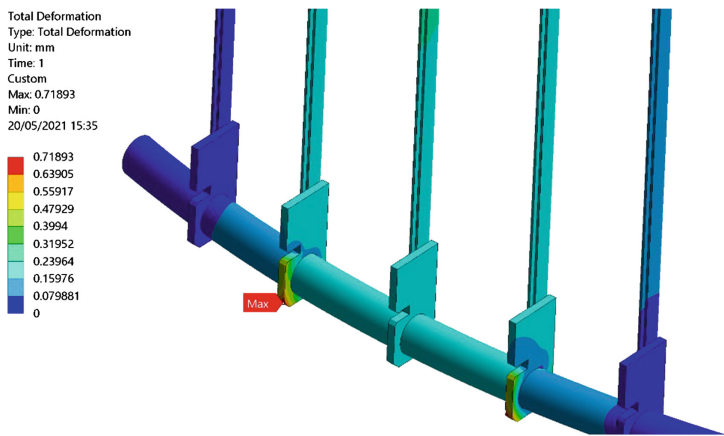


Fig. 10. Displacements on the left-hand side of pivoting joint when frictional contact is used

Maximum angle position of frames, sliding without friction

The geometry representing the maximum angle position is shown in Fig. 11, while values of displacements are given in Figs. 12 and 13.

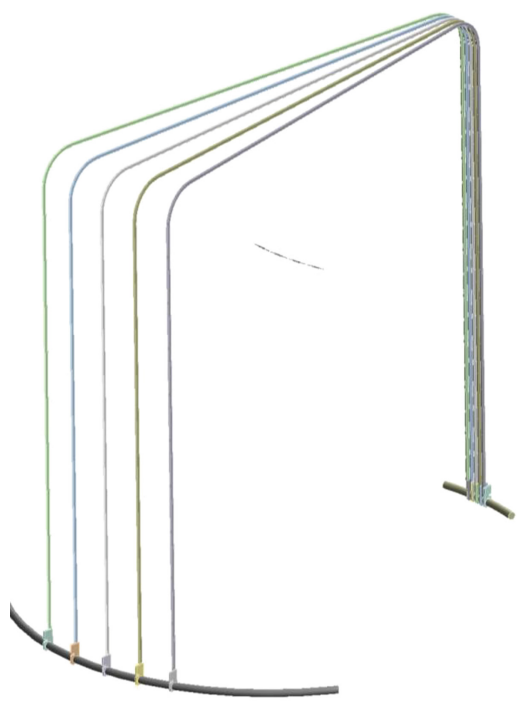


Fig. 11. Five frames connected to the circular rod in the maximum angle position ($\alpha = 45^0$)

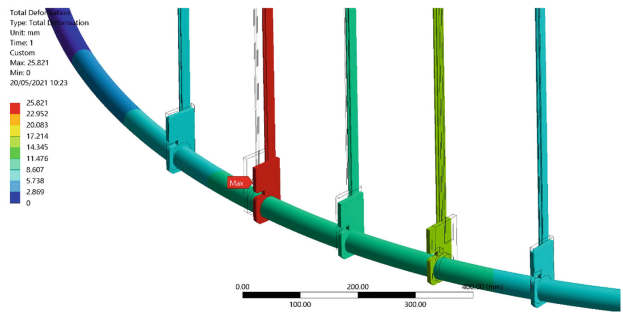


Fig. 12. Displacements on the left-hand side of pivoting joint (maximum 25.8 mm)

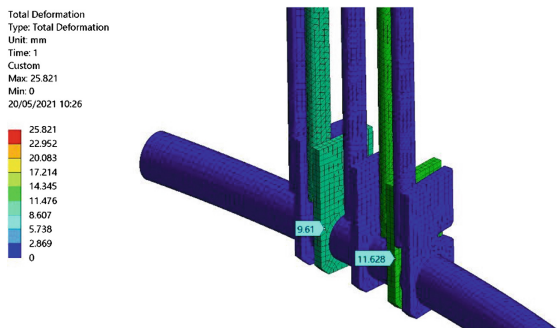


Fig. 13. Displacements on the right-hand side of pivoting joint (maximum 11.6 mm)

Values of stresses are given in Fig. 14. It is important to notice that the maximum stress of 284 MPa is at one node only (singularity) and cannot represent the referent value, while values in the most stressed area are between 170 and 220 MPa (Fig. 15).

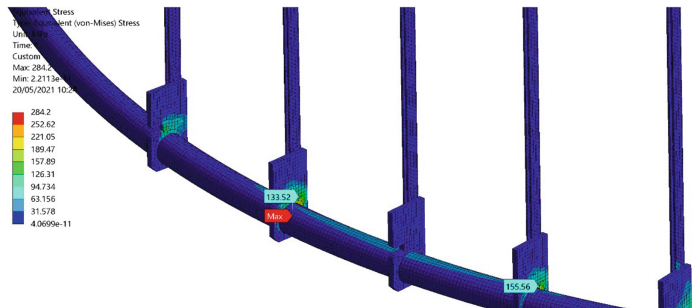


Fig. 14. Maximum value of stress 284.2 MPa obtained on the pivoting joint is singularity

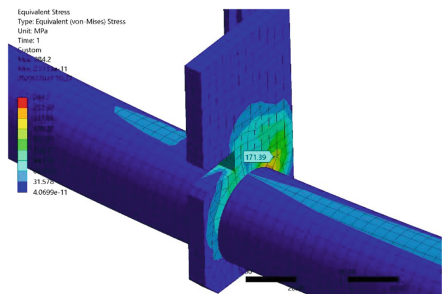


Fig. 15. The maximum stress in the critical area is not greater than 220 MPa

Maximum angle position of frames, sliding with friction $\mu = 0.2$

Similar to the analysis of the firm position of pivoting joint, values of displacements are significantly smaller in the maximum angle position when friction is considered (Fig. 16). However, the maximum displacement is on a different spot than before (Fig. 17). Again, friction produces higher stresses in the contact areas and correct stress values cannot be evaluated without further analysis which includes nonlinear properties of materials.

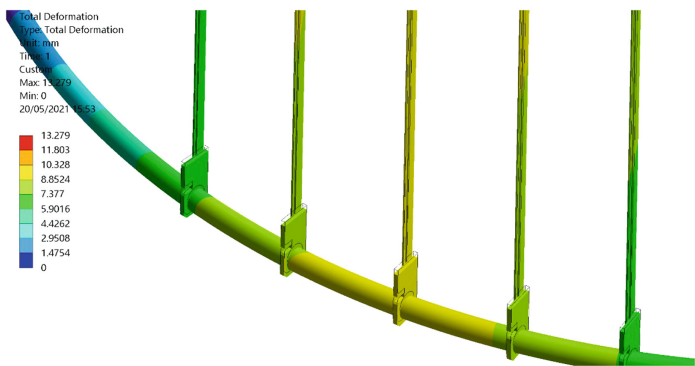


Fig. 16. Displacements on the left-hand side of pivoting joint when frictional contact is used

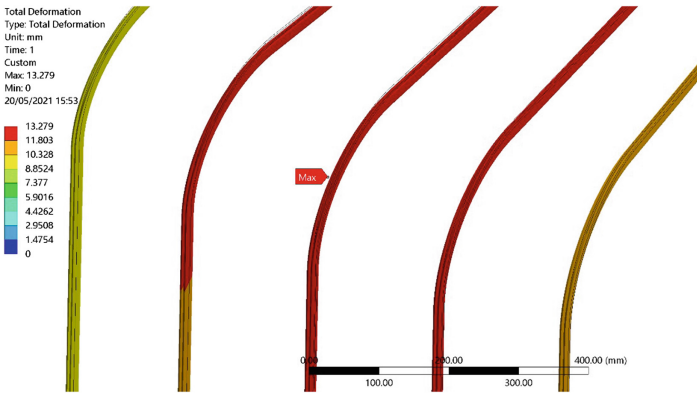


Fig. 17. Maximum displacements is on the top of the middle frame

4 Conclusion

As said above, to consider the influence of the protective bellows, springs with stiffness coefficient $c = 70 \text{ N/mm}$ have been used. Based on the results of FEAs presented in this report, the following conclusions can be drawn:

1. Values of displacement obtained in simulations are acceptable and within the expected range. When friction between ends of aluminum frames and the circular rod is neglected displacement is higher since ends can slide along the circular rod surface; on the contrary, when friction between these elements is considered maximum displacement is much smaller. However, the exact value of the coefficient of friction must be known in order to get the realistic value of displacement. It should be noted that the stiffness of protective bellows influences the total displacement of frames too, and that approximate value of stiffness coefficient was used in calculations. Displacements are generally smaller when frames are in a firm position – this indicates that the maximum angle position is a critical position of pivoting joint.
2. When friction is neglected, stress values are low in a firm position and significantly higher when frames are in maximum angle position but acceptable. Maximum stress is around 50 MPa in a firm position and around 210 MPa when frames are in maximum angle position. This implies that aluminum alloy 6060-T6 (or similar) should be used since it has the yield tensile strength of 170 MPa and an ultimate tensile strength of 220 MPa. Therefore, this alloy can provide desired safety factor $\nu = 2.5$. When arbitrary friction coefficient $\mu = 0.2$ is used in calculations stress values in contact areas rise, but accurate values cannot be calculated without considering the nonlinear properties of materials: maximum stress is higher than the yield strength of aluminum alloy which implies the occurrence of plastic deformation.

References

1. Wenhui, W., Yan, Z.: Design and finite element analysis of corrugated plate boarding bridge. *Adv. Mater. Res.* **97–101**, 3727–3730 (2010). <https://doi.org/10.4028/www.scientific.net/AMR.97-101.3727>
2. Hyun, N.W., Jun, K.H., Yeol, B.S.: Study on the effect of the lift column layout design on structural strength of the passenger boarding bridge. *Trans. Korean Soc. Mech. Eng. C* **3**(4), 307–312 (2015). <https://doi.org/10.3795/KSME-C.2015.3.4.307>
3. Rulin, Y., Long, Yu, Qidong, F., Xuefeng, W.: Experimental and numerical resistance analysis for a cruise ship W/O fin stabilizers. *J. Mar. Sci. Eng.* **10**(8), 1054 (2022). <https://doi.org/10.3390/jmse10081054>
4. Zhang, P., Ding, M., Huang, G., Chen, Q.: FEM analysis of the telescopic tunnel in passenger boarding bridges. *Highlights Sci. Eng. Technol.* **15**, 297–302 (2022)
5. Balac, M., Grbovic, A., Kastratovic, G., Petrovic, A., Sarvas, L.: Fatigue life evaluation of the damaged passenger boarding bridge supports. In: Mitrovic, N., Mladenovic, G., Mitrovic, A. (eds.) *Current Problems in Experimental and Computational Engineering*. CNNTech 2021. *Lecture Notes in Networks and Systems*, vol 323. Springer, Cham. https://doi.org/10.1007/978-3-030-86009-7_16
6. Balac, M., Grbovic, A., Petrovic, A., Popovic, V.: FEM analysis of pressure vessel with an investigation of crack growth on cylindrical surface. *Eksplotacja i Niezawodnosc - Maintenance and Reliability* **20**(3), 378–386 (2018)
7. Grbović, A., Kastratović, G., Božić, Ž., Božić, I., Obradović, A., Sedmak, A., Sedmak, S.: Experimental and numerical evaluation of fracture characteristics of composite material used in the aircraft engine cover manufacturing. *Eng. Failure Anal.* **137**, 106286 (2022). <https://doi.org/10.1016/j.engfailanal.2022.106286>
8. Zečević, B., Maksimović, A., Milović, Lj., Aleksić, V., Grbović, A., Bulatović, S.: Numerical simulation of 14Mn6–3 steel CT-specimen fracture behavior. *Procedia Struct. Integrity* **42**, 1483–1496 (2022). <https://doi.org/10.1016/j.prostr.2022.12.189>
9. Bajić, D., Momčilović, N., Maneski, T., Balać, M., Kozak, D., Čulafić, S.: Numerical and experimental determination of stress concentration factor for a pipe branches. *Technical Gazette* **24**(3), 687–692 (2017). <https://doi.org/10.17559/TV-20151126222916>



Horizontal Boring Mill Machine Feedrate Revitalization with DC Converter and PLC

Igor Kocic¹(✉), Goran Mladenovic², Sasa Nikolic¹, Darko Mitic¹, Nikola Dankovic¹, and Petar Djekic³

¹ Faculty of Electronic Engineering, University of Nis, 18000 Nis, Serbia
igor.kocic@elfak.ni.ac.rs

² Faculty of Mechanical Engineering, University of Belgrade, 11000 Belgrade, Serbia

³ The Academy of Applied Technical and Preschool Studies-Niš, 18000 Niš, Serbia

Abstract. This paper presents the revitalization of the feedrate system of the Stankoimport 2620B horizontal boring mill machine using a PLC controller and a DC converter with special reference to the way of adjusting the speed and current loop parameters of the converter using Matlab and OPC server. Using Matlab, a model of auxiliary movement was created and simulated. The simulation model was taken as a reference and connected to the PLC and the DC converter using the OPC server, and based on the comparison of the response difference between the simulation model and the real system, the parameters of the PI controller of the DC converter were tuned. Revitalization and reconstruction was carried out using modern components for the regulation of auxiliary movement. During the reconstruction, the components were integrated into the old system, which represents a special challenge, because the control system dating from 1970 was combined with the new control system. New electrical documentation was designed, software for the PLC controller was developed and written. After revitalization, testing was carried out in real conditions in metal machining and functionality was proven.

Keywords: Horizontal boring mill machine · DC converter · PLC · Feedrate regulation

1 Introduction

Speed control using a PID controller is commonly applied in different branches of industry [1, 2]. In machining and production of part improper control speed will result in the damage the of the subject being processed. The paper describes the method of adjusting the analog DC converter, wrote the software and developed the hardware for regulating the feedrate. The control task was realized using two PI controllers in cascade loop [3–5] and a programmable logic controller (PLC) Schneider electric type Modicon M211 [6] and DC converter SSD Parker type 514C [7]. The signal of the actual speed and current of the motor is fed to the analog inputs of the PLC from the analog outputs of the DC converter, whereby the reference speed is set by commands located on the control panel.

Models of DC converter and motor for feedrate are identified, a simulation was performed in Matlab [8, 9], the parameters of the PI controller were determined, and a real DC converter [10] was set based on them and the results were experimentally verified on a horizontal boring mill machine.

2 Hardware and Software Solution of the Speed Control of Motor for Feedrate of Horizontal Boring Mill Machine

The controlling system of feedrate for auxiliary movement (Fig. 1) is provided with DC motor (with characteristics in Table 1) connected to gear box, analog DC converter drive and Modicon PLC with additional cards for necessary analog and digital signal. The DC motor which was used has a maximum speed of 1500 rpm or 3000 rpm depending on how the excitation coil is connected. SSD Parker convertor drive for controlling DC motors [10], providing control of the motor speed in all 4 Quadrants of operation. This type of regulator was chosen because of its low cost.

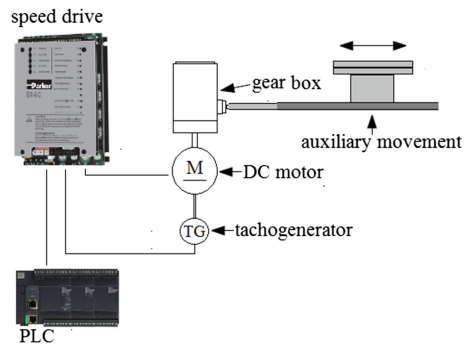


Fig. 1. Block scheme of feedrate regulation

2.1 DC Motor and Converter, Model Identification

Some parameters are taken from nameplate of the motor, and some are determined with the help of the identification procedure and some by simple measurement. To identify the parameters of the DC motor, an experimental platform was used, consisting of a test bench equipped with a Simoreg DC converter of the 6RA70 series [11], which is used to start the motor, and a Micrologix PLC [12] controller with analog cards and a PC with an OPC server [13] and Matlab. Table 1 shows the parameter of the DC motor that drives the mechanical part for feedrate. Part of the parameters was obtained by directly reading the parameters from the nameplate of the engine, part by simple measurement and part of the parameters through identification [14–18]. The model of the DC converter drive is derived on the analysis of voltage waveforms at its input and output [10]. After simplification of the analysis, the function transfer of a single-phase fully controllable thyristor module can be represented by the first-order function transfer with delay (FOPDT) [19].

Table 1. Motor and DC converter parameters

Parameters	Values
Motor power P	2.2 kW
Armature voltage U_a	230 V
Armature current I_a	11.2 A
Motor speed n	1500/3000 rpm
Excitation voltage U_p	230/130 V
Excitation current I_p	0.43/0.88 A
Armature winding resistance R_a	11.5 Ω
Inductance of armature winding L_a	0.136 mH
Excitation windig resistance R_p	110 Ω
Back electromotive force constant k_e	1.23 V
Viscous friction coefficients of motor B_m	0.00221 Nms
Moment of motor rotor inertia J_m	0.0221 kgm ²
Viscous friction coefficients B	0.00712 Nms
Moment of inertia J	0.963 kgm ²
DC converter gain k_t	19.83
DC converter time constant T_t	0.01 s
DC converter time delay θ	0.4 s

2.2 Synthesis of the PI Armature Current and PI Speed Controllers

In applications where purchased DC converters are used, cascade control is always used to control the DC motor and optimize each PI controller separately [11, 20]. PI armature current regulator is designed by the method of technical optimum [21].

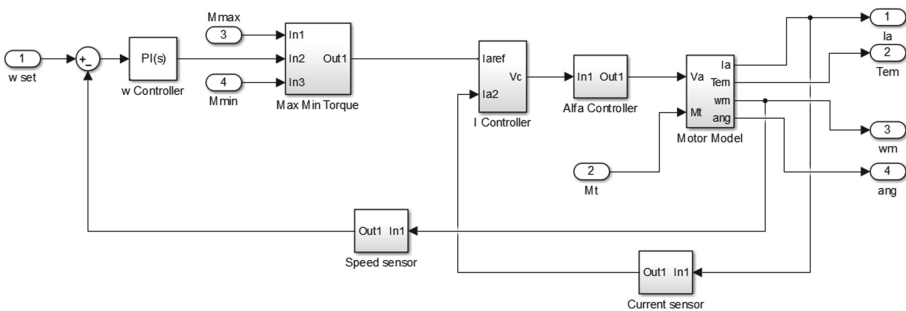


Fig. 2. Block diagram of model motor for feedrate with DC converter

The block diagram of model of auxiliary movement Fig. 2 consists of a PI speed controller, PI current controller, DC converter model, motor model and mechanical part.

When synthesis a PI speed controller, the influence of the response of the internal current loop can be ignored because the time constant of the rotor circuit is much smaller than the mechanical time constant [22, 23]. A dynamic process current loops can be neglected in synthesis and analysis PI speed controller performance and interference rejection performance.

Equation (1) gives the open loop transfer function, and the desired closed-loop transfer function.

$$G_{o\omega} = k_{p\omega} \frac{1 + sT_{i\omega}}{sT_{i\omega}} k_m \frac{k_b}{1 + sT_m} = \frac{a}{s + a} \quad (1)$$

The parameters of the PI speed controller are selected based on the rise time t_r , which also determines the bandwidth of the speed loop. The parameter $T_{i\omega}$ is chosen to compensate for the time constant of the mechanical part of the system T_m Eq. (2), which cancels the old pole, and the parameter $k_{p\omega}$ sets the new pole. The speed performance and the disturbance rejection performance when using PI controller depends on the pole-zero distribution of the desired transfer function.

$$a = \frac{k_{p\omega} k_m k_b}{T_m}, T_m = T_{i\omega}, k_{p\omega} = \frac{a T_m}{k_m k_b}, a \approx \frac{2.2}{t_r} \quad (2)$$

Figure 3 (left) shows the armature current response of the auxiliary motion drive motor based on Matlab simulation when the rotor speed is controlled by a PI controller as the setpoint speed changes, Fig. 3 (right) shows the speed characteristic of the auxiliary motion drive motor obtained by simulation.

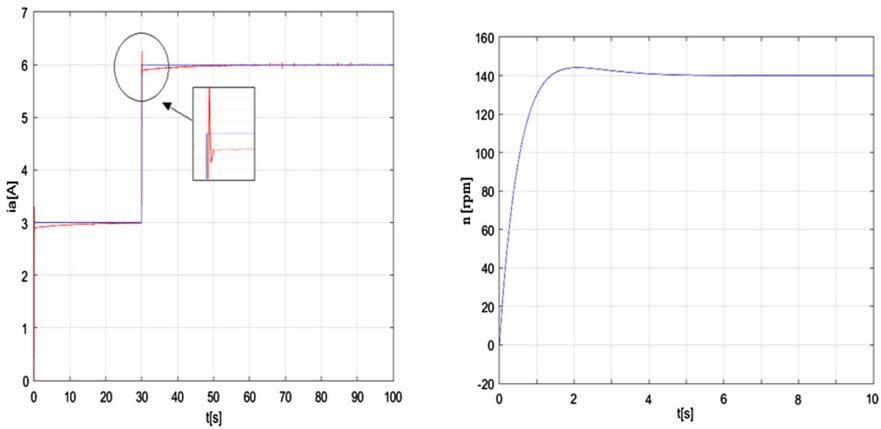


Fig. 3. Response of armature current when changing the set speed in the range from 300 rpm to 700 rpm (left), speed response in time when set speed is 140 rpm (right)

3 Realization Control and Parameter Setup of SSD Converter Drive for Speed Control of Auxiliary Movement

3.1 Parameter Setup of SSD Converter Drive

The procedure for setting the parameters of this type of DC converter is somewhat more complicated compared to converters that have ready-made adjustment procedures. The current loop and speed loop PI controller parameters are adjusted by the method trial and error or Ziegler-Nicols method close loop method, visually observing the response to the step signal. Based on the model and the selected control, it is necessary to establish a connection between the parameters of the PI regulators DC converter [24], which are adjusted by physically turning the potentiometers P_3 , P_4 , P_6 and P_7 on the front panel of the DC converter [7]. Tuning, of the current and speed loop of the DC converter were performed using a PLC controller, HMI connected to PLC and Matlab using Kepware Modbus [25–27]. Kepware server is used for computer interface. On Fig. 4 is illustrated the block scheme of experimental platform for tuning SSD converter and modeling for control applications.

The analog inputs of the PLC controller are connected to output terminals from the DC converter drive that correspond to the current value of motor current and the motor speed of the drive motor for auxiliary movement. The setting of the current loop is done via potentiometers P_6 and P_7 , respectively, for proportional gain and integration time using rules [28].

The setup procedure is divided into two separate procedures. The first is setting the PI parameters of the current loop, and the second is setting the parameters of the speed loop PI controller.

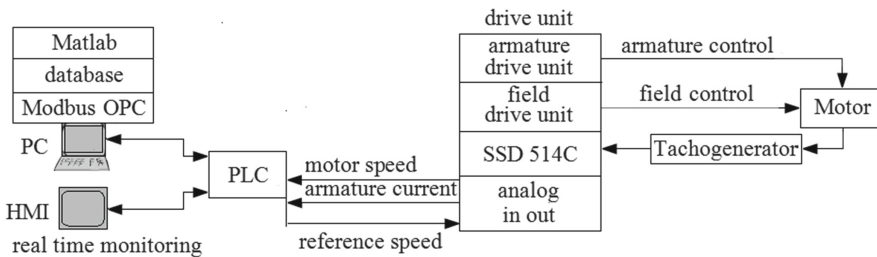


Fig. 4. Block scheme of experimental platform for tuning SSD converter

First, the setup of the PI controller of the current loop was performed using real time monitoring.

Steps of tuning PI controller for current loop:

1. Disconnect the field excitation voltage,
2. Turn on the fan for forced cooling of the motor,
3. Connect the motor to the gear box, if this is physically impossible, it is necessary to brake rotor of the motor,

4. Activate the connection between the PLC and Matlab using Kepware Modbus OPC drive,
5. Start the motor without field excitation and set the maximum current value with potentiometer P_5 [7],
6. Stop motor,
7. Bring the small reference speed signal to the input of the converter using PLC, and start motor,
8. Watch the trend view of PLC tags of motor armature current,
9. Restart the motor and adjust the current loop parameters for several speed reference values, adjust the K_p and T_i parameters (using potentiometers P_6 and P_7) so that the current response is as fast as possible without overshooting, according to the response obtained in the part of the current loop controller model,
10. Repeat point 7 until a satisfactory response is obtained,
11. Reconnect the motor excitation,
12. Deactivate connection between the PLC and Matlab using Kepware Modbus OPC.

The procedure for adjusting the speed loop is performed similar to the procedure of adaptive control with reference model (MRAC) [28–30]. Model composed of the motor model, the DC regulator and the cascade loop of the PI controller modeled in Matlab from was taken as the reference model [31]. At the input of the model and the real process with a DC converter and PLC, a step impulse is simultaneously applied and the response of the system is observed on the HMI panel based on Eq. (3).

$$IAE = \int_0^{+\infty} |e(t)|dt = \int_0^{+\infty} |y_r(t) - y(t)|dt \quad (3)$$

Steps of tuning PI controller for speed loop:

1. Set the potentiometers for the acceleration/deceleration ramp to minimum (P_1 , P_2 [7]),
2. Activate the connection between the PLC and Matlab using Kepware Modbus OPC drive,
3. Watch the trend view of PLC tags of motor speed,
4. Bring the small reference speed signal to the input of the converter using PLC, and start motor,
5. Adjust K_p and T_i (using potentiometers P_3 and P_4) to obtain a critically damped response, i.e. the fastest possible response without overshoot according to the response obtained in the part of the current loop controller model,
6. Repeat step 5 until a satisfactory response is obtained
7. Adjustment P_{10} so that the achieved speed corresponds to the maximum desired speed,
8. Setting P_{11} speed offset for the zero speed signal,
9. Deactivate connection between the PLC and Matlab using Kepware Modbus OPC,
10. Stop motor.

3.2 Realization Control of Feedrate

The hardware configuration of the PLC controller and the writing of the control program for managing the feedrate, as well as the part of the software for Modbus communication and the reading of the current values of the current and the speed of the motor, was done in the software package called “EcoStruxure Machine Expert-Basic” by Schneider Electric.

By combining the contacts of the existing relays from the old system, which are activated by turning the coded rotary switches S_1 and S_2 , commands for 9 slow and 32 fast speeds are generated to control the feedrate. Such commands in the form of a voltage of 0–10 V are sent to the DC converter. Based on the value of the voltage, the motor rotates at the set speed after starting. In the picture Fig. 5 the connection diagram of discrete and analog PLC inputs is shown, and Fig. 6 show DC converter wiring diagram.

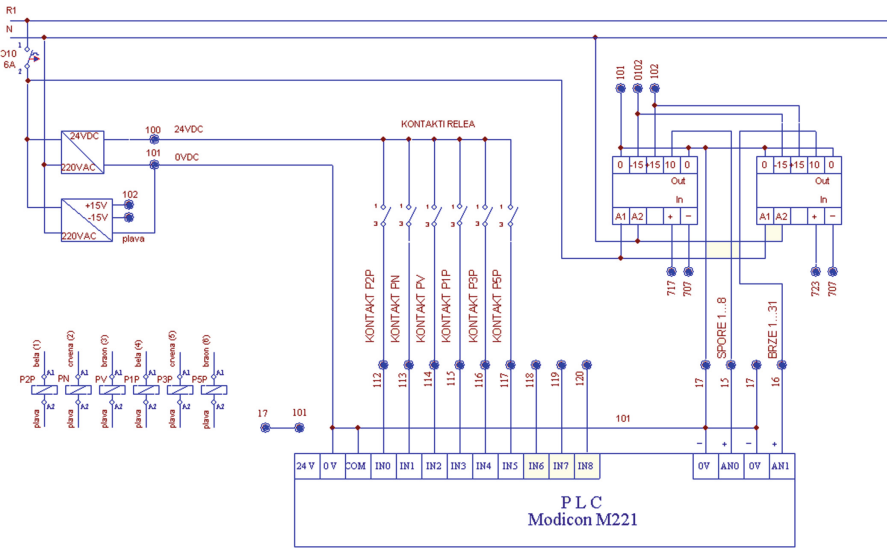


Fig. 5. Input terminal PLC wiring diagram for input system

According to the requirements, it is necessary to completely preserve the old control panel and part of the control logic of the machine, and to carry out the revitalization of only the drive for auxiliary movement, which required ingenuity in the sense of connecting the old and new control system. The relay contacts from the existing old control logic P2P, PN, PV, P1P, P3P and PSP are connected via a 24V DC power supply and introduced to the PLC inputs.

To the analog inputs of the PLC controller using the elements VF_1 , VF_2 for voltage feedback, set values of speeds with slow and fast movement of the drive for auxiliary movement generated in the old control logic are brought. For this reason, it was necessary to design and make cards that are also designed for proportional voltage reduction Fig. 7. Inputs VF_1 and VF_2 are supplied with voltage levels that are generated by turning switches with S_1 and S_2 from multiple positions (order of magnitude 0–120 V), and at

the output pins VF₁ and VF₂ voltages of 0–10 V are obtained, which are introduced as such into the PLC controller.

Depending on the state of the contact (open, closed) and voltage levels and a suitably written program for the PLC controller, a total of 82 movement speeds of the feedrate tool are generated.

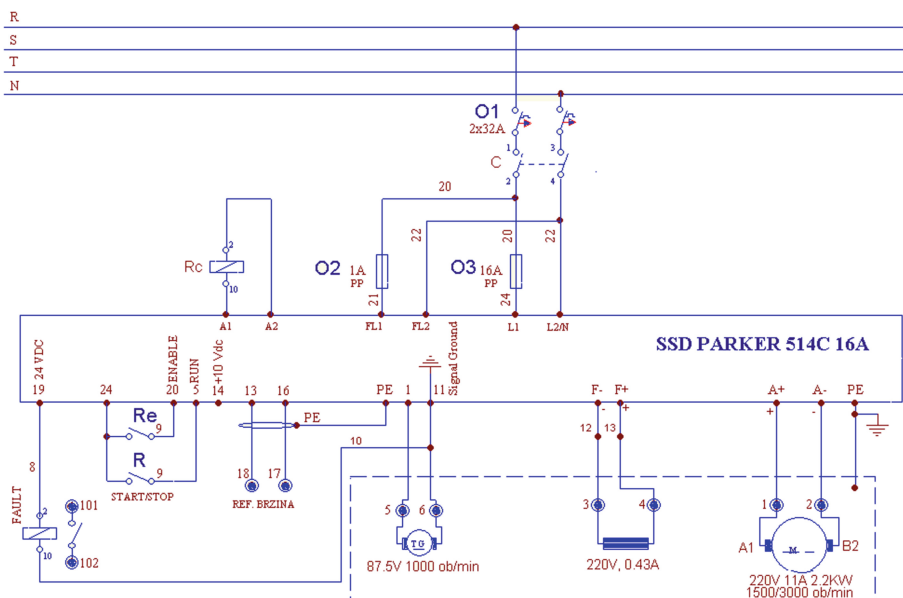


Fig. 6. SSD Parker 514C wiring diagram

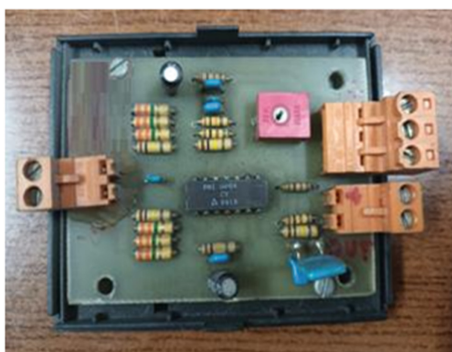
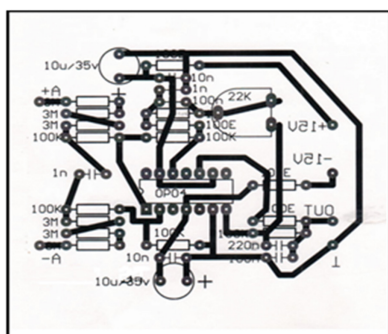


Fig. 7. Voltage feedback card (right), layout of components (left)

Figure 8 shows a part of the software for selecting the operating speed of the drive for auxiliary movement, and turning on and off the engine brake. The speed of the auxiliary motion drive is set by entering the desired value in the register %QW0.100. Speed values in the PLC controller are given in engineering units, ranging from 0 to 10000 eng. unit

which correspond to voltage values from 0 to 10 V, i.e. motor speed from 0 to 1500 rpm. The ramp value is with $t_u = 1$ s and $t_d = 1$ s.

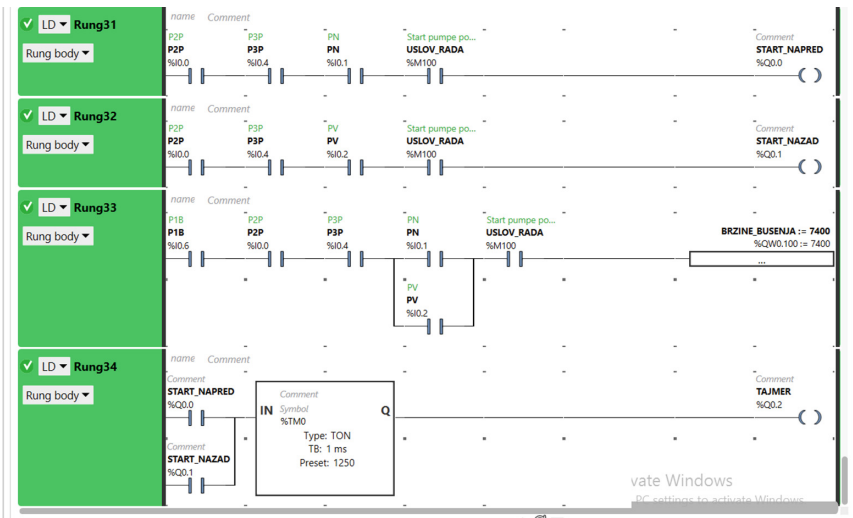


Fig. 8. Part of software for setup speed and activate clutch

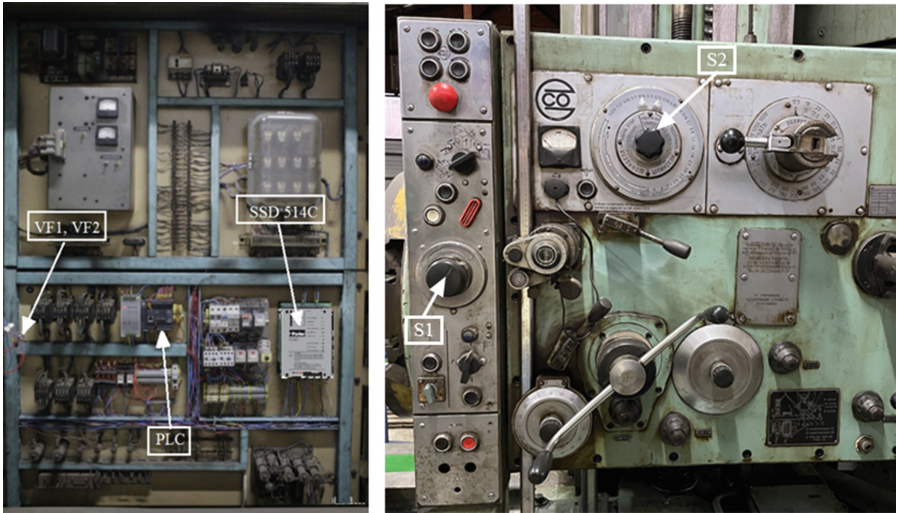


Fig. 9. Drive cabinet with new component (left) and old control panel (right)

Figure 9 on the left shows the real realisation of the drive cabinet in which the PLC M221, SSD 514C converter, voltage coupling cards and other necessary equipment for feedrate controlled are installed. Figure 9, on the right, shows the appearance of the control panel, where the layout of the control commands has been completely preserved.

4 Experimental Results

The experimental results were obtained on a real horizontal boring mill machine type Stankoimport 2620B. Values of the corresponding registers (tags) of the PLC controller which correspond to the real values of speed, current of motor for auxiliary moving are represent in Engineering unit. Figure 10 shows the characteristic of the realized speed of feedrate where the maximal error in tracking the set point speed is 42eng. Unit which corresponds to a voltage of 0.042 V. The value of 1 V or 150 rpm corresponds to the set value of 1000 eng. units.

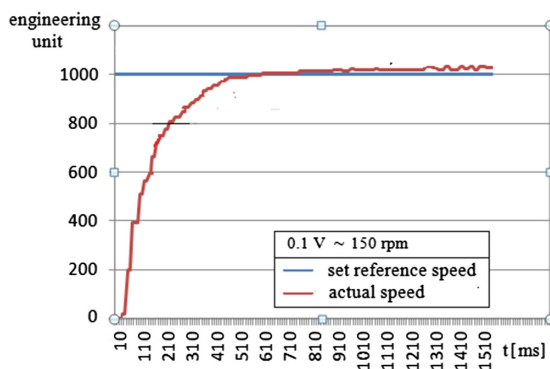


Fig. 10. Characteristic of the speed of motor for feedrate

Figure 11 (up) shows the characteristic of the actual and set referene speed with correspond with armature current Fig. 11 (down) in the feedrate process, where the feedrate speed was changed randomly. From Fig. 11 it can be seen that the DC converter device works in the speed mode, the speed is maintained by the current. A value of 1000 eng. units corresponds to a drive motor current of 1.6 A.

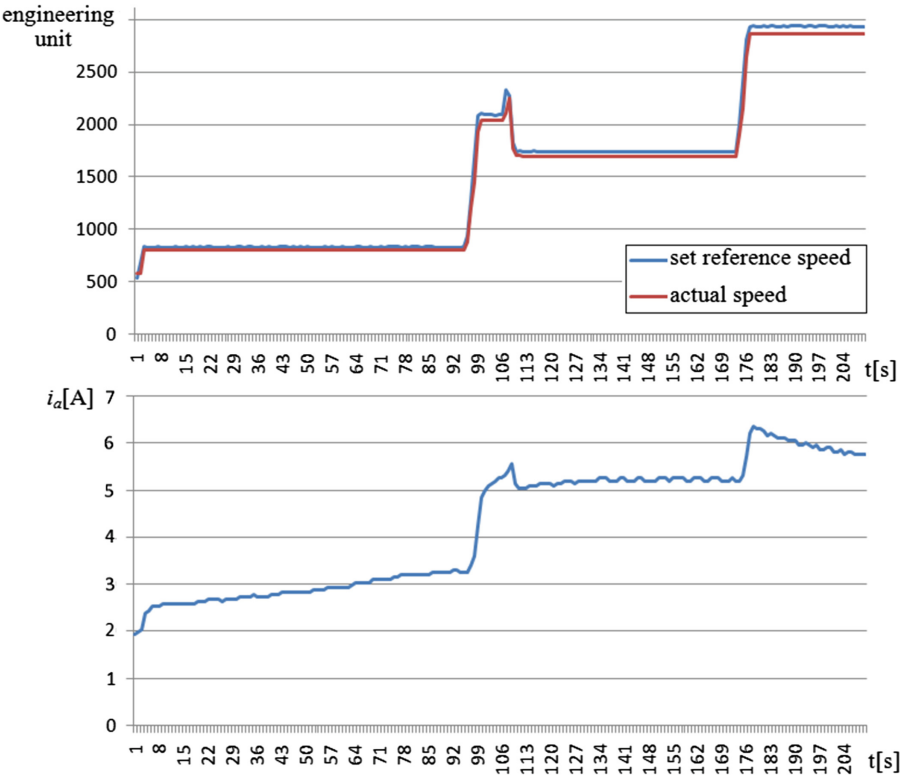


Fig. 11. Characteristic of the actual and set reference speed and actual armature current

5 Conclusion

The most difficult part was to connect the old control system (which dates back to 1970) with the part of the new control system for the auxiliary movement of the machine, which was a significant challenge in terms of knowledge of old control systems (such as Ward Leonard's group, lamps, etc.) and modern control systems. If we add to that the requirement that the cost of the revitalization should not be too high and that the layout of the commands on the command desk be completely maintained, it all represented a challenge. The justification for using the Modicon M221 PLC controller is reflected in its price and modularity, and especially due to intuitive configuration and programming. The used DC converter is of an analog type, based on the simulations performed in the modeling part, it was necessary to connect the obtained results with the simultaneous control, which was solved by the use of PLC and opc drivers. The adjustment of the regulator parameters was performed manually by observing the response on the HMI panel, which is used only in the parameter adjustment process. With the revitalization, the mode of operation and the layout of the control panel commands were kept, which reduced the time for operator training to a minimum.

References

1. Rhinehart, R.R.: The Century's greatest contributions to control practice. *ISA Trans.* **39**, 3–13 (2000)
2. Li, Y., Ang, K.H., Chong, G.C.Y.: Patents, software and hardware for PID control: an overview and analysis of the current art. *IEEE Control. Syst.* **26**(1), 42–54 (2006)
3. Astrom, K.J., Hagglund, T.: Automatic Tuning of PID Controllers. Instrument Society of America, Research Triangle Park, NC (1988)
4. Astrom, K.J., Hagglund, T.: PID Controllers: Theory, Design, and Tuning. Instrument Society of America, Research Triangle Park, NC (1995)
5. Visioli, A.: Practical PID Control. Springer Science & Business Media (2006)
6. Modicon M221 Logic Controller User, available at <https://media.distributordatasolutions.com/schneider2/2020q4/documents/fbb188fbd042afd838384db125b9dad1c2a6a9e9.pdf>. Accessed 5 May 2021
7. 514C DC Controller Product Manual, HA463296, Issue 8, available at <https://www.parker.com/content/dam/Parker-com/Literature/SSD-Drives/DC-Drives/HA463296.pdf>. Accessed 5 May 2023
8. Wang, L.: PID Control System Design and Automatic Tuning using MATLAB/Simulink. Wiley-IEEE PRESS 2020
9. Chau, P.C.: Process Control—A First Course with MATLAB. Cambridge University Press, New York (2002)
10. Leonhard, W.: Control of Electrical Drives. Springer, Berlin Heidelberg (1985)
11. Simoreg DC-Master, Microprocessor-Based Converters from 6kW to 2500kW for Variable-Speed DC Drives, Operating Instructions, 2020, available at <https://support.industry.siemens.com/cs/attachments/22220212/C98130-A1256-A002-14-7619.pdf?download=true>. Accessed 5 May 2021
12. Allen-bradley-controllogix-ethernet-manual, available at <https://www.kepware.com/getattachment/c7cd42b2-e3a8-403e-ac5b-ddff9cb03985/allen-bradley-controllogix-ethernet-manual.pdf>. Accessed 5 May 2021
13. Kepserverex manual, available at <https://www.kepware.com/getattachment/2745a0a9-079a-4630-b15c-8081aba1a91d/kepserverex-manual.pdf>. Accessed 5 May 2021
14. Bos, A.V.: Parmaeter Estimation for Scientists and Engineers, First Edition. Wiley, Inc. (2007)
15. Emhemed, A.A.A., Mamat, R.B.: Modelling and simulation for industrial DC motor using intelligent control. *Procedia Eng.* **41**, 420–425 (2012)
16. Milovanović, M., Antić, D., Spasić, M., Nikolić, S.S., Perić, S., Milojković, M.: Improvement of DC motor velocity estimation using a feedforward neural network. *Acta Polytechnica Hungarica* **12**(6), 107–126 (2015)
17. Bencsik, A.L.: Appropriate mathematical model of DC servo motors applied in SCARA robots. *Acta Polytechnica Hungarica* **1**(2), 99–111 (2004)
18. Danković, N., Antić, D., Nikolić, S., Milojković, M., Perić, S.: New class of digital malmquist-type orthogonal filters based on generalized inner product; application to modeling DPCM system. *FACTA UNIVERSITATIS Series: Mechanical Engineering*, vol. 17, no. 3, (2019), pp. 385–396, Print ISSN: 0354–2025, (Doi No: Publisher: University of Niš. December 2019)
19. Dixon, J.: Chapter 12: Three-phase controlled rectifiers, 2020, available at <https://www.coursehero.com/file/10430607/Three-phase-Controlled-Rectifiers/>. Accessed 5 May 2021
20. Marlin, T.E.: Process Control: Designing Processes and Control Systems for Dynamic Performance. McGraw-Hill (2000)
21. Lee, Y., Park, S.: PID controller tuning to obtain desired closed loop responses for cascade control systems. *Ind. Eng. Chem. Res.* **37**, 1859–1865 (1998)

22. Nikolić, S.S., Kocić, B.I., et al.: Torque regulation of the output pulling device of the cable line for insulation. *Proceedings, 20th International Conference on Thermal Science and Engineering of Serbia – SIMTERM*, Niš, Serbia, pp. 558–572 (2022)
23. Nikolić, S.S., Kocić, I.B., Antić, D.S., Mitić, D.B., Danković, N.B., Milovanović, M.B., Djekić, P.S.: Speed and tensile force control of the pulling devices of the continuous line. *Thermal Sci.* **27**, no. xx, (2023), pp. xx–xx. Print ISSN: 0354–9836, Publisher: Vinča Institute of Nuclear Sciences
24. Vilanova, R., Arrieta, O.: Balanced PID tuning application to series cascade control systems. *International Conference on Computers Communications and Control*, Felix-Spa, Romania, 15–17 May, 2008
25. Lieping, Z., Aiqun, Z., Yunsheng, Z.: On remote realtime communication between MATLAB and PLC based on OPC technology. In: *Chinese Control Conference, 2007 CCC 2007*, Hunan, China, 26–31 July 2007, pp. 545–548, New York: IEEE
26. Igor, K., Saša, S.N., Darko, M., Petar, D., Nikola, D., Nebojša, J.: Data collection tool for process identification using plc and kepware tools. *FACTA UNIVERSITATIS Ser. Autom. Control Robot.* **21**(3), 177–186 (2022)
27. Kim, W., Sung, M.: OPC-UA communication framework for PLC-based industrial IoT applications. In: *Proceedings of the Second International Conference on Internet-of-Things design and implementation*, Pittsburgh, PA, 18–21 April 2017, pp. 327–328. New York: IEEE
28. Ziegler, J.G., Nichols, N.B.: Optimum settings for automatic controllers. *Trans. ASME* **64**, 759–768 (1942)
29. Astrom, K.J., Wittenmark, B.: *Adaptive Control*. 2nd Edition. Prentice-Hall (1994)
30. Landau, I.D.: *Adaptive Control – The Model Reference Approach*. Marcel Dekker, New York (1979)
31. Carripiro, A.B.: Tuning of industrial control systems. *Instrum. Soc. America*, 43–44 (1990)

Author Index

MISC

Šarkočević, Živče

A

Adzic, Vuk

Aleksić, Vujadin

Arsić, Aleksandra

Arsić, Dušan

Arsic, Sinisa

B

Balac, Martina

Bisić, Muhamed

Bojović, Božica

Boljanović, Slobodanka

Bulatović, Srđan

D

Dankovic, Nikola

Devic, Andrija

Dihovicni, Djordje

Djekic, Petar

Djurovic, Marko

Djurović, Strahinja

Dragicevic, Aleksandra

Dragicevic, Iva

G

Gajic, Branislav

Golubović, Zoran

Golubović, Zorana

Grbovic, Aleksandar

I

Ilic, Uros

Ivanovic, Ivana B.

Ivanovska, Aleksandra

J

Jakovljević, Petar

Jevtić, Ivana

K

Kirin, Snežana

Kocic, Igor

Korolija, Nenad

Kovačević, Nada Ratković

Kreculj, Dragan

L

Lazarević, Dragan

Lazarevic, Ilija

Lazarević, Mihailo

M

Maksimović, Ana

Maksimović, Ivana Vasović

Maksimović, Katarina

Maksimović, Mirko

Maksimović, Stevan

Mangovska, Biljana

Mekinjić, Boško

Mihic, Marko

Milivojevic, Aleksandar

Milošević, Miloš

Milovanović, Aleksa

Milovanović, Dragan

Milović, Ljubica

Miščević, Milan

Mišić, Milan

Mišković, Žarko

Mitic, Darko

Mitrovic, Aleksandra

Mitrović, Nenad

Mladenović, Goran

N

Nikolić, Ružica

Nikolic, Sasa

P

Pandžić, Adi
Petrov, Ljubiša

R

Radović, Ljubica
Reljić, Mirjana

S

Sarvas, Lajos
Sedmak, Aleksandar
Stamenic, Mirjana
Stefanović, Dragana Vujičić
Stojčetočić, Bojan
Stojmanovski, Viktor

T

Tadić, Srdjan
Tanasić, Nikola
Trajković, Isaak
Travica, Milan

V

Vidaković, Jelena
Vojnović, Goran Ž.

Z

Zahariev, Aleksandar
Zečević, Bojana
Zivković, Nikola
Zlatanović, Ivan